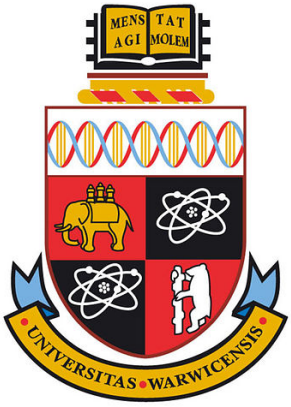

Nano-Probes for Point of Care Diagnostics

By

Alexander Neil Baker

A thesis submitted to The University of Warwick

for the degree of

Doctor of Philosophy

Department of Chemistry

Midlands Integrative Biosciences Training Partnership iCASE

in collaboration with Iceni Diagnostics Ltd.

December 2021

Volume 1 of 2

For all those in the NHS during COVID-19

Especially

Dr O.G. Baker,

Dr T.C. Fernie

&

Dr G.W. Hawker-Bond

And all my colleagues and friends overseas who faced COVID-19 with far less than the United Kingdom.

Contents

Chapters

Chapter 1 – Introduction

Chapter 2 – Lateral Flow Glyco-Assays for the Rapid and Low-Cost Detection of Lectins – Polymeric Linkers and Particle Engineering are Essential for Selectivity and Performance

Chapter 3 – The SARS-COV-2 Spike Protein Binds Sialic Acids, and Enables Rapid Detection in Flow-Through and Lateral Flow Point of Care Diagnostic Devices

Chapter 4 – A Glycan-based Flow-Through Device for the Detection of SARS-COV-2 from Patient Swabs

Chapter 5 – End-Functionalised Poly(Vinyl Pyrrolidone) for Ligand Display in Lateral Flow Device Test Lines

Chapter 6 – The Synthesis of C2 Aminated Monosaccharides with Conserved C2 Hydroxyl Functionality using Mannich Reactions

Chapter 7 – X-ray Photoelectron Spectroscopy for the Elemental Analysis of Glycopolymer-Functionalised Gold Nanoparticles and the Elucidation of Grafting Density

Chapter 8 – Conclusions

Supporting information for each of the chapters can be found in the Appendices (Volume 2)

Contents..... IV

Chapters..... IV

Volume 2 Outline..... XVIII

List of Figures, Tables & Equations XIX

Abbreviations and Acronyms..... XXVII

Acknowledgments..... XXXIII

Declaration XXXVI

Thesis Abstract 1

Chapter 1 3

1.1 Abstract 4

1.2 Declaration 5

1.3 Point of Care 6

1.4 Lateral Flow – an overview 9

1.5 The Components of Lateral Flow 11

1.5.1 The Stationary Phase 11

1.5.2 The Mobile Phase 12

1.5.2.1 Localised Surface Plasmon Resonance (LSPR) 13

1.5.2.2 Gold Nanoparticles 15

1.6 Malaria Rapid Diagnostic Tests – a case study 17

1.6.1 MRDTs in the Field 17

1.6.2 Alternatives to MRDTs and Beyond 19

1.6.3 MRDT Summary 21

1.7 Beyond Antibodies – Glycans as Recognition Units 22

1.7.1 Target and Model Lectins 25

1.7.2 Multivalency and Glyco-Materials 27

1.8 Structural and Synthetic Strategies for Glycan Presentation 28

1.8.1 Non-Polymeric Approaches 28

1.8.1.1 Glycoclusters 28

1.8.1.2 Dendrimers 28

1.8.2 Polymeric Approaches 29

1.8.2.1 Reversible Addition-Fragmentation Chain Transfer (RAFT) 29

1.8.2.2 Linear Polymers 32

1.8.2.3 Pre- versus Post-Polymerisation Functionalisation 33

1.8.2.4 Spherical Polymers.....35
1.8.3 Glycan Presentation Summary.....36
1.9 Glycosylated Gold Nanoparticles.....38
1.10 AuNPs in Sensors and Diagnostics – Aggregation to Lateral Flow Glyco-Assays.....40
1.10.1 Lateral Flow Glyco-Assays.....43
1.11 Conclusions.....46
1.12 References.....48
Chapter 2.....93
2.1 Abstract.....94
2.2 Declaration.....95
2.3 Introduction.....96
2.4 Results and Discussion.....99
2.5. Conclusions.....114
2.6 Experimental.....115
2.6.1 Physical and Analytical Methods.....115
NMR Spectroscopy.....115
Mass Spectrometry.....115
FT-IR Spectroscopy.....115
Size Exclusion Chromatography.....115
X-ray Photoelectron Spectroscopy (XPS).....115
Dynamic Light Scattering.....116
UV-vis Spectroscopy.....116
Transmission Electron Microscopy.....116
Image Collection of Lateral Flow Dipsticks and Devices.....117
2.6.2 Materials.....118
2.6.3 Synthetic Methods.....120

Synthesis of 2-(dodecylthiocarbanothionylthio)-2-methyl propionic acid (DMP) 120

Synthesis of pentafluorophenyl-2-dodecylthiocarbonothioylthio)-2-methylpropanoate (PFP-DMP) 121

Representative Polymerisation of 2-hydroxyethyl acrylamide 122

Representative Poly(N-hydroxyethyl acrylamide) (PHEA40) Glycan Functionalisation 124

Representative Poly(2-hydroxyethyl acrylamide) (PHEA40) PFP Removal with n-pentylamine 124

Synthesis of 1-deoxy-1-amino-galactose 125

Citrate-Stabilised 16 nm Gold Nanoparticle Synthesis 126

Citrate-Stabilised 40 nm Gold Nanoparticle Synthesis 126

Gold Nanoparticle Polymer Coating Functionalisation – 16 nm 126

Gold Nanoparticle Polymer Coating Functionalisation – 40 nm 127

2.6.4 Lateral Flow Strip production, Running and Analysis Protocols 128

Protocol for Manufacturing Lateral Flow Strips 128

Protocol for Test Line Addition to the Lateral Flow Strips 128

Protocol for Running Lateral Flow Test Without Target Analyte in Buffer 128

Protocol for Running Lateral Flow Test with Target Analyte in Buffer 129

Standard Protocol for Lateral Flow Strip Analysis 129

Lateral Flow Signal-to-Noise Analysis 130

Lateral Flow Signal Intensity Analysis 131

Lateral Flow Assay Buffer - 10× HEPES buffer (10% PVP_{400}) in 100 mL H_2O 131

2.6.5 Lateral Flow Complete Device Production, Running and Analysis Protocols 132

Protocol for Manufacturing Lateral Flow Complete Devices/Cassettes 132

Protocol for Conjugate Pad Production....133
10× Conjugate Pad Buffer....133
Protocol for Running Lateral Flow Test Without Target Analyte in Buffer 133
Protocol for Running Lateral Flow Test with Target Analyte in Buffer....133
Lateral Flow Signal Intensity Analysis....134
2.7 References....135
Chapter 3....142
3.1 Abstract....143
3.2 Declaration....144
3.3 Introduction....145
3.4 Results and Discussion....148
3.5 Conclusions....159
3.6.1 Physical and Analytical Methods....161
NMR Spectroscopy....161
Mass spectrometry....161
FT-IR Spectroscopy....161
Size Exclusion Chromatography....161
X-ray Photoelectron Spectroscopy (XPS)....162
Dynamic Light Scattering....162
UV-vis Spectroscopy....162
Transmission Electron Microscopy....163
Biolayer Interferometry (BLI)....163
Protein Modelling....163
^{1}H STD NMR Experiments....163
Protein Thermal Shift Assay....164
3.6.2 Materials....165

3.6.3 Synthetic Methods.....167

Synthesis of 2-(dodecylthiocarbanothionylthio)-2-methyl propionic acid (DMP) 167

Synthesis of Pentafluorophenyl-2-dodecylthiocarbonothioylthio)-2-methylpropanoate (PFP-DMP).....168

Representative Polymerisation of 2-hydroxyethyl acrylamide 169

Representative DP40 Poly(N-hydroxyethyl acrylamide) glycan functionalisation using 2-amino-2-deoxy-N-acetyl-D-neuraminic acid 170

Synthesis of 2-chloro-1,3-dimethylimidazolinium hexafluorophosphate....171

Synthesis of 2-azido-1,3-dimethylimidazolinium hexafluorophosphate (ADMP).....172

Synthesis of 1-Azido-1-deoxy-D-glucose.....173

Synthesis of 1-Amino-1-deoxy-D-glucose 173

Synthesis of O-(N-acetyl-α-neuraminosyl)-(2→3)-O-β-D-galactopyranosyl-(1→4)-1-azido-1-deoxy-glucose. (2,3SL-N_3).....175

Synthesis of O-(N-acetyl-α-neuraminosyl)-(2→3)-O-β-D-galactopyranosyl-(1→4)-1-amino-1-deoxy-glucose. (2,3SL-NH_2).....175

Synthesis of O-(N-acetyl-α-neuraminosyl)-(2→6)-O-β-D-galactopyranosyl-(1→4)-1-azido-1-deoxy-glucose. (2,6 SL-N_3).....178

Synthesis of O-(N-acetyl-α-neuraminosyl)-(2→6)-O-β-D-galactopyranosyl-(1→4)-1-amino-1-deoxy-glucose. (2,6SL-NH_2).....178

N-Acetyl Neuraminic Acid derivative synthesis.....181

Synthesis of Methyl 2,4,7,8,9-penta-O-acetyl-5-(acetamido)-2,3,5-trideoxy-D-glycero-β-D-galacto-non-2-ulopyranosonate (3) 182

Synthesis of Methyl 4,7,8,9-tetra-O-acetyl-2-chloro-5-(acetamido)-2,3,5-trideoxy-D-glycero-β-D-galacto-non-2-ulopyranosonate (4) 184

Synthesis of Methyl 4,7,8,9-tetra-O-acetyl-2-azido-5-(acetamido)-2,3,5-trideoxy-D-glycero-β-D-galacto-non-2-ulopyranosonate (5). 184

Synthesis of 2-azido-5-(acetamido)-3,5-dideoxy-D-glycero-α-D-galacto-non-2-ulopyranosonate (6). α2-azido-2-deoxy-N-acetyl-D-neuraminic acid. 185

Synthesis of α2-Amino-2-deoxy-N-acetyl-D-neuraminic acid (7). 187

Citrate-stabilised 16 nm Gold Nanoparticle Synthesis 190

Citrate-stabilised 35 nm Gold Nanoparticle Synthesis 190

Gold Nanoparticle Polymer Coating Functionalisation – 16 nm 191

Gold Nanoparticle Polymer Coating Functionalisation – 35, 55 and 70 nm 191

BSA/Casein/PVP10 blocking of Nanoparticle surface 191

Expression and purification of SARS-COV-2 Spike S1 in HEK293 Cells .191

Recombinant Expression and Purification of SARS-COV-2 (first 300 amino acids) for Thermal Shift Assay 193

Synthesis of Low Concentration SARS-COV-2 S1-coated Polystyrene Nanoparticle Virus Mimics 194

Synthesis of High Concentration SARS-COV-2 S1-coated Polystyrene Nanoparticle Virus Mimics 194

3.6.4 Flow-Through and Lateral Flow Strip Production, Running and Analysis Protocols.....195

Protocol for manufacturing flow-through and lateral flow strips 195

Protocol for test line addition to the flow-through and lateral flow strips ...195

Protocol for running flow-through and lateral flow tests without target analyte in buffer.....195

Protocol for flow-through and running lateral flow tests with polystyrene nanoparticle virus mimic analyte in buffer 196

Standard protocol for flow-through and lateral flow strip analysis 196

Flow-through and lateral flow signal-to-noise analysis 197

Flow-through and lateral flow signal intensity analysis 198

Silver Staining Procedure.....198

Flow-through and lateral flow assay buffer - 10× HEPES buffer (10% PVP_{400}) in 100 mL H_2O 198
3.6.5 Flow-Thorough Complete Device Production, Running and Analysis Protocols 199
Protocol for manufacturing flow-through complete devices 199
Protocol for Conjugate Pad Production 200
10× Conjugate Pad Buffer 200
Protocol for running flow-through test without target analyte in buffer 201
Flow-through signal-to-noise analysis 202
Flow-through signal intensity analysis 202
3.7 References 203
Chapter 4 212
4.1 Abstract 213
4.2 Declaration 214
4.3 Introduction 215
4.4 Results and Discussion 219
4.5 Conclusions 230
4.6 Experimental 232
4.6.1 Physical and Analytical Methods 232
NMR Spectroscopy 232
Size Exclusion Chromatography 232
X-ray Photoelectron Spectroscopy (XPS) 232
Dynamic Light Scattering 233
UV-vis Spectroscopy 233
Transmission Electron Microscopy 233
Flow-through Cassette Image Collection 233
Protein Thermal Shift Assay 233

4.6.2 Materials....235
Swab Samples....236
4.6.3 Synthetic Methods....237
Polymerisation of 2-hydroxyethyl acrylamide (DP50)....237
DP50 Poly(N-hydroxyethyl acrylamide) glycan functionalisation using 2-amino-2-deoxy-N-acetyl-D-neuraminic acid....239
Citrate-stabilised 35 nm Gold Nanoparticle Synthesis....241
Gold Nanoparticle Polymer Coating Functionalisation....241
Characterisation of 2-Azido-2-deoxy-N-acetyl-D-neuraminic acid....247
Recombinant Expression and Purification of truncated SARS-COV-2 Spike S1 Protein (first 300 amino acids) in E. coli.....249
SARS-COV-2 spike protein variants....251
Expression and purification of SARS-COV-2 Spike S1 in HEK293 Cells.252
4.6.4 Flow-Through Cassette Production, Running and Analysis Protocols...253
Flow-Through Cassette Production, Running and Analysis Protocols....253
Protocol for Manufacturing Flow-Through Cassettes....253
Protocol for Conjugate Pad Production....254
10× Conjugate Pad Buffer....254
Sample Line Addition....255
Protocol for running flow-through tests....255
Silver Staining Procedure....255
Flow-through assay buffer - 10× HEPES buffer (20% PVP_{400}) in 100 mL H_2O....255
Protocol for analysing flow-through tests to determine signal intensity and intensity change....255
4.7 Ethics....257
4.8 References....258

Chapter 5 269
5.1 Abstract 270
5.2 Declaration 271
5.3 Introduction 272
5.4 Results and Discussion 275
5.5 Conclusions 290
5.6 Experimental 291
5.6.1 Physical and Analytical Methods 291
NMR Spectroscopy 291
Mass Spectrometry 291
FT-IR Spectroscopy 291
Size Exclusion Chromatography 291
X-ray Photoelectron Spectroscopy (XPS) 291
Dynamic Light Scattering 292
UV-vis Spectroscopy 292
Transmission Electron Microscopy 292
Image Collection of Lateral Flow Dipsticks and Devices 293
Solvent drying 293
5.6.2 Materials 294
5.6.3 Synthetic Methods 296
Synthesis of 2-(dodecylthiocarbanothionylthio)-2-methyl propionic acid (DMP) 296
Synthesis of pentafluorophenyl-2-(dodecylthiocarbonothioylthio)-2-methylpropanoate (PFP-DMP) 297
Representative Polymerisation of 2-hydroxyethyl acrylamide (PHEA72) 298
Representative Poly(N-hydroxyethyl acrylamide) (PHEA72) Glycan Functionalisation 299

Representative Poly(N-hydroxyethyl acrylamide) (PHEA72) Biotin Functionalisation 300

MADIX Agent Synthesis. 2-(ethoxycarbonothioylthio)-2-methylpropanoic acid N-hydroxsuccinimide ester (MADIX1) 302

Representative Polymerisation of N-vinyl pyrrolidone (PVP80) 304

Representative Poly(N-vinyl pyrrolidone) (PVP80) Glycan Functionalisation 305

Representative Poly(N-vinyl pyrrolidone) (PVP80) Biotin Functionalisation 305

Synthesis of diamine t-BOC 306

Synthesis of biotin diamine t-BOC 307

Synthesis of biotin-NH_2 308

Citrate-Stabilised 16 nm Gold Nanoparticle Synthesis 309

Gold Nanoparticle Polymer Coating Functionalisation – 16 nm 309

Gold Nanoparticle Polymer Coating Functionalisation – 40 nm 309

5.6.4 Lateral Flow Strip Production, Running and Analysis Protocols 310

Protocol for Manufacturing Lateral Flow Strips 310

Protocol for Test Line Addition to the Lateral Flow Strips 310

Protocol for Running Lateral Flow Test Without Target Analyte in Buffer 310

Protocol for Running Lateral Flow Test with Target Analyte in Buffer 311

Standard Protocol for Lateral Flow Strip Analysis 311

Lateral Flow Assay Buffer - 10× HEPES buffer (10% PVP_{400}) in 100 mL H_2O 312

Intensity Calculations 312

Signal-to-Noise Calculations 313

5.7 References 314

Chapter 6 319

6.1 Abstract 320
6.2 Declaration 321
6.3 Introduction 322
6.4 Results and Discussion 326
6.4.1 Synthesis of 2,3,4,6-tetra-O-benzyl mannose 326
6.4.2 Synthesis of N-benzylidone benzamide 329
6.4.3 Mannich reaction 331
6.5 Conclusions 336
6.6 Experimental 337
6.6.1 Physical and Analytical Methods 337
NMR Spectroscopy 337
Mass Spectrometry 337
FT-IR Spectroscopy 337
Solvent drying 337
6.6.2 Materials 338
6.6.3 Synthetic Methods 339
Synthesis of 2,3,4,6-tetra-O-benzyl mannose – Bulman Page method 339
Synthesis of 2,3,4,6-tetra-O-benzyl mannose – Koto method 340
Synthesis of Methyl 2,3,4,6-Tetra-O-Benzyl-Glucopyranoside 342
Synthesis of 2,3,4,6-Tetra-O-Benzyl-Glucose 343
Synthesis of N-trimethylsilylbenzaldimine – method 1 – Bongini 344
Synthesis of N-trimethylsilylbenzaldimine – method 2 – Panunzio[22] 344
Synthesis of N-benzylidone benzamide – method 1 – Bongini-Kupfer 345
Synthesis of N-benzylidone benzamide – method 2 – Colvin-Kupfer 345
Mannich Reaction 346
6.7 References 347

Chapter 7 350
7.1 Abstract 351
7.2 Declaration 352
7.3 Introduction 353
7.3.1 Interfaces, Surfaces and Grafting Density 353
7.3.2 Determining Grafting Density 355
7.3.3 X-ray Photoelectron Spectroscopy 356
7.3.4 X-ray Photoelectron Spectroscopy and Glycopolymer Grafting Density 358
7.4 Results and Discussion 359
7.4.1 Building an XPS Model for Glycosylated Polymeric Gold Nanoparticle Systems 359
7.4.2 Calculating Relative Grafting Density 364
7.4.3 Relative Grafting Density by Spherical Gold Diameter 367
7.4.4 Relative Grafting Density by Polymer 369
7.4.5 Relative Grafting Density by Glycan 371
7.4.6 Relative Grafting Density of Spherical Gold versus Gold Rods 373
7.5 Conclusions 374
7.6 Experimental 375
7.6.1 Physical and Analytical Methods 375
NMR Spectroscopy 375
Mass Spectrometry 375
FT-IR Spectroscopy 375
Size Exclusion Chromatography 375
X-ray Photoelectron Spectroscopy (XPS) 375
Dynamic Light Scattering 376
UV-vis Spectroscopy 376

Transmission Electron Microscopy.....376

Thermogravimetric Analysis.....377

7.6.2 Materials.....378

7.6.3 Synthetic Methods.....379

Synthesis of 2-(dodecylthiocarbanothionylthio)-2-methyl propionic acid (DMP) 379

Synthesis of pentafluorophenyl-2-dodecylthiocarbonothioylthio)-2-methylpropanoate (PFP-DMP).....380

Representative Polymerisation of 2-hydroxyethyl acrylamide (PHEA40) ..381

Representative Poly(N-hydroxyethyl acrylamide) (PHEA40) Glycan Functionalisation 382

Citrate-Stabilised 16 nm Gold Nanoparticle Synthesis.....382

Gold Nanoparticle Polymer Coating Functionalisation – 16 nm 382

7.7 References 383

Chapter 8 389

Volume 2 Outline

Appendix 1 – Supporting Information for Chapter 1 – Introduction

Appendix 2 – Supporting Information for Chapter 2 – Lateral Flow Glyco-Assays for the Rapid and Low-Cost Detection of Lectins – Polymeric Linkers and Particle Engineering are Essential for Selectivity and Performance

Appendix 3 – Supporting Information for Chapter 3 – The SARS-COV-2 Spike Protein Binds Sialic Acids, and Enables Rapid Detection in Flow-Through and Lateral Flow Point of Care Diagnostic Devices

Appendix 4 – Supporting Information for Chapter 4 – A Glycan-based Flow-Through Device for the Detection of SARS-COV-2 from Patient Swabs

Appendix 5 – Supporting Information for Chapter 5 – End-Functionalised Poly(Vinyl Pyrrolidone) for Ligand Display in Lateral Flow Device Test Lines

Appendix 6 – Supporting Information for Chapter 6 – The Synthesis of C2 Aminated Monosaccharides with Conserved C2 Hydroxyl Functionality using Mannich Reactions

Appendix 7 – Supporting Information for Chapter 7 – X-ray Photoelectron Spectroscopy for the Elemental Analysis of Glycopolymer-Functionalised Gold Nanoparticles and the Elucidation of Grafting Density

Appendix 8 – Publications

Volume 2 References

List of Figures, Tables & Equations

Figure 1.1. ASSURED acronym, WHO guidelines for the design of POCT.....7

Figure 1.2. Schematic of a photometric lateral flow device. 10

Figure 1.3. Diagrammatic representation of localised surface plasmon resonance. ..13

Table 1.1. Attenuation coefficients of a selection of nanoparticles and dyes 14

Figure 1.4. Example methods for surface modification of nanoparticles 15

Figure 1.5. *Plasmodium falciparum* Incidence per 1,000 people, 2017[115,116].....17

Figure 1.6. Image of negative and positive MRDT, taken from WHO documents.[127] 18

Figure 1.7. Electron micrograph of goat coronary capillary stained with Alcian blue and diagrammatic representation of the glycocalyx highlighting glycocalyx functions. 24

Figure 1.8. Lectin structures.....26

Figure 1.9. Graphical representation of a selection of glycoconjugates 27

Figure 1.10. Chain Transfer Agents.....30

Figure 1.11. RAFT mechanism.....31

Figure 1.12. Dynamic combinatorial selection of avid lectin binder using poly-aldehydes and acylhydrazide glycans. 33

Figure 1.13. Examples of pre- and post-polymerisation glycan addition approaches34

Figure 1.14. GM1 and synthetic mimics.....36

Figure 1.15. Representation of the three conceptual methods of polymer grafting to surfaces.....38

Figure 1.16. Major nanoparticle design considerations and common lectin analytes for aggregation assays and potential for use in lateral flow assays 40

Figure 1.17. Representative structures of glycosylated AuNPs, and flow-through and lateral flow dipsticks used by the Miura group.....43

Figure 1.18. Representative test lines of flow-through and lateral flow immuno- and glyco-assays 44

Figure 2.1. Synthesis of gold nanoparticle library functionalised with glycan-terminated polymeric tethers at various densities. 101

Table 2.1. Polymers prepared for detecting SBA 102

Figure 2.2. Schematic of dipstick lateral flow assay.....103

Figure 2.3. Optimisation of the gold nanoparticle in dipstick format using SBA as the analyte. 105

Figure 2.4. Lateral flow data from SBA dipstick assays to determine limit of detection. 106

Figure 2.5. Analysed flow-through data from RCA_{120} screen and inset are example dipstick photos. 108

Table 2.2. Additional polymers prepared for detecting RCA_{120} 108

Figure 2.6. Flow-through dipstick assays against RCA_{120}.....110

Figure 2.7. Schematic of complete cassette lateral flow for SBA binding and inlaid images of example cassettes.....112

Figure 2.8. Lateral flow data from SBA cassette assays after 10 minutes to determine limit of detection. 113

Figure E2.1. Lateral flow strip dimensions.....128

Figure E2.2. Representative dipstick (Top), raw grey value plot (Middle) and processed grey value plot (Bottom) 130

Equation E2.1. Equation for determining signal-to-noise ratio 130

Figure E2.3. Lateral flow complete strip dimensions 132

Figure E2.4. Representative cassette (Top left) and strip (Top right), raw grey value plot (Middle) and processed grey value plot (Bottom) 134

Figure 3.1. Sequence alignment of spike protein S1 domains of coronaviruses and a model showing the hypothesised sialic acid binding site for the SARS-COV-2 spike protein trimer.....149

Figure 3.2. Design concept for lateral flow glyco-assay devices.....151

Figure 3.3. Normalised size exclusion chromatography RI molecular weight distributions of telechelic PHEA obtained in DMF versus PMMA standards.....152

Table 3.1. Polymer Characterisation 152

Table 3.2. Nanoparticle Characterisation 153

Figure 3.4. Biolayer interferometry analysis of SARS-COV-2 spike protein with glyconanoparticles 154

Figure 3.5. Flow-through analysis of NeuNAcPHEA$_x$@AuNP$_y$ particles 156

Figure 3.6. Limit of detection of NeuNAc functionalised AuNPs and use in lateral flow and flow-through versus viral mimics 158

Figure E3.1. ^{19}F NMR After (top) and before (bottom) reaction with α2-amino-2-deoxy-*N*-acetyl-D-neuraminic acid functionalisation. 170

Figure E3.2. ^{1}H NMR spectra of GlcNH$_2$. Highlighted areas are the anomeric protons. 174

Figure E3.3. ^{13}C NMR spectra of GlcNH$_2$. Highlighted areas are the anomerics. 174

Figure E3.4. ^{1}H NMR spectrum of *O*-(*N*-acetyl-α-neuraminosyl)-(2→3)-*O*-β-D-galactopyranosyl-(1→4)-1-amino-1-deoxy-glucose. 176

Figure E3.5. ^{13}C NMR spectrum of *O*-(*N*-acetyl-α-neuraminosyl)-(2→3)-*O*-β-D-galactopyranosyl-(1→4)-1-amino-1-deoxy-glucose. 177

Figure E3.6. ^{1}H NMR spectrum of *O*-(*N*-acetyl-α-neuraminosyl)-(2→6)-*O*-β-D-galactopyranosyl-(1→4)-1-amino-1-deoxy-glucose. 180

Figure E3.7. ^{13}C NMR spectrum of *O*-(*N*-acetyl-α-neuraminosyl)-(2→6)-*O*-β-D-galactopyranosyl-(1→4)-1-amino-1-deoxy-glucose. 180

Figure E3.8. α2-Amino-2-deoxy-*N*-acetyl-D-neuraminic acid synthesis 181

Figure E3.9. ^{1}H NMR spectrum of compound 2. 183

Figure E3.10. ^{1}H NMR spectrum of compound 3. 183

Figure E3.11. ^{1}H NMR spectrum of α2-azido-2-deoxy-*N*-acetyl-D-neuraminic acid. 186

Figure E3.12. ^{13}C NMR spectrum of α2-azido-2-deoxy-*N*-acetyl-D-neuraminic acid. 186

Figure E3.13. ^{1}H NMR spectrum of 2-amino-2-deoxy-*N*-acetyl-D-neuraminic acid. 188

Figure E3.14. Zoom in of ^{1}H NMR spectrum (4.15 ppm to 3.15 ppm) of 2-amino-2-deoxy-*N*-acetyl-D-neuraminic acid. 188

Figure E3.15. ^{13}C NMR spectrum of 2-amino-2-deoxy-*N*-acetyl-D-neuraminic acid. 189

Figure E3.16. Gel electrophoresis of expressed spike protein. P1 and P2 were used here. 192

Figure E3.17. Flow-through and lateral flow strip dimensions 195

Figure E3.18. Representative dipstick (Top), raw grey value plot (Middle) and processed grey value plot (Bottom) 197

Equation E3.1. Equation for determining signal-to-noise ratio 197

Figure E3.19. Flow-through complete strip dimensions 199

Figure E3.20. Representative cassette (Top left) and strip (Top right), raw grey value plot (Middle) and processed grey value plot (Bottom) 201

Figure 4.1. Nanoparticle synthesis and flow-through devices. 220

Figure 4.2. Flow though device validation 222

Figure 4.3. Impact of sample volume and stress testing of flow-through devices 224

Figure 4.4. Flow-through device with clinical samples. 226

Figure 4.5. Flow-through (FT) device performance using heat-inactivated primary patient swabs after silver staining step 229

Figure E4.1. ^{1}H NMR spectrum of DP50 PHEA 238

Figure E4.2. Normalised size exclusion chromatography RI molecular weight distribution of telechelic PHEA50 obtained in DMF versus PMMA standards. 238

Figure E4.3. ^{1}H NMR of 2-amino-2-deoxy-*N*-acetyl-D-neuraminic acid functionalised poly(*N*-hydroxyethyl acrylamide)$_{50}$. 240

Figure E4.4. ^{19}F NMR before (Top) and after (Bottom) reaction with α2-amino-2-deoxy-*N*-acetyl-D-neuraminic acid functionalisation. 240

Figure E4.5. Characterisation of unfunctionalised and NeuNAc-functionalised 35 nm AuNPs by A) UV/Vis and B) dynamic light scattering. 242

Table E4.1. Characterisation of unfunctionalised and functionalised AuNPs used in this study. 242

Figure E4.6. TEM images (left) and histograms (right) of citrate stabilised AuNPs. 243

Figure E4.7. X-ray photo-electron spectroscopy (XPS) of citrate stabilised 35 nm AuNP.....244

Figure E4.8. XPS survey scan of neuraminic acid $PHEA_{50}$@$AuNP_{35}$ 245

Figure E4.9. XPS of neuraminic acid $PHEA_{50}$@$AuNP_{35}$ 246

Figure E4.10. ^{1}H NMR of 2-amino-2-deoxy-*N*-acetyl-D-neuraminic acid 247

Figure E4.11. ^{13}C NMR of 2-amino-2-deoxy-*N*-acetyl-D-neuraminic acid 248

Table E4.2. SARS-COV-2 spike protein variants.....251

Figure E4.12. Flow-through complete strip dimensions.....254

Figure E4.13. Representative cassette (Top), raw grey value plot (Middle) and processed grey value plot (Bottom) 256

Figure 5.1. Polymer synthesis. 276

Table 5.1. PVP polymers prepared for the detection of streptavidin.....276

Figure 5.2. Synthesis of biotin-functionalised and galactosamine-functionalised PVP polymers. 277

Figure 5.3. Schematic of dipstick flow-through assay and example dipsticks. 279

Figure 5.4. Analysis of flow-through dipstick assays. 280

Figure 5.5. Synthesis of PHEA polymers and AuNPs. 282

Table 5.2. PHEA polymers prepared for the detection of streptavidin.....282

Figure 5.6. Schematic of dipstick lateral flow assay and example dipsticks. 285

Figure 5.7. Analysis of scanned lateral flow strips using test lines of PVP_{150}-biotin. 286

Figure 5.8. Lateral flow strips and analysis using test lines of PVP_{150}-Gal and PVP_{150} (20 $mg.mL^{-1}$). 289

Figure E5.1. ^{19}F NMR of PHEA72 before (Top) and after (bottom) biotin functionalisation.....301

Figure E5.2. Retrosynthesis of MADIX agent.....303

Figure E5.3. Lateral flow strip dimensions.....310

Figure E5.4. Representative dipstick (Top), raw grey value plot (Middle) and processed grey value plot (Bottom).....312

Figure 6.1. Drugs with Mannich base pharmacophores (highlighted in red).....322

Figure 6.2. Mannich Reaction mechanism.....323

Figure 6.3. Mannose derivatives.....324

Figure 6.4. Scheme presented by Dziedzic *et al.* for the reaction of *N*-benzylidone benzamide with an aldehyde to form an α-hydroxy-β-amino acid[14].....324

Figure 6.5. Proposed Mannich Reaction of mannose derivative adapted from transition state proposed by Córdova group[5].....325

Figure 6.6. Proposed reaction scheme for the synthesis of 2-*C*-phenylmethanamine mannose.....326

Figure 6.7. Reaction schemes for the Koto (A) and Bulman Page (B) approaches for the synthesis of 2,3,4,6-tetra-*O*-benzyl methylmannoside.....327

Figure 6.8. Reaction schemes for Koto (A) and Bulman Page (B) approaches for the synthesis of 2,3,4,6-tetra-*O*-benzyl mannose.....328

Figure 6.9. Reaction schemes for Panunzio (A) and Bongini (B) approaches for the synthesis of *N*-trimethylsilylbenzaldimine.....329

Figure 6.10. Reaction schemes for Bongini-Kupfer (A) and Colvin-Kupfer (B) approaches for the synthesis of *N*-benzylidone benzamide.....330

Figure 6.11. Mannich reaction proline and glycan combinations.....331

Figure 6.12. TLC analysis of Mannich reaction crudes.....331

Figure 6.13. Overlaid representative ^{1}H NMR analysis of Mannich reaction crude products and reagents.....332

Figure 6.14. Observed and anticipated chemical shifts (ppm) for reagents and products in the Mannich reaction.....333

Figure 6.15. Representative 2D NMR analysis of Mannich reaction crude products (2,3,4,6-tetra-*O*-benzyl glucose + L-proline).....334

Equation 7.1. Chemical equilibrium of bound (*ML*) and unbound ligand (*L*) 353

Equation 7.2. Hill-Langmuir Equation.....353

Equation 7.3. Langmuir Adsorption Equation 353

Figure 7.1. Diagrammatic representation of how polymer morphology changes with grafting density on a flat surface. 354

Figure 7.2. Diagrammatic representation of Daoud Cotton Blob model. 355

Equation 7.4. Simplified equation to calculate the binding energy of a photoelectron 356

Equation 7.5. Simplified equation to determine elemental abundance 357

Equation 7.6. Simplified equation to estimate chemical shift as influenced by surrounding charged particles 357

Figure 7.3. C 1*s* character of nanoparticle coatings 360

Figure 7.4. O 1*s* and N 1*s* character of nanoparticle coatings.....360

Figure 7.5. Graphical representation of proposed XPS C 1*s* model with approximate values versus alkane ("A") and approximate signal intensities 361

Figure 7.6. A comparative XPS spectra example of a citrate stabilised AuNP ($AuNP_{16}$, Left column) and a polymer coated AuNP (Galactosamine-$PHEA_{40}$@$AuNP_{16}$, Right column). 362

Figure 7.7. Representative F 1*s* of a fluorinated glycosylated nanoparticle (Gal β1,3 6,6-di-F-GlcNTFAc $PHEA_{45}$@$AuNP_{55}$).....363

Equation 7.7. Equation to calculate relative grafting density from the N 1*s* to Au 4*f* ratio, as determined by XPS.....364

Figure 7.8. Relative grafting density calculated from XPS for synthesised PHEA coated samples on 16 nm gold nanoparticles. 365

Figure 7.9. Thermogravimetric analysis of galactosamine (Gal) functionalised PHEA polymers on 16 nm AuNPs 366

Table 7.1. Equation to calculate relative grafting density from the N 1*s* to Au 4*f* ratio, as determined by XPS 366

Figure 7.10. Relative grafting density calculated from XPS for galactosamine (Gal-2) functionalised PHEA coated samples on varying diameter gold nanoparticles (spheres). 368

Figure 7.11. Relative grafting density calculated from XPS for galactosamine functionalised PHEA (Gal-2-AuNP30) and PHPMA (Gal-2-PHPMA-AuNP30) coated samples on 30 nm gold nanoparticles (spheres). 370

Figure 7.12. Newman projection considering the proposed lowest energy conformer of PHEA (A) and PHPMA (B) polymers.....370

Figure 7.13. Glycans used to functionalise polymer.....371

Figure 7.14. Relative grafting density calculated from XPS for PHEA polymer coated samples on varying diameter gold nanoparticles (spheres) functionalised with various glycans (coding from Figure 7.13).....372

Figure 7.15. Relative grafting density calculated from XPS for PHEA (Glycan-AuNP/AuRod) and PHPMA (Glycan-PHPMA-AuNP/AuRod) coated samples coated on gold spheres (AuNP) and rods (10 nm by 38 nm, AuRod).....373

Abbreviations and Acronyms

A

Abs – absorbance

ACE2 – angiotensin-converting enzyme 2

ACT – artemisinin-based combination therapy

ACVA – 4,4'-azobis(4-cyanovaleric acid)

ADMP – 2-azido-1,3-dimethylimidazolinium hexafluorophosphate

AgNP – silver nanoparticle

Ag stain – silver stain

AMR – antimicrobial resistance

ASSURED – affordable, sensitive, specific, user-friendly, rapid (and robust), equipment-free, delivered (acronym used by WHO guidelines for the design of POCTs)

ATRP – atom-transfer radical-polymerisation

AuNP – gold nanoparticle

B

BE – binding energy

Bn – benzyl

BOC – *tert*-butyloxycarbonyl

BPL – betapropiolactone

BSA – bovine serum albumin

BSA-Gal – Galα1-3Galβ1-4GlcNAc-BSA

C

CBD – carbohydrate-binding domain

CDC – United States Centre for Disease Control and Prevention

$CEID_{50}$ – 50% chicken embryo infectious dose

ConA – concanavalin A

COSY – correlation Spectroscopy

COVAX – COVID-19 vaccines global access

COVID-19 – Coronavirus disease 2019

CPS – counts per second

CRP – controlled radical polymerisation

Cryo-EM – cryogenic electron microscopy

Ct – threshold cycle

CT – computed tomography

CTA – chain transfer agent

CTX – cholera toxin

D

Da – Daltons

DCM – dichloromethane

D_h – hydrodynamic diameters

DLS – dynamic light scattering

DMAP – 4-dimethylaminopyridine

DMF – *N*,*N*-dimethylformamide

DMP – 2-(dodecylthiocarbanothionylthio)-2-methyl propionic acid

DMSO – dimethyl sulphoxide

DNA – deoxyribonucleic acid

DP – degree of polymerisation

DRI – differential refractive index

E

E. coli – *Escherichia coli*

EDCI (EDC) – 1-ethyl-3-(3-dimethylaminopropyl)carbodiimide hydrochloride

EI – electron ionisation

ELISA – enzyme-linked immunosorbent assay

eq. – equivalent

ESCA – electron spectroscopy for chemical analysis

ESI – electrospray ionisation

F

FDA – United States Food and Drug Administration

FGI – functional group interconversion

FP – false positive

FN – false negative

FTIR (FT-IR) – Fourier transform infrared spectroscopy

G

Gal – galactose

Gal-1 – (1-deoxy-1-amino-galactose)

Gal-2 – galactosamine (2-deoxy-2-amino-galactose)

GalNAc – *N*-acetyl galactosamine

GBP – pound Sterling

Glc – glucose

GlcNAc – *N*-acetyl glucosamine

GM1 – a monosialosylganglioside with a high affinity for cholera toxin

G. max – *Glycine max*

H

HCG – human chorionic gonadotrophin

HCP – health care professional

HEA – *N*-hydroxyethyl acrylamide

HEK293 – human embryonic kidney 293

HEPES – 4-(2-hydroxyethyl)-1-piperazineethanesulphonic acid

HIV – human immunodeficiency virus

HMBC – heteronuclear multiple bond correlation

HPMA – *N*-(2-hydroxy propyl)methacrylamide

HRP – histidine-rich protein

HSQC – heteronuclear single quantum coherance

I

IBV-COV – infectious bronchitis virus - coronavirus

IC_{50} – half maximal inhibitory concentration

Iniferter – initiator-transfer-agent-terminator

J-K

K_d – dissociation constant

L

Lac – lactosamine

LAM – less-activated monomer

LAMP – loop-mediated isothermal amplification

LEDC – less economically developed country

LFD – lateral flow diagnostic/device

LFGA – lateral flow glyco-assay

LFIA – lateral flow immunoassay

LoD – limit of detection

LP – lentivirus particle

LRMS – low resolution mass spectra

LS – light scattering

LSP – localised surface plasmon

LSPR – localised surface plasmon resonance

M

MADIX – macromolecular design by interchange of xanthates

MADIX1 – *N*-succinimide 2-(ethyl xanthate)-2-methylpropanoate

MDMA – 3,4-methylenedioxymethamphetamine

MEDC – more economically developed country

MERS – middle east respiratory syndrome

M_n – number average molecular weight

MRDT – malaria rapid diagnostic test

MRI – magnetic resonance imaging

MRSA – methicillin-resistant *Staphylococcus aureus*

M/S – mass spectrometry

$M_{W\ -}$ weight average molecular weight

MW – molecular weight

m/z – mass-to-charge ratio

N

NeuNAc (Neu5NAc) – α,*N*-acetyl neuraminic acid (2-amino-2-deoxy-*N*-acetyl-D-neuraminic acid)

NeuNAc-BSA – α,*N*-acetyl neuraminic acid functionalised BSA

NHS – National Health Service or *N*-hydroxysuccinimide

NIPAM – *N*-isopropyl acrylamide

NMR – nuclear magnetic resonance

NMP – nitroxide-mediated polymerisation

NPV – negative predicative value

NVP – *N*-vinyl pyrrolidone

O

OD – optical density at UV_{max}

ORN178 – *E. coli* bacterial strain with fimbriae I expression

P

PANGO – phylogenetic assignment of named global outbreak

PCR – polymerase chain reaction

PDB – protein data bank

PEG – poly(ethylene glycol)

PET – petroleum ether

P. falciparum – Plasmodium falciparum

PFP – pentafluorophenol

PFP-DMP – pentafluorophenyl-2-(dodecylthiocarbonothioylthio)-2-methylpropanoate

PFU – plaque-forming unit

PHEA – poly(hydroxyethyl acrylamide)

Photo-CRP – photocontrolled radical polymerisation

PHPMA – poly(*N*-(2-Hydroxy propyl)methacrylamide)

P. knowlesi – Plasmodium knowlesi

pLDH – *Plasmodium* lactate dehydrogenase

P. malariae – Plasmodium malariae

PMMA – poly(methyl methacrylate)

PNA – peanut agglutinin

pNIPAM – poly(*N*-isopropylacrylamide)

POC – point of care

POCT – point of care test/testing

P. ovale – Plasmodium ovale

PPV – positive predictive value

PSA – prostate specific antigen

PS-NP – polystyrene nanoparticle

PVP – poly(vinyl pyrrolidone)

PVP40 – $poly(vinyl\ pyrrolidone)_{400}$ (Average Mw ~40,000)

P. vivax – Plasmodium vivax

Q-R

RAFT – reversible addition-fragmentation chain transfer

RCA_{120} (RCAI, RCA120) *Ricinus communis* agglutinin I

RCA_{60} (RCAII) *Ricinus communis* agglutinin II

R. communis – Ricinus communis

RI – refractive index

RNA – ribonucleic acid

ROMP – ring-opening metathesis polymerisation

rRT-PCR – real-time reverse transcription-polymerase chain reaction

RTP – room temperature and pressure

RT-PCR – reverse transcription-polymerase chain reaction

R_0 – reproduction value

S

SARS – severe acute respiratory syndrome

SARS-COV-1 (SC1) – severe acute respiratory syndrome coronavirus 1

SARS-COV-2 (SC2) – severe acute respiratory syndrome coronavirus 2

SAXS – small angle x-ray scattering

SBA – soybean agglutinin

S.D – standard deviation

SEC – size exclusion chromatography

S. epidermidis – Staphylococcus epidermidis

SERS – surface-enhanced Raman scattering

SL – sialyllactose

2,3-SL – 2,3'-sialyllactose

2,6-SL – 2,6'-sialyllactose

2,3SL-BSA – 2,3'-sialyllactose-functionalised BSA

2,6SL-BSA – 2,6'-sialyllactose-functionalised BSA

SPR – surface plasmon resonance

STD NMR – saturation transfer difference nuclear magnetic resonance

STX – Shiga toxin

T

TEA – triethylamine

TEC – total expected costs

TEM – transmission electron microscopy

TFA – trifluoroacetic acid

TGA – thermogravimetric analysis

Theo – theoretical

THF – tetrahydrofuran

TLC – thin layer chromatography

TMS – tetramethylsilane

TN – true negative

TP – true positive

TU – transduction unit

U

UEA – *Ulex Europaeus* Agglutinin I

UHCW – University Hospitals Coventry & Warwickshire

UK – United Kingdom

UNICEF – United Nations Children's Fund

USA ("US") – United States of America

USD – United States dollar

UV – ultraviolet

UV_{max} – ultraviolet value at maximum absorbance

UV-vis (UV/vis) – ultraviolet-visible spectroscopy

V

VAc – vinyl acetate

V. cholerae – Vibrio cholerae

$\nu_{incidence}$ – incident wavelength

VS – viscometry

$\nu_{scattered}$ – scattered wavelength

W

WGA – wheat germ agglutinin

WHO – World Health Organisation

wt/v – weight per unit volume

X-Z

XPS – x-ray photoelectron spectroscopy

Symbols

$Đ_M$ – dispersity (M_w/M_n)

ε – molar attenuation (extinction) coefficients

λ_{max} – maximum wavelength

λ_{spr} (A_{spr}) – wavelength/absorbance of surface plasmon resonance

λ_{450} (A_{450}) – wavelength/absorbance at 450 nm

+Ve – positive

-Ve – negative

Acknowledgments

This thesis is a culmination of the enormous collaborative, and interdisciplinary, efforts of so many excellent scientists, across industry, healthcare, and academia. Without their efforts, this thesis would not exist. Thank you to all our collaborators.

A huge and special thank you to Prof. Matthew Gibson for his unwavering enthusiasm and support. Without Matt's *bon ami* attitude, this work would not exist. I also don't think many people have supervisors as willing as Matt to let their students do as much around their work as Matt has encouraged me to do.

Another huge and special thank you goes to my industry supervisor Dr Simone Dedola. It was always a pleasure to share ideas and understand the industry perspective on the work. Furthermore, thank you for being so welcoming whenever I visited. Thank you to my industry collaborators at Iceni Diagnostics (especially Tanya, Stephan, Giulia, and Simona) and Prof. Rob Field too.

Thank you to all the Gibson group members (both past and present), I could not have hoped to join a more friendly and supportive group. Thank you to Dr Sarah-Jane Richards for teaching, supporting, and advising me across a variety of projects and publications – without your tireless efforts none of the Covid work would have been possible or as enjoyable to do. Thank you to Dr Collette Guy, Dr Ben Graham, Dr Antonio Laezza and Melissa Ligorio for providing organic advice whenever I needed it. Thank you to Dr Tom Congdon, Dr Chris Stubbs and Panos Georgiou for providing polymer advice whenever I needed it. Also thank you to Tom for helping build huge props for Christmas lectures too. Thank you to Dr Caroline Biggs, Dr Kathryn Murray, Dr Tom Whale and Dr Marta Neves for all your support and being there to listen to me rant. Thank you to Dr Ben Graham, Dr Chris Stubbs and Dr Alice Fayter for giving me sound advice and being a riot to work with too. Thank you to Dr Muhammad Hasan and Ashfaq Ahmad for all your biological work, knowledge, and support. Thank you also to Dr Ruben Tomas, Ioanna, Toru, Doug, Huba, Julian, Neer and all the rest of the group for your support and friendship. A special thank you to Angela Hurst for admin support and making sure all the conferences and events were booked and organised.

A huge thank you to Dr Marc Walker for his unfailing humour, patience, and advice throughout the project. He is the sole reason I have a vague understanding of XPS and without him whole sections of this thesis would not exist.

Thank you to Dr Francisco “Paco” Fernandez-Trillo (and group) for allowing me to visit your lab as part of MIBTP. Thank you, Paco, for teaching me the importance of good experiment design and the need for robust controls. Every so often I hear Paco’s voice finding holes in my experiment design – it pushes me to be a better scientist.

Thank you to Midlands Integrative Biosciences Training Partnership and the BBRSC for funding and support. Thank you to its leadership team and administrative staff, especially Prof. Vardis Ntoukakis, Kerry Davies and Prof. Chris Thomas.

Thank you to the Department of Chemistry and the School of Life Sciences who, after four years of an MChem, decided I could stay for another four to do a PhD. Thank you to Dr Manuela Tosin and Prof. Tim Bugg for being such an excellent advisory panel and driving me to always do better science, also Manuela for introducing me to glycobiology and Tim for being my personal tutor for four years. Thank you to Dr Russ Kitson and Dr Stephen Bromfield for supporting my teaching activities and providing advice. Thank you to Dr Bo Kelestyn, Dr Zoë Ayres and others for your efforts in pushing for greater equality, the book club has been a pleasure to write for: I thank the writing team also (Dr Kat Murray, Maria Kariuki, Louis Ammon and Ally McLoughlin). Thank you to the teams that run the fantastic equipment in both Chemistry and Physics at Warwick, and for keeping much of it running for the Gibson group during the pandemic. Thank you to Dr Ivan Prokes and Rob Perry for NMR; Dr Lijiang Song and Lynette Walsh for mass spectrometry; Dr Dan Lester, Dr Rachel Hand and Dr James Town for SEC. Thank you also to the fantastic stores team, finance team and technicians in Chemistry; you guys have kept me safe, helped make and store (thanks Sam Martin!) props for public engagement, repaired stuff I broke and kept the group going in the pandemic – I am forever indebted to you all, you make this department work.

Beyond Chemistry, thank you to those who supported me and my work in the wider University and on committees, especially Prof. Olanrewaju Sorinola, Prof. Peter Scott, Prof. Caroline Meyer, Prof. Ian Tuersley, Prof. Jacqueline Hodgson, Prof. Michael Ward, Carole Harris and Louise Hasler. Thank you to Warwick UCU, we can be proud

of our work across this University. Thank you to colleagues in the SU, especially Ashley Storer-Smith for their work in supporting the faculty reps.

A special thank you to Prof. Gwen van der Velden for her tireless support and advice. Thank you for letting me be a part of WIHEA and its amazing work. Thanks also to Prof. Andy Clark, Dr David Fox, Prof. Dr. Ir. Stefan Bon, Prof. Dave Haddleton, Dr Andy Marsh, Dr Guy Clarkson and Dr Nicola Rogers for their advice and support, both chemical and beyond, over the years. Thank you to Prof. Michael Scott and WIE for their support and advice too. A special thank you to Dr Leanne Williams for mentoring me for my FHEA and helping me think more deeply about pedagogy.

A thank you to all my teachers over the years at WHSB and beyond, especially; Dr Prendergast and Dr Livingston, Mr Wringe, Mrs Skinner, Mr Despres, Mr Hill, Mr Stevens, Mr Senior, Mr Hudson, Mr Brown, Mr Baker, Mrs Wall, Mr Windley, Mr Kersey, Mr Burney and Mr Podbury. As well as colleagues at SIA, Nepal.

Thank you to my family and friends for their ongoing support. Thank you, Mum and Dad, for encouraging my love of Science. Thank you, to my grandparents who often ended up as a taxi service (thank you Grandad Fernie and “Silly” Grandad), or as a stop-over on my way home from school (Nanny and Lee). It is also worth noting that Grandad Fernie will soon have only doctors as direct descendants, not bad going! Thank you to my sister, Dr Olivia Baker (and Mum, Dr Tracy Fernie) for keeping me grounded and aware of the medical perspective. Our constant competition to be the best child and help the most people keeps me going some days. Thank you to wise friends, such as the Greens and Allens, for excellent advice over the years.

A huge and special thank you to my best friend and brother, Dr George Hawker-Bond. You may be exceptionally irritating sometimes, but your support and kindness kept me going during the COVID-19 pandemic and is a big reason why this thesis exists. Thank you also for proof-reading most of my publications and chapters. Thanks to the cat (Munro) also, we had some hairy moments when you sat on my keyboard, but your clock-work desire for food meant I stopped working in the evening.

Finally, thank you to all the students who listened to me drone on while teaching, or doing outreach and public engagement activities. If even one of you makes the world a better place, I have succeeded in some small way.

AB

Declaration

This thesis is submitted to the University of Warwick in support of my application for the degree of Doctor of Philosophy. It has been composed by myself and has not been submitted in any previous application for any degree.

A detailed declaration is provided at the start of each chapter outlining the work carried out by collaborators.

The following chapters have been published or submitted for publication;

Chapter 1 is in preparation for publication as;

A. N. Baker, G. W. Hawker-Bond, P. G. Georgiou, M. I. Gibson, Glycosylated Gold Nanoparticles for Point of Care Diagnostics: from aggregation to Lateral Flow Assays – Manuscript in preparation

Chapter 2 is published as;

A. N. Baker, A. R. Muguruza, S-J. Richards, P. G. Georgiou, S. Goetz, M. Walker, S. Dedola, R. A. Field, M. I. Gibson, *Adv. Healthcare Mater.,* 2021, 2101784.[1]

Chapter 3 is published as;

A. N. Baker, S-J. Richards, C. S. Guy, T. R. Congdon, M. Hasan, A. J. Zwetsloot, A. Gallo, J. R. Lewandowski, P. J. Stansfeld, A. Straube, M. Walker, S. Chessa, G. Pergolizzi, S. Dedola, R. A. Field, M. I. Gibson, *ACS Cent. Sci.,* 2020, *6*, 2046.[2]

A. N. Baker, S-J. Richards, C. S. Guy, T. R. Congdon, M. Hasan, A. J. Zwetsloot, A. Straube, M. Walker, S. Chessa, G. Pergolizzi, S. Dedola, R. A. Field, M. I. Gibson, *Chemrxiv,* 2020*, https://doi.org/10.26434/chemrxiv.12465680.v1*[3]

Chapter 4 is published as;

A. N. Baker, S-J. Richards, S. Pandey, C. S. Guy, A. Ahmad, M. Hasan, C. I. Biggs, P. G. Georgiou, A. J. Zwetsloot, A. Straube, S. Dedola, R. A. Field, N. R. Anderson, M. Walker, D. Grammatopoulos, M. I. Gibson, *ACS Sensors,* 2021, *6*, 10, 3696-3705.[4]

Chapter 5 is published as;

A. N. Baker, T. R. Congdon, S-J. Richards, P. G. Georgiou, M. Walker, S. Dedola, R. A. Field, M. I. Gibson, *ACS Polym. Au,* 2021*, https://doi.org/10.1021/acspolymersau.1c00032*[5]

Chapter 6 is entirely my own work and has not been published.

Chapter 7 contains published work from;

P. G. Georgiou, **A. N. Baker**, S-J. Richards, A. Laezza, M. Walker, M. I. Gibson, Journal of Materials Chemistry B., 2020, *8*, 136-145.[6]

S-J. Richards, **A. N. Baker**, M. Walker, M. I. Gibson, Biomacromolecules, 2020, *21*, 4, 1604-1612.[7]

A. N. Baker, S-J. Richards, C. S. Guy, T. R. Congdon, M. Hasan, A. J. Zwetsloot, A. Gallo, J. R. Lewandowski, P. J. Stansfeld, A. Straube, M. Walker, S. Chessa, G. Pergolizzi, S. Dedola, R. A. Field, M. I. Gibson, *ACS Cent. Sci.,* 2020, *6*, 2046.[2]

A. N. Baker, S-J. Richards, C. S. Guy, T. R. Congdon, M. Hasan, A. J. Zwetsloot, A. Straube, M. Walker, S. Chessa, G. Pergolizzi, S. Dedola, R. A. Field, M. I. Gibson, *Chemrxiv,* 2020*, https://doi.org/10.26434/chemrxiv.12465680.v1*[3]

S-J. Richards, M. I. Gibson, M. A. Fasciae, B. Linclau, M. C. Galan, **A. N. Baker**, H. Ledru, C. S. Webster, C. E. Council, M. Walker, H. Chidwick, D. E. Wheatley, J-B. Vendeville, T. Keenan, D. Budhadev, Chemical Science, 2020, *12*, 905-910. [8]

A. Pancaro, M. Szymonik, P. G. Georgiou, **A. N. Baker**, M. Walker, P. Adriaensens, J. Hendrix, M. I. Gibson, I. Nelissen, Nanoscale, 202, *13* (24), 10837-10848.[9]

P. G. Georgiou, C. S. Guy, M. Hasan, A. Ahmad, S-J. Richards, **A. N. Baker**, N. V. Thakkar, M. Walker, S. Pandey, N. R. Anderson, D. Grammatopoulos, M. I. Gibson, *Plasmonic Detection of SARS-COV-2 with Polymer-Stabilised Glycosylated Gold Nanorods* – Manuscript accepted

A. N. Baker, A. R. Muguruza, S-J. Richards, P. G. Georgiou, S. Goetz, M. Walker, S. Dedola, R. A. Field, M. I. Gibson, *Adv. Healthcare Mater.,* 2021, 2101784.[1]

Thesis Abstract

The COVID-19 pandemic has exposed deep health inequalities between more economically developed and less economically developed countries: both in terms of diagnostics and vaccinations. Robust and low-cost point of care devices are needed to ease these diagnostic inequalities. Current point of care lateral flow immunoassays, utilise proteins, such as antibodies, to sense for analytes. This is epitomised by the malaria rapid diagnostic test and archetypal home pregnancy test. Glycans are emerging as alternative detection units due to their fundamental role in biological signalling and recognition events. Furthermore, the increased robustness, low-cost and synthetic possibilities offered by glycan-based systems, especially glycosylated polymers, make them a promising alternative to antibody-based biosensing and diagnostic systems.

Chapter 1 discusses the current use of protein-based lateral flow and flow-through devices; their advantages and disadvantages versus non-point of care techniques, and the potential of glycan-based lateral flow devices. The concepts introduced in Chapter 1 are then applied in Chapters 2 through 5. **Chapter 2** demonstrates the use of glycosylated polymer-coated nanoparticles, produced by controlled radical polymerisation techniques for the sensitive, label-free detection of lectins in lateral flow and flow-through. The systems produced use only glycans, not antibodies, to provide recognition – a "lateral flow glyco-assay." The lessons learned in Chapter 2 are applied in **Chapter 3** to probe the glycan-binding of the SARS-COV-2 spike protein in a "flow-through glyco-assay" and target a pseudovirus mimic of the target coronavirus in a lateral flow glyco-assay. **Chapter 4** builds on Chapters 2 and 3, applying the fledgling glyco-assay technology to the "real-world" by sensing for the SARS-COV-2 virus in patient samples, alongside exploring the robustness of the devices themselves. Having explored the concept of glycosylated polymer-coated nanoparticles in lateral flow and flow-through setups; **Chapter 5** changes focus and explores the use of polymeric anchors for the design of all-polymer ("vegan") lateral flow and flow-through devices. This work completely removes proteins as either detecting units or anchors from lateral flow for the first time.

Chapters 6 and 7 explore more fundamental Chemistry than the previous chapters. **Chapter 6** considers the use of the Mannich reaction to produce monosaccharides with amine functionality at C2, ideal for polymer conjugation, while maintaining hydroxyl functionality at C2. Although unsuccessful with the reagents used, the chapter highlights a potential avenue of future chemical exploration in novel glycan synthesis. **Chapter 7** pulls together the x-ray photoelectron analysis data and spectra collected across a range of studies, including data collected in previous chapters, and considers if x-ray photoelectron spectroscopy can be used to determine relative grafting density in glycosylated polymer-coated nanoparticle systems.

In summary, the key components of the emerging technology of lateral flow glyco-assays are introduced, interrogated and investigated. The prototype devices tested against model proteins, viral proteins and patient samples, are found to show specificities and sensitivities that rival lateral flow immunoassay systems. The understanding developed in this thesis could pave the way to the first generation of lateral flow glyco-assays that are low-cost, stable in a wide range of conditions, and able to target a wide range of analytes and diseases.

Chapter 1

Introduction

1.1 Abstract

Current point of care lateral flow immunoassays, such as the “pregnancy test”, rely on proteins as detection units (e.g., antibodies) to sense for analytes. Glycans are emerging as alternative detection units, due to their fundamental role in biological signalling and recognition events – hence they are promising alternatives to antibody-based biosensing and diagnostics. In this Introduction the potential of glycans coupled to gold nanoparticles as sensory systems in aggregation assays is reviewed, leading to discussion of how they can be deployed in lateral flow diagnostics. The concept of lateral flow, including specific examples of lateral flow use in the field compared to other diagnostic tools are introduced. Followed by a discussion of glycosylated materials and the affinity gains through the cluster glycoside effect. Finally, the potential role of glycans in lateral flow, including emerging examples and their use are shown.

1.2 Declaration

This Chapter contains a draft review paper discussing the potential use of glycosylated gold nanoparticle systems in lateral flow assays.

George Hawker-Bond assisted in carrying out a literature database search, article screening and drafting the sections around point of care testing in the NHS and similar health services. The search criteria used can be found in Appendix 1.

I led the literature search and drafting of the manuscript.

Myself, George Hawker-Bond, Panagiotis Georgiou and Matthew Gibson were responsible for preparation of the manuscript.

A. N. Baker, G. W. Hawker-Bond, P. G. Georgiou, M. I. Gibson, Glycosylated Gold Nanoparticles for Point of Care Diagnostics: from aggregation to Lateral Flow Assays – Manuscript in preparation

1.3 Point of Care

The diagnosis of infectious diseases should be achieved by; determining infection sites, considering patient needs and gaining a microbiological diagnosis. In many cases, however, diagnosis is guided by symptomatic presentation rather than rational or empirical therapeutic approaches; many methods can take hours or days to produce a result. Observational approaches alone often lead to poor patient outcomes and the injudicious prescribing of broad-spectrum drugs which can contribute to antimicrobial resistance (AMR).[10]

The first point of care (POC) diagnostic was developed in 1962 to measure blood glucose levels.[11] This was followed by the patenting of a rapid pregnancy test circa 1969, by Margaret M. Crane.[12,13] Both of these diagnostics revolutionised care: allowing for testing and diagnosis by or with the patient present, in the case of testing for pregnancy it replaced the *Xenopus laevis* frog (African clawed frog) pregnancy test.[14,15] In 2011, point of care tests (POCT), or "bedside testing", devices were worth $15 billion USD with a projected increase of 4% per annum.[16]

While there is no accepted definition for point of care testing, it can be considered to be rapid testing at, or near to, the point of need that is used to make a medical decision.[17–20] Current POCT devices include the aforementioned glucose biosensor, dipsticks and lateral flow-based devices;[21] such as Malaria Rapid Diagnostic Tests (MRDTs)[22] and pregnancy tests,[23] that separate samples through a solid phase.[16]

Surveys of medical professionals, in relation to POCT, have indicated that sensitivity (> 90%) is considered the most important attribute, followed by a price of less than $20 USD and a short detection time.[24] This is summarised by the World Health Organisation (WHO) guidelines for the design of POCT in the ASSURED acronym (Figure 1.1).[25,26]

Affordable – for those at risk of infection

Sensitive – minimal false negatives

Specific – minimal false positives

User-friendly – minimal steps to carry out

Rapid and robust – short turnaround and easy to store

Equipment-free – no complex equipment

Delivered – to end user

Figure 1.1. ASSURED acronym, WHO guidelines for the design of POCT

The cost-effectiveness of POCT compared to traditional laboratory techniques has been demonstrated in the UK National Health Service (NHS) Health Checks, an early detection tool for cardiovascular disease;[27] a disease which costs the NHS approximately £7 billion GBP per year.[28] The total expected costs (TEC) per completed Health Check was markedly reduced for POCT compared to laboratory techniques – £18 GBP per completed Health Check compared to £25 GBP, respectively, and attendance rates were higher for POCT.[27]

It is equally important to consider the perspectives of patients and health care professionals (HCPs) to POCT. During an increase of Dengue fever cases in Singapore, POCT was found to be more convenient, and marginally better than non-POCT in improving the speed and accuracy of diagnoses.[29]

The alternative to POC testing is laboratory-based testing, however these testing systems require highly trained staff, embedded health infrastructures and specialised facilities. This makes lab-based methods, considered standard in economically wealthier nations, cost-prohibitive in low- and middle-income countries. This is evidenced by the COVID-19 (caused by SARS-COV-2) pandemic.[30] PCR was the primary tool for diagnosis in the initial stages of the COVID-19 pandemic but did not allow for mass testing due to price and the need for centralised infrastructure.[31,32] Furthermore, it is estimated that laboratory-independent POCT for four common infections (syphilis, malaria, tuberculosis and bacterial pneumonia) could prevent more than 1.2 million deaths per annum in low- and middle-income countries.[13] Therefore, chromatographic lateral flow paper-based immunoassays, as highlighted by MRDTs and pregnancy tests, are of particular interest as POCT because of their

low cost, speed of use, laboratory-independence and wide range of devices and analytes currently in use.[33,34]

This chapter will first summarise the chemical basis of the POC lateral flow immunoassay (LFIA) diagnostic, based upon antibodies, as the current standard. It will then explore how glycans, and glyco-materials in particular, may present unique opportunities and advantages. Focus will be paid to glycosylated gold nanoparticles which are the most common, and versatile platform. These have been widely used in aggregation (colourimetric solution diagnostics) assays and are therefore ready to be translated into paper-based lateral flow glyco-assays (LFGA).

1.4 Lateral Flow – an overview

Lateral flow (immuno) assays (LFIA), "sol particle immunoassays" as they were originally termed by Leuvering *et al.*,[35] or more broadly lateral flow devices (LFDs) have been performed on a wide variety of biological targets. These include; complement in plasma;[36] anabolic steroids;[37] prostate-specific antigen,[38] leprosy[39] and meningitis[40] in serum (also identifiable in saliva[41]); evidence of kidney injury in urine;[42] *V. cholerae* in faeces;[43] and other marker proteins[44,45] or pathogens[46] in whole blood samples.[47] This ability to target a broad range of analytes has led to the use of lateral flow devices outside of Medicine. Notably, in policing illicit drug use,[48,49] such as MDMA and other drugs in sweat[50,51] and saliva.[52]

Generic lateral flow devices contain two components; a mobile phase and a stationary phase, these components "sandwich" the analyte and produce a coloured line on the surface if the target analyte is present. When a sample is applied to the strip's sample pad, it passes through the sample pad, drawn by capillary forces caused by the wick (Figure 1.2A, a). Then the sample passes through the conjugate pad. If the sample contains the target analyte it will bind specific antibody-coated gold nanoparticles (or other coloured nanomaterials) within the conjugate pad (Figure 1.2A, b). The sample and nanoparticles (both bound and unbound) pass into the nitrocellulose membrane where they move through two lines of deposited material. One of these lines is a control line that contains antibodies specific for the primary antibody (acting as an antigen for the control line antibody) in the conjugate pad (Figure 1.2A, d). Binding of the nanoparticles to the control line only, indicates a successful test but a negative sample (Figure 1.2B, e). The test line contains antibodies specific for the analyte. If the analyte is "sandwiched" between antibodies immobilised as the test line and antibodies immobilised on the nanoparticles, a line will form (Figure 1.2A, c). A successful and positive test requires both the control and test lines to bind their respective targets. Some researchers have utilised multiple test lines in "multiplexed" lateral flow tests.[53] This multiplexed approach allows for greater efficiency, diagnostic precision and reduces overall cost when tests are combined into one device. An earlier form of the lateral flow test, called a flow-through assay, utilises immobilised sample as a test line – these devices are often less sensitive than lateral flow devices but are

employed when lateral flow is not possible for economic or chemical reasons, or during the prototyping and development stages of LFD design.[16,54]

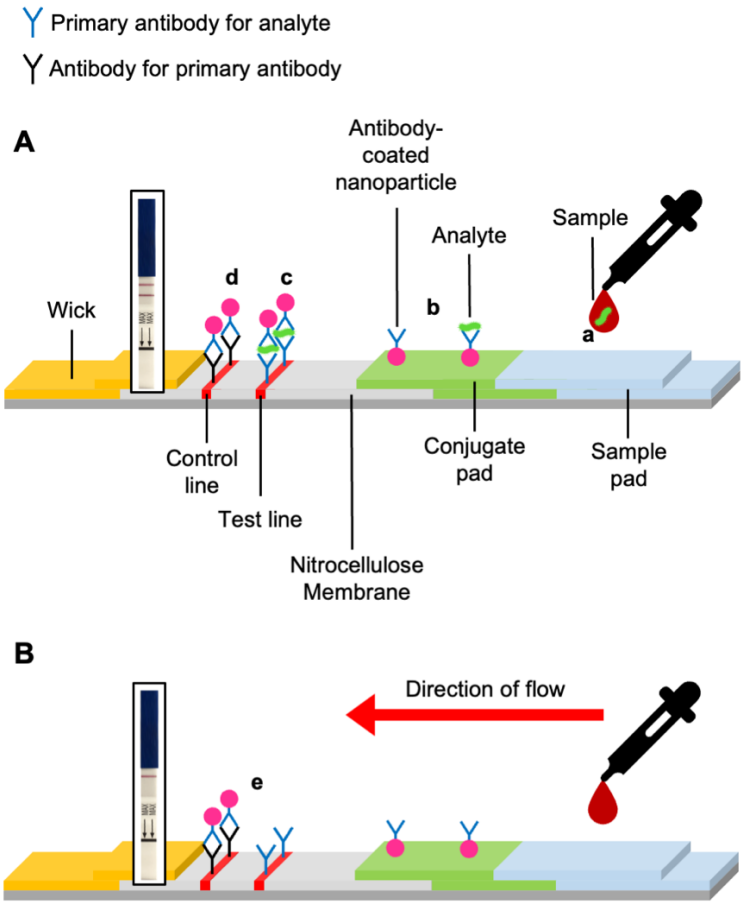

Figure 1.2. Schematic of a photometric lateral flow device.

A) Device constituents in a successful positive test and B) a successful negative test. Generic pregnancy tests for HCG detection inset.

1.5 The Components of Lateral Flow

1.5.1 The Stationary Phase

The stationary (immobile) phase comprises a receptor bound to the surface – in LFIAs this is an antibody. Larger antibodies do not require an immobilisation agent, with Immunoglobulin G isotypes having an absorption of > 100 $\mu g.cm^{-2}$ on nitrocellulose, however protein absorption can decrease with decreasing molecular weight.[55,56] Bovine serum albumin (BSA), or less commonly ovalbumin, are used as carriers/immobilisation agents for small molecules such as nucleotides and small proteins (discussed further in Chapter 5).[33,34] Work by Holstein *et al.* developed less common immobilisation approaches such as covalent epoxide-thiol attachment and "genetic fusion" to custom-designed proteins.[57]

The low absorption of unconjugated antibodies was noted in polymeric systems by Aoyama *et al.*.[58] To overcome this they produced high surface area microcone architectures on polycarbonate sheets. The increased surface area enabled high antibody immobilisation levels. This step was in part inspired by the use of plastic and paper microfluidic systems,[59] a rapidly growing technique that has been used to sense; Ebola virus RNA,[60] *Salmonella typhimurium*[61] and glucose;[62] amongst other biologics.[63,64]

Hiratsuka *et al.* have built on the work of Storhoff *et al.* by using nucleotide-functionalised systems to create a streptavidin immobilising system for polynucleotides.[65,66] Studies with cellulose paper have also exploited biotin and the ability to covalently modify the cellulose surface for easy test line immobilisation.[67,68] It is notable that covalent modification of nitrocellulose has also been carried out.[69] While Tanaka *et al.* and Nagatani *et al.* have utilised the localised surface plasmon resonance (LSPR) phenomenon of gold nanoparticles in the stationary phase to enhance the signal-to-noise ratio when sensing for human chorionic gonadotrophin (HCG) and prostate-specific antigen respectively.[38,70] In these systems, a low concentration of functionalised nanoparticles are placed in the stationary phase to interact with the nanoparticles in the mobile phase, this approach allowed for lower detection limits of 1 $pg.mL^{-1}$ of HCG,[70] the hormone detected in the common pregnancy test, compared to a commercial pregnancy test (~0.7 - 0.07 $nmol.mL^{-1}$).[71]

Others have utilised "proteinticles" (protein-coated nanoparticles) in the stationary phase of reverse lateral flow immunoassays to sense for human antibodies to HIV and hepatitis A and B in the mobile phase.[72] While reverse immunoassays, such as the Epstein-Barr Virus Antibody Test (although not POC) provide precedence for reverse immunoassay approaches;[73] reverse lateral flow immunoassay approaches are not without criticism. During the early stages of the COVID-19 pandemic (2019-20), LFIA tests sensing for an adaptive immune response in patients previously infected with SARS-COV-2 proved controversial.[31,74,75] This was due to a variety of factors including; questions around the ability of tests to differentiate SARS-COV-2 antibodies from other coronaviruses components,[76] the societal risk of false positives and so-called "immunity passports",[77] the time for immunity to develop[78] and data suggesting low immune responses in some patients.[79,80] This led to WHO publishing a scientific briefing, on the 24th of April 2020, discouraging the use of antibody targeting tests for SARS-COV-2[81] and as of the 2nd of November 2020 no CDC or FDA approved antibody tests exist.[82]

Chapter 5 will discuss the development of polymeric anchor systems for immobilising sensing agents onto the surface of lateral flow tests.

1.5.2 The Mobile Phase

Nanoparticles for biosensing have received significant scientific attention because their unique optical properties making them ideal for sensing activities,[83] as well as their tunability in terms of morphology and composition.[84] Plasmonic, especially gold, particles are the most common signal generating units used as the mobile phase in lateral flow devices.

Plasmonic nanoparticles are strongly coloured because their free electron density can couple with incident electromagnetic photons that have a wavelength greater than the size of the nanoparticle. This was quantitively described by Mie over 50 years after being first reported by Faraday; although the phenomenon was utilised far earlier by 4th Century Ancient Roman glassmakers in the Lycurgus Cup.[85–88]

The colour of a nanoparticle is not only dependent on its size but also its shape, the dielectric constant (relative permittivity) of the metal and medium it is in, as shown by the Fröhlich condition.[89–91] Only electromagnetic radiation resonant to electron oscillation can excite the localised surface plasmon and be absorbed by it; this

absorption leads to localised surface plasmon resonance (LSPR), producing the distinctive colour of the nanoparticle system, which in the case of gold is from red to blue.

1.5.2.1 Localised Surface Plasmon Resonance (LSPR)

In these LSPR capable systems photons travelling near parallel to the surface (high angle of incidence) excite free electrons to form collective and uniform oscillating electron systems termed plasmons (Figure 1.3).[90–92] These oscillating free electrons form a dipole displacement away from the lattice equilibrium position. The localised surface plasmon (LSP) formed occurs over the whole surface of the particle. This coherent electron displacement forms a coulombic restoring force that pulls the electrons back to the equilibrium, the system can therefore be considered as a harmonic oscillator driven by the light wave. The energy of the electron system is eventually dissipated through Auger excitations, Landau dampening and thermal dissipation, returning the electrons to below or equal to the Fermi energy. It is notable that only light resonant to the electron oscillation can excite the LSP and be absorbed by it; this absorption produces the distinctive colour of the nanoparticle system. The LSP effect cannot occur in bulk systems due to the low penetration of the electromagnetic radiation below the metal skin depth, preventing plasmon and photon energy curve overlap.

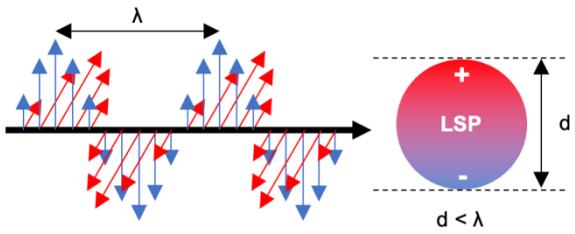

Figure 1.3. Diagrammatic representation of localised surface plasmon resonance.

Light wave present with a wavelength (λ) greater than the diameter of the particle (d).

Plasmonic nanoparticles have high molar attenuation (extinction) coefficients (ε) and Rayleigh scattering far greater than nanoparticles not exhibiting LSPR,[93,94] hence their use in LFDs. For example, 35 nm gold nanoparticles (AuNPs) and 30 nm silver nanoparticles (AgNPs) have attenuation coefficients far higher than common organic dyes such as Sudan III, methylene blue and crystal violet. It is noteworthy, that the best porphyrin dyes, such as 5,10,15,20-tetra-21*H*-23*H*-porphine zinc, have lower

attenuation coefficients than AuNPs (Table 1.1). These high attenuation coefficients lead to bright, vivid colours even at low concentrations, making them ideal for sensing applications.

Chromophore	Molar attenuation coefficient (ε, $M^{-1}\,cm^{-1}$)	Wavelength, λ_{max} (nm)
Gold nanoparticles, 35 nm[95]	~6.1×10^9	506
Silver nanoparticles, 30 nm[96]	~1.5×10^{10}	406
Sudan III[97]	~3.0×10^4	512
Methylene blue[97]	~4.1×10^4	654
Crystal violet[97]	~7.6×10^4	590
5,10,15,20-tetra-21*H*-23*H*-porphine zinc[97]	~5.7×10^5	422

Table 1.1. Attenuation coefficients of a selection of nanoparticles and dyes

An alternative to lateral flow systems, that also harnesses LSPR, is surface-enhanced Raman scattering (SERS), which is outside of the scope of this work but is worth mentioning. Raman scattering occurs when the frequency of photons emitted, from a change in electronic energy level, is different to that of the incident wavelength (i.e. $\nu_{incidence} \neq \nu_{scattered}$). SERS exploits changes in surface chemistry when analytes are deposited on surface-roughened nanoparticles; since this increases the magnitude of scattering. This gives SERS the potential to be used as a technique in POCT.[98] The utility of SERS has been demonstrated in the detection of carbohydrate interactions[99] by both ConA[100] (to pM levels) and different human galectins.[101] DNA targets have also been detected using a SERS primer assay. Namely *S. epidermidis* and MRSA: both common hospital-acquired infections.[102]

1.5.2.2 Gold Nanoparticles

Gold nanoparticles (AuNPs, 15 - 800 nm) are the most widely used plasmonic particles[47] due to their biocompatibility, simple synthesis, low cost (at the concentrations used) and straightforward functionalisation with organic molecules, in particular thiols. The most common method for AuNP synthesis uses $HAuCl_4$, and sodium citrate as both a reducing and capping agent.[103–105] By using seeded growth, anisotropic nanocrystals; such as rods, wires and triangles can be obtained and used in lateral flow systems.[106]

AuNPs can be surface-modified with analyte targeting components by surface passivation using thiol-linked or electrostatically charged antibodies or DNA strands.[65] Example capping ligands include; zwitterions, polymers, peptides, proteins, glycans and nucleic acids (Figure 1.4).[83] The vast majority of lateral flow systems utilise antibody capping groups; these have been extensively reviewed.[33,34,47,107]

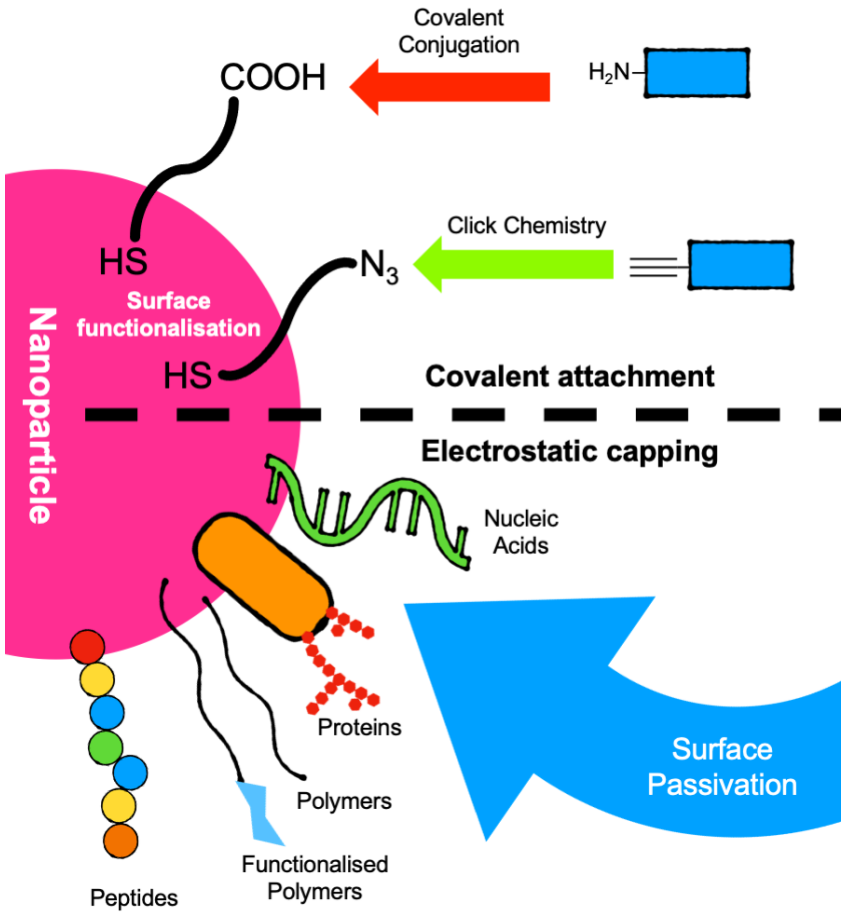

Figure 1.4. Example methods for surface modification of nanoparticles

In addition to gold, but outside the scope of this work, other nanoparticles have also been tested in lateral flow systems, including; core-shell gold nanoparticles,[108] quantum dots,[109] graphene oxide[110] and carbon nanotubes.[111] Furthermore, Dou *et al.* have produced nanomaterial-free antibody systems[112] using crystal violet-stained antibodies, enabling a test to run in 14 minutes, despite the sizeable drop in molar attenuation coefficients (Table 1.1).

In summary, the simplicity, diversity, and broad applicability to many targets has made lateral flow systems an attractive diagnostic. Despite this, many other POCT devices and lab-based diagnostics have been designed for use in more economically developed countries (MEDCs), and are not compatible for use in less economically developed countries (LEDCs).[113,114]

1.6 Malaria Rapid Diagnostic Tests – a case study

1.6.1 MRDTs in the Field

Malaria Rapid Diagnostic Tests (MRDTs) have been deployed primarily in low- and middle-income countries to combat various serotypes of malaria. MRDTs provide a cogent example of the benefits and drawbacks of lateral flow compared to other POC devices.

The World Health Organisation (WHO) estimated that there were 438,000 deaths from malaria in 2014, with 90% of these deaths occurring in sub-Saharan Africa (Figure 1.5).[46,115,116] In 2001, artemisinin-based combination therapies (ACTs) were recommended by WHO as first-line treatments.[117] Within the decade (2009), resistance to first-line ACT treatments was observed in the Greater Mekong Sub-region.[118–120]

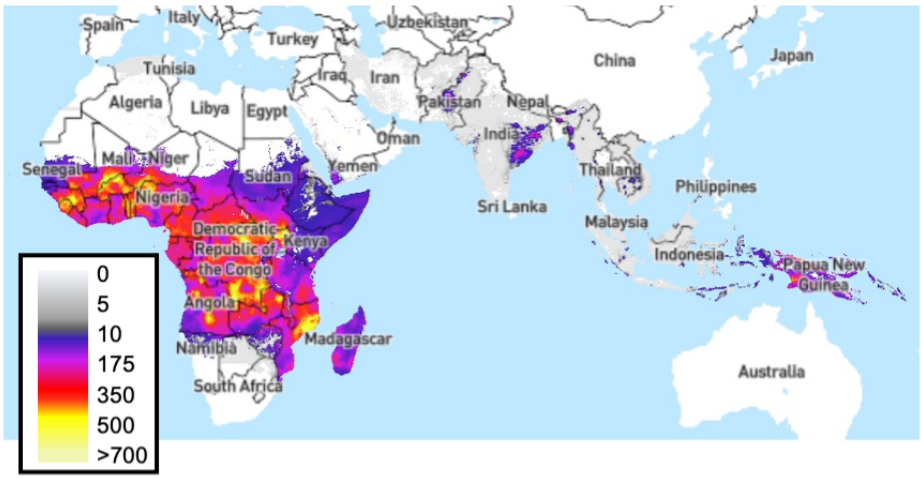

Figure 1.5. *Plasmodium falciparum* Incidence per 1,000 people, 2017[115,116]

Image produced using The Malaria Atlas Project, (Malaria Atlas Project, https://malariaatlas.org, (accessed 6 August 2019)).[116]

Fortunately, resistance to ACTs has not been observed in Africa, however there is growing concern that resistance will soon be observed in Sudan and more widely in travellers returning from Africa.[121–124] This is because health care practitioners in this region and other users of ACTs often do not follow WHO recommendations that the diagnosis of malaria should be based on parasite identification and not just observed patient symptoms.[123,125] For example, during the period from 2008-15, 35% of

suspected malaria cases in Africa were not confirmed with diagnostic tests, which led to antimalarial overuse, increasing the risk of ACT resistance.[46] In the same period, The United Nations Children's Fund (UNICEF) increased its procurement of Malaria Rapid Diagnostic Tests (MRDTs) (Figure 1.6.) from 3.8 million tests to 15 million.[126]

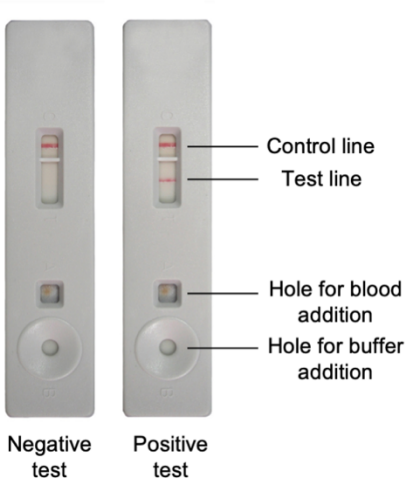

Figure 1.6. Image of negative and positive MRDT, taken from WHO documents.[127]

Resistance is further compounded by wider economic issues. Most malaria-affected countries use treatments costing less than $0.5 USD per capita while artemisinin-based combinatorial therapies cost ~$5 USD per capita.[122,128,129] A shift to a diagnostics-led approach would likely alleviate this problem, with research in Nigerian community pharmacies demonstrating the cost-effectiveness of MRDT-led treatment versus treatment without MRDT diagnosis.[130]

MRDTs are POC immunochromatographic, or photometric lateral flow devices, utilising peripheral blood samples, and selenium dyes or AuNPs conjugated to monoclonal antibodies as sensing units. They are handheld POCT for malaria detection and can differentiate four out of five malaria species (*Plasmodium vivax*, *P. ovale*, *P. malariae* and *P. falciparum*). They are, however, insensitive to *P. knowlesi*: a simian parasite known to infect humans. MRDTs target a variety of antigen analytes such as histidine-rich protein 2 (HRP-2 is synthesised by all *P. falciparum* parasites as an abundant water-soluble protein, unlike HRP-1 and HRP-3)[131], *Plasmodium* lactate dehydrogenase (pLDH) and *Plasmodium* aldolase.[132,133] While the sensitivity and specificity of devices varies by manufacturer and analyte targeted, those tested by Abba *et al.* showed values above 90%.[134,135]

Although MRDTs currently utilise antibodies, antigens of *P. falciparum* have been shown to bind to sialyllactoses and other derivatives found on human erythrocytic glycoprotein A.[136] This highlights the potential for glycan-functionalised MRDTs instead of antibody-functionalised MRDTs, which is discussed later in this chapter.

1.6.2 Alternatives to MRDTs and Beyond

MRDTs are currently less sensitive than alternative non-POCT techniques, such as microscopy of thick blood films and PCR techniques which can detect low parasite concentrations of 50 parasites/μL and 5 parasites/μL, respectively; while MRDTs are not tested by WHO at concentrations below 200 parasites/μL.[46,132] MRDTs are also less capable of determining parasite species beyond *P. falciparum* and *P. vivax*, unlike Giesma-stained blood microscopy,[137] the most common diagnostic technique, that can have a sensitivity of 95% and a specificity of 98%.[46,132,138] Furthermore, this high sensitivity and specificity can be achieved at $0.2 USD per sample at a rate of one sample every 20 minutes.[138] However, microscopy is a lab-based technique that requires an expert to carry out the analysis, leading to a potential sensitivity drop to just 10% in the field.[139]

Beyond malaria diagnostics, a contemporary real-time reverse transcription-PCR (rRT-PCR) system, the GeneXpert® instrument (Cepheid®), deployed in a Liberian mobile laboratory to test for Ebola virus was able to test 180 - 250 samples per day (~2 hours per sample), an improvement from 64 - 100 samples using older rRT-PCR systems. However, the GeneXpert® cost $17,000 USD to purchase with consumable cartridges costing ~$20 USD each, plus storage requirements of 2 - 28 ℃. Moreover, although training was relatively short (~1 week) compared to other rRT-PCR systems, early trainees were required to travel to Toulouse, France for technical training. The GeneXpert® laboratory setup deployed in Liberia performed well (May 2015 to March 2017),[140] with the instrumentation receiving United States Food and Drug Association (FDA) approval in March 2015[141] – however its high cost, infrastructure needs and storage requirements limit its application more broadly in LEDCs.

A timely piece by Phan *et al.*[142] on Ebola virus detection compared rRT-PCR and a lateral flow device (United States Naval Medical Research Centre Ebola virus Lateral Flow Immunoassay) designed to detect Ebola virus nucleoprotein and glycoprotein signature sequences. The average sensitivity of the lateral flow device was > 85% and

its specificity > 95%. The lateral flow assay could be run in 15 minutes compared to the PCR system that required 3 - 6 hours. A comparative study also assessing lateral flow devices versus rRT-PCR techniques showed similar findings.[143] Despite the potential use of lateral flow systems to triage cases, WHO recommended in early 2015 at the start of a major Ebola outbreak, that lateral flow systems should only be used in two extreme scenarios (isolated areas without RT-PCR access and when RT-PCR facilities are overwhelmed) but not for normal triage purposes.[144]

Due to the COVID-19 pandemic, diagnostics have been rapidly rolled out globally with rRT-PCR being the gold standard; but turn-around time and cost remain limiting factors. In July 2020, in the United States, the average wait time for a COVID-19 RT-PCR test was 4 days and only 37% of people received results within 2 days.[145] The availability of RT-PCR testing also varies significantly between countries; per 1000 people (31/7/2020)[146] the United Kingdom (2.27) and the United States (2.91) have significantly out-tested LEDCs such as Zimbabwe (0.07) or Myanmar (0.01).[146] In Iran, for example, CT scanners are used as they are more abundant per person (6.5 per million)[147] than RT-PCR machines.[148,149]

To address the time and cost issues of (the very accurate) rRT-PCRs, several other techniques have emerged. These loop-mediated isothermal amplification assay (LAMP) devices rely on three steps; sample preparation, amplification at a fixed temperature and detection.[150] Bench-top devices integrating all three steps have been produced with detection of the analyte often via immunoassay methods,[150] turbidity,[151] fluorescence[152] or nanoparticles.[153] The overall device however is still expensive, complex and slow, with amplification times ranging between 20 - 90 minutes,[150] this is compared to the 15 - 20 minutes required for an MRDT. A LAMP device for malaria diagnosis was field-tested in India and Thailand, and showed similar sensitivities and specificities to rRT-PCR.[154,155] LAMP devices have also been developed for SARS-COV-2 and compare well to RT-PCR.[156]

Aerts *et al.*,[157] when discussing the cost effectiveness of LAMP, microscopy and lateral flow tests in diagnosing cutaneous leishmaniasis in Afghanistan, suggested that all these diagnostic platforms have a role to play in different healthcare settings. They found that lateral flow systems reduce overall cost when used outside of the clinic. Whereas microscopy is favourable in the clinic except in periods of high demand where LAMP and lateral flow devices are more cost-effective. Ultimately a range of

methods with varying cost versus accuracy parameters are desirable to control outbreaks as illustrated by the rapid development of a range of diagnostics for the COVID-19 pandemic.[158–160]

1.6.3 MRDT Summary

MRDTs provide an excellent case study in the application of POC lateral flow as a low-cost, rapid diagnostic versus lab-based and more expensive POC systems. Moreover, studies carried out in the United States of America have found that MRDTs outperform blood smear microscopy too.[161] In spite of the limited sample size, this study highlights the potential of lateral flow systems in MEDCs where patients and health care professionals value short turnaround times.[16,24]

In summary, MRDT lateral flow systems are cost-effective, faster to run and do not require a specialist to perform; all areas vital to low- and middle-income countries lacking the expertise or funding to carry out lab-based techniques. [138] Furthermore, MRDT use can reduce the cost of artemisinin-based combinatorial therapies where drug price is the greatest barrier in both the short- and long-term.[128,129,162] Therefore, while more expensive reusable POCTs and lab-based diagnostic systems have the potential to provide higher specificities, they do not have the same ease of use, minimal power needs, token maintenance requirements, and low costs of lateral flow POCT deployed in low- and middle- income and, more economically developed countries.

However, some sources argue that MRDTs can be costly and difficult to use.[138,163,164] Furthermore, immuno-based MRDTs degrade when not transported and stored at low temperatures (“cold-chained”), becoming less-sensitive in conditions common in the field.[165] This highlights a potential weakness of protein-based LFDs that could be overcome with glycans.

1.7 Beyond Antibodies – Glycans as Recognition Units

Current POC diagnostics and in particular lateral flow systems as discussed in the previous sections, rely on antibodies as recognition units, owing to their high specificity and established methods for their production and nanoparticle conjugation. However, they are not the only biological recognition motifs; nucleic acids[166] and lectins[167] have also been incorporated into devices; but are still far less common than antibodies. Glycans (carbohydrates) offer an alternative to these recognition units and their study might bring new opportunities.

Glycans are ubiquitous in biological systems;[168] from vancomycin producing bacteria[169] (*Amycolatopsis orientalis*) to glycosylated proteins in humans (e.g. β3 integrin)[170] – with over half of all proteins believed to be glycosylated.[171] Glycosylation covalently adds glycans to proteins, lipids or other molecules (including RNA[172]) to form glycoconjugates in a dynamic fashion, regulated by glycosyl transferases and glycosidases.[173] As it is not template driven, glycosylation cannot be (easily) predicted from genomic information alone.

Glycoconjugates, carbohydrates/glycans covalently linked to other chemical species such as proteins, peptides, lipids etc., perform a vast range of biological roles including; cell signalling,[174] hormonal action,[175] cancer progression,[176] embryonic development,[177] correct protein folding/structure[178,179] and mediating immune responses.[180] Many of these processes are mediated at the glycocalyx (Figure 1.7), a membrane-bound interface layer of glycan-presenting proteins and lipids. This layer is found on many eukaryotic and bacterial cells, providing the primary interface for cells with their external environment.[181] For bacterial cells, the glycocalyx (also termed the "slime" or capsule layer) is known to modulate cell-to-cell binding for the purposes of resistance to host[182,183] and pathogenesis.[184] The nature of glycan presentation on mammalian cells is a key marker of a disease state,[185,186] influenza species specificity[187] and influenza A viruses' zoonotic potential.[188] Antigens from *P. falciparum* have also been shown to bind to sialyllactoses and other derivatives found on human erythrocytic glycoprotein A.[136]

Consequently, there exists a significant opportunity to both target the glycans themselves, or the "glycan-readers" termed lectins. Lectins are a broad family defined as glycan-binding proteins which are neither enzymes, transporters or antibodies.

These proteins often have highly conserved carbohydrate-binding domains (CBD).[189,190] Examples of lectins relevant to healthcare include the Shiga toxins,[191] cholera toxin[192] and ricin;[193] while also being found in snake venoms[194] and biocides in marine algae.[195] Notably, the use of lectins for staining histology samples, has been established for decades.[189]

The use of lectins in biosensor design has been comprehensively reviewed.[196–198] For example, Damborský *et al.* have reported a lectin-based lateral flow device that exploits immobilised lectin as the test line for prostate specific antigen (PSA).[167,199] Just as lectins can be used to recognise glycans, glycans can be used to recognise and differentiate between lectins and other carbohydrate binding proteins. There is extensive literature in the use of glycans in various applications which is beyond the scope of this work, but includes; anti-adhesion therapies,[200–203] glyconanotechnology,[204,205] antimicrobial applications[206,207] and, influenza[208] and human immunodeficiency virus (HIV)[209] vaccine development. A challenge (and an opportunity) lies in the synthesis of oligosaccharides, which inhabit a vast chemical space beyond that of other biological macromolecules of nucleic acid and protein origin.[210] However, access to glycans for recognition studies is rapidly expanding,[211] thanks to the emergence of automated glycan synthesis[212–215] and the use of chemo-enzymatic strategies for greater glycan diversification.[8,216–218]

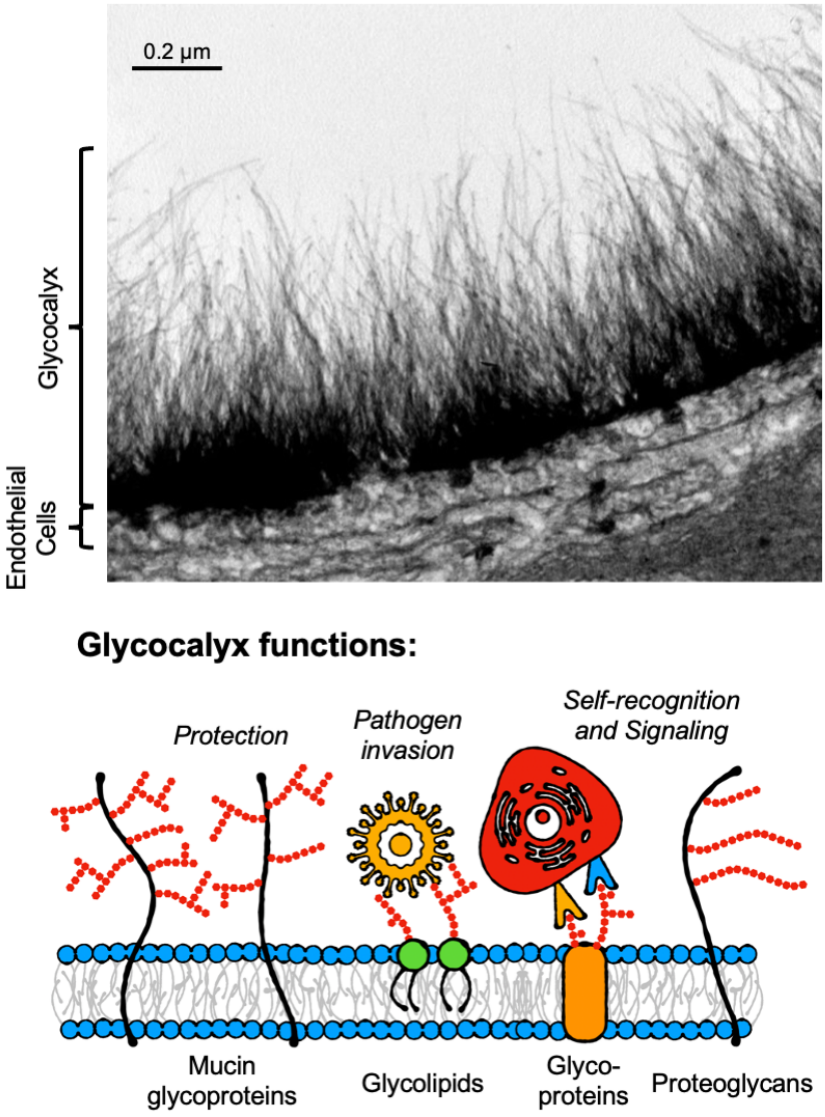

Figure 1.7. Electron micrograph of goat coronary capillary stained with Alcian blue and diagrammatic representation of the glycocalyx highlighting glycocalyx functions. Electron micrograph reproduced from van den Berg *et al.*[219] (figure 75.1.)

1.7.1 Target and Model Lectins

An example target lectin, with real world impact is the Cholera toxin (CTX) (Figure 1.8A) also known as choleragen. CTX was first hypothesised by Koch ("Koch's poison") in the late 19th century[220] before being discovered by De in 1959.[221] It is responsible for the watery diarrhoea symptomatic of *V. cholerae* infections.[221] In 2015, CTX afflicted 2.86 million people in endemic countries and currently threatens the wellbeing of over 1.3 billion in those countries.[222] The CTX lectin is composed of six protein subunits; a single copy of the enzymatic A subunit protomer and five copies of the B subunit involved in binding ganglioside GM1.[192] GM1 contains an oligosaccharide portion (galactose-β 1→3 *N*-acetylgalactosamine-β 1→4 *N*-acetylneuraminic acid-α 2→3 galactose-β 1→4 glucose to lipid) that is bound specifically by CTX.[223] This protein-glycan binding event is necessary for the activity of CTX and its movement into the cell[224–226] and can be inhibited using glycopolymer systems.[227] CTX is therefore a potential target of glycan-based lateral flow technology.

Soybean agglutinin (SBA), harvested from *G. max*, (Figure 1.8B) is far less hazardous than CTX and more economically viable for research purposes. SBA has been used to separate lymphocytes[228] and as a drug delivery system for breast cancer drugs.[229] Like many members of the legume lectin family SBA possesses a carbohydrate binding site that requires Mn^{2+} or Ca^{2+} for activity.[230] The carbohydrate binding site has an affinity for *N*-acetylgalactosamine (GalNAc) and galactose (Gal) although affinity for GalNAc is 40-fold higher than for Gal.[231] Above pH 4.6, SBA is tetrameric allowing for cross-linking and agglutination.[232,233] This makes SBA an attractive model lectin analyte for testing novel glycopolymer-based lateral flow systems and saccharides for diagnostics of particular interest.[234] As such SBA will be a model target for this work.

Similarly, *Ricinus communis* Agglutinin I (RCA I or RCA_{120}, Figure 1.8C) is a lectin from the castor bean or castor bean oil plant (*R. communis*). It is one of the family of ricin lectins used in early erythrocyte agglutination studies (1888) following earlier hemagglutination observations with rattle snake venom.[189] The toxic nature of ricin is well documented and has been harnessed by the United States and British in World War I and II respectively.[235] However, RCA_{120} is a non-toxic (unlike RCA II/RCA_{60}), 120 kDa tetrameric protein composed of two α- (27 kDa) and two β-chains (33 kDa), with an affinity for galactose (Gal) and *N*-acetylgalactosamine (GalNAc); notably it has an ~100 fold greater affinity for Gal > GalNAc (the reverse of SBA).[236–238] The

affinity of RCA_{120} is similar to RCA II, making RCA_{120} an ideal (safe) model target lectin.[239] As such RCA_{120} will also be used as a model target for this work.

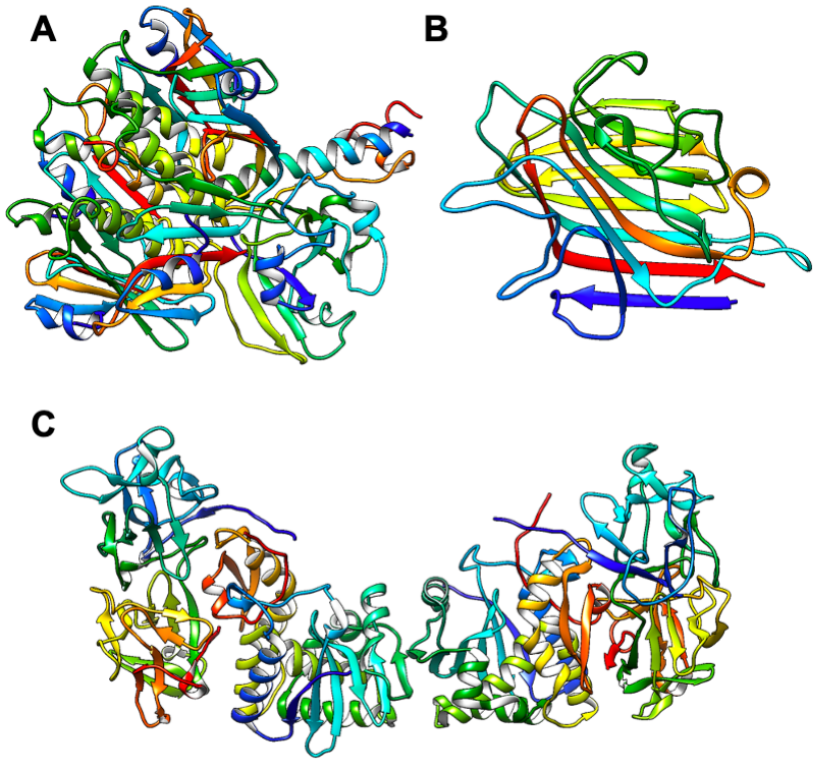

Figure 1.8. Lectin structures

A) Cholera toxin from *V. cholerae*; B) Soybean agglutinin from *G. max* and C) *Ricinus communis* agglutinin I from *R. communis*.

Lectin structures taken from the Protein Data Bank;[240] Cholera toxin (CTX) – 1XTC[241], Soybean agglutinin (SBA) – 1SBF[242] and *Ricinus communis* agglutinin I (RCA_{120}) – 1RZO[243]

1.7.2 Multivalency and Glyco-Materials

Glycan-lectin interactions are typically weak with K_d (dissociation constants) ranging from mM to µM values[244,245] which is significantly weaker than antibody-ligand interactions (in the nM to pM range).[246–248] This is overcome in nature by the presentation of multiple copies of glycans leading to statistical rebinding and chelation, resulting in significant enhancements to binding affinities relative to the free glycans – known as the "cluster glycoside effect".[249,250] The observed affinity enhancement (per glycan) as valency increases is non-linear and is dependent on the architecture of the glycan, its linker and its accessibility to the target. Due to this, there has been significant interest in using materials chemistry (polymers, particles and surfaces) to present multiple copies of glycans to facilitate the cluster glycoside effect.[244]

In the context of diagnostic devices, the cluster glycoside effect is crucial to obtaining the necessary affinity and selectivity, which is not possible using individual glycans. Figure 1.9 shows a summary of 37 glycoconjugates of various valances and architectures taken from a previous review.[244] This simple representation highlights enhancement effects, which can range from 2 to > 10,000-fold increases associated with multivalency. However, it also shows that the simplified assumption that "ever larger, higher valency systems always lead to increased affinity," does not hold true – the effects are more subtle. For example, one of the most potent inhibitors of the cholera toxin, has just five, precisely placed glycans.[251]

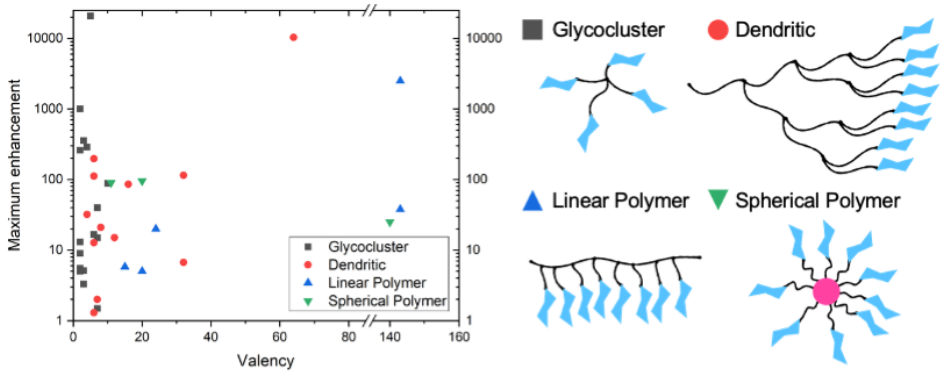

Figure 1.9. Graphical representation of a selection of glycoconjugates

Data adapted from "Table 1" of Lundquist *et al.*,[244] highlighting the maximum enhancement in binding (corrected for ligand valency) as valency changes.

1.8 Structural and Synthetic Strategies for Glycan Presentation

The idea of iterative or modular approaches in carbohydrate chemistry is not novel.[252,253] However, the structures produced can increase valency and mimic more complex polysaccharides facilitating the cluster glycoside effect without requiring expensive and complex syntheses. Glycoclusters, dendrimers, linear polymers and spherical polymers (polymers on a core, often a protein or nanoparticle) (Figure 1.9) provide a variety of ways to present multiple carbohydrates,[254] often monosaccharides, in the correct spatial arrangement for protein binding.[201,255] As such, they have found multiple applications, including as anti-pathogenic agents.[200]

1.8.1 Non-Polymeric Approaches

1.8.1.1 Glycoclusters

Non-polymeric approaches such as glycoclusters provide well defined and controlled glycan presenting architectures often displaying only a handful of glycans. André *et al.* designed a series of glycoclusters to increase affinity relative to the free glycan and enhance selectivity for the target protein.[256] The clusters were based around ethylene glycol, glycerine and pentaerythritol cores. While more complex glycocluster systems have allowed for the tuning of linker length and valency, to target virulence factors such as LecA of *Pseudomonas aeruginosa*[257] and the fimbriae-mediated adhesion of *E. coli*,[258] respectively. Porkolab *et al.* have produced high valences (for glycoclusters), such as 16 glycans on a complex organic core.[259] Whereas others have harnessed non-synthetic cores and directed evolution to design glycoclusters.[260] The structural versatility available in glycoclusters can be used to not only display a glycan but precisely adjust the nature of its presentation in 3D space[261] (as seen for native glycans) providing opportunities to tune the interaction.

1.8.1.2 Dendrimers

In the mid-1980s dendrimers were independently developed by Newkome[262] and Tomalia.[263,264] Dendrimers are oligomeric or even polymeric structures produced iteratively, forming tree-like highly branched regular structures often using poly(amidoamine) cores.[265,266] Many reviews have been carried out into the synthesis and applications of dendrimers[267–269] and glycodendrimers.[270,271] While a study by

Woller *et al.* tracked the binding enhancement realised as dendrimer generation increased in mannose-functionalised dendrimers.[272]

Glycodendrimers often present a compromise. Higher valences are accessible with dendrimers but at the cost of decreased structural control; unlike in glycoclusters where structural control is often favoured over high valences. The high tunability of dendrimers also makes them an attractive approach for glycan presentation; with void spaces in larger dendrimers providing room for molecular cargo, potentially for clinical applications.[273]

1.8.2 Polymeric Approaches

Glycopolymers present glycans, typically, on their side chains but also on end groups[274] therefore they can be considered synthetic glycoconjugates that are capable of presenting a high density of glycans. Due to the relative ease of polymer synthesis, glycopolymers present a convenient route to engineer multivalency. There have been many reviews on this topic[275–280] that have focused on glycopolymer synthesis so this will not be covered here in significant detail.

Advancements in controlled reversible deactivation radical polymerisation techniques, including atom transfer radical polymerisation (ATRP),[281] reversible addition-fragmentation chain transfer (RAFT)[282] polymerisation, ring-opening metathesis polymerisation (ROMP)[283] and nitroxide-mediated polymerisation (NMP)[284] enables the synthesis of macromolecules with different chain lengths, compositions and architectures. This unique class of materials has the potential to harness the discriminatory power of saccharides[285,286] without the thermal instability of proteins, such as antibodies, while maintaining the convenient size and shape tunability of polymers. Furthermore, steric stabilisation from large, bulky polymers can prevent the approach of molecules that may compete for binding sites, increasing the observed affinity.[244]

1.8.2.1 Reversible Addition-Fragmentation Chain Transfer (RAFT)

RAFT (reversible addition-fragmentation chain transfer) is a reversible-deactivation radical living polymerisation technique.[287] It allows for a wide range of functionality, complexity and reaction conditions; while producing low molecular weight dispersity range (degree of polymerisation (DP)) and predictable molecular weight polymers.[288,289] RAFT polymerisation utilises a chain transfer agent (CTA or "RAFT

agent") commonly a thiocarbonylthio compound, however xanthates can be used in a MADIX process (macromolecular design by interchange of xanthate) (Figure 1.10).[290]

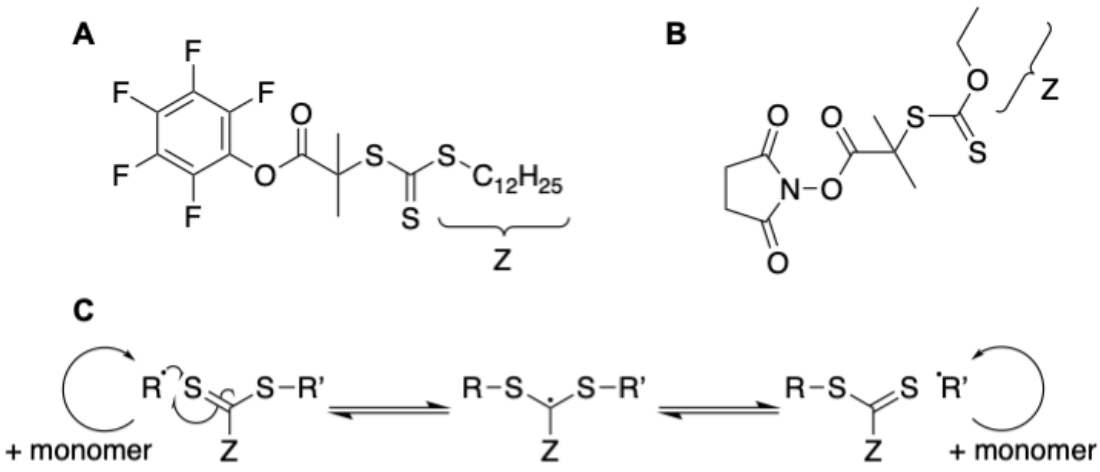

Figure 1.10. Chain Transfer Agents

A) A RAFT agent (Pentafluorophenyl-2-dodecylthiocarbonothioylthio)-2-methylpropanoate (PFP-DMP)); B) A MADIX agent (*N*-succinimide 2-(ethyl xanthate)-2-methylpropanoate ("MADIX1")) and C) Reversible addition-fragmentation of a chain transfer agent, highlighting the Z and R/R' groups

The chain transfer agent in RAFT mediates the polymerisation, an example being thiocarbonylthio compounds that are used in this work. CTAs are made up of three key groups; a group that is reactive to radical addition (e.g., C=S), a Z-group that modifies addition and fragmentation rates by dictating radical stability and R groups that are able to reinitiate polymerisation and act as a free radical leaving group (Figure 1.10C).[289,291] By adjusting these groups CTAs can be designed to control polymerisations of a wide range of monomers.[292]

The monomers used in RAFT polymerisations must be able to form stable radical structures, an example monomer is 2-hydroxyethyl acrylamide (HEA) that will be used in this work. Previous work using HEA monomers has shown the monomer to be suitable for RAFT polymerisations, giving reasonable degrees of polymerisation under benign reaction conditions.[293]

The RAFT mechanism using PFP-DMP (Figure 1.11) is initiated by radical formation, for example thermal initiation using a radical initiator such as 4,4'-azobis(4-

cyanovaleric acid) (ACVA) (Figure 1.11A) and propagation/chain growth on a monomer (Figure 1.11B). This radical species then reacts with the CTA forming an intermediate that collapses back into a π-system with loss of a CTA R-group (a constituent of the CTA that can stabilise a radical) as a radical. The radical R-group then propagates the cycle by reacting with another monomer (radical polymeric chain). The rapid equilibrium that forms between the active chain (radical polymeric chain) and the dormant chain (polymeric chain attached to a CTA) controls molecular weight growth. To maintain controlled polymer growth the radical polymeric chain should undergo chain growth by only a few monomers (ideally one) before returning to the dormant chain. Thus, the CTA R groups cycle in and out of the radical and dormant chain.

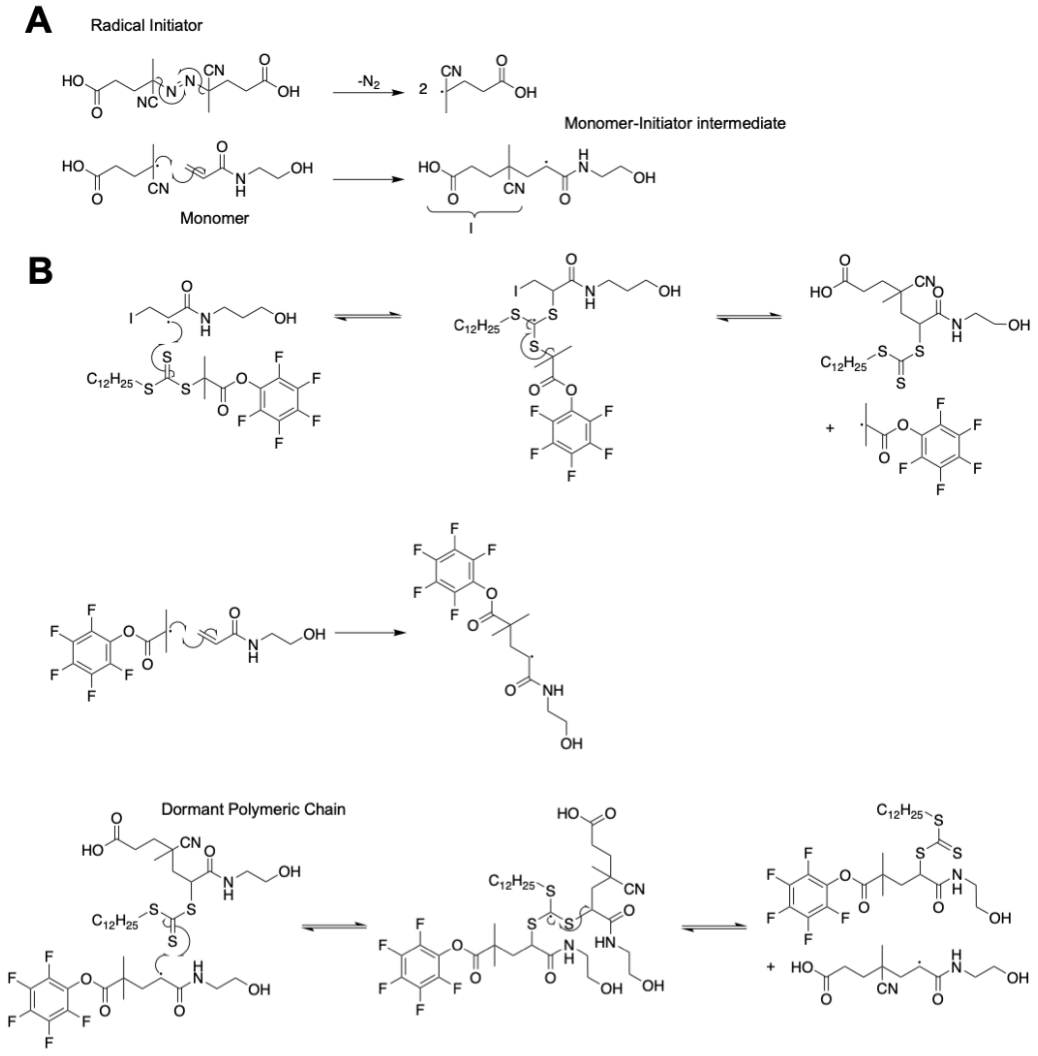

Figure 1.11. RAFT mechanism

A) Initiation and B) Propagation

Molecular weight control is achieved by controlling the initial ratio between the [monomer] and [CTA] and the rate of addition/fragmentation, controlled by the Z-group. Deviations from this ratio give broader molecular weight ranges and are often due to incorrect Z-group choice[292] and poor handling of the CTA – thiocarbonylthio groups are sensitive to oxidizing agents in some solvents, pH changes, high temperatures and light.[294] The ratio of [CTA]:[initiator] is also usually greater than one to make sure the number of dormant CTA chains is greater than the number of free radicals.

Most polymerisation reactions use thermally-initiated systems – however externally controllable alternatives do exist, such as; light,[295,296] voltage in atom transfer radical polymerisation (ATRP),[297] chemical redox in ring-opening metathesis polymerisation (ROMP)[298] and mechanical force.[299] This work will use thermally-initiated polymer reactions. Although, photo-controlled radical polymerisations (photo-CRPs) using either separate photo-induced initiators or RAFT/MADIX agents as an initiator-transfer-agent-terminator (iniferter) allow for more controlled and sustained polymerisations by removing additional thermal radical initiator, therefore favouring photolysis of the C-S bond as the initiation step.[300–302] This can allow for higher conversions and better dispersities in the synthesis of higher M_n polymers of both telechelic PHEA and PVP.[302] Photo-polymerisation has the added advantages of being possible at room temperature and in the presence of oxygen – this makes the process more industrially viable than standard RAFT approaches.[300]

1.8.2.2 Linear Polymers

Linear polymers (unlike dendrimers) provide a simple synthetic approach to present a high valence system with limited structural control. This is because the polymer backbone is flexible, decreasing topological control of the molecular architecture; however, the backbone is functionalised with multiple glycan units allowing for higher valences. Glucose-functionalised linear polymers have been used to interfere with quorum sensing and sequester bacteria,[303,304] building on work discussed by Pieters, that shows bacterial adhesion can be interfered with by multivalent carbohydrate systems.[305] While sialoside-functionalised linear polymers have been used to inhibit virus binding.[306] It is emerging how the polymer backbone, which presents the glycans, can itself play a key role in fine tuning affinity and selectivity. For example Kiessling showed that *cis*-backbones (from ROMP) gave mucin mimetics which were

more potent inhibitors than *trans* equivalents.[307] Whereas amide-linked mannose side-chains were found to bind ConA less than ester-linked side-chains, this difference was attributed to subtle mobility differences.[308]

The glycan unit of linear glycopolymers is often attached to the polymer backbone by a pendent linker such as ethylene glycol or similar short chain unit. This is not always the case though with some groups making polymers out of glycopeptides such as vancomycin.[309] In this study the polymer was found to have a higher affinity for cell wall intermediate mimics than monomeric vancomycin. Interestingly a dendrimer-based approach has also been developed to target drug-resistant cell walls.[310] While others have tuned the length of the pedant linker and glycan density on the backbone to influence affinity.[311–313] Semsarilar *et al.* increased the valency of the linear backbone by hyperbranching at the pendent sites, overcoming the chain length limitations of a linear polymer where one monomer unit often has a valency of one.[314] While Mahon *et al.* used Polymer-Scaffolded Dynamic Combinatorial Libraries and a lectin scaffold to increase the affinity of a linear polymer, by dynamically selecting for high affinity pendent groups (Figure 1.12).[286]

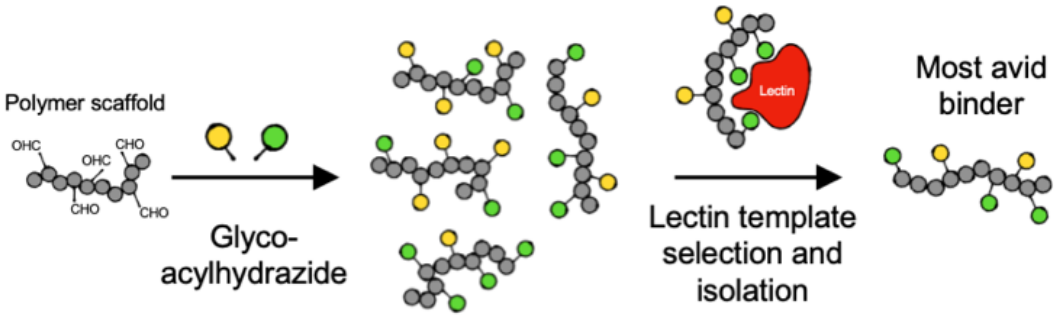

Figure 1.12. Dynamic combinatorial selection of avid lectin binder using poly-aldehydes and acylhydrazide glycans.

1.8.2.3 Pre- versus Post-Polymerisation Functionalisation

A key consideration in the synthesis of linear (and spherical polymers) is whether to add glycans pre-polymerisation or post-polymerisation. The addition of glycans onto monomer units pre-polymerisation,[315] can be done by chemical or enzymatic means.[316] Pre-polymerisation glycan functionalisation, can lead to excessive and unnecessary use of a glycan (e.g. loss during synthesis and incomplete monomer conversion) unless used in a copolymerisation technique.[317] This can make it

unfeasible for economic reasons when using complex saccharides. It is also usually necessary to protect the glycan before polymerisation (Figure 1.13A),[318,319] however, this is not always the case.[320] Post-polymerisation functionalisation along the length of the polymer chain has been carried out by click chemistry (Figure 1.13B)[321,322] but often requires priming of the glycan[323,324] or full conversion is not realised.[325] Activated esters and aminated glycans have also been used to carry out post-polymerisation chain functionalisation, however the conversion was not total.[326] While a ring-opening approach utilising poly(azalactone) yielded high conversions with aminated monosaccharides; however this approach does limit monomer choice, a key design variable of polymer chemistry.[327] Post-polymerisation terminal functionalisation using amino-oxy terminated polymers and reducing glycans has also been developed.[328] Notably, terminal functionalisation can also be obtained using pre-polymerisation glycan functionalisation, but this additional, usually hydrophilic, glycan group can interfere with the polymerisation reaction.

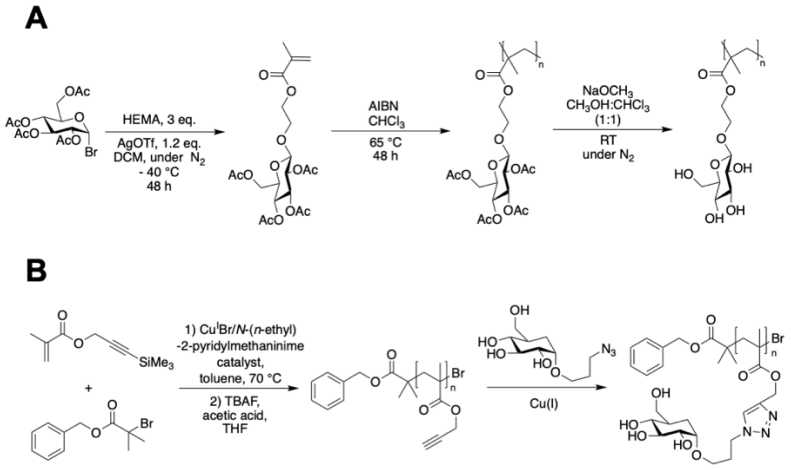

Figure 1.13. Examples of pre- and post-polymerisation glycan addition approaches

A) pre-polymerisation[319] and B) post-polymerisation[322]

Further structural diversity can be achieved by varying the carbon position on the glycan used for attachment, this can also tailor binding.[230,329] For example pyranose glycans are often functionalised through C1, with aminated glycans such as galactosamine favouring functionalisation via C2, while C3[330] and C6[331,332] functionalisation is less common. A rare example of C4 functionalisation was carried out using a vinyl-benzaldehyde monomer at the *para*-position, but the linkage was also via C6.[333]

1.8.2.4 Spherical Polymers

The Miura and Gibson groups have independently shown that linear glycopolymer constructs on spherical gold cores ("spherical polymers") can mimic GM1[334–336] (Figure 1.14A), a membrane-bound monosialosylganglioside with a high affinity for cholera toxin.[337] These approaches build on work illustrating lectins, such as cholera toxin, show good affinity for fragments of their polysaccharide target.[338] While the Miura group focused on heterogenous glycan functionalisation along the length of the polymer chain (Figure 1.14B),[335] the Gibson group sought to mimic the structure of the GM1 scaffold and its terminal groups using bifunctional monomer units (Figure 1.14C).[334] Interestingly, both groups mimicked the same two glycans in their structures, the terminal glycans of GM1; galactose and neuraminic acid, illustrating well that glycan presentation can tune binding. Others have varied side chain length (i.e. linker length between backbone and glycan) to enable control over the access of galactose into the relatively deep GM1 binding pocket of the Cholera toxin.[202,339] While by adding branching units on the glycan-polymer linker, the allosteric sialic acid binding site could be targeted to further increase selectivity.[334,340,341] This approach also utilised multiple different glycans within a single polymer chain and was shown to increase affinity through a range of mechanisms[342] beyond just targeting a second binding site – potentially steric shielding too.[343]

Other groups have moved away from the commonly used protein and nanoparticle cores. Wu *et al.* has favoured self-assembling polymeric glycomicelles that use polyester cores.[344] While the Percec group have harnessed amphiphilicity to make coreless glycodendrimersomes from dendritic units.[345,346]

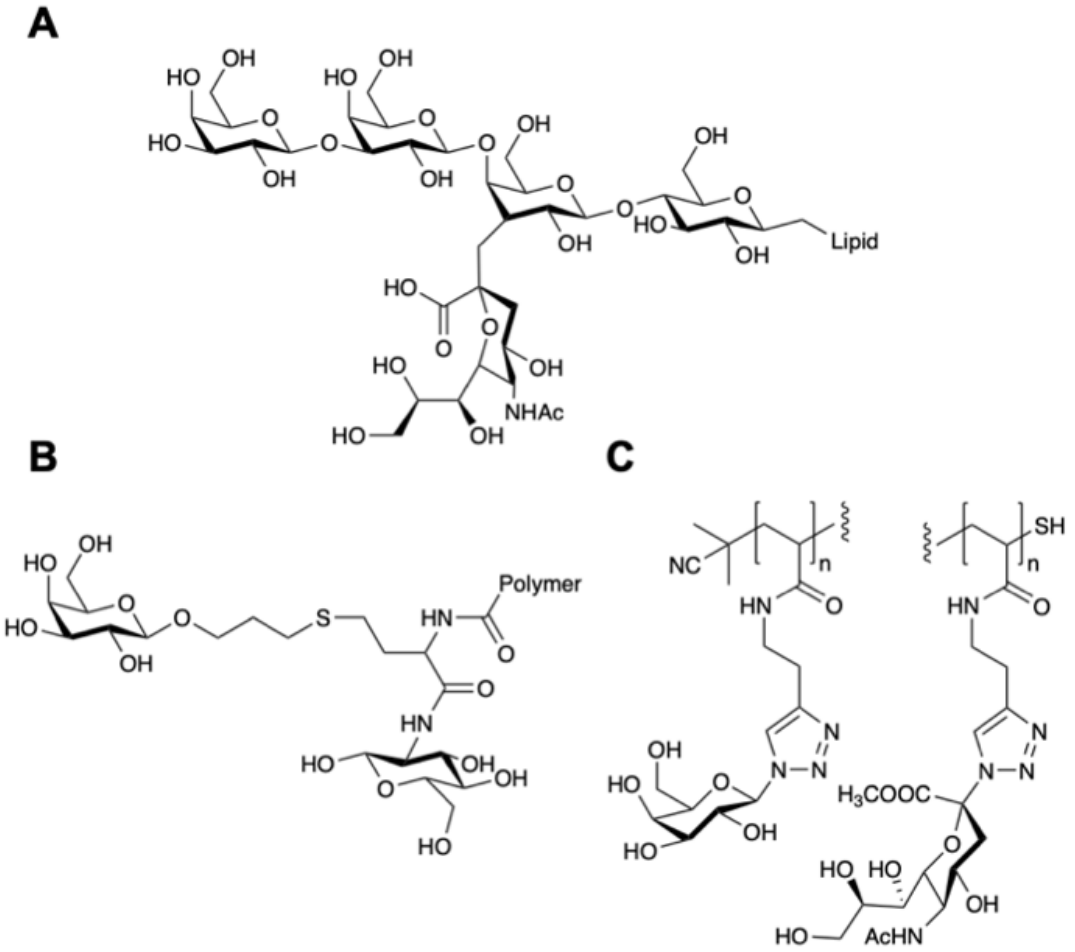

Figure 1.14. GM1 and synthetic mimics

A) GM1; B) Gibson Group GM1 mimic and C) Miura Group GM1 mimic

1.8.3 Glycan Presentation Summary

The synthetic mimicking of GM1 to bind cholera toxin,[347] highlights well the structural variety and number of different synthetic avenues that researchers have taken to imitate the same binding event. For example, galactose dendrimers have been used to mimic GM1 and were shown in an octavalent system to have an IC_{50}, lower than GM1, for cholera toxin.[348] While the work of the Miura and Gibson groups highlights the use of spherical polymers for the same target.[334–336] Plus linear polymers have also been used as GM1 mimics.[349]

In summary, the structural versatility of multivalent glycan presenting systems can be used to overcome a broad range of challenges. Glycopolymers have been deployed, or show potential for, a variety of therapeutic roles and biomedical applications[350,351] including; binding flu virus[352] (glycopolymers in vaccine development is discussed in

detail by Sunasee *et al.*),[280] MRI contrast agents,[353,354] drug delivery,[355–357] anti-cancer agents,[358] metabolic labelling of cell-surfaces[359] and to re-program the glycocalyx.[360] Chikae *et al.*[361] demonstrated that glycopolymer-coated nanoparticles, immobilised on carbon electrodes can detect amyloid-β, a peptide produced in Alzheimer's disease. Others have shown the potential of glycopolymer-coated AuNPs as anti-cancer[362] and transfection agents.[363] Notably, Miura *et al.* have written a review that discusses the role of glycopolymers in nanobiotechnology in more depth.[279] The final sections of this chapter will focus more directly on spherical polymers, specifically those that use a gold nanoparticle core.

1.9 Glycosylated Gold Nanoparticles

As with antibody-functionalised gold nanoparticles which form the basis of most lateral flow devices, there are extensive reports of glycans being immobilised onto gold nanoparticles. Several reports conjugate the glycan directly to the nanoparticle surface, or with short linkers, which give a high density (valency) but can lead to problems with colloidal stability. This can lead to irreversible aggregation when used in biologically relevant media, such as saline buffers or blood plasma. Hence the use of polymeric tethers which provide steric stabilisation, as well as acting as non-fouling interfaces, has been explored.[364]

Polymer chains can be added to the surface of AuNPs by three methods; *grafting to* (a polymer is added to the surface of pre-prepared AuNPs), *in situ* (a polymer is added to the surface of growing AuNPs) and *grafting from* (polymerisation occurs on CTAs or initiators bound to the pre-prepared AuNP surface) (Figure 1.15).[365] The advantage of *grafting to* is that a well-defined polymer can be synthesised before addition to the surface: this allows for increased control of the reaction. However, the diffusion rate of a large macromolecule to the target surface is low and decreases as more bound macromolecules impede the path to the surface. This is overcome with *grafting from* at the expense of losing control over the polymer synthesis, as the polymer is grown from the surface in a poorly-defined manner.[366,367] In addition, to analyse a *grafting from* polymer, the polymer must be laboriously cleaved from the surface.

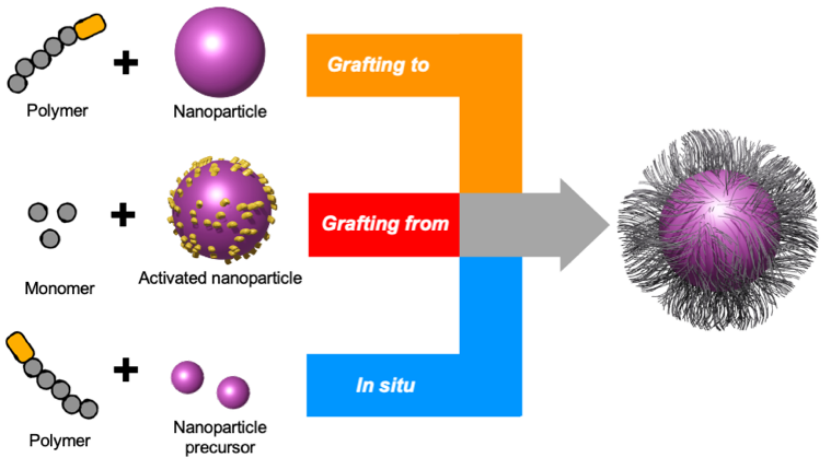

Figure 1.15. Representation of the three conceptual methods of polymer grafting to surfaces

Poly(ethylene glycol) (PEG) is widely used as a nanoparticle coating, due to its low-biofouling, low cytotoxicity and commercial availability. Russel and co-workers used a PEG linker to immobilise a tri-functional sialoside to gold nanoparticles, enabling tuning of avian versus human influenza binding (dictated by the 2,3 versus 2,6 linkages).[368] Penadés and co-workers have used PEGylated gold nanoparticles[369] to investigate glycosphingolipid mediated carbohydrate-carbohydrate interactions when coupled with an SPR sensor.[370]

Whilst PEG is widely used, there are thousands of other potential monomeric building blocks for the polymer tether. RAFT polymerisation has attracted interest in this respect, as it installs an α-terminal (protected) thiol on every chain (the α-terminal di/tri-thioester (trithiocarbonate) is easily reduced to a thiol for direct gold particle immobilisation[371]), which is suitable for immobilisation onto gold surfaces.[372,373] There has been particular interest in exploiting RAFT polymerisation to generate polymeric ligands for gold nanoparticles. The loading of thiol-terminated glycopolymers produced by RAFT was investigated by Dave *et al.*.[374] In this work, fluorescein isothiocyanate was displaced from the gold surface to determine the effects of polymer length on loading. Similarly, Jin *et al.* used thiols projecting from a poly(methyl methacrylate) surface to immobilised AuNPs. The AuNPs were further functionalised with glycopolymers via a thiol linker.[375] Cameron and co-workers used poly(galactosides) derived by RAFT for the *in situ* formation of small (< 20 nm) glycosylated AuNPs, capable of lectin recognition, to generate glyco-conjugate cancer vaccines.[376] RAFT polymerisation has also been used to make pH responsive[357] and thermo-responsive[377] glycopolymers on AuNPs. Other approaches using disulphide, double-headed ATRP initiators[378] or grafting-from methods have also been used.[367,379] A more novel approach for gold functionalisation was used by Boyer *et al.* to immobilise glycopolymers.[380] Their "layer-by-layer" approach formed a charged spherical polymer, around a gold core, that was later functionalised with a charged glycopolymer.

1.10 AuNPs in Sensors and Diagnostics – Aggregation to Lateral Flow Glyco-Assays

The surface plasmon absorption energy maximum of a plasmonic nanoparticle is altered by collective conduction-band electron oscillation that occurs when nanoparticles become localised – i.e when they aggregate there is strong colour change.[83,89] Zsigmondy and Thiessen established that proteins could be used to stabilise gold and prevent gold aggregation.[420] While Mirkin *et al.* demonstrated that oligonucleotide-functionalised AuNPs aggregated in the presence of complementary DNA sticky ends showing how specific DNA sequences can be identified by a simple colour change in solution.[381] Due to the fact that many lectins have multiple binding sites (i.e. Concanavalin A (ConA) has 4,[382] Soybean agglutinin (SBA) has 4)[383], multivalent glycosylated gold nanoparticles have been explored as colourimetric sensors for lectins based on red-blue colour shifts.

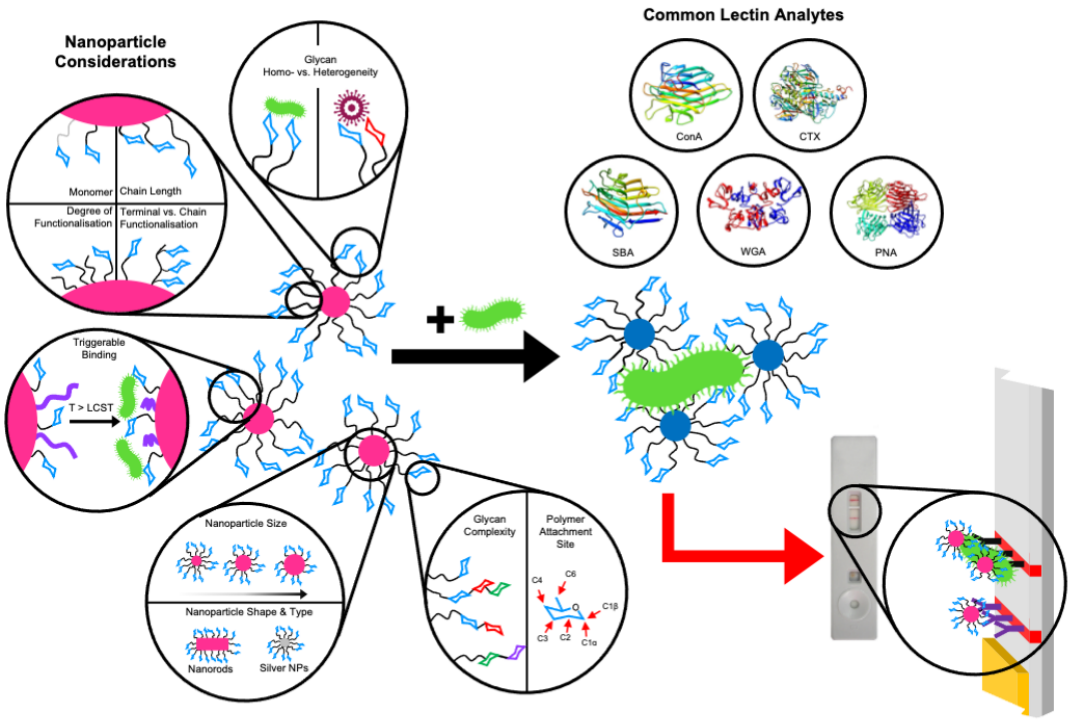

Figure 1.16. Major nanoparticle design considerations and common lectin analytes for aggregation assays and potential for use in lateral flow assays

Lectin structures were taken from the Protein Data Bank[240] as follows; Soybean agglutinin (SBA) – 1SBF,[242] Concanavalin A (ConA) – 3CNA,[384] Cholera toxin

(CTX) – 1XTC,[241] Wheat germ agglutinin (WGA) – 2X52[385] and Peanut agglutinin (PNA) – 2DVD.[386]

While early aggregation studies using glycopolymer functionalised AuNPs did not harness the potential of glycans to bind lectins, instead using biotin functionalised polymers, in conjunction with glycopolymers, to bind streptavidin.[387,388] More contemporary studies have focused on model (plant) lectins, using; mannose-functionalised poly(ethylene glycol) chains to bind ConA,[389,390] galactose-functionalised glycopolymers to bind RCA_{120}[390] and lactose-functionalised glycopolymers to bind cholera toxin.[391] Although Jiang *et al.* would later show bifunctional systems of glycan and biotin are able to bind both streptavidin and lectins (ConA, ricin and WGA), allowing for lectin immobilisation on an avidin-coated dotLab Sensor Surface.[392,393]

Aggregation assay users have deployed many different polymer linkers. The use of polymeric linkers introduces steric stabilisation ensuring particles do not aggregate in e.g. saline conditions, compared to using glycans directly-conjugated to the AuNP surface.[394] Von der Ehe *et al.*[395] synthesised a copolymer of unfunctionalised *N*-isopropylacrylamide (NIPAM) and 2-mercaptoethylacrylamide functionalised with monosaccharides via a sulphur linker. Despite using RAFT polymerisation, the thiocarbonylthio group was not degraded to a thiol before immobilisation onto gold nanoparticles.[396] Aggregation assays were carried out using ConA – no aggregation was observed with the glucose-functionalised copolymer or poly(NIPAM) homopolymer. Aggregation was only observed with the mannose-functionalised copolymer, leading to a small shift in the UV-vis spectra on aggregation.

The use of polymer tethers also enables additional functionality and properties, such as thermoresponsivity.[397] This was further developed by Won *et al.* who deployed gold nanoparticles functionalised with poly(hydroxyethyl acrylamide) glycopolymers and poly(NIPAM). These systems demonstrated that lectin binding can be triggered by both temperature changes,[398] and changes in calcium ion concentrations.[399] In both cases glycan functionalisation was through an amide or ester linker, either before or after polymerisation. Samoilova *et al.* also used an amide linker for glycan functionalisation but with poly(ethylene-*alt*-maleic anhydride) and poly(*N*-vinylpyrrolidone-*alt*-maleic anhydride).[400] This study also found negligible differences between gold and silver nanoparticles, highlighting the potential of

possible alternatives to spherical AuNPs. It is also notable that gold nanorods have reported protein detection, down to 100 pg.mL^{-1}.[401] This was built on by Georgiou *et al.* who harnessed gold nanorods functionalised with neuraminic acids to sense for SARS-COV-2 in clinical samples (unpublished data).

Click reactions have also been used to form glycan linkages. This can require "priming" (preparation before use) of the glycan and protection of the glycan hydroxyls,[323] something not necessary in other syntheses.[402,403] A click approach allowed Boden *et al.* to present mannose, sequestered via the C1 position, on a variety of precision-made polymers using solid phase polymer synthesis.[317] Three short polymers of varying hydrophobicity with either monovalent or pentavalent mannose functionalisation were produced. Although, all the glycopolymers successfully bound the lectin, the pentavalent system exhibited the lowest binding. This is likely due to steric hindrance preventing the lectin from binding the mannose residues. While precise solid phase polymer synthesis is unlikely to be industrially viable for integration into POC devices, this work does illustrate the importance of appropriate glycan presentation, regardless of high glycan concentrations.[404]

The importance of glycan presentation was further illustrated by Otten *et al.* who presented two different monosaccharides: mannosamine and galactosamine, on AuNPs. This heterogenous approach allowed for differentiation of lectins such as ConA, SBA and *Ricinus communis* agglutinin I (RCA_{120}).[405] These modest changes to glycan heterogeneity allowed for increased discriminatory power and emphasises the ease with which monosaccharides can be deployed to good effect.

Toyoshima *et al.*[406] synthesised mannose- and *N*-acetylglucosamine-functionalised glycopolymers immobilised on 15, 40 and 100 nm AuNPs. Pre-functionalised *p*-acrylamidophenyl α-mannoside and *p*-acrylamidophenyl *N*-acetyl-β-glucosamine were polymerised by RAFT. The level of glycan functionalisation on the backbone varied from 13% to 100%. Aggregation experiments were carried out with target and off-target lectins; and the colour change measured by UV-vis and aggregation confirmed by TEM. The mannose functionalised AuNPs were assayed against ORN178 (an *E. coli* species specific for α-mannose) and aggregated (Figure 1.17A).[406] Similar work was carried out by Richards *et al.* who showed how fimbrae-differing phenotypes (FimH+ and FimH-) of *E. coli* can be discriminated by glycosylated AuNPs.[407]

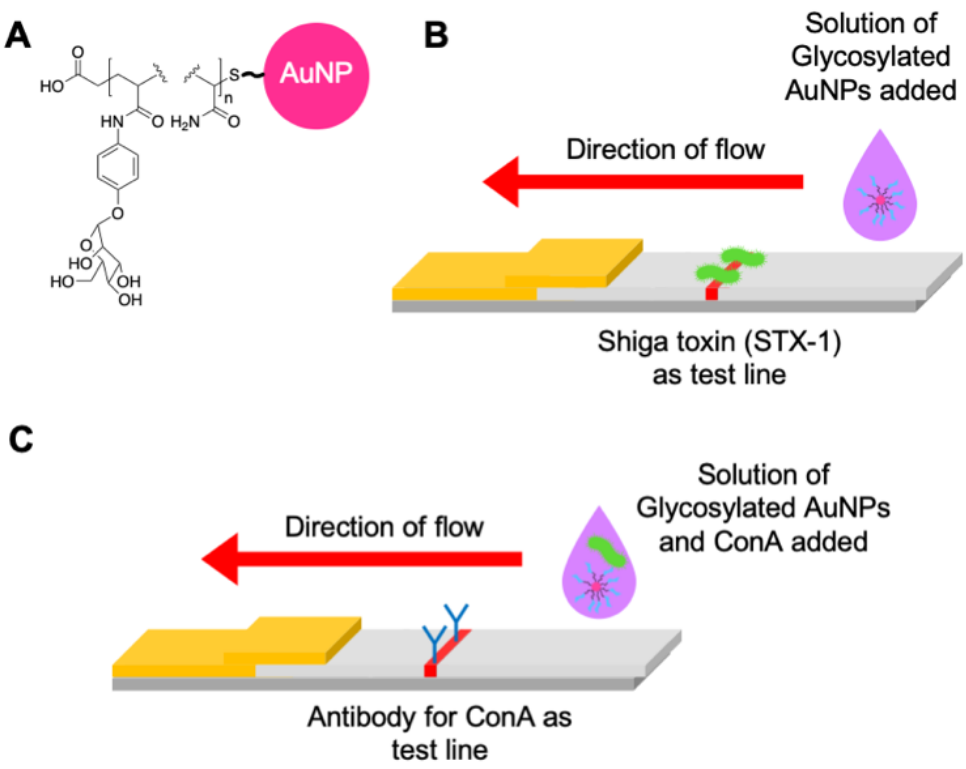

Figure 1.17. Representative structures of glycosylated AuNPs, and flow-through and lateral flow dipsticks used by the Miura group

A) Representative structure of glycosylated acrylamide coated AuNPs used by Toyoshima *et al.*[315] and Ishii *et al.*;[408] B) Schematic of the flow-through dipstick used by Toyoshima *et al.*[315] and C) Schematic of the lateral flow dipstick used by Ishii *et al.*.[408]

1.10.1 Lateral Flow Glyco-Assays

Considering the large body of literature showing that multivalent presentation significantly increases glycan binding affinity and the importance of carbohydrate binding to proteins as biomarkers, there exists a significant opportunity to develop lateral flow-based diagnostics using glycans as the capture/recognition units. As glycans can be chemically synthesised, there is no need to raise antibodies against emergent pathogens and the sheer range of tools to alter their presentation make them appealing targets. However, thus far there have been few lateral flow glyco-assays (LFGAs).

The first step towards a lateral flow glyco assay was carried out by Toyoshima *et al.*[315] who utilised α-galactose- and α-mannose- *p*-acrylamidophenyl pyranosides against

target and off-target lectins in aggregation assays and surface plasmon resonance (SPR) (Figure 1.17A). This work highlighted that glycopolymers could be used to sense for targets, such as Shiga toxin-1, by aggregation assay and SPR. Interestingly, a flow-through glyco-assay using Shiga toxin-1 as the test line (Figure 1.17B), showed mild levels of binding to a galactose-functionalised AuNP system (Figure 1.18C).

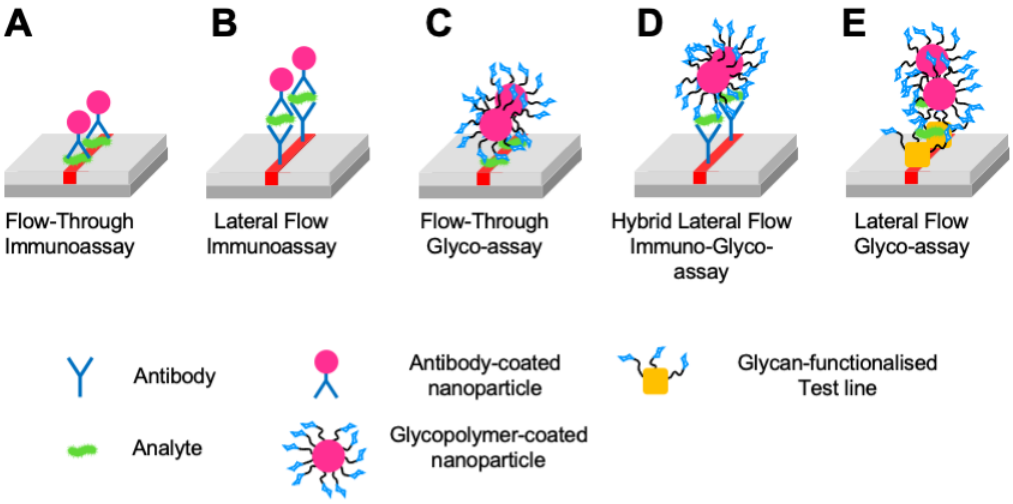

Figure 1.18. Representative test lines of flow-through and lateral flow immuno- and glyco-assays

This minor foray into lateral flow technology was advanced by the Miura group using mannose-functionalised *p*-acrylamidophenyl polymers to sense for ConA in the mobile phase.[408] They employed RAFT polymerisation to form a polymer with varying amounts of mannose-functionalised groups (0% to 50%) along the length of the polymer. This was immobilised on 40 nm AuNPs and run in the mobile phase. The test line was a rabbit anti-ConA antibody (Figures 1.17C & 1.18D) – a hybrid lateral flow immuno-glyco-assay. The results were analysed by UV-vis, but the red line response from higher concentrations could be seen with the naked eye.

Further work was carried out using similarly synthesised AuNPs to determine whether copolymers with varying glycan (mannose) densities or a mixture of functionalised and unfunctionalised polymers gave the best responses in aggregation and lateral flow assays.[409] They found that an AuNP coated in functionalised and unfunctionalised chains with high glycan concentrations gave excellent responses. It is notable that smearing of the nanoparticles was observed in some cases, indicating the importance of the polymer coating, and using an appropriate particle blocking agent such as BSA or casein. The importance of the polymer coating has previously been observed in

aggregation assays where a compromise must be struck between stability in aqueous media and rapid optical readout, usually tuned by adjusting polymer length.[394,407] Similarly, alterations to the polymer itself i.e. to a more sterically bulky polymer can be used to stabilise AuNPs[410] and favour binding, but avoid aggregation.[6]

This is likely to be of importance in lateral flow assays where early deposition leads to smearing and undesirable signal-to-noise ratios. Nevertheless, the work of the Miura group has shown the knowledge transfer possible from aggregation assays to flow-through assays to lateral flow assays. This coupled with knowledge gained from glycosylated AuNP aggregation studies into targets such as Influenza hemagglutinins,[7] has led to the development of the first lateral flow glyco-assay (LFGA) diagnostic devices by the Gibson Group, presented in this work and the following publications.

Baker *et al.*, discovered that SARS-COV-2 (the causative agent of COVID-19) spike protein has affinity towards certain sialic acids,[2,3] and later further confirmed with microarrays[411] and STD NMR.[412] This built on research highlighting sialic acid affinity in other coronaviruses,[413,414] such as the coronavirus that causes Middle East Respiratory syndrome (MERS).[415] *N*-acetyl neuraminic acid functionalised hydroxyethyl acrylamide polymers immobilised on AuNPs were used to detect a SARS-COV-2 spike protein bearing pseudovirus in a lateral flow glyco-assay device (using a BSA-glycoconjugate test-line) (Figure 1.18E), discussed further in Chapter 3. While a flow-through glyco-assay device, where the specimen is deposited as the test line, was used for the diagnosis of SARS-COV-2 in primary clinical samples (Figure 1.18C), discussed further in Chapter 4.[4] These works established that lateral flow glyco-assays have potential applications in rapid diagnostics, surveillance and as accessible research tools for evaluating glycan-binding protein function. Further work showed that by tuning the polymer coating (glycan density and polymer length) and AuNP size, different lectins could be targeted, discussed further in Chapter 2.[1] This demonstrated the tuneability and robustness of lateral flow glyco-assay systems.

1.11 Conclusions

Research into carbohydrate-based, rather than antibody- or nucleotide-based, aggregation assays highlights the potential of carbohydrate-based systems to provide cost-effective and sensitive diagnostics for healthcare at the point of care and need.[416] This collection of research builds on the extensive role of carbohydrates in nature, and coupled with the robustness of glycan-based systems and the benefits of lateral flow POCT, could allow for the targeting of a wider range of potential epitopes and analytes.[325,417]

In summary, glycan-based systems offer an alternative to immuno-based detection systems.[418] The potential benefits of glycan-based systems compared to proteomic or immuno-based systems are the ease of both storage and manufacture.[202] The potential for glycopolymer-functionalised AuNPs, integrated into lateral flow systems, for use as POCT devices is vast. This is especially true if the glycopolymers can be functionalised economically with monosaccharides or branched polysaccharide mimics. These low-cost immuno-free glycopolymer-based lateral flow diagnostic devices (Lateral Flow Glyco-Assays (LFGA)) could be ideal for low- and middle-income, and more economically developed countries alike.[202,419]

Herein, the first created lateral flow glyco-assay is discussed (Chapter 2) and its performance tuned against a variety of lectin analytes by adjusting, polymer chain length, glycan linkage position and particle engineering. The first published LFGA is then discussed in Chapter 3 and its use demonstrated against the S1 spike protein of SARS-COV-2 and a pseudovirus system bearing the S1 spike protein. This device, in a flow-through glyco-assay format, is then applied to a real-world problem, as it is used to detect the presence of the SARS-COV-2 virus in clinical samples (Chapter 4).

In Chapter 5, the focus shifts away from the nanoparticle system to the stationary phase, where the first fully synthetic ("vegan") lateral flow test is demonstrated using a glycan functionalised poly(vinyl pyrrolidone) test line. The performance of this fully synthetic test line is interrogated using a variety of analytes.

In Chapter 6, the synthesis of mannose and glucose derivatives with C2 conjugate functionality but conserved C2 hydroxyl functionality is explored using a Mannich-based approach.

Finally in Chapter 7, the x-ray photoelectron spectroscopy data collected over the course of this work and others is collated and explored for its potential to study grafting density and its effects in nanoparticle systems.

1.12 References

(1) Baker, A. N.; Muguruza, A. R.; Richards, S.-J.; Georgiou, P. G.; Goetz, S.; Walker, M.; Dedola, S.; Field, R. A.; Gibson, M. I. Lateral Flow Glyco-Assays for the Rapid and Low-Cost Detection of Lectins–Polymeric Linkers and Particle Engineering Are Essential for Selectivity and Performance. *Advanced Healthcare Materials* **2021**, 2101784.

(2) Baker, A. N.; Richards, S.-J.; Guy, C. S.; Congdon, T. R.; Hasan, M.; Zwetsloot, A. J.; Gallo, A.; Lewandowski, J. R.; Stansfeld, P. J.; Straube, A.; Walker, M.; Chessa, S.; Pergolizzi, G.; Dedola, S.; Field, R. A.; Gibson, M. I. The SARS-COV-2 Spike Protein Binds Sialic Acids and Enables Rapid Detection in a Lateral Flow Point of Care Diagnostic Device. *ACS Central Science* **2020**, *6* (11), 2046–2052.

(3) Baker, A. N.; Richard, S.-J.; Guy, C. S.; Congdon, T. R.; Hasan, M.; Zwetsloot, A. J.; Straube, A.; Walker, M.; Chessa, S.; Pergolizzi, G.; Dedola, S.; Field, R.; Gibson, M. The SARS-COV-2 Spike Protein Binds Sialic Acids, and Enables Rapid Detection in a Lateral Flow Point of Care Diagnostic Device. *chemrxiv.org* **2020**.

(4) Baker, A. N.; Richards, S.-J.; Pandey, S.; Guy, C. S.; Ahmad, A.; Hasan, M.; Biggs, C. I.; Georgiou, P. G.; Zwetsloot, A. J.; Straube, A.; Dedola, S.; Field, R. A.; Anderson, N. R.; Walker, M.; Grammatopoulos, D.; Gibson, M. I. Glycan-Based Flow-Through Device for the Detection of SARS-COV-2. *ACS Sensors* **2021**, *6* (10), 3696–3705.

(5) Baker, A. N.; Congdon, T. R.; Richards, S.-J.; Georgiou, P. G.; Walker, M.; Dedola, S.; Field, R. A.; Gibson, M. I. End-Functionalized Poly(Vinylpyrrolidone) for Ligand Display in Lateral Flow Device Test Lines. *ACS Polymers Au* **2021**, acspolymersau.1c00032.

(6) Georgiou, P. G.; Baker, A. N.; Richards, S.-J.; Laezza, A.; Walker, M.; Gibson, M. I. Tuning Aggregative versus Non-Aggregative Lectin Binding with Glycosylated Nanoparticles by the Nature of the Polymer Ligand. *Journal of Materials Chemistry. B* **2020**, *8* (1), 136–145.

(7) Richards, S.-J.; Baker, A. N.; Walker, M.; Gibson, M. I. Polymer-Stabilized Sialylated Nanoparticles: Synthesis, Optimization, and Differential Binding to Influenza Hemagglutinins. *Biomacromolecules* **2020**, *21* (4), 1604–1612.

(8) Richards, S.-J.; Keenan, T.; Vendeville, J.-B. B.; Wheatley, D. E.; Chidwick, H.; Budhadev, D.; Council, C. E.; Webster, C. S.; Ledru, H.; Baker, A. N.; Walker, M.; Galan, M. C.; Linclau, B.; Fascione, M. A.; Gibson, M. I. Introducing Affinity and Selectivity into Galectin-Targeting Nanoparticles with Fluorinated Glycan Ligands. *Chemical Science* **2021**, *12* (3), 905–910.

(9) Pancaro, A.; Szymonik, M.; Georgiou, P. G.; Baker, A. N.; Walker, M.; Adriaensens, P.; Hendrix, J.; Gibson, M. I.; Nelissen, I. The Polymeric Glyco-Linker Controls the Signal Outputs for Plasmonic Gold Nanorod Biosensors Due to Biocorona Formation. *Nanoscale* **2021**, *13* (24), 10837–10848.

(10) Leekha, S.; Terrell, C. L.; Edson, R. S. General Principles of Antimicrobial Therapy. *Mayo Clinic Proceedings* **2011**, *86* (2), 156–167.

(11) Clark, L. C.; Lyons, C. Electrode Systems for Continuous Monitoring in Cardiovascular Surgery. *Annals of the New York Academy of Sciences* **1962**, *102*, 29–45.

(12) Crane, M. M.; Organon MV. *Diagnostic Test Device - US3579306A*; 1969.

(13) Drain, P. K.; Hyle, E. P.; Noubary, F.; Freedberg, K. A.; Wilson, D.; Bishai, W. R.; Rodriguez, W.; Bassett, I. V. Diagnostic Point-of-Care Tests in Resource-Limited Settings. *The Lancet Infectious Diseases* **2014**, *14*, 239–249.

(14) Shapiro, H.; Zwarenstein, H. A. A Test for the Early Diagnosis of Pregnancy on the South African Clawed Toad (Xenopus Loevis). *South African Medical Journal* **1930**, *9* (6), 202–205.

(15) Elkan, E. R. The Xenopus Pregnancy Test. *British medical journal* **1938**, *2* (4067), 1253–1256.

(16) St John, A.; Price, C. P. Point-of-Care Testing Technologies Existing and Emerging Technologies for Point-of-Care Testing. *Clin Biochem Rev* **2014**, *35* (3), 155–167.

(17) Price, C. P.; St John, A.; Hicks, J. *Point-of-Care Testing*, 2nd ed.; American Association for Clinical Chemistry: Washington D.C, 2004.

(18) Ehrmeyer, S. S.; Laessig, R. H. Point-of-Care Testing, Medical Error, and Patient Safety: A 2007 Assessment. *Clinical Chemistry and Laboratory Medicine* **2007**, No. 45, 766–773.

(19) Pai, N. P.; Vadnais, C.; Denkinger, C.; Engel, N.; Pai, M. Point-of-Care Testing for Infectious Diseases: Diversity, Complexity, and Barriers in Low-And Middle-Income Countries The Promise of Point-of-Care Testing. *PLoS Medicine* **2012**, *9* (9).

(20) Pai, N. P.; Pai, M. Point-of-Care Diagnostics for HIV and Tuberculosis: Landscape, Pipeline, and Unmet Needs. *Discovery medicine* **2012**, *13*, 34–45.

(21) Hsieh, H.; Dantzler, J.; Weigl, B. Analytical Tools to Improve Optimization Procedures for Lateral Flow Assays. *Diagnostics* **2017**, *7* (2), 29.

(22) Liang, T.; Robinson, R.; Houghtaling, J.; Fridley, G.; Ramsey, S. A.; Fu, E. Investigation of Reagent Delivery Formats in a Multivalent Malaria Sandwich Immunoassay and Implications for Assay Performance. *Analytical Chemistry* **2016**, *88* (4), 2311–2320.

(23) Vaitukaitis, J. L. Development of the Home Pregnancy Test. *Annals of the New York Academy of Sciences* **2004**, *1038* (1), 220–222.

(24) Hsieh, Y.-H.; Gaydos, C. A.; Hogan, M. T.; Uy, O. M.; Jackman, J.; Jett-Goheen, M.; Albertie, A.; Dangerfield, D. T.; Neustadt, C. R.; Wiener, Z. S.; Rompalo, A. M. What Qualities Are Most Important to Making a Point of Care Test Desirable for Clinicians and Others Offering Sexually Transmitted Infection Testing? *PLoS ONE* **2011**, *6* (4), e19263.

(25) Peeling, R. W.; Holmes, K. K.; Mabey, D.; Ronald, A. Rapid Tests for Sexually Transmitted Infections (STIs): The Way Forward. *Sexually transmitted infections* **2006**, *82* (S5), 1–6.

(26) Kosack, C. S.; Page, A.-L.; Klatser, P. R. *Bulletin of the World Health Organization: A Guide to Aid the Selection of Diagnostic Tests*; 2017.

(27) El-Osta, A.; Woringer, M.; Pizzo, E.; Verhoef, T.; Dickie, C.; Ni, M. Z.; Huddy, J. R.; Soljak, M.; Hanna, G. B.; Majeed, A. Does Use of Point-of-Care Testing Improve Cost-Effectiveness of the NHS Health Check Programme in the Primary Care Setting? A Cost-Minimisation Analysis. *BMJ Open* **2017**, *7* (8), e015494.

(28) Bhatnagar, P.; Wickramasinghe, K.; Williams, J.; Rayner, M.; Townsend, N. The Epidemiology of Cardiovascular Disease in the UK 2014. *Heart* **2015**, *101* (15), 1182–1189.

(29) Tan, Q.; Hildon, Z. J. L.; Singh, S.; Jing, J.; Thein, T. L.; Coker, R.; Vrijhoef, H. J. M.; Leo, Y. S. Comparing Patient and Healthcare Worker Experiences during a Dengue Outbreak in Singapore: Understanding the Patient Journey and the Introduction of a Point-of-Care Test (POCT) toward Better Care Delivery. *BMC Infectious Diseases* **2017**, *17* (1), 503–519.

(30) Ramchandani, R.; Kazatchkine, M.; Liu, J.; Sudan, P.; Dybul, M.; Matsoso, P.; Nordström, A.; Phelan, A.; Legido-Quigley, H.; Singh, S.; Mabuchi, S. Vaccines, Therapeutics, and Diagnostics for Covid-19: Redesigning Systems to Improve Pandemic Response. *BMJ (Clinical research ed.)* **2021**, *375*, e067488.

(31) Li, Z.; Yi, Y.; Luo, X.; Xiong, N.; Liu, Y.; Li, S.; Sun, R.; Wang, Y.; Hu, B.; Chen, W.; Zhang, Y.; Wang, J.; Huang, B.; Lin, Y.; Yang, J.; Cai, W.; Wang, X.; Cheng, J.; Chen, Z.; Sun, K.; Pan, W.; Zhan, Z.; Chen, L.; Ye, F. Development and Clinical Application of a Rapid IgM-IgG Combined Antibody Test for SARS-CoV-2 Infection Diagnosis. *Journal of Medical Virology* **2020**, *92* (9), 1518−1524.

(32) Kolifarhood, G.; Aghaali, M.; Mozafar Saadati, H.; Taherpour, N.; Rahimi, S.; Izadi, N.; Hashemi Nazari, S. S. Epidemiological and Clinical Aspects of COVID-19; a Narrative Review. *Archives of academic emergency medicine* **2020**, *8* (1), e41.

(33) Posthuma-Trumpie, G. A.; Korf, J.; van Amerongen, A. Lateral Flow (Immuno)Assay: Its Strengths, Weaknesses, Opportunities and Threats. A Literature Survey. *Analytical and Bioanalytical Chemistry* **2009**, *393* (2), 569–582.

(34) Bahadır, E. B.; Sezgintürk, M. K. Lateral Flow Assays: Principles, Designs and Labels. *TrAC Trends in Analytical Chemistry* **2016**, *82*, 286–306.

(35) Leuvering, J. H. W.; Thal, P. J. H. M.; Waart, M. van der; Schuurs, A. H. W. M. Sol Particle Immunoassay (SPIA). *Journal of Immunoassay* **1980**, *1* (1), 77–91.

(36) Schramm, E. C.; Staten, N. R.; Zhang, Z.; Bruce, S. S.; Kellner, C.; Atkinson, J. P.; Kyttaris, V. C.; Tsokos, G. C.; Petri, M.; Sander Connolly, E.; Olson, P. K. A Quantitative Lateral Flow Assay to Detect Complement Activation in Blood. *Analytical Biochemistry* **2015**, *477*, 78–85.

(37) Liu, L.; Peng, C.; Jin, Z.; Xu, C. Development and Evaluation of a Rapid Lateral Flow Immunochromatographic Strip Assay for Screening 19-Nortestosterone. *Biomedical Chromatography* **2007**, *21* (8), 861–866.

(38) Nagatani, N.; Yuhi, T.; Chikae, M.; Kerman, K.; Endo, T.; Kobori, Y.; Takata, M.; Konaka, H.; Namiki, M.; Ushijima, H.; Takamura, Y.; Tamiya, E. A Sensitive Immunochromatographic Assay Using Gold Nanoparticles for the Semiquantitative Detection of Prostate-Specific Antigen in Serum. *NanoBiotechnology* **2006**, *2* (3–4), 79–86.

(39) Buhrer-Sekula, S.; Smits, H. L.; Gussenhoven, G. C.; van Leeuwen, J.; Amador, S.; Fujiwara, T.; Klatser, P. R.; Oskam, L. Simple and Fast Lateral Flow Test for Classification of Leprosy Patients and Identification of Contacts with High Risk of Developing Leprosy. *Journal of Clinical Microbiology* **2003**, *41* (5), 1991–1995.

(40) Jarvis, J. N.; Percival, A.; Bauman, S.; Pelfrey, J.; Meintjes, G.; Williams, G. N.; Longley, N.; Harrison, T. S.; Kozel, T. R. Evaluation of a Novel Point-of-Care Cryptococcal Antigen Test on Serum, Plasma, and Urine From Patients With HIV-Associated Cryptococcal Meningitis. *Clinical Infectious Diseases* **2011**, *53* (10), 1019–1023.

(41) Kwizera, R.; Nguna, J.; Kiragga, A.; Nakavuma, J.; Rajasingham, R.; Boulware, D. R.; Meya, D. B. Performance of Cryptococcal Antigen Lateral Flow Assay Using Saliva in Ugandans with CD4 <100. *PLoS ONE* **2014**, *9* (7), e103156.

(42) Vaidya, V. S.; Ford, G. M.; Waikar, S. S.; Wang, Y.; Clement, M. B.; Ramirez, V.; Glaab, W. E.; Troth, S. P.; Sistare, F. D.; Prozialeck, W. C.; Edwards, J. R.; Bobadilla, N. A.; Mefferd, S. C.; Bonventre, J. V. A Rapid Urine Test for Early Detection of Kidney Injury. *Kidney International* **2009**, *76*, 108–114.

(43) Page, A.-L.; Alberti, K. P.; Mondonge, V.; Rauzier, J.; Quilici, M.-L.; Guerin, P. J. Evaluation of a Rapid Test for the Diagnosis of Cholera in the Absence of a Gold Standard. *PLoS ONE* **2012**, *7* (5), e37360.

(44) Ang, S. H.; Rambeli, M.; Thevarajah, T. M.; Alias, Y. B.; Khor, S. M. Quantitative, Single-Step Dual Measurement of Hemoglobin A1c and Total Hemoglobin in Human Whole Blood Using a Gold Sandwich Immunochromatographic Assay for Personalized Medicine. *Biosensors and Bioelectronics* **2016**, No. 78, 187–193.

(45) Biagini, R. E.; Sammons, D. L.; Smith, J. P.; MacKenzie, B. A.; Striley, C. A. F.; Snawder, J. E.; Robertson, S. A.; Quinn, C. P. Rapid, Sensitive, and Specific Lateral-Flow Immunochromatographic Device to Measure Anti-Anthrax Protective Antigen

Immunoglobulin G in Serum and Whole Blood. *Clinical and Vaccine Immunology* **2006**, *12*, 541–546.

(46) World Health Organisation. *Malaria Rapid Diagnostic Test Performance: Summary Results of WHO Product Testing of Malaria RDTs: Rounds 1-6 (2008-2015)*; 2015.

(47) Banerjee, R.; Jaiswal, A. Recent Advances in Nanoparticle-Based Lateral Flow Immunoassay as a Point-of-Care Diagnostic Tool for Infectious Agents and Diseases. *Analyst* **2018**, *143* (9), 1970–1996.

(48) Gentili, S.; Solimini, R.; Tittarelli, R.; Mannocchi, G.; Busardò, F. P. A Study on the Reliability of an On-Site Oral Fluid Drug Test in a Recreational Context. *Journal of Analytical Methods in Chemistry* **2016**, *2016*, 1–10.

(49) Arkell, T. R.; Kevin, R. C.; Stuart, J.; Lintzeris, N.; Haber, P. S.; Ramaekers, J. G.; McGregor, I. S. Detection of Δ 9 THC in Oral Fluid Following Vaporized Cannabis with Varied Cannabidiol (CBD) Content: An Evaluation of Two Point-of-collection Testing Devices. *Drug Testing and Analysis* **2019**, *11* (10), 1486–1497.

(50) De Giovanni, N.; Fucci, N. The Current Status of Sweat Testing for Drugs of Abuse: A Review. *Current Medicinal Chemistry* **2013**, No. 20, 545–561.

(51) Pacifici, R.; Farre, M.; Pichini, S.; Ortuno, J.; Roset, P. N.; Zuccaro, P.; Segura, J.; de la Torre, R. Sweat Testing of MDMA with the Drugwipe(R) Analytical Device: A Controlled Study with Two Volunteers. *Journal of Analytical Toxicology* **2001**, *25* (2), 144−146.

(52) Carrio, A.; Sampedro, C.; Sanchez-Lopez, J.; Pimienta, M.; Campoy, P. Automated Low-Cost Smartphone-Based Lateral Flow Saliva Test Reader for Drugs-of-Abuse Detection. *Sensors* **2015**, *15* (11), 29569–29593.

(53) Huang, L.; Tian, S.; Zhao, W.; Liu, K.; Ma, X.; Guo, J. Multiplexed Detection of Biomarkers in Lateral-Flow Immunoassays. *The Analyst* **2020**, *145* (8), 2828–2840.

(54) Zheng, M. Z.; Richard, J. L.; Binder, J. A Review of Rapid Methods for the Analysis of Mycotoxins. *Mycopathologia* **2006**, *161* (5), 261–273.

(55) Mansfield, M. M. The Use of Nitrocellulose Membranes in Lateral Flow Assays. In *Drugs of Abuse: Body Fluid Testing*; 2005; pp 74–85.

(56) Mansfield, M. A. Nitrocellulose Membranes for Lateral Flow Immunoassays: A Technical Treatise. In *Lateral Flow Immunoassay*; 2009; pp 95–114.

(57) Holstein, C. A.; Chevalier, A.; Bennett, S.; Anderson, C. E.; Keniston, K.; Olsen, C.; Li, B.; Bales, B.; Moore, D. R.; Fu, E.; Baker, D.; Yager, P. Immobilizing Affinity Proteins to Nitrocellulose: A Toolbox for Paper-Based Assay Developers. *Analytical and Bioanalytical Chemistry* **2016**, *408* (5), 1335–1346.

(58) Aoyama, S.; Akiyama, Y.; Monden, K.; Yamada, M.; Seki, M. Thermally Imprinted Microcone Structure-Assisted Lateral-Flow Immunoassay Platforms for Detecting Disease Marker Proteins. *The Analyst* **2019**, *144* (5), 1519–1526.

(59) Ng, A. H. C.; Uddayasankar, U.; Wheeler, A. R. Immunoassays in Microfluidic Systems. *Analytical and Bioanalytical Chemistry* **2010**, *397* (3), 991–1007.

(60) Magro, L.; Jacquelin, B.; Escadafal, C.; Garneret, P.; Kwasiborski, A.; Manuguerra, J.-C.; Monti, F.; Sakuntabhai, A.; Vanhomwegen, J.; Lafaye, P.; Tabeling, P. Paper-Based RNA Detection and Multiplexed Analysis for Ebola Virus Diagnostics. *Scientific Reports* **2017**, *7* (1), 1347.

(61) Srisa-Art, M.; Boehle, K. E.; Geiss, B. J.; Henry, C. S. Highly Sensitive Detection of *Salmonella Typhimurium* Using a Colorimetric Paper-Based Analytical Device Coupled with Immunomagnetic Separation. *Analytical Chemistry* **2018**, *90* (1), 1035–1043.

(62) Gabriel, E.; Garcia, P.; Lopes, F.; Coltro, W. Paper-Based Colorimetric Biosensor for Tear Glucose Measurements. *Micromachines* **2017**, *8* (4), 104.

(63) Carrell, C.; Kava, A.; Nguyen, M.; Menger, R.; Munshi, Z.; Call, Z.; Nussbaum, M.; Henry, C. Beyond the Lateral Flow Assay: A Review of Paper-Based Microfluidics. *Microelectronic Engineering* **2019**, *206*, 45–54.

(64) Oyama, Y.; Osaki, T.; Kamiya, K.; Sawai, M.; Sakai, M.; Takeuchi, S. A Sensitive Point-of-Care Testing Chip Utilizing Superabsorbent Polymer for the Early Diagnosis of Infectious Disease. *Sensors and Actuators B: Chemical* **2017**, *240*, 881–886.

(65) Hiratsuka, M.; Ebisawa, A.; Matsubara, Y.; Kure, S.; Konno, Y.; Sasaki, T.; Mizugaki, M. Genotyping of Single Nucleotide Polymorphisms (SNPs) Influencing Drug Response by Competitive Allele-Specific Short Oligonucleotide Hybridization

(CASSOH) with Immunochromatographic Strip. *Drug Metabolism and Pharmacokinetics* **2004**, *19* (4), 303–307.

(66) Storhoff, J. J.; Elghanian, R.; Mucic, R. C.; Mirkin, C. A.; Letsinger, R. L. One-Pot Colorimetric Differentiation of Polynucleotides with Single Base Imperfections Using Gold Nanoparticle Probes. *Journal of the American Chemical Society* **1998**, *120* (9), 1959–1964.

(67) Kaneko, K.; Hara, M.; Nishino, T.; Maruyama, T. One-Step Biotinylation of Cellulose Paper by Polymer Coating to Prepare a Paper-Based Analytical Device. *Analytical Chemistry* **2020**, *92* (2), 1978–1987.

(68) Yu, A.; Shang, J.; Cheng, F.; Paik, B. A.; Kaplan, J. M.; Andrade, R. B.; Ratner, D. M. Biofunctional Paper via the Covalent Modification of Cellulose. *Langmuir* **2012**, *28* (30), 11265–11273.

(69) Másson, M.; Lauritzen, E.; Holm, A. Chemical Activation of Nitrocellulose Membranes for Peptide Antigen-Antibody Binding Studies: Direct Substitution of the Nitrate Group with Diaminoalkane. *Electrophoresis* **1993**, *14* (1), 860–865.

(70) Tanaka, R.; Yuhi, T.; Nagatani, N.; Endo, T.; Kerman, K.; Takamura, Y.; Tamiya, E. A Novel Enhancement Assay for Immunochromatographic Test Strips Using Gold Nanoparticles. *Analytical and Bioanalytical Chemistry* **2006**, *385* (8), 1414–1420.

(71) Alfthan, H.; Björses, U.-M.; Tiitinen, A.; Stenman, U.-H. Specificity and Detection Limit of Ten Pregnancy Tests. *Scandinavian Journal of Clinical and Laboratory Investigation* **1993**, *53*, 105–113.

(72) Lee, J.-H.; Seo, H. S.; Kwon, J.-H.; Kim, H.-T.; Kwon, K. C.; Sim, S. J.; Cha, Y. J.; Lee, J. Multiplex Diagnosis of Viral Infectious Diseases (AIDS, Hepatitis C, and Hepatitis A) Based on Point of Care Lateral Flow Assay Using Engineered Proteinticles. *Biosensors and Bioelectronics* **2015**, *69*, 213–225.

(73) De Paschale, M. Serological Diagnosis of Epstein-Barr Virus Infection: Problems and Solutions. *World Journal of Virology* **2012**, *1* (1), 31.

(74) Liu, Y.; Liu, Y.; Diao, B.; Ren, F.; Wang, Y.; Ding, J.; Huang, Q. Diagnostic Indexes of a Rapid IgG/IgM Combined Antibody Test for SARS-CoV-2. *medRxiv* **2020**.

(75) Wen, T.; Huang, C.; Shi, F.-J.; Zeng, X.-Y.; Lu, T.; Ding, S.-N.; Jiao, Y.-J. Development of a Lateral Flow Immunoassay Strip for Rapid Detection of IgG Antibody against SARS-CoV-2 Virus. *The Analyst* **2020**, *145* (15), 5345–5352.

(76) Long, Q.-X.; Liu, B.-Z.; Deng, H.-J.; Wu, G.-C.; Deng, K.; Chen, Y.-K.; Liao, P.; Qiu, J.-F.; Lin, Y.; Cai, X.-F.; Wang, D.-Q.; Hu, Y.; Ren, J.-H.; Tang, N.; Xu, Y.-Y.; Yu, L.-H.; Mo, Z.; Gong, F.; Zhang, X.-L.; Tian, W.-G.; Hu, L.; Zhang, X.-X.; Xiang, J.-L.; Du, H.-X.; Liu, H.-W.; Lang, C.-H.; Luo, X.-H.; Wu, S.-B.; Cui, X.-P.; Zhou, Z.; Zhu, M.-M.; Wang, J.; Xue, C.-J.; Li, X.-F.; Wang, L.; Li, Z.-J.; Wang, K.; Niu, C.-C.; Yang, Q.-J.; Tang, X.-J.; Zhang, Y.; Liu, X.-M.; Li, J.-J.; Zhang, D.-C.; Zhang, F.; Liu, P.; Yuan, J.; Li, Q.; Hu, J.-L.; Chen, J.; Huang, A.-L. Antibody Responses to SARS-CoV-2 in Patients with COVID-19. *Nature Medicine* **2020**, *26* (6), 845–848.

(77) Phelan, A. L. COVID-19 Immunity Passports and Vaccination Certificates: Scientific, Equitable, and Legal Challenges. *The Lancet* **2020**, *395* (10237), 1595–1598.

(78) Burbelo, P. D.; Riedo, F. X.; Morishima, C.; Rawlings, S.; Smith, D.; Das, S.; Strich, J. R.; Chertow, D. S.; Davey, R. T.; Cohen, J. I. Sensitivity in Detection of Antibodies to Nucleocapsid and Spike Proteins of Severe Acute Respiratory Syndrome Coronavirus 2 in Patients With Coronavirus Disease 2019. *The Journal of Infectious Diseases* **2020**, *222* (2), 206–213.

(79) Wu, F.; Wang, A.; Liu, M.; Wang, Q.; Chen, J.; Xia, S.; Ling, Y.; Zhang, Y.; Xun, J.; Lu, L.; Jiang, S.; Lu, H.; Wen, Y.; Huang, J. Neutralizing Antibody Responses to SARS-CoV-2 in a COVID-19 Recovered Patient Cohort and Their Implications. *medRxiv* **2020**.

(80) Ward, H.; Cooke, G.; Atchison, C.; Whitaker, M.; Elliott, J.; Moshe, M.; Brown, J. C.; Flower, B.; Daunt, A.; Ainslie, K.; Ashby, D.; Donnelly, C.; Riley, S.; Darzi, A.; Barclay, W.; Elliott, P.; team, for the R. study. Declining Prevalence of Antibody Positivity to SARS-CoV-2: A Community Study of 365,000 Adults. *medRxiv* **2020**

(81) World Health Organization. *"Immunity Passports" in the Context of COVID-19, Scientific Brief, 24th of April*; 2020.

(82) Centres for Disease Control and Prevention. Overview of Testing for SARS-CoV-2 (COVID-19) | CDC https://www.cdc.gov/coronavirus/2019-ncov/hcp/testing-overview.html (accessed Nov 2, 2020).

(83) Howes, P. D.; Chandrawati, R.; Stevens, M. M. Colloidal Nanoparticles as Advanced Biological Sensors. *Science* **2014**, *346* (6205), 53–64.

(84) Dreaden, E. C.; Alkilany, A. M.; Huang, X.; Murphy, C. J.; El-Sayed, M. A. The Golden Age: Gold Nanoparticles for Biomedicine. *Chem. Soc. Rev.* **2012**, *41* (7), 2740–2779.

(85) Roduner, E. Size Matters: Why Nanomaterials Are Different. *Chemical Society Reviews* **2006**, *35* (7), 583.

(86) Mie, G. Beiträge Zur Optik Trüber Medien, Speziell Kolloidaler Metallösungen. *Annalen der Physik* **1908**, *330* (3), 377–445.

(87) Faraday, M. X. The Bakerian Lecture. —Experimental Relations of Gold (and Other Metals) to Light. *Philosophical Transactions of the Royal Society of London* **1857**, *147*, 145–181.

(88) Bhagyaraj, S. M.; Oluwafemi, O. S. Nanotechnology: The Science of the Invisible. In *Synthesis of Inorganic Nanomaterials*; Woodhead Publishing, 2018; pp 1–18.

(89) Eustis, S.; El-Sayed, M. A. Why Gold Nanoparticles Are More Precious than Pretty Gold: Noble Metal Surface Plasmon Resonance and Its Enhancement of the Radiative and Nonradiative Properties of Nanocrystals of Different Shapes. *Chemical Society Reviews* **2006**, *35*, 209–217.

(90) Amendola, V.; Pilot, R.; Frasconi, M.; Maragò, O. M.; Iatì, M. A. Surface Plasmon Resonance in Gold Nanoparticles: A Review. *Journal of Physics: Condensed Matter* **2017**, *29* (20), 203002.

(91) Kreibig, U.; Vollmer, M. *Optical Properties of Metal Clusters*; Springer Series in Materials Science; Springer Berlin Heidelberg: Berlin, Heidelberg, Heidelberg, 1995; Vol. 25.

(92) Maier, S. A. *Plasmonics: Fundamentals and Applications*; Springer US: New York, NY, 2007.

(93) Petryayeva, E.; Krull, U. J. Localized Surface Plasmon Resonance: Nanostructures, Bioassays and Biosensing—A Review. *Analytica Chimica Acta* **2011**, *706* (1), 8–24.

(94) Yguerabide, J.; Yguerabide, E. E. Light-Scattering Submicroscopic Particles as Highly Fluorescent Analogs and Their Use as Tracer Labels in Clinical and Biological Applications: I. Theory. *Analytical Biochemistry* **1998**, *262* (2), 137–156.

(95) Liu, X.; Atwater, M.; Wang, J.; Huo, Q. Extinction Coefficient of Gold Nanoparticles with Different Sizes and Different Capping Ligands. *Colloids and Surfaces B: Biointerfaces* **2007**, *58* (1), 3–7.

(96) Paramelle, D.; Sadovoy, A.; Gorelik, S.; Free, P.; Hobley, J.; Fernig, D. G. A Rapid Method to Estimate the Concentration of Citrate Capped Silver Nanoparticles from UV-Visible Light Spectra. *The Analyst* **2014**, *139* (19), 4855–4861.

(97) Taniguchi, M.; Lindsey, J. S. Database of Absorption and Fluorescence Spectra of >300 Common Compounds for Use in PhotochemCAD. *Photochemistry and Photobiology* **2018**, *94* (2), 290–327.

(98) Joseph, M. M.; Narayanan, N.; Nair, J. B.; Karunakaran, V.; Ramya, A. N.; Sujai, P. T.; Saranya, G.; Arya, J. S.; Vijayan, V. M.; Maiti, K. K. Exploring the Margins of SERS in Practical Domain: An Emerging Diagnostic Modality for Modern Biomedical Applications. *Biomaterials* **2018**, *181*, 140–181.

(99) García, I.; Mosquera, J.; Plou, J.; Liz-Marzán, L. M. Plasmonic Detection of Carbohydrate-Mediated Biological Events. *Advanced Optical Materials* **2018**, *6* (23), 1800680.

(100) Craig, D.; Simpson, J.; Faulds, K.; Graham, D. Formation of SERS Active Nanoparticle Assemblies via Specific Carbohydrate–Protein Interactions. *Chem. Commun.* **2013**, *49* (1), 30–32.

(101) Langer, J.; García, I.; Liz-Marzán, L. M. Real-Time Dynamic SERS Detection of Galectin Using Glycan-Decorated Gold Nanoparticles. *Faraday Discussions* **2017**, *205* (0), 363–375.

(102) van Lierop, D.; Faulds, K.; Graham, D. Separation Free DNA Detection Using Surface Enhanced Raman Scattering. *Analytical Chemistry* **2011**, *83* (15), 5817–5821.

(103) Turkevich, J.; Stevenson, P. C.; Hillier, J. A Study of the Nucleation and Growth Processes in the Synthesis of Colloidal Gold. *Discussions of the Faraday Society* **1951**, *11*, 55–75.

(104) Ziegler, C.; Eychmüller, A. Seeded Growth Synthesis of Uniform Gold Nanoparticles with Diameters of 15−300 Nm. *The Journal of Physical Chemistry C* **2011**, *115* (11), 4502–4506.

(105) Bastús, N. G.; Comenge, J.; Puntes, V. Kinetically Controlled Seeded Growth Synthesis of Citrate-Stabilized Gold Nanoparticles of up to 200 Nm: Size Focusing versus Ostwald Ripening. *Langmuir* **2011**, *27* (17), 11098–11105.

(106) Venkataramasubramani, M.; Tang, L. Development of Gold Nanorod Lateral Flow Test for Quantitative Multi-Analyte Detection. In *IFMBE Proceedings*; 2009; pp 199–202.

(107) Sajid, M.; Kawde, A.-N.; Daud, M. Designs, Formats and Applications of Lateral Flow Assay: A Literature Review. *Journal of Saudi Chemical Society* **2015**, *19* (6), 689–705.

(108) Lu, X.; Mei, T.; Guo, Q.; Zhou, W.; Li, X.; Chen, J.; Zhou, X.; Sun, N.; Fang, Z. Improved Performance of Lateral Flow Immunoassays for Alpha-Fetoprotein and Vanillin by Using Silica Shell-Stabilized Gold Nanoparticles. *Mikrochimica acta* **2018**, *186* (1), 2.

(109) Wu, J.; Ma, J.; Wang, H.; Qin, D.; An, L.; Ma, Y.; Zheng, Z.; Hua, X.; Wang, T.; Wu, X. Rapid and Visual Detection of Benzothiostrobin Residue in Strawberry Using Quantum Dot-Based Lateral Flow Test Strip. *Sensors and Actuators B: Chemical* **2019**, *283*, 222–229.

(110) Yu, L.; Li, P.; Ding, X.; Zhang, Q. Graphene Oxide and Carboxylated Graphene Oxide: Viable Two-Dimensional Nanolabels for Lateral Flow Immunoassays. *Talanta* **2017**, *165*, 167–175.

(111) Yao, L.; Teng, J.; Zhu, M.; Zheng, L.; Zhong, Y.; Liu, G.; Xue, F.; Chen, W. MWCNTs Based High Sensitive Lateral Flow Strip Biosensor for Rapid Determination of Aqueous Mercury Ions. *Biosensors and Bioelectronics* **2016**, *85*, 331–336.

(112) Dou, L.; Bu, T.; Zhang, W.; Zhao, B.; Yang, Q.; Huang, L.; Li, S.; Yang, C.; Wang, J.; Zhang, D. Chemical-Staining Based Lateral Flow Immunoassay: A Nanomaterials-Free and Ultra-Simple Tool for a Small Molecule Detection. *Sensors and Actuators B: Chemical* **2019**, *279*, 427–432.

(113) Peeling, R. W.; Mabey, D. Point-of-Care Tests for Diagnosing Infections in the Developing World. *Clinical Microbiology and Infection* **2010**, *16*, 1062–1069.

(114) Morel, C. M. Neglected Diseases: Under-funded Research and Inadequate Health Interventions. *EMBO reports* **2003**, *4*, S35–S38.

(115) Weiss, D. J.; Lucas, T. C. D.; Nguyen, M.; Nandi, A. K.; Bisanzio, D.; Battle, K. E.; Cameron, E.; Twohig, K. A.; Pfeffer, D. A.; Rozier, J. A.; Gibson, H. S.; Rao, P. C.; Casey, D.; Bertozzi-Villa, A.; Collins, E. L.; Dalrymple, U.; Gray, N.; Harris, J. R.; Howes, R. E.; Kang, S. Y.; Keddie, S. H.; May, D.; Rumisha, S.; Thorn, M. P.; Barber, R.; Fullman, N.; Huynh, C. K.; Kulikoff, X.; Kutz, M. J.; Lopez, A. D.; Mokdad, A. H.; Naghavi, M.; Nguyen, G.; Shackelford, K. A.; Vos, T.; Wang, H.; Smith, D. L.; Lim, S. S.; Murray, C. J. L.; Bhatt, S.; Hay, S. I.; Gething, P. W. Mapping the Global Prevalence, Incidence, and Mortality of Plasmodium Falciparum, 2000-17: A Spatial and Temporal Modelling Study. *The Lancet* **2019**, *394* (10195), 322–331.

(116) Hay, S. I.; Snow, R. W. The Malaria Atlas Project: Developing Global Maps of Malaria Risk. *PLoS Medicine* **2006**, *3* (12), e473.

(117) World Health Organization. *Global Report on Antimalarial Drug Efficacy and Drug Resistance: 2000-2010*; 2010.

(118) Dondorp, A. M.; Nosten, F.; Yi, P.; Das, D.; Phyo, A. P.; Tarning, J.; Lwin, K. M.; Ariey, F.; Hanpithakpong, W.; Lee, S. J.; Ringwald, P.; Silamut, K.; Imwong, M.; Chotivanich, K.; Lim, P.; Herdman, T.; An, S. S.; Yeung, S.; Singhasivanon, P.; Day, N. P. J.; Lindegardh, N.; Socheat, D.; White, N. J. Artemisinin Resistance in Plasmodium Falciparum Malaria. *New England Journal of Medicine* **2009**, *361* (5), 455–467.

(119) Fairhurst, R. M.; Dondorp, A. M. Artemisinin-Resistant Plasmodium Falciparum Malaria. *Microbiology Spectrum* **2016**, *4* (3), doi:10.1128/microbiolspec.EI10-0013-2016.

(120) Otienoburu, S. D.; Suay, I.; Garcia, S.; Thomas, N. V.; Srisutham, S.; Björkman, A.; Humphreys, G. S. An Online Mapping Database of Molecular Markers of Drug Resistance in Plasmodium Falciparum: The ACT Partner Drug Molecular Surveyor. *Malaria Journal* **2019**, *18* (1), 12–21.

(121) Shahinas, D.; Lau, R.; Khairnar, K.; Hancock, D.; Pillai, D. R. Artesunate Misuse and Plasmodium Falciparum Malaria in Traveler Returning from Africa. *Emerging Infectious Diseases* **2010**, *16* (10), 1608–1610.

(122) White, N. J. Antimalarial Drug Resistance. *The Journal of clinical investigation* **2004**, *113* (8), 1084–1092.

(123) Elmannan, A. A. A.; Elmardi, K. A.; Idris, Y. A.; Spector, J. M.; Ali, N. A.; Malik, E. M. Anti-Malarial Prescribing Practices in Sudan Eight Years after Introduction of Artemisinin-Based Combination Therapies and Implications for Development of Drug Resistance. *BMC Pharmacology and Toxicology 2015 16:1* **2015**, *360* (5), 491–499.

(124) Biamonte, M. A.; Wanner, J.; Le Roch, K. G. Recent Advances in Malaria Drug Discovery. *Bioorganic & Medicinal Chemistry Letters* **2013**, *23*, 2829–2843.

(125) World Health Organization. *Guidelines for the Treatment of Malaria*, 2nd ed.; World Health Organization, 2010.

(126) UNICEF. *Malaria Rapid Diagnostic Tests Market & Supply Update*; 2016.

(127) World Health Organization. *How To Use a Rapid Diagnostic Test (RDT)*; 2008.

(128) Njau, J. D.; Goodman, C. A.; Kachur, S. P.; Mulligan, J.; Munkondya, J. S.; Mchomvu, N.; Abdulla, S.; Bloland, P.; Mills, A. The Costs of Introducing Artemisinin-Based Combination Therapy: Evidence from District-Wide Implementation in Rural Tanzania. *Malaria Journal* **2008**, *7* (1), 4–17.

(129) Olliaro, P.; Taylor, W. R. J.; Rigal, J.; Mulligan, J.; Munkondya, J. S.; Mchomvu, N.; Abdulla, S.; Bloland, P.; Mills, A. Controlling Malaria: Challenges and Solutions. *Tropical Medicine and International Health* **2001**, *6* (11), 922–927.

(130) Ezennia, I. J.; Nduka, S. O.; Ekwunife, O. I. Cost Benefit Analysis of Malaria Rapid Diagnostic Test: The Perspective of Nigerian Community Pharmacists. *Malaria Journal* **2017**, *16* (1), 7–16.

(131) Rock, E. P.; Marsh, K.; Saul, A. J.; Wellems, T. E.; Taylor, D. W.; Maloy, W. L.; Howard, R. J. Comparative Analysis of the Plasmodium Falciparum Histidine-Rich Proteins HRP-I, HRP-II and HRP-III in Malaria Parasites of Diverse Origin. *Parasitology* **1987**, *95 (Pt 2)*, 209–227.

(132) Moody, A. Rapid Diagnostic Tests for Malaria Parasites. *Clinical microbiology reviews* **2002**, *15* (1), 66–78.

(133) Barber, B. E.; Grigg, M. J.; William, T.; Yeo, T. W.; Anstey, N. M. The Treatment of Plasmodium Knowlesi Malaria. *Trends in Parasitology* **2017**, *33* (3), 242–253.

(134) Abba, K.; Deeks, J. J.; Olliaro, P. L.; Naing, C.-M.; Jackson, S. M.; Takwoingi, Y.; Donegan, S.; Garner, P. Rapid Diagnostic Tests for Diagnosing Uncomplicated P. Falciparum Malaria in Endemic Countries. *Cochrane Database of Systematic Reviews* **2011**, No. 7.

(135) Wilson, M. L. Malaria Rapid Diagnostic Tests. *Clinical Infectious Diseases* **2012**, *54* (11), 1637–1641.

(136) Tolia, N. H.; Enemark, E. J.; Sim, B. K. L.; Joshua-Tor, L. Structural Basis for the EBA-175 Erythrocyte Invasion Pathway of the Malaria Parasite Plasmodium Falciparum. *Cell* **2005**, *122* (2), 183–193.

(137) Field, J.; Shute, P.; Sandosham, A. *The Microscopic Diagnosis of Human Malaria*; Kuala Lumpur, 1956.

(138) Cordray, M. S.; Richards-Kortum, R. R. Review: Emerging Nucleic Acid-Based Tests for Point-of-Care Detection of Malaria. *Am. J. Trop. Med. Hyg* **2012**, *87* (2), 223–230.

(139) Coleman, R. E.; Maneechai, N.; Rachaphaew, N.; Kumpitak, C.; Miller, R. S.; Soyseng, V.; Thimasarn, K.; Sattabongkot, J. Comparison of Field and Expert Laboratory Microscopy for Active Surveillance for Asymptomatic Plasmodium Falciparum and Plasmodium Vivax in Western Thailand. *American Journal of Tropical Medicine and Hygiene* **2002**, *67*, 141–144.

(140) Raftery, P.; Condell, O.; Wasunna, C.; Kpaka, J.; Zwizwai, R.; Nuha, M.; Fallah, M.; Freeman, M.; Harris, V.; Miller, M.; Baller, A.; Massaquoi, M.; Katawera, V.; Saindon, J.; Bemah, P.; Hamblion, E.; Castle, E.; Williams, D.; Gasasira, A.; Nyenswah, T. Establishing Ebola Virus Disease (EVD) Diagnostics Using GeneXpert Technology at a Mobile Laboratory in Liberia: Impact on Outbreak Response, Case Management and Laboratory Systems Strengthening. *PLOS Neglected Tropical Diseases* **2018**, *12* (1), e0006135.

(141) United States Food and Drug Association. *Xpert Ebola Assay (Cepheid) - FDA Emergency Use Authorization - March 23, 2015*; 2015.

(142) Phan, J. C.; Pettitt, J.; George, J. S.; Fakoli, L. S.; Taweh, F. M.; Bateman, S. L.; Bennett, R. S.; Norris, S. L.; Spinnler, D. A.; Pimentel, G.; Sahr, P. K.; Bolay, F. K.; Schoepp, R. J. Lateral Flow Immunoassays for Ebola Virus Disease Detection in Liberia. *Journal of Infectious Diseases* **2016**, *214* (suppl 3), S222–S228.

(143) Wonderly, B.; Jones, S.; Gatton, M. L.; Barber, J.; Killip, M.; Hudson, C.; Carter, L.; Brooks, T.; Simpson, A. J. H.; Semper, A.; Urassa, W.; Chua, A.; Perkins, M.; Boehme, C. Comparative Performance of Four Rapid Ebola Antigen-Detection Lateral Flow Immunoassays during the 2014-2016 Ebola Epidemic in West Africa. *PLOS ONE* **2019**, *14* (3), e0212113.

(144) World Health Organisation. *Interim Guidance on the Use of Rapid Ebola Antigen Detection Tests*; 2015.

(145) Lazer, D.; Baum, M. A.; Quintana, A.; Druckman, J.; Della, J.; Simonson, M. *The State Of The Nation: A 50-State Covid-19 Survey - Report #8: Failing the Test: Waiting Times for COVID Diagnostic Tests Across The U.S*; 2020.

(146) Hannah Ritchie; Mathieu, E.; Rodés-Guirao, L.; Appel, C.; Giattino, C.; Ortiz-Ospina, E.; Hasell, J.; Macdonald, B.; Beltekian, D.; Roser, M. Coronavirus Pandemic (COVID-19) Statistics and Research https://ourworldindata.org/coronavirus (accessed Jul 31, 2020).

(147) Abedini, Z.; Sari, A. A.; Foroushani, A. R.; Jaafaripooyan, E. Diffusion of Advanced Medical Imaging Technology, CT, and MRI Scanners, in Iran: A Qualitative Study of Determinants. *The International Journal of Health Planning and Management* **2019**, *34* (1), e397–e410.

(148) Mahdavi, A.; Khalili, N.; Davarpanah, A. H.; Faghihi, T.; Mahdavi, A.; Haseli, S.; Sabri, A.; Kahkouee, S.; Kazemi, M. A.; Mehrian, P.; Falahati, F.; Bakhshayeshkaram, M.; Sanei Taheri, M. Radiologic Management of COVID-19: Preliminary Experience of the Iranian Society of Radiology COVID-19 Consultant Group (ISRCC). *Iranian Journal of Radiology* **2020**, *17* (2), e102324.

(149) Fields, B. K. K.; Demirjian, N. L.; Gholamrezanezhad, A. Coronavirus Disease 2019 (COVID-19) Diagnostic Technologies: A Country-Based Retrospective Analysis of Screening and Containment Procedures during the First Wave of the Pandemic. *Clinical Imaging* **2020**, *67*, 219–225.

(150) Niemz, A.; Ferguson, T. M.; Boyle, D. S. Point-of-Care Nucleic Acid Testing for Infectious Diseases. *Trends in Biotechnology* **2011**, *29* (5), 240–250.

(151) Hattori, T.; Chagan-Yasutan, H.; Shiratori, B.; Egawa, S.; Izumi, T.; Kubo, T.; Nakajima, C.; Suzuki, Y.; Niki, T.; Alisjahbana, B.; Telan, E. Development of Point-of-Care Testing for Disaster-Related Infectious Diseases. *The Tohoku journal of experimental medicine* **2016**, *238* (4), 287–293.

(152) Cao, Y.; Wang, L.; Duan, L.; Li, J.; Ma, J.; Xie, S.; Shi, L.; Li, H. Development of a Real-Time Fluorescence Loop-Mediated Isothermal Amplification Assay for Rapid and Quantitative Detection of Ustilago Maydis. *Scientific Reports* **2017**, *7* (1), 13394.

(153) Garrido-Maestu, A.; Azinheiro, S.; Carvalho, J.; Abalde-Cela, S.; Carbó-Argibay, E.; Diéguez, L.; Piotrowski, M.; Kolen'ko, Y. V.; Prado, M. Combination of Microfluidic Loop-Mediated Isothermal Amplification with Gold Nanoparticles for Rapid Detection of Salmonella Spp. in Food Samples. *Frontiers in Microbiology* **2017**, *8*, 2159.

(154) Patel, J. C.; Lucchi, N. W.; Srivastava, P.; Lin, J. T.; Sug-aram, R.; Aruncharus, S.; Bharti, P. K.; Shukla, M. M.; Congpuong, K.; Satimai, W.; Singh, N.; Udhayakumar, V.; Meshnick, S. R. Field Evaluation of a Real-Time Fluorescence Loop-Mediated Isothermal Amplification Assay, RealAmp, for the Diagnosis of Malaria in Thailand and India. *Journal of Infectious Diseases* **2014**, *210* (8), 1180–1187.

(155) Hsiang, M. S.; Greenhouse, B.; Rosenthal, P. J. Point of Care Testing for Malaria Using LAMP, Loop Mediated Isothermal Amplification. *Journal of Infectious Diseases* **2014**, *210* (8), 1167–1169.

(156) Park, G.-S.; Ku, K.; Baek, S.-H.; Kim, S.-J.; Kim, S. Il; Kim, B.-T.; Maeng, J.-S. Development of Reverse Transcription Loop-Mediated Isothermal Amplification Assays Targeting Severe Acute Respiratory Syndrome Coronavirus 2 (SARS-CoV-2). *The Journal of Molecular Diagnostics* **2020**, *22* (6), 729–735.

(157) Aerts, C.; Vink, M.; Pashtoon, S. J.; Nahzat, S.; Picado, A.; Cruz, I.; Sicuri, E. Cost Effectiveness of New Diagnostic Tools for Cutaneous Leishmaniasis in Afghanistan. *Applied Health Economics and Health Policy* **2019**, *17* (2), 213–230.

(158) Nguyen, N. N. T.; McCarthy, C.; Lantigua, D.; Camci-Unal, G. Development of Diagnostic Tests for Detection of SARS-CoV-2. *Diagnostics* **2020**, *10* (11), 905.

(159) Kailasa, S. K.; Mehta, V. N.; Koduru, J. R.; Basu, H.; Singhal, R. K.; Murthy, Z. V. P.; Park, T.-J. An Overview of Molecular Biology and Nanotechnology Based Analytical Methods for the Detection of SARS-CoV-2: Promising Biotools for the Rapid Diagnosis of COVID-19. *The Analyst* **2021**, *146* (5), 1489–1513.

(160) Shiaelis, N.; Tometzki, A.; Peto, L.; McMahon, A.; Hepp, C.; Bickerton, E.; Favard, C.; Muriaux, D.; Andersson, M.; Oakley, S.; Vaughan, A.; Matthews, P. C.; Stoesser, N.; Crook, D.; Kapanidis, A. N.; Robb, N. C. Virus Detection and Identification in Minutes Using Single-Particle Imaging and Deep Learning. *medRxiv*. 2020.

(161) Stauffer, W. M.; Cartwright, C. P.; Olson, D. A.; Juni, B. A.; Taylor, C. M.; Bowers, S. H.; Hanson, K. L.; Rosenblatt, J. E.; Boulware, D. R. Diagnostic Performance of Rapid Diagnostic Tests versus Blood Smears for Malaria in US Clinical Practice. *Clinical Infectious Diseases* **2009**, *49* (6), 908–913.

(162) Tawiah, T.; Hansen, K. S.; Baiden, F.; Bruce, J.; Tivura, M.; Delimini, R.; Amengo-Etego, S.; Chandramohan, D.; Owusu-Agyei, S.; Webster, J. Cost-Effectiveness Analysis of Test-Based versus Presumptive Treatment of Uncomplicated Malaria in Children under Five Years in an Area of High Transmission in Central Ghana. *PLOS ONE* **2016**, *11* (10), e0164055.

(163) Jorgensen, P.; Chanthap, L.; Rebueno, A.; Tsuyuoka, R.; Bell, D. Malaria Rapid Diagnostic Tests in Tropical Climates: The Need for a Cool Chain. *American Journal of Tropical Medicine and Hygiene* **2006**, *74* (5), 750–754.

(164) Hawkes, M.; Katsuva, J. P.; Masumbuko, C. K. Use and Limitations of Malaria Rapid Diagnostic Testing by Community Health Workers in War-Torn Democratic Republic of Congo. *Malaria Journal* **2009**, *8* (1), 308.

(165) Jorgensen, P.; Chanthap, L.; Rebueno, A.; Tsuyuoka, R.; Bell, D. Malaria Rapid Diagnostic Tests in Tropical Climates: The Need for a Cool Chain. *American Journal of Tropical Medicine and Hygiene* **2006**, *74* (5), 750–754.

(166) Mao, X.; Ma, Y.; Zhang, A.; Zhang, L.; Zeng, L.; Liu, G. Disposable Nucleic Acid Biosensors Based on Gold Nanoparticle Probes and Lateral Flow Strip. *Analytical Chemistry* **2009**, *81* (4), 1660–1668.

(167) Damborský, P.; Koczula, K. M.; Gallotta, A.; Katrlík, J. Lectin-Based Lateral Flow Assay: Proof-of-Concept. *The Analyst* **2016**, *141* (23), 6444–6448.

(168) Bertozzi, C. R.; Kiessling; L., L.; Kiessling, L. L. Chemical Glycobiology. *Science* **2001**, *291* (5512), 2357–2364.

(169) Levine, D. P. Vancomycin: A History. *Clinical Infectious Diseases* **2006**, *42* (Supplement_1), S5–S12.

(170) Wang, Y.-C.; Peterson, S. E.; Loring, J. F. Protein Post-Translational Modifications and Regulation of Pluripotency in Human Stem Cells. *Nature Publishing Group* **2013**, *24* (24), 143–160.

(171) Apweiler, R.; Hermjakob, H.; Sharon, N. On the Frequency of Protein Glycosylation, as Deduced from Analysis of the SWISS-PROT Database. *Biochimica et Biophysica Acta - General Subjects* **1999**, *1473* (1), 4–8.

(172) Flynn, R. A.; Pedram, K.; Malaker, S. A.; Batista, P. J.; Smith, B. A. H.; Johnson, A. G.; George, B. M.; Majzoub, K.; Villalta, P. W.; Carette, J. E.; Bertozzi, C. R. Small RNAs Are Modified with N-Glycans and Displayed on the Surface of Living Cells. *Cell* **2021**, *184* (12), 3109-3124.e22.

(173) Dedola, S.; Rugen, M. D.; Young, R. J.; Field, R. A. Revisiting the Language of Glycoscience: Readers, Writers and Erasers in Carbohydrate Biochemistry. *ChemBioChem* **2020**, *21* (3), 423–427.

(174) Haltiwanger, R. S. Regulation of Signal Transduction by Glycosylation. *International Journal of Experimental Pathology* **2004**, *85* (4), A49–A77.

(175) Bustamante, J. J.; Gonzalez, L.; Carroll, C. A.; Weintraub, S. T.; Aguilar, R. M.; Muñoz, J.; Martinez, A. O.; Haro, L. S. O-Glycosylated 24 KDa Human Growth Hormone Has a Mucin-like Biantennary Disialylated Tetrasaccharide Attached at Thr-60. *Proteomics* **2009**, *9* (13), 3474–3488.

(176) Varki, A.; Kannagi, R.; Toole, B. P. *Glycosylation Changes in Cancer*; Cold Spring Harbor Laboratory Press, 2009.

(177) Yan, Q.; Yao, D.; Wei, L. L.; Huang, Y.; Myers, J.; Zhang, L.; Xin, W.; Shim, J.; Man, Y.; Petryniak, B.; Gerson, S.; Lowe, J. B.; Zhou, L. O-Fucose Modulates Notch-Controlled Blood Lineage Commitment. *The American journal of pathology* **2010**, *176* (6), 2921–2934.

(178) Shental-Bechor, D.; Levy, Y. Folding of Glycoproteins: Toward Understanding the Biophysics of the Glycosylation Code. *Current Opinion in Structural Biology* **2009**, *19* (5), 524–533.

(179) Helenius, A.; Aebi, M. Roles of N-Linked Glycans in the Endoplasmic Reticulum. *Annual Review of Biochemistry* **2004**, *73* (1), 1019–1049.

(180) Marth, J. D.; Grewal, P. K. Mammalian Glycosylation in Immunity. *Nature Reviews Immunology* **2008**, *8* (11), 874–887.

(181) Yilmaz, O.; Afsar, B.; Ortiz, A.; Kanbay, M. The Role of Endothelial Glycocalyx in Health and Disease. *Clinical Kidney Journal* **2019**, *12* (5), 611–619.

(182) Daffé, M.; Etienne, G. The Capsule of Mycobacterium Tuberculosis and Its Implications for Pathogenicity. *Tubercle and Lung Disease* **1999**, *79* (3), 153–169.

(183) Campos, M. A.; Vargas, M. A.; Regueiro, V.; Llompart, C. M.; Alberti, S.; Bengoechea, J. A. Capsule Polysaccharide Mediates Bacterial Resistance to Antimicrobial Peptides. *Infection and Immunity* **2004**, *72* (12), 7107–7114.

(184) Hori, K.; Matsumoto, S. Bacterial Adhesion: From Mechanism to Control. *Biochemical Engineering Journal* **2010**, *48* (3), 424–434.

(185) Xiong, Y.; Chen, Y.; Ding, L.; Liu, X.; Ju, H. Fluorescent Visual Quantitation of Cell-Secreted Sialoglycoconjugates by Chemoselective Recognition and Hybridization Chain Reaction. *The Analyst* **2019**, *144* (15), 4545–4551.

(186) Chaudhary, P. M.; Murthy, R. V.; Yadav, R.; Kikkeri, R. A Rationally Designed Peptidomimetic Biosensor for Sialic Acid on Cell Surfaces. *Chemical Communications* **2015**, *51* (38), 8112–8115.

(187) Long, J. S.; Mistry, B.; Haslam, S. M.; Barclay, W. S. Host and Viral Determinants of Influenza A Virus Species Specificity. *Nature Reviews Microbiology* **2019**, *17* (2), 67–81.

(188) Mostafa, A.; Abdelwhab, E.; Mettenleiter, T.; Pleschka, S. Zoonotic Potential of Influenza A Viruses: A Comprehensive Overview. *Viruses* **2018**, *10* (9), 497.

(189) Manning, J. C.; Romero, A.; Habermann, F. A.; García Caballero, G.; Kaltner, H.; Gabius, H.-J. Lectins: A Primer for Histochemists and Cell Biologists. *Histochemistry and Cell Biology* **2017**, *147* (2), 199–222.

(190) Ghazarian, H.; Idoni, B.; Oppenheimer, S. B. A Glycobiology Review: Carbohydrates, Lectins and Implications in Cancer Therapeutics. *Acta Histochemica* **2011**, *113* (3), 236–247.

(191) Lindberg, A. A.; Brown, J. E.; Strömberg, N.; Westling-Ryd, M.; Schultz, J. E.; Karlsson, K. A. Identification of the Carbohydrate Receptor for Shiga Toxin Produced by Shigella Dysenteriae Type 1. *The Journal of biological chemistry* **1987**, *262* (4), 1779–1785.

(192) Richards, R. L.; Moss, J.; Alving, C. R.; Fishman, P. H.; Brady, R. O. Choleragen (Cholera Toxin): A Bacterial Lectin. *Proceedings of the National Academy of Sciences of the United States of America* **1979**, *76* (4), 1673–1676.

(193) Li, S. S.; Wei, C. H.; Lin, J.-Y.; Tung, T.-C. Amino-Terminal Sequences of the Anti-Tumor Lectin Ricin A- and B-Chains. *Biochemical and Biophysical Research Communications* **1975**, *65* (4), 1191–1195.

(194) Sartim, M. A.; Sampaio, S. V. Snake Venom Galactoside-Binding Lectins: A Structural and Functional Overview. *Journal of Venomous Animals and Toxins including Tropical Diseases* **2015**, *21* (1), 35.

(195) Liao, W.-R.; Lin, J.-Y.; Shieh, W.-Y.; Jeng, W.-L.; Huang, R. Antibiotic Activity of Lectins from Marine Algae against Marine Vibrios. *Journal of Industrial Microbiology and Biotechnology* **2003**, *30* (7), 433–439.

(196) Jelinek, R.; Kolusheva, S. Carbohydrate Biosensors. *Chemical Reviews* **2004**, *104* (12), 5987–6016.

(197) Cunningham, S.; Gerlach, J. Q.; Kane, M.; Joshi, L. Glyco-Biosensors: Recent Advances and Applications for the Detection of Free and Bound Carbohydrates. *The Analyst* **2010**, *135* (10), 2471–2480.

(198) Zeng, X.; Andrade, C. A. S.; Oliveira, M. D. L.; Sun, X.-L. Carbohydrate--Protein Interactions and Their Biosensing Applications. *Analytical and Bioanalytical Chemistry* **2012**, *402* (10), 3161–3176.

(199) Damborský, P.; Damborská, D.; Belický, Š.; Tkáč, J.; Katrlík, J. Sweet Strategies in Prostate Cancer Biomarker Research: Focus on a Prostate Specific Antigen. *BioNanoScience* **2018**, *8* (2), 690–700.

(200) Bernardi, A.; Jiménez-Barbero, J.; Casnati, A.; De Castro, C.; Darbre, T.; Fieschi, F.; Finne, J.; Funken, H.; Jaeger, K.-E.; Lahmann, M.; Lindhorst, T. K.; Marradi, M.; Messner, P.; Molinaro, A.; Murphy, P. V; Nativi, C.; Oscarson, S.; Penadés, S.; Peri, F.; Pieters, R. J.; Renaudet, O.; Reymond, J.-L.; Richichi, B.; Rojo, J.; Sansone, F.; Schäffer, C.; Turnbull, W. B.; Velasco-Torrijos, T.; Vidal, S.; Vincent, S.; Wennekes, T.; Zuilhof, H.; Imberty, A. Multivalent Glycoconjugates as Anti-Pathogenic Agents. *Chem. Soc. Rev.* **2013**, *42* (42), 4709–4727.

(201) Jones, M. W. W.; Otten, L.; Richards, S.-J.; Lowery, R.; Phillips, D. J. J.; Haddleton, D. M. M.; Gibson, M. I. I. Glycopolymers with Secondary Binding Motifs Mimic Glycan Branching and Display Bacterial Lectin Selectivity in Addition to Affinity. *Chem. Sci.* **2014**, *5* (4), 1611–1616.

(202) Richards, S.-J.; Jones, M. W.; Hunaban, M.; Haddleton, D. M.; Gibson, M. I. Probing Bacterial-Toxin Inhibition with Synthetic Glycopolymers Prepared by Tandem Post-Polymerization Modification: Role of Linker Length and Carbohydrate Density. *Angewandte Chemie International Edition* **2012**, *51* (31), 7812–7816.

(203) Sharon, N. Carbohydrates as Future Anti-Adhesion Drugs for Infectious Diseases. *Biochimica et Biophysica Acta - General Subjects*. 2006, pp 527–537.

(204) Marradi, M.; Chiodo, F.; García, I.; Penadés, S.; Whitesides, G. M.; Lee, D. Y.; Shin, H.; Pieters, R. J.; Fuente, J. M. de la; Nishimura, S.-H.; Arosio, P.; Lascialfari, A.; Gatteschi, D.; Sangregorio, C. Glyconanoparticles as Multifunctional and Multimodal Carbohydrate Systems. *Chemical Society Reviews* **2013**, *42* (11), 4728–4745.

(205) Reichardt, N. C.; Martín-Lomas, M.; Penadés, S.; Andersson, M.; Thran, A.; Proksa, R.; Fayad, Z. A.; Cormode, D. P.; Wu, C. Y.; Wong, C. H.; Green, M. L. H.; Kostarelos, K.; Davis, B. G.; Vincent, S. P. Glyconanotechnology. *Chemical Society Reviews* **2013**, *42* (10), 4358–4376.

(206) Lui, L. T.; Xue, X.; Sui, C.; Brown, A.; Pritchard, D. I.; Halliday, N.; Winzer, K.; Howdle, S. M.; Fernandez-Trillo, F.; Krasnogor, N.; Alexander, C. Bacteria Clustering by Polymers Induces the Expression of Quorum-Sensing-Controlled Phenotypes. *Nature chemistry* **2013**, *5* (12), 1058–1065.

(207) Otten, L.; Fullam, E.; Gibson, M. I. Discrimination between Bacterial Species by Ratiometric Analysis of Their Carbohydrate Binding Profile. *Mol. BioSyst. Mol. BioSyst* **2016**, *12* (12), 341–344.

(208) Chang, D.; Zaia, J. Why Glycosylation Matters in Building a Better Flu Vaccine. *Molecular & Cellular Proteomics* **2019**, *18* (12), 2348–2358.

(209) Tokatlian, T.; Read, B. J.; Jones, C. A.; Kulp, D. W.; Menis, S.; Chang, J. Y. H.; Steichen, J. M.; Kumari, S.; Allen, J. D.; Dane, E. L.; Liguori, A.; Sangesland, M.; Lingwood, D.; Crispin, M.; Schief, W. R.; Irvine, D. J. Innate Immune Recognition of Glycans Targets HIV Nanoparticle Immunogens to Germinal Centers. *Science* **2019**, *363* (6427), 649–654.

(210) Boons, G.-J. Strategies in Oligosaccharide Synthesis. *Tetrahedron* **1996**, *52* (4), 1095–1121.

(211) Lepenies, B.; Yin, J.; Seeberger, P. H. Applications of Synthetic Carbohydrates to Chemical Biology. *Current Opinion in Chemical Biology* **2010**, *14* (3), 404–411.

(212) Seeberger, P. H.; Haase, W.-C. Solid-Phase Oligosaccharide Synthesis and Combinatorial Carbohydrate Libraries. *Chemical Reviews* **2000**, *100* (12), 4349–4394.

(213) Plante, Obadiah. J.; Palmacci, Emma. R.; Seeberger, P. H. Automated Solid-Phase Synthesis of Oligosaccharides. *Science* **2001**, *291* (5508), 1523–1527.

(214) Joseph, A. A.; Pardo-Vargas, A.; Seeberger, P. H. Total Synthesis of Polysaccharides by Automated Glycan Assembly. *Journal of American Chemical Society* **2020**, No. 142, 8561–8564.

(215) Guberman, M.; Seeberger, P. H. Automated Glycan Assembly: A Perspective. *Journal of the American Chemical Society* **2019**, *141* (14), 5581–5592.

(216) Flitsch, S. Chemical and Enzymatic Synthesis of Glycopolymers. *Current Opinion in Chemical Biology* **2000**, *4* (6), 619–625.

(217) Li, T.; Liu, L.; Wei, N.; Yang, J.-Y.; Chapla, D. G.; Moremen, K. W.; Boons, G.-J. An Automated Platform for the Enzyme-Mediated Assembly of Complex Oligosaccharides. *Nature Chemistry* **2019**, *11* (3), 229–236.

(218) Unverzagt, C. Chemoenzymatic Synthesis of a Sialylated Undecasaccharide–Asparagine Conjugate. *Angewandte Chemie International Edition in English* **1996**, *35* (20), 2350–2353.

(219) van den Berg, B. M.; Nieuwdorp, M.; Stroes, E.; Vink, H. Endothelial Luminal Glycocalyx: Protective Barrier between Endothelial Cells and Flowing Blood. In

Endothelial Biomedicine; Aird, W. C., Ed.; Cambridge University Press: Cambridge, 2007; pp 689–695.

(220) Koch, R. An Address on Cholera and Its Bacillus. *British Medical Journal* **1884**, *2* (1235), 403.

(221) Bharati, K.; Ganguly, N. K. Cholera Toxin: A Paradigm of a Multifunctional Protein. *The Indian journal of medical research* **2011**, *133* (2), 179–187.

(222) Ali, M.; Nelson, A. R.; Lopez, A. L.; Sack, D. A. Updated Global Burden of Cholera in Endemic Countries. *PLoS neglected tropical diseases* **2015**, *9* (6), 1–13.

(223) Staerk, J.; Ronneberger, H. J.; Wiegandt, H.; Ziegler, W. Interaction of Ganglioside GGtet1 and Its Derivatives with Choleragen. *European Journal of Biochemistry* **1974**, *48* (1), 103–110.

(224) Torgersen, M. L.; Skretting, G.; van Deurs, B.; Sandvig, K. Internalization of Cholera Toxin by Different Endocytic Mechanisms. *Journal of Cell Science* **2001**, *114* (20), 3737–3747.

(225) Basu, I.; Mukhopadhyay, C. Insights into Binding of Cholera Toxin to GM1 Containing Membrane. *Langmuir* **2014**, *30* (50), 15244–15252.

(226) Wolf, A. A.; Fujinaga, Y.; Lencer, W. I. Uncoupling of the Cholera Toxin-G(M1) Ganglioside Receptor Complex from Endocytosis, Retrograde Golgi Trafficking, and Downstream Signal Transduction by Depletion of Membrane Cholesterol. *The Journal of biological chemistry* **2002**, *277* (18), 16249–16256.

(227) Wands, A. M.; Cervin, J.; Huang, H.; Zhang, Y.; Youn, G.; Brautigam, C. A.; Matson Dzebo, M.; Björklund, P.; Wallenius, V.; Bright, D. K.; Bennett, C. S.; Wittung-Stafshede, P.; Sampson, N. S.; Yrlid, U.; Kohler, J. J. Fucosylated Molecules Competitively Interfere with Cholera Toxin Binding to Host Cells. *ACS Infectious Diseases* **2018**, *4* (5), 758–770.

(228) Reisner, Y.; Ravid, A.; Sharon, N. Use of Soybean Agglutinin for the Separation of Mouse B and T Lymphocytes. *Biochemical and Biophysical Research Communications* **1976**, *72* (4), 1585–1591.

(229) Casañas Pimentel, R. G.; Robles Botero, V.; San Martín Martínez, E.; Gómez García, C.; Hinestroza, J. P. Soybean Agglutinin-Conjugated Silver Nanoparticles

Nanocarriers in the Treatment of Breast Cancer Cells. *Journal of Biomaterials Science, Polymer Edition* **2016**, *27* (3), 218–234.

(230) Rao, V. S. R.; Lam, K.; Qasba, P. K. Three Dimensional Structure of the Soybean Agglutinin-Gal/GalNAc Complexes by Homology Modeling. *Journal of Biomolecular Structure and Dynamics* **1998**, *15* (5), 853–860.

(231) Pereira, M. E.; Kabat, E. A.; Sharon, N. Immunochemical Studies on the Specificity of Soybean Agglutinin. *Carbohydrate research* **1974**, *37* (1), 89–102.

(232) Huet, M. Factors Affecting the Molecular Structure and the Agglutinating Ability of Concanavalin A and Other Lectins. *European Journal of Biochemistry* **1975**, *59* (2), 627–632.

(233) Mandal, D. K.; Nieves, E.; Bhattacharyya, L.; Orr, G. A.; Roboz, J.; Yu, Q. -t; Brewer, C. F. Purification and Characterization of Three Isolectins of Soybean Agglutinin: Evidence for C-terminal Truncation by Electrospray Ionization Mass Spectrometry. *European Journal of Biochemistry* **1994**, *221* (1), 547–553.

(234) Ernst, B.; Magnani, J. L. From Carbohydrate Leads to Glycomimetic Drugs. *Nature Reviews Drug Discovery* **2009**, *8* (8), 661–677.

(235) Sharon, N.; Lis, H. History of Lectins: From Hemagglutinins to Biological Recognition Molecules. *Glycobiology* **2004**, *14* (11), 53R-62R.

(236) Park, S.; Lee, M.-R.; Shin, I. Construction of Carbohydrate Microarrays by Using One-Step, Direct Immobilizations of Diverse Unmodified Glycans on Solid Surfaces. *Bioconjugate Chemistry* **2009**, *20* (1), 155–162.

(237) Manimala, J. C.; Roach, T. A.; Li, Z.; Gildersleeve, J. C. High-Throughput Carbohydrate Microarray Analysis of 24 Lectins. *Angewandte Chemie International Edition* **2006**, *45* (22), 3607–3610.

(238) Wu, A. M.; Wu, J. H.; Singh, T.; Lai, L.-J.; Yang, Z.; Herp, A. Recognition Factors of Ricinus Communis Agglutinin 1 (RCA1). *Molecular Immunology* **2006**, *43* (10), 1700–1715.

(239) Baenzigers, J. U.; Fiete, D. Structural Determinants of Ricinus Communis Agglutinin and Toxin Specificity for Oligosaccharides*. *The Journal of Biological Chemistry* **1979**, *254* (19), 9795–9799.

(240) Berman, H. M.; Westbrook, J.; Feng, Z.; Gilliland, G.; Bhat, T. N.; Weissig, H.; Shindyalov, I. N.; Bourne, P. E. The Protein Data Bank. *Nucleic Acids Research* **2000**, *28* (1), 235–242.

(241) Zhang, R. G.; Scott, D. L.; Westbrook, M. L.; Nance, S.; Spangler, B. D.; Shipley, G. G.; Westbrook, E. M. The Three-Dimensional Crystal Structure of Cholera Toxin. *J.Mol.Biol.* **1995**, *251*, 563–573.

(242) Olsen, L. R.; Dessen, A.; Gupta, D.; Sabesan, S.; Sacchettini, J. C.; Brewer, C. F. X-Ray Crystallographic Studies of Unique Cross-Linked Lattices between Four Isomeric Biantennary Oligosaccharides and Soybean Agglutinin. *Biochemistry* **1997**, *36*, 15073–15080.

(243) Gabdoulkhakov, A. G.; Savochkina, Y.; Konareva, N.; Krauspenhaar, R.; Stoeva, S.; Nikonov, S. V.; Voelter, W.; Betzel, C.; Mikhailov, A. M. RCSB PDB - 1RZO: Agglutinin from Ricinus communis with galactoaza https://www.rcsb.org/structure/1RZO (accessed Jul 6, 2021).

(244) Lundquist, J. J.; Toone, E. J. The Cluster Glycoside Effect. *Chemical Reviews* **2002**, *102*, 555–578.

(245) Hořejší, V.; Chaloupecká, O.; Kocourek, J. Studies on Lectins: XLIII. Isolation and Characterization of the Lectin from Restharrow Boots (Ononis Hircina Jacq.). *Biochimica et Biophysica Acta (BBA) - General Subjects* **1978**, *539* (3), 287–293.

(246) Pan, Y.; Sackmann, E. K.; Wypisniak, K.; Hornsby, M.; Datwani, S. S.; Herr, A. E. Determination of Equilibrium Dissociation Constants for Recombinant Antibodies by High-Throughput Affinity Electrophoresis. *Scientific Reports* **2016**, *6* (1), 39774.

(247) Stubenrauch, K.; Wessels, U.; Essig, U.; Kowalewsky, F.; Vogel, R.; Heinrich, J. Characterization of Murine Anti-Human Fab Antibodies for Use in an Immunoassay for Generic Quantification of Human Fab Fragments in Non-Human Serum Samples Including Cynomolgus Monkey Samples. *Journal of Pharmaceutical and Biomedical Analysis* **2013**, *72*, 208–215.

(248) Ambrosi, M.; Cameron, N. R.; Davis, B. G. Lectins: Tools for the Molecular Understanding of the Glycocode. *Organic & Biomolecular Chemistry* **2005**, *3* (9), 1593–1608.

(249) Lee, Y. C.; Lee, R. T. Carbohydrate-Protein Interactions: Basis of Glycobiology. *Accounts of Chemical Research* **1995**, *28* (8), 321–327.

(250) Pieters, R. J. Maximising Multivalency Effects in Protein–Carbohydrate Interactions. *Organic & Biomolecular Chemistry* **2009**, *7* (10), 2013–2025.

(251) Branson, T. R.; McAllister, T. E.; Garcia-Hartjes, J.; Fascione, M. A.; Ross, J. F.; Warriner, S. L.; Wennekes, T.; Zuilhof, H.; Turnbull, W. B. A Protein-Based Pentavalent Inhibitor of the Cholera Toxin B-Subunit. *Angewandte Chemie - International Edition* **2014**, *53* (32), 8323–8327.

(252) Unverzagt, C.; Gundel, G.; Eller, S.; Schuberth, R.; Seifert, J.; Weiss, H.; Niemietz, M.; Pischl, M.; Raps, C. Synthesis of Multiantennary Complex Type N-Glycans by Use of Modular Building Blocks. *Chemistry - A European Journal* **2009**, *15* (45), 12292–12302.

(253) Ogawa, T.; Sugimoto, M.; Kitajima, T.; Sadozai, K. K.; Nukada, T. Total Synthesis of a Undecasaccharide: A Typical Carbohydrate Sequence for the Complex Type of Glycan Chains of a Glycoprotein. *Tetrahedron Letters* **1986**, *27* (47), 5739–5742.

(254) Okada, M. Molecular Design and Syntheses of Glycopolymers. *Progress in Polymer Science* **2001**, *26* (1), 67–104.

(255) Müller, C.; Despras, G.; Lindhorst, T. K. Organizing Multivalency in Carbohydrate Recognition. *Chem. Soc. Rev.* **2016**, *45* (11), 3275–3302.

(256) André, S.; Lahmann, M.; Gabius, H.-J.; Oscarson, S. Glycocluster Design for Improved Avidity and Selectivity in Blocking Human Lectin/Plant Toxin Binding to Glycoproteins and Cells. *Molecular Pharmaceutics* **2010**, *7* (6), 2270–2279.

(257) Wang, S.; Dupin, L.; Noël, M.; Carroux, C. J.; Renaud, L.; Géhin, T.; Meyer, A.; Souteyrand, E.; Vasseur, J.-J.; Vergoten, G.; Chevolot, Y.; Morvan, F.; Vidal, S. Toward the Rational Design of Galactosylated Glycoclusters That Target Pseudomonas Aeruginosa Lectin A (LecA): Influence of Linker Arms That Lead to Low-Nanomolar Multivalent Ligands. *Chemistry - A European Journal* **2016**, *22* (33), 11785–11794.

(258) Lindhorst, T. K.; Kieburg, C.; Krallmann-Wenzel, U. Inhibition of the Type 1 Fimbriae-Mediated Adhesion of Escherichia Coli to Erythrocytes by Multiantennary

α-Mannosyl Clusters: The Effect of Multivalency. *Glycoconjugate Journal* **1998**, *15*, 605–613.

(259) Porkolab, V.; Pifferi, C.; Sutkeviciute, I.; Ordanini, S.; Taouai, M.; Thépaut, M.; Vivès, C.; Benazza, M.; Bernardi, A.; Renaudet, O.; Fieschi, F. Development of C-Type Lectin-Oriented Surfaces for High Avidity Glycoconjugates: Towards Mimicking Multivalent Interactions on the Cell Surface. *Organic & Biomolecular Chemistry* **2020**, *18* (25), 4763–4772.

(260) MacPherson, I. S.; Temme, J. S.; Habeshian, S.; Felczak, K.; Pankiewicz, K.; Hedstrom, L.; Krauss, I. J. Multivalent Glycocluster Design through Directed Evolution. *Angewandte Chemie International Edition* **2011**, *50* (47), 11238–11242.

(261) Wang, Z.; Chinoy, Z. S.; Ambre, S. G.; Peng, W.; McBride, R.; de Vries, R. P.; Glushka, J.; Paulson, J. C.; Boons, G.-J. A General Strategy for the Chemoenzymatic Synthesis of Asymmetrically Branched N-Glycans. *Science* **2013**, *341* (6144), 379–383.

(262) Newkome, G. R.; Yao, Z.; Baker, G. R.; Gupta, V. K. Micelles. Part 1. Cascade Molecules: A New Approach to Micelles. A [27]-Arborol. *The Journal of Organic Chemistry* **1985**, *50* (11), 2003–2004.

(263) Tomalia, D. A.; Baker, H.; Dewald, J.; Hall, M.; Kallos, G.; Martin, S.; Roeck, J.; Ryder, J.; Smith, P. A New Class of Polymers: Starburst-Dendritic Macromolecules. *Polymer Journal* **1985**, *17* (1), 117–132.

(264) Bosman, A. W.; Janssen, H. M.; Meijer, E. W. About Dendrimers: Structure, Physical Properties, and Applications. *Chemical Reviews* **1999**, *99* (7), 1665–1688.

(265) Roy, R. Syntheses and Some Applications of Chemically Defined Multivalent Glycoconjugates. *Current Opinion in Structural Biology* **1996**, *6* (5), 692–702.

(266) Okada, M. Molecular Design and Syntheses of Glycopolymers. *Progress in Polymer Science* **2001**, *26* (1), 67–104.

(267) Kim, Y.; Zimmerman, S. C. Applications of Dendrimers in Bio-Organic Chemistry. *Current Opinion in Chemical Biology* **1998**, *2* (6), 733–742.

(268) Cloninger, M. J. Biological Applications of Dendrimers. *Current opinion in chemical biology* **2002**, *6* (6), 742–748.

(269) Lee, C. C.; MacKay, J. A.; Fréchet, J. M. J.; Szoka, F. C. Designing Dendrimers for Biological Applications. *Nature Biotechnology* **2005**, *23* (12), 1517–1526.

(270) Jayaraman, N.; Nepogodiev, S. A.; Stoddart, J. F. Synthetic Carbohydrate-Containing Dendrimers. *Chemistry - A European Journal* **1997**, *3* (8), 1193–1199.

(271) Turnbull, W. B.; Kalovidouris, S. A.; Stoddart, J. F. Large Oligosaccharide-Based Glycodendrimers Synthetic Carbohydrate Dendrimers. *Chemistry - A European Journal* **2002**, *8* (13), 2988–3000.

(272) Woller, E. K.; Cloninger, M. J. The Lectin-Binding Properties of Six Generations of Mannose-Functionalized Dendrimers. *Organic Letters* **2002**, *4* (1), 7–10.

(273) Mignani, S.; Rodrigues, J.; Tomas, H.; Roy, R.; Shi, X.; Majoral, J.-P. Bench-to-Bedside Translation of Dendrimers: Reality or Utopia? A Concise Analysis. *Advanced Drug Delivery Reviews* **2018**, *136–137*, 73–81.

(274) Abdouni, Y.; Yilmaz, G.; Becer, C. R. Sequence and Architectural Control in Glycopolymer Synthesis. *Macromolecular Rapid Communications* **2017**, *38* (24), 1700212.

(275) Pramudya, I.; Chung, H. Recent Progress of Glycopolymer Synthesis for Biomedical Applications. *Biomaterials Science* **2019**, *7* (12), 4848–4872.

(276) Becer, C. R. The Glycopolymer Code: Synthesis of Glycopolymers and Multivalent Carbohydrate-Lectin Interactions. *Macromolecular Rapid Communications* **2012**, *33* (9), 742–752.

(277) Spain, S. G.; Gibson, M. I.; Cameron, N. R. Recent Advances in the Synthesis of Well-Defined Glycopolymers. *Journal of Polymer Science Part A: Polymer Chemistry* **2007**, *45* (11), 2059–2072.

(278) von der Ehe, C.; Weber, C.; Gottschaldt, M.; Schubert, U. S. Immobilized Glycopolymers: Synthesis, Methods and Applications. *Progress in Polymer Science* **2016**, *57*, 64–102.

(279) Miura, Y.; Hoshino, Y.; Seto, H. Glycopolymer Nanobiotechnology. *Chemical Reviews* **2016**, *116* (4), 1673–1692.

(280) Sunasee, R.; Narain, R. Glycopolymers and Glyco-Nanoparticles in Biomolecular Recognition Processes and Vaccine Development. *Macromolecular Bioscience* **2013**, *13* (1), 9–27.

(281) Vázquez-Dorbatt, V.; Maynard, H. D. Biotinylated Glycopolymers Synthesized by Atom Transfer Radical Polymerization. *Biomacromolecules* **2006**, *7* (8), 2297–2302.

(282) Lowe, A. B.; Sumerlin, B. S.; McCormick, C. L. The Direct Polymerization of 2-Methacryloxyethyl Glucoside via Aqueous Reversible Addition-Fragmentation Chain Transfer (RAFT) Polymerization. *Polymer* **2003**, *44* (22), 6761–6765.

(283) Strong, L. E.; Kiessling, L. L. A General Synthetic Route to Defined, Biologically Active Multivalent Arrays. *Journal of the American Chemical Society* **1999**, *121* (26), 6193–6196.

(284) Ohno, K.; Tsujii, Y.; Miyamoto, T.; Fukuda, T.; Goto, M.; Kobayashi, K.; Akaike, T. Synthesis of a Well-Defined Glycopolymer by Nitroxide-Controlled Free Radical Polymerization. *Macromolecules* **1998**, *31* (4), 1064–1069.

(285) Godula, K.; Bertozzi, C. R. Synthesis of Glycopolymers for Microarray Applications via Ligation of Reducing Sugars to a Poly(Acryloyl Hydrazide) Scaffold. *Journal of the American Chemical Society* **2010**, *132* (29), 9963–9965.

(286) Mahon, C. S.; Fascione, M. A.; Sakonsinsiri, C.; McAllister, T. E.; Bruce Turnbull, W.; Fulton, D. A.; Turnbull, W. B.; Fulton, D. A. Templating Carbohydrate-Functionalised Polymer-Scaffolded Dynamic Combinatorial Libraries with Lectins. *Organic & Biomolecular Chemistry* **2015**, *13* (9), 2756–2761.

(287) Moad, G.; Rizzardo, E.; Postma, A.; Thang, S. H. Synthesis of Dithioester Chain Transfer Agents and Use of Bis(Thioacyl) Disulfides or Dithioesters as Chain Transfer Agents, July 20, 1998.

(288) Vinet, L.; Zhedanov, A. A "Missing" Family of Classical Orthogonal Polynomials. *Australian Journal of Chemistry* **2010**, *58* (6), 379.

(289) Moad, G.; Rizzardo, E.; Thang, S. H. Radical Addition–Fragmentation Chemistry in Polymer Synthesis. *Polymer* **2008**, *49* (5), 1079–1131.

(290) Perrier, S.; Takolpuckdee, P. Macromolecular Design via Reversible Addition-Fragmentation Chain Transfer (RAFT)/Xanthates (MADIX) Polymerization. *Journal of Polymer Science Part A: Polymer Chemistry* **2005**, *43* (22), 5347–5393.

(291) Moad, G.; Mayadunne, R. T. A.; Rizzardo, E.; Skidmore, M.; Thang, S. H. Chapter 36 - Kinetics and Mechanism of RAFT Polymerization. In *Advances in Controlled/Living Radical Polymerization*; 2003; pp 520–535.

(292) Keddie, D. J.; Moad, G.; Rizzardo, E.; Thang, S. H. RAFT Agent Design and Synthesis. *Macromolecules* **2012**, *45* (13), 5321–5342.

(293) Steinhauer, W.; Hoogenboom, R.; Keul, H.; Moeller, M. Copolymerization of 2-Hydroxyethyl Acrylate and 2-Methoxyethyl Acrylate via RAFT: Kinetics and Thermoresponsive Properties. *Macromolecules* **2010**, *43*, 7041–7047.

(294) Stenzel, M. H. Hairy Core-Shell Nanoparticles via RAFT: Where Are the Opportunities and Where Are the Problems and Challenges? *Macromolecular Rapid Communications* **2009**, *30*, 1603–1624.

(295) Otsu, T.; Yoshida, M. Role of Initiator-transfer Agent-terminator (Iniferter) in Radical Polymerizations: Polymer Design by Organic Disulfides as Iniferters. *Die Makromolekulare Chemie, Rapid Communications* **1982**, *3* (2), 127–132.

(296) Stubbs, C.; Congdon, T. R.; Gibson, M. I. Photo-Polymerisation and Study of the Ice Recrystallisation Inhibition of Hydrophobically Modified Poly(Vinyl Pyrrolidone) Co-Polymers. *European Polymer Journal* **2019**, *110*, 330–336.

(297) Chmielarz, P.; Fantin, M.; Park, S.; Isse, A. A.; Gennaro, A.; Magenau, A. J. D.; Sobkowiak, A.; Matyjaszewski, K. Electrochemically Mediated Atom Transfer Radical Polymerization (EATRP). *Progress in Polymer Science* **2017**, *69*, 47–78.

(298) Broderick, E. M.; Guo, N.; Vogel, C. S.; Xu, C.; Sutter, J.; Miller, J. T.; Meyer, K.; Mehrkhodavandi, P.; Diaconescu, P. L. Redox Control of a Ring-Opening Polymerization Catalyst. *Journal of the American Chemical Society* **2011**, *133* (24), 9278–9281.

(299) Caruso, M. M.; Davis, D. A.; Shen, Q.; Odom, S. A.; Sottos, N. R.; White, S. R.; Moore, J. S. Mechanically-Induced Chemical Changes in Polymeric Materials. *Chemical Reviews* **2009**, *109* (11), 5755–5798.

(300) Perrier, S. S. 50th Anniversary Perspective: RAFT Polymerization - A User Guide. *Macromolecules* **2017**, *50*, 7433–7447.

(301) Lewis, R. W.; Evans, R. A.; Malic, N.; Saito, K.; Cameron, N. R. Ultra-Fast Aqueous Polymerisation of Acrylamides by High Power Visible Light Direct Photoactivation RAFT Polymerisation. *Polymer Chemistry* **2018**, *9* (1), 60–68.

(302) Chen, M.; Zhong, M.; Johnson, J. A. Light-Controlled Radical Polymerization: Mechanisms, Methods, and Applications. *Chemical Reviews* **2016**, *116* (17), 10167–10211.

(303) Xue, X.; Pasparakis, G.; Halliday, N.; Winzer, K.; Howdle, S. M.; Cramphorn, C. J.; Cameron, N. R.; Gardner, P. M.; Davis, B. G.; Fernµndez-Trillo, F.; Alexander, C.; Fernández-Trillo, F.; Alexander, C. Synthetic Polymers for Simultaneous Bacterial Sequestration and Quorum Sense Interference. *Angewandte Chemie International Edition* **2011**, *50* (42), 9852–9856.

(304) Mammen, M.; Dahmann, G.; Whitesides, G. M. Effective Inhibitors of Hemagglutination by Influenza Virus Synthesized from Polymers Having Active Ester Groups. Insight into Mechanism of Inhibition. *Journal of Medicinal Chemistry* **1995**, *38* (21), 4179–4190.

(305) Pieters, R. J. Intervention with Bacterial Adhesion by Multivalent Carbohydrates. *Medicinal Research Reviews* **2007**, *27* (6), 796–816.

(306) Sigal, G. B.; Mammen, M.; Dahmann, G.; Whitesides, G. M. Polyacrylamides Bearing Pendent α-Sialoside Groups Strongly Inhibit Agglutination of Erythrocytes by Influenza Virus: The Strong Inhibition Reflects Enhanced Binding through Cooperative Polyvalent Interactions. *Journal of the American Chemical Society* **1996**, *118* (16), 3789–3800.

(307) Kruger, A. G.; Brucks, S. D.; Yan, T.; Cárcarmo-Oyarce, G.; Wei, Y.; Wen, D. H.; Carvalho, D. R.; Hore, M. J. A.; Ribbeck, K.; Schrock, R. R.; Kiessling, L. L. Stereochemical Control Yields Mucin Mimetic Polymers. *ACS Central Science* **2021**, *7* (4), acscentsci.0c01569.

(308) Nagao, M.; Kichize, M.; Hoshino, Y.; Miura, Y. Influence of Monomer Structures for Polymeric Multivalent Ligands: Consideration of the Molecular Mobility of Glycopolymers. *Biomacromolecules* **2021**, *22* (7), 3119–3127.

(309) Arimoto, H.; Oishi, T.; Nishijima, M.; Kinumi, T. Affinity of a Vancomycin Polymer with Bacterial Surface Models. *Tetrahedron Letters* **2001**, *42* (19), 3347–3350.

(310) Choi, S. K.; Myc, A.; Silpe, J. E.; Sumit, M.; Wong, P. T.; McCarthy, K.; Desai, A. M.; Thomas, T. P.; Kotlyar, A.; Holl, M. M. B.; Orr, B. G.; Baker, J. R. Dendrimer-Based Multivalent Vancomycin Nanoplatform for Targeting the Drug-Resistant Bacterial Surface. *ACS Nano* **2013**, *7* (1), 214–228.

(311) Trinadh, M.; Kannan, G.; Rajasekhar, T.; Sesha Sainath, A. V.; Dhayal, M. Synthesis of Glycopolymers at Various Pendent Spacer Lengths of Glucose Moiety and Their Effects on Adhesion, Viability and Proliferation of Osteoblast Cells. *RSC Adv.* **2014**, *4* (70), 37400–37410.

(312) Trinadh, M.; Govindaraj, K.; Santosh, V.; Dhayal, M.; Sainath, A. V. S. Synthesis of PEO-Based Di-Block Glycopolymers at Various Pendent Spacer Lengths of Glucose Moiety and Their in-Vitro Biocompatibility with MC3T3 Osteoblast Cells. *Designed Monomers and Polymers* **2016**, *19* (1), 24–33.

(313) Takasu, A.; Kojima, H. Synthesis and Ring-Opening Polymerizations of Novel S-Glycooxazolines. *Journal of Polymer Science Part A: Polymer Chemistry* **2010**, *48* (24), 5953–5960.

(314) Semsarilar, M.; Ladmiral, V.; Perrier, S. Highly Branched and Hyperbranched Glycopolymers via Reversible Addition−Fragmentation Chain Transfer Polymerization and Click Chemistry. *Macromolecules* **2010**, *43* (3), 1438–1443.

(315) Toyoshima, M.; Oura, T.; Fukuda, T.; Matsumoto, E.; Miura, Y. Biological Specific Recognition of Glycopolymer- Modified Interfaces by RAFT Living Radical Polymerization. *Polymer Journal* **2010**, *42* (2), 172–178.

(316) Miura, Y.; Ikeda, T.; Kobayashi, K. Chemoenzymatically Synthesized Glycoconjugate Polymers †. *Biomacromolecules* **2003**, *4* (2), 410–415.

(317) Boden, S.; Wagner, K.; Karg, M.; Hartmann, L. Presenting Precision Glycomacromolecules on Gold Nanoparticles for Increased Lectin Binding. *Polymers* **2017**, *9* (12), 716.

(318) Ting, S. R. S.; Min, E. H.; Escalé, P.; Save, M.; Billon, L.; Stenzel, M. H. Lectin Recognizable Biomaterials Synthesized via Nitroxide-Mediated Polymerization of a Methacryloyl Galactose Monomer. *Macromolecules* **2009**, *42* (24), 9422–9434.

(319) Ambrosi, M.; Batsanov, A. S.; Cameron, N. R.; Davis, B. G.; Howard, J. A. K.; Hunter, R. Influence of Preparation Procedure on Polymer Composition: Synthesis

and Characterisation of Polymethacrylates Bearing β-D-Glucopyranoside and β-D-Galactopyranoside Residues. *Journal of the Chemical Society, Perkin Transactions 1* **2002**, No. 1, 45–52.

(320) Tanaka, T.; Inoue, G.; Shoda, S.-I.; Kimura, Y. Protecting-Group-Free Synthesis of Glycopolymers Bearing Thioglycosides via One-Pot Monomer Synthesis from Free Saccharides. *Journal of Polymer Science Part A: Polymer Chemistry* **2014**, *52*, 3513–3520.

(321) Slavin, S.; Burns, J.; Haddleton, D. M.; Becer, C. R. Synthesis of Glycopolymers via Click Reactions. *European Polymer Journal* **2011**, *47* (4), 435–446.

(322) Ladmiral, V.; Mantovani, G.; Clarkson, G. J.; Cauet, S.; Irwin, J. L.; Haddleton, D. M. Synthesis of Neoglycopolymers by a Combination of "Click Chemistry" and Living Radical Polymerization. *Journal of the American Chemical Society* **2006**, *128* (14), 4823–4830.

(323) Li, J.; Tian, X.-Y.; Zong, L.-P.; Zhang, Q.; Zhang, X.-J.; Marks, R.; Cosnier, S.; Shan, D. Uniform and Easy-To-Prepare Glycopolymer-Brush Interface for Rapid Protein (Anti-)Adhesion Sensing. *ACS Applied Materials & Interfaces* **2019**, *11* (35), 32366–32372.

(324) Vinson, N.; Gou, Y.; Becer, C. R.; Haddleton, D. M.; Gibson, M. I. Optimised "click" Synthesis of Glycopolymers with Mono/Di- and Trisaccharides. *Polymer Chemistry* **2011**, *2* (1), 107–113.

(325) Godula, K.; Bertozzi, C. R. Synthesis of Glycopolymers for Microarray Applications via Ligation of Reducing Sugars to a Poly(Acryloyl Hydrazide) Scaffold. *Journal of the American Chemical Society* **2010**, *132* (29), 9963–9965.

(326) Gibson, M. I.; Fröhlich, E.; Klok, H.-A. Postpolymerization Modification of Poly(Pentafluorophenyl Methacrylate): Synthesis of a Diverse Water-Soluble Polymer Library. *Journal of Polymer Science Part A: Polymer Chemistry* **2009**, *47* (17), 4332–4345.

(327) Jones, M. W.; Richards, S.-J.; Haddleton, D. M.; Gibson, M. I. Poly(Azlactone)s: Versatile Scaffolds for Tandem Post-Polymerisation Modification and Glycopolymer Synthesis. *Polym. Chem.* **2013**, *4* (3), 717–723.

(328) Laezza, A.; Georgiou, P. G.; Richards, S.-J.; Baker, A. N.; Walker, M.; Gibson, M. I. Protecting Group Free Synthesis of Glyconanoparticles Using Amino–Oxy-Terminated Polymer Ligands. *Bioconjugate Chemistry* **2020**, *31* (10), 2392–2403.

(329) Yahara, I.; Edelman, G. M. Restriction of the Mobility of Lymphocyte Immunoglobulin Receptors by Concanavalin A. *Proceedings of the National Academy of Sciences* **1972**, *69* (3), 608–612.

(330) Ayres, N.; Holt, D. J.; Jones, C. F.; Corum, L. E.; Grainger, D. W. Polymer Brushes Containing Sulfonated Sugar Repeat Units: Synthesis, Characterization, and in Vitro Testing of Blood Coagulation Activation. *Journal of Polymer Science Part A: Polymer Chemistry* **2008**, *46* (23), 7713–7724.

(331) Pfaff, A.; Barner, L.; Müller, A. H. E.; Granville, A. M. Surface Modification of Polymeric Microspheres Using Glycopolymers for Biorecognition. *European Polymer Journal* **2011**, *47* (4), 805–815.

(332) Hashimoto, K.; Ohsawa, R.; Imai, N.; Okada, M. Glycopolymeric Inhibitors of ?-Glucuronidase I. Synthesis and Polymerization of Styrene Derivatives Having PendentD-Glucaric Moieties. *Journal of Polymer Science Part A: Polymer Chemistry* **1999**, *37* (3), 303–312.

(333) Mancini, R. J.; Lee, J.; Maynard, H. D. Trehalose Glycopolymers for Stabilization of Protein Conjugates to Environmental Stressors. *Journal of the American Chemical Society* **2012**, *134* (20), 8474–8479.

(334) Wilkins, L. E.; Badi, N.; Du Prez, F.; Gibson, M. I. Double-Modified Glycopolymers from Thiolactones to Modulate Lectin Selectivity and Affinity. *ACS Macro Letters* **2018**, *7* (12), 1498–1502.

(335) Terada, Y.; Hoshino, Y.; Miura, Y. Glycopolymers Mimicking GM1 Gangliosides: Cooperativity of Galactose and Neuraminic Acid for Cholera Toxin Recognition. *Chemistry – An Asian Journal* **2019**, *14* (7), 1021–1027.

(336) Kimoto, Y.; Terada, Y.; Hoshino, Y.; Miura, Y. Screening of a Glycopolymer Library of GM1 Mimics Containing Hydrophobic Units Using Surface Plasmon Resonance Imaging. *ACS Omega* **2019**, *4* (24), 20690–20696.

(337) Svennerholm, L. Interaction of Cholera Toxin and Ganglioside G(M1). *Advances in experimental medicine and biology* **1976**, *71*, 191–204.

(338) Turnbull, W. B.; Precious, B. L.; Homans, S. W. Dissecting the Cholera Toxin−Ganglioside GM1 Interaction by Isothermal Titration Calorimetry. *Journal of the American Chemical Society* **2004**, *126* (4), 1047–1054.

(339) Polizzotti, B. D.; Kiick, K. L. Effects of Polymer Structure on the Inhibition of Cholera Toxin by Linear Polypeptide-Based Glycopolymers. *Biomacromolecules* **2006**, *7* (2), 483–490.

(340) Tran, H.-A.; Kitov, P. I.; Paszkiewicz, E.; Sadowska, J. M.; Bundle, D. R. Multifunctional Multivalency: A Focused Library of Polymeric Cholera Toxin Antagonists. *Organic & biomolecular chemistry* **2011**, *9* (10), 3658–3671.

(341) Jones, M. W.; Otten, L.; Richards, S.-J.; Lowery, R.; Phillips, D. J.; Haddleton, D. M.; Gibson, M. I. Glycopolymers with Secondary Binding Motifs Mimic Glycan Branching and Display Bacterial Lectin Selectivity in Addition to Affinity. *Chemical Science* **2014**, *5* (4), 1611–1616.

(342) Martyn, B.; Biggs, C. I.; Gibson, M. I. Comparison of Systematically Functionalized Heterogeneous and Homogenous Glycopolymers as Toxin Inhibitors. *Journal of Polymer Science Part A: Polymer Chemistry* **2019**, *57* (1), 40–47.

(343) Ponader, D.; Maffre, P.; Aretz, J.; Pussak, D.; Ninnemann, N. M.; Schmidt, S.; Seeberger, P. H.; Rademacher, C.; Nienhaus, G. U.; Hartmann, L. Carbohydrate-Lectin Recognition of Sequence-Defined Heteromultivalent Glycooligomers. *Journal of the American Chemical Society* **2014**, *136* (5), 2008–2016.

(344) Wu, L.; Zhang, Y.; Li, Z.; Yang, G.; Kochovski, Z.; Chen, G.; Jiang, M. “Sweet” Architecture-Dependent Uptake of Glycocalyx-Mimicking Nanoparticles Based on Biodegradable Aliphatic Polyesters by Macrophages. *Journal of the American Chemical Society* **2017**, *139* (41), 14684–14692.

(345) Zhang, S.; Xiao, Q.; Sherman, S. E.; Muncan, A.; Ramos Vicente, A. D. M.; Wang, Z.; Hammer, D. A.; Williams, D.; Chen, Y.; Pochan, D. J.; Vértesy, S.; André, S.; Klein, M. L.; Gabius, H. J.; Percec, V. Glycodendrimersomes from Sequence-Defined Janus Glycodendrimers Reveal High Activity and Sensor Capacity for the Agglutination by Natural Variants of Human Lectins. *Journal of the American Chemical Society* **2015**, *137* (41), 13334–13344.

(346) Zhang, S.; Moussodia, R.-O.; Vértesy, S.; André, S.; Klein, M. L.; Gabius, H.-J.; Percec, V. Unraveling Functional Significance of Natural Variations of a Human Galectin by Glycodendrimersomes with Programmable Glycan Surface. *Proceedings of the National Academy of Sciences of the United States of America* **2015**, *112* (18), 5585–5590.

(347) Kumar, V.; Turnbull, W. B. Carbohydrate Inhibitors of Cholera Toxin. *Beilstein Journal of Organic Chemistry*. Beilstein-Institut 2018, pp 484–498.

(348) Branderhorst, H. M.; Liskamp, R. M. J.; Visser, G. M.; Pieters, R. J. Strong Inhibition of Cholera Toxin Binding by Galactose Dendrimers. *Chemical Communications* **2007**, No. 47, 5043.

(349) Cervin, J.; Boucher, A.; Youn, G.; Björklund, P.; Wallenius, V.; Mottram, L.; Sampson, N. S.; Yrlid, U. Fucose-Galactose Polymers Inhibit Cholera Toxin Binding to Fucosylated Structures and Galactose-Dependent Intoxication of Human Enteroids. *ACS Infectious Diseases* **2020**, *6* (5), 1192–1203.

(350) Seidi, F.; Jenjob, R.; Phakkeeree, T.; Crespy, D. Saccharides, Oligosaccharides, and Polysaccharides Nanoparticles for Biomedical Applications. *Journal of Controlled Release* **2018**, *284*, 188–212.

(351) Yilmaz, G.; Becer, C. R. Glycopolymer Code: Programming Synthetic Macromolecules for Biological Targeting. *Macromolecular Chemistry and Physics* **2020**, *221* (7), 2000006.

(352) Umemura, M.; Makimura, Y.; Itoh, M.; Yamamoto, T.; Mine, T.; Mitani, S.; Simizu, I.; Ashida, H.; Yamamoto, K. One-Step Synthesis of Efficient Binding-Inhibitor for Influenza Virus through Multiple Addition of Sialyloligosaccharides on Chitosan. *Carbohydrate Polymers* **2010**, *81* (2), 330–334.

(353) Qu, Y.; Li, Y.; Liao, S.; Sun, J.; Li, M.; Wang, D.; Xia, C.; Luo, Q.; Hu, J.; Luo, K.; Gong, Q.; Song, B. Linear and Core-Crosslinked Glycopolymer-Gadolinium Conjugates: Preparation and Their Behaviors as Nanoscale Magnetic Resonance Imaging Contrast Agents. *Journal of Biomedical Nanotechnology* **2019**, *15* (8), 1637–1653.

(354) Wang, Y.; Dai, Y.; Luo, Q.; Wei, X.; Xiao, X.; Li, H.; Hu, J.; Gong, Q.; Wu, J.; Luo, K. Tumor Environment-Responsive Degradable Branched Glycopolymer Magnetic

Resonance Imaging Contrast Agent and Its Tumor-Targeted Imaging. *Journal of Biomedical Nanotechnology* **2019**, *15* (7), 1384–1400.

(355) Cao, C.; Zhao, J.; Lu, M.; Garvey, C. J.; Stenzel, M. H. Correlation between Drug Loading Content and Biological Activity: The Complexity Demonstrated in Paclitaxel-Loaded Glycopolymer Micelle System. *Biomacromolecules* **2019**, *20* (4), 1545–1554.

(356) Wu, J.; Yuan, J.; Ye, B.; Wu, Y.; Xu, Z.; Chen, J.; Chen, J. Dual-Responsive Core Crosslinking Glycopolymer-Drug Conjugates Nanoparticles for Precise Hepatocarcinoma Therapy. *Frontiers in Pharmacology* **2018**, *9*, 663.

(357) Yilmaz, G.; Guler, E.; Geyik, C.; Demir, B.; Ozkan, M.; Odaci Demirkol, D.; Ozcelik, S.; Timur, S.; Becer, C. R. PH Responsive Glycopolymer Nanoparticles for Targeted Delivery of Anti-Cancer Drugs. *Molecular Systems Design & Engineering* **2018**, *3* (1), 150–158.

(358) Loka, R. S.; Sletten, E. T.; Barash, U.; Vlodavsky, I.; Nguyen, H. M. Specific Inhibition of Heparanase by a Glycopolymer with Well-Defined Sulfation Pattern Prevents Breast Cancer Metastasis in Mice. *ACS Applied Materials & Interfaces* **2019**, *11* (1), 244–254.

(359) Tomás, R. M. F.; Gibson, M. I. Optimization and Stability of Cell-Polymer Hybrids Obtained by "Clicking" Synthetic Polymers to Metabolically Labeled Cell Surface Glycans. *Biomacromolecules* **2019**, *20*, 2726–2736.

(360) Huang, M. L.; Smith, R. A. A.; Trieger, G. W.; Godula, K. Glycocalyx Remodeling with Proteoglycan Mimetics Promotes Neural Specification in Embryonic Stem Cells. *Journal of the American Chemical Society* **2014**, *136* (30), 10565–10568.

(361) Chikae, M.; Fukuda, T.; Kerman, K.; Idegami, K.; Miura, Y.; Tamiya, E. Amyloid-β Detection with Saccharide Immobilized Gold Nanoparticle on Carbon Electrode. *Bioelectrochemistry* **2008**, *74* (1), 118–123.

(362) Adokoh, C. K.; Quan, S.; Hitt, M.; Darkwa, J.; Kumar, P.; Narain, R. Synthesis and Evaluation of Glycopolymeric Decorated Gold Nanoparticles Functionalized with Gold-Triphenyl Phosphine as Anti-Cancer Agents. *Biomacromolecules* **2014**, *15* (10), 3802–3810.

(363) Ahmed, M.; Deng, Z.; Narain, R. Study of Transfection Efficiencies of Cationic Glyconanoparticles of Different Sizes in Human Cell Line. *ACS Applied Materials & Interfaces* **2009**, *1* (9), 1980–1987.

(364) Hucknall, A.; Rangarajan, S.; Chilkoti, A. In Pursuit of Zero: Polymer Brushes That Resist the Adsorption of Proteins. *Advanced Materials* **2009**, *21* (23), 2441–2446.

(365) Zoppe, J. O.; Ataman, N. C.; Mocny, P.; Wang, J.; Moraes, J.; Klok, H. A. Surface-Initiated Controlled Radical Polymerization: State-of-the-Art, Opportunities, and Challenges in Surface and Interface Engineering with Polymer Brushes. *Chemical Reviews* **2017**, *117* (3), 1105–1318.

(366) Michalek, L.; Barner, L.; Barner-Kowollik, C. Polymer on Top: Current Limits and Future Perspectives of Quantitatively Evaluating Surface Grafting. *Advanced Materials* **2018**, *30* (21), 1706321.

(367) Wu, L.; Glebe, U.; Böker, A. Surface-Initiated Controlled Radical Polymerizations from Silica Nanoparticles, Gold Nanocrystals, and Bionanoparticles. *Polymer Chemistry* **2015**, *6* (29), 5143–5184.

(368) Marín, M. J.; Rashid, A.; Rejzek, M.; Fairhurst, S. A.; Wharton, S. A.; Martin, S. R.; McCauley, J. W.; Wileman, T.; Field, R. A.; Russell, D. A. Glyconanoparticles for the Plasmonic Detection and Discrimination between Human and Avian Influenza Virus. *Organic & Biomolecular Chemistry* **2013**, *11* (41), 7101.

(369) Barrientos, Á. G.; De la Fuente, J. M.; Rojas, T. C.; Fernández, A.; Penadés, S. Gold Glyconanoparticles: Synthetic Polyvalent Ligands Mimicking Glycocalyx-like Surfaces as Tools for Glycobiological Studies. *Chemistry - A European Journal* **2003**, *9* (9), 1909–1921.

(370) Hernáiz, M. J.; De La Fuente, J. M.; Barrientos, Á. G.; Penadés, S. A Model System Mimicking Glycosphingolipid Clusters to Quantify Carbohydrate Self-Interactions by Surface Plasmon Resonance. *Angewandte Chemie International Edition* **2002**, *41* (9), 1554–1557.

(371) Lowe, A. B.; Sumerlin, B. S.; Donovan, M. S.; McCormick, C. L.; Barbey, R.; Lavanant, L.; Paripovic, D.; Schuwer, N.; Sugnaux, C.; Tugulu, S.; Klok, H.-A. Facile Preparation of Transition Metal Nanoparticles Stabilized by Well-Defined

(Co)Polymers Synthesized via Aqueous Reversible Addition-Fragmentation Chain Transfer Polymerization. *J. Am. Chem. Soc.* **2002**, *124* (39), 5437–5527.

(372) Lowe, A. B.; Sumerlin, B. S.; Donovan, M. S.; McCormick, C. L. Facile Preparation of Transition Metal Nanoparticles Stabilized by Well-Defined (Co)Polymers Synthesized via Aqueous Reversible Addition-Fragmentation Chain Transfer Polymerization. *J. Am. Chem. Soc.* **2002**, *124* (39), 11562–11563.

(373) Spain, S. G.; Albertin, L.; Cameron, N. R. Facile in Situ Preparation of Biologically Active Multivalent Glyconanoparticles. *Chemical Communications* **2006**, *96* (40), 4198–4200.

(374) Dave, K.; Malleswara Rao, N. N.; Trinadh, M.; Monisha, B. A.; Sesha Sainath, A. V.; Dhayal, M. Spectroscopic and Electron Microscopic Analysis of Bi-Ligand Functionalized Glycopolymer/FITC–Gold Nanoparticles. *RSC Advances* **2016**, *6* (50), 44392–44401.

(375) Jin, Y.; Wong, K. H.; Granville, A. M. Enhancement of Localized Surface Plasmon Resonance Polymer Based Biosensor Chips Using Well-Defined Glycopolymers for Lectin Detection. *Journal of Colloid and Interface Science* **2016**, *462*, 19–28.

(376) Parry, A. L.; Clemson, N. A.; Ellis, J.; Bernhard, S. S. R.; Davis, B. G.; Cameron, N. R. 'Multicopy Multivalent' Glycopolymer-Stabilized Gold Nanoparticles as Potential Synthetic Cancer Vaccines. *Journal of the American Chemical Society* **2013**, *135* (25), 9362–9365.

(377) Shen, F.-W.; Zhou, K.-C.; Cai, H.; Zhang, Y.-N.; Zheng, Y.-L.; Quan, J. One-Pot Synthesis of Thermosensitive Glycopolymers Grafted Gold Nanoparticles and Their Lectin Recognition. *Colloids and Surfaces B: Biointerfaces* **2019**, *173*, 504–511.

(378) Mizukami, K.; Takakura, H.; Matsunaga, T.; Kitano, H. Binding of Ricinus Communis Agglutinin to a Galactose-Carrying Polymer Brush on a Colloidal Gold Monolayer. *Colloids and Surfaces B: Biointerfaces* **2008**, *66* (1), 110–118.

(379) Nuß, S.; Böttcher, H.; Wurm, H.; Hallensleben, M. L. Gold Nanoparticles with Covalently Attached Polymer Chains. *Angewandte Chemie International Edition* **2001**, *40* (21), 4016–4018.

(380) Boyer, C.; Bousquet, A.; Rondolo, J.; Whittaker, M. R.; Stenzel, M. H.; Davis, T. P. Glycopolymer Decoration of Gold Nanoparticles Using a LbL Approach. *Macromolecules* **2010**, *43* (8), 3775–3784.

(381) Mirkin, C. A.; Letsinger, R. L.; Mucic, R. C.; Storhoff, J. J. A DNA-Based Method for Rationally Assembling Nanoparticles into Macroscopic Materials. *Nature* **1996**, *382* (6592), 607–609.

(382) Wang, J. L.; Edelman, G. M. Binding and Functional Properties of Concanavalin A and Its Derivatives. II. A Proteolytic Product with Saccharide Binding Activity. *Journal of Biological Chemistry* **1978**, *253* (9), 3008–3015.

(383) de Boeck, H.; Lis, H.; van Tilbeurgh, H.; Sharon, N.; Loontiens, F. G. Binding of Simple Carbohydrates and Some of Their Chromophoric Derivatives to Soybean Agglutinin as Followed by Titrimetric Procedures and Stopped Flow Kinetics. *Journal of Biological Chemistry* **1984**, *259* (11), 7067–7074.

(384) Hardman, K. D.; Ainsworth, C. F. Structure of Concanavalin A at 2.4-Ang Resolution. *Biochemistry* **1972**, *11* (26), 4910–4919.

(385) Schwefel, D.; Maierhofer, C.; Beck, J. G.; Seeberger, S.; Diederichs, K.; Moller, H. M.; Welte, W.; Wittmann, V. Structural Basis of Multivalent Binding to Wheat Germ Agglutinin. *J.Am.Chem.Soc.* **2010**, *132*, 8704–8719.

(386) Natchiar, S. K.; Srinivas, O.; Mitra, N.; Surolia, A.; Jayaraman, N.; Vijayan, M. Structural Studies on Peanut Lectin Complexed with Disaccharides Involving Different Linkages: Further Insights into the Structure and Interactions of the Lectin. *Acta Crystallographica Section D* **2006**, *62*, 1413–1421.

(387) Housni, A.; Cai, H.; Liu, S.; Pun, S. H.; Narain, R. Facile Preparation of Glyconanoparticles and Their Bioconjugation to Streptavidin. *Langmuir* **2007**, *23* (9), 5056–5061.

(388) Narain, R.; Housni, A.; Gody, G.; Boullanger, P.; Charreyre, M.-T.; Delair, T. Preparation of Biotinylated Glyconanoparticles via a Photochemical Process and Study of Their Bioconjugation to Streptavidin. *Langmuir* **2007**, *23* (26), 12835–12841.

(389) Toyoshima, M.; Ooya, K.; Miura, Y.; Kobayashi, K. Preparation and Biological Properties of Saccharide-Modified Gold Nanoparticles. *Journal of the Japan Society of Powder and Powder Metallurgy* **2007**, *54* (12), 843–848.

(390) Schofield, C. L.; Mukhopadhyay, B.; Hardy, S. M.; McDonnell, M. B.; Field, R. A.; Russell, D. A. Colorimetric Detection of Ricinus Communis Agglutinin 120 Using Optimally Presented Carbohydrate-Stabilised Gold Nanoparticles. *The Analyst* **2008**, *133* (5), 626–634.

(391) Schofield, C. L.; Field, R. A.; Russell, D. A. Glyconanoparticles for the Colorimetric Detection of Cholera Toxin. *Analytical Chemistry* **2007**, *79* (4), 1356–1361.

(392) Deng, Z.; Li, S.; Jiang, X.; Narain, R. Well-Defined Galactose-Containing Multi-Functional Copolymers and Glyconanoparticles for Biomolecular Recognition Processes. *Macromolecules* **2009**, *42* (17), 6393–6405.

(393) Jiang, X.; Housni, A.; Gody, G.; Boullanger, P.; Charreyre, M.-T.; Delair, T.; Narain, R. Synthesis of Biotinylated α-d-Mannoside or *N*-Acetyl-β-d-Glucosaminoside Decorated Gold Nanoparticles: Study of Their Biomolecular Recognition with Con A and WGA Lectins. *Bioconjugate Chemistry* **2010**, *21* (3), 521–530.

(394) Richards, S.-J.; Gibson, M. I. Optimization of the Polymer Coating for Glycosylated Gold Nanoparticle Biosensors to Ensure Stability and Rapid Optical Readouts. *ACS Macro Letters* **2014**, *3* (10), 1004–1008.

(395) von der Ehe, C.; Kretschmer, F.; Weber, C.; Crotty, S.; Stumpf, S.; Hoeppener, S.; Gottschaldt, M.; Schubert, U. S. RAFT Copolymerization of Thioglycosidic Glycomonomers with N IPAm and Subsequent Immobilization onto Gold Nanoparticles. In *Controlled Radical Polymerization: Materials*; 2015; pp 221–256.

(396) Ebeling, B.; Vana, P. RAFT-Polymers with Single and Multiple Trithiocarbonate Groups as Uniform Gold-Nanoparticle Coatings. *Macromolecules* **2013**, *46* (12), 4862–4871.

(397) Shen, F.-W.; Zhou, K.-C.; Cai, H.; Zhang, Y.-N.; Zheng, Y.-L.; Quan, J. One-Pot Synthesis of Thermosensitive Glycopolymers Grafted Gold Nanoparticles and Their Lectin Recognition. *Colloids and Surfaces B: Biointerfaces* **2019**, *173*, 504–511.

(398) Won, S.; Richards, S.-J.; Walker, M.; Gibson, M. I. Externally Controllable Glycan Presentation on Nanoparticle Surfaces to Modulate Lectin Recognition. *Nanoscale Horizons* **2017**, *2* (2), 106–109.

(399) Won, S.; Hindmarsh, S.; Gibson, M. I. Triggerable Multivalent Glyconanoparticles for Probing Carbohydrate-Carbohydrate Interactions. *ACS Macro Letters* **2018**, *7* (2), 178–183.

(400) Samoilova, N. A.; Krayukhina, M. A.; Babushkina, T. A.; Yamskov, I. A.; Likhosherstov, L. M.; Piskarev, V. E. Silver- and Gold-Labeled Colloidal and Crosslinked Glycopolymers Based on Glycyl Glycosynthons and Maleic Anhydride Copolymers for Lectin Binding. *Journal of Applied Polymer Science* **2017**, *134* (16), 44718.

(401) Otsuka, H.; Muramatsu, Y.; Matsukuma, D. Gold Nanorods Functionalized with Self-Assembled Glycopolymers for Ultrasensitive Detection of Proteins. *Chemistry Letters* **2015**, *44* (2), 132–134.

(402) Álvarez-Paino, M.; Bordegé, V.; Cuervo-Rodríguez, R.; Muñoz-Bonilla, A.; Fernández-García, M. Well-Defined Glycopolymers via RAFT Polymerization: Stabilization of Gold Nanoparticles. *Macromolecular Chemistry and Physics* **2014**, *215* (19), 1915–1924.

(403) Pei, D.; Li, Y.; Huang, Q.; Ren, Q.; Li, F.; Shi, T. Biomimetic Glycopolymers Tethered Gold Nanoparticles: Preparation, Self-Assembly and Lectin Recognition Properties. *Colloids and Surfaces B: Biointerfaces* **2015**, *126*, 367–373.

(404) Gerke, C.; Ebbesen, M. F.; Jansen, D.; Boden, S.; Freichel, T.; Hartmann, L. Sequence-Controlled Glycopolymers via Step-Growth Polymerization of Precision Glycomacromolecules for Lectin Receptor Clustering. *Biomacromolecules* **2017**, *18* (3), 787–796.

(405) Otten, L.; Vlachou, D.; Richards, S.-J.; Gibson, M. I. Glycan Heterogeneity on Gold Nanoparticles Increases Lectin Discrimination Capacity in Label-Free Multiplexed Bioassays. *The Analyst* **2016**, *141* (14), 4305–4312.

(406) Toyoshima, M.; Miura, Y. Preparation of Glycopolymer-Substituted Gold Nanoparticles and Their Molecular Recognition. *Journal of Polymer Science Part A: Polymer Chemistry* **2009**, *47* (5), 1412–1421.

(407) Richards, S.-J.; Fullam, E.; Besra, G. S.; Gibson, M. I. Discrimination between Bacterial Phenotypes Using Glyco-Nanoparticles and the Impact of Polymer Coating on Detection Readouts. *J. Mater. Chem. B* **2014**, *2* (11), 1490–1498.

(408) Ishii, J.; Toyoshima, M.; Chikae, M.; Takamura, Y.; Miura, Y. Preparation of Glycopolymer-Modified Gold Nanoparticles and a New Approach for a Lateral Flow Assay. *Bulletin of the Chemical Society of Japan* **2011**, *84* (5), 466–470.

(409) Takara, M.; Toyoshima, M.; Seto, H.; Hoshino, Y.; Miura, Y. Polymer-Modified Gold Nanoparticles via RAFT Polymerization: A Detailed Study for a Biosensing Application. *Polymer Chemistry* **2014**, *5* (3), 931–939.

(410) Sze Ieong, N.; Biggs, C. I.; Walker, M.; Gibson, M. I. Comparison of RAFT-Derived Poly(Vinylpyrrolidone) Verses Poly(Oligoethyleneglycol Methacrylate) for the Stabilization of Glycosylated Gold Nanoparticles. *Journal of Polymer Science Part A: Polymer Chemistry* **2017**, *55* (7), 1200–1208.

(411) Nguyen, L.; McCord, K. A.; Bui, D. T.; Bouwman, K. A.; Kitova, E. N.; Kumawat, D.; Daskan, G. C.; Tomris, I.; Han, L.; Chopra, P.; Yang, T.-J.; Williows, S. D.; Lowary, T. L.; West, L. J.; Hsu, S.-T. D.; Tompkins, S. M.; Boons, G.-J.; Mason, A. L.; Vries, R. P. de; Macauley, M. S.; Klassen, J. S. Sialic Acid-Dependent Binding and Viral Entry of SARS-CoV-2. *bioRxiv* **2021**, 2021.03.08.434228.

(412) Buchanan, C. J.; Gaunt, B.; Harrison, P. J.; Bas, A. Le; Khan, A.; Giltrap, A. M.; Ward, P. N.; Dumoux, M.; Daga, S.; Picchiotti, N.; Baldassarri, M.; Benetti, E.; Fallerini, C.; Fava, F.; Giliberti, A.; Koukos, P. I.; Lakshminarayanan, A.; Xue, X.; Papadakis, G.; Deimel, L. P.; Casablancas-Antras, V.; Claridge, T. D. W.; Bonvin, A. M. J. J.; Sattentau, Q. J.; Furini, S.; Gori, M.; Huo, J.; Owens, R. J.; Renieri, A.; Study, G.-C. M.; Naismith, J. H.; Baldwin, A.; Davis, B. G. Cryptic SARS-CoV2-Spike-with-Sugar Interactions Revealed by “universal” Saturation Transfer Analysis. *bioRxiv* **2021**, 2021.04.14.439284.

(413) Huang, X.; Dong, W.; Milewska, A.; Golda, A.; Qi, Y.; Zhu, Q. K.; Marasco, W. A.; Baric, R. S.; Sims, A. C.; Pyrc, K.; Li, W.; Sui, J. Human Coronavirus HKU1 Spike Protein Uses O -Acetylated Sialic Acid as an Attachment Receptor Determinant and Employs Hemagglutinin-Esterase Protein as a Receptor-Destroying Enzyme. *Journal of Virology* **2015**, *89* (14), 7202–7213.

(414) Hulswit, R. J. G.; Lang, Y.; Bakkers, M. J. G.; Li, W.; Li, Z.; Schouten, A.; Ophorst, B.; Van Kuppeveld, F. J. M.; Boons, G. J.; Bosch, B. J.; Huizinga, E. G.; De Groot, R. J. Human Coronaviruses OC43 and HKU1 Bind to 9-O-Acetylated Sialic Acids via a Conserved Receptor-Binding Site in Spike Protein Domain A. *Proceedings of the National Academy of Sciences of the United States of America* **2019**, *116* (7), 2681–2690.

(415) Park, Y. J.; Walls, A. C.; Wang, Z.; Sauer, M. M.; Li, W.; Tortorici, M. A.; Bosch, B. J.; DiMaio, F.; Veesler, D. Structures of MERS-CoV Spike Glycoprotein in Complex with Sialoside Attachment Receptors. *Nature Structural and Molecular Biology* **2019**, *26* (12), 1151–1157.

(416) Sheng-, S.; Wang, K.; Cheng, C.-M.; Wang, S.-K. Glycan-Based Diagnostic Devices: Current Progress, Challenges and Perspectives. *Chem. Commun. Chem. Commun* **2015**, *51* (51), 16750–16762.

(417) Purohit, S.; Li, T.; Guan, W.; Song, X.; Song, J.; Tian, Y.; Li, L.; Sharma, A.; Dun, B.; Mysona, D.; Ghamande, S.; Rungruang, B.; Cummings, R. D.; Wang, P. G.; She, J.-X. Multiplex Glycan Bead Array for High Throughput and High Content Analyses of Glycan Binding Proteins. *Nature communications* **2018**, *9* (1), 258.

(418) Reichardt, N.-C.; Martín-Lomas, M.; Penadés, S. Opportunities for Glyconanomaterials in Personalized Medicine. *Chem. Commun.* **2016**, *52* (92), 13430–13439.

(419) Engel, N.; Ganesh, G.; Patil, M.; Yellappa, V.; Vadnais, C.; Pai, N. P.; Pai, M. Point-of-Care Testing in India: Missed Opportunities to Realize the True Potential of Point-of-Care Testing Programs. *BMC Health Services Research* **2015**, *15* (1), 550–563.

(420) Zsigmondy, R.; Thiessen, P. A. Das Kolloide Gold; 1925

Chapter 2

Lateral Flow Glyco-Assays for the Rapid and Low-Cost Detection of Lectins – Polymeric Linkers and Particle Engineering are Essential for Selectivity and Performance

2.1 Abstract

Lateral flow immunoassays, such as the home pregnancy test, are rapid point of care diagnostics that use antibody-coated nanoparticles to bind antigens/analytes (e.g., viruses, toxins, or hormones). Ease of use, no need for centralised infrastructure and low-cost, makes these devices appealing for rapid disease identification, especially in low-resource environments. Here glycosylated polymer-coated nanoparticles are demonstrated for the sensitive, label-free detection of lectins in lateral flow and flow-through. The systems introduced here use glycans, not antibodies, to provide recognition: a "lateral flow glyco-assay," providing unique biosensing opportunities. Glycans are installed onto polymer termini and immobilised onto gold nanoparticles, providing colloidal stability but crucially also introducing assay tunability and selectivity. Using soybean agglutinin and *Ricinus communis* agglutinin I (RCA_{120}) as model analytes, the impact of polymer chain length and nanoparticle core size are evaluated, with chain length found to have a significant effect on signal generation – highlighting the need to control the macromolecular architecture to tune response. With optimised systems, lectins are detectable at sub-nanomolar concentrations, comparable to antibody-based systems. Complete lateral flow devices are also assembled to show how these devices could be deployed in the "real world." This work shows that glycan-binding can be a valuable tool in rapid diagnostics.

2.2 Declaration

This chapter has been published as a paper discussing the detection of SBA and RCA_{120} using flow-through and lateral flow diagnostics by harnessing glycans as capture agents.

Asier Muguruza helped carry out some of the DLS and UV-vis analysis of the particles and helped prepare and carry out the lateral flow testing targeting SBA, Sarah-Jane Richards helped prepare and carry out the lateral flow testing targeting RCA_{120}, Panagiotis Georgiou carried out the TEM analysis, Stephan Goetz provided guidance and support in designing the LFD systems and Marc Walker supported the XPS analysis and supported model fitting the XPS data.

I synthesised the RAFT agent, the polymers, the gold particles; functionalised the polymers with glycans; characterised the polymer systems by NMR, SEC and FTIR; characterised the particles by XPS; and synthesised and characterised the glycans by NMR. I designed, constructed, and ran the prototype flow-through and lateral flow devices, and analysed the data from the devices.

Myself, Simone Dedola, Robert A. Field and Matthew Gibson were responsible for preparation of the manuscript.

A. N. Baker, A. R. Muguruza, S-J. Richards, P. G. Georgiou, S. Goetz, M. Walker, S. Dedola, R. A. Field, M. I. Gibson, *Adv. Healthcare Mater.,* 2021, 2101784.

2.3 Introduction

Lateral flow devices (LFDs), such as the home pregnancy test,[1] can be used to provide rapid point of care testing at low cost. The cost-effectiveness and clinical usefulness of LFDs has been well demonstrated by malaria rapid diagnostic tests,[2,3] in the diagnosis of cutaneous leishmaniasis[4] and in comparisons with reverse transcription-polymerase chain reaction (RT-PCR) approaches for Ebola diagnosis.[5] More recently LFDs have been used to detect SARS-COV-2, as rapid and low-cost diagnostics allowing for early detection when deployed appropriately.[6] LFDs are chromatographic paper-based devices which function by flowing the analyte past a functionalised stationary phase with affinity for the analyte. As the analyte passes through the device it is bound by both the stationary phase and the signal generating mobile phase, most commonly gold nanoparticles functionalised with receptors for the analyte, "sandwiching" the analyte.[7] This leads to a visible colour forming at the test line, indicating a positive test. Gold nanoparticles are the most commonly[7] used mobile phase due to their strong colouration associated with their localised surface plasmon resonance band,[8–10] and ease of functionalisation by nonspecific surface passivation (e.g., absorption of proteins), or through aurophilic functionalities such as thiols. Gold nanoparticles are also easy to synthesise by reduction of gold salts. Notably, other signal generating units such as; quantum dots,[11] graphene oxide[12,13] and carbon nanotubes[14] have also been used in LFDs.

Typically, the capture units for the analyte, on both the test line and nanoparticle surface, are antibodies, owing to their high affinity and selectivity. However, antibodies are not essential components in lateral flow devices. Other recognition units such as; nucleic acids,[15] lectins[16] and glycans can also be used, so long as the analyte is bound with sufficient affinity and specificity. Glycans are ubiquitous in biological systems[17] with over half of all mammalian proteins estimated to be glycosylated[18] and glycoconjugates playing a variety of roles from cell signalling[19] to mediating immune responses.[20] They are also the site of pathogen adhesion during many viral infections,[21,22] especially respiratory viruses such as influenzas.[23]

The diverse range of biological recognition processes driven by glycans presents many opportunities to either target the glycans themselves or the proteins that sense for them (lectins) in biosensing or diagnostic applications. Lectins are found in a wide-array of

environments, for example the cholera toxin,[24] ricin,[25] lectins in snake venoms[26] and as biocides in algae.[27] Furthermore, lectins have been used for decades as histological stains, to identify diseased tissue based on glycosylation,[28] while lectins-containing biosensors have been extensively reviewed.[29–31] Damborský *et al.* have reported a lateral flow device that utilises immobilised lectins (in place of antibodies) as test lines for prostate specific antigen[16,32] and Bayoumy *et al.* have used antibodies to target glycans.[33] However, to the best of our knowledge, there are very few examples of the exploration of glycans as the detection units in lateral flow, that is, using glycans to sense for an analyte – rather than targeting glycans as an analyte or a glycosylated analyte. A mannose-functionalised *p*-acrylamidophenyl polymer coated AuNP, with an antibody as the test line, was used by Ishii *et al.* to detect Concanavalin A (ConA) in a lateral flow device.[34] We believe this is the first report of glycans forming part of an LFD. Miura and co-workers built on this work further by preparing a small panel of glycopolymer functionalised AuNPs for the detection of ConA – again using an antibody as the stationary phase.[35] These two examples demonstrated that glyco-nanoparticles could be deployed in LFDs, however, both reports relied on using antibodies in part, and were only demonstrated against the plant lectin ConA. Baker *et al.*, discovered that SARS-COV-2 (the causative agent of COVID-19) spike protein has affinity towards sialic acids,[36] as had been reported for previous coronaviruses[37,38] including the coronavirus that causes Middle East Respiratory syndrome (MERS).[39] Using *N*-acetyl neuraminic acid-terminated polymer ligands, immobilised onto gold nanoparticles, it was demonstrated that a SARS-COV-2 spike protein bearing pseudovirus could be detected in a lateral flow glyco-assay (using a BSA-glycoconjugate test-line), and that a flow-through assay (LFD without a test line) device could be used for the detection of S1 spike protein.[36] This clearly demonstrated that lateral flow glyco-assays, lateral flow devices that use glycans as capture agents (on the test line and particle) for an analyte, have potential applications in rapid diagnostics, surveillance, and as accessible research tools for evaluating glycan-binding protein function. Further work utilising a flow-through glyco-assay demonstrated that glycans could be used as capture agents to sense for the SARS-COV-2 virus in patient samples and that these tests were thermally robust,[40] which could be an advantage of glycan-based devices versus antibody-based devices.[41] To advance the study of glyco-LFD technology, LFDs that use glycans as capture agents

on test lines and/or particles, it is crucial to understand how each component (particle, surface) impacts performance.

Herein we explore how the role of polymer chain length, glycan density and nanoparticle size affect the performance of lateral flow glyco-assays, for the detection of lectin analytes, as a model system to further validate glyco-LFDs. This study reveals that the outputs (signal, nonspecific binding and background) were dependent on the nanoparticle's structural parameters. In particular, the precise chain length of the polymeric tether required for optimal detection of different lectins (SBA (soybean agglutinin) and RCA_{120} (*Ricinus communis* agglutinin I)) was shown to be different. This provides the opportunity to introduce selectivity not just through the glycan, but also through macromolecular engineering, which is a unique feature of this technology. Guided by these results, complete diagnostic devices were fabricated and used to detect SBA in 10 minutes at concentrations as low as 5 $\mu g.mL^{-1}$.

2.4 Results and Discussion

The primary aim of this work was to develop lateral flow glyco-assay technology to enable the sensitive detection of lectins, using glycosylated polymer-stabilised gold nanoparticles, as an alternative to traditional antibody-based detection systems. To achieve this, an understanding of how particle/polymer structure impacts lateral flow performance was required. Therefore, a library-based screening approach was undertaken, with SBA chosen as the model lectin for detection. The precise chain length, surface glycan density, and particle size have been previously shown to be crucial in plasmonic (aggregation) glyco-assays, by modulating particle/analyte interactions and outcomes, while also ensuring colloidal stability in complex media.[42,43] Reversible addition-fragmentation chain transfer (RAFT) polymerisation was used to synthesise a panel of poly(hydroxyethyl acrylamide)s (PHEA) using pentafluorophenyl-2-(dodecylthiocarbonothioylthio)-2-methylpropanoate (PFP-DMP) as the RAFT agent to install a pentafluorophenyl group at the ω-chain end, and a protected thiol at the α-end (for AuNP immobilisation), Figure 2.1. PHEA was chosen because of its solubility and colloidal stability when immobilised onto gold nanoparticles.[44] The polymers were characterised (Table 2.1) by size exclusion chromatography (SEC, Figure 2.1C) showing low dispersity values, and the structure confirmed by ^{1}H, ^{13}C and ^{19}F NMR spectroscopy (Experimental section and Appendix 2). Galactosamine (2-deoxy-2-amino-galactose) was conjugated to the polymer by displacement of the PFP end-group, to mimic the structure of *N*-acetyl galactosamine (GalNAc) due to formation of the amide linkage. Glycan addition was confirmed by FTIR, ^{19}F and ^{1}H NMR. Non-glycosylated polymers were produced by reaction with n-pentylamine and used (below) to dilute the density of glycans on the particle surface.

Citrate stabilised 16 and 40 nm gold nanoparticles (AuNPs) were synthesised by a seeded growth approach and characterised by dynamic light scattering (DLS), transmission electron microscopy (Appendix 2 Figure S8) and UV-vis analysis.[45,46] The AuNPs were then functionalised with varying ratios of glycosylated and non-glycosylated polymers to produce 100%, 66%, 33% and 0% glycan-densities on the AuNPs for each polymer length and AuNP size, to produce a library of 34 particles (including the two citrate-stabilised AuNPs), Figure 2.1. UV-vis spectroscopy and DLS confirmed functionalisation (Appendix 2 Figures S9-S17 and Table S1). In some

cases, the particles were unstable (fully aggregated): all GalPHEA$_{26@}$AuNP$_{40}$'s and all GalPHEA$_{40}$@AuNP$_{40}$'s aggregated except 100% glycan functionalised; hence these particles were excluded from further analysis. It is worth noting that a hydrophobic amine was used in place of the glycan for the non-glycosylated polymers (to remove the PFP group) which contributes to the observed aggregation. A hydrophobic amine was chosen as some aggregation of the particles with both antigen and test line in an LFD may aid detection, and therefore even the dispersed samples showed some populations of larger particles in the DLS (Appendix 2) but were all suitable for this screening step. Therefore, this does not prevent their application here where the LFD performance is the primary outcome. To further characterise the surface of the particles, x-ray photoelectron spectroscopy (XPS) was conducted on dried particles (Appendix 2 Figures S32-S42 and Tables S15-S16). XPS confirmed the presence of amide (*C*(O)NC) and amine (C(O)N*C*) peaks in the C 1*s* (Figure 2.1D), and N 1*s* scans (amine and amides have similar/overlapping binding energies so were not distinguishable), showing the presence of the PHEA, which were not present in the naked AuNP samples. Similarly, ether (XPS cannot easily distinguish ether from alcohol and are combined in the model employed here) peaks in the C 1*s* scans were far larger in samples containing 100% glycan than in the citrate stabilised AuNPs with no polymer functionalisation. It is important to note the presence of carbonyls and carboxylic acid carbons are from atmospheric contaminants, and the presence of carbide likely from the silicon wafer/particle interface.

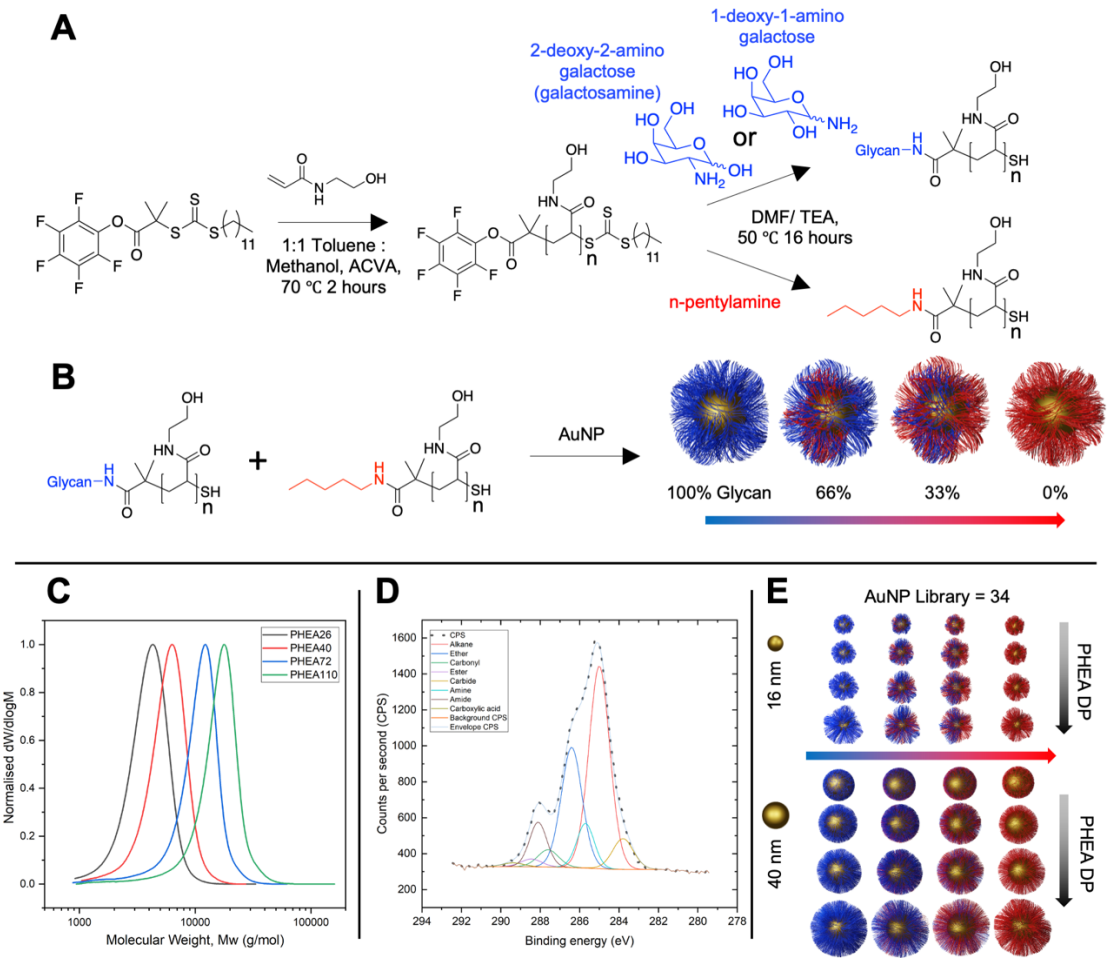

Figure 2.1. Synthesis of gold nanoparticle library functionalised with glycan-terminated polymeric tethers at various densities.

A) Polymerisation of *N*-hydroxyethyl acrylamide (HEA) by RAFT, followed by displacement of the PFP ester with amino-glycans; B) Assembly of polymers onto pre-formed gold nanoparticles to give variable glycan densities; C) Normalised size exclusion chromatography analysis of PHEA polymers from Table 2.1; D) C 1*s* x-ray photoelectron spectrum of 100% GalPHEA$_{72}$@AuNP$_{16}$; E) Graphical representation of AuNP library illustrating the 3 variables of diameter, coating DP, and glycan density.

Table 2.1. Polymers prepared for detecting SBA

Polymer	[M]:[CTA]	$M_{n(theo)}$ (g.mol^{-1})[a]	$M_{n(SEC)}$ (g.mol^{-1})[b]	$M_{n(NMR)}$ (g.mol^{-1})[c]	$Đ_M$[b]
$PHEA_{26}$	10	1700	3600	4100	1.17
$PHEA_{40}$	20	2800	5100	5000	1.19
$PHEA_{72}$	40	5100	8900	8600	1.28
$PHEA_{110}$	70	8600	13000	14000	1.27

[a)] Calculated from the feed ratio of monomer to chain transfer agent; [b)] Calculated against poly(methyl methacrylate) standards using 5 mM NH_4BF_4 in DMF as eluent; [c)] Determined from ^{1}H NMR end-group analysis.

With this library of glycoparticles to hand, their function was screened in a lateral flow assay. Figure 2.2 shows the set-up of the assay. A dipstick was made, where the test line (to capture the lectin analyte) was made by depositing 1 μL of 1 mg.mL^{-1} Galα1-3Galβ1-4GlcNAc-bovine serum albumin conjugate (Galα1-3Galβ1-4GlcNAc-BSA) which has affinity for SBA (Figure 2.2A). For this evaluation no control line was employed, which would be essential for a real diagnostic to demonstrate a device is functioning (and is used in the final devices at the end of this study, below).[47] The mobile phase was SBA (0.05 mg.mL^{-1}, ~0.4 nmol.mL^{-1}) and OD1 (optical density at UV_{max}, the standard measurement for concentration) AuNPs (Figure 2.2D). Notably the OD used was kept constant (OD = 1) for all dipsticks and devices to provide a constant concentration across and between assays allowing for easy comparison. Negative controls were run of the AuNPs versus Galα1-3Galβ1-4GlcNAc-BSA only (Figure 2.2C), and unfunctionalised BSA (Figure 2.2B) test lines to determine if any off-target binding to the test line itself occurred. Further negative controls were run using AuNPs versus Galα1-3Galβ1-4GlcNAc-BSA test lines with *Ulex Europaeus* Agglutinin I (UEA, 0.05 mg.mL^{-1}, Figure 2.2E), a lectin with no affinity for GalNAc.

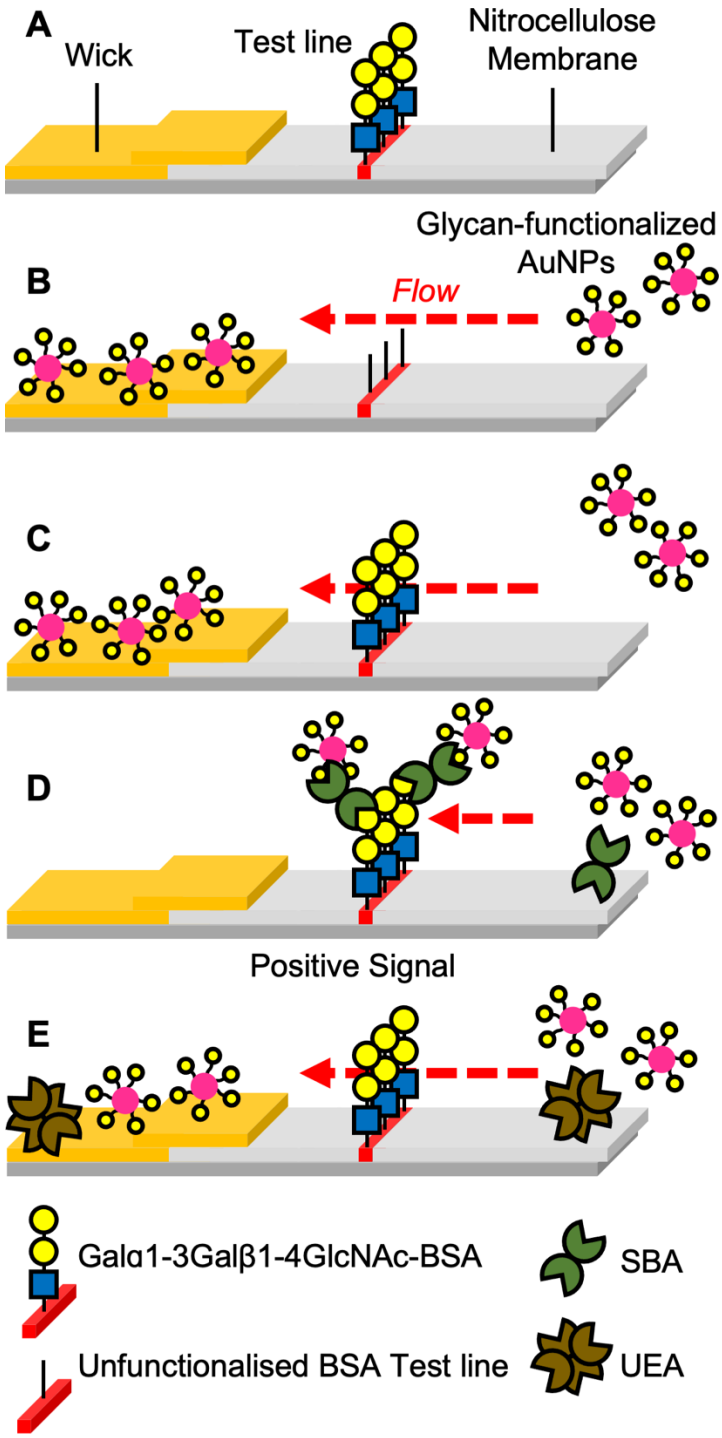

Figure 2.2. Schematic of dipstick lateral flow assay.

A) Design of dipstick; B) Lateral flow with unfunctionalised BSA - particles flow without engaging the test line; C) Lateral flow with Galα1-3Galβ1-4GlcNAc-BSA test line and no analyte - particles do not engage test line; D) Lateral flow with Galα1-3Galβ1-4GlcNAc-BSA test line and SBA (analyte) resulting in capture and signal generation; E) Lateral flow with Galα1-3Galβ1-4GlcNAc-BSA test line and UEA (negative control) - hence no signal generation.

All dipsticks were run in triplicate for 20 minutes before being scanned and analysed with image analysis software[48] to evaluate binding (photographs of all strips are in Appendix 2 Figures S18-S22, S24-27 and Tables S2-S6, S8-11). This process of running in triplicate and averaging (mean) the data was carried out for all dipsticks and devices in this study. The test line is situated on the strip around 15 to 35 relative distance units (i.e., x-axis output from image analysis) along the strip, noting that the strip length is set to 100 relative distance units. An example of positive (with SBA as analyte) and negative (buffer alone) dipsticks are shown in Figure 2.3A, with the direction of flow, the test line area and the wick area labeled. The wick area, where unbound nanoparticles gather (at the end of the assay), is typically "hidden" in the housing of a full lateral flow cassette. An example image analysis of these dipsticks is shown in Figure 2.3B and a summary of the best performing systems is show in Figure 2.3C. Full analysis of all strips as a function of nanoparticle composition and original images are included in Appendix 2.

Consideration of the data revealed three trends; i) as polymer length increases the total amount of binding to SBA decreases, but the nonspecific binding in negative controls was also reduced; ii) decreasing the density of the glycan on the particles decreases binding to SBA but also leads to some increases in nonspecific binding; and iii) increasing AuNP diameter led to increased signal intensity but also increased noise from the background. Taking this into account, the particles that gave optimal performance against SBA were 100% glycan functionalised GalPHEA$_{72}$@AuNP$_{16}$ and GalPHEA$_{72}$@AuNP$_{40}$. While GalPHEA$_{110}$@AuNP$_{40}$ gave higher signals the background signal was also very high. These three particle systems were further analysed by considering their signal-to-noise ratios (Figure 2.3C, Appendix 2 Figures S23&S28 and Tables S7&S12); 100% glycan functionalised GalPHEA$_{72}$@AuNP$_{16}$ was found to have the highest signal-to-noise ratio despite producing less signal than 100% glycan functionalised GalPHEA$_{72}$@AuNP$_{40}$.

There are limited examples of lateral flow assays based only on glycans, but in our previous report of a system for SARS-COV-2 detection, larger nanoparticles (35 nm) were optimal.[36] This highlights how each system can be fine-tuned to the detection challenge, with this data illustrating how tuning the particle/polymer/ligand interfaces enables modulation of the observable outputs. Notably buffer conditions, and

materials used in the LFD were kept constant in this work but could also be further optimised to modulate output.

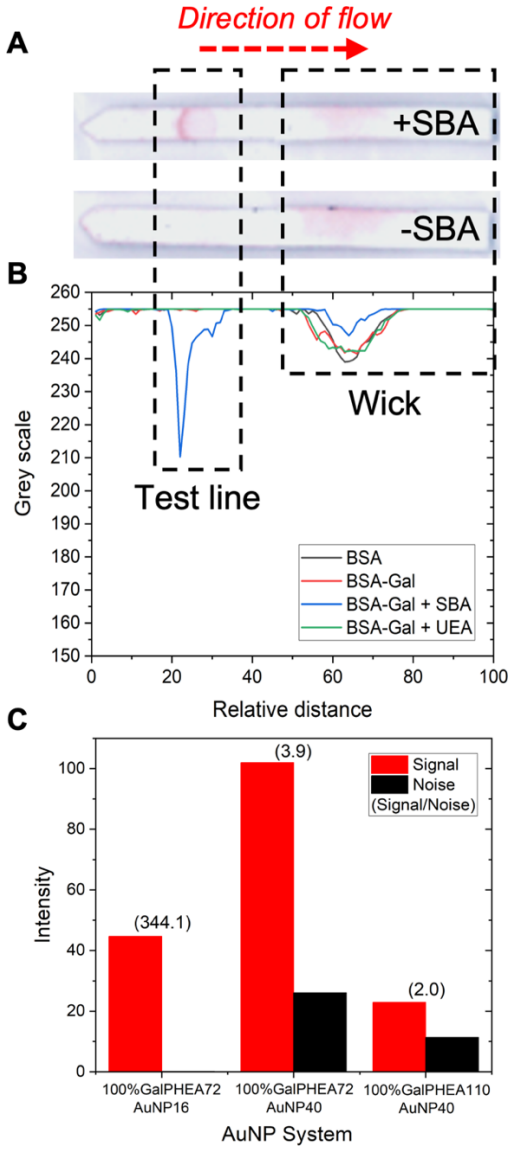

Figure 2.3. Optimisation of the gold nanoparticle in dipstick format using SBA as the analyte.

A) Example lateral flow dipsticks showing test line (Galα1-3Galβ1-4GlcNAc-BSA, 1 mg.mL^{-1}) and direction of flow; B) Example image analysis result using 100% GalPHEA$_{72}$@AuNP$_{16}$; C) Summary of selected nanoparticle performance from image analysis. Signal-to-noise ratio is indicated above each pair of bars. Images shown have been enhanced for clarity (all original dipstick photos and image analyses are included in Appendix 2). Test lines for (B) are unfunctionalised BSA (BSA, 1 mg.mL^{-1}), and Galα1-3Galβ1-4GlcNAc-BSA (BSA-Gal, 1 mg.mL^{-1}) with (or without) lectins in solution (SBA or UEA, 0.05 mg.mL^{-1}).

The identified optimum particle, 100% glycan functionalised GalPHEA$_{72}$@AuNP$_{16}$, was next explored for its limit of detection (LoD) in the dipstick assays. A serial dilution of SBA was prepared in the buffer and run, Figure 2.4 (Appendix 2 Table S13 and Figure S29). The limit of detection was found to be 0.02 mg.mL^{-1} (0.17 nmol.mL^{-1}). This is similar to a commercial pregnancy test (~0.7 – 0.07 nmol.mL^{-1})[49] showing that glycans can achieve the necessary LoD to be a viable alternative/companion, to antibody-based LFDs. It should be noted that no attempts to reduce background (*via* buffer tuning) were made here, but a lower background was achieved in the final device (below).

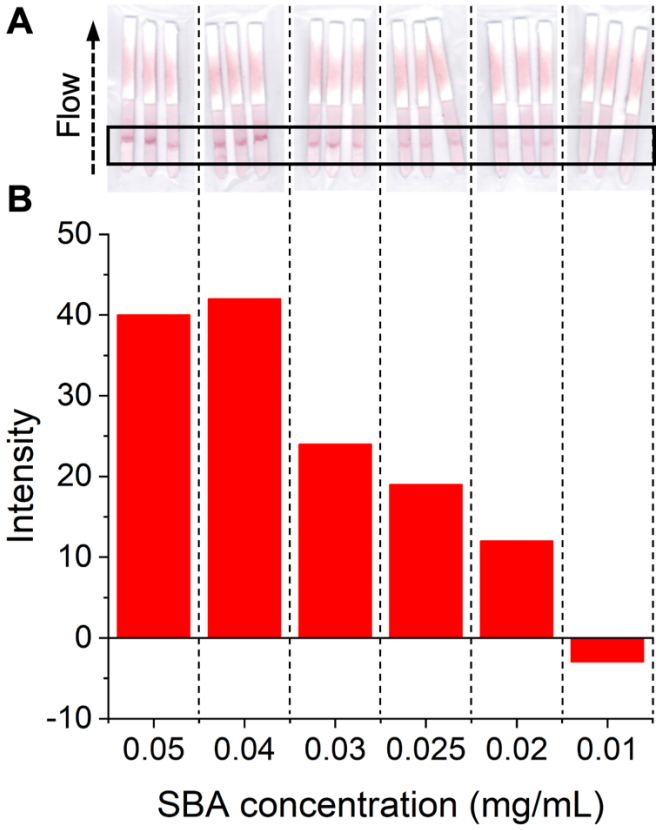

Figure 2.4. Lateral flow data from SBA dipstick assays to determine limit of detection.

A) Lateral flow dipsticks run with the indicated concentrations of SBA using 100% GalPHEA$_{72}$@AuNP$_{16}$; B) Analysed lateral flow intensity data from the lateral flow strips in A.

The above data showed that the lateral flow glyco-assay approach can be used to detect SBA and that the exact nanoparticle used (size, coating, density of ligands) can be easily tuned and is a key determinant in their output. Therefore, another lectin was also explored, RCA$_{120}$, which has affinity towards galactose and *N*-

acetylgalactosamine (GalNAc).[50,51] $PHEA_{40}$, $PHEA_{72}$ and $PHEA_{110}$ were functionalised with 1-deoxy-1-amino-galactose due to known affinity of this isomer towards RCA_{120}. This is a different galactosamine isomer than used for the SBA study above. Shorter polymers, less than 100% glycan functionalisation and 40 nm gold nanoparticles were not explored based on the experiments with SBA where there was significant particle aggregation. Particle characterisation is provided in Appendix 2 Figures S43-S44, S49-S54 and Tables S17, S20-S21.

It was not possible to find a commercially available BSA-glycoconjugate with sufficient affinity for RCA_{120} to generate a suitable test line. Therefore, an alternative approach, a "flow-through assay,"[52,53] was used based on direct deposition of the target (RCA_{120} at 5 $mg.mL^{-1}$) onto the test line, followed by running the dipstick. Whilst unconventional, we have previously used this methodology in S1 spike protein detection.[36] The dipsticks were run in the same manner as the SBA system and the results are summarised in Figure 2.5. In addition to RCA_{120} the following controls were tested; Wheat Germ Agglutinin (WGA) at 5 $mg.mL^{-1}$, a lectin with known affinity for *N*-acetyl-glucosamine,[54] used to assess off-target binding; Galα1-3Galβ1-4GlcNAc-BSA at 1 $mg.mL^{-1}$, used to determine if a BSA glycoconjugate may serve as a viable test line in the future; and SBA at 5 $mg.mL^{-1}$. SBA was used as it has a known affinity to galactose residues,[55] providing a challenge to design a flow-through assay that only generates signal against RCA_{120}. All images and analysis are available in Figure S45 and Table S18 of Appendix 2.

In contrast to what was observed with SBA, the averaged triplicate dipstick data for $GalPHEA_{40}@AuNP_{16}$ (Figure 2.5A) showed binding to RCA_{120} (and SBA) while the longer polymer $PHEA_{72}$ (Figure 2.5B) showed very weak binding to RCA_{120} only ($GalPHEA_{110}@AuNP_{16}$ (Figure 2.5C) showed no clear binding to any lectins or controls). Notably 2-deoxy-2-amino-$GalPHEA_{72}@AuNP_{16}$ (Figure 2.5D) showed binding to both RCA_{120} and SBA but gave a stronger signal with SBA. This further shows that the optimal presentation of the glycan for each lectin is subtly different; but offers opportunities for tuning selectivity and affinity. Two additional polymers were therefore synthesised to fall between the 40 to 72 range of chain lengths already tested, to improve the assay, Table 2.2.

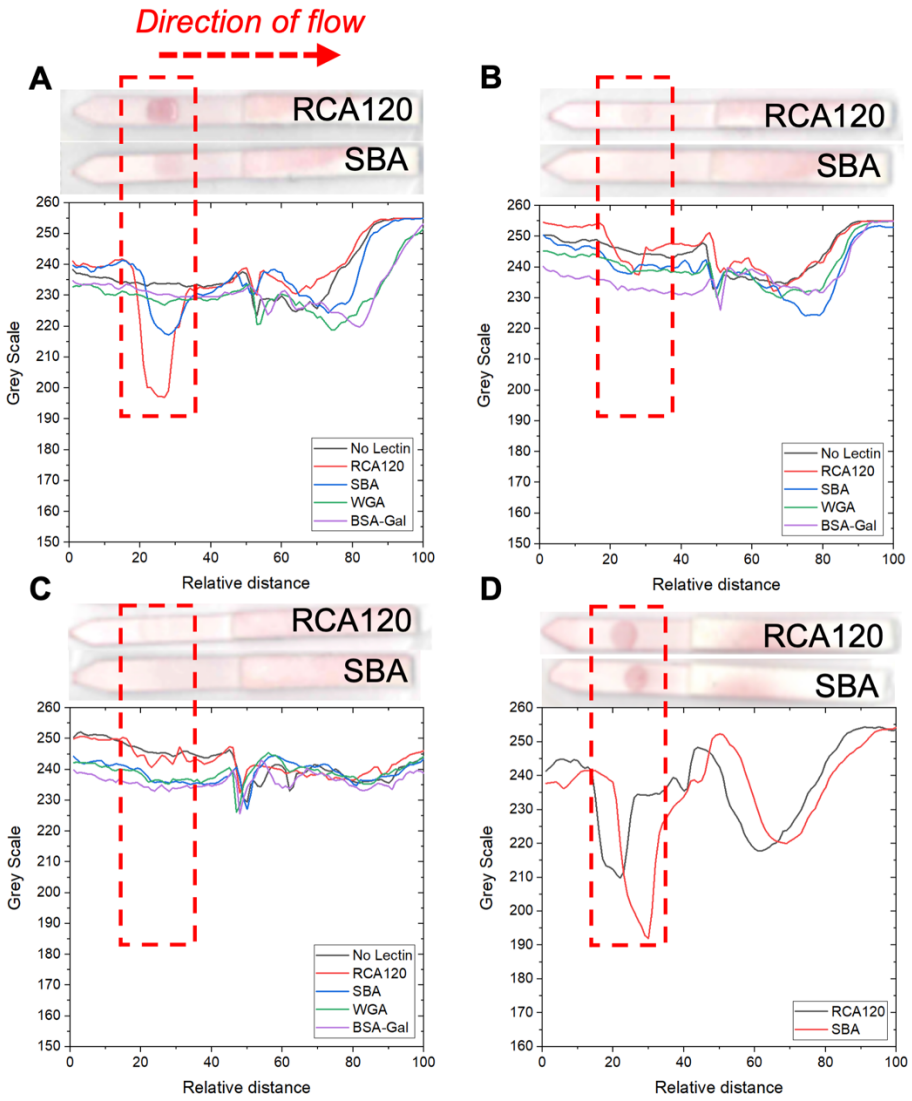

Figure 2.5. Analysed flow-through data from RCA_{120} screen and inset are example dipstick photos.

A) $GalPHEA_{40}@AuNP_{16}$; B) $GalPHEA_{72}@AuNP_{16}$; C) $GalPHEA_{110}@AuNP_{16}$; D) 2-deoxy-2-amino-$GalPHEA_{72}@AuNP_{16}$. Test lines were RCA_{120}, SBA or WGA at 5 $mg.mL^{-1}$, or BSA-Gal (Galα1-3Galβ1-4GlcNAc-BSA) at 1 $mg.mL^{-1}$.

Table 2.2. Additional polymers prepared for detecting RCA_{120}

Polymer	[M]:[CTA]	$M_{n(theo)}$ ($g.mol^{-1}$)[a]	$M_{n(SEC)}$ ($g.mol^{-1}$)[b]	$M_{n(NMR)}$ ($g.mol^{-1}$)[c]	$Đ_M$[b]
$PHEA_{50}$	25	3400	6400	5500	1.27
$PHEA_{58}$	30	4000	7200	6700	1.26

[a)] Calculated from the feed ratio of monomer to chain transfer agent; [b)] Calculated from SEC using poly(methyl methacrylate) standards; [c)] Determined from ^1H NMR end-group analysis.

The two additional polymers, $PHEA_{50}$ and $PHEA_{58}$ (Table 2.2) were functionalised with 1-deoxy-1-amino-galactose, immobilised onto 16 nm AuNPs, as described above, and fully characterised (Appendix 2). Subsequent evaluation in the same dipstick format found both bound to RCA_{120}, generating positive test lines. Whilst both AuNPs bound to the RCA_{120}, the $GalPHEA_{58}@AuNP_{16}$ generated significantly weaker signal intensity against SBA and WGA controls (Figure 2.6B) compared to $GalPHEA_{50}@AuNP_{16}$ (Figure 2.6A). This confirmed that precision tuning the polymer chain length enables control of the overall signal generated and can provide additional discriminatory power to the assay. The identified optimum particle, 100% glycan functionalised $GalPHEA_{58}@AuNP_{16}$, was next explored for its limit of detection in the dipstick assay. A serial dilution of RCA_{120} was prepared and deposited onto the strips (Figure 2.6C and D, Appendix 2 Table S19 and Figure S47). The lowest concentration that could be detected, above the signal of a 5 $mg.mL^{-1}$ SBA control, was found to be 0.5 $mg.mL^{-1}$ (4.2 $nmol.mL^{-1}$).[56]

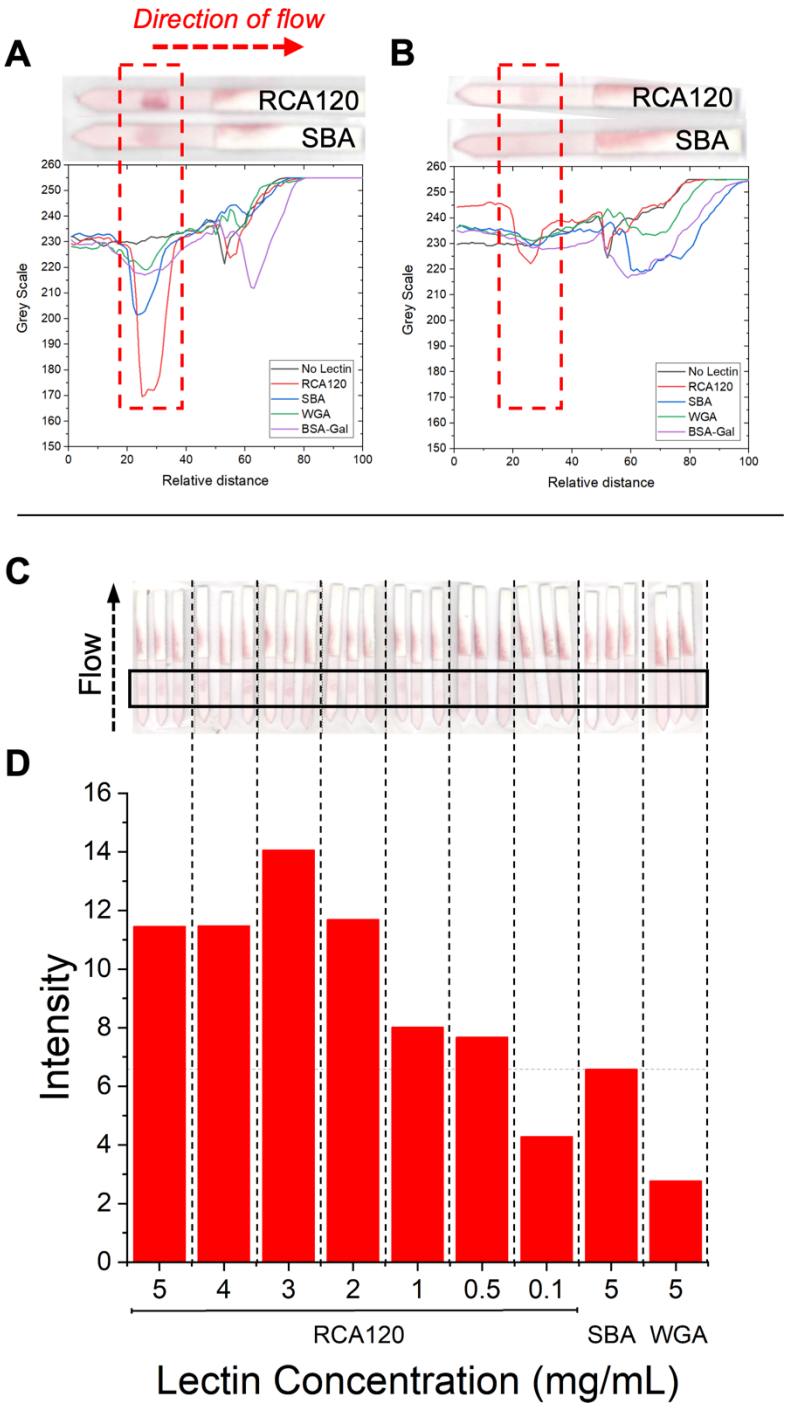

Figure 2.6. Flow-through dipstick assays against RCA_{120}.

A) Data from $GalPHEA_{50}@AuNP_{16}$ and inset example dipsticks; B) Data from $GalPHEA_{58}@AuNP_{16}$ and inset example dipsticks; C) $GalPHEA_{58}@AuNP_{16}$ dipstick assays to determine limit of detection of RCA_{120}; D) Analysed limit of detection data of $GalPHEA_{58}@AuNP_{16}$ for RCA_{120}. Test lines for (A) and (B) were RCA_{120}, SBA or WGA at 5 $mg.mL^{-1}$; or BSA-Gal (Galα1-3Galβ1-4GlcNAc-BSA) at 1 $mg.mL^{-1}$.

The dipsticks used above demonstrate the principle of lateral flow and flow-through glyco-assays for detecting lectins. However, a full device in a cassette format is required for a diagnostic which can be packaged, stored, distributed, and used easily. Therefore, cassettes designed to detect SBA (for which valid test and control lines were available) were assembled as proof of principle and as a prototype for a complete lateral flow glyco-assay for lectin detection.

2-deoxy-2-amino-GalPHEA$_{72}$@AuNP$_{16}$ was selected as the optimal particle setup (from above), so particles were dried onto conjugate pads (from which they are released when the analyte solution is applied) and integrated into a complete cassette. A control line of 1 μL (5 mg.mL^{-1}) SBA was also added to the cassettes. A control line is essential in a functioning device to prove the device is running correctly (e.g., to distinguish between a negative result, and one where the particles did not flow) but was not used in the screening experiments above. Design schematics (Figure 2.7) and images of complete cassettes are shown in Figure 2.8 (and in full detail in Appendix 2 Figure S31 and Table S14). Using this setup, concentrations of SBA as low as 5 μg.mL^{-1} (0.042 nmol.mL^{-1}) could be detected in the buffer in 10 minutes (Figure 2.8). The drop in binding at 0.03 and 0.02 mg.mL^{-1} indicates the difficulty in scanning the cassettes (when visually compared to the strips after removal from the devices, Appendix 2 Table S14) and variability between the hand-made devices. Notably all devices in the triplicates produced an observable signal and when averaged gave the values presented in Figure 2.8. In summary, Figure 2.8 validates the principle of the lateral flow glyco-assay, which can be adapted to other glycan-binding antigens, such as toxins or viruses. In each cassette a control line was also visible, confirming the devices ran correctly.

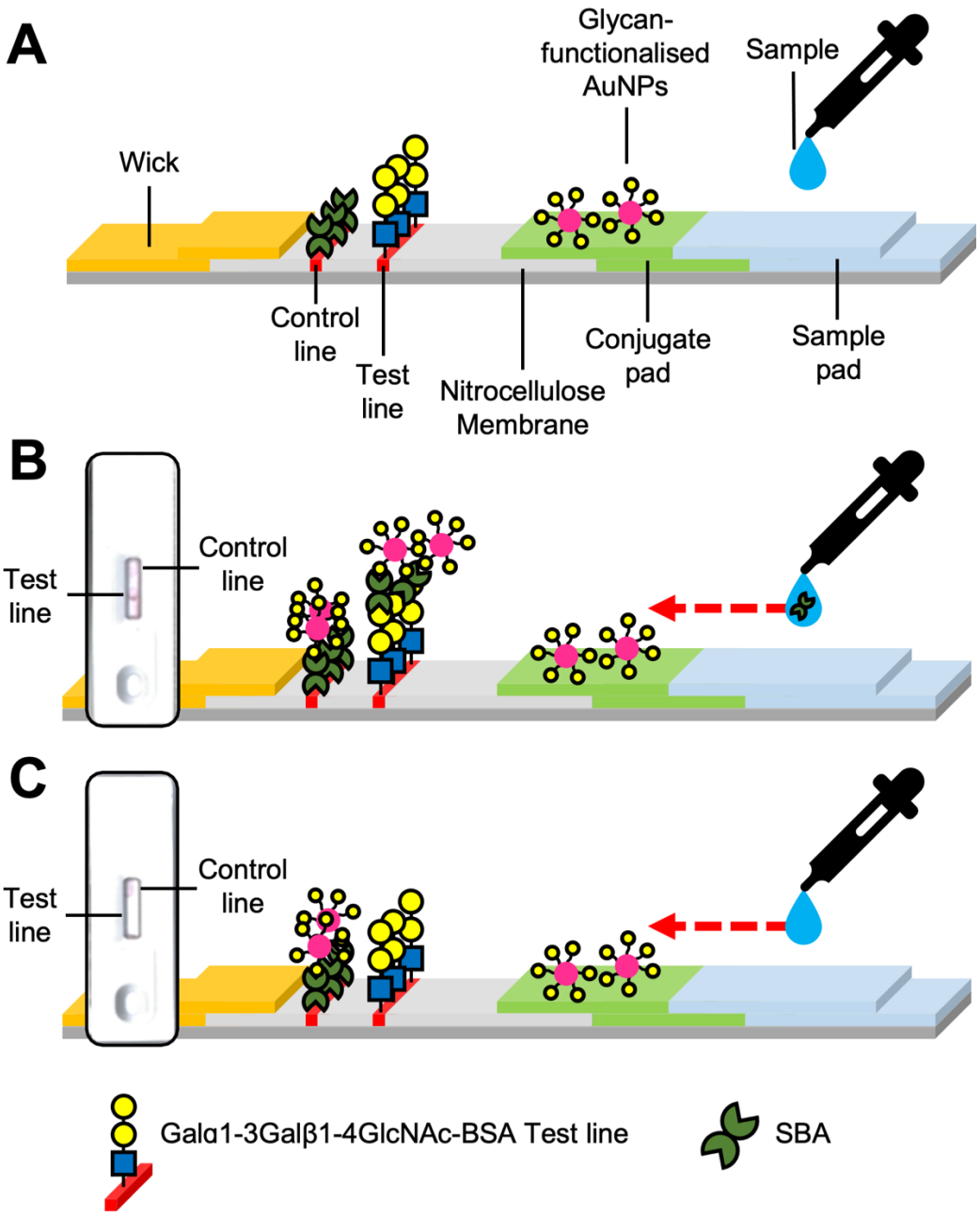

Figure 2.7. Schematic of complete cassette lateral flow for SBA binding and inlaid images of example cassettes.

A) Labelled schematic of cassette; B) Lateral flow with SBA target in sample buffer; C) Lateral flow with no protein in buffer.

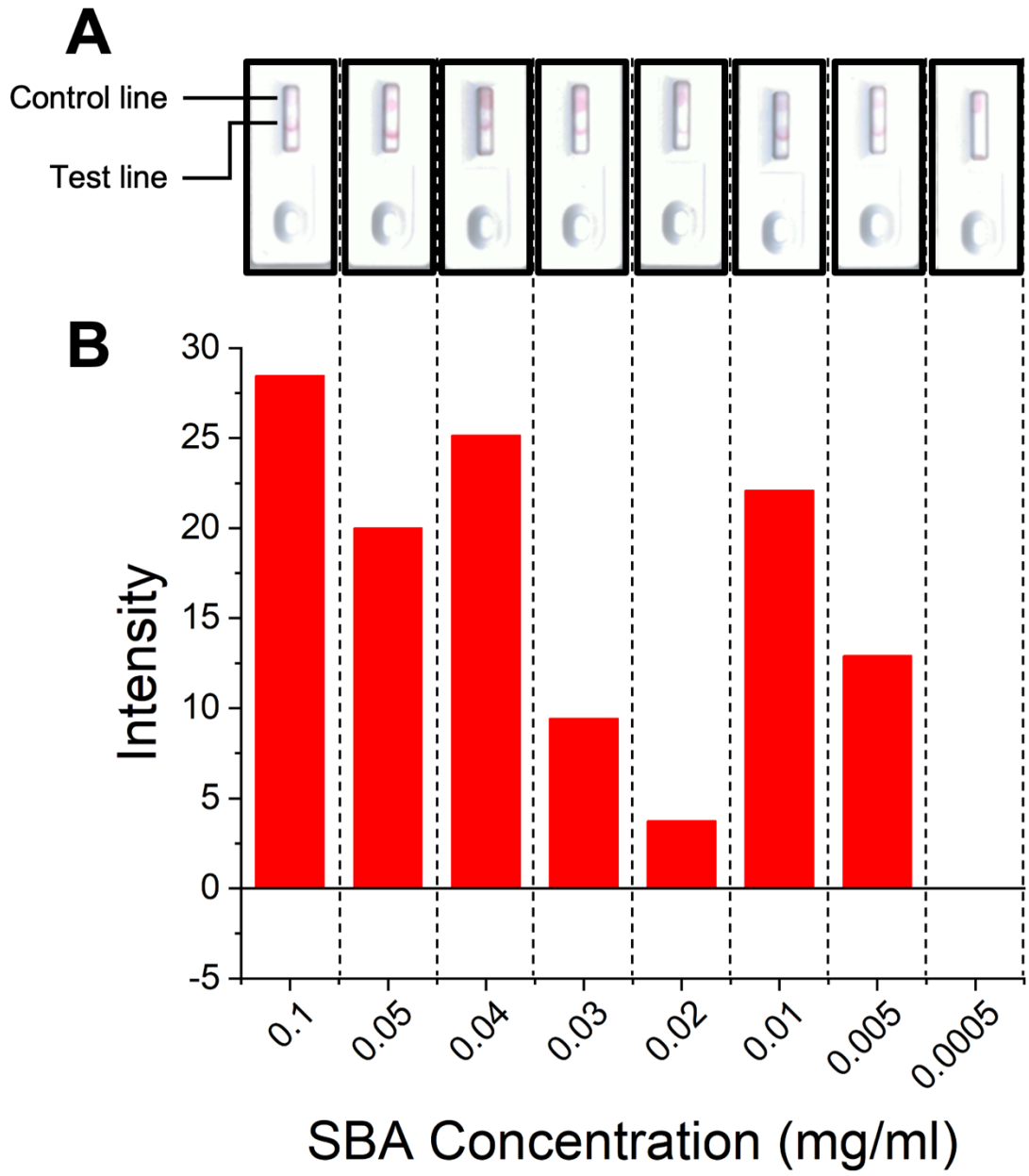

Figure 2.8. Lateral flow data from SBA cassette assays after 10 minutes to determine limit of detection.

A) Example lateral flow cassette photographs for varying concentrations of SBA; B) Analysed lateral flow intensity data for varying concentrations of SBA.

2.5. Conclusions

Here the emerging concept of lateral flow glyco-assays, as a tool for rapid diagnostics/sensing of glycan-binding analytes is validated. Polymeric ligands were used to install glycans onto gold nanoparticles (which are the signal generating units) and provide both colloidal stability in solution while ensuring that the particles resuspend and flow in the lateral flow devices. A library of polymer linker lengths (synthesised using RAFT polymerisation), glycan density (by using polymers without glycans) and nanoparticle size was assembled and the impact of each feature on performance evaluated. A crucial observation was that the optimal polymer-coating required for the detection of SBA was not the same as required for RCA_{120}. This is a unique advantage of employing the polymeric tethers, in that the final device's performance and specificity can be tuned by macromolecular engineering, in addition to varying the exact glycan used. In general, too short polymers increase nonspecific binding, longer polymers reduced nonspecific binding but could reduce signal intensity also, while larger gold particles increase the signal of both nonspecific and specific binding. Therefore, tuning is essential to ensure that accurate and specific diagnostics can be developed.

The optimised glyconanoparticles were incorporated into "real" lateral flow cassettes, that is, a single device where a solution of analyte is applied to a well and run without any additional machine/user interfaces. Using this setup, SBA could be detected as low as 5 $\mu g.mL^{-1}$ (0.042 $nmmol.mL^{-1}$) which is below the (molar) detection limits of commercial lateral flow pregnancy tests which use antibody-functionalised gold nanoparticles and falls within the range of values (microgram to nanogram per millilitre) for antibody-based LFDs.[49,57] Taken together, this work demonstrates the power of using glycans in easy to use, disposable, paper-based lateral flow glyco-assay diagnostics. By using glycans it is possible to probe function (e.g., is the antigen folded) and may provide opportunities for monitoring pathogenic state, rather than simply identifying if a pathogen is present.

2.6 Experimental

2.6.1 Physical and Analytical Methods

NMR Spectroscopy

^{1}H-NMR, ^{13}C-NMR and ^{19}F-NMR spectra were recorded at 300 MHz or 400 MHz on a Bruker DPX-300 or DPX-400 spectrometer respectively, with chloroform-*d* ($CDCl_3$) or deuterium oxide (D_2O) as the solvent. Chemical shifts of protons are reported as δ in parts per million (ppm) and are relative to either $CDCl_3$ (7.26) or D_2O (4.79).

Mass Spectrometry

Low resolution mass spectra (LRMS) were recorded on a Bruker Esquire 2000 spectrometer using electrospray ionisation (ESI). m/z values are reported in Daltons.

FT-IR Spectroscopy

Fourier Transform-Infrared (FT-IR) spectroscopy measurements were carried out using an Agilent Cary 630 FT-IR spectrometer, in the range of 650 to 4000 cm^{-1}.

Size Exclusion Chromatography

Size exclusion chromatography (SEC) analysis was performed on an Agilent Infinity II MDS instrument equipped with differential refractive index (DRI), viscometry (VS), dual angle light scattering (LS) and variable wavelength UV detectors. The system was equipped with 2 x PLgel Mixed D columns (300 x 7.5 mm) and a PLgel 5 µm guard column. The mobile phase used was DMF (HPLC grade) containing 5 mM NH_4BF_4 at 50 °C at flow rate of 1.0 $mL.min^{-1}$. Poly(methyl methacrylate) (PMMA) standards (Agilent EasyVials) were used for calibration between 955,000 – 550 $g.mol^{-1}$. Analyte samples were filtered through a nylon membrane with 0.22 µm pore size before injection. Number average molecular weights (M_n), weight average molecular weights (M_w) and dispersities ($Đ_M = M_w/M_n$) were determined by conventional calibration using Agilent GPC/SEC software.

X-ray Photoelectron Spectroscopy (XPS)

The samples were attached to electrically-conductive carbon tape, mounted on to a sample bar and loaded into a Kratos Axis Ultra DLD spectrometer which possesses a base pressure below 1 x 10^{-10} mbar. XPS measurements were performed in the main analysis chamber, with the sample being illuminated using a monochromated Al Kα

x-ray source. The measurements were conducted at room temperature and at a take-off angle of 90° with respect to the surface parallel. The core level spectra were recorded using a pass energy of 20 eV (resolution approx. 0.4 eV), from an analysis area of 300 μm x 700 μm. The spectrometer work function and binding energy scale of the spectrometer were calibrated using the Fermi edge and $3d_{5/2}$ peak recorded from a polycrystalline Ag sample prior to the commencement of the experiments. In order to prevent surface charging the surface was flooded with a beam of low energy electrons throughout the experiment and this necessitated recalibration of the binding energy scale. To achieve this, the C-C/C-H component of the C 1*s* spectrum was referenced to 285.0 eV. The data were analysed in the CasaXPS package, using Shirley backgrounds and mixed Gaussian-Lorentzian (Voigt) lineshapes. For compositional analysis, the analyser transmission function has been determined using clean metallic foils to determine the detection efficiency across the full binding energy range.

Dynamic Light Scattering

Hydrodynamic diameters (D_h) and size distributions of particles were determined by dynamic light scattering (DLS) using a Malvern Zetasizer Nano ZS with a 4 mW He-Ne 633 nm laser module operating at 25 °C. Measurements were carried out at an angle of 173° (back scattering), and results were analysed using Malvern DTS 7.03 software. All determinations were repeated 5 times with at least 10 measurements recorded for each run. D_h values were calculated using the Stokes-Einstein equation where particles are assumed to be spherical.

UV-vis Spectroscopy

Absorbance measurements were recorded on an Agilent Cary 60 UV-Vis Spectrophotometer and on a BioTek Epoch microplate reader.

Transmission Electron Microscopy

Dry-state stained TEM imaging was performed on a JEOL JEM-2100Plus microscope operating at an acceleration voltage of 200 kV. All dry-state samples were diluted with deionised water and then deposited onto formvar-coated copper grids.

Image Collection of Lateral Flow Dipsticks and Devices

All devices were scanned using a Kyocera TASKalfa 5550ci printer to a pdf file that was converted to a jpeg. The jpeg was analysed in ImageJ 1.51.[48] None of the images in Appendix 2 have been image adjusted i.e. no changes/enhancements have been made from the original scan images.

2.6.2 Materials

All chemicals were used as supplied unless otherwise stated. *N*-Hydroxyethyl acrylamide (97%), 4,4'-azobis(4-cyanovaleric acid) (ACVA, 98%), 4-dimethylaminopyridine (DMAP, > 98%), mesitylene (reagent grade), triethylamine (> 99%), sodium citrate tribasic dihydrate (> 99%), gold(III) chloride trihydrate (99.9%), ammonium carbonate (reagent grade), potassium phosphate tribasic (≥ 98%, reagent grade), potassium hexafluorophosphate (99.5%), deuterium oxide (D_2O, 99.9%), deuterated chloroform ($CDCl_3$, 99.8%), diethyl ether (≥ 99.8%, ACS reagent grade), methanol (≥ 99.8%, ACS reagent grade), toluene (≥ 99.7%,), Tween-20 (molecular biology grade), HEPES, PVP40 (poly(vinyl pyrrolidone)$_{400}$ (Average Mw ~40,000)), sucrose (Bioultra grade), carbon disulphide (≥ 99.8%), acetone (≥ 99%), 1-dodecane thiol (≥ 98%), n-pentylamine (99%) and pentafluorophenol (≥ 99%, reagent plus) were purchased from Sigma-Aldrich. Anhydrous trehalose was purchased from Alfa Aesar. DMF (> 99%) and 2-bromo-2-methyl propionic acid (98%) were purchased from Acros Organics. Galactosamine HCl and 1-Ethyl-3-(3-dimethylaminopropyl)carbodiimide hydrochloride (EDCI, > 98%) were purchased from Carbosynth. HPLC grade acetonitrile (≥ 99.8%), glucose (lab-reagent grade), hexane fraction from petrol (lab reagent grade), DCM (99% lab reagent grade), sodium hydrogen carbonate (≥ 99%), ethyl acetate (≥ 99.7%, analytical reagent grade), sodium chloride (≥ 99.5%), calcium chloride, 40-60 petroleum ether (lab reagent grade), hydrochloric acid (~37%, analytical grade), glacial acetic acid (analytical grade) and magnesium sulphate (reagent grade) were purchased from Thermo Fisher Scientific.

Nitrocellulose Immunopore RP 90-150 s/4cm 25 mm was purchased from GE Healthcare. Lateral flow backing cards 60 mm by 301.58 mm (KN-PS1060.45 with KN211 adhesive) and lateral flow cassettes (KN-CT105) were purchased from Kenosha Tapes. Cellulose fibre wick material 20 cm by 30 cm by 0.825 mm (290 gsm and 180 mL/min) (Surewick CFSP223000) was purchased from EMD Millipore. Glass fibre conjugate pads (GFCP103000) 10 mm by 300 mm and unfunctionalised BSA were purchased from Merck. Thick Chromatography Paper (for sample pads), Grade 237, Ahlstrom 20 cm by 20 cm was purchased from VWR International.

Soybean agglutinin, *Ricinus communis* Agglutinin I (RCA_{120}), *Ulex Europaeus* Agglutinin I and wheat germ agglutinin (WGA) were purchased from Vector

Laboratories. Galα1-3Galβ1-4GlcNAc-BSA (3 atom spacer, NGP0334) was purchased from Dextra Laboratories.

Ultra-pure water used for buffers was MilliQ grade 18.2 mΩ resistance.

2.6.3 Synthetic Methods

Synthesis of 2-(dodecylthiocarbanothionylthio)-2-methyl propionic acid (DMP)

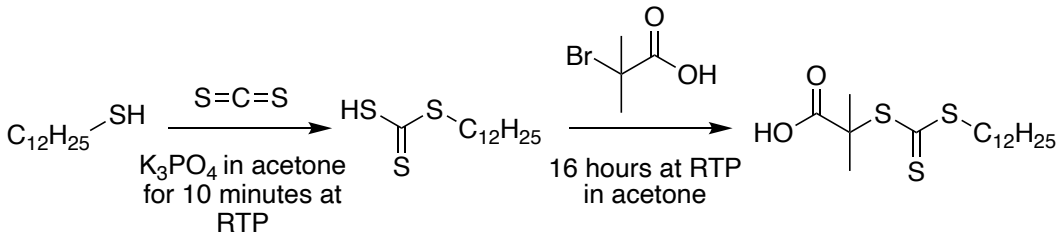

This was synthesised, according to a previously published procedure.[58] 2.00 g (9.88 mmol) of 1-dodecane thiol was added dropwise to stirring 2.10 g (9.89 mmol) of K_3PO_4 in 30 mL of acetone at RTP, the mixture was left to stir for 25 minutes to form a white suspension. 2.05 g (26.93 mmol) of carbon disulphide was then added and left for 10 minutes, a yellow solution formed. 1.5 g (8.98 mmol) of 2-bromo-2-methyl-propionic acid was then added and the solution left to stir for 16 hours. The solvent was removed under vacuum. The crude product was dissolved in 100 mL of 1 M HCl and extracted with DCM (2×100 mL). The organic layer was washed with 200 mL of water and 200 mL of brine. The organic layer was dried with $MgSO_4$ and filtered under gravity. The solvent was then removed from the filtrate under vacuum. The crude product was purified using a silica column (40-60 PET:DCM:glacial acetic acid 75:24:1) and recrystalised in n-hexane to give a yellow solid (58%). δ_H (300 MHz, $CDCl_3$) 3.28 (2H, t, *J* 7.5, SCH_2CH_2), 1.80 - 1.45 (8H, m, $C(CH_3)_2$ and SCH_2CH_2), 1.45 - 1.2 (18H, m, $(CH_2)_9CH_3$), 0.87 (3H, t, *J* 6.0, CH_3). δ_C (400 MHz, $CDCl_3$) 221.0 (1C, SC(S)S), 178.3 (1C, C(O)), 55.7 (1C, $C(CH_3)_2$), 37.7 (1C, SCH_2), 32.1 - 28.0 (9C, $SCH_2(CH_2)_9$), 25.4 (2C, $C(CH_3)_2$), 22.8 (1C, CH_2CH_3), 14.3 (1C, CH_2CH_3). m/z calculated as 364.16; found for ESI $[M+H]^+$ 365.3 and $[M+Na]^+$ 387.3. FTIR (cm^{-1}) – 2956, 2916.6 & 2850 (methyl and methylene), 1702 (ester C=O), 1459, 1437 & 1413 (methyl and methylene), 1280 ($C(CH_3)_2$), 1064 (S-C(S)-S).

Synthesis of pentafluorophenyl-2-dodecylthiocarbonothioylthio)-2-methylpropanoate (PFP-DMP)

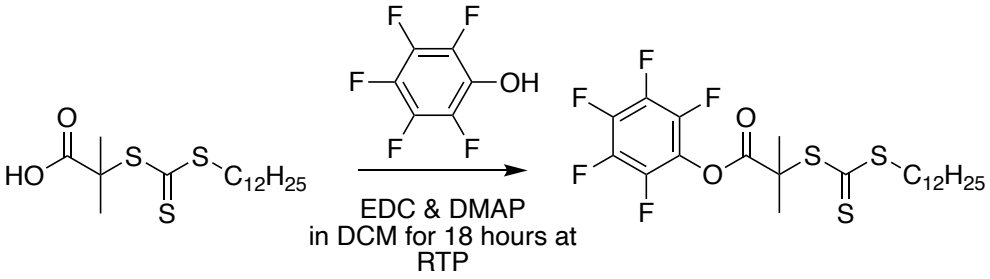

This was synthesised, according to a previously published procedure.[58] 4.06 g (11.13 mmol) of DMP, 3.65 g (19.04 mmol) of EDC and 2.30 g (18.82 mmol) of DMAP were dissolved in 160 mL of DCM and degassed for 30 minutes. 7.28 g (39.55 mmol) of pentaflurophenol was added in 20 mL of DCM and the mixture stirred for 18 hours at RTP. The organic layer was washed with 3 M HCl (200 mL), 1 M $NaHCO_3$ (200 mL) and 0.5 M NaCl (200 mL). The organic layer was dried with $MgSO_4$ and filtered under gravity. The solvent was then removed from the filtrate under vacuum. The crude product was recrystallised from ethyl acetate (or hexane) overnight at -8 °C and dried to give yellow crystals (90.9%). δ_H (300 MHz, $CDCl_3$) 3.31 (2H, t, *J* 7.5, SCH_2CH_2), 1.86 (6H, s, $C(CH_3)_2$), 1.69 (2H, qn, *J* 7.5, SCH_2), 1.48 - 1.16 (18H, m, $CH_2CH_2CH_2CH_2CH_2CH_2CH_2CH_2CH_3$), 0.94 - 0.82 (3H, m, CH_3). δ_C (300 MHz, $CDCl_3$) 220.1 (1C, SC(S)S), 169.7 (1C, C(O)), 143.1 (2C, meta C), 139.8 (1C, ipso C), 139.6 (1C, para C), 136.3 (2C, Ortho C), 55.5 (1C, $C(CH_3)_2$), 37.3 (1C, SCH_2), 32.0 - 22.8 (10C, $SCH_2(CH_2)_{10}$), 25.4 (2C, $C(CH_3)_2$), 14.1 (1C, CH_2CH_3). δ_F (300 MHz, $CDCl_3$) -151.4 - -151.6 (2F, m, $OCC_2H_2C_2H_2CH$), -148.5 (1F, t, *J* 21.5, $OCC_2H_2C_2H_2CH$), -162.2 - -162.5 (2F, m, $OCC_2H_2C_2H_2CH$). m/z calculated as 530.14; found for ESI $[M+Na]^+$ 553.3 and $[M+CH_3CN+Na]^+$ 593.5. FTIR (cm^{-1}) – 2956, 2917 & 2850 (methyl and methylene), 1702 (ester C=O), 1519 (aromatic C=C or C-F), 1460, 1437 & 1413 (methyl and methylene), 1280 ($C(CH_3)_2$), 1068 (S-C(S)-S).

Representative Polymerisation of 2-hydroxyethyl acrylamide

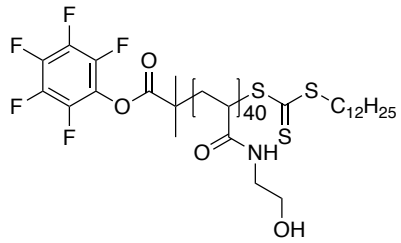

PHEA40 as representative example. 2.0 g (17.37 mmol) of 2-hydroxyethyl acrylamide, 0.043 g (0.15 mmol) of ACVA and 0.368 g (0.69 mmol) of PFP-DMP was added to 16 mL 1:1 toluene:methanol and degassed with nitrogen for 30 minutes. The reaction vessel was stirred and heated to 70 °C for 2 hours. The solvent was removed under vacuum. The crude product was dissolved in the minimum amount of methanol. Diethyl ether cooled in liquid nitrogen was added to the methanol to form a precipitate. The mixture was centrifuged for 2 minutes at 13 krpm and the liquid decanted off. The solid was dissolved in methanol and removed under vacuum to give a yellow crystalline solid.

PHEA40 - δ_H (300 MHz, D_2O) 8.35 - 7.95 (21H, m, N*H*), 3.97 - 3.56 (78H, m, NHC*H*$_2$), 3.56 - 3.03 (80H, m, C*H*$_2$OH & SC*H*$_2$), 2.41 - 1.90 (41H, m, $CH_2CHC(O)$ & $C(CH_3)_2$), 1.90 - 0.99 (108H, m, $CH_2CHC(O)$ & $CH_2CH_2CH_2CH_2CH_2CH_2CH_2CH_2CH_2CH_2CH_3$), 0.83 - 0.72 (5H, m, CH_2CH_3). δ_F (300 MHz, D_2O) -152.0 - -164.3 (5F, m, C_6F_5). FTIR (cm^{-1}) – 3263 (OH, broad), 3088 & 2924 (C(O)NH and NH), 1638 & 1541 (C(O)NH). Yield - 73%

PHEA26 - δ_H (300 MHz, D_2O) 8.38 - 7.88 (13H, m, N*H*), 3.96 - 3.54 (55H, m, NHC*H*$_2$), 3.55 - 3.09 (78H, m, C*H*$_2$OH & SC*H*$_2$), 2.53 - 1.90 (31H, m, $CH_2CHC(O)$ & $C(CH_3)_2$), 1.90 – 1.01 (86H, m, $CH_2CHC(O)$ & $CH_2CH_2CH_2CH_2CH_2CH_2CH_2CH_2CH_2CH_2CH_3$), 0.84 - 0.73 (5H, m, CH_2CH_3)

PHEA50 - δ_H (300 MHz, D_2O) 8.31 - 7.97 (23H, m, N*H*), 3.99 - 3.55 (86H, m, NHC*H*$_2$), 3.55 - 3.09 (100H, m, C*H*$_2$OH & SC*H*$_2$), 2.49 - 1.90 (46H, m, $CH_2CHC(O)$ & $C(CH_3)_2$), 1.90 - 0.98 (110H, m, $CH_2CHC(O)$ & $CH_2CH_2CH_2CH_2CH_2CH_2CH_2CH_2CH_2CH_2CH_3$), 0.84 - 0.72 (5H, m, CH_2CH_3)

PHEA58 - δ_H (300 MHz, D_2O) 8.36 - 7.98 (29H, m, N*H*), 4.00 - 3.55 (H, 108H, m, NHC*H*$_2$), 3.55 - 3.15 (127H, m, C*H*$_2$OH & SC*H*$_2$), 2.36 - 1.88 (56H, m, $CH_2CHC(O)$

& C(C*H*$_3$)$_2$), 1.87 - 1.09 (128H, m, C*H*$_2$CHC(O) & C*H*$_2$C*H*$_2$C*H*$_2$C*H*$_2$C*H*$_2$C*H*$_2$C*H*$_2$C*H*$_2$C*H*$_2$CH$_2$CH$_3$), 0.83 - 0.72 (5H, m, C*H*$_2$C*H*$_3$)

PHEA72 - δ_H (300 MHz, D_2O) 8.30 - 7.96 (34H, m, N*H*), 3.96 - 3.52 (126H, m, NHC*H*$_2$), 3.52 - 3.07 (155H, m, C*H*$_2$OH & SC*H*$_2$), 2.36 - 1.88 (70H, m, CH$_2$C*H*C(O) & C(C*H*$_3$)$_2$), 1.88 - 1.03 (148H, m, C*H*$_2$CHC(O) & C*H*$_2$C*H*$_2$C*H*$_2$C*H*$_2$C*H*$_2$C*H*$_2$C*H*$_2$C*H*$_2$C*H*$_2$CH$_2$CH$_3$), 0.82 - 0.70 (5H, m, C*H*$_2$C*H*$_3$)

PHEA110 - δ_H (300 MHz, D_2O) 8.24 - 8.02 (28H, m, N*H*), 3.83 - 3.51 (239H, m, NHC*H*$_2$), 3.51 - 3.08 (293H, m, C*H*$_2$OH & SC*H*$_2$), 2.40 - 1.90 (117H, m, CH$_2$C*H*C(O) & C(C*H*$_3$)$_2$), 1.90 - 1.03 (273H, m, C*H*$_2$CHC(O) & C*H*$_2$C*H*$_2$C*H*$_2$C*H*$_2$C*H*$_2$C*H*$_2$C*H*$_2$C*H*$_2$C*H*$_2$CH$_2$CH$_3$), 0.86 - 0.73 (5H, m, C*H*$_2$C*H*$_3$)

Representative Poly(N-hydroxyethyl acrylamide) (PHEA40) Glycan Functionalisation

0.25 g (0.088 mmol) of poly(2-hydroxyethyl acrylamide) and 0.090 g (0.50 mmol) of galactosamine HCl were added to 25 ml of DMF containing 0.05 M TEA. The reaction was stirred at 50 ℃ for 16 hours. Solvent was removed under vacuum. The crude product was dissolved in the minimum amount of methanol at RTP before cooling in a liquid nitrogen bath. Diethyl ether cooled in liquid nitrogen was added to the methanol to form a precipitate. The mixture was centrifuged for 2 minutes at 13 krpm and the liquid decanted off. The solid was dissolved in methanol and removed under vacuum to give an orange/brown crystalline solid. δ_H (300 MHz, D_2O) 8.03 - 7.86 (6H, m, NH), 4.96 - 4.87 (2H, anomeric protons), 4.13 - 3.51 (~90H, m, NHCH_2 & glycan protons), 3.51 - 3.09 (~80H, m, CH_2OH & SCH_2 & glycan protons), 2.47 - 1.90 (~50H, m, $CH_2CHC(O)$, $C(CH_3)_2$ & glycan protons), 1.90 - 1.42 (98H, m, CH_2CHC(O) & CH_2CH_2CH_2CH_2CH_2CH_2CH_2CH_2CH_2CH$_3$), 0.93 - 0.72 (5H, m, CH_2CH_3). FTIR (cm^{-1}) – 3267 (OH, broad), 3094 & 2926 (C(O)NH and NH), 1638 & 1545 (C(O)NH).

Representative Poly(2-hydroxyethyl acrylamide) (PHEA40) PFP Removal with n-pentylamine

0.4 g (0.14 mmol) of poly(2-hydroxyethyl acrylamide) and 0.05 ml (3.28 mmol) of n-pentylamine were added to 40 ml of DMF containing 0.05 $moldm^{-3}$ TEA. The reaction was stirred at 50 ℃ for 16 hours. Solvent was removed under vacuum. The crude product was dissolved in the minimum amount of methanol at RTP before cooling in a liquid nitrogen bath. The crude product was dissolved in the minimum amount of methanol. Diethyl ether cooled in liquid nitrogen was added to the methanol to form a precipitate. The mixture was centrifuged for 2 minutes at 13 krpm and the liquid decanted off. The solid was dissolved in methanol and removed under vacuum to give a pale yellow crystalline solid. Removal of PFP was determined by ^{19}F NMR.

Synthesis of 1-deoxy-1-amino-galactose

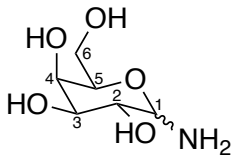

This was synthesised, according to previously published procedures.[59,60] 0.36 g (2 mmol) of galactose and 0.158 g (2 mmol) ammonium hydrogen carbonate were added to a 10 mL solution of 16 mol.dm^{-3} ammonia solution. The mixture was heated for 16 hours at 42 °C. The liquid was removed under vacuum and resuspended in 5 mL of water. The solution was lyophilised to give a cream or off-white crystalline solid, that did not smell of ammonia. (94.6%) (α:β 0.71:0.38). δ_H (300 MHz, $CDCl_3$) 4.24 (0.38H, d, *J* 8.81, C^1H^{α}), 4.03 (0.71H, d, *J* 8.75, C^1H^{β}), 3.93 (1H, d, *J* 3.00, C^3H or C^4H), 3.90 - 3.45 (8H, m, C^3H or C^4H, C^6H_2, C^5H and hydroxyls), 3.39 (1H, t, *J* 9.0, C^2H). δ_C (300 MHz, $CDCl_3$) 87.6 (1C, C^1H^{α}), 85.5 (1C, C^1H^{β}), 76.0 (1C, C^5), 73.4 (1C, C^3 or C^4), 72.0 (1C, C^2), 68.96 (1C, C^3 or C^4), 61.1 (1C, C^6). m/z calculated as 179.171; found for ESI $[2M+Na]^+$ 381.3 and $[M-H^+]^-$ 178.1. FTIR (cm^{-1}) – 3650 - 2500 (hydroxyl), 2924 & 2878 (alkane), 1646 & 1584 (amine), 1465 & 1420 (hydroxyl).

Citrate-Stabilised 16 nm Gold Nanoparticle Synthesis

Synthesised by a previously reported protocol.[61] To 500 mL of water was added 0.163 g (0.414 mmol) of gold(III) chloride trihydrate, the mixture was heated to reflux and 14.6 mL of water containing 0.429 g (1.46 mmol) of sodium citrate tribasic dihydrate was added. The reaction was allowed to reflux for 30 minutes before cooling to room temperature over 3 hours. The solution was centrifuged at 13 krpm for 30 minutes and the pellet resuspended in 40 mL of water to give an absorbance at 520 nm of ~1Abs.

Citrate-Stabilised 40 nm Gold Nanoparticle Synthesis

40 nm gold nanoparticles were synthesised by a modified step growth method developed by Bastús *et al.*.[46] A solution of 2.2 mM sodium citrate in Milli-Q water (150 mL) was heated under reflux for 15 min under vigorous stirring. After boiling had commenced, 1 mL of $HAuCl_4$ (25 mM) was injected. The colour of the solution changed from yellow to bluish gray and then to soft pink in 10 min, 1 mL was taken for DLS and UV/Vis analysis. Immediately after the synthesis of the Au seeds and in the same reaction vessel, the reaction was cooled until the temperature of the solution reached 90 °C. Then, 1 mL of a $HAuCl_4$ solution (25 mM) was injected. After 20 min, the reaction was finished. This process was repeated twice. After that, the sample was diluted by adding 85 mL of MilliQ water and 3.1 mL of 60 mM sodium citrate. This solution was then used as a seed solution, and three further portions of 1.6 mL of 25 mM $HAuCl_4$ were added with 20 min between each addition. Following completion of this step 1 mL was taken for DLS and UV/Vis analysis. The sample was diluted by adding 135 mL of MilliQ water and 4.9 mL of 60 mM sodium citrate. This solution was then used as a seed solution, and the process was repeated with three further additions of 2.5 mL of 25 mM $HAuCl_4$, this solution was analysed by DLS and UV/Vis and target size of 40 nm was reached, so the solution was allowed to cool.

Gold Nanoparticle Polymer Coating Functionalisation – 16 nm

100 mg of glycopolymer was agitated overnight with 10 mL of 16 nm AuNPs ~1Abs at UV_{max}. The solution was centrifuged at 13 krpm for 30 minutes and the pellet resuspended in 10 mL of water, the solution was centrifuged again at 13 krpm for 30 minutes and the pellet resuspended in 1 mL aliquots and centrifuged at 14.5 krpm for 10 minutes. The pellets were combined into a 1 mL solution with an absorbance at 520 nm of ~10 Abs.

Gold Nanoparticle Polymer Coating Functionalisation – 40 nm

100 mg of glycopolymer was agitated overnight with 10 mL of 40 nm AuNPs ~1Abs at UV_{max}. The solution was centrifuged at 8 krpm for 30 minutes and the pellet resuspended in 10 mL of water, the solution was centrifuged again at 8 krpm for 30 minutes and the pellet resuspended in 1 mL aliquots and centrifuged at 8 krpm for 10 minutes. The pellets were combined into a 1 mL solution with an absorbance at UV_{max} of ~10 Abs.

2.6.4 Lateral Flow Strip production, Running and Analysis Protocols

The procedure to produce flow-through and lateral flow devices was identical, apart from the deposition of the analyte directly to the nitrocellulose (flow-through), versus application of tests lines to the nitrocellulose (lateral flow).

Protocol for Manufacturing Lateral Flow Strips

Backing cards were cut to size by removal of 20 mm using a guillotine. Nitrocellulose was added to the backing card by attaching the plastic backing of the nitrocellulose to the self-adhesive on the card. The wick material was then added to the backing card so it overlaps with the nitrocellulose by ~5 mm. The lateral flow strips were cut to size of width 2 - 3 mm.

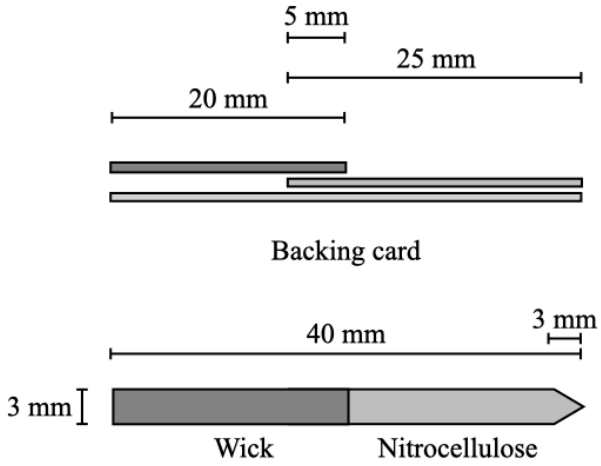

Figure E2.1. Lateral flow strip dimensions

Protocol for Test Line Addition to the Lateral Flow Strips

1 µL of the test line solution was added to the test strip using a micropipette fitted with 10 µL tip, the test line was spotted ~1 cm from the non-wick end of the strip. The strips were dried at 37 ℃ in an oven for 30 minutes. The test strips were allowed to cool to room temperature before testing.

Protocol for Running Lateral Flow Test Without Target Analyte in Buffer

The running buffer of total volume 50 µL was made as follows; 5 µL AuNPs (OD10), 5 µL lateral flow assay buffer – 10 × HEPES buffer, 40 µL water. The running solution was then agitated on a roller for 5 minutes. 45 µL of this solution was added to a 0.2 mL PCR tube, standing vertically.

A small "v" (~3 mm) was cut into the test strips at the non-wick end and the strips added to the PCR tubes, so they protrude from the top and the immobile phase (1 cm from non-wick end) is not below the solvent line. There was one test per tube. All tests were run in triplicate.

The tests were run for 20 minutes before removal from the tubes. The test strips were allowed to dry at room temperature for ~5 minutes. The test strips were mounted test-face down onto a clear and colourless piece of acetate sheeting.

The *Protocol for Running Lateral Flow Test Without Target Analyte in Buffer* was used for the flow-through assays as the target analyte is deposited on the nitrocellulose as a "test line" i.e. the analyte is not in the running buffer.

Protocol for Running Lateral Flow Test with Target Analyte in Buffer

The running buffer of total volume 50 µL was made as follows; 5 µL AuNPs (OD10), 5 µL lateral flow assay buffer – 10 × HEPES buffer, 40 µL of water - *x* µL, where *x* is the volume of target analyte added to make the required concentration of the lectin. The running solution was then agitated on a roller for 5 minutes. 45 µL of this solution was added to a 0.2 mL PCR tube, standing vertically.

A small "v" (~3 mm) was cut into the test strips at the non-wick end and the strips added to the PCR tubes, so they protrude from the top and the immobile phase (1 cm from non-wick end) is not below the solvent line. There was one test per tube. All tests were run in triplicate.

The tests were run for 20 minutes before removal from the tubes. The test strips were allowed to dry at room temperature for ~5 minutes. The test strips were mounted test-face down onto a clear and colourless piece of acetate sheeting.

Standard Protocol for Lateral Flow Strip Analysis

The acetate sheets were scanned using a Kyocera TASKalfa 5550ci printer to a pdf file that was converted to a jpeg, scans were taken within 1 hour of strip drying. The jpeg was analysed in ImageJ 1.51[48] using the plot profile function to create a data set exported to Microsoft Excel for Mac. The data was exported to Origin 2019 64Bit and trimmed to remove pixel data not from the strip surface. The data was aligned and averaged (mean). The data was then reduced by number of groups to 100 data points

(nitrocellulose and wick) and plotted as Grey value (scale) vs Relative distance along the 100 data points.

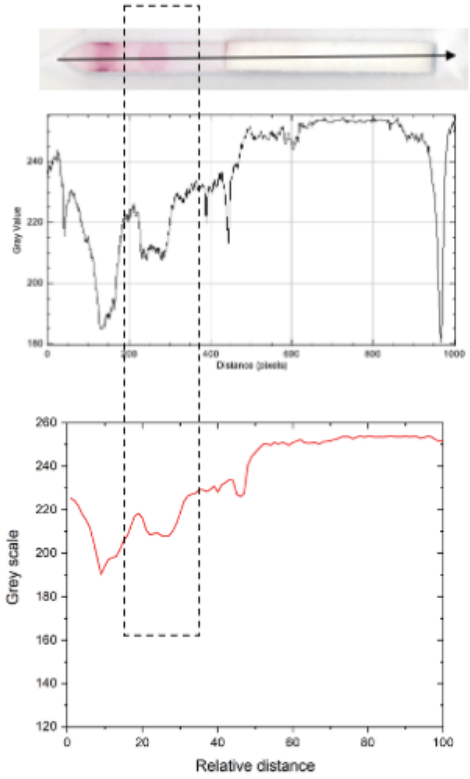

Figure E2.2. Representative dipstick (Top), raw grey value plot (Middle) and processed grey value plot (Bottom)

Lateral Flow Signal-to-Noise Analysis

Relative distance pixel 15 to 35 (area around the test line) was averaged (mean) to provide average noise around the test line for strips vs. Galα1-3Galβ1-4GlcNAc-BSA (BSA-Gal) (1 mg/mL) as a test line. The signal value was determined by selecting the lowest grey value between 15 to 35 relative distance pixels as a test line. Equation E2.1 was then used to determine the signal-to-noise ratio.

$$Signal - to - noise = \frac{255 - Signal}{255 - Noise}$$

Equation E2.1. Equation for determining signal-to-noise ratio

NB: 255 is the grey value for the blank nitrocellulose surface.

Lateral Flow Signal Intensity Analysis

Relative distance pixel 15 to 35 (area around the test line), excluding pixels that contributed to the signal peak were averaged (mean). This average was subtracted from the lowest grey value between 15 to 35.

Lateral Flow Assay Buffer - 10× HEPES buffer (10% PVP_{400}) in 100 mL H_2O

2.38 g (100 mmol.dm^{-3}) of HEPES, 8.77 g (1.50 mol.dm^{-3}) of NaCl, 0.011 g (1.0 mmol.dm^{-3}) of $CaCl_2$, 0.8 g (0.8% w/v., 123 mmol.dm^{-3}) of NaN_3, 0.5 g (0.5% w/v., 4.07 mmol.dm^{-3}) of Tween-20 and 10 g (10% w/v.) of poly(vinyl pyrrolidone)$_{400}$ (PVP_{400}, Average Mw ~40,000) were dissolved in 100 mL of water. The buffer was not pH adjusted.

2.6.5 Lateral Flow Complete Device Production, Running and Analysis Protocols

Protocol for Manufacturing Lateral Flow Complete Devices/Cassettes

Nitrocellulose was added to the backing card by attaching the plastic backing of the nitrocellulose to the self-adhesive on the card. The wick material was then added to the backing card so it overlaps with the nitrocellulose by ~5 mm. The strips were then cut to size of width ~3 mm so they sit in the cassettes without the need for excess force to fit. Tests lines were then added before addition of the conjugate pad. 1 µL of the test line solution was added to the nitrocellulose strip using a micropipette fitted with 10 µL tip, the test line was spotted ~1 cm from the non-wick end of the nitrocellulose surface. A control line was added ~1.5 cm from non-wick end of the nitrocellulose surface. The control for galactosamine systems was 1 µL (5 $mg.mL^{-1}$) SBA. The strips were dried at 37 ℃ in an oven for 30 minutes. The test strips were allowed to cool to room temperature before addition of the conjugate pad. The conjugate pad was added to the backing card so it overlaps with the nitrocellulose by ~3.5 mm. The sample pad, was cut to size (20 mm by 6 mm) and added to the backing card, overlapping with the conjugate pad by ~6.5 mm and straddling the backing card evenly. The completed strip was then added to the cassettes and sealed.

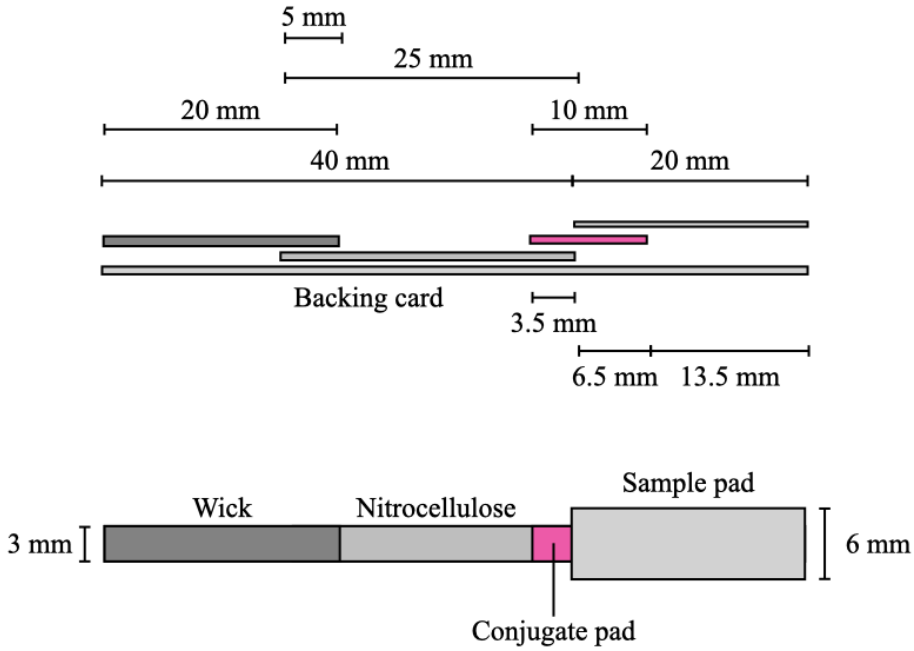

Figure E2.3. Lateral flow complete strip dimensions

Protocol for Conjugate Pad Production

Strips of the conjugate pad material were agitated for 30 minutes in a solution of 0.1% Tween-20 (blocking solution). The strips were then patted dry and baked overnight at 37 ℃ in an oven. The conjugate pads were cut to size (3 mm width) and placed individually into the wells of a 384-well microplate. 20 µL 1× conjugate pad buffer solution containing OD1 AuNPs was added to the top of each conjugate pad in the wells. The pads were dried for 3 hours at 37 ℃ in an oven before curing overnight in an airtight box containing desiccant. The completed pads were always stored in an airtight box containing desiccant.

10× Conjugate Pad Buffer

10% w/v. of poly(vinyl pyrrolidone)$_{400}$ (Average Mw ~40,000 g.mol^{-1}), 50% w/v. trehalose, 10% w/v. sucrose and 0.1% w/v. Tween-20 were added to distilled water and allowed to dissolve.

Protocol for Running Lateral Flow Test Without Target Analyte in Buffer

8 µL 10× HEPES buffer (20% PVP$_{400}$) was added to 72 µL distilled water. 80 µL was added to the sample pad and allowed to absorb. The test was run for 10 minutes before scanning the cassettes using a Kyocera TASKalfa 5550ci printer, the images were exported to a pdf file that was converted to a jpeg. Within ~1 hour the strips were removed from the cassettes and added to acetate sheets. These were scanned using a Kyocera TASKalfa 5550ci printer to a pdf file that was converted to a jpeg, acetate scans were taken within 1 hour of strip drying. The jpegs were analysed in Image J 1.51 using the plot profile function to create a data set exported to Microsoft Excel for Mac. The data was exported to Origin 2019 64Bit and trimmed to remove pixel data not from the strip surface. The data was aligned and averaged (mean). The data was then reduced by number of groups to 100 data points (just the nitrocellulose surface) and plotted as Grey value (scale) vs Relative distance along the 100 data points.

Protocol for Running Lateral Flow Test with Target Analyte in Buffer

8 µL 10× HEPES buffer (20% PVP$_{400}$) was added to 72 µL of water - x µL, where x is the volume of target analyte added to make the required concentration of the lectin. 80 µL was added to the sample pad and allowed to absorb. The test was run for 10 minutes before scanning the cassettes using a Kyocera TASKalfa 5550ci printer, the images were exported to a pdf file that was converted to a jpeg. Within ~1 hour the

strips were removed from the cassettes and added to acetate sheets. These were scanned using a Kyocera TASKalfa 5550ci printer to a pdf file that was converted to a jpeg, acetate scans were taken within 1 hour of strip drying. The jpegs were analysed in Image J 1.51 using the plot profile function to create a data set exported to Microsoft Excel for Mac. The data was exported to Origin 2019 64Bit and trimmed to remove pixel data not from the strip surface. The data was aligned and averaged (mean). The data was then reduced by number of groups to 100 data points (just the nitrocellulose surface) and plotted as Grey value (scale) vs Relative distance along the 100 data points.

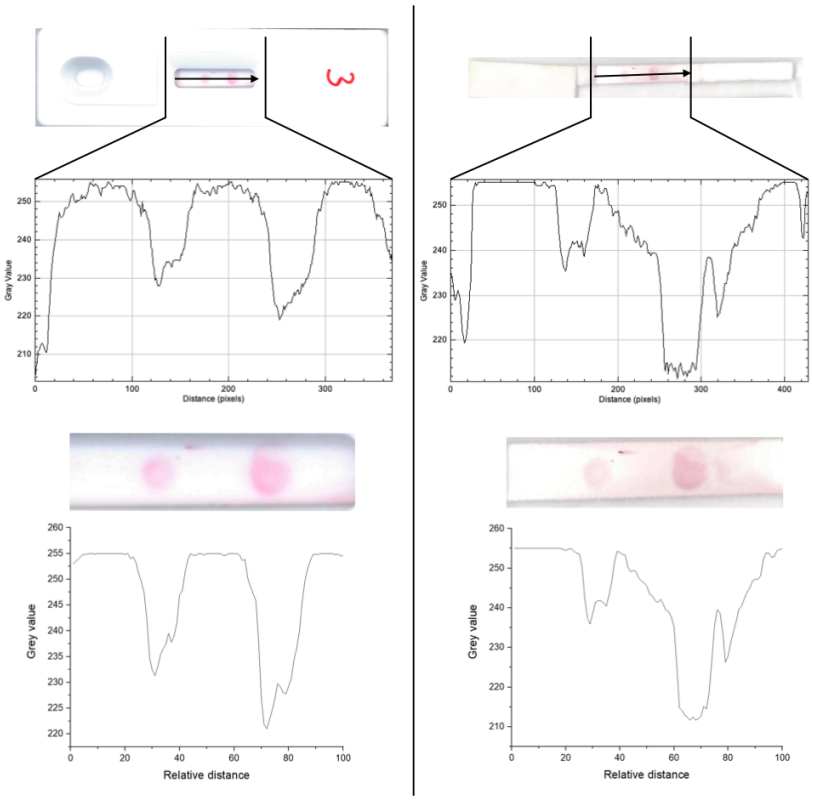

Figure E2.4. Representative cassette (Top left) and strip (Top right), raw grey value plot (Middle) and processed grey value plot (Bottom)

Lateral Flow Signal Intensity Analysis

Relative distance pixel 1 to 10 and 51 to 60 (area around the test line), excluding pixels that contributed to the signal peak were averaged (mean). This average was subtracted from the lowest grey value between 11 to 50 (test line region).

2.7 References

(1) Crane, M. M.; Organon MV. *Diagnostic Test Device - US3579306A*; 1969.

(2) Ezennia, I. J.; Nduka, S. O.; Ekwunife, O. I. Cost Benefit Analysis of Malaria Rapid Diagnostic Test: The Perspective of Nigerian Community Pharmacists. *Malaria Journal* **2017**, *16* (1), 7–16.

(3) Tawiah, T.; Hansen, K. S.; Baiden, F.; Bruce, J.; Tivura, M.; Delimini, R.; Amengo-Etego, S.; Chandramohan, D.; Owusu-Agyei, S.; Webster, J. Cost-Effectiveness Analysis of Test-Based versus Presumptive Treatment of Uncomplicated Malaria in Children under Five Years in an Area of High Transmission in Central Ghana. *PLOS ONE* **2016**, *11* (10), e0164055.

(4) Aerts, C.; Vink, M.; Pashtoon, S. J.; Nahzat, S.; Picado, A.; Cruz, I.; Sicuri, E. Cost Effectiveness of New Diagnostic Tools for Cutaneous Leishmaniasis in Afghanistan. *Applied Health Economics and Health Policy* **2019**, *17* (2), 213–230.

(5) Phan, J. C.; Pettitt, J.; George, J. S.; Fakoli, L. S.; Taweh, F. M.; Bateman, S. L.; Bennett, R. S.; Norris, S. L.; Spinnler, D. A.; Pimentel, G.; Sahr, P. K.; Bolay, F. K.; Schoepp, R. J. Lateral Flow Immunoassays for Ebola Virus Disease Detection in Liberia. *Journal of Infectious Diseases* **2016**, *214* (suppl 3), S222–S228.

(6) Crozier, A.; Rajan, S.; Buchan, I.; McKee, M. Put to the Test: Use of Rapid Testing Technologies for Covid-19. *BMJ* **2021**, *372*, n208.

(7) Banerjee, R.; Jaiswal, A. Recent Advances in Nanoparticle-Based Lateral Flow Immunoassay as a Point-of-Care Diagnostic Tool for Infectious Agents and Diseases. *Analyst* **2018**, *143* (9), 1970–1996.

(8) Amendola, V.; Pilot, R.; Frasconi, M.; Maragò, O. M.; Iatì, M. A. Surface Plasmon Resonance in Gold Nanoparticles: A Review. *Journal of Physics: Condensed Matter* **2017**, *29* (20), 203002.

(9) Dreaden, E. C.; Alkilany, A. M.; Huang, X.; Murphy, C. J.; El-Sayed, M. A. The Golden Age: Gold Nanoparticles for Biomedicine. *Chem. Soc. Rev.* **2012**, *41* (7), 2740–2779.

(10) Saha, K.; Agasti, S. S.; Kim, C.; Li, X.; Rotello, V. M. Gold Nanoparticles in Chemical and Biological Sensing. *Chemical Reviews* **2012**, *112* (5), 2739–2779.

(11) Wu, J.; Ma, J.; Wang, H.; Qin, D.; An, L.; Ma, Y.; Zheng, Z.; Hua, X.; Wang, T.; Wu, X. Rapid and Visual Detection of Benzothiostrobin Residue in Strawberry Using Quantum Dot-Based Lateral Flow Test Strip. *Sensors and Actuators B: Chemical* **2019**, *283*, 222–229.

(12) Yu, L.; Li, P.; Ding, X.; Zhang, Q. Graphene Oxide and Carboxylated Graphene Oxide: Viable Two-Dimensional Nanolabels for Lateral Flow Immunoassays. *Talanta* **2017**, *165*, 167–175.

(13) Hassan, A. H. A.; Bergua, J. F.; Morales-Narváez, E.; Mekoçi, A. Validity of a Single Antibody-Based Lateral Flow Immunoassay Depending on Graphene Oxide for Highly Sensitive Determination of E. Coli O157:H7 in Minced Beef and River Water. *Food Chemistry* **2019**, *297*, 124965.

(14) Yao, L.; Teng, J.; Zhu, M.; Zheng, L.; Zhong, Y.; Liu, G.; Xue, F.; Chen, W. MWCNTs Based High Sensitive Lateral Flow Strip Biosensor for Rapid Determination of Aqueous Mercury Ions. *Biosensors and Bioelectronics* **2016**, *85*, 331–336.

(15) Mao, X.; Ma, Y.; Zhang, A.; Zhang, L.; Zeng, L.; Liu, G. Disposable Nucleic Acid Biosensors Based on Gold Nanoparticle Probes and Lateral Flow Strip. *Analytical Chemistry* **2009**, *81* (4), 1660–1668.

(16) Damborský, P.; Koczula, K. M.; Gallotta, A.; Katrlík, J. Lectin-Based Lateral Flow Assay: Proof-of-Concept. *The Analyst* **2016**, *141* (23), 6444–6448.

(17) Bertozzi, C. R.; Kiessling; L., L.; Kiessling, L. L. Chemical Glycobiology. *Science* **2001**, *291* (5512), 2357–2364.

(18) Apweiler, R.; Hermjakob, H.; Sharon, N. On the Frequency of Protein Glycosylation, as Deduced from Analysis of the SWISS-PROT Database. *Biochimica et Biophysica Acta - General Subjects* **1999**, *1473* (1), 4–8.

(19) Haltiwanger, R. S. Regulation of Signal Transduction by Glycosylation. *International Journal of Experimental Pathology* **2004**, *85* (4), A49–A77.

(20) Marth, J. D.; Grewal, P. K. Mammalian Glycosylation in Immunity. *Nature Reviews Immunology* **2008**, *8* (11), 874–887.

(21) Ströh, L. J.; Stehle, T. Glycan Engagement by Viruses: Receptor Switches and Specificity. *Annual Review of Virology* **2014**, *1* (1), 285–306.

(22) Olofsson, S.; Bergström, T. Glycoconjugate Glycans as Viral Receptors. *Annals of Medicine* **2005**, *37* (3), 154–172.

(23) Viswanathan, K.; Chandrasekaran, A.; Srinivasan, A.; Raman, R.; Sasisekharan, V.; Sasisekharan, R. Glycans as Receptors for Influenza Pathogenesis. *Glycoconjugate journal* **2010**, *27* (6), 561–570.

(24) Richards, R. L.; Moss, J.; Alving, C. R.; Fishman, P. H.; Brady, R. O. Choleragen (Cholera Toxin): A Bacterial Lectin. *Proceedings of the National Academy of Sciences of the United States of America* **1979**, *76* (4), 1673–1676.

(25) Li, S. S.; Wei, C. H.; Lin, J.-Y.; Tung, T.-C. Amino-Terminal Sequences of the Anti-Tumor Lectin Ricin A- and B-Chains. *Biochemical and Biophysical Research Communications* **1975**, *65* (4), 1191–1195.

(26) Sartim, M. A.; Sampaio, S. V. Snake Venom Galactoside-Binding Lectins: A Structural and Functional Overview. *Journal of Venomous Animals and Toxins including Tropical Diseases* **2015**, *21* (1), 35.

(27) Liao, W.-R.; Lin, J.-Y.; Shieh, W.-Y.; Jeng, W.-L.; Huang, R. Antibiotic Activity of Lectins from Marine Algae against Marine Vibrios. *Journal of Industrial Microbiology and Biotechnology* **2003**, *30* (7), 433–439.

(28) Manning, J. C.; Romero, A.; Habermann, F. A.; García Caballero, G.; Kaltner, H.; Gabius, H.-J. Lectins: A Primer for Histochemists and Cell Biologists. *Histochemistry and Cell Biology* **2017**, *147* (2), 199–222.

(29) Jelinek, R.; Kolusheva, S. Carbohydrate Biosensors. *Chemical Reviews* **2004**, *104* (12), 5987–6016.

(30) Cunningham, S.; Gerlach, J. Q.; Kane, M.; Joshi, L. Glyco-Biosensors: Recent Advances and Applications for the Detection of Free and Bound Carbohydrates. *The Analyst* **2010**, *135* (10), 2471–2480.

(31) Zeng, X.; Andrade, C. A. S.; Oliveira, M. D. L.; Sun, X.-L. Carbohydrate--Protein Interactions and Their Biosensing Applications. *Analytical and Bioanalytical Chemistry* **2012**, *402* (10), 3161–3176.

(32) Damborský, P.; Damborská, D.; Belický, Š.; Tkáč, J.; Katrlík, J. Sweet Strategies in Prostate Cancer Biomarker Research: Focus on a Prostate Specific Antigen. *BioNanoScience* **2018**, *8* (2), 690–700.

(33) Bayoumy, S.; Hyytiä, H.; Leivo, J.; Talha, S. M.; Huhtinen, K.; Poutanen, M.; Hynninen, J.; Perheentupa, A.; Lamminmäki, U.; Gidwani, K.; Pettersson, K. Glycovariant-Based Lateral Flow Immunoassay to Detect Ovarian Cancer–Associated Serum CA125. *Communications Biology* **2020**, *3* (1), 460.

(34) Ishii, J.; Toyoshima, M.; Chikae, M.; Takamura, Y.; Miura, Y. Preparation of Glycopolymer-Modified Gold Nanoparticles and a New Approach for a Lateral Flow Assay. *Bulletin of the Chemical Society of Japan* **2011**, *84* (5), 466–470.

(35) Takara, M.; Toyoshima, M.; Seto, H.; Hoshino, Y.; Miura, Y. Polymer-Modified Gold Nanoparticles via RAFT Polymerization: A Detailed Study for a Biosensing Application. *Polymer Chemistry* **2014**, *5* (3), 931–939.

(36) Baker, A. N.; Richards, S.-J.; Guy, C. S.; Congdon, T. R.; Hasan, M.; Zwetsloot, A. J.; Gallo, A.; Lewandowski, J. R.; Stansfeld, P. J.; Straube, A.; Walker, M.; Chessa, S.; Pergolizzi, G.; Dedola, S.; Field, R. A.; Gibson, M. I. The SARS-COV-2 Spike Protein Binds Sialic Acids and Enables Rapid Detection in a Lateral Flow Point of Care Diagnostic Device. *ACS Central Science* **2020**, *6* (11), 2046–2052.

(37) Huang, X.; Dong, W.; Milewska, A.; Golda, A.; Qi, Y.; Zhu, Q. K.; Marasco, W. A.; Baric, R. S.; Sims, A. C.; Pyrc, K.; Li, W.; Sui, J. Human Coronavirus HKU1 Spike Protein Uses O -Acetylated Sialic Acid as an Attachment Receptor Determinant and Employs Hemagglutinin-Esterase Protein as a Receptor-Destroying Enzyme. *Journal of Virology* **2015**, *89* (14), 7202–7213.

(38) Hulswit, R. J. G.; Lang, Y.; Bakkers, M. J. G.; Li, W.; Li, Z.; Schouten, A.; Ophorst, B.; van Kuppeveld, F. J. M.; Boons, G.-J.; Bosch, B.-J.; Huizinga, E. G.; de Groot, R. J. Human Coronaviruses OC43 and HKU1 Bind to 9- O -Acetylated Sialic Acids via a Conserved Receptor-Binding Site in Spike Protein Domain A. *Proceedings of the National Academy of Sciences* **2019**, *116* (7), 2681–2690.

(39) Park, Y. J.; Walls, A. C.; Wang, Z.; Sauer, M. M.; Li, W.; Tortorici, M. A.; Bosch, B. J.; DiMaio, F.; Veesler, D. Structures of MERS-CoV Spike Glycoprotein in Complex with Sialoside Attachment Receptors. *Nature Structural and Molecular Biology* **2019**, *26* (12), 1151–1157.

(40) Baker, A. N.; Richards, S.-J.; Pandey, S.; Guy, C. S.; Ahmad, A.; Hasan, M.; Biggs, C. I.; Georgiou, P. G.; Zwetsloot, A. J.; Straube, A.; Dedola, S.; Field, R. A.; Anderson, N. R.; Walker, M.; Grammatopoulos, D.; Gibson, M. I. Glycan-Based

Flow-Through Device for the Detection of SARS-COV-2. *ACS Sensors* **2021**, *6* (10), 3696–3705.

(41) Jorgensen, P.; Chanthap, L.; Rebueno, A.; Tsuyuoka, R.; Bell, D. Malaria Rapid Diagnostic Tests in Tropical Climates: The Need for a Cool Chain. *American Journal of Tropical Medicine and Hygiene* **2006**, *74* (5), 750–754.

(42) Richards, S.-J.; Baker, A. N.; Walker, M.; Gibson, M. I. Polymer-Stabilized Sialylated Nanoparticles: Synthesis, Optimization, and Differential Binding to Influenza Hemagglutinins. *Biomacromolecules* **2020**, *21* (4), 1604–1612.

(43) Georgiou, P. G.; Baker, A. N.; Richards, S.-J.; Laezza, A.; Walker, M.; Gibson, M. I. "Tuning Aggregative versus Non-Aggregative Lectin Binding with Glycosylated Nanoparticles by the Nature of the Polymer Ligand." *Journal of Materials Chemistry B* **2020**, *8* (1), 136–145.

(44) Richards, S.-J.; Otten, L.; Besra, G. S.; Gibson, M. I. Glycosylated Gold Nanoparticle Libraries for Label-Free Multiplexed Lectin Biosensing. *J. Mater. Chem. B* **2016**, *4* (18), 3046–3053.

(45) He, Y. Q.; Liu, S. P.; Kong, L.; Liu, Z. F. A Study on the Sizes and Concentrations of Gold Nanoparticles by Spectra of Absorption, Resonance Rayleigh Scattering and Resonance Non-Linear Scattering. *Spectrochimica Acta - Part A: Molecular and Biomolecular Spectroscopy* **2005**, *16* (13–14), 2861–2866.

(46) Bastús, N. G.; Comenge, J.; Puntes, V. Kinetically Controlled Seeded Growth Synthesis of Citrate-Stabilized Gold Nanoparticles of up to 200 Nm: Size Focusing versus Ostwald Ripening. *Langmuir* **2011**, *27* (17), 11098–11105.

(47) Sajid, M.; Kawde, A.-N.; Daud, M. Designs, Formats and Applications of Lateral Flow Assay: A Literature Review. *Journal of Saudi Chemical Society* **2015**, *19* (6), 689–705.

(48) Schneider, C. A.; Rasband, W. S.; Eliceiri, K. W. NIH Image to ImageJ: 25 Years of Image Analysis. *Nature Methods* **2012**, *9* (7), 671–675.

(49) Alfthan, H.; Björses, U.-M.; Tiitinen, A.; Stenman, U.-H. Specificity and Detection Limit of Ten Pregnancy Tests. *Scandinavian Journal of Clinical and Laboratory Investigation* **1993**, *53*, 105–113.

(50) Park, S.; Lee, M.-R.; Shin, I. Construction of Carbohydrate Microarrays by Using One-Step, Direct Immobilizations of Diverse Unmodified Glycans on Solid Surfaces. *Bioconjugate Chemistry* **2009**, *20* (1), 155–162.

(51) Manimala, J. C.; Roach, T. A.; Li, Z.; Gildersleeve, J. C. High-Throughput Carbohydrate Microarray Analysis of 24 Lectins. *Angewandte Chemie International Edition* **2006**, *45* (22), 3607–3610.

(52) St John, A.; Price, C. P. Point-of-Care Testing Technologies Existing and Emerging Technologies for Point-of-Care Testing. *Clin Biochem Rev* **2014**, *35* (3), 155–167.

(53) Zheng, M. Z.; Richard, J. L.; Binder, J. A Review of Rapid Methods for the Analysis of Mycotoxins. *Mycopathologia* **2006**, *161* (5), 261–273.

(54) Monsigny, M.; Roche, A.-C.; Sene, C.; Maget-Dana, R.; Delmotte, F. Sugar-Lectin Interactions: How Does Wheat-Germ Agglutinin Bind Sialoglycoconjugates? *European Journal of Biochemistry* **1980**, *104* (1), 147–153.

(55) Pereira, M. E.; Kabat, E. A.; Sharon, N. Immunochemical Studies on the Specificity of Soybean Agglutinin. *Carbohydrate research* **1974**, *37* (1), 89–102.

(56) Green, E. D.; Brodbeck, R. M.; Baenziger, J. U. Lectin Affinity High-Performance Liquid Chromatography. Interactions of N-Glycanase-Released Oligosaccharides with Ricinus Communis Agglutinin I and Ricinus Communis Agglutinin II. *Journal of Biological Chemistry* **1987**, *262* (25), 12030–12039.

(57) Bahadır, E. B.; Sezgintürk, M. K. Lateral Flow Assays: Principles, Designs and Labels. *TrAC Trends in Analytical Chemistry* **2016**, *82*, 286–306.

(58) Richards, S.-J.; Gibson, M. I. Optimization of the Polymer Coating for Glycosylated Gold Nanoparticle Biosensors to Ensure Stability and Rapid Optical Readouts. *ACS Macro Letters* **2014**, *3* (10), 1004–1008.

(59) Campa, C.; Donati, I.; Vetere, A.; Gamini, A.; Paoletti, S. Synthesis of Glycosylamines: Indentification and Quantification of Side Products. *Journal of Carbohydrate Chemistry* **2001**, *20* (3–4), 263–273.

(60) Lubineau, A.; Augé, J.; Drouillat, B. Improved Synthesis of Glycosylamines and a Straightforward Preparation of N-Acylglycosylamines as Carbohydrate-Based Detergents. *Carbohydrate Research* **1995**, *266* (2), 211–219.

(61) Ieong, N. S.; Brebis, K.; Daniel, L. E.; O'Reilly, R. K.; Gibson, M. I. The Critical Importance of Size on Thermoresponsive Nanoparticle Transition Temperatures: Gold and Micelle-Based Polymer Nanoparticles. *Chemical Communications* **2011**, *47* (42), 11627–11629.

Chapter 3

The SARS-COV-2 Spike Protein Binds Sialic Acids, and Enables Rapid Detection in Flow-Through and Lateral Flow Point of Care Diagnostic Devices

3.1 Abstract

There is an urgent need to understand the behavior of the novel coronavirus (SARS-COV-2), which is the causative agent of COVID-19, and to develop point of care diagnostics. Here, a glyconanoparticle platform is used to discover that *N*-acetyl neuraminic acid has affinity toward the SARS-COV-2 spike glycoprotein, demonstrating its glycan-binding function. Optimisation of the particle size and coating enabled detection of the spike glycoprotein in flow-through and showed selectivity over the SARS-COV-1 spike protein. Using a virus-like particle and a pseudotyped lentivirus model, paper-based lateral flow detection was demonstrated in under 30 minutes showing the potential of this system as a low-cost detection platform.

3.2 Declaration

This chapter contains the paper discussing the detection of SARS-COV-2 spike protein using flow-through and lateral flow diagnostics by harnessing sialic acids as capture agents.

Sarah-Jane Richards carried out the BLI studies, synthesised the 35 to 70 nm gold particles, functionalised the polymers with glycans, characterised the particles by DLS and UV-vis, and helped run the flow-through and lateral flow devices; Collette Guy, Simona Chessa and Giulia Pergolizzi synthesised the *N*-acetyl neuraminic acid derivatives; Collette Guy also carried out the pseudotyped lentivirus experiments; Tom Congdon assisted with LFD construction and polymer characterisation; Muhammad Hasan carried out the sequence alignments, expressed the spike protein used for the thermal shift assays and carried out the thermal shift assays; Alexander Zwetsloot and Anne Straube expressed the spike protein used for testing the devices; Angelo Gallo and Józef Lewandowski carried out the STD NMR; Peter Stansfeld produced the hypothesised sialic binding site model of the spike protein; and Marc Walker carried out the XPS analysis and supported model fitting the XPS data.

I synthesised the RAFT agent, the polymers, the 16 nm gold particles; functionalised the polymers with glycans; characterised the polymer systems by NMR, SEC and FTIR; characterised the particles by XPS; and characterised the glycans by NMR. I designed, constructed, and ran the prototype flow-through and lateral flow devices (including the synthesis of the polystyrene systems), and analysed the data from the devices.

Myself, Sarah-Jane Richards, Simone Dedola, Robert Field and Matthew Gibson were responsible for preparation of the manuscript.

A. N. Baker, S-J. Richards, C. S. Guy, T. R. Congdon, M. Hasan, A. J. Zwetsloot, A. Gallo, J. R. Lewandowski, P. J. Stansfeld, A. Straube, M. Walker, S. Chessa, G. Pergolizzi, S. Dedola, R. A. Field, M. I. Gibson, *ACS Cent. Sci.,* **2020**, *6*, 2046.

A. N. Baker, S-J. Richards, C. S. Guy, T. R. Congdon, M. Hasan, A. J. Zwetsloot, A. Straube, M. Walker, S. Chessa, G. Pergolizzi, S. Dedola, R. A. Field, M. I. Gibson, *Chemrxiv, 2020, https://doi.org/10.26434/chemrxiv.12465680.v1*

Myself, Sarah-Jane Richards and Matthew Gibson have a patent related to this work.

3.3 Introduction

In December 2019 a novel zoonotic coronavirus (SARS-COV-2), reported in Wuhan (China), led to a pandemic of the respiratory disease COVID-19.[1] While vaccinations are becoming available (if unequally despite the COVID-19 Vaccines Global Access Facility (COVAX)),[2,3] there are still no therapeutics. Diagnostics, surveillance and case isolation are the primary tools for many countries for controlling the spread of the virus and driving down the basic reproduction (R_0) value. Following the successful genome sequencing of SARS-COV-2, RT-PCR-based (reverse transcription-polymerase chain reaction) diagnostics were rapidly developed. These require dedicated laboratory facilities, trained personnel and do not provide an instant output, and while highly specific, false negative results are reported at 3% versus chest CT scans.[4] There are also reports of conflicting RT-PCR results in samples from the same patient.[5,6] The results can depend on the sampling location *i.e.* throat *versus* lower respiratory tract,[7] and the false negative rate is highest during the early stages of infection.[8]

An alternative detection platform to RT-PCR is the lateral flow device (LFD), such as the home pregnancy test,[9] which typically uses antibodies as the detection units immobilised to both the stationary phase (e.g., nitrocellulose paper) and the mobile phase (e.g., gold nanoparticle), forming a "sandwich" with the analyte. While flow-through devices utilise deposition of sample as a test line (stationary) phase, sometimes termed a "Half" lateral flow assay.[10] Both systems show a positive (red line) response by eye at the test line. Such devices require little or no clinical infrastructure or training, and they can be used in the patient's home. The cost-effectiveness of these inexpensive devices has been demonstrated by various studies of malaria rapid diagnostic tests[11,12] and were found to compare well to the more expensive RT-PCR for Ebola diagnosis.[13] In addition to antibodies, other biological recognition units such as nucleic acids,[14] glycans, and lectins[15] could be used. Glycans have not been widely applied in lateral flow[16] but offer new opportunities and advantages compared with antibody-based systems. Glycans have reduced cold chain needs compared with proteins[17] and are thus suited to low resource, triage, or emergency settings. A further benefit of glycans, as the capture unit, would be the detection of intact viruses. For SARS-COV-2, viral RNA (e.g., from a positive RT-

PCR result) is detected past the point where patients are no longer infectious, resulting in extended hospital stays.[18]

Glycans (carbohydrates) direct myriad binding and recognition events in biology from cell-cell communication to being markers of disease. Analysis of the 2009 swine (zoonotic) influenza pandemic showed that porcine viral hemagglutinins, which normally bind α2,3'-linked sialic acids, switched to binding α2,6'-linked sialic acids found in human respiratory tracts.[19,20] This demonstrates the importance of glycan-binding during infection. This switch in glycan specificity has enabled the establishment of glycan-functional biosensors to rapidly identify strains without using nucleic acid based detection methods.[21,22] All coronaviruses display homotrimers of spike glycoproteins on their surface. Sialic acid binding by the S1 spike protein subunits is crucial for coronavirus to engage host cells, while the S2 domain initiates viral fusion.[23] Tortorici *et al*. showed the structural basis for 9-*O*-acetylated sialic acid binding to a human coronavirus (strain OC43) by cryo-EM, and affinity of this ligand to the HKU1-HE strain, has also been reported.[24,25] MERS S1 preferentially binds α2,3'-linked over α2,6'-linked sialic acids but any acetylation of the sialic acids decreases affinity,[26] which is distinct from OC43. This evidence shows that sialic acid binding is crucial in coronavirus infection and potentially in its zoonosis to human hosts,[27,28] but that the exact glycan partner can vary between strains. It has also emerged that sulphated glycosaminoglycans (including heparin sulphates) bind SARS-COV-2 spike protein, and can inhibit viral entry.[29–31] The above examples demonstrate that glycan "anchoring" of coronaviruses may offer opportunities for detection using capture techniques such as LFD. Since this was first demonstrated by Baker *et al.*[32] further reports showing the binding of sialic acids to SARS-COV-2 *in silico*,[3334] and *in vitro*[35,36] have occurred.

Individual glycans display low affinity to their protein targets, but this is overcome in nature by multivalent display. Due to the cluster glycoside effect,[37] displaying multiple copies of glycans can result in several orders of magnitude enhancement in the observed affinity. This has been widely exploited in materials chemistry[38,39] using dendrimers,[40,41] peptides/proteins,[42] polymers[43,44] and nanoparticles[22,45] to generate high avidity.

Here we report the synthesis of polymer-stabilised, multivalent gold nanoparticles bearing sialic acid derivatives and their interaction with the spike glycoprotein from

SARS-COV-2. We find that α,*N*-acetyl neuraminic acid binds the spike glycoprotein and subsequently exploit this interaction as the detection unit in prototype flow-through glyco-assay and lateral flow glyco-assay rapid diagnostics, which requires no centralised infrastructure.

3.4 Results and Discussion

Figure 3.1A shows the sequence alignments between the S1 domains of coronavirus spike proteins from MERS and SARS-COV-2. There is some conservation of the sialic acid binding site, notably residues His69 and Phe79. Figure 3.1B and C shows models constructed from the Cryo-EM structure of SARS-COV,[46] with missing loops and the α2,3'-sialyllactose modeled into it using the Cryo-EM structure of MERS.[47] The modeling data suggests that Arg21 and Leu24 coordinates the glycan, while Gln23 may also have a role in binding. Adjacent to the hairpin containing His69 and Phe79, it seems likely that Arg246 also has a role in coordination. The limited conservation of the sialic acid binding groove sequence (Appendix 3 Figure S1) is in marked contrast to the entirety of the spike S protein, which is often highly conserved between coronaviruses.[48] In the MERS sialic acid binding site in complex with α2,3'-sialyllactose, only the neuraminic acid unit, not the lactose, is engaged. This is in contrast to influenza hemagglutinins, which contact the galactose residues.[49] This evidence suggests that *N*-acetyl neuraminic acid is a reasonable target for SARS-COV-2 binding (also hypothesised here[50]) and hence a potential capture ligand for a new "glyco-LFD" diagnostic device.

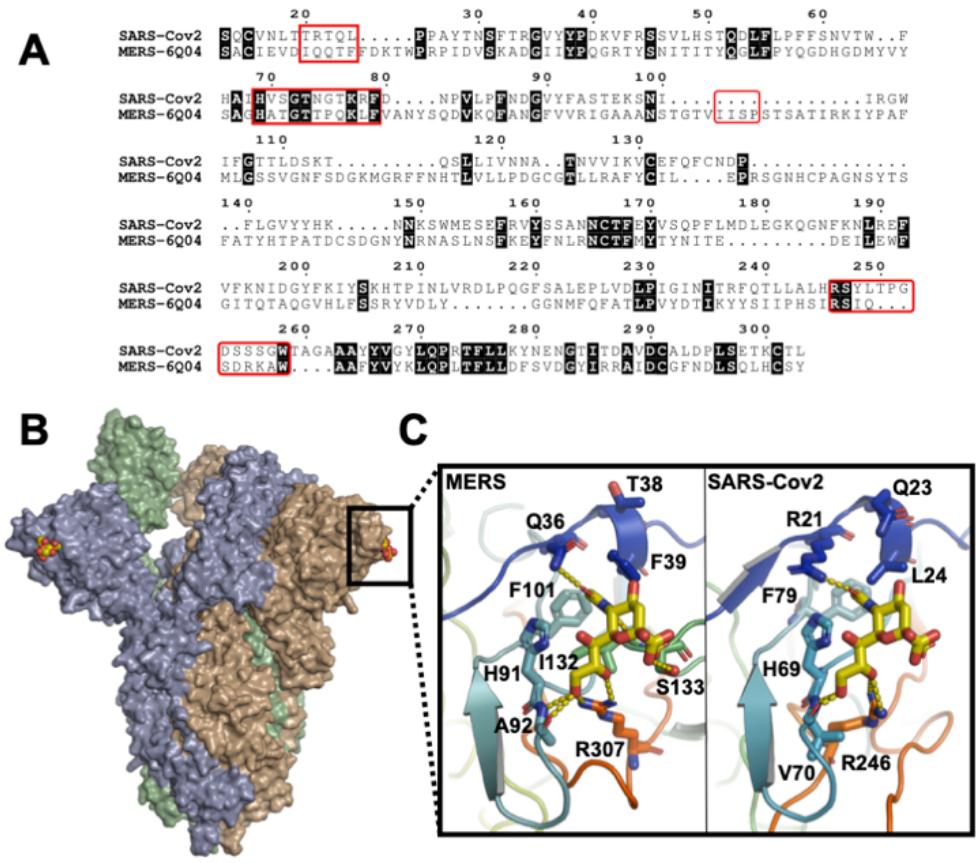

Figure 3.1. Sequence alignment of spike protein S1 domains of coronaviruses and a model showing the hypothesised sialic acid binding site for the SARS-COV-2 spike protein trimer

A) Sequence alignment between the S1 domains of the SARS-COV-2 and MERS spike proteins. Regions important for sialic acid binding are highlighted by red boxes; B) Model showing the hypothesised sialic acid binding sites (yellow CPK colouring) for the SARS-COV-2 spike protein trimer; C) A comparison between the sialic acid binding sites from MERS (PDB entry 6Q04) and the SARS-COV-2 model (PDB entry 6VSB) in complex with α2,3'-sialyllactose.

Figure 3.2A shows a design schematic for a "lateral flow glyco-assay" ("glyco-LFD"). Typically LFDs use antibodies, but here the glycan is immobilised (as a BSA-glycoconjugate) on the test strip and also in the mobile phase onboard gold nanoparticles, providing multivalency (and hence affinity), for dissecting SARS-COV-2 binding and for the LFD. Our nanoparticle design concept uses telechelic polymer tethers which conjugate the glycans, by displacement of an ω-terminal

pentafluorophenyl (PFP) group, and immobilisation onto gold particles *via* the α-terminal thiol. Poly(*N*-hydroxyethyl acrylamide), PHEA, was chosen as the polymer to give colloidally stable particles and as an acrylamide, it is not easily hydrolysable unlike acrylates for example (Figure 3.2B and Table 3.1).[45,51] PHEA was synthesised using RAFT (reversible addition-fragmentation chain transfer) polymerisation resulting in dispersities below 1.3. The PHEA lengths were selected on the basis of performance in initial lateral flow screening assays (Chapter 2) and from reports of their colloidal stability.[45,51] Amino-glycans were synthesised by reduction of anomeric azides and subsequently conjugated to the PHEAs by displacement of the PFP group, which was confirmed by ^{19}F NMR. Polymers were then assembled onto citrate-stabilised gold nanoparticles and excess ligand removed by centrifugation/resuspension cycles. The nanoparticles were elucidated by UV-Vis, dynamic light scattering (DLS), transmission electron microscopy (TEM) and XPS (x-ray photoelectron spectroscopy) to confirm surface coating (Table 3.2 and Appendix 3). Following observations *via* DLS and UV-vis that 16 nm sialyllactose particles were less stable than 35 nm particles, the latter were selected for initial glycan-binding assays.

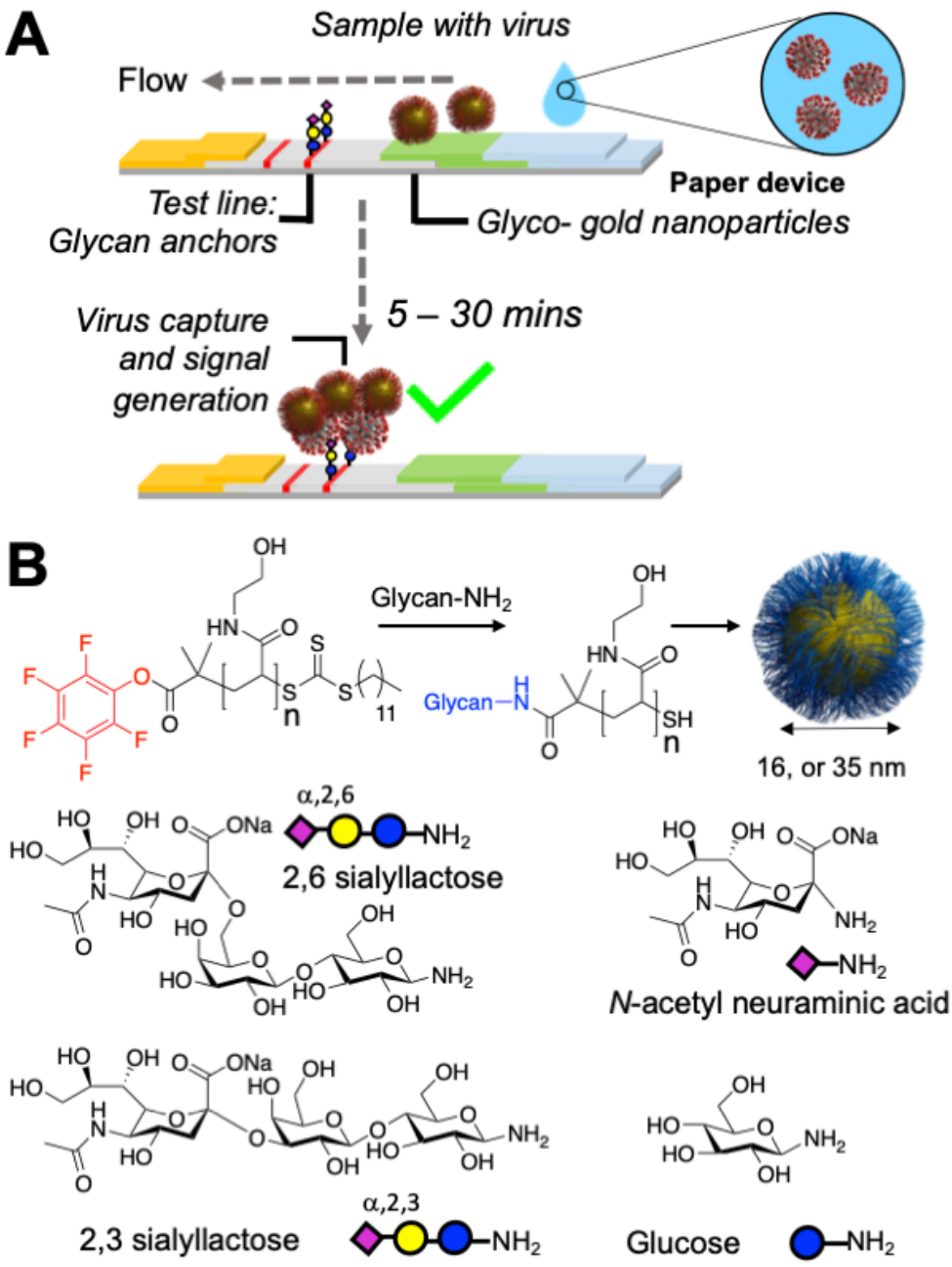

Figure 3.2. Design concept for lateral flow glyco-assay devices.

A) Lateral flow assay for virus, using glycan capture units; B) Synthetic procedure for glyconanoparticles.

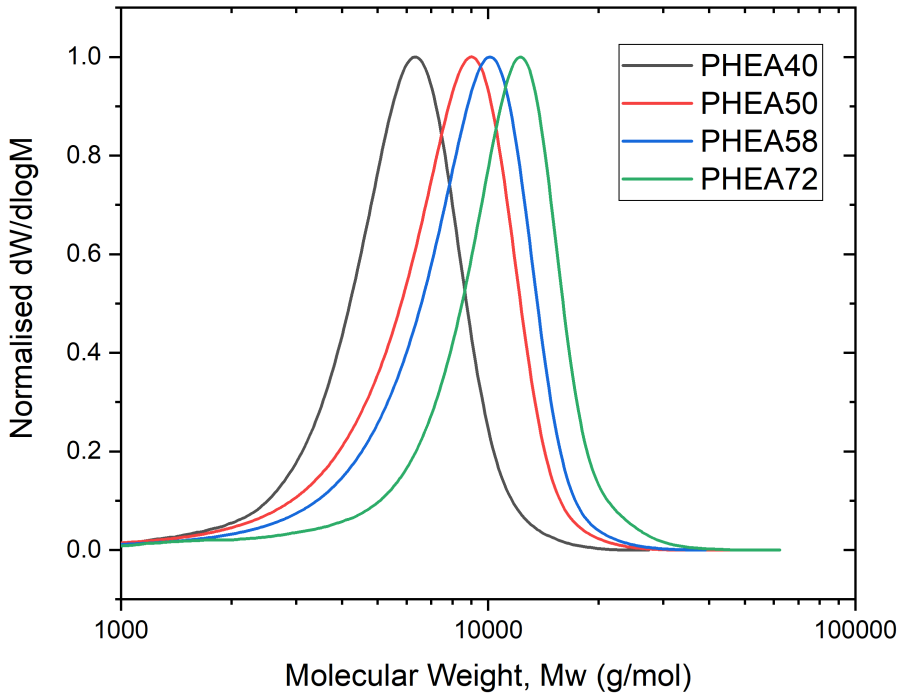

Figure 3.3. Normalised size exclusion chromatography RI molecular weight distributions of telechelic PHEA obtained in DMF versus PMMA standards.

Table 3.1. Polymer Characterisation

Code	M:CTA	$M_{n(theo)}$[a] (g.mol^{-1})	$M_{n(SEC)}$[b] (g.mol^{-1})	$M_{n(NMR)}$[c] (g.mol^{-1})	$Đ_M$[b]
$PHEA_{40}$	20	2800	5100	5000	1.19
$PHEA_{50}$	25	3400	6400	5500	1.27
$PHEA_{58}$	30	4000	7200	6700	1.26
$PHEA_{72}$	40	5100	8900	8600	1.28

[a)] Estimated from [M]:[CTA]; [b)] From DMF SEC versus PMMA standards; [c)] ^{1}H NMR end-group analysis.

Table 3.2. Nanoparticle Characterisation

Code	UV_{max}[a] (nm)	A_{SPR}/A_{450}[b]	$D_{h(UV)}$[c] (nm)	$D_{h\,(DLS)}$[d] (nm)	$D_{(TEM)}$[e] (nm)
$AuNP_{16}$	519	1.64	16	20.7±0.8	14±2
NeuNAc-$PHEA_{40}AuNP_{16}$	527	1.66	16	40.9±0.5	
NeuNAc-$PHEA_{50}AuNP_{16}$	526	1.68	18	44.2±0.8	
$AuNP_{35}$	526	1.91	35	34.5±0.5	35±3
NeuNAc-$PHEA_{40}AuNP_{35}$	531	1.98	45	46.2±0.7	
NeuNAc-$PHEA_{50}AuNP_{35}$	531	1.99	45	55.3±0.8	

[a] SPR absorption maximum; [b] Absorbance ratio of SPR to 450 nm; [c] Estimated from UV-Vis;[52] [d] From dynamic light scattering; [e] From TEM, from average of > 100 particles, showing ±S.D.

With the glyconanoparticles to hand, recombinant S1 subunit (SARS-COV-2 S1) spike protein was immobilised onto biolayer interferometry (BLI) sensors[22] to replicate a lateral flow situation, which is the primary aim of this work. Since there are 22 *N*-linked glycans per protein which are not present in bacteria-expressed protein,[53] we used protein expressed in mammalian cells (HEK) to ensure glycosylation. Figure 3.4A shows α,NeuNAc-AuNPs bind to a greater extent compared to both sialyllactose isomers (α2,3'/α2,6') and the monosaccharide control (glucose). X-ray photoelectron spectroscopy analysis (Appendix 3) of these particles revealed that the NeuNAc/Glc monosaccharide-terminated polymers had a higher relative grafting density than the sialyllactose trisaccharides by a ratio of 2:1 (35 nm)/ 3:1 (16 nm), because of the difference in glycan size. It is therefore important to note that this data does not rule out sialyllactose binding (and indeed, in LFD we do see binding), but that in this system NeuNAc gave the strongest response and consequently was taken forward. Thermal shift assays further confirmed that NeuNAc bound selectively over galactose and glucose, and preliminary STD (saturation transfer difference) NMR spectroscopy showed NeuNAc binding also (both in Appendix 3). While outside the scope of this work, the identification of the sialic acid binding function of the spike protein may provide fundamental guidance as to how the virus engages host cells, or is processed within them, and this (to the best of our knowledge) is the first report of this matter.[32]

The next step was to evaluate the impact of particle size on binding. Both 16 and 35 nm gold (relevant diameters for LFDs) NeuNAc particles were used to interrogate

SARS-COV-2 S1 (Figures 3.4B and C). End point dose dependency (Fig 3.3D) showed similar binding trends for both particles, with an apparent K_d ~1 nM, noting that for multivalent systems exact K_d's cannot be extracted. The plots are shown in terms of OD (SPR absorption maximum) as this is standard for AuNP concentration.

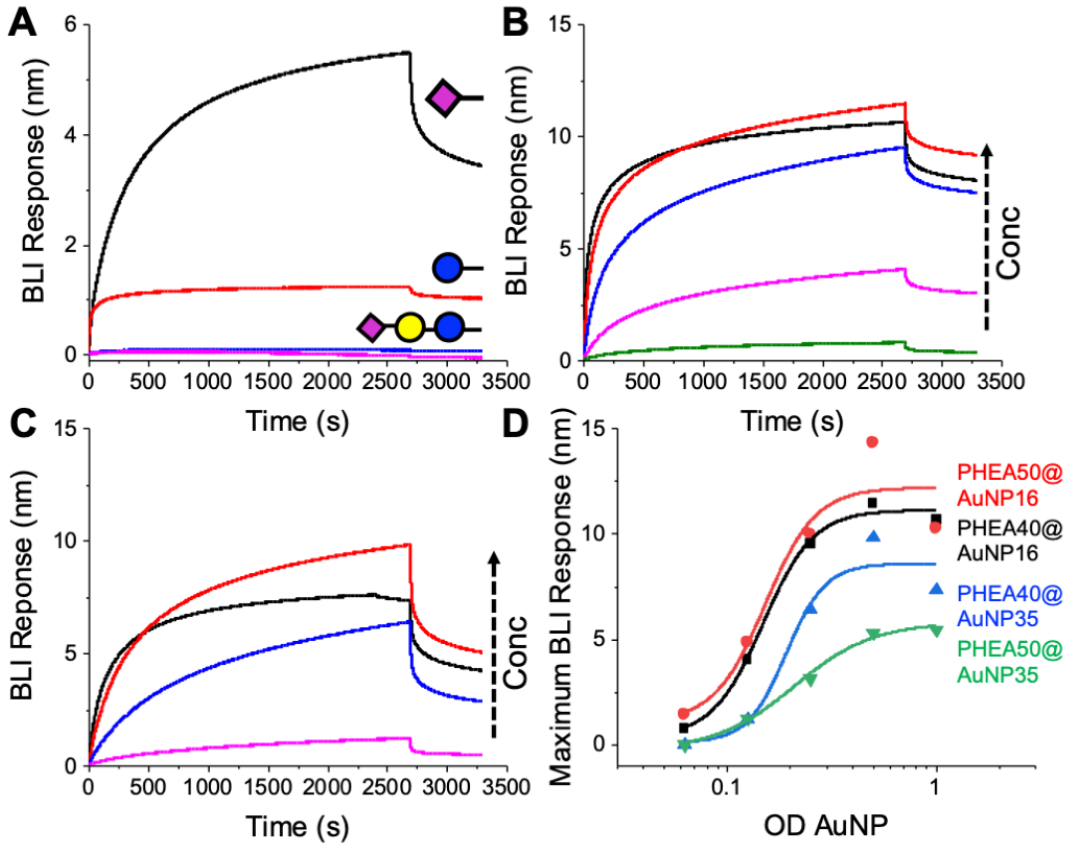

Figure 3.4. Biolayer interferometry analysis of SARS-COV-2 spike protein with glyconanoparticles.

A) Screening using $PHEA_{50}$@$AuNP_{35}$ at OD = 1; Dose dependent binding of NeuNAc-$PHEA_{50}$ using B) @$AuNP_{16}$ and C) @$AuNP_{35}$. OD = 1 (-, black), 0.5(-, red), 0.25(-, blue), 0.125(-, pink); D) Binding curves.

With the successful identification of NeuNAc as a target ligand, its application as the capture unit in lateral flow was examined. The performance of an LFD depends on not only the affinity of the capture ligand (NeuNAc) but also the flow of the particles. Flow-through ("Half" lateral flow assays) (Figure 3.5A) were established to optimise the particles. The negative test line was (commercial) 2,3'-sialyllactose-BSA, which the glyco-nanoparticle should not bind to (to avoid false positives in "full" lateral flow where it would serve to capture viral antigen). The positive control was immobilised

(monomeric) SARS-COV-2 S1 (which mimics capture in full lateral flow) and the nanoparticles were flowed over them (original strips are in Appendix 3). Pleasingly, all particles bound SARS-COV-2 S1 showing this detection method is valid. NeuNAcPHEA$_{50}$@AuNP$_{35}$ gave the strongest signal-to-noise compared to other particles, owing to their lower background compared to 16 nm particles (noting that the 16 nm did give a strong signal too). The 16 nm also showed some binding to the 2,3'-sialyllactose-BSA control, however. Hence, NeuNAcPHEA$_{50}$@AuNP$_{35}$ particles were used from this point onward (Figure 3.5B and C). α2,3'- and α2,6'-sialiyllactosamine particles were also tested, and on larger AuNPs (55 - 70 nm) and longer polymers (PHEA$_{72}$) too but gave no improvement over NeuNAcPHEA$_{50}$@AuNP$_{35}$ (Appendix 3). Blocking of the NeuNAc particles with BSA before running was also explored in an attempt to further reduce the background, as is common in LFDs. BSA blocking did not improve the performance of the NeuNAc systems but it did reduce off-target binding in the α2,3'-sialyllactosamine systems tested (casein and PVP$_{10}$ were also used) (Appendix 3). Encouraged by these results, the specificity and function of the NeuNAcPHEA$_{50}$@AuNP$_{35}$ particles were tested against a panel of test-line immobilised lectins 1 mg.mL^{-1}. Total signal intensity is plotted in Figure 3.5D confirming that NeuNAc-AuNPs have no nonspecific binding. The only lectin that bound was RCA$_{120}$, which is known to have some affinity toward sialic acids.[54] WGA and SNA also have some affinity to sialic acids but did not show signal here, highlighting an advantage (and challenge) of LFDs, that glycan presentation is a strong determinant of the signal generation in addition to binding affinity. To test binding specificity in a more challenging scenario, the particles were screened against the spike protein, SARS-COV-2 S1, (the desired target) and also against the S1 spike domain of a previous zoonotic coronavirus SARS-COV-1,[55] responsible for the 2003 "SARS" outbreak. As can be seen in Figure 3.5E, the NeuNAc particle system has a clear preference for SARS-COV-2, demonstrating selectivity in this glyconanoparticle system. While this does not rule out binding, it does show the particles/glycan do not generate sufficient signal against SARS-COV-1. This data further supports the notion that the terminal NeuNAc is the key binding motif.

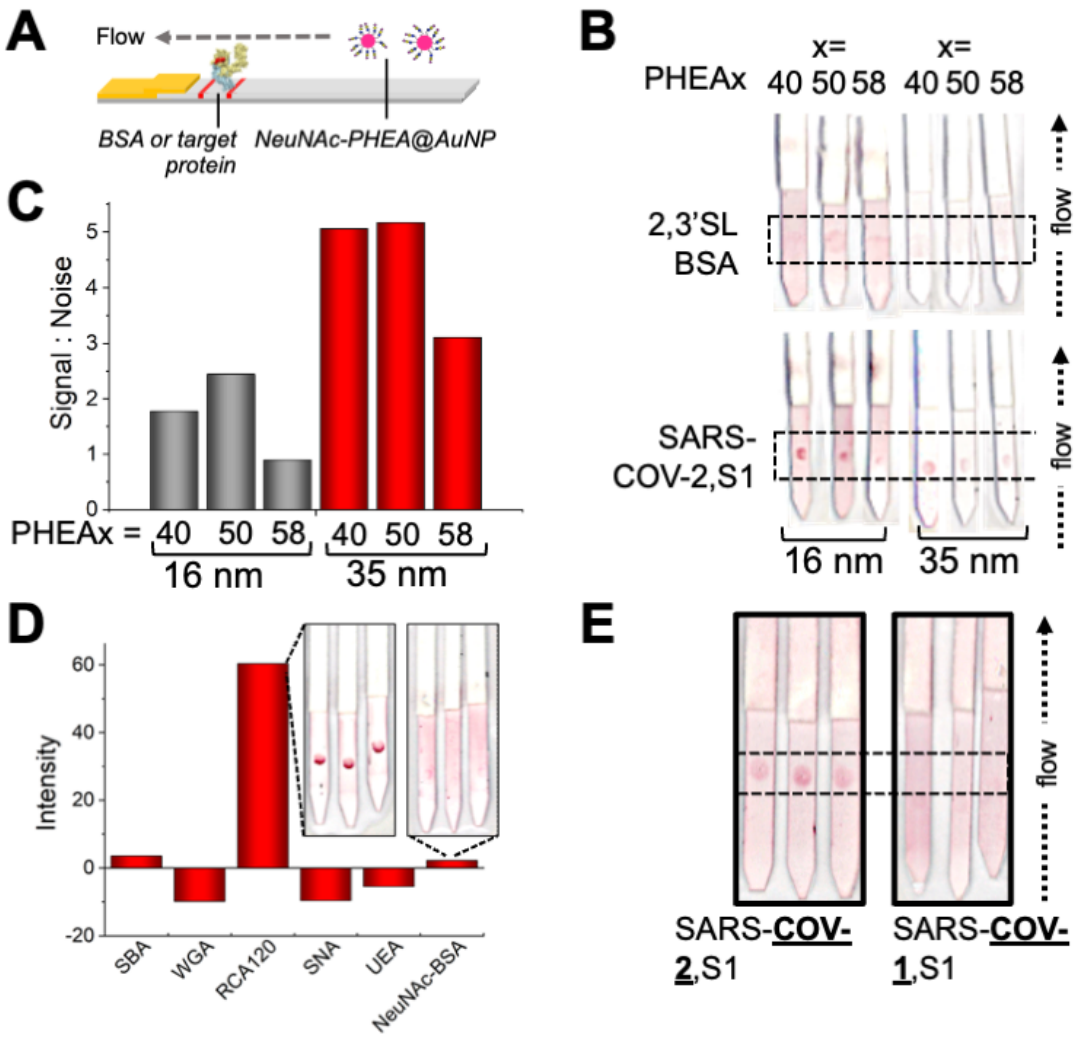

Figure 3.5. Flow-through analysis of NeuNAcPHEA$_x$@AuNP$_y$ particles.

A) Flow-through assay setup with target protein immobilised on the test line; B) Effect of polymer chain length and particle size on flow-through binding; C) Signal:noise analysis; D) Selectivity of NeuNAcPHEA$_{50}$@AuNP$_{35}$ against a panel of lectins (inset example strips). E) Selectivity of NeuNAcPHEA$_{50}$@AuNP$_{35}$ against S1 protein from different coronavirus strains. Data is the mean from 3 repeats. Original LFD strips are in Appendix 3. Test lines are within the dashed-line box. 2,3'SL-BSA = 2,3'-sialyllactose-functionalised BSA.

To explore the detection limits and specificity of this system, NeuNAc (positive) and galactose (negative) nanoparticles were screened against a dilution series of SARS-COV-2 S1 (Figure 3.6A and B). At the highest concentration (0.5 mg.mL^{-1}) galactose particles showed weak binding to SARS-COV-2 S1. NeuNAc particles showed

significantly stronger binding, with an apparent limit of detection below 8 μg.mL^{-}1 or 8 nM. Encouraged by successful binding, a dipstick sandwich assay was established where the analyte was added to the gold particle solution, rather than dried onto the nitrocellulose paper. The test line was NeuNAc-BSA (validated to capture the particles by BLI, Appendix 3) and RCA_{120} as a control line, which is essential in lateral flow devices to ensure each device is functional. To mimic the virus in a model system without cell debris, which may complicate initial LFD development, the spike glycoprotein was immobilised onto 100 nm polystyrene nanoparticles which match the diameter of the coronavirus. Figure 3.7C shows the results of testing this system (original lateral flow strips with no image enhancement are in the Appendix 3). In this system 2,3'-sialyllactose-BSA is the test (capture) line as the data in Figure 3.5 confirmed no nonspecific binding by the nanoparticles to this line. The lateral flow devices could clearly detect the virus-like particles at a concentration of just 5 μg.mL^{-1} (5 nM) protein, which is in line with the detection limits from Figure 3.6B. Controls using naked polystyrene colloids showed no binding to the test line, ruling out nonspecific interactions, and a control (with no polystyrene analyte) only showed control line binding. The resolution of the test spots could be further enhanced using a silver-staining protocol,[56] which improves the "by eye" detection (Figure 3.6C). An additional control of two influenza strains (which bind sialyllactoses) were shown to have little off-target binding as influenza hemagglutinins require the galactose linker in addition to the sialic acid, for strong binding (Appendix 3).[57] As a final proof-of-concept, SARS-COV-2 spike protein pseudotyped lentivirus were tested in flow-through devices. Pseudovirus was applied to the test line and ran in a flow-through cassette (Appendix 3 for full photos). Using NeuNAc particles, detection at $1.5x10^4$ transduction units/mL was achieved. Galactose-functional particles failed to detect the virus, confirming the role of sialic acid binding. Direct comparison of transduction units/mL to viral load (typical copies/mL) is not possible, but values as high as 10^8 copies.mL^{-1} are reported from COVID positive swabs,[18] suggesting this method may have relevant detection limits. A hybrid LFD using antibody capture in one component may also be possible to further improve this.[16]

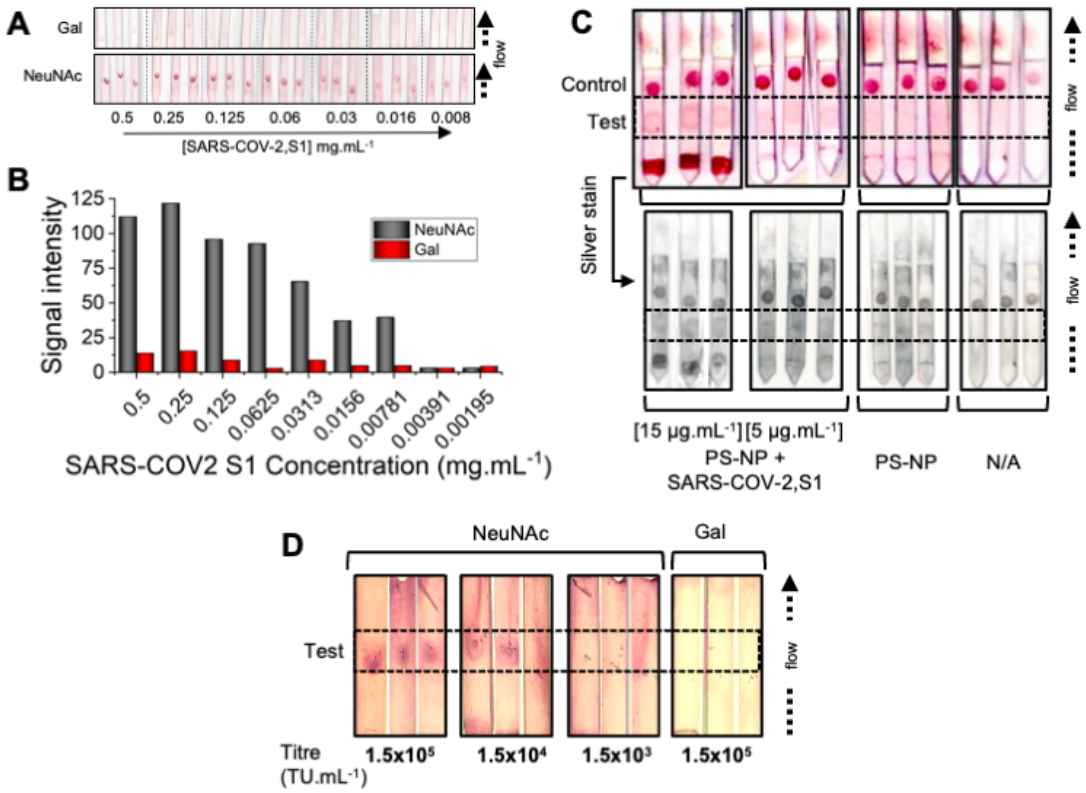

Figure 3.6. Limit of detection of NeuNAc functionalised AuNPs and use in lateral flow and flow-through versus viral mimics

A) Detection limit analysis of galactose or NeuNAc functionalised AuNPs against immobilised SARS-COV-2 S1 using flow-through assays and, B) Signal intensity analysis; C) Dipstick lateral flow tests using NeuNAcPHEA$_{50}$@AuNP$_{35}$ and NeuNAc-BSA as the test line and RCA$_{120}$ as the control line. PS-NP = 100 nm polystyrene colloid, or + SARS-COV-2 S1. N/A is with no polystyrene analyte. D) Flow-through analysis of SARS-COV-2 Spike pseudotyped lentivirus against NeuNAcPHEA$_{50}$@AuNP$_{35}$ or GalPHEA$_{50}$@AuNP$_{35}$ nanoparticles. In each image, the test line region is indicated by the dashed box. Complete original images are in Appendix 3.

3.5 Conclusions

In conclusion, we have demonstrated flow-through glyco-assay and lateral flow glyco-assay detection systems that can detect the spike glycoprotein from the SARS-COV-2 virus in under 30 mins. Guided by sequence alignment against other coronavirus spike proteins it was hypothesised that sialic acids may bind this protein, to enable capture/detection. Using a nanoparticle based biolayer interferometry platform we demonstrated that α,*N*-acetyl neuraminic acid is a ligand for the spike glycoprotein. The gold nanoparticles and polymer tethers (for glycan capture) were optimised and it was found in flow-through assays that α,*N*-acetyl neuraminic acid particles have selectivity toward the SARS-COV-2 spike protein, including specificity over SARS-COV-1 and a panel of lectins. Guided by this, we successfully detected a virus mimic particle bearing SARS-COV-2 S1 in under 30 mins, with a detection limit of the spike protein around 5 $\mu g.mL^{-1}$ in a lateral flow assay. Furthermore, a SARS-COV-2 spike protein-presenting pseudotyped lentivirus was successfully detected in a robust flow-through proof-of-concept. This work provides proof that glycan binding can be exploited to create rapid point of care diagnostics in a format which requires no infrastructure and limited training and, to the best of our knowledge, is the first reported all-glycan lateral flow system. This approach may find application for disease surveillance or mass testing at transport/work hubs or even for self/home testing. Finally, the observation that SARS-COV-2 can engage sialic acids found on human respiratory cells may provide insight into its zoonosis and infection pathways to help guide new interventions.

Following publication of the paper underlying this chapter in September 2020[58] (and pre-print in June 2020),[32] the binding of sialic acids to the SARS-COV-2 spike protein has been further verified *in silico*[34] and, *in vitro* by saturation transfer difference (STD) NMR,[59] glycan microarray[60] and ELISA[61] – validating that lateral flow and flow-through systems can be used to study glycan binding. The concept of targeting the spike protein over the nucleocapsid of the virus has also been discussed and considered further too.[62] This has occurred alongside broader studies that discuss the immunological role of the spike protein,[63,64] and if the spike protein or sialic acids on the cell surface can be a target for combatting SARS-COV-2.[65,66] While the

importance of sialic acid glycolipids in mediating SARS-COV-2 viral entry has also been shown too.[67]

3.6 Experimental

3.6.1 Physical and Analytical Methods

NMR Spectroscopy

^{1}H-NMR, ^{13}C-NMR and ^{19}F-NMR spectra were recorded at 300 MHz, 400 MHz or 500 MHZ on a Bruker DPX-300, DPX-400 or DPX-500 spectrometer respectively, with chloroform-*d* ($CDCl_3$), acetonitrile-d_3 (CD_3CN) or deuterium oxide (D_2O) as the solvent. Chemical shifts of protons are reported as δ in parts per million (ppm) and are relative to either $CDCl_3$ (7.26), CD_3CN (1.94) or D_2O (4.79).

Mass spectrometry

Low resolution mass spectra (LRMS) were recorded on a Bruker Esquire 2000 spectrometer using electrospray ionisation (ESI). m/z values are reported in Daltons.

FT-IR Spectroscopy

Fourier Transform-Infrared (FT-IR) spectroscopy measurements were carried out using an Agilent Cary 630 FT-IR spectrometer, in the range of 650 to 4000 cm^{-1}.

Size Exclusion Chromatography

Size exclusion chromatography (SEC) analysis was performed on an Agilent Infinity II MDS instrument equipped with differential refractive index (DRI), viscometry (VS), dual angle light scattering (LS) and variable wavelength UV detectors. The system was equipped with 2 x PLgel Mixed D columns (300 x 7.5 mm) and a PLgel 5 μm guard column. The mobile phase used was DMF (HPLC grade) containing 5 mM NH_4BF_4 at 50 °C at flow rate of 1.0 $mL.min^{-1}$. Poly(methyl methacrylate) (PMMA) standards (Agilent EasyVials) were used for calibration between 955,000 – 550 $g.mol^{-1}$. Analyte samples were filtered through a nylon membrane with 0.22 μm pore size before injection. Number average molecular weights (M_n), weight average molecular weights (M_w) and dispersities ($Đ_M = M_w/M_n$) were determined by conventional calibration using Agilent GPC/SEC software.

X-ray Photoelectron Spectroscopy (XPS)

The samples were attached to electrically-conductive carbon tape, mounted on to a sample bar and loaded in to a Kratos Axis Ultra DLD spectrometer which possesses a base pressure below 1 x 10^{-10} mbar. XPS measurements were performed in the main analysis chamber, with the sample being illuminated using a monochromated Al Kα x-ray source. The measurements were conducted at room temperature and at a take-off angle of 90° with respect to the surface parallel. The core level spectra were recorded using a pass energy of 20 eV (resolution approx. 0.4 eV), from an analysis area of 300 μm x 700 μm. The spectrometer work function and binding energy scale of the spectrometer were calibrated using the Fermi edge and $3d_{5/2}$ peak recorded from a polycrystalline Ag sample prior to the commencement of the experiments. In order to prevent surface charging the surface was flooded with a beam of low energy electrons throughout the experiment and this necessitated recalibration of the binding energy scale. To achieve this, the C-C/C-H component of the C 1*s* spectrum was referenced to 285.0 eV. The data were analysed in the CasaXPS package, using Shirley backgrounds and mixed Gaussian-Lorentzian (Voigt) lineshapes. For compositional analysis, the analyser transmission function has been determined using clean metallic foils to determine the detection efficiency across the full binding energy range.

Dynamic Light Scattering

Hydrodynamic diameters (D_h) and size distributions of particles were determined by dynamic light scattering (DLS) using a Malvern Zetasizer Nano ZS with a 4 mW He-Ne 633 nm laser module operating at 25 ℃. Measurements were carried out at an angle of 173° (back scattering), and results were analysed using Malvern DTS 7.03 software. All determinations were repeated 5 times with at least 10 measurements recorded for each run. D_h values were calculated using the Stokes-Einstein equation where particles are assumed to be spherical.

UV-vis Spectroscopy

Absorbance measurements were recorded on an Agilent Cary 60 UV-Vis Spectrophotometer and on a BioTek Epoch microplate reader.

Transmission Electron Microscopy

Dry-state stained TEM imaging was performed on a JEOL JEM-2100Plus microscope operating at an acceleration voltage of 200 kV. All dry-state samples were diluted with deionised water and then deposited onto formvar-coated copper grids.

Biolayer Interferometry (BLI)

Biolayer Interferometry was carried out on ForteBio Octet Red96 (Forte Bio, USA). Assays were performed in black 96 well plates. Assays were carried out at 30 °C and agitated at 1,000 rpm. Amine reactive (ARG2) biosensor tips (Forte Bio, USA) were hydrated in milliQ H_2O water for at least 10 mins prior to use. A stable baseline was established in milliQ water for 1 minute. The biosensors were first activated using EDC/NHS for 10 minutes and functionalised by loading with 50 $\mu g.mL^{-1}$ protein in pH 6 Acetate buffer for 10 mins followed by 5 minutes quenching with 1 M ethanolamine and 1 minute equilibration step in 10 mM HEPES with 0.15 M NaCl, 0.1 mM $CaCl_2$ and 0.01 mM $MnCl_2$ to remove any unbound protein and to establish a stable baseline. Following protein immobilisation, the binding association with glycan-functionalised AuNPs was carried out in 10 mM HEPES with 0.15 M NaCl, 0.1 mM CaCl2 and 0.01 mM $MnCl_2$, for 30 minutes followed by dissociation in 10 mM HEPES with 0.15 M NaCl, 0.1 mM $CaCl_2$ and 0.1 mM $MnCl_2$ for 10 minutes.

Protein Modelling

Models of the S1 domain were constructed based principally on the Cryo-EM structure of SARS-COV-2 (PDB entry 6VSB), with missing loops and the α2,3'-sialyllactose modeled in from the Cryo-EM structure of MERS (PDB entry 6Q04), using a combination of Swiss-model, Pymol and energy minimisation using Gromacs.

^{1}H STD NMR Experiments

All the STD NMR spectra were acquired on a Bruker Avance 700.24 MHz at 298 K. The STD NMR experiments were performed in Potassium Phosphate 50 mM and 10% D_2O buffer, pH 7.4. For the complexes SARS-COV-2 Spike protein, the protein concentration was ~50 μM while each ligand concentration was 5 mM. The on- and off-resonance spectra were acquired using a train of 50 ms Gaussian selective saturation pulses (4 mW) using a total of 3s of saturation time, and a relaxation delay (D1) of 3.5s. The water signal was suppressed using the excitation sculpting technique (*stddiffesgp.3*) while the residual protein resonances were filtered using a $T_{1\rho}$-filter of

50 ms. All the spectra were acquired with a spectral width of 15 kHz (20 ppm) and 32K data points using 128 scans. The on-resonance spectra were acquired by saturating at 0.91 ppm while the off-resonance spectra were acquired by saturating at 40 ppm.

Protein Thermal Shift Assay

The thermal shift reaction was performed with a BioRad CFX96 real-time PCR machine. The sample was heated from 25 ℃ to 95 ℃ and the fluorescence intensity change monitored using the Protein Thermal Shift™ Dye kit (Thermo Fisher Scientific, Cat # 4461146). Analysis for binding induced shifts in thermal transition was performed in PBS buffer with Precision Melt Analysis Software provided by the manufacturer (BioRad) and a protein concentration of 0.2 mg/mL. The data was collected over 5 runs for each glycan and glycan concentration.

3.6.2 Materials

All chemicals were used as supplied unless otherwise stated. *N*-Hydroxyethyl acrylamide (97%), 4,4'-azobis(4-cyanovaleric acid) (98%), mesitylene (reagent grade), triethylamine (> 99%), sodium citrate tribasic dihydrate (> 99%), gold(III) chloride trihydrate (99.9%), ammonium carbonate (reagent grade), potassium phosphate tribasic (≥ 98%, reagent grade), potassium hexafluorophosphate (99.5%), deuterium oxide (D_2O, 99.9%), deuterated chloroform ($CDCl_3$, 99.8%), acetonitrile-d_3 (CD_3CN, ≥ 99.8%,) , diethyl ether ((≥ 99.8%, ACS reagent grade), sodium azide (≥ 99.5%, reagent plus grade), hydrazine hydrate (50 - 60%), methanol (≥ 99.8%, ACS reagent grade), Amberlite® IR120 (H^+ form), toluene (≥ 99.7%,), Tween-20 (molecular biology grade), HEPES, PVP40 (poly(vinyl pyrrolidone)$_{400}$ (PVP400, PVP_{400}) (Average Mw ~40,000)), sucrose (Bioultra grade), carbon disulphide (≥ 99.8%), acetone (≥ 99%), 1-dodecane thiol (≥ 98%), pentafluorophenol (≥ 99%, reagent plus), micro particles based on polystyrene (100 nm), silver staining kit (Silver Enhancer Kit), Dowex 50WX8 hydrogen Form 100-200 mesh, acetic anhydride, *N*-acetyl neuraminic acid, acetyl chloride, Polyvinylpyrrolidone 10 (PVP_{10}, wt 10,000) and Casein from bovine milk (technical grade) were purchased from Sigma-Aldrich. 2,3'-sialyllactose, 2,6'-sialyllactose, lactosamine and galactosamine HCl were purchased from Carbosynth. Palladium hydroxide (20% on carbon) and anhydrous trehalose were purchased from Alfa Aesar. 2-chloro-1,3-dimethylimidazolimium chloride (90%), DMF (> 99%) and 2-bromo-2-methyl propionic acid (98%) were purchased from Acros Organics. HPLC grade acetonitrile (≥ 99.8%), glucose (lab-reagent grade), hexane fraction from petrol (lab reagent grade), DCM (99% lab reagent grade), sodium hydrogen carbonate (≥ 99%), ethyl acetate (≥ 99.7%, analytical reagent grade), sodium chloride (≥ 99.5%), calcium chloride, 40-60 petroleum ether (lab reagent grade), hydrochloric acid (~37%, analytical grade), glacial acetic acid (analytical grade) and magnesium sulphate (reagent grade) were purchased from Thermo Fisher Scientific.

Nitrocellulose Immunopore RP 90-150 s/4cm 25 mm was purchased from GE Healthcare. Lateral flow backing cards 60 mm by 301.58 mm (KN-PS1060.45 with KN211 adhesive) and lateral flow cassettes (KN-CT105) were purchased from Kenosha Tapes. Cellulose fibre wick material 20 cm by 30 cm by 0.825 mm (290 gsm and 180 mL/min) (Surewick CFSP223000) was purchased from EMD Millipore.

Glass fibre conjugate pads (GFCP103000) 10 mm by 300 mm was purchased from Merck. Thick Chromatography Paper (for sample pads), Grade 237, Ahlstrom 20 cm by 20 cm were purchased from VWR International.

Soybean agglutinin, Ricinus communis Agglutinin I (RCA_{120}), Ulex Europaeus Agglutinin I and wheat germ agglutinin were purchased from Vector Laboratories. 2,3'-sialyllactose-BSA (3 atom spacer, NGP0702), 2,6'-sialyllactose-BSA (3 atom spacer, NGP0706), Galα1-3Galβ1-4GlcNAc-BSA (3 atom spacer, NGP0330) and *N*-acetylneuraminic acid-BSA (6 atom spacer, NGP6111) were purchased from Dextra Laboratories. Appendix 3 Figures S18, 19, 20 and 21; and Tables S2, 3, 4, 5, 6, 7, 13, 14 and 15 used SARS-COV-2 spike glycoprotein S1, Sheep Fc-Tag (HEK293) from The Native Antigen Company; SARS-COV-1 spike glycoprotein S1, His-Tag (HEK293) was also purchased from here. Commercial spike protein was used for the BLI studies (Figure 3.4). Commercial and expressed (details are included below) in-house spike protein was used for flow-through and lateral flow analyses.

Clear and black half area 96-well plates were purchased from Greiner Bio-one. Streptavidin (SA) biosensors were purchased from Forte Bio.

Spike (SARS-COV-2) pseudotyped lentivirus (*Luc* Reporter) (Catalogue number: 79942, Lot number: 200730) was purchased from amsbio.

Biological reagents are listed as used in *Expression and Purification of SARS-COV-2 Spike S1 in HEK293 Cells* and *Recombinant Expression and Purification of SARS-COV-2 (first 300 amino acids) for Thermal Shift Assay.*

Distilled water used for buffers was MilliQ grade 18.2 mΩ resistance.

3.6.3 Synthetic Methods

Synthesis of 2-(dodecylthiocarbanothionylthio)-2-methyl propionic acid (DMP)

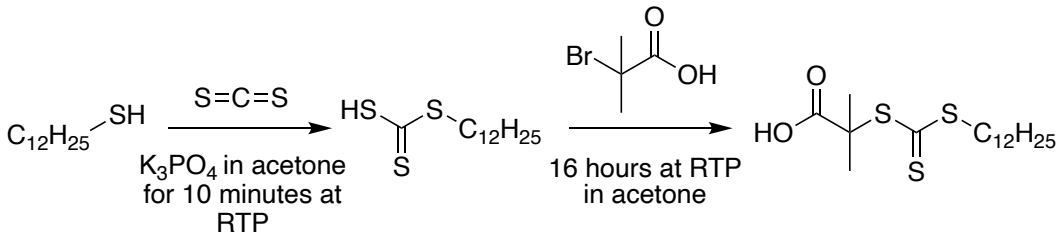

This was synthesised, according to a previously published procedure.[45] 2.00 g (9.88 mmmol) of 1-dodecane thiol was added dropwise to stirring 2.10 g (9.89 mmol) of K_3PO_4 in 30 mL of acetone at RTP, the mixture was left to stir for 25 minutes to form a white suspension. 2.05 g (26.93 mmol) of carbon disulphide was then added and left for 10 minutes, a yellow solution formed. 1.5 g (8.98 mmol) of 2-bromo-2-methyl-propionic acid was then added and the solution left to stir for 16 hours. The solvent was removed under vacuum. The crude product was dissolved in 100 mL of 1 M HCl and extracted with DCM (2×100 mL). The organic layer was washed with 200 mL of water and 200 mL of brine. The organic layer was dried with $MgSO_4$ and filtered under gravity. The solvent was then removed from the filtrate under vacuum. The crude product was purified using a silica column (40-60 PET:DCM:glacial acetic acid 75:24:1) and recrystalised in n-hexane to give a yellow solid (58%). δ_H (300 MHz, $CDCl_3$) 3.28 (2H, t, *J* 7.5, SCH_2CH_2), 1.80 - 1.45 (8H, m, $C(CH_3)_2$ and SCH_2CH_2), 1.45 - 1.2 (18H, m, $(CH_2)_9CH_3$), 0.87 (3H, t, *J* 6.0, CH_3). δ_C (400 MHz, $CDCl_3$) 221.0 (1C, SC(S)S), 178.3 (1C, C(O)), 55.7 (1C, $C(CH_3)_2$), 37.7 (1C, SCH_2), 32.1 - 28.0 (9C, $SCH_2(CH_2)_9$), 25.4 (2C, $C(CH_3)_2$), 22.8 (1C, CH_2CH_3), 14.3 (1C, CH_2CH_3). m/z calculated as 364.16; found for ESI $[M+H]^+$ 365.3 and $[M+Na]^+$ 387.3. FTIR (cm^{-1}) – 2955.8, 2916.6 & 2849.5 (methyl and methylene), 1701.5 (ester C=O), 1459.3, 1436.9 & 1412.7 (methyl and methylene), 1280.3 ($C(CH_3)_2$), 1064.2 (S-C(S)-S).

Synthesis of Pentafluorophenyl-2-dodecylthiocarbonothioylthio)-2-methylpropanoate (PFP-DMP)

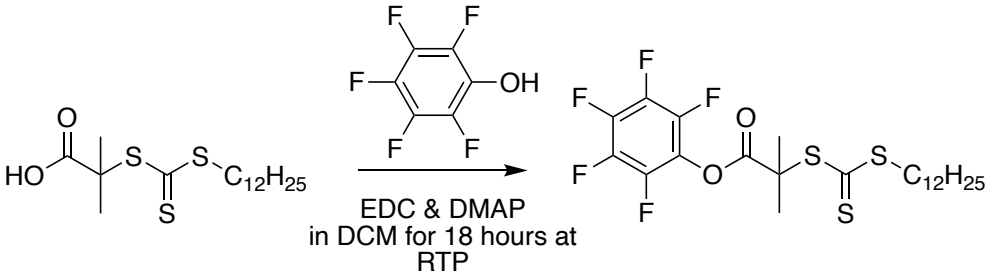

This was synthesised, according to a previously published procedure.[45] 4.06 g (11.13 mmol) of DMP, 3.65 g (19.04 mmol) of EDC and 2.30 g (18.82 mmol) of DMAP were dissolved in 160 mL of DCM and degassed for 30 minutes. 7.28 g (39.55 mmol) of pentaflurophenol was added in 20 mL of DCM and the mixture stirred for 18 hours at RTP. The organic layer was washed with 3 M HCl (200 mL), 1 M $NaHCO_3$ (200 mL) and 0.5 M NaCl (200 mL). The organic layer was dried with $MgSO_4$ and filtered under gravity. The solvent was then removed from the filtrate under vacuum. The crude product was recrystallised from ethyl acetate (or hexane) overnight at -8 °C and dried to give yellow crystals (90.9%). δ_H (300 MHz, $CDCl_3$) 3.31 (2H, t, *J* 7.5, SCH_2CH_2), 1.86 (6H, s, $C(CH_3)_2$), 1.69 (2H, qn, *J* 7.5, SCH_2), 1.48 - 1.16 (18H, m, $CH_2CH_2CH_2CH_2CH_2CH_2CH_2CH_2CH_3$), 0.94 - 0.82 (3H, m, CH_3). δ_C (300 MHz, $CDCl_3$) 220.1 (1C, SC(S)S), 169.7 (1C, C(O)), 143.1 (2C, meta C), 139.8 (1C, ipso C), 139.6 (1C, para C), 136.3 (2C, Ortho C), 55.5 (1C, $C(CH_3)_2$), 37.3 (1C, SCH_2), 32.0 - 22.8 (10C, $SCH_2(CH_2)_{10}$), 25.4 (2C, $C(CH_3)_2$), 14.1 (1C, CH_2CH_3). δ_F (300 MHz, $CDCl_3$) -151.4 - -151.6 (2F, m, $OCC_2H_2C_2H_2CH$), -148.5 (1F, t, *J* 21.5, $OCC_2H_2C_2H_2CH$), -162.2 - -162.5 (2F, m, $OCC_2H_2C_2H_2CH$). m/z calculated as 530.14; found for ESI $[M+Na]^+$ 553.3 and $[M+CH_3CN+Na]^+$ 593.5. FTIR (cm^{-1}) – 2955.8, 2916.6 & 2849.5 (methyl and methylene), 1701.5 (ester C=O), 1518.9 (aromatic C=C or C-F), 1459.3, 1436.9 & 1412.7 (methyl and methylene), 1280.3 ($C(CH_3)_2$), 1067.9 (S-C(S)-S).

Representative Polymerisation of 2-hydroxyethyl acrylamide

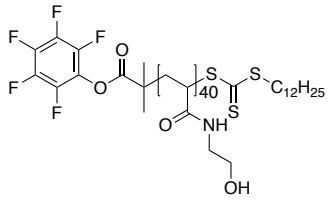

PHEA40 as representative example. 2.0 g (17.37 mmol) of 2-hydroxyethyl acrylamide, 0.043 g (0.15 mmol) of ACVA and 0.368 g (0.69 mmol) of PFP-DMP was added to 16 mL 1:1 toluene:methanol and degassed with nitrogen for 30 minutes. The reaction vessel was stirred and heated to 70 °C for 2 hours. The solvent was removed under vacuum. The crude product was dissolved in the minimum amount of methanol. Diethyl ether cooled in liquid nitrogen was added to the methanol to form a precipitate. The mixture was centrifuged for 2 minutes at 13 krpm and the liquid decanted off. The solid was dissolved in methanol and removed under vacuum to give a yellow crystalline solid.

PHEA40 - δ_H (300 MHz, D_2O) 8.35 - 7.95 (21H, m, N*H*), 3.97 - 3.56 (78H, m, NHC*H*$_2$), 3.56 - 3.03 (80H, m, C*H*$_2$OH & SC*H*$_2$), 2.41 - 1.90 (41H, m, $CH_2CHC(O)$ & $C(CH_3)_2$), 1.90 - 0.99 (108H, m, C*H*$_2$CHC(O) & C*H*$_2$C*H*$_2$C*H*$_2$C*H*$_2$C*H*$_2$C*H*$_2$C*H*$_2$C*H*$_2$C*H*$_2$C*H*$_2$CH$_2$CH$_3$), 0.83 - 0.72 (5H, m, C*H*$_2$C*H*$_3$). δ_F (300 MHz, D_2O) -152.0 - -164.3 (5F, m, C_6F_5). FTIR (cm^{-1}) – 3263.3 (OH, broad), 3088.1 & 2924.1 (C(O)NH and NH), 1638.2 & 1541.3 (C(O)NH). Yield - 73%

PHEA50 - δ_H (300 MHz, D_2O) 8.31 - 7.97 (23H, m, N*H*), 3.99 - 3.55 (86H, m, NHC*H*$_2$), 3.55 - 3.09 (100H, m, C*H*$_2$OH & SC*H*$_2$), 2.49 - 1.90 (46H, m, $CH_2CHC(O)$ & $C(CH_3)_2$), 1.90 - 0.98 (110H, m, C*H*$_2$CHC(O) & C*H*$_2$C*H*$_2$C*H*$_2$C*H*$_2$C*H*$_2$C*H*$_2$C*H*$_2$C*H*$_2$C*H*$_2$C*H*$_2$CH$_3$), 0.84 - 0.72 (5H, m, C*H*$_2$C*H*$_3$)

PHEA58 - δ_H (300 MHz, D_2O) 8.36 - 7.98 (29H, m, N*H*), 4.00 - 3.55 (H, 108H, m, NHC*H*$_2$), 3.55 - 3.15 (127H, m, C*H*$_2$OH & SC*H*$_2$), 2.36 - 1.88 (56H, m, $CH_2CHC(O)$ & $C(CH_3)_2$), 1.87 - 1.09 (128H, m, C*H*$_2$CHC(O) & C*H*$_2$C*H*$_2$C*H*$_2$C*H*$_2$C*H*$_2$C*H*$_2$C*H*$_2$C*H*$_2$C*H*$_2$C*H*$_2$CH$_3$), 0.83 - 0.72 (5H, m, C*H*$_2$C*H*$_3$)

PHEA72 - δ_H (300 MHz, D_2O) 8.30 - 7.96 (34H, m, N*H*), 3.96 - 3.52 (126H, m, NHC*H*$_2$), 3.52 - 3.07 (155H, m, C*H*$_2$OH & SC*H*$_2$), 2.36 - 1.88 (70H, m, $CH_2CHC(O)$ & $C(CH_3)_2$), 1.88 - 1.03 (148H, m, C*H*$_2$CHC(O) & C*H*$_2$C*H*$_2$C*H*$_2$C*H*$_2$C*H*$_2$C*H*$_2$C*H*$_2$C*H*$_2$C*H*$_2$C*H*$_2$CH$_3$), 0.82 - 0.70 (5H, m, C*H*$_2$C*H*$_3$)

Representative DP40 Poly(N-hydroxyethyl acrylamide) glycan functionalisation using 2-amino-2-deoxy-N-acetyl-D-neuraminic acid

0.2 g (0.039 mmol) of poly(2-hydroxyethyl acrylamide)$_{40}$ and 0.078 mmol of glycan were added to 20 mL of DMF containing 0.05 M TEA. The reaction was stirred at 50 °C for 16 hours. Solvent was removed under vacuum. The crude product was dissolved in the minimum amount of methanol. Diethyl ether cooled in liquid nitrogen was added to the methanol to form a precipitate. The mixture was centrifuged for 2 minutes at 13 krpm and the liquid decanted off. The solid was dissolved in methanol and solvent removed under vacuum to give an orange/brown crystalline solid. Loss of fluorine signal in the ^{19}F NMR was used to indicate the reaction had gone to completion. δ_H (300 MHz, D_2O) 8.21 - 7.99 (25H, m, NH), 4.10 - 3.57 (~90H, m, NHC*H*$_2$ & glycan protons), 3.57 - 2.99 (~82H, m, C*H*$_2$OH & SC*H*$_2$ & glycan protons), 2.40 - 1.87 (50H, m, $CH_2CHC(O)$, $C(CH_3)_2$ & glycan protons), 1.87 - 0.99 (110H, m, C*H*$_2$CHC(O) & C*H*$_2$C*H*$_2$C*H*$_2$C*H*$_2$C*H*$_2$C*H*$_2$C*H*$_2$C*H*$_2$C*H*$_2$$CH_3$ & glycan protons), 0.86 - 0.74 (5H, m, CH_2CH_3).

NB: This approach was used for other glycans also.

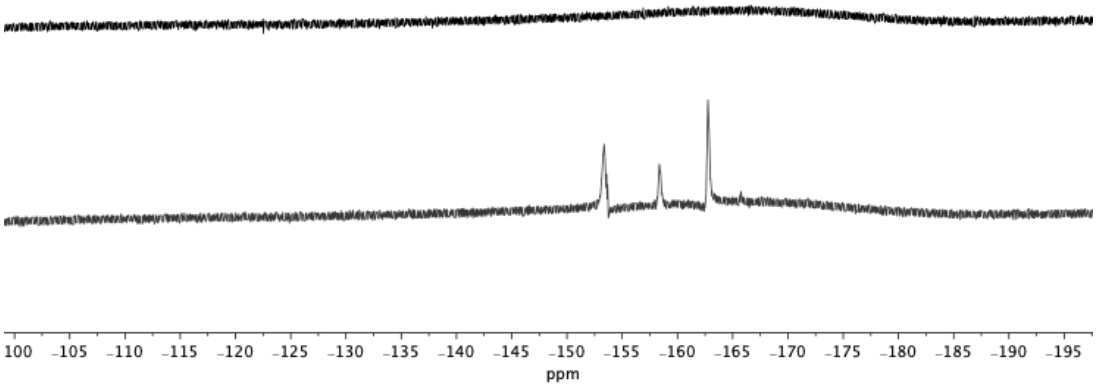

Figure E3.1. ^{19}F NMR After (top) and before (bottom) reaction with α2-amino-2-deoxy-*N*-acetyl-D-neuraminic acid functionalisation.

Synthesis of 2-chloro-1,3-dimethylimidazolinium hexafluorophosphate

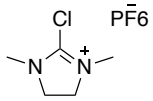

Synthesis was carried out following the procedure of Lim *et al.*[68] In a 100 mL round bottom flask equipped with a rubber septum, 2-chloro-1,3-dimethylimidazolinium chloride **1** (5 g, 29.6 mmol, 1.0 eq.) is dissolved in anhydrous acetonitrile (15 mL) and stirred under an N_2 atmosphere. KPF_6 (5.40 g, 29.6 mmol, 1 eq.) is added by temporary removal of the septum. After 2 h the mixture is filtered off using a sintered funnel packed with dry Celite® (2 g). The filtered cake is washed with acetonitrile and the filtrate is concentrated in vacuo. The resultant solid is dissolved in a small amount of acetonitrile and diethyl ether is added until a precipitate is formed. Stir for 3 - 5 min. The precipitate is collected by suction filtration, washed with diethyl ether and dry under vacuum to afford product as an off-white solid (7.5 g, 90%). δ_H (400 MHz, CD_3CN) 3.93 (4H, s, CH_2), 3.13 (6H, s, CH_3). δ_C (400 MHz, CD_3CN) 50.7 (2C, CH_2), 35.1 (2C, CH_3).

Synthesis of 2-azido-1,3-dimethylimidazolinium hexafluorophosphate (ADMP)

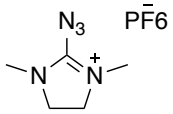

Synthesis was carried out following the procedure of Lim *et al.*[68] 2-chloro-1,3-dimethylimidazolinium hexafluorophosphate (7 g, 25.1 mmol, 1.0 eq.) was dissolved in anhydrous acetonitrile (25 mL) and stirred at 0 °C under N_2 atmosphere. NaN_3 (2.45 g, 27.7 mmol, 1.5 eq.) was added. The reaction mixture was stirred for 6 h, then filtered off using a sintered funnel packed with dry Celite® (2 g). The resultant solid was dissolved in a small amount of acetonitrile and diethyl ether was added until a precipitate was formed. The precipitate was collected by suction filtration, washed with diethyl ether and dried under vacuum for 12 h to afford the crude product which recrystallised from toluene:acetone (1:1) to give the product as a white solid. (6.5 g, 90%). δ_H (400 MHz, CD_3CN) 3.78 (4H, s, CH_2), 3.05 (6H, s, CH_3). δ_C (400 MHz, CD_3CN) 49.8 (2C, CH_2), 33.8 (2C, CH_3).

Synthesis of 1-Azido-1-deoxy-D-glucose

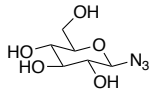

Synthesis was carried out following the procedure of Lim *et al.*[68] Glucose (100 mg, 0.555 mmol) was dissolved in 4:1 D_2O/MeCN (2 mL) under nitrogen and cooled to 0 °C. Triethylamine (387 μL, 2.78 mmol) was then added and mixture stirred at 0 °C for 10 mins. 2-azido-1,3-dimethylimidazolinium hexafluorophosphate (475 mg, 1.66 mmol) was then added and the reaction stirred at 0 °C for 3 hours, and then left at 4 °C for a further 16 hours. The reaction mixture was then diluted with water (15 mL) and washed with DCM (3 x 20 mL). The aqueous phase was then passed through a column of Amberlite® IR120 (H^+, previously treated with 1 M NaOH solution), and lyophilised to give a white solid (279 mg) which was used directly in the next reaction.

Synthesis of 1-Amino-1-deoxy-D-glucose

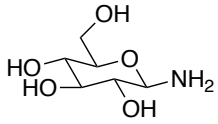

1-Azido-1-deoxy-D-glucose (0.555 mmol) (from above) was dissolved in methanol (5 mL) under nitrogen. $Pd(OH)_2/C$ (20 wt%, 39 mg, 0.055 mmol) and hydrazine hydrate (50%, 89 μL, 1.39 mmol) were then added and the reaction heated to reflux for 16 hours. The reaction mixture was then cooled, filtered (to remove Pd/C) and concentrated *in vacuo* (to remove hydrazine) to give the product as a white solid (257 mg). This reagent was used directly, as unreacted azide would not take part in the reaction with pentafluorophenyl leaving group on the polymer. Reduction was confirmed by TLC and ninhydrin staining. ^1H and ^{13}C NMR confirmed multiple anomeric peaks supported by HSQC) including starting material. Product was a mixture of anomers.

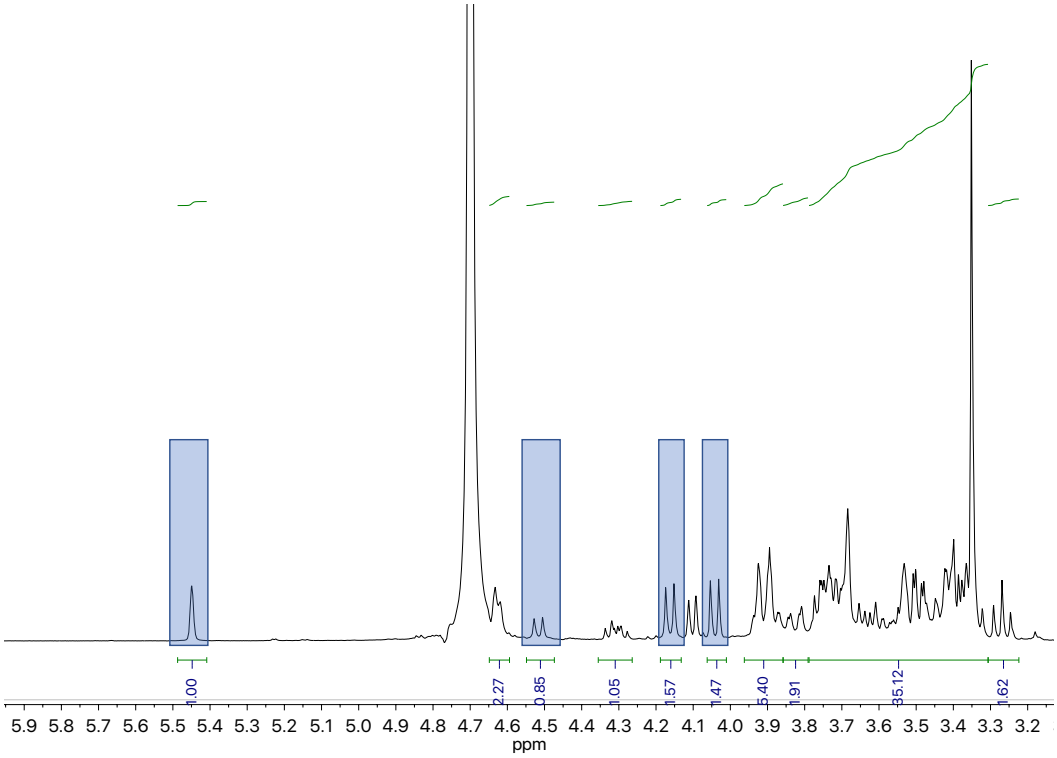

Figure E3.2. ^{1}H NMR spectra of $GlcNH_2$. Highlighted areas are the anomeric protons.

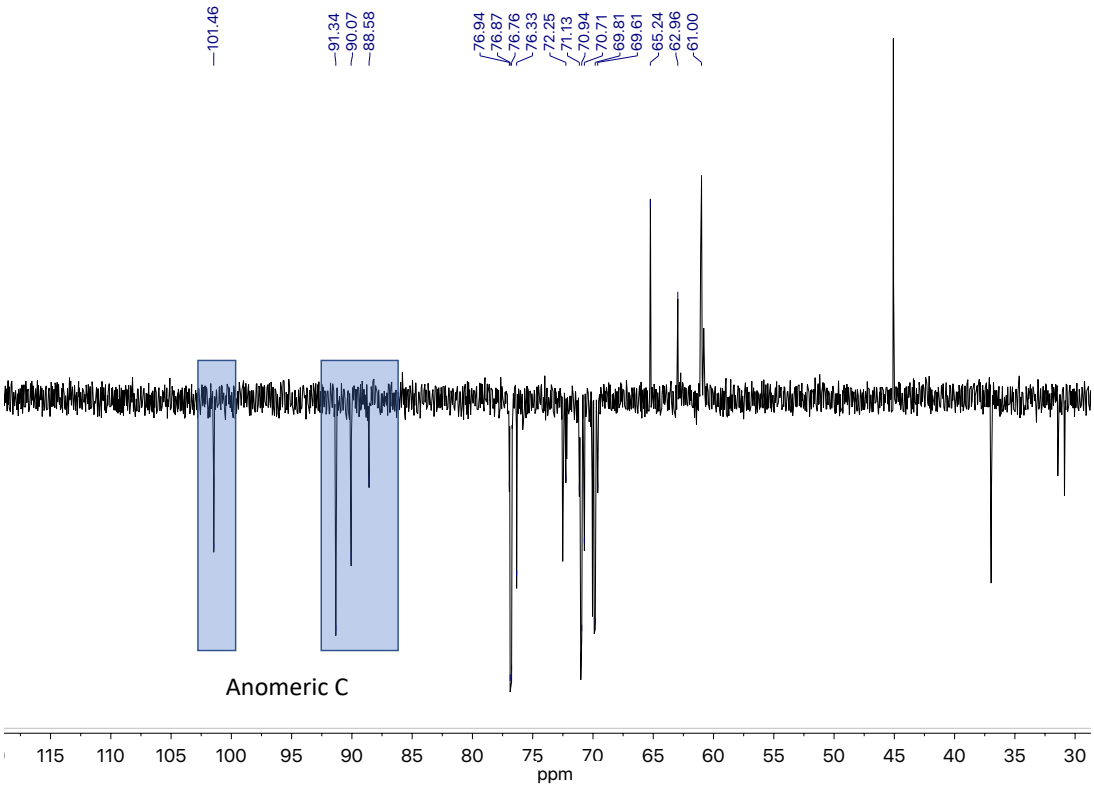

Figure E3.3. ^{13}C NMR spectra of $GlcNH_2$. Highlighted areas are the anomerics.

Synthesis of O-(N-acetyl-a-neuraminosyl)-(2→3)-O-β-D-galactopyranosyl-(1→4)-1-azido-1-deoxy-glucose. (2,3SL-N_3)

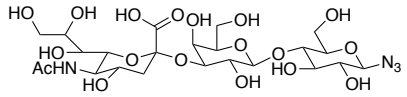

O-(*N*-acetyl-α-neuraminosyl)-(2→3)-*O*-β-D-galactopyranosyl-(1→4)-glucose (50 mg, 0.076 mmol) was dissolved in 4:1 D_2O/MeCN (1 mL) under nitrogen and cooled to 0 °C. Triethylamine (53 μL, 0.381 mmol) was then added and mixture stirred at 0 °C for 10 mins. 2-azido-1,3-dimethylimidazolinium hexafluorophosphate (65 mg, 0.229 mmol) was then added and the reaction stirred at 0 °C for 3 hours, and then left at 4 °C for a further 16 hours. The reaction mixture was then diluted with water (15 mL) and washed with DCM (3 x 20 mL). The aqueous phase was then passed through a column of Amberlite® IR120 (H^+, previously treated with 1 M NaOH solution), and lyophilised to give a white solid (95 mg) which was used directly in the next reaction. m/z calculated as 658.22; found for ESI $[M-H]^-$ 657.1

Synthesis of O-(N-acetyl-a-neuraminosyl)-(2→3)-O-β-D-galactopyranosyl-(1→4)-1-amino-1-deoxy-glucose. (2,3SL-NH_2)

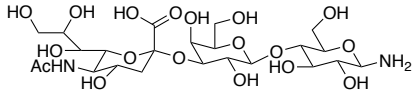

Crude *O*-(*N*-acetyl-α-neuraminosyl)-(2→3)-*O*-β-D-galactopyranosyl-(1→4)-1-azido-1-deoxy-glucose (0.076 mmol) was dissolved in methanol (5 mL) under nitrogen. $Pd(OH)_2/C$ (20 wt%, 5.4 mg, 0.0076 mmol) and hydrazine hydrate (50%, 12.2 μL, 0.191 mmol) were then added and the reaction heated to reflux for 16 hours. The reaction mixture was then cooled, filtered (to remove Pd/C) and concentrated *in vacuo* (to remove hydrazine) to give the product as a white solid (51 mg). Product was a 2:1 mix of α:β anomers at the Glc anomeric centre. δ_H (500 MHz, D_2O) 5.37 (0.65H, d, *J* 1.5, Glc α anomeric CH), 4.54 (1H d, *J* 8.0, Gal anomeric CH), 4.44 (0.35H, d, *J* 7.5, Glc β anomeric CH), 4.04 (1H, dd, *J* 10.0, 3.0), 3.98 - 4.02 (1H, m), 3.43 - 3.92 (18H, m), 2.68 (1H, dd, *J* 12.5, 4.5, Neu5Ac H^{3a}), 1.95 (3H, s, CH_3), 1.76 - 1.68 (1H, m, Neu5Ac H^{3b}). δ_C (126 MHz, D_2O) 175.0, 173.9 (2C, CO), 102.6, 101.8, 101.4 (3C, anomeric CH), 99.8 (1C, anomeric C), 77.7, 75.5, 75.1, 74.1, 72.8, 71.8, 71.4, 70.0, 69.1, 68.4, 68.1, 67.4 (12C, CH), 65.1, 62.5, 61.1 (3C, CH_2O), 51.7 (1C, CH_2N), 39.7 (1C, CCH_2C), 22.0 (1C, CH_3).

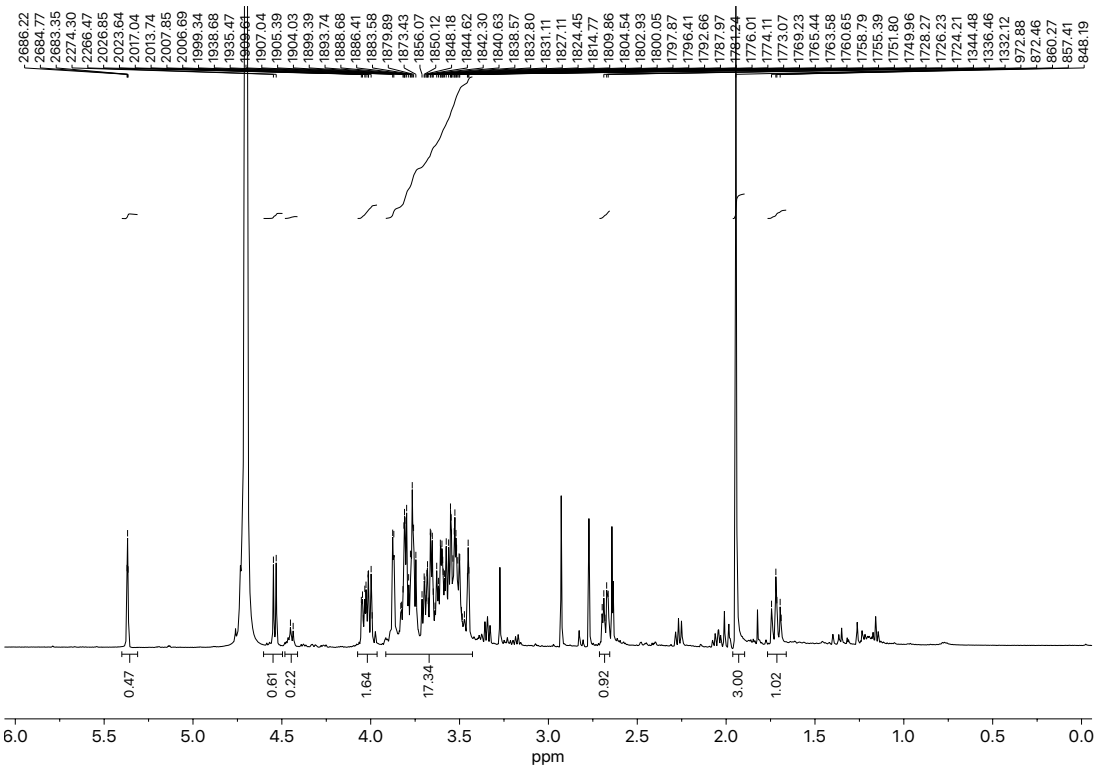

Figure E3.4. ^{1}H NMR spectrum of *O*-(*N*-acetyl-α-neuraminosyl)-(2→3)-*O*-β-D-galactopyranosyl-(1→4)-1-amino-1-deoxy-glucose.

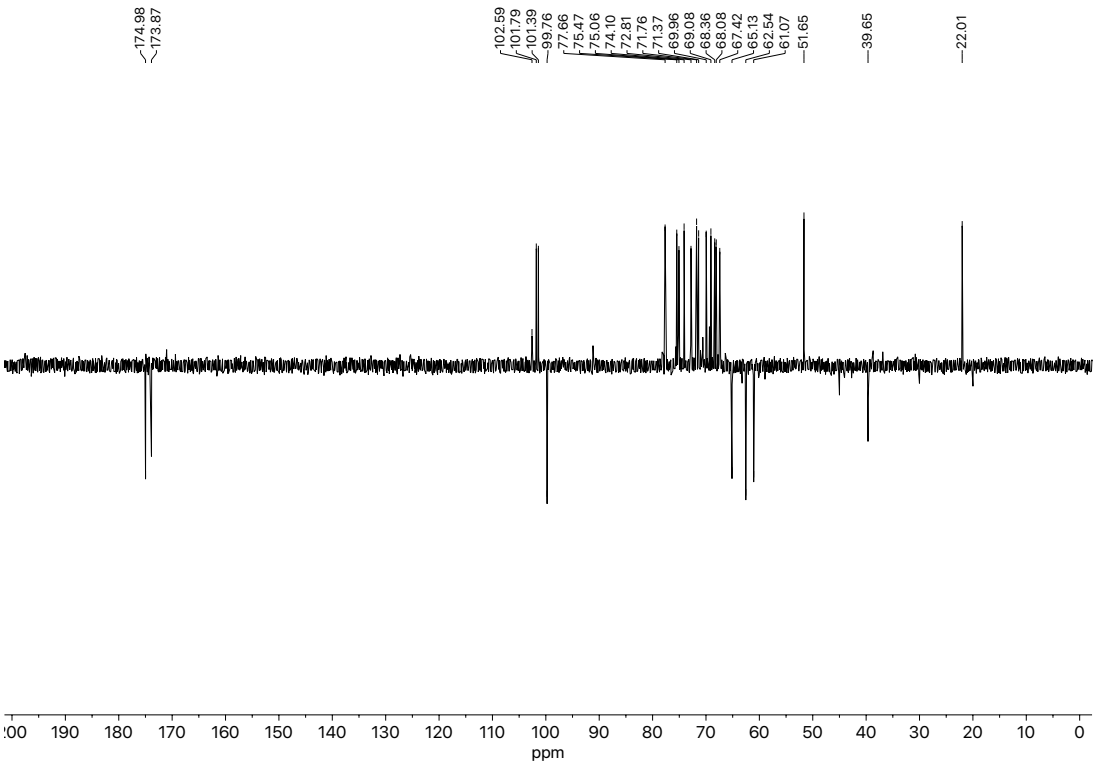

Figure E3.5. ^{13}C NMR spectrum of *O*-(*N*-acetyl-α-neuraminosyl)-(2→3)-*O*-β-D-galactopyranosyl-(1→4)-1-amino-1-deoxy-glucose.

Synthesis of O-(N-acetyl-a-neuraminosyl)-(2→6)-O-β-D-galactopyranosyl-(1→4)-1-azido-1-deoxy-glucose. (2,6 SL-N_3)

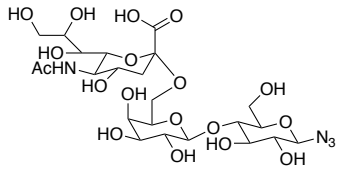

O-(*N*-acetyl-α-neuraminosyl)-(2→6)-*O*-β-D-galactopyranosyl-(1→4)-glucose (50 mg, 0.076 mmol) was dissolved in 4:1 D_2O/MeCN (1 mL) under nitrogen and cooled to 0 °C. Triethylamine (53 μL, 0.381 mmol) was then added and mixture stirred at 0 °C for 10 mins. 2-azido-1,3-dimethylimidazolinium hexafluorophosphate (65 mg, 0.229 mmol) was then added and the reaction stirred at 0 °C for 3 hours, and then left at 4 °C for a further 16 hours. The reaction mixture was then diluted with water (15 mL) and washed with DCM (3 x 20 mL). The aqueous phase was then passed through a column of Amberlite® IR120 (H^+, previously treated with 1 M NaOH solution), and lyophilised to give a white solid (86 mg) which was used directly in the next reaction. m/z calculated as 658.22; found for ESI $[M-H]^-$ 657.1

Synthesis of O-(N-acetyl-a-neuraminosyl)-(2→6)-O-β-D-galactopyranosyl-(1→4)-1-amino-1-deoxy-glucose. (2,6SL-NH_2)

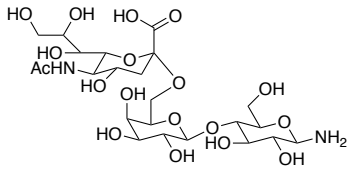

Crude *O*-(*N*-acetyl-α-neuraminosyl)-(2→6)-*O*-β-D-galactopyranosyl-(1→4)-1-azido-1-deoxy-glucose (0.076 mmol) was dissolved in methanol (5 mL) under nitrogen. $Pd(OH)_2/C$ (20 wt%, 5.4 mg, 0.0076 mmol) and hydrazine hydrate (50%, 12.2 μL, 0.191 mmol) were then added and the reaction heated to reflux for 16 hours. The reaction mixture was then cooled, filtered (to remove Pd/C) and concentrated *in vacuo* (to remove hydrazine) to give the product as a white solid (48 mg). Product was a 2.35:1 mix of α:β anomers at the Glc anomeric centre. δ_H (500 MHz, D_2O) 5.37 (0.58H (relative to Glc β anomeric), s, Glc α anomeric CH), 4.44 (1H, d, *J* 8.0, Gal anomeric CH), 4.33 (0.42H (relative to Glc α anomeric), d, *J* 7.5, Glc β anomeric CH), 4.02 (1H, d, *J* 8.0), 3.93 - 3.37 (19H, m), 2.66 - 2.60 (1H, m, Neu5Ac H^{3a}), 1.94 (3H, s, CH_3), 1.67 - 1.56 (1H, m, Neu5Ac H^{3b}). δ_C (126 MHz, D_2O) 175.0, 173.5 (2C, CO),

101.9, 101.3, 100.5 (3C, anomeric CH), 98.5 (1C, anomeric C), 77.1, 76.2, 73.9, 73.6, 73.5, 71.7, 71.6, 71.3, 70.5, 69.7, 68.4, 68.2 (12C, CH), 65.0, 63.5, 62.6 (3C, CH_2O), 51.8 (1C, CH_2N), 39.5 (1C, CCH_2C), 22.0 (1C, CH_3).

^{13}C spectra were assigned using HSQC and HMBC.

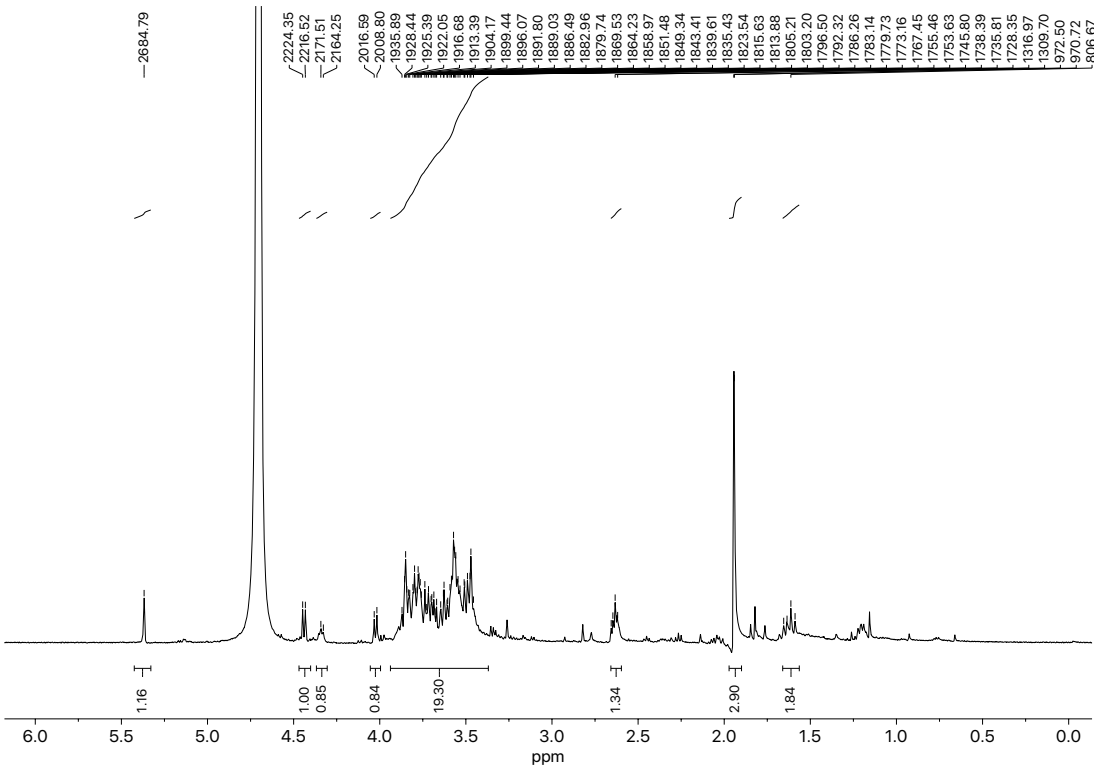

Figure E3.6. ^{1}H NMR spectrum of *O*-(*N*-acetyl-α-neuraminosyl)-(2→6)-*O*-β-D-galactopyranosyl-(1→4)-1-amino-1-deoxy-glucose.

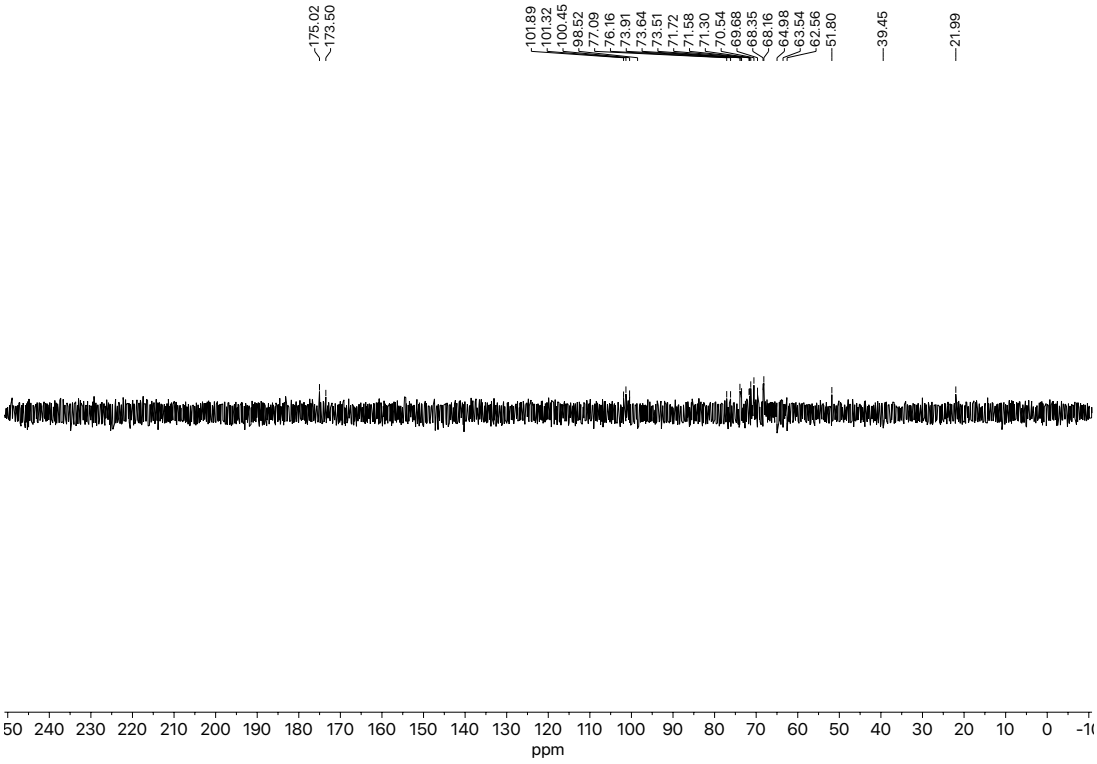

Figure E3.7. ^{13}C NMR spectrum of *O*-(*N*-acetyl-α-neuraminosyl)-(2→6)-*O*-β-D-galactopyranosyl-(1→4)-1-amino-1-deoxy-glucose.

N-Acetyl Neuraminic Acid derivative synthesis

The overall procedure is shown in Figure E3.8. based upon established procedures, which are indicated.

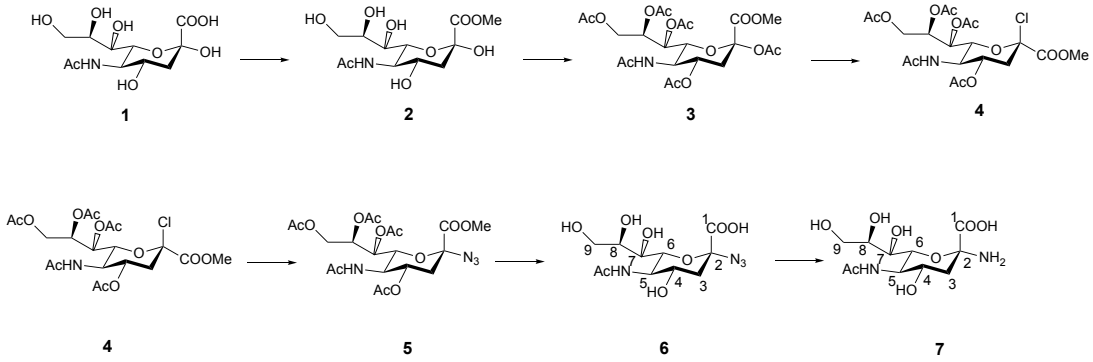

Figure E3.8. α2-Amino-2-deoxy-*N*-acetyl-D-neuraminic acid synthesis

Synthesis of Methyl 2,4,7,8,9-penta-O-acetyl-5-(acetamido)-2,3,5-trideoxy-D-glycero-β-D-galacto-non-2-ulopyranosonate (3)

Compound **3** was prepared according to the literature.[69] Briefly, *N*-acetyl neuraminic acid (**1**) (5g, 16 mmol) and Dowex 50WX8 200 (H^+) resin (12 g) were stirred in anhydrous MeOH (120 mL) at RTP overnight. The mixture was filtered and the resin extensively washed with MeOH; the combined filtrates were evaporated under reduced pressure to dryness to give compound **2** as a white solid (5.8 g). Compound **2** (2 g, 6.1 mmol) was suspended in acetic anhydride (16 mL) and the mixture cooled down to 0°C in ice bath. Then, pyridine (14 mL) was added dropwise and the reaction was left to warm up to RTP overnight. After TLC (toluene:acetone, 1:1) showed complete conversion, the reaction was evaporated under reduced pressure to dryness and co-evaporated with toluene (3x). The residue was dissolved in dichloromethane and the organic phase washed successively with 10% HCl solution, sat. $NaHCO_3$ and water. The organic phase was dried over anhydrous MgSO4, filtered and evaporated under reduced pressure to dryness to give compound **3** as a glassy solid (3.4 g, quantitative), and used directly in the next step.

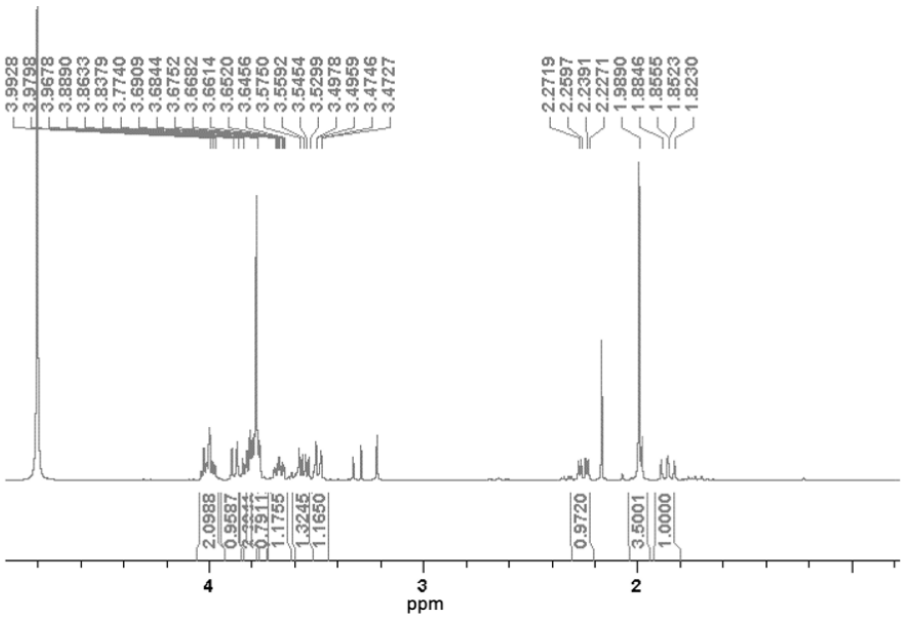

Figure E3.9. ^{1}H NMR spectrum of compound 2.

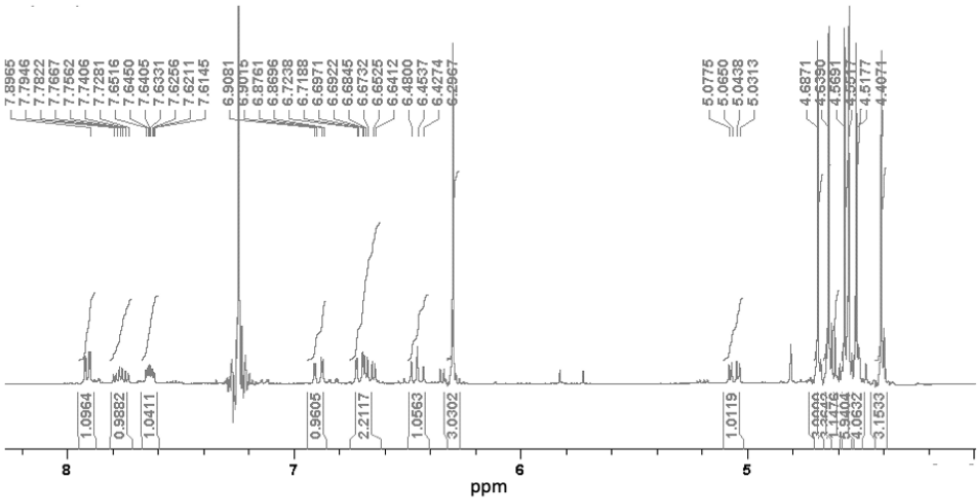

Figure E3.10. ^{1}H NMR spectrum of compound 3.

Synthesis of Methyl 4,7,8,9-tetra-O-acetyl-2-chloro-5-(acetamido)-2,3,5-trideoxy-D-glycero-β-D-galacto-non-2-ulopyranosonate (4)

Synthesis was conducted following an established procedure.[70] Anhydrous MeOH (3 mL, 11.5eq.) was added dropwise to a round bottom flask containing AcCl (5.5 mL, 12eq.) cooled with an ice bath. The resulting mixture was added to a solution of compound **3** (3.4 g, 1eq.) in 30 mL of anhydrous dichloromethane and 5.5 mL of AcCl (12eq.) cooled with an ice bath. The reaction was allowed up to RTP and stirred overnight. After TLC (elution with 100% EtOAc for 3 times) showed complete conversion of the starting material, the volatile were evaporated under reduced pressure to dryness and the oily residue co-evaporated with toluene (3x) to give compound **4** as a glassy solid (3.2 g, quantitative). It was used directly in the next step.

Synthesis of Methyl 4,7,8,9-tetra-O-acetyl-2-azido-5-(acetamido)-2,3,5-trideoxy-D-glycero-β-D-galacto-non-2-ulopyranosonate (5).

Synthesis was conducted following an established procedure.[71] To a solution of halide **4** (1 g, 1eq.), TBAHS (0.665 g, 1eq.) and NaN_3 (0.637 g, 5eq.) in dichloromethane (1 mL/100 mg of halide), saturated $NaHCO_3$ (1 mL/100 mg of halide) was added. The two-phase mixture was stirred vigorously at RTP overnight after which time TLC showed complete conversion (TLC 100% EtOH). To the crude reaction mixture, EtOAc was added (10 times the volume of dichloromethane); then, the organic phase was separated and successively washed with sat. $NaHCO_3$, water (2x) and brine. The combined organic extracts were dried over anhydrous Na_2SO_4, filtered, and evaporated under reduced pressure to dryness. Flash chromatography (Hex/EtOAc) afforded the product (**5**) as a white solid (0.750 g, 74% yield). This was used directly in the next step.

Synthesis of 2-azido-5-(acetamido)-3,5-dideoxy-D-glycero-a-D-galacto-non-2-ulopyranosonate (6). a2-azido-2-deoxy-N-acetyl-D-neuraminic acid.

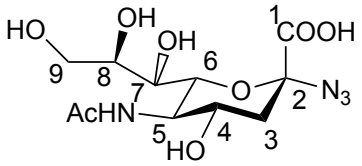

Compound **5** (0.4 g) was dissolved in MeOH:TEA:H2O (4:1:5) (55 mL) and stirred at RTP overnight. The reaction mixture was evaporated under reduced pressure to dryness, dissolved in water, and freeze-dried to afford the Neu5Ac azide (**6**) as a white solid (0.256 g, full conversion). A single anomer was obtained (α) based on the ^{13}C shift at 90.9 of C2 (anomeric carbon), in agreement with literature value of 89.1 for the per-acetylated equivalent.[71] There is no anomeric proton in his compound, hence the use of ^{13}C. δ_H (400 MHz, D_2O) 3.93 - 3.80 (3H, m, H^4, H^6, H^9), 3.80 - 3.72 (1H, m, H^5), 3.66 - 3.61 (1H, m, H^8), 3.61 - 3.53(1H, m, H^9), 3.39 (1H, q, *J* 7, H^7), 2.68 (1H, dd, *J* 12.5, 4.5, H^3), 2.03 (3H ,s , CH_3), 1.63 (1H, t, *J* 12.5, H^3). δ_C (400 MHz, D_2O) 175.1 (1C, NHCO), 172.4 (1C, C^1), 90.9 (1C, C^2), 73.8 (1C, C^6), 71.5 (1C, C^8), 68.1 (1C, C^7), 62.7 (1C, C^9), 51.6 (1C, C^5), 38.9 (1C, C^3), 22.0 (1C, CH_3)

NB: The peaks at ~1.25 ppm and ~3.25 ppm in the proton NMR and ~9 ppm and ~45 ppm are triethylamine salt impurities

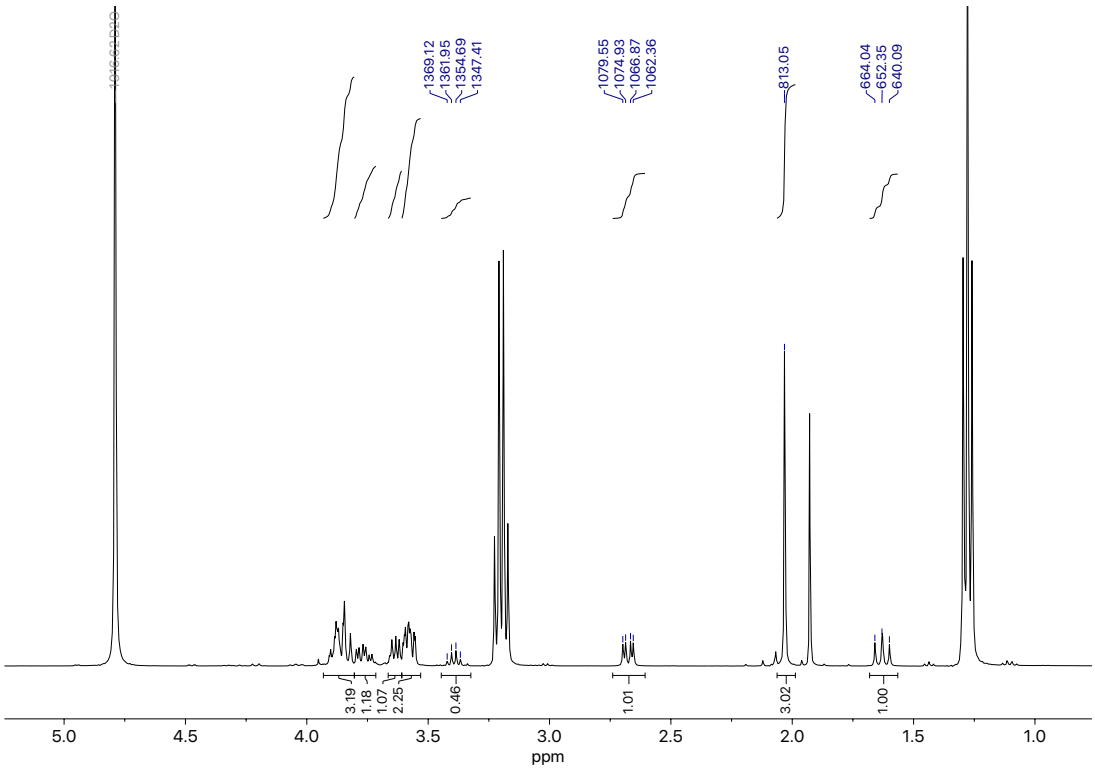

Figure E3.11. ^{1}H NMR spectrum of α2-azido-2-deoxy-*N*-acetyl-D-neuraminic acid.

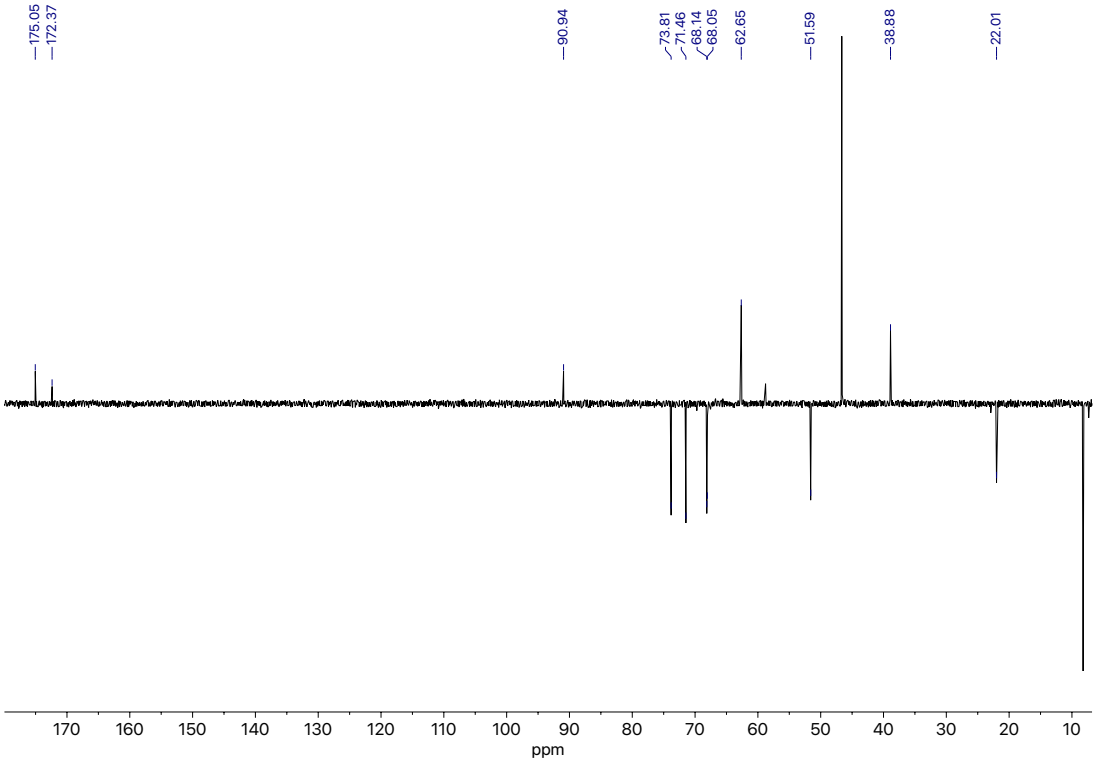

Figure E3.12. ^{13}C NMR spectrum of α2-azido-2-deoxy-*N*-acetyl-D-neuraminic acid.

Synthesis of a2-Amino-2-deoxy-N-acetyl-D-neuraminic acid (7).

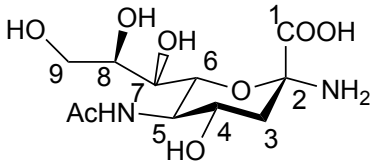

2-Azido-2-deoxy-*N*-acetyl-D-neuraminic acid (40 mg, 0.120 mmol) was dissolved in methanol (5 mL) under nitrogen. $Pd(OH)_2/C$ (20 wt%, 8.4 mg, 0.012 mmol) and hydrazine hydrate (50%, 19.2 μL, 0.299 mmol) were then added and the reaction heated to reflux for 4 hours. The reaction mixture was then cooled, filtered (to remove Pd/C) and concentrated *in vacuo* (to remove hydrazine) to give the product as a colourless oil (35 mg). A single anomer was identified in the ^{13}C spectra with a chemical shift of 96.1, compared to 89.1 in the azido precursor, consistent with no anomeric inversion during the reduction of azide to amine. δ_H (500 MHz, D_2O) 3.93 - 3.98 (1H, m, H^4), 3.89 - 3.93 (1H, m, H^6), 3.84 (1H, q, *J* 10.0, H^5), 3.75 (1H, dd, *J* 12.0, 2.5, H^{9a}), 3.67 (1H, ddd, *J* 9.0, 6.5, 2.5, H^8), 3.50 - 3.55 (1H, m, H^{9b}), 3.42 - 3.45 (1H, m, H^7), 2.15 (1H, dd, *J* 13.0, 5.0, H^{3a}), 1.96 (3H, s, CH_3), 1.75 (1H, dd, *J* 13.0, 11.5, H^{3b}). δ_C NMR (126 MHz, D_2O) 175.8 (1C, *C*OCH_3), 174.7 (1C, C^1), 96.1 (1C, C^2), 70.2, 70.2 (2C, C^6 and C^8), 68.4 (1C, C^7) 67.1 (1C, C^4), 63.2 (1C, C^9), 52.2 (1C, C^5), 39.2 (1C, C^3), 22.1 (1C, CH_3).

NB: The peaks at ~2.7 ppm and ~2.9 ppm in the proton NMR are DMF impurities

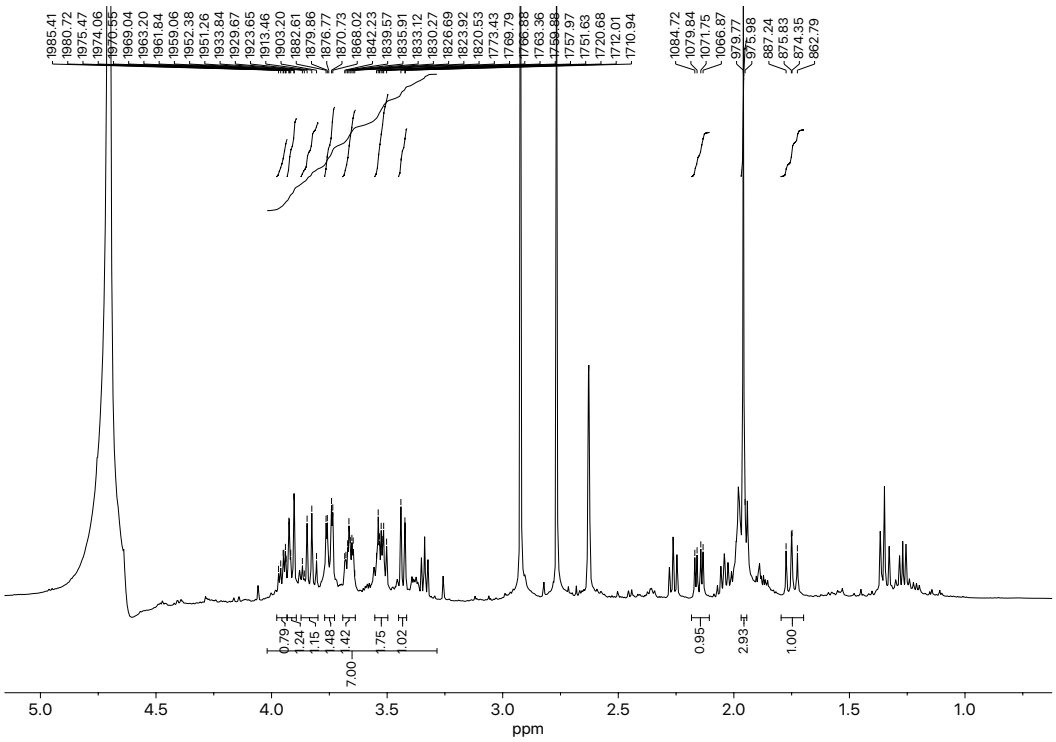

Figure E3.13. ^{1}H NMR spectrum of 2-amino-2-deoxy-*N*-acetyl-D-neuraminic acid.

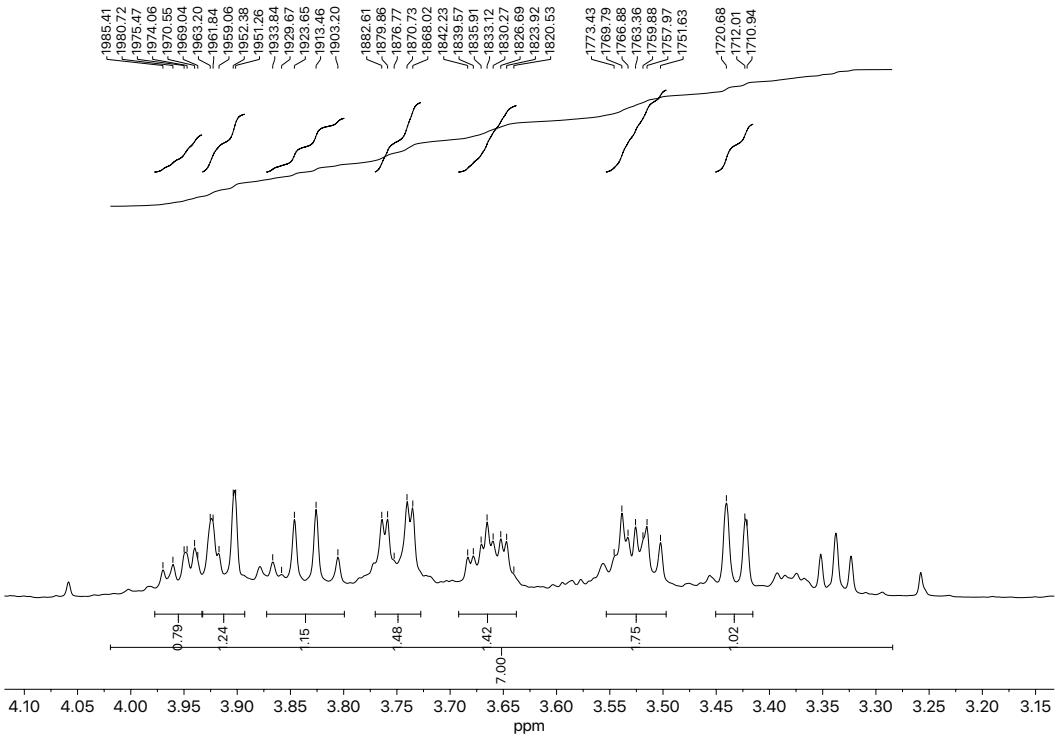

Figure E3.14. Zoom in of ^{1}H NMR spectrum (4.15 ppm to 3.15 ppm) of 2-amino-2-deoxy-*N*-acetyl-D-neuraminic acid.

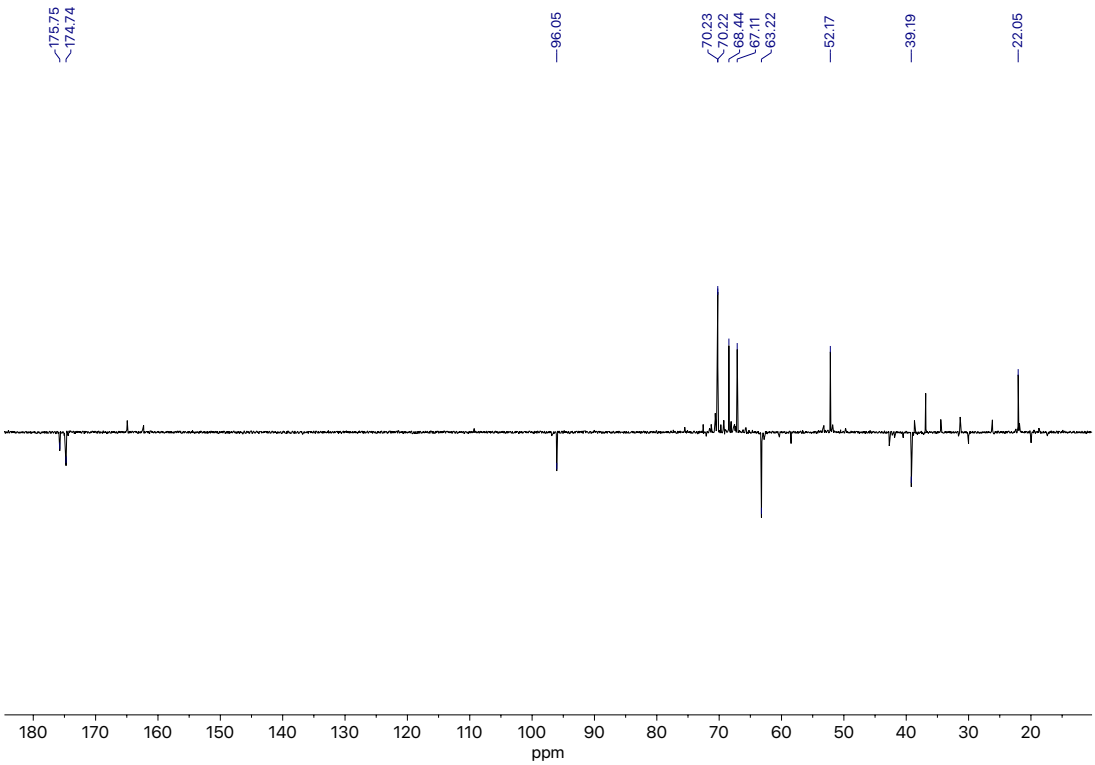

Figure E3.15. ^{13}C NMR spectrum of 2-amino-2-deoxy-*N*-acetyl-D-neuraminic acid. A single anomeric signal was observed (96 ppm).

Citrate-stabilised 16 nm Gold Nanoparticle Synthesis

Synthesised by a previously reported protocol.[72] To 500 mL of water was added 0.163 g (0.414 mmol) of gold(III) chloride trihydrate, the mixture was heated to reflux and 14.6 mL of water containing 0.429 g (1.46 mmol) of sodium citrate tribasic dihydrate was added. The reaction was allowed to reflux for 30 minutes before cooling to room temperature over 3 hours. The solution was centrifuged at 13 krpm for 30 minutes and the pellet resuspended in 40 mL of water to give an absorbance at 520 nm of ~1Abs.

Citrate-stabilised 35 nm Gold Nanoparticle Synthesis

35 nm gold nanoparticles were synthesised by a modified step growth method developed by Bastús *et al.*[73] A solution of 2.2 mM sodium citrate in Milli-Q water (150 mL) was heated under reflux for 15 min under vigorous stirring. After boiling had commenced, 1 mL of $HAuCl_4$ (25 mM) was injected. The colour of the solution changed from yellow to bluish gray and then to soft pink in 10 min, 1 mL was taken for DLS and UV/Vis analysis. Immediately after the synthesis of the Au seeds and in the same reaction vessel, the reaction was cooled until the temperature of the solution reached 90 °C. Then, 1 mL of a $HAuCl_4$ solution (25 mM) was injected. After 20 min, the reaction was finished. This process was repeated twice. After that, the sample was diluted by adding 85 mL of MilliQ water and 3.1 mL of 60 mM sodium citrate. This solution was then used as a seed solution, and three further portions of 1.6 mL of 25 mM $HAuCl_4$ were added with 20 min between each addition. Following completion of this step 1 mL was taken for DLS and UV/Vis analysis. The sample was diluted by adding 135 mL of MilliQ water and 4.9 mL of 60 mM sodium citrate. This solution was then used as a seed solution, and the process was repeated with three further additions of 2.5 mL of 25 mM $HAuCl_4$, this solution was analysed by DLS and UV/Vis and target size of 35 nm was reached and the solution was cooled and a sample taken for TEM analysis.

This process of $HAuCl_4$ additions followed by dilution was repeated until a size of 55 nm and 70 nm was reached as determined by UV/Vis and DLS.

Gold Nanoparticle Polymer Coating Functionalisation – 16 nm

100 mg of glycopolymer was agitated overnight with 10 mL of 16 nm AuNPs ~1Abs at UV_{max}. The solution was centrifuged at 13 krpm for 30 minutes and the pellet resuspended in 10 mL of water, the solution was centrifuged again at 13 krpm for 30 minutes and the pellet resuspended in 1 mL aliquots and centrifuged at 14.5 krpm for 10 minutes. The pellets were combined into a 1 mL solution with an absorbance at 520 nm of ~10 Abs.

Gold Nanoparticle Polymer Coating Functionalisation – 35, 55 and 70 nm

100 mg of glycopolymer was agitated overnight with 10 mL of 35 nm AuNPs ~1Abs at UV_{max}. The solution was centrifuged at 8 krpm for 30 minutes and the pellet resuspended in 10 mL of water, the solution was centrifuged again at 8 krpm for 30 minutes and the pellet resuspended in 1 mL aliquots and centrifuged at 8 krpm for 10 minutes. The pellets were combined into a 1 mL solution with an absorbance at UV_{max} of ~10 Abs.

BSA/Casein/PVP10 blocking of Nanoparticle surface

1 mL of UV_{max} at 2.5 Abs AuNPs were centrifuged at 15,00 rpm for 30 mins and supernatant was removed and replaced with 1 mL 1 mg/mL BSA for 30 minutes. The blocking agent was then removed by centrifugation (2 × 30 minutes at 15,000 krpm for 16 nm AuNPs and 2 × 30 minutes at 8,000 rpm for 35 nm AuNPs). The particles were then taken to an Absorbance of ~10 at UV_{max}.

Expression and purification of SARS-COV-2 Spike S1 in HEK293 Cells

Codon-optimised SARS-COV-2 Spike S1 subunit (amino acids 1-685) with a C-terminal 10x polyhistidine tag was expressed under control of a CMV promoter (pCMV3-S1-10xHis, Sino Biological, #VG40591-CH). HEK293 cells were grown in suspension to a density of 1.0 x 10^6 cells/mL in FreeStyle 293 Expression Medium (Thermo Scientific, #12338018), then transfected with 0.5 µg of pCMV3-S1-10xHis, 1.5 µg of linear polyethyleneimine (Alfa Aesar, #43896.01) and 50 µL Opti-MEM-I per 1 mL of cells (Thermo Scientific, #31985-062). After transfection, cells were grown to a density of 2.0 x 10^6 cells/mL and supplemented with 4 mM valproic acid (Sigma Aldrich, #P4543). 96 hours post transfection, the media was cleared by centrifugation, 6,000 x g in a Fiberlite F10-4 x 1000 LEX rotor (Thermo Scientific, #096-041053) for 10 minutes.

To purify Spike S1, cleared media was adjusted to 20 mM HEPES pH 7.5 and 10 mM imidazole, and was loaded on to a 5 mL HisTrap HP column (cytiva, #17524801) at a flow rate of 20 mL/min for ~16 hours. A purification buffer comprising 20 mM HEPES, 300 mM NaCl and 1 mM DTT +/- 1 M imidazole was used (for buffer lines A and B respectively), and the column was washed with 30 CVs of 2% buffer B (20 mM imidazole) before eluting the protein over a 2 - 50% gradient over 30 CVs. Fractions containing Spike S1 were pooled and concentrated using a 10 KDa molecular-weight cut-off spin concentrator (Sigma Aldrich, #UFC910008), before being buffer exchanged into 20 mM HEPES 7.5, 300 mM NaCl, 10% glycerol using a 5 mL HiTrap desalting column (cytiva, #29048684). Peak fractions were pooled, and the final concentration was measured by absorbance at 280 nm, yielding a concentration of 1.25 mg/mL. Aliquots of protein were snap-frozen in liquid nitrogen and stored at -80 ℃.

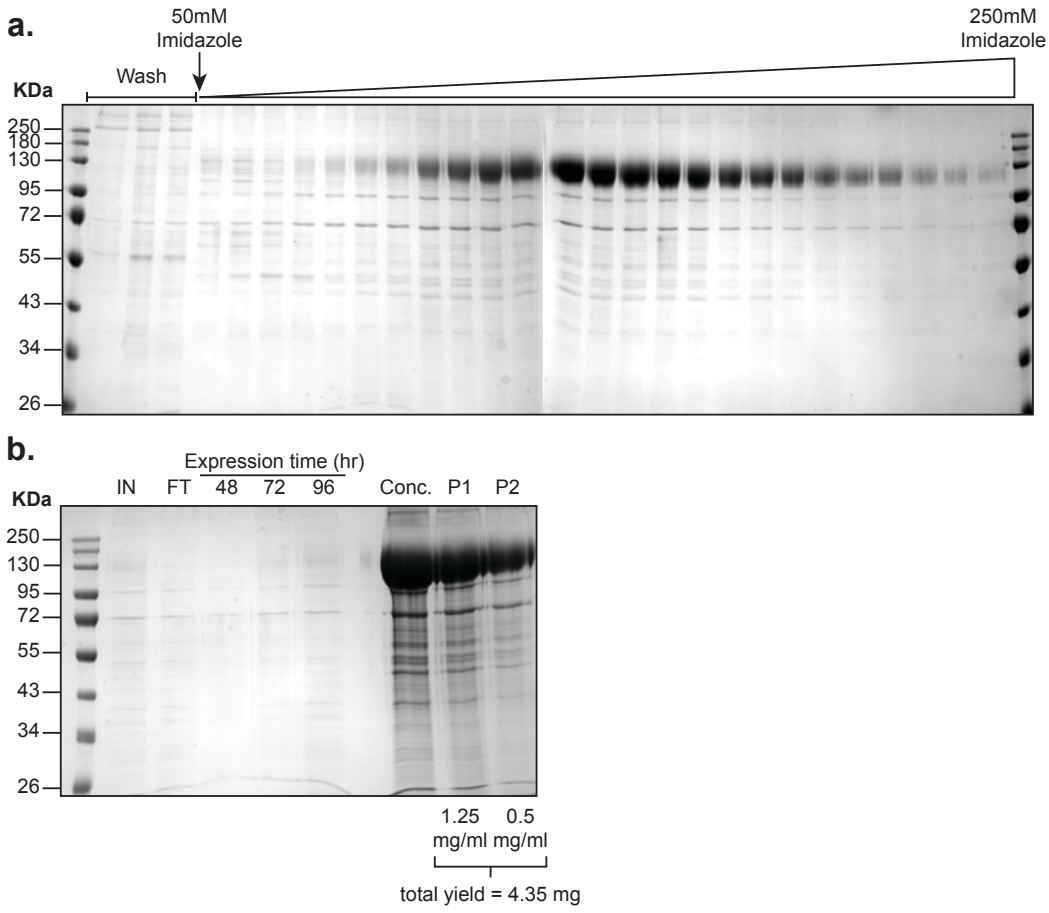

Figure E3.16. Gel electrophoresis of expressed spike protein. P1 and P2 were used here.

Recombinant Expression and Purification of SARS-COV-2 (first 300 amino acids) for Thermal Shift Assay

A pET21a plasmid encoding for a hexahistidine-tag, SUMO-tag and the first 300 amino acids of SARS-COV-2 was purchased from Genscript Inc. The plasmid was transformed into competent Escherichia coli BL21(DE3) cells (New England Biolabs). A colony was selected to inoculate 100 mL of LB-medium containing 100 µg.mL-1 kanamycin and was grown overnight at 37 °C under continuous shaking of 180 rpm. The following day, 10 mL of the preculture was added to 1 L of LB-medium (supplemented with 100 µg.mL-1 kanamycin) in a 2.5 L Ultra Yield™ flask and grown at 37 °C with a shaking speed of 180 rpm until an OD600 of 0.6 was reached. The temperature was then reduced to 16 °C and the cells incubated for another hour before adding IPTG to a final concentration of 0.2 mM. The overexpression of the protein was allowed to take place overnight following which the cells were centrifuged at 5000 g for 10 minutes at 4 °C. Pelleted cells were resuspended in PBS supplemented with Pierce protease inhibitor mini-tablets. The suspension was passed through a STANSTED "Pressure Cel" FPG12800 homogenizer in order to lyse the cells. The cell lysate was centrifuged at 48,000 g and the supernatant was passed through a 0.45 µm filter before being added to a 3 mL column of IMAC cOmplete His-Tag Purification Resin (Roche) pre-equilibrated with PBS. The column was washed with 20 column volumes of PBS. Bound protein was eluted using 6 mL of 300 mM Imidazole in PBS. Further purification of was achieved using a HiLoad 16/600 Superdex 200 pg gel filtration column (GE Healthcare) with PBS as the running buffer. Purity was estimated using SDS-PAGE and protein concentration determined using Thermo Scientific Pierce BCA assay kit. Various volumes of the protein contained in PBS solution were aliquoted into 1.5 mL microcentrifuge tubes and snap-frozen in liquid nitrogen to store at -80 °C until required.

Synthesis of Low Concentration SARS-COV-2 S1-coated Polystyrene Nanoparticle Virus Mimics

12.5 µL of 0.5 mg/mL SC2 S1 from Pool 2 and 125 µL of polystyrene nanoparticles were added to 1000 µL 10 mM HEPES saline buffer (0.15 M NaCl). This was agitated for 1 hour. It was not centrifuged before use in testing. This gave a maximum SC2 S1 concentration on polystyrene of of 5.5 µg/mL.

The low concentration naked polystyrene control was made up as above except the SC2 S1 protein was replaced with distilled water of equal volume (12.5 µL).

Synthesis of High Concentration SARS-COV-2 S1-coated Polystyrene Nanoparticle Virus Mimics

30 µL of 0.5 mg/mL SC2 S1 from Pool 2 and 125 µL of polystyrene nanoparticles were added to 845 µL 10 mM HEPES saline buffer (0.15 M NaCl). This was agitated for 1 hour. It was not centrifuged before use in testing. This gave a maximum SC2 S1 concentration on polystyrene of 15 µg/mL.

The high concentration naked polystyrene control was made up as above except the SC2 S1 protein was replaced with distilled water of equal volume (12.5 µL).

3.6.4 Flow-Through and Lateral Flow Strip Production, Running and Analysis Protocols

Protocol for manufacturing flow-through and lateral flow strips

Backing cards were cut to size by removal of 20 mm using a guillotine. Nitrocellulose was added to the backing card by attaching the plastic backing of the nitrocellulose to the self-adhesive on the card. The wick material was then added to the backing card so it overlaps with the nitrocellulose by ~5 mm. The strips were cut to size of width 2 - 3 mm.

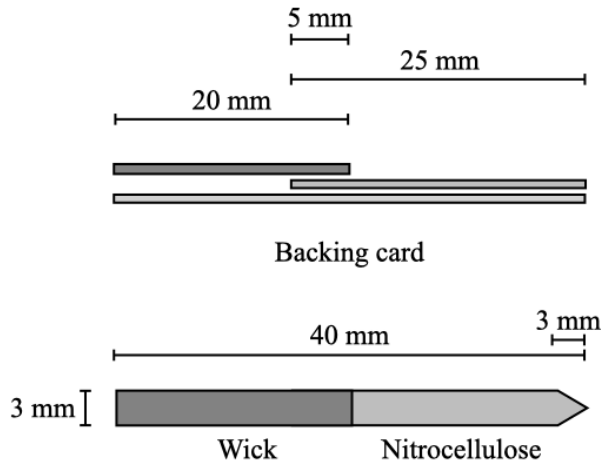

Figure E3.17. Flow-through and lateral flow strip dimensions

Protocol for test line addition to the flow-through and lateral flow strips

1 µL of the test line solution was added to the test strip using a micropipette fitted with 10 µL tip, the test line was spotted ~1 cm from the non-wick end of the strip. The strips were dried at 37 ℃ in an oven for 30 minutes. The test strips were allowed to cool to room temperature before testing.

Protocol for running flow-through and lateral flow tests without target analyte in buffer

The running buffer of total volume 50 µL was made as follows; 5 µL AuNPs (OD10), 5 µL flow-through and lateral flow assay buffer – 10 × HEPES buffer, 40 µL water. The running solution was then agitated on a roller for 5 minutes. 45 µL of this solution was added to a 0.2 mL PCR tube, standing vertically.

A small "v" (~3 mm) was cut into the test strips at the non-wick end and the strips added to the PCR tubes so they protrude from the top and the immobile phase (1 cm

from non-wick end) is not below the solvent line. There was one test per tube. All tests were run in triplicate.

The tests were run for 20 minutes before removal from the tubes. The test strips were allowed to dry at room temperature for ~5 minutes. The test strips were mounted test-face down onto a clear and colourless piece of acetate sheeting.

Protocol for flow-through and running lateral flow tests with polystyrene nanoparticle virus mimic analyte in buffer

The running buffer of total volume 50 µL was made as follows; 5 µL AuNPs (OD10), 5 µL flow-through and lateral flow assay buffer – 10 × HEPES buffer, 40 µL polystyrene solution. The running solution was then agitated on a roller for 5 minutes. 45 µL of this solution was added to a 0.2 mL PCR tube, standing vertically.

A small "v" (~3 mm) was cut into the test strips at the non-wick end and the strips added to the PCR tubes so they protrude from the top and the immobile phase (1 cm from non-wick end) is not below the solvent line. There was one test per tube. All tests were run in triplicate.

The tests were run for 20 minutes before removal from the tubes. The test strips were allowed to dry at room temperature for ~5 minutes. The test strips were mounted test-face down onto a clear and colourless piece of acetate sheeting.

Standard protocol for flow-through and lateral flow strip analysis

The acetate sheets were scanned using a Kyocera TASKalfa 5550ci printer to a pdf file that was converted to a jpeg, scans were taken within 1 hour of strip drying. The jpeg was analysed in Image J 1.51 using the plot profile function to create a data set exported to Microsoft Excel for Mac. The data was exported to Origin 2019 64Bit and trimmed to remove pixel data not from the strip surface. The data was aligned and averaged (mean). The data was then reduced by number of groups to 100 data points (nitrocellulose and wick) and plotted as Grey value (scale) vs Relative distance along the 100 data points.

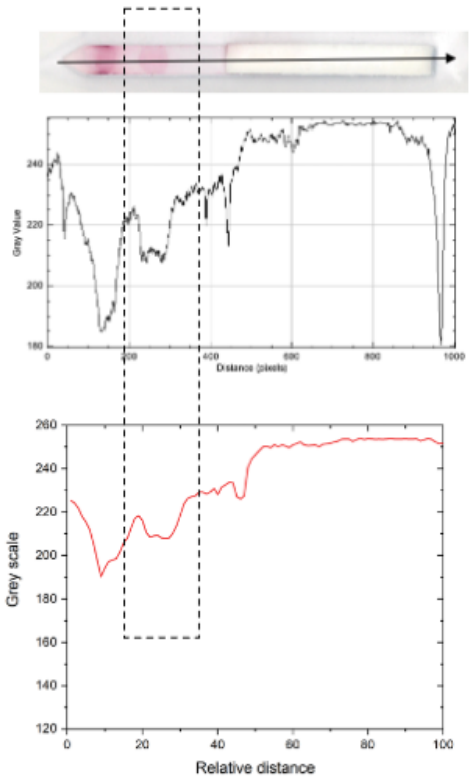

Figure E3.18. Representative dipstick (Top), raw grey value plot (Middle) and processed grey value plot (Bottom)

Flow-through and lateral flow signal-to-noise analysis

Relative distance pixel 15 to 35 (area around the test line) was averaged (mean) to provide average noise around the test line for strips vs. 2,3'-sialyllactosamine-BSA (1 mg/mL) as a test line. The signal value was determined by selecting the lowest grey value between 15 to 35 relative distance pixels for strips vs. SARS-COV-2 S1 (0.39 mg/mL) as a testline. Equation E3.1 was then used to determine the signal-to-noise ratio.

$$Signal - to - Noise = \frac{255 - Signal}{255 - Noise}$$

Equation E3.1. Equation for determining signal-to-noise ratio

NB: 255 is the grey value for the blank nitrocellulose surface.

Flow-through and lateral flow signal intensity analysis

Relative distance pixel 15 to 35 (area around the test line), excluding pixels that contributed to the signal peak were averaged (mean). This average was subtracted from the lowest grey value between 15 to 35.

Silver Staining Procedure

Staining solution was prepared as kit guidelines. 2 mL of solution A and 2 mL of solution B were added to a watch glass and mixed thoroughly. The wick of the strip was removed and the nitrocellulose strip immersed for 1 minute. Samples were removed from the solution, washed with still water and dried room temperature for 10 minutes before scanning with a Kyocera TASKalfa 5550ci printer to a pdf file that was converted to a jpeg.

Flow-through and lateral flow assay buffer - 10× HEPES buffer (10% PVP_{400}) in 100 mL H_2O

2.38 g (100 $mmoldm^{-3}$) of HEPES, 8.77 g (1.50 $moldm^{-3}$) of NaCl, 0.011 g (1.0 $mmoldm^{-3}$) of $CaCl_2$, 0.8 g (0.8% w/v., 123 $mmoldm^{-3}$) of NaN_3, 0.5 g (0.5% w/v., 4.07 $mmoldm^{-3}$) of Tween-20 and 10 g (10% w/v.) of poly(vinyl pyrrolidone)$_{400}$ (PVP_{400}, Average Mw ~40,000) was dissolved in 100 mL of water. The buffer is not pH adjusted. All experiments with 2,3'- and 2,6'-Sialyllactosamine (2,6SL) functionalised PHEA polymers used a 1% PVP_{400} buffer.

Neuraminic acid (NeuNAc) functionalised PHEA polymers of varying lengths on 35 nm AuNPs with BSA versus a test line of SARS-COV-2 S1 protein (SC2, 0.39 mg/mL), SARS-COV-1 spike protein (SC1, 0.4 mg/mL) or neuraminic acid-BSA (NeuNAc-BSA, 1 mg/mL) also used a 1% PVP_{400} buffer. Neuraminic acid (NeuNAc) functionalised PHEA polymers of varying lengths on 16 nm and 35 nm AuNPs versus a test line of SARS-COV-2 S1 protein (SC2, 0.39 mg/mL) or 2,3'-sialyllactosamine BSA (2,3SL-BSA, 1 mg/mL) also used a 1% PVP_{400} buffer.

All other experiments with neuraminic acid glycopolymer functionalised AuNPs used a 10× HEPES buffer (20% PVP_{400}) buffer to further decrease background noise.

The percentage of PVP_{400} in the buffer is listed in the supplementary figure and table headings (Appendix 3).

3.6.5 Flow-Thorough Complete Device Production, Running and Analysis Protocols

Protocol for manufacturing flow-through complete devices

Nitrocellulose was added to the backing card by attaching the plastic backing of the nitrocellulose to the self-adhesive on the card. The wick material was then added to the backing card so it overlaps with the nitrocellulose by ~5 mm. The strips were then cut to size of width ~3 mm so they sit in the cassettes without the need for excess force to fit. Tests lines were then added before addition of the conjugate pad. 1 µL of the test line solution was added to the nitrocellulose strip using a micropipette fitted with 10 µL tip, the test line was spotted ~1 cm from the non-wick end of the nitrocellulose surface. A control line was added ~1.5 cm from non-wick end of the nitrocellulose surface. The strips were dried at 37 °C in an oven for 30 minutes. The test strips were allowed to cool to room temperature before addition of the conjugate pad. The conjugate pad was added to the backing card so it overlaps with the nitrocellulose by ~3.5 mm. The sample pad, was cut to size of 20 mm by 6 mm and was added to the backing card, overlapping with the conjugate pad by ~6.5 mm and straddling the backing card evenly. The completed strip was then added to the cassettes and sealed.

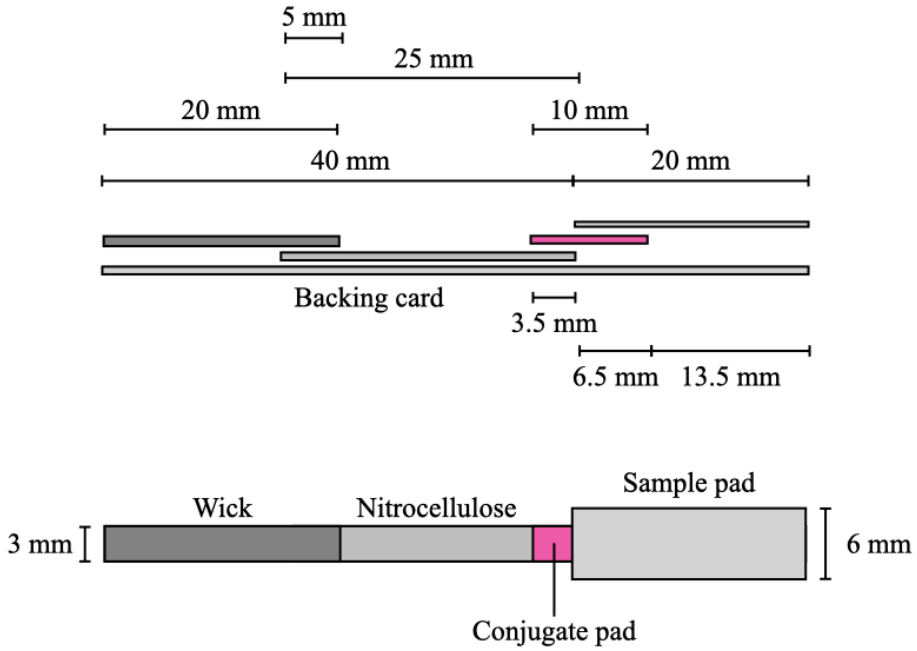

Figure E3.19. Flow-through complete strip dimensions

Protocol for Conjugate Pad Production

Strips of the conjugate pad material were agitated for 30 minutes in a solution of 0.1% Tween-20 (blocking solution). The strips were then patted dry and baked overnight at 37 ℃ in an oven overnight. The conjugate pads were cut to size (3 mm width) and placed individually into the wells of a 384-well microplate. 20 µL 1× conjugate pad buffer solution containing OD1 (unless otherwise specified) AuNPs was added to the top of each conjugate pad in the wells. The pads were dried for 3 hours at 37 ℃ in an oven before curing overnight in an airtight box containing desiccant. The completed pads were always stored in an airtight box containing desiccant.

10× Conjugate Pad Buffer

10% w/v. of poly(vinyl pyrrolidone)$_{400}$ (Average Mw ~40,000 g.mol^{-1}), 50% w/v. trehalose, 10% w/v. sucrose and 0.1% w/v. Tween-20 were added to distilled water and allowed to dissolve.

Protocol for running flow-through test without target analyte in buffer

8 µL 10× HEPES buffer (20% PVP_{400}) was added to 72 µL distilled water. 80 µL was added to the sample pad and allowed to absorb. The test was run for 10 minutes before scanning in the cassettes by a Kyocera TASKalfa 5550ci printer to a pdf file that was converted to a jpeg. After ~1 hour the strips were removed from the cassettes, and added to acetate sheets. These were scanned using a Kyocera TASKalfa 5550ci printer to a pdf file that was converted to a jpeg, acetate scans were taken within 1 hour of strip drying. The jpegs were analysed in Image J 1.51 using the plot profile function to create a data set exported to Microsoft Excel for Mac. The data was exported to Origin 2019 64Bit and trimmed to remove pixel data not from the strip surface. The data was aligned and averaged (mean). The data was then reduced by number of groups to 100 data points (just the nitrocellulose surface) and plotted as Grey value (scale) vs Relative distance along the 100 data points.

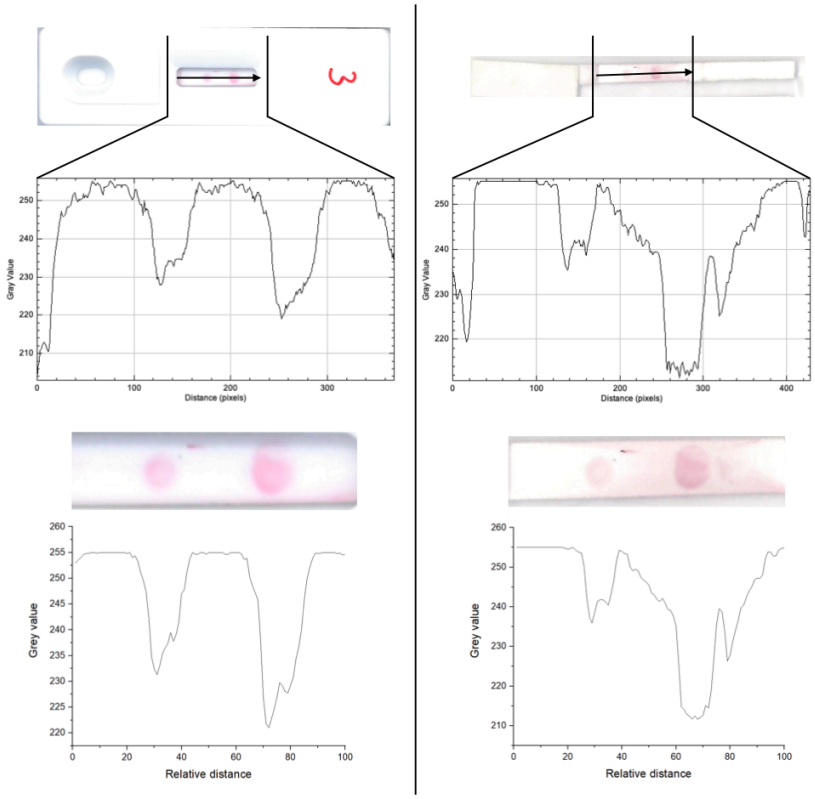

Figure E3.20. Representative cassette (Top left) and strip (Top right), raw grey value plot (Middle) and processed grey value plot (Bottom)

Flow-through signal-to-noise analysis

Relative distance pixel 1 to 10 and 51 to 60 (area around the test line) was averaged (mean) to provide average noise around the test line for strips. The signal value was determined by selecting the lowest grey value between 11 to 50 relative distance pixels. Equation 1 was then used to determine the signal-to-noise ratio.

Flow-through signal intensity analysis

Relative distance pixel 1 to 10 and 51 to 60 (area around the test line), excluding pixels that contributed to the signal peak were averaged (mean). This average was subtracted from the lowest grey value between 11 to 50.

3.7 References

(1) Zhou, P.; Yang, X.-L.; Wang, X.-G.; Hu, B.; Zhang, L.; Zhang, W.; Si, H.-R.; Zhu, Y.; Li, B.; Huang, C.-L.; Chen, H.-D.; Chen, J.; Luo, Y.; Guo, H.; Jiang, R.-D.; Liu, M.-Q.; Chen, Y.; Shen, X.-R.; Wang, X.; Zheng, X.-S.; Zhao, K.; Chen, Q.-J.; Deng, F.; Liu, L.-L.; Yan, B.; Zhan, F.-X.; Wang, Y.-Y.; Xiao, G.-F.; Shi, Z.-L. A Pneumonia Outbreak Associated with a New Coronavirus of Probable Bat Origin. *Nature* **2020**, *579* (7798), 270–273.

(2) Sharma, S.; Kawa, N.; Gomber, A. WHO's Allocation Framework for COVAX: Is It Fair? *Journal of medical ethics* **2021**, 107152.

(3) The Lancet, T. Access to COVID-19 Vaccines: Looking beyond COVAX. *Lancet (London, England)* **2021**, *397* (10278), 941.

(4) Xie, X.; Zhong, Z.; Zhao, W.; Zheng, C.; Wang, F.; Liu, J. Chest CT for Typical Coronavirus Disease 2019 (COVID-19) Pneumonia: Relationship to Negative RT-PCR Testing. *Radiology* **2020**, *296* (2), E41–E45.

(5) Li, Y.; Yao, L.; Li, J.; Chen, L.; Song, Y.; Cai, Z.; Yang, C. Stability Issues of RT-PCR Testing of SARS-CoV-2 for Hospitalized Patients Clinically Diagnosed with COVID-19. *Journal of Medical Virology* **2020**, *92* (7), 903-908.

(6) Huang, P.; Liu, T.; Huang, L.; Liu, H.; Lei, M.; Xu, W.; Hu, X.; Chen, J.; Liu, B. Use of Chest CT in Combination with Negative RT-PCR Assay for the 2019 Novel Coronavirus but High Clinical Suspicion. *Radiology* **2020**, *295* (1), 22–23.

(7) Hase, R.; Kurita, T.; Muranaka, E.; Sasazawa, H.; Mito, H.; Yano, Y. A Case of Imported COVID-19 Diagnosed by PCR-Positive Lower Respiratory Specimen but with PCR-Negative Throat Swabs. *Infectious Diseases* **2020**, *52* (6), 423–426.

(8) Kucirka, L. M.; Lauer, S. A.; Laeyendecker, O.; Boon, D.; Lessler, J. Variation in False-Negative Rate of Reverse Transcriptase Polymerase Chain Reaction–Based SARS-CoV-2 Tests by Time Since Exposure. *Annals of Internal Medicine* **2020**, *173* (4), 262-267.

(9) Crane, M. M.; Organon MV. *Diagnostic Test Device - US3579306A*; 1969.

(10) Zheng, M. Z.; Richard, J. L.; Binder, J. A Review of Rapid Methods for the Analysis of Mycotoxins. *Mycopathologia* **2006**, *161* (5), 261–273.

(11) Ezennia, I. J.; Nduka, S. O.; Ekwunife, O. I. Cost Benefit Analysis of Malaria Rapid Diagnostic Test: The Perspective of Nigerian Community Pharmacists. *Malaria Journal* **2017**, *16* (1), 7–16.

(12) Tawiah, T.; Hansen, K. S.; Baiden, F.; Bruce, J.; Tivura, M.; Delimini, R.; Amengo-Etego, S.; Chandramohan, D.; Owusu-Agyei, S.; Webster, J. Cost-Effectiveness Analysis of Test-Based versus Presumptive Treatment of Uncomplicated Malaria in Children under Five Years in an Area of High Transmission in Central Ghana. *PLOS ONE* **2016**, *11* (10), e0164055.

(13) Phan, J. C.; Pettitt, J.; George, J. S.; Fakoli, L. S.; Taweh, F. M.; Bateman, S. L.; Bennett, R. S.; Norris, S. L.; Spinnler, D. A.; Pimentel, G.; Sahr, P. K.; Bolay, F. K.; Schoepp, R. J. Lateral Flow Immunoassays for Ebola Virus Disease Detection in Liberia. *Journal of Infectious Diseases* **2016**, *214* (suppl 3), S222–S228.

(14) Mao, X.; Ma, Y.; Zhang, A.; Zhang, L.; Zeng, L.; Liu, G. Disposable Nucleic Acid Biosensors Based on Gold Nanoparticle Probes and Lateral Flow Strip. *Analytical Chemistry* **2009**, *81* (4), 1660–1668.

(15) Damborský, P.; Koczula, K. M.; Gallotta, A.; Katrlík, J. Lectin-Based Lateral Flow Assay: Proof-of-Concept. *The Analyst* **2016**, *141* (23), 6444–6448.

(16) Ishii, J.; Toyoshima, M.; Chikae, M.; Takamura, Y.; Miura, Y. Preparation of Glycopolymer-Modified Gold Nanoparticles and a New Approach for a Lateral Flow Assay. *Bulletin of the Chemical Society of Japan* **2011**, *84* (5), 466–470.

(17) Jorgensen, P.; Chanthap, L.; Rebueno, A.; Tsuyuoka, R.; Bell, D. Malaria Rapid Diagnostic Tests in Tropical Climates: The Need for a Cool Chain. *American Journal of Tropical Medicine and Hygiene* **2006**, *74* (5), 750–754.

(18) Wölfel, R.; Corman, V. M.; Guggemos, W.; Seilmaier, M.; Zange, S.; Müller, M. A.; Niemeyer, D.; Jones, T. C.; Vollmar, P.; Rothe, C.; Hoelscher, M.; Bleicker, T.; Brünink, S.; Schneider, J.; Ehmann, R.; Zwirglmaier, K.; Drosten, C.; Wendtner, C. Virological Assessment of Hospitalized Patients with COVID-2019. *Nature* **2020**, *581* (7809), 465–469.

(19) Connor, R. J.; Kawaoka, Y.; Webster, R. G.; Paulson, J. C. Receptor Specificity in Human, Avian, and Equine H2 and H3 Influenza Virus Isolates. *Virology* **1994**, *205* (1), 17–23.

(20) Childs, R. A.; Palma, A. S.; Wharton, S.; Matrosovich, T.; Liu, Y.; Chai, W.; Campanero-Rhodes, M. A.; Zhang, Y.; Eickmann, M.; Kiso, M.; Hay, A.; Matrosovich, M.; Feizi, T. Receptor-Binding Specificity of Pandemic Influenza A (H1N1) 2009 Virus Determined by Carbohydrate Microarray. *Nature Biotechnology* **2009**, *27* (9), 797–799.

(21) Marín, M. J.; Rashid, A.; Rejzek, M.; Fairhurst, S. A.; Wharton, S. A.; Martin, S. R.; McCauley, J. W.; Wileman, T.; Field, R. A.; Russell, D. A. Glyconanoparticles for the Plasmonic Detection and Discrimination between Human and Avian Influenza Virus. *Organic & Biomolecular Chemistry* **2013**, *11* (41), 7101.

(22) Richards, S.-J.; Baker, A. N.; Walker, M.; Gibson, M. I. Polymer-Stabilized Sialylated Nanoparticles: Synthesis, Optimization, and Differential Binding to Influenza Hemagglutinins. *Biomacromolecules* **2020**, *21* (4), 1604–1612.

(23) Qing, E.; Hantak, M.; Perlman, S.; Gallagher, T. Distinct Roles for Sialoside and Protein Receptors in Coronavirus Infection. *mBio* **2020**, *11* (1).

(24) Hulswit, R. J. G.; Lang, Y.; Bakkers, M. J. G.; Li, W.; Li, Z.; Schouten, A.; Ophorst, B.; Van Kuppeveld, F. J. M.; Boons, G. J.; Bosch, B. J.; Huizinga, E. G.; De Groot, R. J. Human Coronaviruses OC43 and HKU1 Bind to 9-O-Acetylated Sialic Acids via a Conserved Receptor-Binding Site in Spike Protein Domain A. *Proceedings of the National Academy of Sciences of the United States of America* **2019**, *116* (7), 2681–2690.

(25) Huang, X.; Dong, W.; Milewska, A.; Golda, A.; Qi, Y.; Zhu, Q. K.; Marasco, W. A.; Baric, R. S.; Sims, A. C.; Pyrc, K.; Li, W.; Sui, J. Human Coronavirus HKU1 Spike Protein Uses O -Acetylated Sialic Acid as an Attachment Receptor Determinant and Employs Hemagglutinin-Esterase Protein as a Receptor-Destroying Enzyme. *Journal of Virology* **2015**, *89* (14), 7202–7213.

(26) Li, W.; Hulswit, R. J. G.; Widjaja, I.; Raj, V. S.; McBride, R.; Peng, W.; Widagdo, W.; Tortorici, M. A.; van Dieren, B.; Lang, Y.; van Lent, J. W. M.; Paulson, J. C.; de Haan, C. A. M.; de Groot, R. J.; van Kuppeveld, F. J. M.; Haagmans, B. L.; Bosch, B.-J. Identification of Sialic Acid-Binding Function for the Middle East Respiratory Syndrome Coronavirus Spike Glycoprotein. *Proceedings of the National Academy of Sciences* **2017**, *114* (40), E8508–E8517.

(27) Bolles, M.; Donaldson, E.; Baric, R. SARS-CoV and Emergent Coronaviruses: Viral Determinants of Interspecies Transmission. *Current Opinion in Virology* **2011**, *1* (6), 624–634.

(28) Li, W.; Hulswit, R. J. G.; Widjaja, I.; Raj, V. S.; McBride, R.; Peng, W.; Widagdo, W.; Tortorici, M. A.; van Dieren, B.; Lang, Y.; van Lent, J. W. M.; Paulson, J. C.; de Haan, C. A. M.; de Groot, R. J.; van Kuppeveld, F. J. M.; Haagmans, B. L.; Bosch, B.-J. Identification of Sialic Acid-Binding Function for the Middle East Respiratory Syndrome Coronavirus Spike Glycoprotein. *Proceedings of the National Academy of Sciences* **2017**, *114* (40), E8508–E8517.

(29) Kwon, P. S.; Oh, H.; Kwon, S.-J.; Jin, W.; Zhang, F.; Fraser, K.; Hong, J. J.; Linhardt, R. J.; Dordick, J. S. Sulfated Polysaccharides Effectively Inhibit SARS-CoV-2 in Vitro. *Cell Discovery* **2020**, *6* (1), 50.

(30) Clausen, T. M.; Sandoval, D. R.; Spliid, C. B.; Pihl, J.; Painter, C. D.; Thacker, B. E.; Glass, C. A.; Narayanan, A.; Majowicz, S. A.; Zhang, Y.; Torres, J. L.; Golden, G. J.; Porell, R.; Garretson, A. F.; Laubach, L.; Feldman, J.; Yin, X.; Pu, Y.; Hauser, B.; Caradonna, T. M.; Kellman, B. P.; Martino, C.; Gordts, P. L. S. M.; Leibel, S. L.; Chanda, S. K.; Schmidt, A. G.; Godula, K.; Jose, J.; Corbett, K. D.; Ward, A. B.; Carlin, A. F.; Esko, J. D. SARS-CoV-2 Infection Depends on Cellular Heparan Sulfate and ACE2. *bioRxiv* **2020**, 10.1101/2020.07.14.201616.

(31) Mycroft-West, C. J.; Su, D.; Pagani, I.; Rudd, T. R.; Elli, S.; Guimond, S. E.; Miller, G.; Meneghetti, M. C. Z.; Nader, H. B.; Li, Y.; Nunes, Q. M.; Procter, P.; Mancini, N.; Clementi, M.; Bisio, A.; Forsyth, N. R.; Turnbull, J. E.; Guerrini, M.; Fernig, D. G.; Vicenzi, E.; Yates, E. A.; Lima, M. A.; Skidmore, M. A. Heparin Inhibits Cellular Invasion by SARS-CoV-2: Structural Dependence of the Interaction of the Surface Protein (Spike) S1 Receptor Binding Domain with Heparin. *bioRxiv* **2020**, 2020.04.28.066761.

(32) Baker, A. N.; Richard, S.-J.; Guy, C. S.; Congdon, T. R.; Hasan, M.; Zwetsloot, A. J.; Straube, A.; Walker, M.; Chessa, S.; Pergolizzi, G.; Dedola, S.; Field, R.; Gibson, M. The SARS-COV-2 Spike Protein Binds Sialic Acids, and Enables Rapid Detection in a Lateral Flow Point of Care Diagnostic Device. *chemrxiv.org* **2020**.

(33) Milanetti, E.; Miotto, M.; Di Rienzo, L.; Nagaraj, M.; Monti, M.; Golbek, T. W.; Gosti, G.; Roeters, S. J.; Weidner, T.; Otzen, D. E.; Ruocco, G. In-Silico Evidence for

a Two Receptor Based Strategy of SARS-CoV-2. *Frontiers in Molecular Biosciences* **2021**, *8*, 509.

(34) Bò, L.; Miotto, M.; Di Rienzo, L.; Milanetti, E.; Ruocco, G. Exploring the Association Between Sialic Acid and SARS-CoV-2 Spike Protein Through a Molecular Dynamics-Based Approach. *Frontiers in Medical Technology* **2021**, *2*, 24.

(35) Buchanan, C. J.; Gaunt, B.; Harrison, P. J.; Bas, A. Le; Khan, A.; Giltrap, A. M.; Ward, P. N.; Dumoux, M.; Daga, S.; Picchiotti, N.; Baldassarri, M.; Benetti, E.; Fallerini, C.; Fava, F.; Giliberti, A.; Koukos, P. I.; Lakshminarayanan, A.; Xue, X.; Papadakis, G.; Deimel, L. P.; Casablancas-Antras, V.; Claridge, T. D. W.; Bonvin, A. M. J. J.; Sattentau, Q. J.; Furini, S.; Gori, M.; Huo, J.; Owens, R. J.; Renieri, A.; Study, G.-C. M.; Naismith, J. H.; Baldwin, A.; Davis, B. G. Cryptic SARS-CoV2-Spike-with-Sugar Interactions Revealed by "universal" Saturation Transfer Analysis. *bioRxiv* **2021**, 2021.04.14.439284.

(36) Nguyen, L.; McCord, K. A.; Bui, D. T.; Bouwman, K. A.; Kitova, E. N.; Kumawat, D.; Daskan, G. C.; Tomris, I.; Han, L.; Chopra, P.; Yang, T.-J.; Williows, S. D.; Lowary, T. L.; West, L. J.; Hsu, S.-T. D.; Tompkins, S. M.; Boons, G.-J.; Mason, A. L.; Vries, R. P. de; Macauley, M. S.; Klassen, J. S. Sialic Acid-Dependent Binding and Viral Entry of SARS-CoV-2. *bioRxiv* **2021**, 2021.03.08.434228.

(37) Lundquist, J. J.; Toone, E. J. The Cluster Glycoside Effect. *Chemical Reviews* **2002**, *102*, 555–578.

(38) Reichardt, N. C.; Martín-Lomas, M.; Penadés, S.; Andersson, M.; Thran, A.; Proksa, R.; Fayad, Z. A.; Cormode, D. P.; Wu, C. Y.; Wong, C. H.; Green, M. L. H.; Kostarelos, K.; Davis, B. G.; Vincent, S. P. Glyconanotechnology. *Chemical Society Reviews* **2013**, *42* (10), 4358–4376.

(39) Branson, T. R.; Turnbull, W. B. Bacterial Toxin Inhibitors Based on Multivalent Scaffolds. *Chemical Society Reviews* **2013**, *42* (11), 4613–4622.

(40) Kiessling, L. L.; Gestwicki, J. E.; Strong, L. E. Synthetic Multivalent Ligands as Probes of Signal Transduction. *Angewandte Chemie International Edition* **2006**, *45* (15), 2348–2368.

(41) Zhang, S.; Moussodia, R.-O.; Vértesy, S.; André, S.; Klein, M. L.; Gabius, H.-J.; Percec, V. Unraveling Functional Significance of Natural Variations of a Human

Galectin by Glycodendrimersomes with Programmable Glycan Surface. *Proceedings of the National Academy of Sciences of the United States of America* **2015**, *112* (18), 5585–5590.

(42) Branson, T. R.; McAllister, T. E.; Garcia-Hartjes, J.; Fascione, M. A.; Ross, J. F.; Warriner, S. L.; Wennekes, T.; Zuilhof, H.; Turnbull, W. B. A Protein-Based Pentavalent Inhibitor of the Cholera Toxin B-Subunit. *Angewandte Chemie - International Edition* **2014**, *53* (32), 8323–8327.

(43) Richards, S.-J.; Jones, M. W.; Hunaban, M.; Haddleton, D. M.; Gibson, M. I. Probing Bacterial-Toxin Inhibition with Synthetic Glycopolymers Prepared by Tandem Post-Polymerization Modification: Role of Linker Length and Carbohydrate Density. *Angewandte Chemie International Edition* **2012**, *51* (31), 7812–7816.

(44) Becer, C. R.; Gibson, M. I.; Geng, J.; Ilyas, R.; Wallis, R.; Mitchell, D. A.; Haddleton, D. M. High-Affinity Glycopolymer Binding to Human DC-SIGN and Disruption of DC-SIGN Interactions with HIV Envelope Glycoprotein. *Journal of the American Chemical Society* **2010**, *132* (43), 15130–15132.

(45) Richards, S.-J.; Gibson, M. I. Optimization of the Polymer Coating for Glycosylated Gold Nanoparticle Biosensors to Ensure Stability and Rapid Optical Readouts. *ACS Macro Letters* **2014**, *3* (10), 1004–1008.

(46) Wrapp, D.; Wang, N.; Corbett, K. S.; Goldsmith, J. A.; Hsieh, C.-L.; Abiona, O.; Graham, B. S.; McLellan, J. S. Cryo-EM Structure of the 2019-NCoV Spike in the Prefusion Conformation. *Science* **2020**, *367* (6483), 1260–1263.

(47) Park, Y. J.; Walls, A. C.; Wang, Z.; Sauer, M. M.; Li, W.; Tortorici, M. A.; Bosch, B. J.; DiMaio, F.; Veesler, D. Structures of MERS-CoV Spike Glycoprotein in Complex with Sialoside Attachment Receptors. *Nature Structural and Molecular Biology* **2019**, *26* (12), 1151–1157.

(48) Vandelli, A.; Monti, M.; Milanetti, E.; Ponti, R. D.; Tartaglia, G. G. Structural Analysis of SARS-CoV-2 and Prediction of the Human Interactome. *bioRxiv* **2020**, DOI 10.1101/2020.03.28.013789.

(49) Weis, W.; Brown, J. H.; Cusack, S.; Paulson, J. C.; Skehel, J. J.; Wiley, D. C. Structure of the Influenza Virus Haemagglutinin Complexed with Its Receptor, Sialic Acid. *Nature* **1988**, *333* (6172), 426–431.

(50) Milanetti, E.; Miotto, M.; Rienzo, L. Di; Monti, M.; Gosti, G.; Ruocco, G. In-Silico Evidence for Two Receptors Based Strategy of SARS-CoV-2. *bioRxiv* **2020**, 2020.03.24.006197.

(51) Georgiou, P. G.; Baker, A. N.; Richards, S.-J.; Laezza, A.; Walker, M.; Gibson, M. I. Tuning Aggregative versus Non-Aggregative Lectin Binding with Glycosylated Nanoparticles by the Nature of the Polymer Ligand. *Journal of Materials Chemistry. B* **2020**, *8* (1), 136–145.

(52) Haiss, W.; Thanh, N. T. K.; Aveyard, J.; Fernig, D. G. Determination of Size and Concentration of Gold Nanoparticles from UV - Vis Spectra. *Analytical Chemistry* **2007**, *79* (11), 4215–4221.

(53) Watanabe, Y.; Allen, J. D.; Wrapp, D.; McLellan, J. S.; Crispin, M. Site-Specific Glycan Analysis of the SARS-CoV-2 Spike. *Science* **2020**, eabb9983.

(54) Song, X.; Yu, H.; Chen, X.; Lasanajak, Y.; Tappert, M. M.; Air, G. M.; Tiwari, V. K.; Cao, H.; Chokhawala, H. A.; Zheng, H.; Cummings, R. D.; Smith, D. F. A Sialylated Glycan Microarray Reveals Novel Interactions of Modified Sialic Acids with Proteins and Viruses. *Journal of Biological Chemistry* **2011**, *286* (36), 31610–31622.

(55) Bolles, M.; Donaldson, E.; Baric, R. SARS-CoV and Emergent Coronaviruses: Viral Determinants of Interspecies Transmission. *Current Opinion in Virology* **2011**, *1* (6), 624–634.

(56) Fu, E.; Liang, T.; Houghtaling, J.; Ramachandran, S.; Ramsey, S. A.; Lutz, B.; Yager, P. Enhanced Sensitivity of Lateral Flow Tests Using a Two-Dimensional Paper Network Format. *Analytical Chemistry* **2011**, *83* (20), 7941–7946.

(57) Weis, W.; Brown, J. H.; Cusack, S.; Paulson, J. C.; Skehel, J. J.; Wiley, D. C. Structure of the Influenza Virus Haemagglutinin Complexed with Its Receptor, Sialic Acid. *Nature* **1988**, *333* (6172), 426–431.

(58) Baker, A. N.; Richards, S.-J.; Guy, C. S.; Congdon, T. R.; Hasan, M.; Zwetsloot, A. J.; Gallo, A.; Lewandowski, J. R.; Stansfeld, P. J.; Straube, A.; Walker, M.; Chessa, S.; Pergolizzi, G.; Dedola, S.; Field, R. A.; Gibson, M. I. The SARS-COV-2 Spike Protein Binds Sialic Acids and Enables Rapid Detection in a Lateral Flow Point of Care Diagnostic Device. *ACS Central Science* **2020**, *6* (11), 2046–2052.

(59) Buchanan, C. J.; Gaunt, B.; Harrison, P. J.; Bas, A. Le; Khan, A.; Giltrap, A. M.; Ward, P. N.; Dumoux, M.; Daga, S.; Picchiotti, N.; Baldassarri, M.; Benetti, E.; Fallerini, C.; Fava, F.; Giliberti, A.; Koukos, P. I.; Lakshminarayanan, A.; Xue, X.; Papadakis, G.; Deimel, L. P.; Casablancas-Antràs, V.; Claridge, T. D. W.; Bonvin, A. M. J. J.; Sattentau, Q. J.; Furini, S.; Gori, M.; Huo, J.; Owens, R. J.; Renieri, A.; Study, G.-C. M.; Naismith, J. H.; Baldwin, A.; Davis, B. G. Cryptic SARS-CoV2-Spike-with-Sugar Interactions Revealed by 'Universal' Saturation Transfer Analysis. *bioRxiv* **2021**, 2021.04.14.439284.

(60) Dhar, C.; Sasmal, A.; Diaz, S.; Verhagen, A.; Yu, H.; Li, W.; Chen, X.; Varki, A. Are Sialic Acids Involved in COVID-19 Pathogenesis? *Glycobiology* **2021**, *31* (9), 1068–1071.

(61) Ryzhikov, A. B.; Onkhonova, G. S.; Imatdinov, I. R.; Gavrilova, E. V.; Maksyutov, R. A.; Gordeeva, E. A.; Pazynina, G. V.; Ryzhov, I. M.; Shilova, N. V.; Bovin, N. V. Recombinant SARS-CoV-2 S Protein Binds to Glycans of the Lactosamine Family in Vitro. *Biochemistry (Moscow)* **2021**, *86* (3), 243–247.

(62) Barlev-Gross, M.; Weiss, S.; Ben-Shmuel, A.; Sittner, A.; Eden, K.; Mazuz, N.; Glinert, I.; Bar-David, E.; Puni, R.; Amit, S.; Kriger, O.; Schuster, O.; Alcalay, R.; Makdasi, E.; Epstein, E.; Noy-Porat, T.; Rosenfeld, R.; Achdout, H.; Mazor, O.; Israely, T.; Levy, H.; Mechaly, A. Spike vs Nucleocapsid SARS-CoV-2 Antigen Detection: Application in Nasopharyngeal Swab Specimens. *Analytical and Bioanalytical Chemistry* **2021**, *413* (13), 3501–3510.

(63) Sun, X.-L. The Role of Cell Surface Sialic Acids for SARS-CoV-2 Infection. *Glycobiology* **2021**, *31* (10), 1245–1253.

(64) Nguyen, L.; McCord, K. A.; Bui, D. T.; Bouwman, K. M.; Kitova, E. N.; Kumawat, D.; Daskhan, G. C.; Tomris, I.; Han, L.; Chopra, P.; Yang, T.-J.; Willows, S. D.; Mason, A. L.; Lowary, T. L.; West, L. J.; Hsu, S.-T. D.; Tompkins, S. M.; Boons, G.-J.; Vries, R. P. de; Macauley, M. S.; Klassen, J. S. Sialic Acid-Dependent Binding and Viral Entry of SARS-CoV-2. *bioRxiv* **2021**, 2021.03.08.434228.

(65) Di Gaetano, S.; Capasso, D.; Delre, P.; Pirone, L.; Saviano, M.; Pedone, E.; Mangiatordi, G. F. More Is Always Better Than One: The N-Terminal Domain of the Spike Protein as Another Emerging Target for Hampering the SARS-CoV-2

Attachment to Host Cells. *International Journal of Molecular Sciences* **2021**, *22* (12), 6462.

(66) Fantini, J.; Di Scala, C.; Chahinian, H.; Yahi, N. Structural and Molecular Modelling Studies Reveal a New Mechanism of Action of Chloroquine and Hydroxychloroquine against SARS-CoV-2 Infection. *International Journal of Antimicrobial Agents* **2020**, *55* (5), 105960.

(67) Nguyen, L.; McCord, K. A.; Bui, D. T.; Bouwman, K. M.; Kitova, E. N.; Elaish, M.; Kumawat, D.; Daskhan, G. C.; Tomris, I.; Han, L.; Chopra, P.; Yang, T.-J.; Willows, S. D.; Mason, A. L.; Mahal, L. K.; Lowary, T. L.; West, L. J.; Hsu, S.-T. D.; Hobman, T.; Tompkins, S. M.; Boons, G.-J.; de Vries, R. P.; Macauley, M. S.; Klassen, J. S. Sialic Acid-Containing Glycolipids Mediate Binding and Viral Entry of SARS-CoV-2. *Nature Chemical Biology* **2021**, 1–10.

(68) Lim, D.; Brimble, M. A.; Kowalczyk, R.; Watson, A. J. A.; Fairbanks, A. J. Protecting-Group-Free One-Pot Synthesis of Glycoconjugates Directly from Reducing Sugars. *Angewandte Chemie International Edition* **2014**, *53* (44), 11907–11911.

(69) Kuhn, R.; Lutz, P.; Macdonald, D. L. Synthese Anomerer Sialinsäure-methylketoside. *Chemische Berichte* **1966**, *99* (2), 611–617.

(70) Orlova, A. V.; Shpirt, A. M.; Kulikova, N. Y.; Kononov, L. O. N,N-Diacetylsialyl Chloride-a Novel Readily Accessible Sialyl Donor in Reactions with Neutral and Charged Nucleophiles in the Absence of a Promoter. *Carbohydrate Research* **2010**, *345* (6), 721–730.

(71) Tropper, F. D.; Andersson, F. O.; Braun, S.; Roy, R. Phase Transfer Catalysis as a General and Stereoselective Entry into Glycosyl Azides from Glycosyl Halides. *Synthesis* **1992**, *1992* (07), 618–620.

(72) Ieong, N. S.; Brebis, K.; Daniel, L. E.; O'Reilly, R. K.; Gibson, M. I. The Critical Importance of Size on Thermoresponsive Nanoparticle Transition Temperatures: Gold and Micelle-Based Polymer Nanoparticles. *Chemical Communications* **2011**, *47* (42), 11627–11629.

(73) Bastús, N. G.; Comenge, J.; Puntes, V. Kinetically Controlled Seeded Growth Synthesis of Citrate-Stabilized Gold Nanoparticles of up to 200 Nm: Size Focusing versus Ostwald Ripening. *Langmuir* **2011**, *27* (17), 11098–11105.

Chapter 4

A Glycan-based Flow-Through Device for the Detection of SARS-COV-2 from Patient Swabs

4.1 Abstract

The COVID-19 pandemic, and future pandemics, require diagnostic tools to track disease spread and guide the isolation of (a)symptomatic individuals. Lateral flow diagnostics (LFDs) are rapid and of lower cost than molecular (genetic) tests, with current LFDs using antibodies as their recognition units. Herein, we develop a prototype flow-through device (related, but distinct to LFDs), utilizing *N*-acetyl neuraminic acid functionalised, polymer-coated, gold nanoparticles as the detection/capture unit for SARS-COV-2, by targeting the sialic-acid binding site of the spike protein. The prototype devices give rapid results, with higher viral loads being faster than lower viral loads. The prototype's effectiveness is demonstrated using spike protein, lentiviral models and a panel of heat-inactivated primary patient nasal swabs. The device was also shown to retain detection capability toward recombinant spike proteins from several variants (mutants) of concern. This demonstrates the proof of principle that glyco-assays could be used in the tracking and monitoring of infectious agents, to complement, or as alternatives to antibody-based systems.

4.2 Declaration

This chapter contains the paper discussing the detection of SARS-COV-2 in clinical samples in a flow-through assay by harnessing sialic acids as capture agents.

Sarah-Jane Richards synthesised the gold particles, functionalised the polymers with glycans, characterised the particles by DLS and UV-vis, and ran the flow-through; Sarojini Pandey prepared the patient samples at UHCW and ran the RT-PCR analysis – this was supported and overseen by Dimitris Grammatopoulos and Neil Anderson. Collette Guy synthesised the *N*-acetyl neuraminic acid derivatives and carried out the pseudotyped lentivirus experiments; Asfaq Ahmad and Muhammad Hasan expressed the spike proteins (including the mutants) and carried out the thermal shift assays; Caroline Biggs helped prepare the flow-through materials; Panagiotis Georgiou prepared and analysed the TEM samples; Alexander Zwetsloot and Anne Straube synthesised the spike protein used for quality control of the gold nanoparticle batches and the cassettes produced; and Marc Walker carried out the XPS analysis and supported model fitting the XPS data.

The work of the front-line NHS staff who collected the samples from patients is also acknowledged and appreciated.

I synthesised the RAFT agent, the polymers; functionalised the polymers with glycans; characterised the polymer systems by NMR, SEC and FTIR; characterised the particles by XPS; and characterised the glycans by NMR. I designed, constructed, and ran the prototype flow-through devices, and analysed the results from the devices.

Myself, Sarah-Jane Richards, Simone Dedola, Robert Field and Matthew Gibson were responsible for preparation of the manuscript.

A. N. Baker, S-J. Richards, S. Pandey, C. S. Guy, A. Ahmad, M. Hasan, C. I. Biggs, P. G. Georgiou, A. J. Zwetsloot, A. Straube, S. Dedola, R. A. Field, N. R. Anderson, M. Walker, D. Grammatopoulos, M. I. Gibson, *ACS Sensors,* **2021**, 6, 10, 3696-3705

Myself, Sarah-Jane Richards and Matthew Gibson have a patent related to this work.

4.3 Introduction

The COVID-19 pandemic has led to > 171 million confirmed cases and ~3.7 million deaths worldwide, reported to WHO, as of the 4th of June 2021.[1] COVID-19 is caused by the coronavirus SARS-COV-2, first reported in Wuhan (China).[2] Despite global efforts, there are still a limited number of effective therapeutics. Vaccines have now been approved for use, but with limited supplies, a major mechanism for controlling disease spread remains testing, identification, and patient isolation.

The testing system deployed by more economically developed countries (MEDCs) and less economically developed countries (LEDCs) has been based primarily on molecular (genetic) approaches such as real-time reverse transcription-polymerase chain reaction (rRT-PCR).[3–6] However, RT-PCR-based approaches require dedicated laboratory facilities and trained personnel, meaning early in the pandemic CT scans, which are not recommended for routine use, were initially employed.[7]

Due to the infrastructure needs of RT-PCR and long processing times, RT-PCR does not typically provide a rapid turnaround, especially in a high-volume laboratory setting, although it is considered the gold standard for COVID-19 diagnosis. In July 2020 during the early stages of the COVID-19 pandemic, in the United States, the average wait time for a RT-PCR test result was 4 days with 37% of people receiving the results within 2 days.[8] The availability of RT-PCR testing also varies significantly between countries; per 1000 people (31/7/2020)[9] the United Kingdom (2.27) and the United States (2.91) have significantly out-tested LEDCs such as Zimbabwe (0.07) or Myanmar (0.01).[9] In Iran, for example, CT scanners are more abundant[10] than RT-PCR machines.[11,12] Faster RT-PCR devices, such as the those based on DNAnudge™, have been developed and allow for decentralised testing outside of hospital or lab environments but do have capacity requirements of one machine to one test.[13] Other molecular genetic techniques have also been developed, which similarly do not require centralised testing infrastructure. For example, loop-mediated isothermal amplification (LAMP)[14] can return a diagnosis in just over 90 minutes (LamPORE™ device). Although faster than conventional RT-PCR, neither of these offer rapid results at a capacity that would facilitate mass screening or at a cost per device that would allow point of care testing in the home or in lower-resource enviroments.[15,16]

Lateral flow devices (LFD) are established tools for rapid diagnosis, giving results often in under 30 minutes and therefore can rapidly identify infected individuals. LFDs, such as the home-pregnancy test,[17] use antibodies as detection units in both the stationary phase (test line bound to nitrocellulose) and as a coating for the mobile phase (on the surface of a gold nanoparticle). Upon binding the target analyte, the stationary and mobile phase form a "sandwich" with the analyte in the middle. The results are visible by eye as a red or blue line depending on the precise gold formulation, although other nanomaterials, such as fluorescent particles, can be used.[18] LFDs are typically cheap (compared to molecular methods), require little to no training or clinical infrastructure to use, and can be scaled up to enable large population testing. LFDs tend to have lower sensitivity (some false negatives) but high selectivity (few false positives). The cost-effectiveness and clinical usefulness of LFDs has been demonstrated by malaria rapid diagnostic tests,[19,20] in the diagnosis of cutaneous leishmaniasis[21] and in comparisons with more expensive RT-PCR approaches for Ebola diagnosis.[22] Consequently, the appeal of LFDs in the COVID-19 pandemic are that their low cost and rapid turnaround time may enable mass testing of large populations.[23] This is especially true in non-clinical environments. Moreover, modelling from Müller *et al.* argues that the cost/performance trade off of a cheaper test used to carry out large scale testing could be used to track and control virus spread in conjunction with RT-PCR for symptomatic patients.[24] This mirrors analysis by Moghadas and Fitzpatrick *et al.* who argue that asymptomatic transmission accounts for over 50% of the attack rate in outbreaks and that scaling up testing of asymptomatic and presymptomatic cases is crucial.[25] In both studies, the likely viable solution to mass testing, estimated at ~1 million tests per day in Switzerland by Müller *et al.* – is the use of LFD POC devices. The "Vò experiment" further highlights the importance of mass testing and its positive application in a municipality in Italy.[26] In summary, a mass testing approach, facilitated by LFDs, could find asymptomatic individuals spreading the virus, who would not be identified by symptomatic RT-PCR testing only,[24,25,27] currently the preferred option in most healthcare systems.

The first LFDs for the COVID-19 pandemic were designed to detect antibodies in patient blood samples produced in response to SARS-COV-2 infections.[28–30] These were intended to report if a patient has previously been infected; not to indicate active infection, so could not effectively be used in screening/triage settings or mass testing

for active infections. Antigen LFDs, in contrast, are designed to diagnose the presence of the virus i.e., an active infection. Several antigen lateral flow tests, by late 2020, had passed Phase 3 testing in the United Kingdom,[31] gained WHO "Emergency Use Listing" approval[32] or had emergency approval granted by The United States Food & Drug Administration.[33,34] These devices all utilise antibodies as detection/capture units. To the best of our knowledge, these devices all use antibodies to target the nucleocapsid protein of SARS-COV-2. A university-based validation process, between LFDs and PCR, confirmed that LFDs cannot detect lower viral loads but were estimated to be capable of identifying up to 85% of infections in the cohort trialed.[35] This illustrates their potential for frequent, low cost testing when deployed appropriately.

It is important to note that antibodies are not essential components in LFDs, and other recognition moieties could be used, including nucleic acids,[36] glycans, and lectins.[37] Glycan-based LFDs could offer advantages over other recognition moieties. For example, glycans are the site of pathogen adhesion during many viral infections[38,39] especially respiratory viruses such as influenzas,[40] and glycans can be chemically synthesised at scale. Glycan binding can also explore the "state" of a pathogen; for example, LecA/B are upregulated by *Pseudomonas aeruginosa* during infection.[41,42] Furthermore, glycans are often more thermally robust than proteins[43] making them ideal candidates for low-resource environments. Glycosylated gold-nanoparticles (the mobile phase) are well established having been used in colourimetric/aggregation-based diagnostics, surface enhanced Raman and other bioassays.[44–47] Despite this, glycans as capture units have not been widely applied in lateral flow[48] and to the best of our knowledge have not been shown to function using clinical samples, only models.

We have previously reported that the S1 domain of the SARS-COV-2 spike protein can bind α,*N*-acetyl neuraminic acid (Neu5NAc), a sialic acid (Chapter 3),[49] and similar binding has been observed for other zoonotic coronaviruses toward sialic acids[50–52] (e.g., SARS or MERS). Incorporation of α,*N*-acetyl neuraminic acid onto a polymer-stabilised glyconanoparticle platform enabled detection of (purified) spike protein in a LFD (5 $\mu g.mL^{-1}$) and also detection of a pseudotyped lentivirus presenting the SARS-COV-2 spike protein at 1.5×10^4 transduction $units.mL^{-1}$ in a dipstick test (Chapter 3).[49] The exact biological role of sialic-acid binding is not yet fully

understood for SARS-COV-2, with clear differences in its role in cell entry compared to SARS and MERS.[53] Microarray, ELISA and STD NMR have been used to further demonstrate that sialic acids are receptors for the SARS-COV-2 spike protein.[54–56] It has also emerged that sulphated glycosaminoglycans (including heparin sulphates) bind SARS-COV-2 spike protein, and can inhibit viral entry.[57–59] Glycans (including those carrying terminal sialic acids) have also been shown to participate in angiotensin-converting enzyme 2 (ACE2) receptor binding during SARS-COV-2 cell adhesion/entry.[60]

Herein, we demonstrate that glycan-based flow-through devices can detect SARS-COV-2 in heat-inactivated primary patient swabs and validate these initial results against RT-PCR. Compared to an LFD format, no test line was used, rather the sample is directly absorbed onto the nitrocellulose target. Device optimisation was achieved using a lentivirus and recombinant SARS-COV-2 spike protein showing that heat (or chemical) inactivation did not prevent usage. The prototype devices were then used with a panel of primary heat-inactivated clinical swabs, demonstrating that flow-through glyco-assays can be used to detect viral infection and therefore that glyco-LFDs could be made with suitable test lines. Furthermore, the devices were shown to detect recombinant mutant spike proteins showing glycan-based detection may still detect variants of concern. This conceptual approach could be broadly applied to other pathogens/disease states and provide redundancy in testing regimes compared to using antibodies alone.

4.4 Results and Discussion

Our synthetic strategy to generate α-Neu5NAc-polymer tethered gold nanoparticles was employed.[49] Telechelic poly(*N*-hydroxyethyl acrylamide), pHEA, was synthesised using RAFT (reversible addition-fragmentation chain transfer) polymerisation, and 2-amino-2-deoxy-*N*-acetyl-neuraminic acid conjugated to the ω-terminus by displacement of a pentafluorophenyl ester (allowing monitoring by ^{19}F NMR).[61] These polymers were then assembled onto gold nanoparticles (~35 nm by TEM), Figure 4.1A-C, and characterised by DLS/UV-Vis and XPS (Figure 4.1C). Just 10 mg of glycan-terminated polymer, can produce sufficient gold colloid for > 2500 assays, highlighting the scalability of this approach. The use of a polymer linker between the particle and glycan provides colloidal stability and reduces nonspecific binding.

In a standard lateral flow device, a test line is printed onto the paper to capture the antigen (e.g., a virus) which is then "sandwiched" by the nanoparticle detection unit. To streamline the development process no test line was used, and instead, the patient sample is directly deposited and dried onto the strip with the viral components absorbing onto the stationary phase; therefore this is a flow-through, rather than lateral flow, device.[23,62] This removes the need for a validated, stable and specific test line, accelerating the development process and allowing us to prove the potential of glycan recognition for future complete lateral flow devices. The setup of this approach is shown in Figure 4.1D, with sample application, the flow of the glycan-gold conjugate and then detection. Figure 4.1D also shows a silver staining step which can improve detection limits in flow-through devices (and LFDs) (discussed in detail later). The silver stain enhances the signal, as silver ions that are soluble in water are reduced to insoluble metallic silver catalysed by the gold nanoparticles. This causes the silver to precipitate onto the surface of the gold increasing the signal.

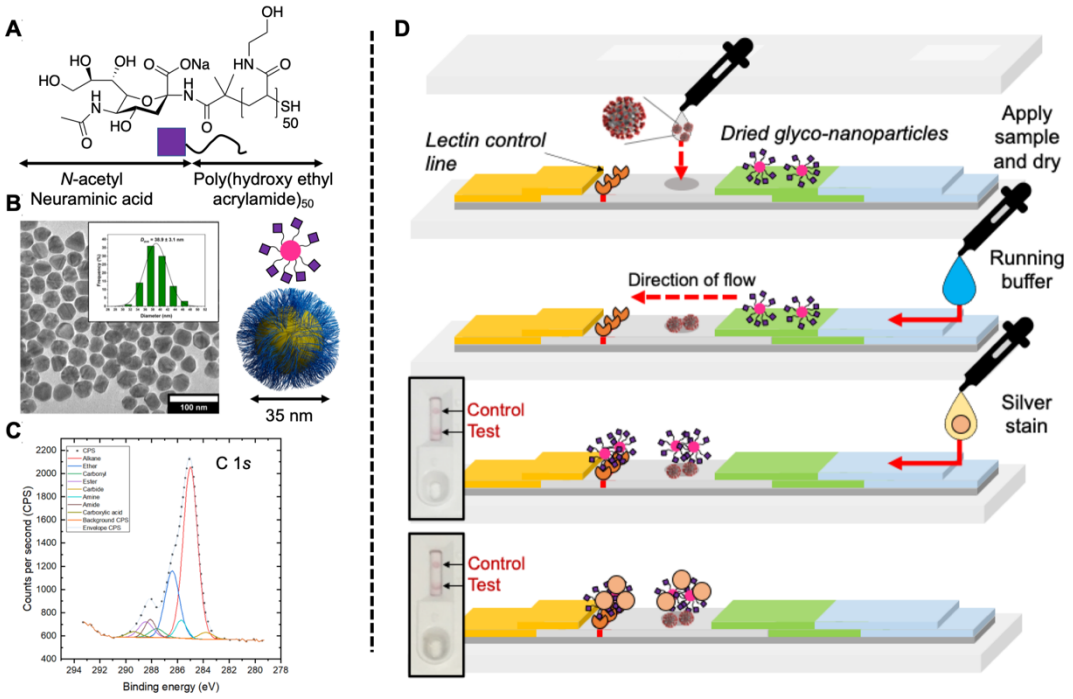

Figure 4.1. Nanoparticle synthesis and flow-through devices.

A) Neu5NAc-terminated polymer coating; B) TEM micrograph of polymer-coated AuNPs; C) C 1*s* portion of XPS spectrum of polymer-coated AuNPs; D) Flow-through device layout and assay procedure (top to bottom).

Flow-through cassettes were manufactured in-house as described in the Experimental Section. SARS-COV-2 spike protein-bearing lentivirus was applied to the test line in 20 devices at 10^4 transduction units.mL^{-1} – a concentration within the expected viral range of COVID positive patient respiratory swabs, Figure 4.2A.[63,64] 19 out of 20 devices showed a positive result on the test line (no silver staining used). As a negative control, bald virus (without the spike protein) was also run in 20 cassettes. 5/20 Showed potential weak positives, confirming the role of spike protein as the binding partner for the nanoparticles. The control line used in these devices was *Ricinus communis* agglutinin I (RCA_{120}) lectin at 5 mg.mL^{-1}, so a strong red line/crescent formed as the AuNPs were sequestered by the high concentration of RCA_{120} used. Later the RCA_{120} control spot concentration was lowered to 1 mg.mL^{-1} to improve performance. In the development of a "real" finished device, the control line also has to be validated, which is outside of the scope of this work. As 1 mL of the lentiviral solution was applied to each device, approximately 10 transduction units/device were applied, which would suggest a very low limit of detection. A possible explanation for this observation is that inert (non-transducible) particles, which also display spike

protein, may contribute but are not counted in the transduction unit concentration, i.e., there are more potentially detectable particles than expected. Lentiviral vectors have been reported to show variance between the number of transduction units to genome copy in a range of 60 – 600, supporting this hypothesis.[65]

In current PCR testing laboratory protocols, nasal swabs are heat-treated during the processing cycle to sterilise and deactivate the virus prior to RNA extraction steps.[66] To evaluate if our flow-through device was compatible with a heat-inactivated virus, the lentivirus was heated to 60 °C for 30 minutes, and 20 repeats were run – all cases gave a positive result. (Please note, when using primary swab samples, below, a different inactivation temperature is used, which was following a clinical workflow). To probe the origin of thermal tolerance, a truncated SARS-COV-2 spike-protein (expressed in-house in *E. coli,* see Experimental Section) was heated to 60 °C for 30 minutes, then applied to devices (Figure 4.2B). As can be seen, heat-treatment did not prevent binding. These observations show that glycan-based diagnostics may detect both intact and deactivated virus; this is also a condition of PCR, the current gold standard. Chemical deactivation medium was also explored, to probe the tolerance. Tergitol NP-40 is a surfactant, which has been validated to inactive SARS-COV-2 at 0.1 and 0.5 wt% within 30 minutes.[67] Figure 4.2C shows devices with spike protein (expressed in HEK293 cells[49]) and Tergitol showing detection with 0.1 wt%, but more spreading of the sample spot, which reduced the intensity. At the higher 0.5 wt% the signal was reduced significantly due to the spreading of the test spot.

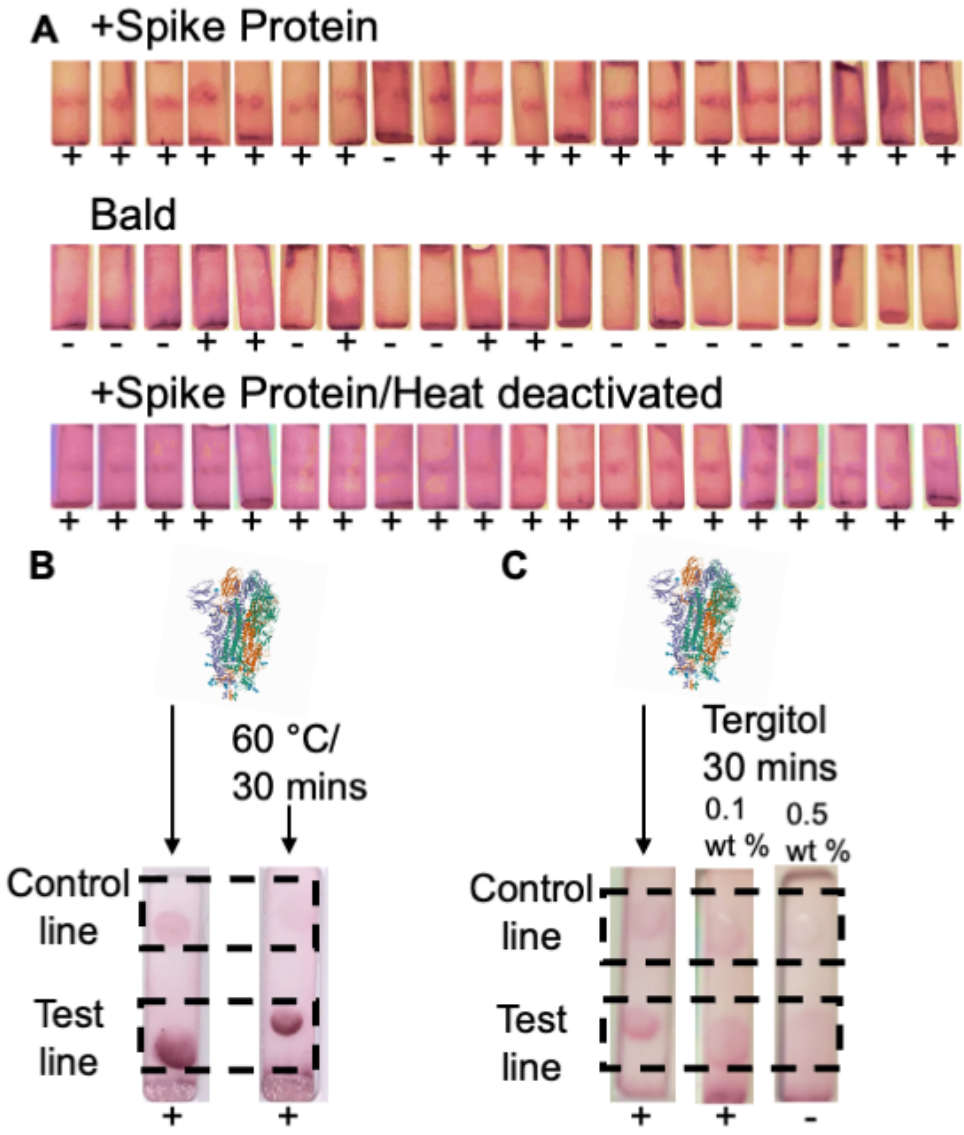

Figure 4.2. Flow though device validation.

A) Photographs of the test line of lentivirus (no silver staining) positive for spike protein, negative (bald) and after heat-treatment at 60 °C for 30 minutes. Recombinant S1 domain of spike protein in flow-through devices; B) heat-treatment at 60 °C for 30 mins [spike] = 0.25 mg.mL^{-1}. (*E. coli* expressed); C) Tergitol treatment for 30 mins [spike] = 0.5 mg.mL^{-1} (HEK293 expressed). Note control lines are not optimised but weak signals are present. "+" indicates a positive response and "-" indicates a negative response.

As this flow-through approach requires direct addition of the swab-extracts onto the test zone, the impact of volume applied was explored to optimise the deposition

process. Figure 4.3A shows test zones of devices run as a function of the volume of a heat-inactivated primary nasal swab sample, which was validated as positive by RT-PCR (Ct = 8.3 from swab eluted with 2 mL of water) and an RT-PCR negative sample. Up to 3 μL (0.15 vol% of the total sample) could be applied to the test line without problems. However, further study (Appendix 4 Tables S5 and S7) highlighted problems with 3 μL with high viral load samples. Larger volumes (> 3 μL) captured essentially all of the particles in flow, preventing the development of the control line. Some false positives also occurred with larger volumes, therefore 2 μL was chosen as the optimal application volume for experiments from here on.

Antibody-based LFDs (lateral flow immunoassays) should not be exposed to extremes of humidity and heat, but it is expected that the glycan/polymer particles used here could be more robust. Devices were manufactured and left in the laboratory (on a shelf, with no desiccant) for 21 days, while some were baked in an oven for 12 hours at 70 °C (Appendix 4 Tables S4 and S8). Figure 4.3B shows the results of these preliminary stability tests, indicating that the tests retained function compared to cassettes not exposed to the atmosphere for 21 days (Appendix 4 Tables S2 and S3) or subjected to heating (Appendix 4 Table S8). It is important to note that the heat-treated devices did give weaker signals, but the conditions used for this were extreme and no silver staining was used at this point – hence the weaker signal. These initial robustness studies highlight the promise of glycopolymer systems; however, further studies and control line optimisation are necessary. Device robustness is crucial for use “in the community” or in low-resource settings where cold chains are not established and more widely to reduce the number of failed devices.

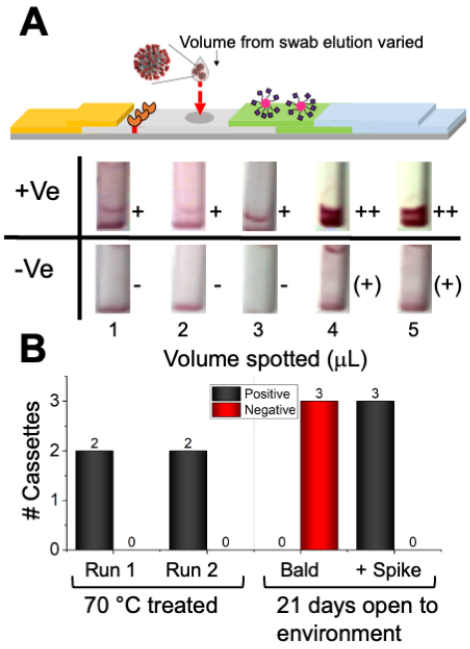

Figure 4.3. Impact of sample volume and stress testing of flow-through devices

A) Impact of sample volume applied to the test line. From 2 mL primary swab elution of Ct 8.3 (+Ve), and a primary swab elution negative by RT-PCR (-Ve), no silver staining used. B) Impact of stress conditions on device function. Heat-treated devices tested with swab sample (Ct 6.29), or after 21 days using indicated lentivirus ("Bald" ~1×10^4 LP.mL^{-1} and "+ Spike" 1.5×10^4 TU.mL^{-1}). "+" indicates a positive response on the test strips, "++" indicates a very strong positive response, "(+)" indicates a weak positive response, and "-" indicates a negative response.

Encouraged by the positive results with pseudotyped lentivirus, primary clinical samples were the next step. For this, surplus nasal swabs eluates (which had been eluted and heat inactivated as part of clinical investigation of symptomatic patient/staff and assessed by RT-PCR) were used. These tests were not conducted blind, with the PCR result known to the user. After specimen application, devices were dried at 37 °C to ensure consistency across this study in terms of drying conditions. Figure 4.4A shows devices, following the addition of buffer: note that a lower Ct value indicates a higher viral load. A positive result (red line/spot at the test position) was clear, whereas control line/spot intensity varied between samples. It is crucial to note that a usable real-world device requires both control and test lines for a valid result. Converting Ct to viral concentration is not a linear relationship and varies between the methods used, but Figure 4.4 covers a wide range from weak to very strong positives. As these tests are "homemade" there is likely to be more variance than in mass-manufactured

devices, therefore a silver staining step was employed here to provide signal enhancement. Figure 4.4B exemplifies this with 5 other swab samples, which despite having relatively low Ct values gave weaker signals on the test line. After silver staining, Figure 4.4C shows that these (From Figure 4.4B) all now give clear and strong positives. Negative samples, after silver staining, did not lead to false positives (discussed further below in the context of larger sample numbers), (Appendix 4 Tables S12-14), unless longer developing times were used. Figure 4.4D shows the impact of silver staining on the signal intensity (from image analysis), confirming that low viral loads benefitted more from the signal increase, compared to higher viral loads (low Ct). It is notable that commercial lateral flow diagnostics have a time window for reading results, as over-development can lead to false positives.

As previously discussed for the lentiviral data, as only 2 mL of the specimen is applied, the total number of viral particles/device is expected to be very low. A Ct of 26 (using the RT-PCR method cited here)[68] is approximately 100 PFU.mL^{-1} or ~10^5 RNA copies.mL^{-1}.[69] This would mean detection of ~200 RNA copies per devices, or < 1 PFU per device. Ct to PFU and RNA copy numbers are known to vary between RT-PCR machine, method, and calibration,[69–72] Therefore, while Ct can give an indication of PFU and viral load, it is not an exact equivalence,[73] and hence, for a test that detects the spike protein correlating these different measurements is challenging. Ct values used here were from the Abbott assay.[68,72] It is important to note here that the numbers above do not include defective viral particles (e.g., capsid only and RNA-deficient particles),[74,75] which may still have spike protein components (targeted in this work). In the case of the (cultured) Ebola virus, for example,[76] contingent on the passage number, the ratio of total viral particles to plaque-forming units (intact virus) has been reported in the range of 10^2 to 10^5 which, depending on the nature of particles, may contribute to diagnostic performance. To the best of our knowledge, the particle:PFU ratio is not available for SARS-COV-2, but we hypothesise that the detection limit maybe be enhanced due to these additional (non-plaque forming) viral particles or fragments of the released spike protein. Preliminary experiments on heat-treated, purified SARS-COV-2 (from cell culture not patients) showed higher limits of detection, supporting the hypothesis that defective particles may be contributing, rather than the release of spike protein from viral particles, which would also occur in this control.

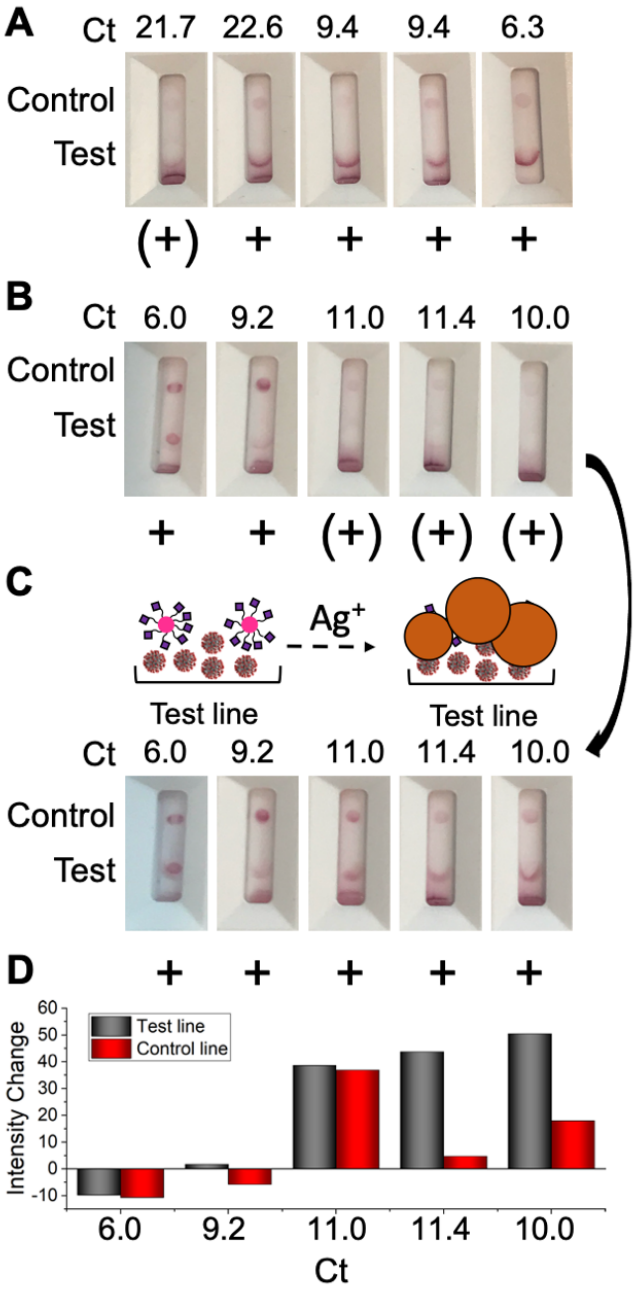

Figure 4.4. Flow-through device with clinical samples.

2 µL total of the sample was applied to each test line. A) Photographs taken after 20 minutes of the buffer; B) Photographs from different panels taken after 20 minutes of the buffer and then C) subjected to silver-staining enhancement. D) Impact of silver-staining on signal intensity of control and test lines, obtained by image analysis.

Encouraged by the above results, a panel of 50 positive and 54 negative, PCR-validated patient-derived swab samples were tested (See experimental section for how these were handled, including dry transport, and heat inactivation). Each sample was

analysed twice, on independent devices, treated in the analysis as an independent run, and reported as such in the results below. The tests were not run blind, and the Ct values were known to the user. Failed devices (where gold conjugate did not flow, for example) were excluded from the analysis (1 positive sample device and 2 negative sample devices). As above, to ensure consistency, all samples were dried onto the devices at 37 °C before running the devices. Figure 4.5A shows the distribution of positive samples as a function of the Ct values after silver staining, with high viral loads (lower Ct) giving fewer false negatives – as would be expected. Figure 4.5A is annotated showing the sensitivity (% true positives) by the Ct value. Analysis of non-silver-stained devices is provided in Appendix 4 (Figures S1-S2) for comparison purposes.

Confusion matrices were produced from both positive and negative sample sets Figure 4.5B. After silver staining, a sensitivity value of 85% and specificity of 93% were achieved. The sensitivity is comparable, or exceeds, some commercial LFDs (when clinical swabs were used),[69] whereas the specificity is lower, but is anticipated to be improved by manufacturing processes and further optimisation of the components and running conditions. Before silver staining (where control lines were not always visible, so judged by the test line presence only) a lower sensitivity (68%) but higher specificity (96%) was observed. The total number of false positives was 8 (from 6 samples) across the study. Considering that this is a prototype the values are very promising. It is important to note that this data uses primary samples, rather than artificial doped-samples which would be expected to give higher values for specificity, but our aim was to evaluate under conditions as close to 'application' as possible. To the best of our knowledge, this is the first example of a flow-through glyco-assay assessed with clinical samples, providing proof-of-principle that this methodology can be applied to complement antibody-based systems.

SARS-COV-2 variants with mutations in the spike protein have (and continue to) emerge, and any diagnostics should retain the ability to detect these. Davis and co-workers have reported that the B1.1.7 and B1.351 spike mutants have reduced NMR STD signal to the NAc protons of a α2,3-sialyllactoside compared to the wild type, consequently there is potential that the glycan-binding affinity may be decreased.[77]To test the impact of this, 3 mutant truncated spike protein varients; B1.1.7, B.1.351 and P1 (variants first detected in Kent (UK), South Africa and Brazil) were expressed in

E. coli and tested in our devices. In all cases a positive test line was seen (Figure 4.5C, no silver staining), showing detection capability is retained. It is crucial to again note that binding affinity does not relate linearly to signal output in flow-through (or lateral flow) devices, therefore this does not rule out differences in the individual protein/glycan interactions.

Influenza has haemagglutinins and neuraminidases, which target sialosides (including *N*-acetyl neuraminic acid),[78] and sialic acid nanoparticles which bind influenza are well known,[79,80] so it was important to consider cross-reactivity. Heating is known to reduce haemagglutination activity;[81] hence, our diagnostic specificity (above) might have been improved by the heat-inactivation of the sample. To explore influenza cross-reactivity, haemagglutinins from H1N1, H3N2, H7N8 and H7N3 as well as betapropiolactone (BPL)-inactivated influenza virions were tested and the devices are shown in Appendix 4. H3N2 haemagglutinins were detected in the devices but H1N1, H7N9 and H7N3 haemagglutinins were not, noting relatively high concentrations were used (0.5 $mg.mL^{-1}$). In contrast, using intact influenza virus there was no cross-reactivity observed. A further control of heat-inactivated SARS-COV-2 remained detectable under these conditions (Appendix 4). The lack of apparent influenza cross-reactivity can be attributed to the effective low haemagglutinin concentration on the viral surface, compared to using just 'pure' protein along with differential absorption onto the nitrocellulose. From a structural biology perspective, haemagglutinins make binding contacts to not only the terminal glycan used here (Neu5NAc) but can also contact linker units (e.g., the lactose, in sialylactose). Our preliminary data[49] and addition thermal shift assays (Appendix 4) suggest that the SARS-COV-2 spike protein had a similar affinity toward Neu5NAc as to sialylactose (2,3 and 2,6). Therefore, the use of the Neu5NAc monosaccharide as the detection unit may lead to reduced overall affinity toward influenzas, while maintaining SARS-COV-2 affinity, and thus providing selectivity in the flow-through format.

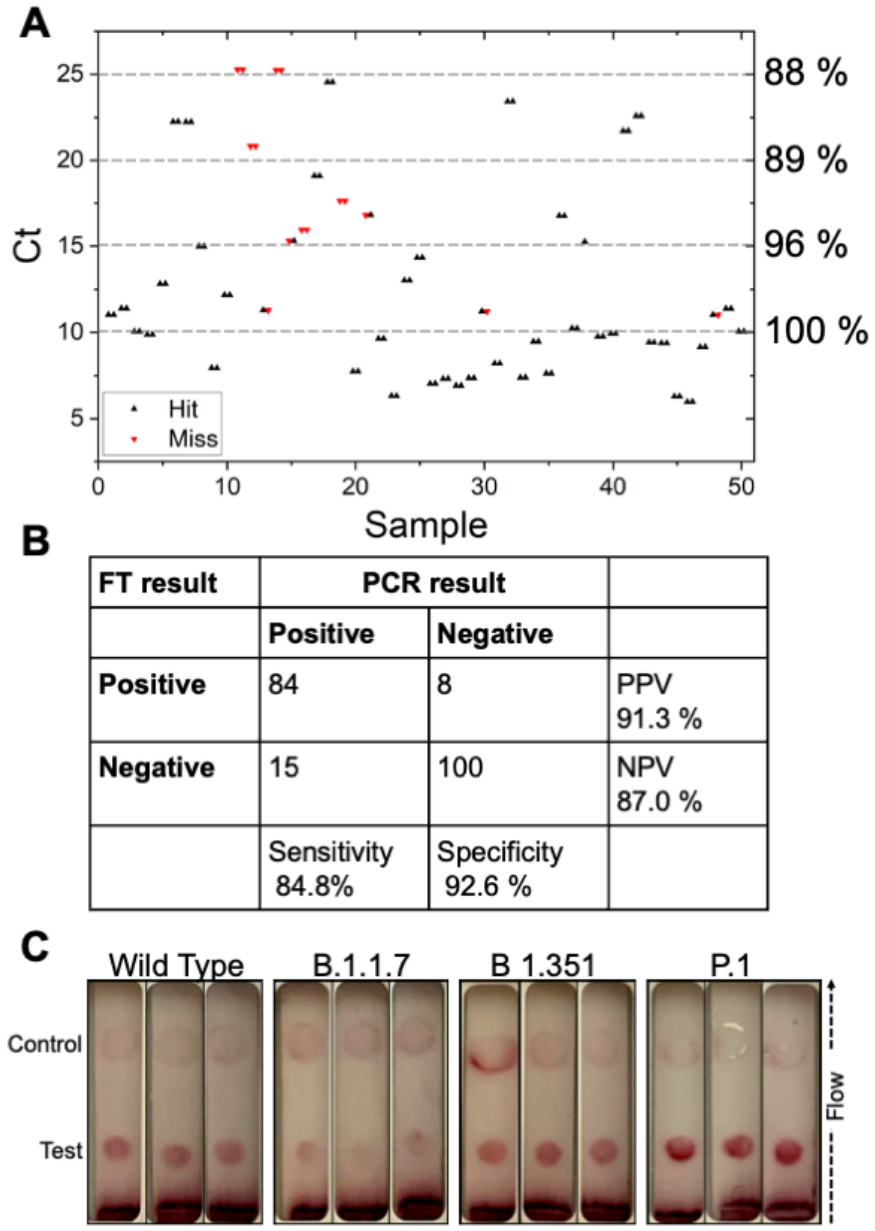

FT result	PCR result		
	Positive	**Negative**	
Positive	84	8	PPV 91.3 %
Negative	15	100	NPV 87.0 %
	Sensitivity 84.8%	Specificity 92.6 %	

Figure 4.5. Flow-through (FT) device performance using heat-inactivated primary patient swabs after silver staining step

A) Results of device performance (hit or miss) as a function of Ct for devices ran alone. Thresholds indicated are the sensitivity as a function of the Ct value; B) Confusion matrices after silver staining. Sensitivity = TP/(TP+FN); Specificity = TN/(TN+FP); PPV = TP/(TP+FP); NPV = TN/(TN+FN). TP = true positive; TN = true negative; FN = false negative; FP = false positive. C) Devices using recombinant spike protein from variant strains. Sequence information in Experimental Section. Larger versions of Figure 4.5A can be found as Figures S3A and 3B in the Supporting Information for clarity. A positive result has a visible test and control.

4.5 Conclusions

Here, we have demonstrated a prototype flow-through glyco-assay device, which is capable of detecting SARS-COV-2 infection by exploiting the interaction between *N*-acetyl neuraminic acid and the viral spike protein. Rather than a traditional lateral flow design where there is a capture unit on the stationary phase ("test line"), we developed our system so that the primary sample (in this case derived from nasal swabs) was directly deposited as the test line and hence is a "flow-through" device. This approach removed the need to develop a test line, speeding up the initial development process, and allowing us to prove the principle that glycans could be used in complete lateral flow devices with primary samples. Crucial to achieving this is the use of a non-fouling polymeric coating, which reduces nonspecific interaction with any deposited biological components (e.g., mucus, cell debris) as well as providing the tether to display the glycan. Using a lentiviral model, the flow-through devices were specific toward spike bearing lentiviruses, compared to bald lentiviruses. Using recombinant, truncated spike protein, we demonstrated that the protein retains sialic-acid binding capacity even after heating or limited detergent treatment. This observation shows that this device may detect damaged viruses and so it cannot be claimed to only detect intact virus (similar to other diagnostic tools for SARS-COV-2). Using a panel of RT-PCR-validated swab samples, these prototype flow devices were shown to achieve, after silver staining, 85% sensitivity and 93% specificity, using Ct values as high as 25. (An upper limit in line with recent UK-wide lateral flow device validation methods[82]). These results compare well to commercially available tests (Appendix 4 Table S21). The apparently low detection limit may be in part due to the detection of defective viral particles, which also bear the spike protein. This will require further studies to validate their contribution and the role of using heat-inactivated swabs. Further optimisation of the device, and running buffers are expected to lead to improvements, especially to further reduce any nonspecific interactions, as well as the potential to develop a full lateral flow device.

With any diagnostic or sensor, there is potential for cross-interaction with other agents. Cross-reactivity with two influenza strains (H1N1 and H3N2) was not seen, even though the nanoparticles do have an affinity toward H3N2 haemagglutinins, which may be due to differential absorbance to the test zone or differences in overall

detection limits. The molecular details of reported spike protein mutations (including the H69/V70 deletions) on the actual binding affinity toward sialosides (and this detection method) are still under study.[83] The devices developed here were shown to be capable of detecting recombinant spike proteins from several variants, demonstrating that these mutations do not remove glycan-binding function. Future work will further explore the roles of sample preparation including the heat-inactivation step, mechanism of application of specimens, and fundamental studies of the glycan recognition function and its biochemical basis. Consideration must also be given to removing the need for a pipette as an application system to the device, followed by the time delay for drying the specimen onto the pad. Both of these could be improved, or further developed into a complete lateral flow (test line) device. The evidence provided here shows that glycan flow technology (lateral flow and flow-through glyco-assays) could be translated to clinical settings to be used alongside more traditional antibody-based approaches.

4.6 Experimental

4.6.1 Physical and Analytical Methods

NMR Spectroscopy

^{1}H-NMR, ^{13}C-NMR and ^{19}F-NMR spectra were recorded at 300 MHz or 400 MHz on a Bruker DPX-300 or DPX-400 spectrometer respectively, with deuterium oxide (D_2O) as the solvent. Chemical shifts of protons are reported as δ in parts per million (ppm) and are relative to D_2O (4.79).

Size Exclusion Chromatography

Size exclusion chromatography (SEC) analysis was performed on an Agilent Infinity II MDS instrument equipped with differential refractive index (DRI), viscometry (VS), dual angle light scattering (LS) and variable wavelength UV detectors. The system was equipped with 2 x PLgel Mixed D columns (300 x 7.5 mm) and a PLgel 5 μm guard column. The mobile phase used was DMF (HPLC grade) containing 5 mM NH_4BF_4 at 50 °C at flow rate of 1.0 mL.min^{-1}. Poly(methyl methacrylate) (PMMA) standards (Agilent EasyVials) were used for calibration between 955,000 – 550 g.mol^{-1}. Analyte samples were filtered through a nylon membrane with 0.22 μm pore size before injection. Number average molecular weights (M_n), weight average molecular weights (M_w) and dispersities ($Đ_M = M_w/M_n$) were determined by conventional calibration using Agilent GPC/SEC software.

X-ray Photoelectron Spectroscopy (XPS)

The samples were attached to electrically-conductive carbon tape, mounted on to a sample bar and loaded in to a Kratos Axis Ultra DLD spectrometer which possesses a base pressure below 1 x 10^{-10} mbar. XPS measurements were performed in the main analysis chamber, with the sample being illuminated using a monochromated Al Kα x-ray source. The measurements were conducted at room temperature and at a take-off angle of 90° with respect to the surface parallel. The core level spectra were recorded using a pass energy of 20 eV (resolution approx. 0.4 eV), from an analysis area of 300 μm x 700 μm. The spectrometer work function and binding energy scale of the spectrometer were calibrated using the Fermi edge and $3d_{5/2}$ peak recorded from a polycrystalline Ag sample prior to the commencement of the experiments. In order to prevent surface charging the surface was flooded with a beam of low energy

electrons throughout the experiment and this necessitated recalibration of the binding energy scale. To achieve this, the C-C/C-H component of the C 1*s* spectrum was referenced to 285.0 eV. The data were analysed in the CasaXPS package, using Shirley backgrounds and mixed Gaussian-Lorentzian (Voigt) lineshapes. For compositional analysis, the analyser transmission function has been determined using clean metallic foils to determine the detection efficiency across the full binding energy range.

Dynamic Light Scattering

Hydrodynamic diameters (D_h) and size distributions of particles were determined by dynamic light scattering (DLS) using a Malvern Zetasizer Nano ZS with a 4 mW He-Ne 633 nm laser module operating at 25 °C. Measurements were carried out at an angle of 173° (back scattering), and results were analysed using Malvern DTS 7.03 software. All determinations were repeated 5 times with at least 10 measurements recorded for each run. D_h values were calculated using the Stokes-Einstein equation where particles are assumed to be spherical.

UV-vis Spectroscopy

Absorbance measurements were recorded on an Agilent Cary 60 UV-Vis Spectrophotometer and on a BioTek Epoch microplate reader.

Transmission Electron Microscopy

Dry-state stained TEM imaging was performed on a JEOL JEM-2100Plus microscope operating at an acceleration voltage of 200 kV. All dry-state samples were diluted with deionised water and then deposited onto formvar-coated copper grids.

Flow-through Cassette Image Collection

Images of the flow-through cassettes were collected on an iPhone XR or an iPhone 7, using standard/automatic photo settings i.e. no manual adjustments were made by the authors to improve photo quality on capture. Images in main paper have been cropped and brightness/contrast changed. Original images are included in full in Appendix 4.

Protein Thermal Shift Assay

The thermal shift reaction was performed with a BioRad CFX96 real-time PCR machine. The sample was heated from 25 °C to 95 °C and the fluorescence intensity change monitored using the Protein Thermal Shift™ Dye kit (Thermo Fisher Scientific, Cat # 4461146). Analysis for binding induced shifts in thermal transition

was performed in PBS buffer with Precision Melt Analysis Software provided by the manufacturer (BioRad) and a protein concentration of 0.2 mg/mL. The data was collected over 5 runs for each glycan and glycan concentration. Glucose and Galactose data are from a prior publication,[49] with the addition of sialyllactoses here.

4.6.2 Materials

All chemicals were used as supplied unless otherwise stated. *N*-Hydroxyethyl acrylamide (97%), 4,4'-azobis(4-cyanovaleric acid) (98%), triethylamine (> 99%), sodium citrate tribasic dihydrate (> 99%), gold(III) chloride trihydrate (99.9%), potassium phosphate tribasic (≥ 98%, reagent grade), deuterium oxide (D_2O, 99.9%), diethyl ether ((≥ 99.8%, ACS reagent grade), sodium azide (≥ 99.5%, reagent plus grade), methanol (≥ 99.8%, ACS reagent grade), toluene (≥ 99.7%,), Tween-20 (molecular biology grade), HEPES, PVP40 (poly(vinyl pyrrolidone)$_{400}$ (Average Mw ~40,000)), sucrose (Bioultra grade), acetone (≥ 99%) and a silver staining kit (Silver Enhancer Kit) were purchased from Sigma-Aldrich. Anhydrous trehalose was purchased from Alfa Aesar. DMF (> 99%) was purchased from Acros Organics. Sodium chloride (≥ 99.5%) and calcium chloride were purchased from Thermo Fisher Scientific.

Nitrocellulose Immunopore RP 90-150 s/4cm 25 mm was purchased from GE Healthcare. Lateral flow backing cards 60 mm by 301.58 mm (KN-PS1060.45 with KN211 adhesive) and lateral flow cassettes (KN-CT105) were purchased from Kenosha Tapes. Cellulose fibre wick material 20 cm by 30 cm by 0.825 mm (290 gsm and 180 mL/min) (Surewick CFSP223000) was purchased from EMD Millipore. Glass fibre conjugate pads (GFCP103000) 10 mm by 300 mm was purchased from Merck. Thick chromatography paper (for sample pads), Grade 237, Ahlstrom 20 cm by 20 cm were purchased from VWR International.

Ricinus communis Agglutinin I (RCA_{120}) was purchased from Vector Laboratories.

Spike (SARS-COV2) pseudotyped lentivirus (*Luc* Reporter) (Catalogue number: 79942, Lot number: 200730) and Bald lentiviral pseudovirion (*Luc* reporter) (Catalogue number: 79943, Lot number: 200727) were purchased from amsbio.

Influenza A virus (A/Brisbane/10/2007 (H3N2)) BPL-inactivated (Catalogue number: NR-19321), Influenza A virus (A/Puerto Rico/8/1934 (H1N1)) BPL-inactivated (Catalogue number: NR-19325), H7 Hemagglutinin (HA) protein from influenza virus (A/Canada/rv444/2004 (H7N3)) – recombinant from Baculovirus (Catalogue number: NR-43740), H7 Hemagglutinin (HA) protein from influenza virus (A/Shanghai/1/2013 (H7N9)) – recombinant from Baculovirus (Catalogue number: NR-44079), H3 Hemagglutinin (HA) protein from influenza virus (A/New

York/55/2004 (H3N2)) – recombinant from Baculovirus (Catalogue number: NR-19241), H1 Hemagglutinin (HA) protein with C-terminal histidine tag from influenza virus (A/Brisbane/59/2007 (H1N1)) – recombinant from Baculovirus (Catalogue number: NR-28607) and SARS-related Coronavirus 2 (SARS-COV-2) (USA-WA1/2020) heat-inactivated at 65 ℃ for 30 minutes (Catalogue number: NR-52286) were obtained through BEI Resources.

Water used for buffers was MilliQ grade > 18.2 mΩ resistance.

Swab Samples

This study used remnant elutions from nasal, or nasal + oral swab samples collected from symptomatic staff/patients at the University Hospital Coventry and Warwickshire NHS Trust and routinely tested by standard PCR protocols employing the Abbott assay (Ref: 09N77-095, https://www.molecular.abbott/sal/9N77-095_SARS-CoV-2_US_EUA_Amp_PI.pdf) during April-September 2020.[84] As this evaluation study used left-over anonymised material no written informed consent was obtained, although the project was registered with the local COVID-19 research committee.

Dry cotton swabs, one nose and one throat, were obtained in a single universal container. To each primary swab sample was added 2000 µL of molecular grade water (if one swab) or 2500 µL of molecular grade water (if two swabs are in universal container). These were then vortexed and allowed to settle for 5 minutes. All liquid was transferred from primary container into 13 mm × 75 mm tube. These tubes were heat inactivated at 85 ℃ for 10 minutes. The specimens were then used for testing. All testing was conducted on samples which had not been frozen, but had been stored in a fridge, and tested within 48 hours of receipt.

4.6.3 Synthetic Methods

The following synthetic methods have been previously reported,[49] but have been provided for the reader as the glycopolymer synthesis and AuNP functionalisation have been optimised and materials were made specifically for this work. Note the synthesis of 2-azido-2-deoxy-*N*-acetyl-D-neuraminic acid and the SARS-COV-2 S1 spike protein can be found in the previous report (Chapter 3)[49] but a full characterisation of the 2-azido-2-deoxy-*N*-acetyl-D-neuraminic acid has been provided as this was synthesised again here.

Polymerisation of 2-hydroxyethyl acrylamide (DP50)

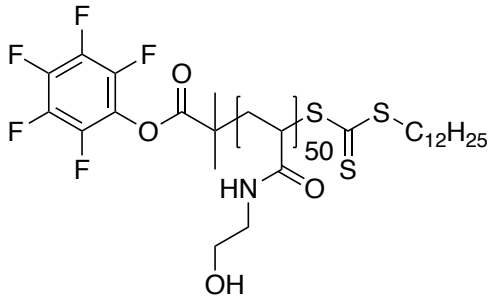

2.7635 g (24.00 mmol) of 2-hydroxyethyl acrylamide, 0.0607 g (0.22 mmol) of ACVA and 0.5273 g (2.87 mmol) of PFP-DMP (synthesised previously[49]) was added to 22 mL 1:1 toluene:methanol and degassed with nitrogen for 30 minutes. The reaction vessel was stirred and heated at 70 °C for 2 hours. The solvent was removed under vacuum. The crude product was dissolved in the minimum amount of methanol. Diethyl ether cooled in liquid nitrogen was added to the methanol to form a precipitate. The mixture was centrifuged for 2 minutes at 13 krpm and the liquid decanted off. The solid was dissolved in methanol and removed under vacuum to give a yellow crystalline solid. δ_H (300 MHz, D_2O) 8.31 - 7.97 (23H, m, N*H*), 3.99 - 3.55 (86H, m, NHC*H*$_2$), 3.55 - 3.09 (100H, m, C*H*$_2$OH & SC*H*$_2$), 2.49 - 1.90 (46H, m, $CH_2CHC(O)$ & $C(CH_3)_2$), 1.90 - 0.98 (110H, m, C*H*$_2$CHC(O) & C*H*$_2$C*H*$_2$C*H*$_2$C*H*$_2$C*H*$_2$C*H*$_2$C*H*$_2$C*H*$_2$C*H*$_2$CH$_2$CH$_3$), 0.84 - 0.72 (5H, m, C*H*$_2$C*H*$_3$).

$M_{n,Theoretical}$ = 3400 g.mol^{-1}. $M_{n,NMR}$ = 5500 g.mol^{-1}. SEC (5 mM NH_4BF_4 in DMF) $M_{n,\ SEC\ RI}$ = 6400 g.mol^{-1} ($DP_{PHEa,\ SEC}$ = 50), $Đ_{M,\ SEC\ RI}$ = 1.27. Yield - 75%.

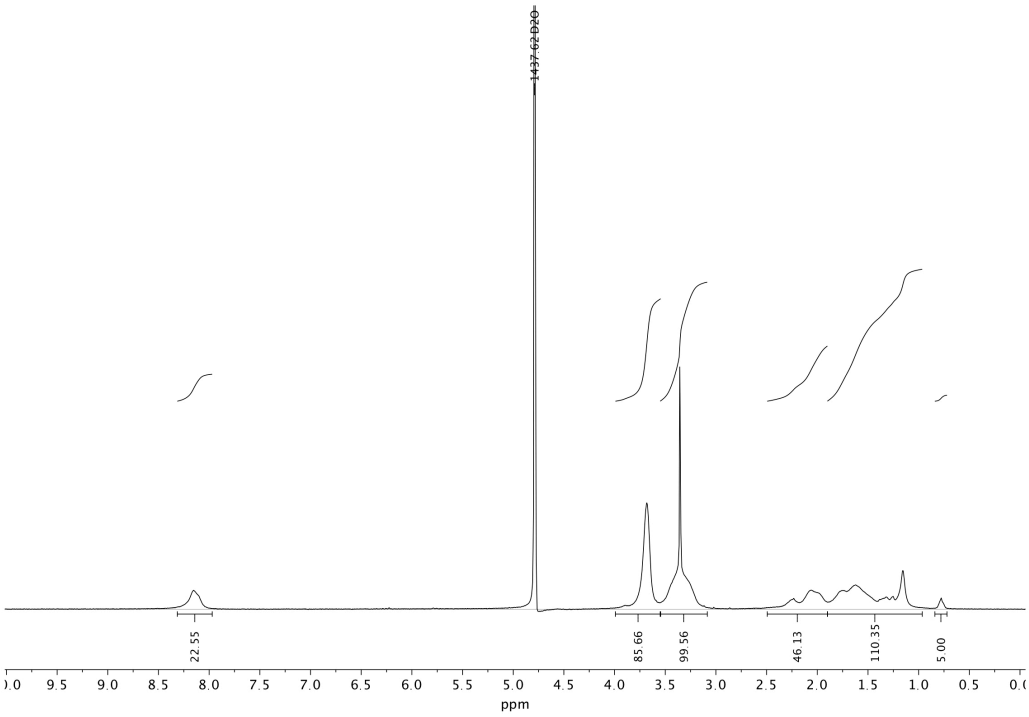

Figure E4.1. ^{1}H NMR spectrum of DP50 PHEA

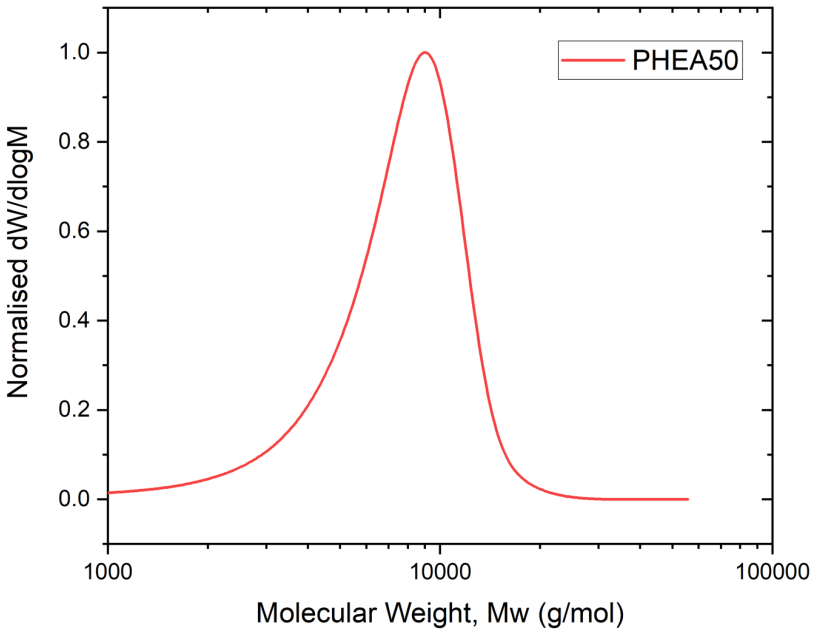

Figure E4.2. Normalised size exclusion chromatography RI molecular weight distribution of telechelic PHEA50 obtained in DMF versus PMMA standards.

DP50 Poly(N-hydroxyethyl acrylamide) glycan functionalisation using 2-amino-2-deoxy-N-acetyl-D-neuraminic acid

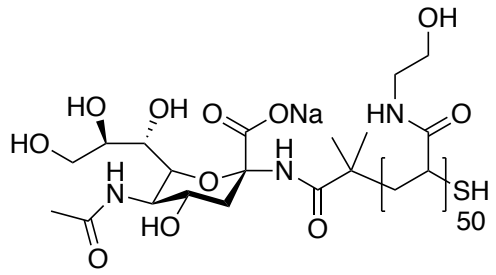

0.1 g (0.016 mmol) of poly(2-hydroxyethyl acrylamide)$_{50}$ and 25 mg (0.64 mmol) of 2-amino-2-deoxy-*N*-acetyl-D-neuraminic acid were added to 3 mL of DMF containing 100 µL TEA. The reaction was stirred at RTP for 16 hours. Solvent was removed under vacuum. The crude product was dissolved in the minimum amount of methanol. Diethyl ether cooled in liquid nitrogen was added to the methanol to form a precipitate. The mixture was centrifuged for 2 minutes at 13 krpm and the liquid decanted off. The solid was dissolved in methanol and solvent removed under vacuum to give an orange/brown crystalline solid. Loss of fluorine signals in the ^{19}F NMR was used to indicate the reaction had gone to completion. δ_H (400 MHz, D_2O) 3.99 - 3.55 (~117H, m, NHC*H*$_2$ & glycan protons), 3.55 - 3.09 (~98H, m, C*H*$_2$OH & SC*H*$_2$ & glycan protons), 2.49 - 1.90 (~63H, m, $CH_2CHC(O)$, $C(CH_3)_2$ & glycan protons), 1.90 - 0.98 (~95H, m, C*H*$_2$CHC(O) & glycan protons).

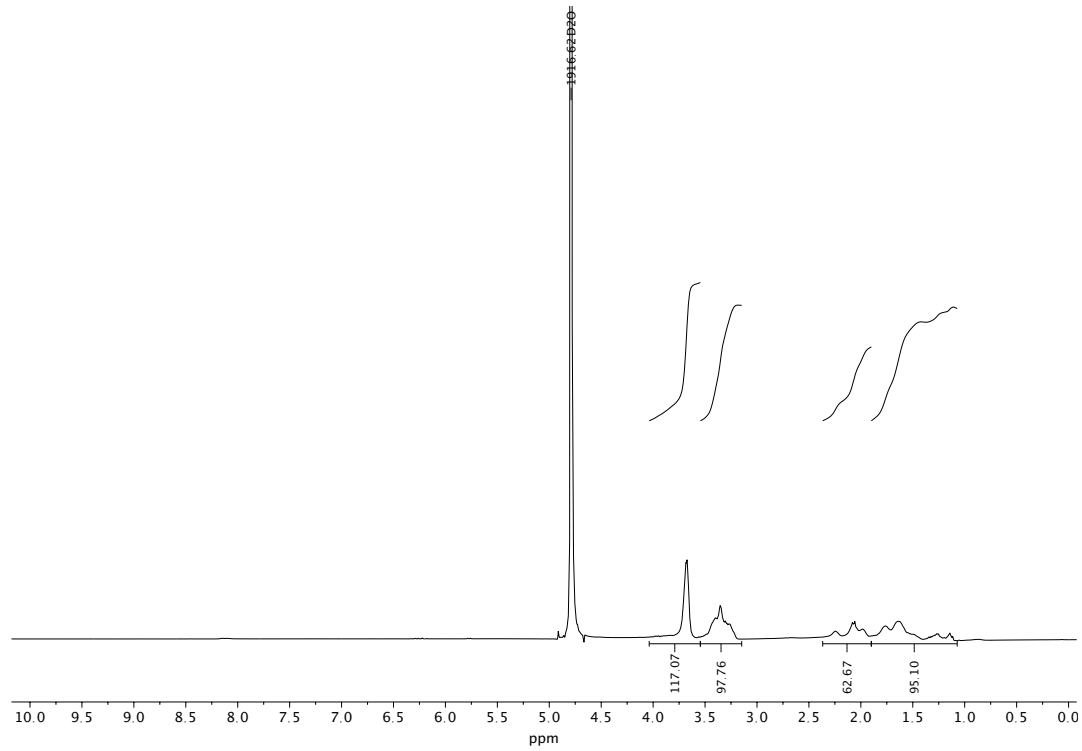

Figure E4.3. ^{1}H NMR of 2-amino-2-deoxy-*N*-acetyl-D-neuraminic acid functionalised poly(*N*-hydroxyethyl acrylamide)$_{50}$.

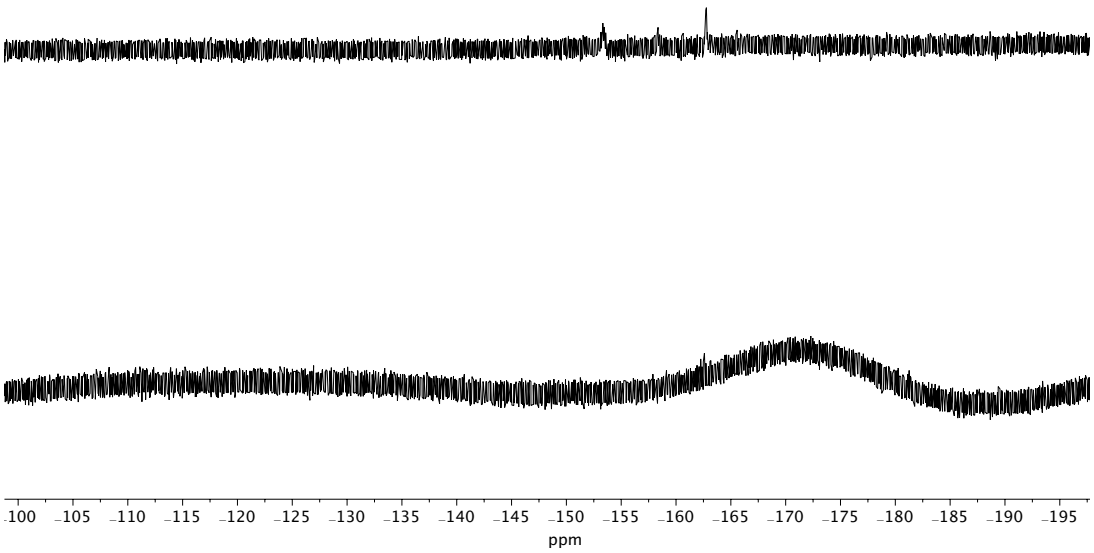

Figure E4.4. ^{19}F NMR before (Top) and after (Bottom) reaction with α2-amino-2-deoxy-*N*-acetyl-D-neuraminic acid functionalisation.

Citrate-stabilised 35 nm Gold Nanoparticle Synthesis

35 nm gold nanoparticles were synthesised by a modified step growth method developed by Bastús *et al.*.[85] A solution of 2.2 mM sodium citrate in Milli-Q water (150 mL) was heated under reflux for 15 min while vigorously stirring. After boiling had commenced, 1 mL of $HAuCl_4$ (25 mM) was injected. The colour of the solution changed from yellow to bluish gray and then to soft pink in 10 min, 1 mL was taken for DLS and UV/Vis analysis. Immediately after the synthesis of the Au seeds and in the same reaction vessel, the reaction was cooled until the temperature of the solution reached 90 °C. Then, 1 mL of a $HAuCl_4$ solution (25 mM) was injected. After 20 min, the reaction was finished. This process was repeated twice. After that, the sample was diluted by adding 85 mL of MilliQ water and 3.1 mL of 60 mM sodium citrate. This solution was then used as a seed solution, and three further portions of 1.6 mL of 25 mM $HAuCl_4$ were added with 20 min between each addition. Following completion of this step, 1 mL was taken for DLS and UV/Vis analysis. The sample was diluted by adding 135 mL of MilliQ water and 4.9 mL of 60 mM sodium citrate. This solution was then used as a seed solution, and the process was repeated with three further additions of 2.5 mL of 25 mM $HAuCl_4$, this solution was analysed by DLS and UV/Vis. When the target size of 35 nm was reached, the solution was cooled, and a sample taken for TEM analysis.

Gold Nanoparticle Polymer Coating Functionalisation

1 mg of glycopolymer was agitated overnight with 10 mL of 35 nm AuNPs ~2 Abs at UV_{max}. The solution was centrifuged at 8 krpm for 30 minutes and the pellet resuspended in 10 mL of water, the solution was centrifuged again at 8 krpm for 30 minutes and the pellet resuspended in 1 mL aliquots and centrifuged at 8 krpm for 10 minutes. The pellets were combined into a 1 mL solution with an absorbance at UV_{max} of ~10 Abs.

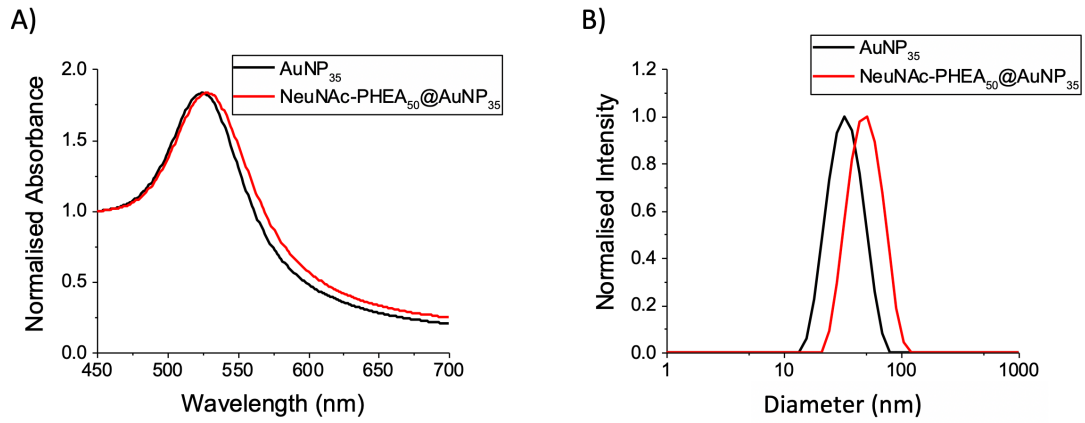

Figure E4.5. Characterisation of unfunctionalised and NeuNAc-functionalised 35 nm AuNPs by A) UV/Vis and B) dynamic light scattering.

Code	UVmax[a] (nm)	A_{SPR}/A_{450}[b]	D_h[c] (nm)	$D_{h(DLS)}$[d] (nm)	$D_{(TEM)}$[e] (nm)
Citrate AuNP35	526	1.91	35	34.5±1	35±3
NeuNAc-PHEA50AuNP35	531	1.99	45	55.3±1	38.9±3.1

Table E4.1. Characterisation of unfunctionalised and functionalised AuNPs used in this study.

[a)] SPR absorption maximum; [b)] Absorbance ratio of SPR to 450 nm; [c)] Estimated from UV-Vis[86]; [d)] From dynamic light scattering; [e)] From TEM, from average of > 100 particles, showing ±S.D.

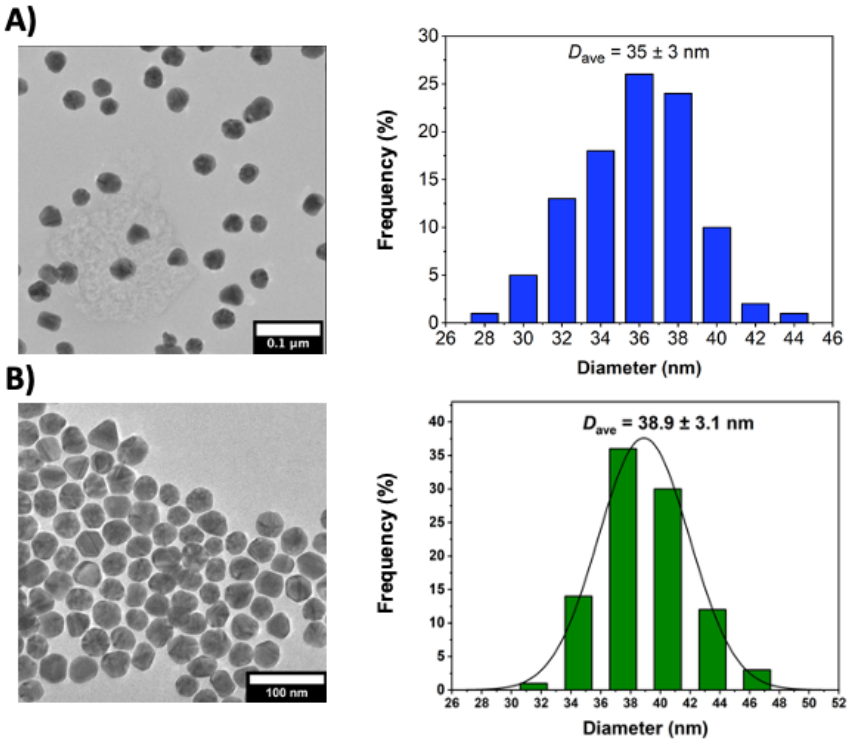

Figure E4.6. TEM images (left) and histograms (right) of citrate stabilised AuNPs.

A) 35 nm unfunctionalised AuNP and B) NeuNAcPHEA$_{50}$@AuNP$_{35}$. Histograms from analysis of > 100 particles

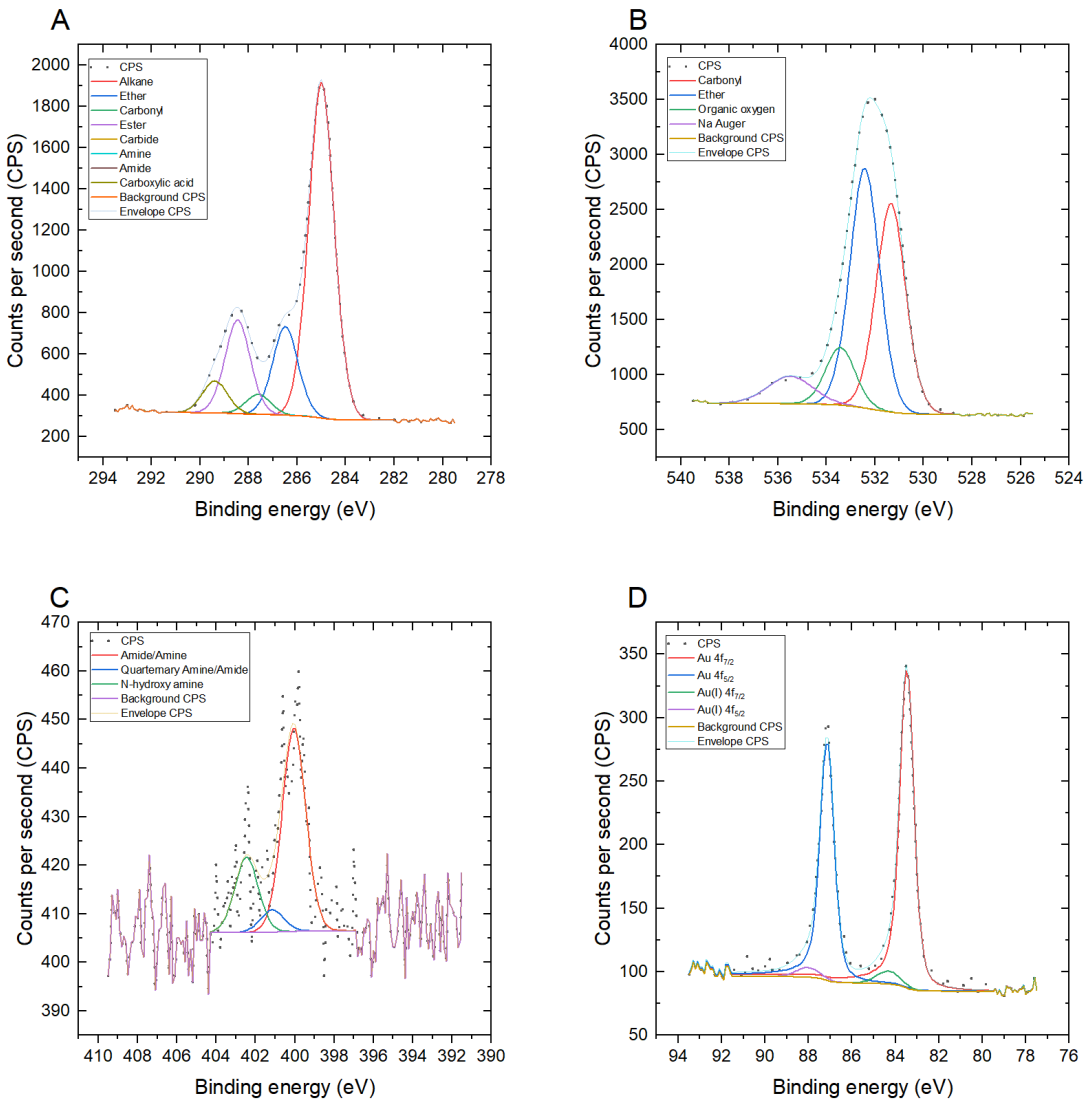

Figure E4.7. X-ray photo-electron spectroscopy (XPS) of citrate stabilised 35 nm AuNP

A) C 1*s* B) O 1*s* C) N 1*s* and D) Au 4*f*

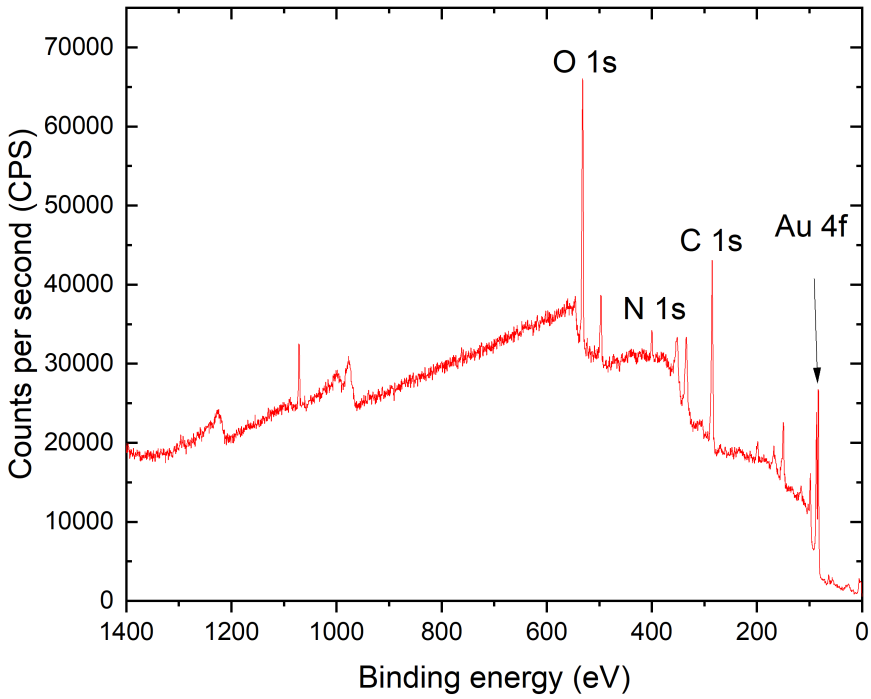

Figure E4.8. XPS survey scan of neuraminic acid $PHEA_{50}$@$AuNP_{35}$

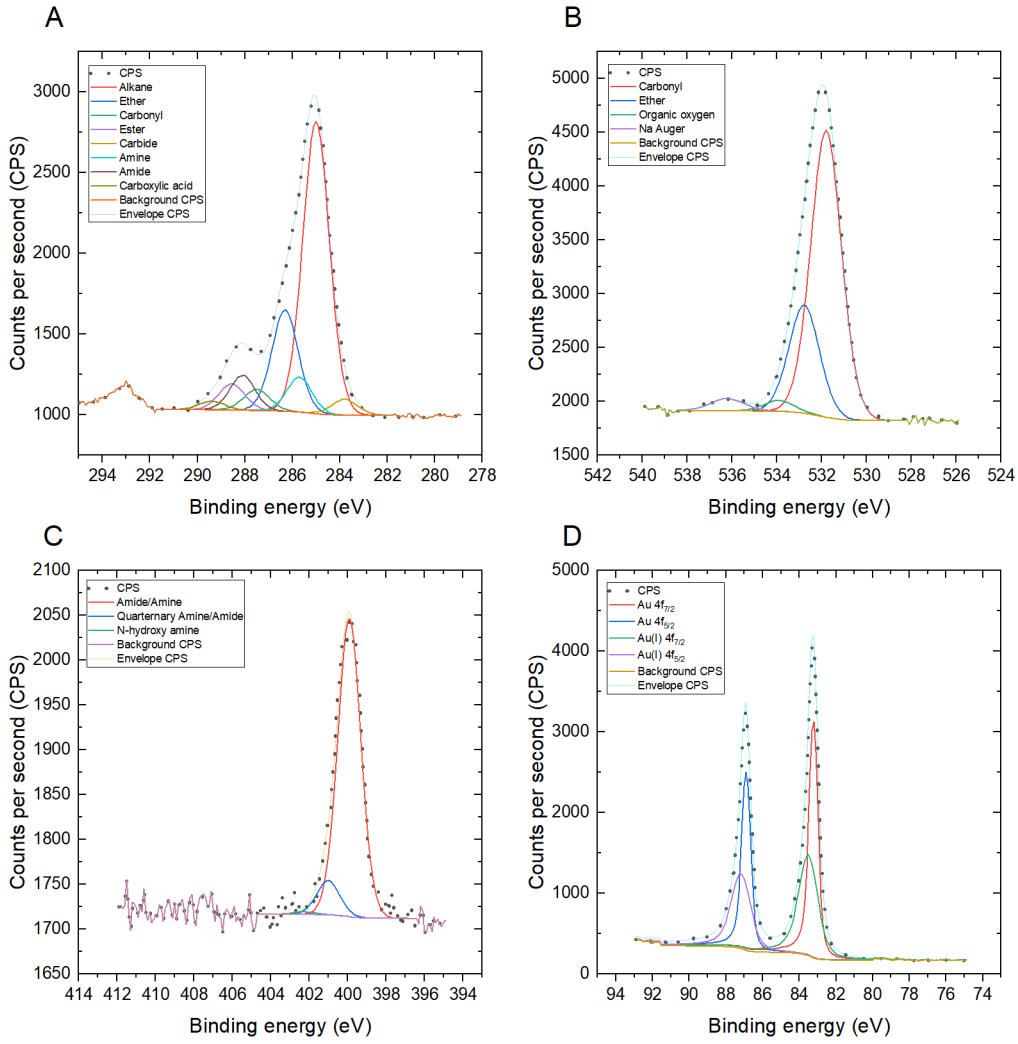

Figure E4.9. XPS of neuraminic acid $PHEA_{50}$@$AuNP_{35}$

A) C 1*s* B) O 1*s* C) N 1*s* and D) Au 4*f*

Characterisation of 2-Azido-2-deoxy-N-acetyl-D-neuraminic acid

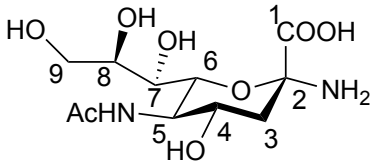

δ_H (400 MHz, D_2O) 4.05 - 3.89 (3H, m, H^4, H^5 and H^6), 3.83 (1H, dd, *J* 11.5, 1.5, H^{9a}), 3.78 - 3.71 (1H, m, H^8), 3.62 (1H, dd, *J* 11.5, 6.5, H^{9b}), 3.48 - 3.43 (1H, m, H^7), 2.13 - 2.00 (~5H, m, H^{3a}, H^{3b} and CH_3). δ_C NMR (400 MHz, D_2O) 174.6 (1C, *C*OCH_3), 174.4 (1C, C^1), 96.4 (1C, C^2),70.7, 69.4 (2C, C^6 and C^8), 67.8 (1C, C^7) 66.0 (1C, C^4), 63.2 (1C, C^9), 53.3 (1C, C^5), 38.6 (1C, C^3), 22.0 (1C, CH_3).

NB: The peaks at ~4.3 ppm and ~1.25 ppm in the ^{1}H NMR are TEA impurities

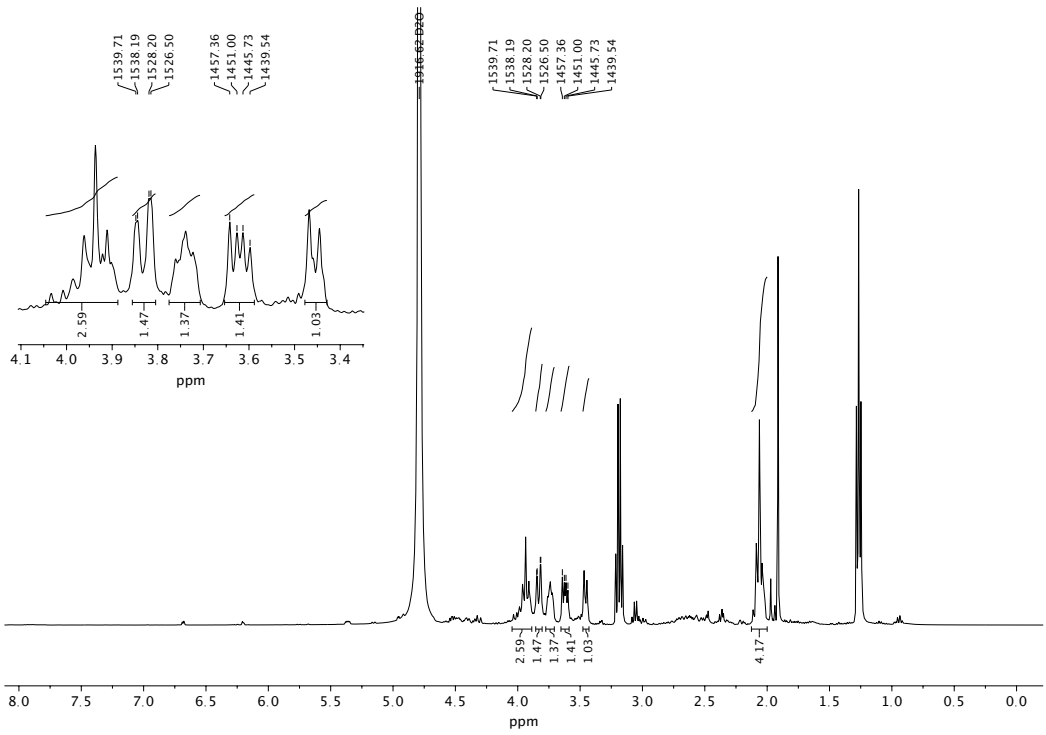

Figure E4.10. ^{1}H NMR of 2-amino-2-deoxy-*N*-acetyl-D-neuraminic acid

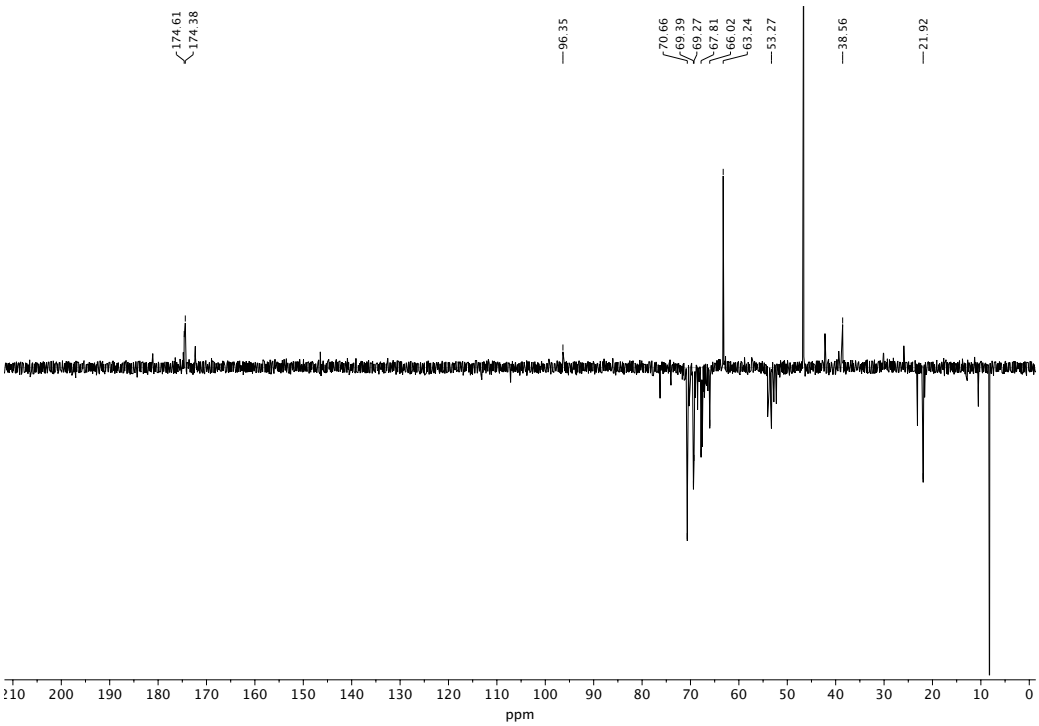

Figure E4.11. ^{13}C NMR of 2-amino-2-deoxy-*N*-acetyl-D-neuraminic acid

Recombinant Expression and Purification of truncated SARS-COV-2 Spike S1 Protein (first 300 amino acids) in E. coli.

(All data reported in the chapter/Appendix 4 uses this protein, not that from HEK293 expression (detailed below), unless specified).

A pET21a plasmid encoding for a hexahistidine-tag, SUMO-tag and the first 300 amino acids of SARS-COV-2 was purchased from Genscript Inc. The plasmid was transformed into competent *Escherichia coli* BL21(DE3) cells (New England Biolabs). A colony was selected to inoculate 100 mL of LB-medium containing 100 $\mu g.mL^{-1}$ kanamycin and was grown overnight at 37 ℃ under continuous shaking of 180 rpm. The following day, 10 mL of the preculture was added to 1 L of LB-medium (supplemented with 100 $\mu g.mL^{-1}$ kanamycin) in a 2.5 L Ultra Yield™ flask and grown at 37 ℃ with a shaking speed of 180 rpm till an OD_{600} of 0.6 was reached. The temperature was then reduced to 16 ℃ and the cells incubated for another hour before adding IPTG to a final concentration of 0.2 mM. The overexpression of the protein was allowed to take place overnight following which the cells were centrifuged at 5000 g for 10 minutes at 4 ℃. Pelleted cells were resuspended in PBS supplemented with Pierce protease inhibitor mini-tablets. The suspension was passed through a STANSTED "Pressure Cell" FPG12800 homogenizer in order to lyse the cells. The cell lysate was centrifuged at 48,000 g and the supernatant was passed through a 0.45 µm filter before being added to a 3 mL column of IMAC cOmplete His-Tag Purification Resin (Roche) pre-equilibrated with PBS. The column was washed with 20 column volumes of PBS. Bound protein was eluted using 6 mL of 300 mM Imidazole in PBS. Further purification of was achieved using a HiLoad 16/600 Superdex 200 pg gel-filtration column (GE Healthcare) with PBS as the running buffer. Purity was estimated using SDS-PAGE and protein concentration determined using Thermo Scientific Pierce BCA assay kit. Various volumes of the protein contained in PBS solution were aliquoted into 1.5 mL microcentrifuge tubes and snap-frozen in liquid nitrogen to store at -80 °C until required.

Protein sequence expressed (N-terminal polyhistidine and SUMO tags with the first 300 amino acids of the spike protein);

MGSSHHHHHHGSGMSDSEVNQEAKPEVKPEVKPETHINLKVSDGSSEIFFKI
KKTTPLRRLMEAFAKRQGKEMDSLRFLYDGIRIQADQTPEDLDMEDNDIIEA

HREQIGGGSEFELMFVFLVLLPLVSSQCVNLTTRTQLPPAYTNSFTRGVYYP
DKVFRSSVLHSTQDLFLPFFSNVTWFHAIHVSGTNGTKRFDNPVLPFNDGVY
FASTEKSNIIRGWIFGTTLDSKTQSLLIVNNATNVVIKVCEFQFCNDPFLGVY
YHKNNKSWMESEFRVYSSANNCTFEYVSQPFLMDLEGKQGNFKNLREFVF
KNIDGYFKIYSKHTPINLVRDLPQGFSALEPLVDLPIGINITRFQTLLALHRSYL
TPGDSSSGWTAGAAAYYVGYLQPRTFLLKYNENGTITDAVDCALDPLSETK

NB: The 300 amino acids of the spike protein are underlined

SARS-COV-2 spike protein variants

In order to establish whether the glycan flow-through concept was capable of detecting new variants of SARS-COV-2, a number of truncated recombinant spike proteins containing mutations associated with SARS-COV-2 variants were expressed (in *E. coli*). The plasmids encoding the variants were purchased from Genscript Inc and expressed using the above protocol (entitled *Recombinant Expression and Purification of truncated SARS-COV-2 Spike S1 Protein (first 300 amino acids) in E. coli).*

First detection location	PANGO lineage	Relevant mutations
Brazil	P.1	L18F, T20N, P26S, D138Y, R190S
United Kingdom	B.1.1.7	H69-V70 deletion, Y144 deletion
South Africa	B.1.351	L18F, D80A, D215G, R246I

Table E4.2. SARS-COV-2 spike protein variants

Expression and purification of SARS-COV-2 Spike S1 in HEK293 Cells

(reproduced from[49] where we previously expressed this protein)

Codon-optimised SARS-COV-2 Spike S1 subunit (amino acids 1-685) with a C-terminal 10x polyhistidine tag was expressed under control of a CMV promoter (pCMV3-S1-10xHis, Sino Biological, #VG40591-CH). HEK293 cells were grown in suspension to a density of 1.0 x 10^6 cells/mL in FreeStyle 293 Expression Medium (Thermo Scientific, #12338018), then transfected with 0.5 µg of pCMV3-S1-10xHis, 1.5 µg of linear polyethyleneimine (Alfa Aesar, #43896.01) and 50 µL Opti-MEM-I per 1 mL of cells (Thermo Scientific, #31985-062). After transfection, cells were grown to a density of 2.0 x 10^6 cells/mL and supplemented with 4 mM valproic acid (Sigma Aldrich, #P4543). 96 hours post transfection, the media was cleared by centrifugation, 6,000 x g in a Fiberlite F10-4 x 1000 LEX rotor (Thermo Scientific, #096-041053) for 10 minutes.

To purify Spike S1, cleared media was adjusted to 20 mM HEPES pH 7.5 and 10 mM imidazole, and was loaded on to a 5 mL HisTrap HP column (cytiva, #17524801) at a flow rate of 20 mL/min for ~16 hours. A purification buffer comprising 20 mM HEPES, 300 mM NaCl and 1 mM DTT +/- 1 M imidazole was used (for buffer lines A and B respectively), and the column was washed with 30 CVs of 2% buffer B (20 mM imidazole) before eluting the protein over a 2 - 50% gradient over 30 CVs. Fractions containing Spike S1 were pooled and concentrated using a 10 KDa molecular-weight cut-off spin concentrator (Sigma Aldrich, #UFC910008), before being buffer exchanged into 20 mM HEPES 7.5, 300 mM NaCl, 10% glycerol using a 5 mL HiTrap desalting column (cytiva, #29048684). Peak fractions were pooled, and the final concentration was measured by absorbance at 280 nm, yielding a concentration of 1.25 mg/mL. Aliquots of protein were snap-frozen in liquid nitrogen and stored at -80 °C.

The protein produced by this method (*Expression and purification of SARS-COV-2 Spike S1 in HEK293 Cells*) was used to check new gold nanoparticle batches and cassettes produced during the initial development of this work and for the Tergitol experiments (Figure 4.2C). *E. coli* expressed spike protein was used for all other analysis, as this enabled variant sequences to be expressed, ensuring consistency.

4.6.4 Flow-Through Cassette Production, Running and Analysis Protocols

Flow-Through Cassette Production, Running and Analysis Protocols

The following Flow-through Cassette buffers have been previously reported,[49] but have been provided for the reader. Minor optimisations have been made to the other protocols, so the full procedure has been provided for clarity.

Protocol for Manufacturing Flow-Through Cassettes

Nitrocellulose was added to the backing card by attaching the plastic backing of the nitrocellulose to the self-adhesive on the card. The wick material was then added to the backing card so it overlaps with the nitrocellulose by ~5 mm. The strips were then cut to size of width ~3 mm so they sit in the cassettes without the need for excess force to fit. The conjugate pad was added to the backing card, so it overlaps with the nitrocellulose by ~3.5 mm. The sample pad, was cut to size of 20 mm by 6 mm and was added to the backing card, overlapping with the conjugate pad by ~6.5 mm and straddling the backing card evenly. The completed strip was then added to the cassettes and sealed.

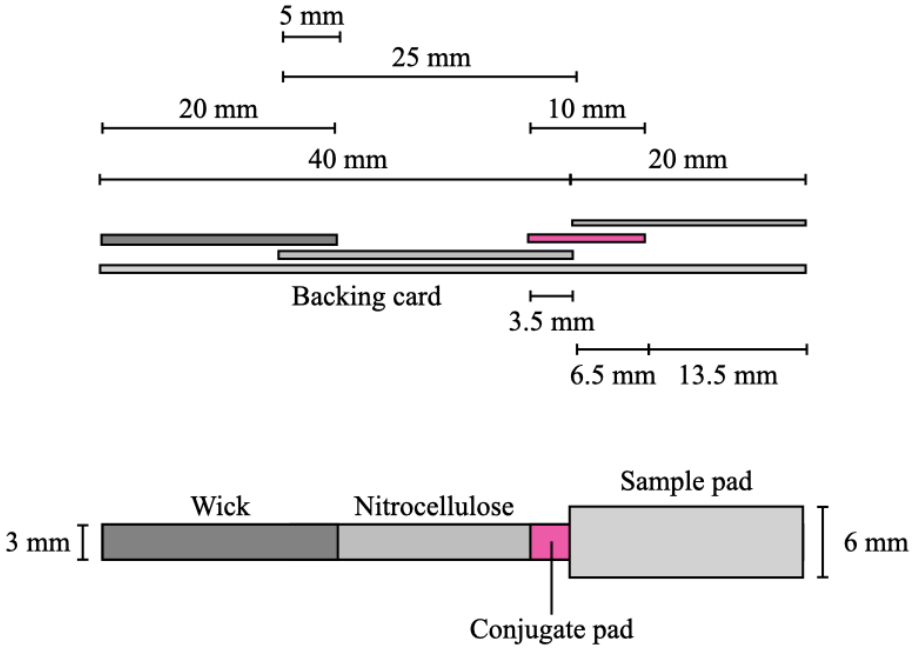

Figure E4.12. Flow-through complete strip dimensions

Protocol for Conjugate Pad Production

Strips of the conjugate pad material were agitated for 30 minutes in a solution of 0.1% Tween-20 (blocking solution). The strips were then patted dry and baked overnight at 37 °C in an oven. The conjugate pads were cut to size (3 mm width) and placed individually into the wells of a 384-well microplate. 20 µL 1× conjugate pad buffer solution containing OD3 (unless otherwise specified) AuNPs was added to the top of each conjugate pad in the wells. The pads were dried overnight at 37 °C in an oven. The completed pads were stored in an airtight box containing desiccant until addition to the strips.

10× Conjugate Pad Buffer

10% w/v. of poly(vinyl pyrrolidone)$_{400}$ (Average Mw ~40,000 g.mol^{-1}), 50% w/v. trehalose, 10% w/v. sucrose and 0.1% w/v. Tween-20 were added to distilled water and allowed to dissolve.

Control Line Addition

Control lines of 1 µL of RCA$_{120}$ were added to the nitrocellulose strips using a micropipette fitted with a 10 µL tip. A control line was added ~1.5 cm from the non-

wick end of the nitrocellulose surface. The strips were dried at 37 °C in an oven for 30 minutes.

Sample Line Addition

Sample lines of 1 µL were added to the nitrocellulose strip using a micropipette fitted with a 10 µL tip, the sample was spotted ~1 cm from the non-wick end of the nitrocellulose surface. The strips were dried at 37 °C in an oven as described in the figures.

Protocol for running flow-through tests

10 µL 10× HEPES buffer (20% PVP_{400}) was added to 90 µL distilled water. 100 µL was added to the cassette well and allowed to absorb. The test was run for X minutes, as described in the figures, before photos were taken.

Silver Staining Procedure

Staining solution was prepared following the kit guidelines. 50 µL of solution A and 50 µL of solution B were mixed and added to the cassette well. The test was run for X minutes, as described in the figures, before photos were taken.

Flow-through assay buffer - 10× HEPES buffer (20% PVP_{400}) in 100 mL H_2O

2.38 g (100 $mmoldm^{-3}$) of HEPES, 8.77 g (1.50 $moldm^{-3}$) of NaCl, 0.011 g (1.0 $mmoldm^{-3}$) of $CaCl_2$, 0.8 g (0.8% w/v., 123 $mmoldm^{-3}$) of NaN_3, 0.5 g (0.5% w/v., 4.07 $mmoldm^{-3}$) of Tween-20 and 20 g (20% w/v.) of poly(vinyl pyrrolidone)$_{400}$ (PVP_{400}, Average Mw ~40,000) was dissolved in 100 mL of water. The buffer is not pH adjusted.

Protocol for analysing flow-through tests to determine signal intensity and intensity change

Images collected were analysed in Image J 1.51 using the plot profile function to create a data set exported to Microsoft Excel for Mac. The data was exported to Origin 2019 64Bit and trimmed to remove pixel data not from the strip surface. The data was then reduced by number of groups to 100 data points (just the nitrocellulose surface) and plotted as Grey value (scale) vs Relative distance along the 100 data points.

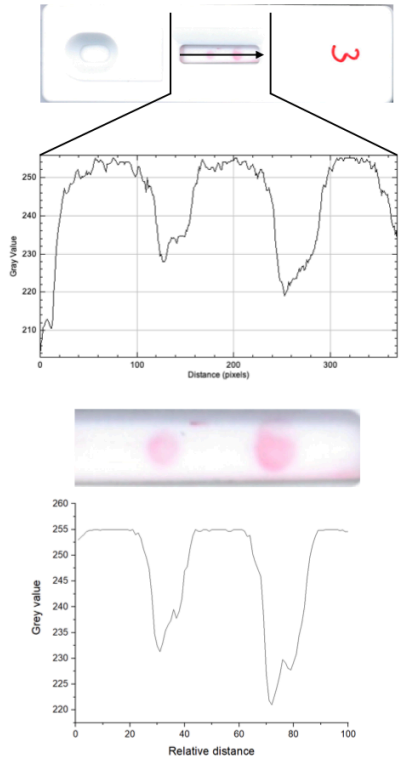

Figure E4.13. Representative cassette (Top), raw grey value plot (Middle) and processed grey value plot (Bottom)

Relative distance pixel 1 to 50 and 51 to 100 (area around the test line and control line, respectively), excluding pixels that contributed to the signal peaks were averaged (mean). This average was subtracted from the lowest grey value between 1 to 50 (test spot) and 51 to 100 (control spot) respectively. To determine the change after silver staining, the signal intensity before and after silver staining was calculated and subtracted from one another to give Intensity Change (Figure 4.4D).

4.7 Ethics

This study used remnant elutions from nasal swab samples routinely collected from symptomatic staff/patients at the University Hospital Coventry and Warwickshire NHS Trust and tested by standard PCR protocols employing the Abbott RealTime SARS-COV-2 assay (09N77-095) during April-September 2020. As this was an evaluation study using left-over anonymised material (which had been heat-treated to render acellular) no written informed consent was required/obtained, although the project was registered with the local COVID-19 research committee.

4.8 References

(1) World Health Organization. WHO Coronavirus Disease (COVID-19) Dashboard | WHO Coronavirus Disease (COVID-19) Dashboard https://covid19.who.int/ (accessed Dec 16, 2020).

(2) Zhou, P.; Yang, X.-L.; Wang, X.-G.; Hu, B.; Zhang, L.; Zhang, W.; Si, H.-R.; Zhu, Y.; Li, B.; Huang, C.-L.; Chen, H.-D.; Chen, J.; Luo, Y.; Guo, H.; Jiang, R.-D.; Liu, M.-Q.; Chen, Y.; Shen, X.-R.; Wang, X.; Zheng, X.-S.; Zhao, K.; Chen, Q.-J.; Deng, F.; Liu, L.-L.; Yan, B.; Zhan, F.-X.; Wang, Y.-Y.; Xiao, G.-F.; Shi, Z.-L. A Pneumonia Outbreak Associated with a New Coronavirus of Probable Bat Origin. *Nature* **2020**, *579* (7798), 270–273.

(3) Carter, L. J.; Garner, L. V.; Smoot, J. W.; Li, Y.; Zhou, Q.; Saveson, C. J.; Sasso, J. M.; Gregg, A. C.; Soares, D. J.; Beskid, T. R.; Jervey, S. R.; Liu, C. Assay Techniques and Test Development for COVID-19 Diagnosis. *ACS Central Science* **2020**, *6* (5), 591–605.

(4) Yüce, M.; Filiztekin, E.; Özkaya, K. G. COVID-19 Diagnosis —A Review of Current Methods. *Biosensors and Bioelectronics* **2021**, *172*, 112752.

(5) World Health Organization. *Laboratory Testing for 2019 Novel Coronavirus (2019-NCoV) in Suspected Human Cases - Interim Guidance - 17 January 2020*; 2020.

(6) World Health Organization. *Laboratory Testing for Coronavirus Disease (COVID-19) in Suspected Human Cases - Interim Guidance - 19 March 2020*; 2020.

(7) Xie, X.; Zhong, Z.; Zhao, W.; Zheng, C.; Wang, F.; Liu, J. Chest CT for Typical Coronavirus Disease 2019 (COVID-19) Pneumonia: Relationship to Negative RT-PCR Testing. *Radiology* **2020**, *296* (2), E41–E45.

(8) Lazer, D.; Baum, M. A.; Quintana, A.; Druckman, J.; Della, J.; Simonson, M. *The State Of The Nation: A 50-State Covid-19 Survey - Report #8: Failing the Test: Waiting Times for COVID Diagnostic Tests Across The U.S*; 2020.

(9) Hannah Ritchie; Mathieu, E.; Rodés-Guirao, L.; Appel, C.; Giattino, C.; Ortiz-Ospina, E.; Hasell, J.; Macdonald, B.; Beltekian, D.; Roser, M. Coronavirus Pandemic (COVID-19) Statistics and Research https://ourworldindata.org/coronavirus (accessed Jul 31, 2020).

(10) Abedini, Z.; Sari, A. A.; Foroushani, A. R.; Jaafaripooyan, E. Diffusion of Advanced Medical Imaging Technology, CT, and MRI Scanners, in Iran: A Qualitative Study of Determinants. *The International Journal of Health Planning and Management* **2019**, *34* (1), e397–e410.

(11) Mahdavi, A.; Khalili, N.; Davarpanah, A. H.; Faghihi, T.; Mahdavi, A.; Haseli, S.; Sabri, A.; Kahkouee, S.; Kazemi, M. A.; Mehrian, P.; Falahati, F.; Bakhshayeshkaram, M.; Sanei Taheri, M. Radiologic Management of COVID-19: Preliminary Experience of the Iranian Society of Radiology COVID-19 Consultant Group (ISRCC). *Iranian Journal of Radiology* **2020**, *17* (2), e102324.

(12) Fields, B. K. K.; Demirjian, N. L.; Gholamrezanezhad, A. Coronavirus Disease 2019 (COVID-19) Diagnostic Technologies: A Country-Based Retrospective Analysis of Screening and Containment Procedures during the First Wave of the Pandemic. *Clinical Imaging* **2020**, *67*, 219–225.

(13) Gibani, M. M.; Toumazou, C.; Sohbati, M.; Sahoo, R.; Karvela, M.; Hon, T.-K.; De Mateo, S.; Burdett, A.; Leung, K. Y. F.; Barnett, J.; Orbeladze, A.; Luan, S.; Pournias, S.; Sun, J.; Flower, B.; Bedzo-Nutakor, J.; Amran, M.; Quinlan, R.; Skolimowska, K.; Herrera, C.; Rowan, A.; Badhan, A.; Klaber, R.; Davies, G.; Muir, D.; Randell, P.; Crook, D.; Taylor, G. P.; Barclay, W.; Mughal, N.; Moore, L. S. P.; Jeffery, K.; Cooke, G. S. Assessing a Novel, Lab-Free, Point-of-Care Test for SARS-CoV-2 (CovidNudge): A Diagnostic Accuracy Study. *The Lancet Microbe* **2020**, *1* (7), e300–e307.

(14) Park, G.-S.; Ku, K.; Baek, S.-H.; Kim, S.-J.; Kim, S. Il; Kim, B.-T.; Maeng, J.-S. Development of Reverse Transcription Loop-Mediated Isothermal Amplification Assays Targeting Severe Acute Respiratory Syndrome Coronavirus 2 (SARS-CoV-2). *The Journal of Molecular Diagnostics* **2020**, *22* (6), 729–735.

(15) Peto, L.; Rodger, G.; Carter, D. P.; Osman, K. L.; Yavuz, M.; Johnson, K.; Raza, M.; Parker, M. D.; Wyles, M. D.; Andersson, M.; Justice, A.; Vaughan, A.; Hoosdally, S.; Stoesser, N.; Matthews, P. C.; Eyre, D. W.; Peto, T. E. A.; Carroll, M. W.; de Silva, T. I.; Crook, D. W.; Evans, C. M.; Pullan, S. T. Diagnosis of SARS-CoV-2 Infection with LamPORE, a High-Throughput Platform Combining Loop-Mediated Isothermal Amplification and Nanopore Sequencing. *Journal of Clinical Microbiology* **2021**, *59* (6), e03271-20.

(16) Jiang, N.; Tansukawat, N. D.; Gonzalez-Macia, L.; Ates, H. C.; Dincer, C.; Güder, F.; Tasoglu, S.; Yetisen, A. K. Low-Cost Optical Assays for Point-of-Care Diagnosis in Resource-Limited Settings. *ACS Sensors* **2021**, *6* (6), 2108–2124.

(17) Crane, M. M.; Organon MV. *Diagnostic Test Device - US3579306A*; 1969.

(18) Xu, F.; Jin, Z.; Zou, S.; Chen, C.; Song, Q.; Deng, S.; Xiao, W.; Zhang, X.; Jia, A.; Tang, Y. EuNPs-MAb Fluorescent Probe Based Immunochromatographic Strip for Rapid and Sensitive Detection of Porcine Epidemic Diarrhea Virus. *Talanta* **2020**, *214*, 120865.

(19) Ezennia, I. J.; Nduka, S. O.; Ekwunife, O. I. Cost Benefit Analysis of Malaria Rapid Diagnostic Test: The Perspective of Nigerian Community Pharmacists. *Malaria Journal* **2017**, *16* (1), 7–16.

(20) Tawiah, T.; Hansen, K. S.; Baiden, F.; Bruce, J.; Tivura, M.; Delimini, R.; Amengo-Etego, S.; Chandramohan, D.; Owusu-Agyei, S.; Webster, J. Cost-Effectiveness Analysis of Test-Based versus Presumptive Treatment of Uncomplicated Malaria in Children under Five Years in an Area of High Transmission in Central Ghana. *PLOS ONE* **2016**, *11* (10), e0164055.

(21) Aerts, C.; Vink, M.; Pashtoon, S. J.; Nahzat, S.; Picado, A.; Cruz, I.; Sicuri, E. Cost Effectiveness of New Diagnostic Tools for Cutaneous Leishmaniasis in Afghanistan. *Applied Health Economics and Health Policy* **2019**, *17* (2), 213–230.

(22) Phan, J. C.; Pettitt, J.; George, J. S.; Fakoli, L. S.; Taweh, F. M.; Bateman, S. L.; Bennett, R. S.; Norris, S. L.; Spinnler, D. A.; Pimentel, G.; Sahr, P. K.; Bolay, F. K.; Schoepp, R. J. Lateral Flow Immunoassays for Ebola Virus Disease Detection in Liberia. *Journal of Infectious Diseases* **2016**, *214* (suppl 3), S222–S228.

(23) St John, A.; Price, C. P. Point-of-Care Testing Technologies Existing and Emerging Technologies for Point-of-Care Testing. *Clin Biochem Rev* **2014**, *35* (3), 155–167.

(24) Müller, M.; Derlet, P. M.; Mudry, C.; Aeppli, G. Testing of Asymptomatic Individuals for Fast Feedback-Control of COVID-19 Pandemic. *Physical Biology* **2020**, *17* (6), 065007.

(25) Moghadas, S. M.; Fitzpatrick, M. C.; Sah, P.; Pandey, A.; Shoukat, A.; Singer, B. H.; Galvani, A. P. The Implications of Silent Transmission for the Control of COVID-19

Outbreaks. *Proceedings of the National Academy of Sciences* **2020**, *117* (30), 17513–17515.

(26) Lavezzo, E.; Franchin, E.; Ciavarella, C.; Cuomo-Dannenburg, G.; Barzon, L.; Del Vecchio, C.; Rossi, L.; Manganelli, R.; Loregian, A.; Navarin, N.; Abate, D.; Sciro, M.; Merigliano, S.; De Canale, E.; Vanuzzo, M. C.; Besutti, V.; Saluzzo, F.; Onelia, F.; Pacenti, M.; Parisi, S. G.; Carretta, G.; Donato, D.; Flor, L.; Cocchio, S.; Masi, G.; Sperduti, A.; Cattarino, L.; Salvador, R.; Nicoletti, M.; Caldart, F.; Castelli, G.; Nieddu, E.; Labella, B.; Fava, L.; Drigo, M.; Gaythorpe, K. A. M.; Brazzale, A. R.; Toppo, S.; Trevisan, M.; Baldo, V.; Donnelly, C. A.; Ferguson, N. M.; Dorigatti, I.; Crisanti, A. Suppression of a SARS-CoV-2 Outbreak in the Italian Municipality of Vo'. *Nature* **2020**, *584* (7821), 425–429.

(27) Ferguson, J.; Dunn, S.; Best, A.; Mirza, J.; Percival, B.; Mayhew, M.; Megram, O.; Ashford, F.; White, T.; Moles-Garcia, E.; Crawford, L.; Plant, T.; Bosworth, A.; Kidd, M.; Richter, A.; Deeks, J.; McNally, A. Validation Testing to Determine the Sensitivity of Lateral Flow Testing for Asymptomatic SARS-CoV-2 Detection in Low Prevalence Settings: Testing Frequency and Public Health Messaging Is Key. *Plos Biology* **2021**, *19* (4), e3001216.

(28) Li, Z.; Yi, Y.; Luo, X.; Xiong, N.; Liu, Y.; Li, S.; Sun, R.; Wang, Y.; Hu, B.; Chen, W.; Zhang, Y.; Wang, J.; Huang, B.; Lin, Y.; Yang, J.; Cai, W.; Wang, X.; Cheng, J.; Chen, Z.; Sun, K.; Pan, W.; Zhan, Z.; Chen, L.; Ye, F. Development and Clinical Application of a Rapid IgM-IgG Combined Antibody Test for SARS-CoV-2 Infection Diagnosis. *Journal of Medical Virology* **2020**, *92* (9), 1518−1524.

(29) Liu, Y.; Liu, Y.-P.; Diao, B.; Ding, J.-Y.; Yuan, M.-X.; Ren, F.-F.; Wang, Y.; Huang, Q.-C. Diagnostic Indexes of a Rapid Immunoglobulin G/Immunoglobulin M Combined Antibody Test for Severe Acute Respiratory Syndrome Coronavirus 2. *Chinese medical journal* **2020**, *134* (4), 475–477.

(30) Wen, T.; Huang, C.; Shi, F.-J.; Zeng, X.-Y.; Lu, T.; Ding, S.-N.; Jiao, Y.-J. Development of a Lateral Flow Immunoassay Strip for Rapid Detection of IgG Antibody against SARS-CoV-2 Virus. *The Analyst* **2020**, *145* (15), 5345–5352.

(31) Department of Health and Social Care. First wave of non-machine based lateral flow technology (LFT) assessment - GOV.UK https://www.gov.uk/government/publications/assessment-and-procurement-of-

coronavirus-covid-19-tests/lateral-flow-devices-results#test-1-sd-biosensor-lateral-flow-test (accessed Nov 5, 2020).

(32) World Health organization. Global partnership to make available 120 million affordable, quality COVID-19 rapid tests for low- and middle-income countries https://www.who.int/news/item/28-09-2020-global-partnership-to-make-available-120-million-affordable-quality-covid-19-rapid-tests-for-low--and-middle-income-countries (accessed Nov 5, 2020).

(33) United States Food & Drug Administration. *BinaxNOW COVID-19 Ag Card - FDA Letter of Authorization*; 2020.

(34) United States Food & Drug Administration. *CareStart COVID-19 Antigen Test - FDA Letter of Authorization*; 2020.

(35) Ferguson, J.; Dunn, S.; Best, A.; Mirza, J.; Percival, B.; Mayhew, M.; Megram, O.; Ashford, F.; White, T.; Moles-Garcia, E.; Crawford, L.; Plant, T.; Bosworth, A.; Kidd, M.; Richter, A.; Deeks, J.; McNally, A. Validation Testing to Determine the Sensitivity of Lateral Flow Testing for Asymptomatic SARS-CoV-2 Detection in Low Prevalence Settings: Testing Frequency and Public Health Messaging Is Key. *Plos Biology* **2021**, *19* (4), e3001216.

(36) Mao, X.; Ma, Y.; Zhang, A.; Zhang, L.; Zeng, L.; Liu, G. Disposable Nucleic Acid Biosensors Based on Gold Nanoparticle Probes and Lateral Flow Strip. *Analytical Chemistry* **2009**, *81* (4), 1660–1668.

(37) Damborský, P.; Koczula, K. M.; Gallotta, A.; Katrlík, J. Lectin-Based Lateral Flow Assay: Proof-of-Concept. *The Analyst* **2016**, *141* (23), 6444–6448.

(38) Ströh, L. J.; Stehle, T. Glycan Engagement by Viruses: Receptor Switches and Specificity. *Annual Review of Virology* **2014**, *1* (1), 285–306.

(39) Olofsson, S.; Bergström, T. Glycoconjugate Glycans as Viral Receptors. *Annals of Medicine* **2005**, *37* (3), 154–172.

(40) Viswanathan, K.; Chandrasekaran, A.; Srinivasan, A.; Raman, R.; Sasisekharan, V.; Sasisekharan, R. Glycans as Receptors for Influenza Pathogenesis. *Glycoconjugate journal* **2010**, *27* (6), 561–570.

(41) Gilboa-Garber, N. [32] Pseudomonas Aeruginosa Lectins. In *Methods in Enzymology*; Academic Press, 1982; Vol. 83, pp 378–385.

(42) Diggle, S. P.; Stacey, R. E.; Dodd, C.; Cámara, M.; Williams, P.; Winzer, K. The Galactophilic Lectin, LecA, Contributes to Biofilm Development in Pseudomonas Aeruginosa. *Environmental Microbiology* **2006**, *8* (6), 1095–1104.

(43) Jorgensen, P.; Chanthap, L.; Rebueno, A.; Tsuyuoka, R.; Bell, D. Malaria Rapid Diagnostic Tests in Tropical Climates: The Need for a Cool Chain. *American Journal of Tropical Medicine and Hygiene* **2006**, *74* (5), 750–754.

(44) Compostella, F.; Pitirollo, O.; Silvestri, A.; Polito, L. Glyco-Gold Nanoparticles: Synthesis and Applications. *Beilstein Journal of Organic Chemistry* **2017**, *13*, 1008–1021.

(45) Richards, S.-J.; Keenan, T.; Vendeville, J.-B. B.; Wheatley, D. E.; Chidwick, H.; Budhadev, D.; Council, C. E.; Webster, C. S.; Ledru, H.; Baker, A. N.; Walker, M.; Galan, M. C.; Linclau, B.; Fascione, M. A.; Gibson, M. I. Introducing Affinity and Selectivity into Galectin-Targeting Nanoparticles with Fluorinated Glycan Ligands. *Chemical Science* **2021**, *12* (3), 905–910.

(46) Schofield, C. L.; Mukhopadhyay, B.; Hardy, S. M.; McDonnell, M. B.; Field, R. A.; Russell, D. A. Colorimetric Detection of Ricinus Communis Agglutinin 120 Using Optimally Presented Carbohydrate-Stabilised Gold Nanoparticles. *The Analyst* **2008**, *133* (5), 626–634.

(47) Pancaro, A.; Szymonik, M.; Georgiou, P. G.; Baker, A. N.; Walker, M.; Adriaensens, P.; Hendrix, J.; Gibson, M. I.; Nelissen, I. The Polymeric Glyco-Linker Controls the Signal Outputs for Plasmonic Gold Nanorod Biosensors Due to Biocorona Formation. *Nanoscale* **2021**, *13* (24), 10837–10848.

(48) Ishii, J.; Toyoshima, M.; Chikae, M.; Takamura, Y.; Miura, Y. Preparation of Glycopolymer-Modified Gold Nanoparticles and a New Approach for a Lateral Flow Assay. *Bulletin of the Chemical Society of Japan* **2011**, *84* (5), 466–470.

(49) Baker, A. N.; Richards, S.-J.; Guy, C. S.; Congdon, T. R.; Hasan, M.; Zwetsloot, A. J.; Gallo, A.; Lewandowski, J. R.; Stansfeld, P. J.; Straube, A.; Walker, M.; Chessa, S.; Pergolizzi, G.; Dedola, S.; Field, R. A.; Gibson, M. I. The SARS-COV-2 Spike Protein Binds Sialic Acids and Enables Rapid Detection in a Lateral Flow Point of Care Diagnostic Device. *ACS Central Science* **2020**, *6* (11), 2046–2052.

(50) Alejandra Tortorici, M.; Walls, A. C.; Lang, Y.; Wang, C.; Li, Z.; Koerhuis, D.; Boons, G. J.; Bosch, B. J.; Rey, F. A.; de Groot, R. J.; Veesler, D. Structural Basis for Human Coronavirus Attachment to Sialic Acid Receptors. *Nature Structural and Molecular Biology* **2019**, *26* (6), 481–489.

(51) Huang, X.; Dong, W.; Milewska, A.; Golda, A.; Qi, Y.; Zhu, Q. K.; Marasco, W. A.; Baric, R. S.; Sims, A. C.; Pyrc, K.; Li, W.; Sui, J. Human Coronavirus HKU1 Spike Protein Uses O -Acetylated Sialic Acid as an Attachment Receptor Determinant and Employs Hemagglutinin-Esterase Protein as a Receptor-Destroying Enzyme. *Journal of Virology* **2015**, *89* (14), 7202–7213.

(52) Park, Y. J.; Walls, A. C.; Wang, Z.; Sauer, M. M.; Li, W.; Tortorici, M. A.; Bosch, B. J.; DiMaio, F.; Veesler, D. Structures of MERS-CoV Spike Glycoprotein in Complex with Sialoside Attachment Receptors. *Nature Structural and Molecular Biology* **2019**, *26* (12), 1151–1157.

(53) Chu, H.; Hu, B.; Huang, X.; Chai, Y.; Wang, Y.; Shuai, H.; Yang, D.; Hou, Y.; Zhang, X.; Yuen, T. T.-T.; Cai, J.-P.; Zhang, A. J.; Zhou, J.; Yuan, S.; To, K. K.-W.; Chan, I. H.-Y.; Sit, K.-Y.; Foo, D. C.-C.; Wong, I. Y.-H.; Ng, A. T.-L.; Cheung, T. T.; Law, S. Y.-K.; Au, W.-K.; Kok, K.-H.; Chan, J. F.-W.; Yuen, K.-Y. Host and Viral Determinants for Efficient SARS-CoV-2 Infection of the Human Lung. *Nature Communications* **2020**, *12* (1), 134.

(54) Buchanan, C. J.; Gaunt, B.; Harrison, P. J.; Bas, A. Le; Khan, A.; Giltrap, A. M.; Ward, P. N.; Dumoux, M.; Daga, S.; Picchiotti, N.; Baldassarri, M.; Benetti, E.; Fallerini, C.; Fava, F.; Giliberti, A.; Koukos, P. I.; Lakshminarayanan, A.; Xue, X.; Papadakis, G.; Deimel, L. P.; Casablancas-Antras, V.; Claridge, T. D. W.; Bonvin, A. M. J. J.; Sattentau, Q. J.; Furini, S.; Gori, M.; Huo, J.; Owens, R. J.; Renieri, A.; Study, G.-C. M.; Naismith, J. H.; Baldwin, A.; Davis, B. G. Cryptic SARS-CoV2-Spike-with-Sugar Interactions Revealed by “universal” Saturation Transfer Analysis. *bioRxiv* **2021**, 2021.04.14.439284.

(55) Nguyen, L.; McCord, K. A.; Bui, D. T.; Bouwman, K. A.; Kitova, E. N.; Kumawat, D.; Daskan, G. C.; Tomris, I.; Han, L.; Chopra, P.; Yang, T.-J.; Williows, S. D.; Lowary, T. L.; West, L. J.; Hsu, S.-T. D.; Tompkins, S. M.; Boons, G.-J.; Mason, A. L.; Vries, R. P. de; Macauley, M. S.; Klassen, J. S. Sialic Acid-Dependent Binding and Viral Entry of SARS-CoV-2. *bioRxiv* **2021**, 2021.03.08.434228.

(56) Ryzhikov, A. B.; Onkhonova, G. S.; Imatdinov, I. R.; Gavrilova, E. V.; Maksyutov, R. A.; Gordeeva, E. A.; Pazynina, G. V.; Ryzhov, I. M.; Shilova, N. V.; Bovin, N. V. Recombinant SARS-CoV-2 S Protein Binds to Glycans of the Lactosamine Family in Vitro. *Biochemistry (Moscow)* **2021**, *86* (3), 243–247.

(57) Kwon, P. S.; Oh, H.; Kwon, S.-J.; Jin, W.; Zhang, F.; Fraser, K.; Hong, J. J.; Linhardt, R. J.; Dordick, J. S. Sulfated Polysaccharides Effectively Inhibit SARS-CoV-2 in Vitro. *Cell Discovery* **2020**, *6* (1), 50.

(58) Clausen, T. M.; Sandoval, D. R.; Spliid, C. B.; Pihl, J.; Perrett, H. R.; Painter, C. D.; Narayanan, A.; Majowicz, S. A.; Kwong, E. M.; McVicar, R. N.; Thacker, B. E.; Glass, C. A.; Yang, Z.; Torres, J. L.; Golden, G. J.; Bartels, P. L.; Porell, R. N.; Garretson, A. F.; Laubach, L.; Feldman, J.; Yin, X.; Pu, Y.; Hauser, B. M.; Caradonna, T. M.; Kellman, B. P.; Martino, C.; Gordts, P. L. S. M.; Chanda, S. K.; Schmidt, A. G.; Godula, K.; Leibel, S. L.; Jose, J.; Corbett, K. D.; Ward, A. B.; Carlin, A. F.; Esko, J. D. SARS-CoV-2 Infection Depends on Cellular Heparan Sulfate and ACE2. *Cell* **2020**, *183* (4), 1043-1057.e15.

(59) Mycroft-West, C. J.; Su, D.; Pagani, I.; Rudd, T. R.; Elli, S.; Gandhi, N. S.; Guimond, S. E.; Miller, G. J.; Meneghetti, M. C. Z.; Nader, H. B.; Li, Y.; Nunes, Q. M.; Procter, P.; Mancini, N.; Clementi, M.; Bisio, A.; Forsyth, N. R.; Ferro, V.; Turnbull, J. E.; Guerrini, M.; Fernig, D. G.; Vicenzi, E.; Yates, E. A.; Lima, M. A.; Skidmore, M. A. Heparin Inhibits Cellular Invasion by SARS-CoV-2: Structural Dependence of the Interaction of the Spike S1 Receptor-Binding Domain with Heparin. *Thrombosis and Haemostasis* **2020**, *120* (12), 1700–1715.

(60) Mehdipour, A. R.; Hummer, G. Dual Nature of Human ACE2 Glycosylation in Binding to SARS-CoV-2 Spike. *Proceedings of the National Academy of Sciences* **2021**, *118* (19), e2100425118.

(61) Richards, S.-J.; Gibson, M. I. Optimization of the Polymer Coating for Glycosylated Gold Nanoparticle Biosensors to Ensure Stability and Rapid Optical Readouts. *ACS Macro Letters* **2014**, *3* (10), 1004–1008.

(62) Zheng, M. Z.; Richard, J. L.; Binder, J. A Review of Rapid Methods for the Analysis of Mycotoxins. *Mycopathologia* **2006**, *161* (5), 261–273.

(63) Zheng, S.; Fan, J.; Yu, F.; Feng, B.; Lou, B.; Zou, Q.; Xie, G.; Lin, S.; Wang, R.; Yang, X.; Chen, W.; Wang, Q.; Zhang, D.; Liu, Y.; Gong, R.; Ma, Z.; Lu, S.; Xiao,

Y.; Gu, Y.; Zhang, J.; Yao, H.; Xu, K.; Lu, X.; Wei, G.; Zhou, J.; Fang, Q.; Cai, H.; Qiu, Y.; Sheng, J.; Chen, Y.; Liang, T. Viral Load Dynamics and Disease Severity in Patients Infected with SARS-CoV-2 in Zhejiang Province, China, January-March 2020: Retrospective Cohort Study. *BMJ* **2020**, *369*, m1443.

(64) Pan, Y.; Zhang, D.; Yang, P.; Poon, L. L. M.; Wang, Q. Viral Load of SARS-CoV-2 in Clinical Samples. *The Lancet Infectious Diseases* **2020**, *20* (4), 411–412.

(65) Geraerts, M.; Willems, S.; Baekelandt, V.; Debyser, Z.; Gijsbers, R. Comparison of Lentiviral Vector Titration Methods. *BMC Biotechnology* **2006**, *6* (1), 34.

(66) Richter, A.; Plant, T.; Kidd, M.; Bosworth, A.; Mayhew, M.; Megram, O.; Ashworth, F.; Crawford, L.; White, T.; Moles-Garcia, E.; Mirza, J.; Percival, B.; McNally, A. How to Establish an Academic SARS-CoV-2 Testing Laboratory. *Nature Microbiology* **2020**, *5* (12), 1452–1454.

(67) Public Health England. *SARS-CoV-2 Inactivation Testing: Interim Report (HCM/CoV2/025/v1 - 16 July 2020)*; 2020.

(68) Arnaout, R.; Lee, R. A.; Lee, G. R.; Callahan, C.; Cheng, A.; Yen, C. F.; Smith, K. P.; Arora, R.; Kirby, J. E. The Limit of Detection Matters: The Case for Benchmarking Severe Acute Respiratory Syndrome Coronavirus 2 Testing. *Clinical Infectious Diseases* **2021**, *73* (9), e3042-3046.

(69) PHE Porton Down & University of Oxford SARS-CoV-2 LFD test development and validation cell. *Preliminary Report from the Joint PHE Porton Down & University of Oxford SARS-CoV-2 Test Development and Validation Cell: Rapid Evaluation of Lateral Flow Viral Antigen Detection Devices (LFDs) for Mass Community Testing - 8th of November, 2020*; 2020.

(70) Rabaan, A. A.; Tirupathi, R.; Sule, A. A.; Aldali, J.; Mutair, A. Al; Alhumaid, S.; Muzaheed; Gupta, N.; Koritala, T.; Adhikari, R.; Bilal, M.; Dhawan, M.; Tiwari, R.; Mitra, S.; Emran, T. Bin; Dhama, K. Viral Dynamics and Real-Time RT-PCR Ct Values Correlation with Disease Severity in COVID-19. *Diagnostics* **2021**, *11* (6), 1091.

(71) Yu, F.; Yan, L.; Wang, N.; Guo, Y.; Zhang, F. Reply to Aquino-Jarquin. *Clinical Infectious Diseases* **2021**, *72* (8), 1490–1491.

(72) Berg, M. G.; Zhen, W.; Lucic, D.; Degli-Angeli, E. J.; Anderson, M.; Forberg, K.; Olivo, A.; Sheikh, F.; Toolsie, D.; Greninger, A. L.; Cloherty, G. A.; Coombs, R. W.; Berry, G. J. Development of the RealTime SARS-CoV-2 Quantitative Laboratory Developed Test and Correlation with Viral Culture as a Measure of Infectivity. *Journal of Clinical Virology* **2021**, *143*, 104945.

(73) Aquino-Jarquin, G. The Raw Cycle Threshold Values From Reverse-Transcription Polymerase Chain Reaction Detection Are Not Viral Load Quantitation Units. *Clinical Infectious Diseases* **2021**, *72* (8), 1489–1490.

(74) Klasse, P. J. Chapter Ten - Molecular Determinants of the Ratio of Inert to Infectious Virus Particles. In *Progress in Molecular Biology and Translational Science*; NIH Public Access, 2015; Vol. 129, pp 285–326.

(75) Schwerdt, C. E.; Fogh, J. The Ratio of Physical Particles per Infectious Unit Observed for Poliomyelitis Viruses. *Virology* **1957**, *4* (1), 41–52.

(76) Alfson, K. J.; Avena, L. E.; Beadles, M. W.; Staples, H.; Nunneley, J. W.; Ticer, A.; Dick, E. J.; Owston, M. A.; Reed, C.; Patterson, J. L.; Carrion, R.; Griffiths, A. Particle-to-PFU Ratio of Ebola Virus Influences Disease Course and Survival in Cynomolgus Macaques. *Journal of Virology* **2015**, *89* (13), 6773–6781.

(77) Buchanan, C. J.; Gaunt, B.; Harrison, P. J.; Bas, A. Le; Khan, A.; Giltrap, A. M.; Ward, P. N.; Dumoux, M.; Daga, S.; Picchiotti, N.; Baldassarri, M.; Benetti, E.; Fallerini, C.; Fava, F.; Giliberti, A.; Koukos, P. I.; Lakshminarayanan, A.; Xue, X.; Papadakis, G.; Deimel, L. P.; Casablancas-Antras, V.; Claridge, T. D. W.; Bonvin, A. M. J. J.; Sattentau, Q. J.; Furini, S.; Gori, M.; Huo, J.; Owens, R. J.; Renieri, A.; Study, G.-C. M.; Naismith, J. H.; Baldwin, A.; Davis, B. G. Cryptic SARS-CoV2-Spike-with-Sugar Interactions Revealed by “universal” Saturation Transfer Analysis. *bioRxiv* **2021**, 2021.04.14.439284.

(78) Childs, R. A.; Palma, A. S.; Wharton, S.; Matrosovich, T.; Liu, Y.; Chai, W.; Campanero-Rhodes, M. A.; Zhang, Y.; Eickmann, M.; Kiso, M.; Hay, A.; Matrosovich, M.; Feizi, T. Receptor-Binding Specificity of Pandemic Influenza A (H1N1) 2009 Virus Determined by Carbohydrate Microarray. *Nature Biotechnology* **2009**, *27* (9), 797–799.

(79) Marín, M. J.; Rashid, A.; Rejzek, M.; Fairhurst, S. A.; Wharton, S. A.; Martin, S. R.; McCauley, J. W.; Wileman, T.; Field, R. A.; Russell, D. A. Glyconanoparticles for the

Plasmonic Detection and Discrimination between Human and Avian Influenza Virus. *Organic & Biomolecular Chemistry* **2013**, *11* (41), 7101–7107.

(80) Richards, S.-J.; Baker, A. N.; Walker, M.; Gibson, M. I. Polymer-Stabilized Sialylated Nanoparticles: Synthesis, Optimization, and Differential Binding to Influenza Hemagglutinins. *Biomacromolecules* **2020**, *21* (4), 1604–1612.

(81) Jonges, M.; Liu, W. M.; van der Vries, E.; Jacobi, R.; Pronk, I.; Boog, C.; Koopmans, M.; Meijer, A.; Soethout, E. Influenza Virus Inactivation for Studies of Antigenicity and Phenotypic Neuraminidase Inhibitor Resistance Profiling. *Journal of clinical microbiology* **2010**, *48* (3), 928–940.

(82) PHE Porton Down & University of Oxford SARS-CoV-2 LFD test development and validation cell. *Preliminary Report from the Joint PHE Porton Down & University of Oxford SARS-CoV-2 Test Development and Validation Cell: Rapid Evaluation of Lateral Flow Viral Antigen Detection Devices (LFDs) for Mass Community Testing - 8th of November, 2020*; 2020.

(83) Kemp, S.; Datir, R.; Collier, D.; Ferreira, I.; Carabelli, A.; Harvey, W.; Robertson, D.; Gupta, R. Recurrent Emergence and Transmission of a SARS-CoV-2 Spike Deletion ΔH69/ΔV70. *bioRxiv* **2020**, 2020.12.14.422555.

(84) Abbott Molecular Inc. *Abbot RealTime SARS-CoV-2 Instructions for Use (Ref: 09N77-095)*; 2020.

(85) Bastús, N. G.; Comenge, J.; Puntes, V. Kinetically Controlled Seeded Growth Synthesis of Citrate-Stabilized Gold Nanoparticles of up to 200 Nm: Size Focusing versus Ostwald Ripening. *Langmuir* **2011**, *27* (17), 11098–11105.

(86) Haiss, W.; Thanh, N. T. K.; Aveyard, J.; Fernig, D. G. Determination of Size and Concentration of Gold Nanoparticles from UV - Vis Spectra. *Analytical Chemistry* **2007**, *79* (11), 4215–4221.

Chapter 5

End-Functionalised Poly(Vinyl Pyrrolidone) for Ligand Display in Lateral Flow Device Test Lines

5.1 Abstract

Lateral flow devices are rapid (and often low cost) point of care diagnostics – the classic example being the home pregnancy test. A test line (the stationary phase) is typically prepared by the physisorption of an antibody, which binds to analytes/antigens such as viruses, toxins, or hormones. However, there is no intrinsic requirement for the detection unit to be an antibody, and incorporating other ligand classes may bring new functionalities, or detection capabilities. To enable other (non-protein) ligands to be deployed in lateral flow devices, they must be physiosorbed to the stationary phase as a conjugate, which currently would be a high-molecular-weight carrier protein, which requires (challenging) chemoselective modifications and purification. Here, we demonstrate that poly(vinyl pyrrolidone), PVP, is a candidate for a polymeric, protein-free test line, owing to its unique balance of water solubility (for printing) and adhesion to the nitrocellulose stationary phase. End-functionalised PVPs were prepared by RAFT polymerisation and the model capture ligands of biotin and galactosamine were installed on PVP and subsequently immobilised on nitrocellulose. This polymeric test line was validated in both flow-through and full lateral flow formats using streptavidin and soybean agglutinin; and is the first demonstration of an "all polymer" approach for installation of capture units. This work illustrates the potential of polymeric scaffolds as anchoring agents for small molecule capture agents in the next generation of robust and modular lateral flow devices and that macromolecular engineering may provide real benefit.

5.2 Declaration

This paper has been submitted for publication as a paper discussing the synthesis and application of a synthetic glycopolymer for use as a test line in lateral flow and flow-through diagnostics for the detection of streptavidin and SBA.

Thomas Congdon and Panagiotis Georgiou help design the PVP synthesis, Sarah-Jane Richards assisted with running the lateral flow testing and Marc Walker supported the XPS analysis and supported model fitting the XPS data.

I synthesised the RAFT agent, the polymers, the gold particles; functionalised the polymers with glycans; characterised the polymer systems by NMR, SEC and FTIR; and characterised the particles by XPS. I designed, constructed, and ran the flow-through and lateral flow devices, and analysed the data from the devices.

Myself, Simone Dedola, Robert A. Field and Matthew Gibson were responsible for preparation of the manuscript.

A. N. Baker, T. R. Congdon, S-J. Richards, P. G. Georgiou, M. Walker, S. Dedola, R. A. Field, M. I. Gibson, *ACS Polym. Au,* 2021*, https://doi.org/10.1021/acspolymersau.1c00032*

5.3 Introduction

Lateral flow devices (LFDs) are point of care (POC) diagnostics that are suited to primary care, triage, and emergency applications.[1] The most widely known LFD is the home pregnancy test, which detects the presence of the hormone human chorionic gonadotrophin (HCG) in urine in under 20 minutes.[2,3] In these devices, the stationary phase of the LFD is nitrocellulose functionalised with an antibody that binds HCG. Gold nanoparticles (AuNPs) functionalised with the same antibody are in the mobile phase. This leads to the sandwiching of HCG between the immobilised antibody on the device surface and the antibody on the AuNPs, producing an optical signal – often a red line; notably, other signal producing elements can be used such as quantum dots,[4] graphene oxide,[5,6] and carbon nanotubes.[7]

LFDs have many applications beyond detecting HCG; for example, they have been deployed for analytes such as; drugs of abuse,[8] Ebola virus,[9] meningitis[10] and SARS-COV-2.[11] The common design principle shared by the above tests is they all use antibodies as capture agents (lateral flow immunoassays) due to the very high affinity and selectivity of antibodies toward their ligands (in the range of nM to pM). Despite the ubiquity of antibodies in LFDs, there is no functional requirement that these be used as the capture agent. There are examples of LFDs that use protein-anchored nucleotides,[12] protein-anchored glycans[13] and lectins[14] as capture agents in the mobile phase and as test lines in the stationary phase. There are potential benefits of using alternative ligand capture molecules. For example, Baker *et al.* have demonstrated that the spike protein from SARS-COV-2 (causative agent of COVID-19) can be detected in a lateral flow/flow-through setup by using *N*-acetyl neuraminic acid (NeuNAc, a glycan) as the recognition agent but required a glycosylated protein as the test line.[13] The same system could be deployed in flow-through (no test line) to detect COVID-19 in primary patient swab samples.[15]

Miura *et al.* have made hybrid LFDs to detect plant proteins, using glycosylated nanoparticles as the mobile phase but still using an antibody as the test line.[16] By moving away from (or combining with) antibody-based detection, it may be possible to more rapidly develop new LFDs, by enabling the development of fully synthetic systems removing the need to raise antibodies (in e.g., rabbits). This new approach

could allow for easier manufacture (including scaling) as well as bringing additional discriminatory power to tests.

Nearly all current LFDs use antibodies (lateral flow immunoassays) as the stationary phase (as well as the mobile phase) or use proteins that are functionalised with other ligands, such as nucleic acids, in the stationary phase. These approaches lead to three fundamental challenges. First, the molecular weight of the test line conjugate must be large enough to attach to the surface, with absorption ability decreasing with decreasing molecular weight, limiting scope to very high-molecular-weight macromolecules.[17,18] This limit can be overcome by increasing the surface area of the stationary phase membrane, although this limits the choice of stationary phase membrane material.[19] Second, bovine serum albumin (BSA) or other proteins must be used as "anchors" to immobilise small capture agents such as nucleotides or glycans onto the surface of an LFD; this is further limited by the small number of easy-to-use chemical conjugations available to functionalise carrier-proteins. Moreover, the chemical conjugation approaches used do not provide a clear picture of the number of capture units per protein. For example, when using glycan-functionalised BSA, a range of degrees of glycosylation are obtained, with the number of glycans differing by glycan used too.[20] Third, the temperature instability of many protein-based LFDs above 30 - 40 °C, may prevent devices from being deployed in various low-resource settings that lack established health infrastructures and cold chains.[21,22] This is especially problematic, as more expensive lab-based diagnostic techniques are also not applicable, as exemplified by the COVID-19 crisis, creating a clear health inequality between higher- and lower-income countries.[23]

When considering test line design, all test lines used in LFDs must be sufficiently hydrophobic to remain immobilised on the surface of the LFD as the mobile phase passes by, but must also be hydrophilic enough to dissolve in water for application to the stationary phase (many organic solvents can damage stationary phase materials). It is also common practice when designing LFDs to use a series of proteins or polymers such as bovine serum albumin, casein, or poly(vinyl pyrrolidone) (PVP) as blocking agents (i.e. substances that coat ("block") the surface of the stationary phase, to prevent nonspecific binding of the mobile phase to the stationary phase).[17,18] Blocking agents are either applied to the stationary phase as a pre-treatment before the LFD is run or contained within the buffer of the LFD and run as a component of the

mobile phase. PVP is an interesting case, as it is widely used in LFDs as a blocking agent, is hydrophilic enough to dissolve in water but hydrophobic enough to be immobilised onto nitrocellulose (reflected by vinyl pyrrolidone's LogP of ~0.37),[24] is widely used in biomedical applications[25] and is a synthetic polymer allowing for chemical modification. Therefore, it seemed an ideal candidate to prove the principle that a universal polymeric anchor for LFDs could be discovered.

Herein, we explore the use of capture-agent-functionalised PVP as a test line in flow-through assays, lateral flow assays and lateral flow glyco-assays, as the first example (to the best of our knowledge) of creating a synthetic polymer test line. The performance of the test line was investigated using biotin-functionalised PVP with streptavidin-functionalised AuNPs (as the mobile phase) in a flow-through assay as well as free streptavidin and biotin-functionalised AuNPs in a lateral flow assay. Further exemplification is provided using glycosylated PVP to detect a lectin in a lateral flow glyco-assay. Crucially, the polymer molecular weight can be tuned to impact the final output, providing a unique fine-tuning tool, not possible with current technologies. The polymer approach is also highly modular, as shown here. This new approach to immobilising ligands onto the test line will help develop the next generation of LFDs and simplify workflows.

5.4 Results and Discussion

The primary aim of this work was to synthesise and test the first generation of fully synthetic, protein-free test lines for use in LFD devices, to facilitate the development pipeline of new LFDs, using robust polymeric anchoring agents. Poly(vinyl pyrrolidone), PVP, was chosen as the polymeric anchor, as it is widely used in LFDs as a blocking agent – it is flowed over the nitrocellulose stationary phase to reduce nonspecific interactions of analytes or media components. Hence, if it is blocking nonspecific binding, we reasoned that PVP must be sufficiently hydrophobic to interact with/coat the nitrocellulose, while also being hydrophilic enough to dissolve in water,[26,27] which is an essential criterion for test line printing from aqueous solution.

Reversible addition-fragmentation chain transfer (RAFT) polymerisation was employed, as it enables the synthesis of polymers with defined chain lengths and control over end-groups (crucial to add the binding ligand of interest). Furthermore, RAFT or MADIX (macromolecular design by the interchange of xanthates, a specific type of RAFT) is compatible with less-activated monomers (LAMs) such as NVP (*N*-vinyl pyrrolidone) or VAc (vinyl acetate), which are more challenging than, for example, (meth)acrylates to polymerise.[28–30] A xanthate chain transfer agent (CTA) of 2-(ethoxycarbonothioylthio)-2-methylpropanoic acid *N*-hydroxsuccinimide ester was designed by retrosynthetic methods using Keddie *et al.*[31] (Figure E5.2) and synthesised with a *N*-hydroxsuccinimide (NHS) end-group that could be substituted by primary amines (such as galactosamine) as shown in Figure 5.1A. Loss of the NHS end-group could also be tracked using ^{1}H NMR analysis.

Three chain lengths of PVP telechelic homopolymers (DP = 50, 80 and 150) were synthesised (as determined by ^{1}H NMR end-group analysis, spectra in Appendix 5) *via* thermally-initiated RAFT polymerisation using 4,4′-azobis(4-cyanovaleric acid) (ACVA) as a radical initiator (Figure 5.1B). Due to low conversions, that are typically observed in the polymer synthesis of LAMs,[32] monomer to CTA ratios were higher than the target DPs ([M]:[CTA] = 200, 300 and 500, of 50, 80 and 150 respectively). Polymerisation was also stopped at less than 100% conversion to maximise the retention of end-groups. Size exclusion chromatography (SEC) analysis in DMF with 5 mM NH_4BF_4 revealed monomodal molecular weight distribution peaks with relatively low dispersities ($Đ_M \leq$ 1.7) (Figure 5.1C and Table 5.1).

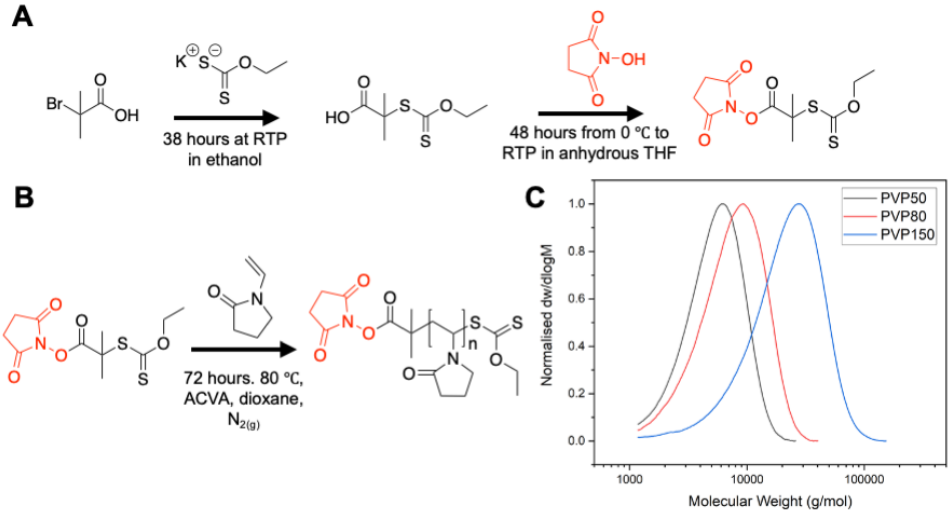

Figure 5.1. Polymer synthesis.

A) Synthesis of MADIX chain transfer agent (CTA); B) Polymerisation of *N*-vinyl pyrrolidone (NVP); C) Normalised molecular weight distributions from size exclusion chromatography of PVP polymers from Table 5.1.

Table 5.1. PVP polymers prepared for the detection of streptavidin

Polymer	[M]:[CTA]	$M_{n(theo)}$ ($g.mol^{-1}$)[a]	$M_{n(SEC)}$ ($g.mol^{-1}$)[b]	$M_{n(NMR)}$ ($g.mol^{-1}$)[c]	$Đ_M$[b]
PVP_{50}	200	22500	4500	5900	1.33
PVP_{80}	300	33600	6000	9200	1.47
PVP_{150}	500	55900	15100	17000	1.72

[a)] Determined from the feed ratio of the monomer to chain transfer agent assuming 100% conversion; [b)] Calculated against poly(methyl methacrylate) standards using 5 mM NH_4BF_4 in DMF as an eluent; [c)] Determined from ^{1}H NMR end-group analysis by comparing the integrations of the $–CH_2$ signals (δ ~2.8 ppm) of the NHS end-group with those of the corresponding signals of the polymer.

To determine if PVP provided a suitable anchor, a model flow-through system was devised using a biotin-end group, which has well-characterised and strong binding to streptavidin to test the capture principle. It is important to note that flow-through is distinct from full lateral flow, which has analyte and functionalised gold particles in the mobile phase, which is evaluated in full later. An amino-biotin derivative was synthesised in three steps from ethylene diamine and biotin following procedures from Eisenführ *et al.*[33] and Kaufman *et al.* (Figure 5.2A).[34] A mono-*t*-BOC-protected

diamine was synthesised (*N*-BOC-ethylene diamine) and conjugated with biotin. The BOC protecting group was then removed using TFA to produce "biotin-NH_2" – a biotin derivative with amine functionality.[35] The biotin-NH_2 was characterised by ^{1}H and ^{13}C NMR, FTIR, and ESI mass spectrometry (Experimental section). Functionalisation of the PVP polymers was confirmed by the loss of the NHS protons in the ^{1}H NMR spectra and the addition of biotin-NH_2 protons.

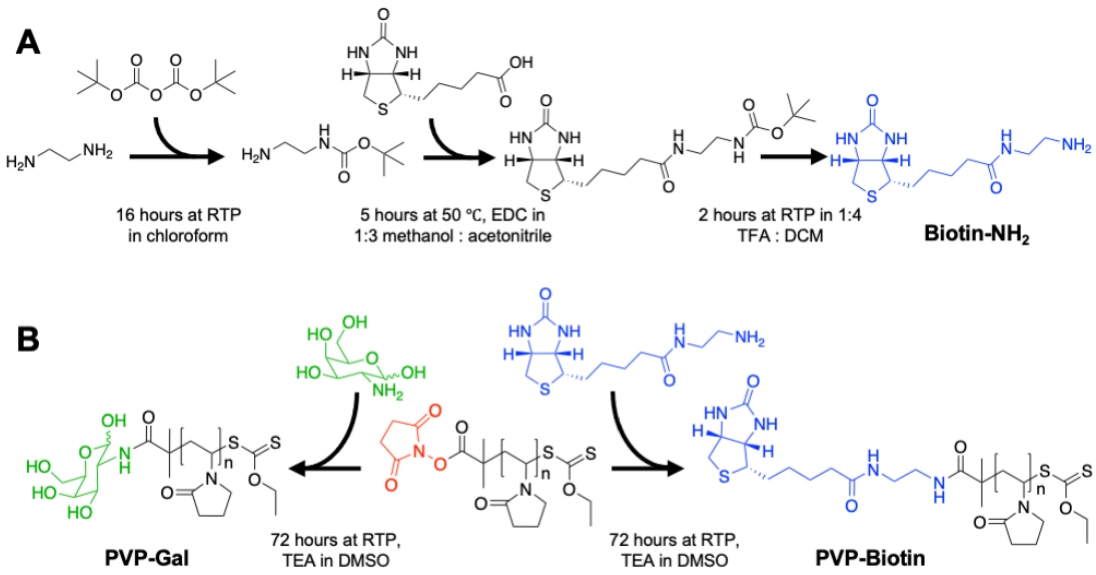

Figure 5.2. Synthesis of biotin-functionalised and galactosamine-functionalised PVP polymers.

A) Synthesis of biotin derivative; B) Synthesis of biotin-functionalised PVP polymers and galactosamine-functionalised PVP polymers

The biotin-functionalised PVP and an "unfunctionalised" PVP control were deposited onto the nitrocellulose dipsticks as test lines, in triplicate, of varying concentrations in water (20 $mg.mL^{-1}$, 10 $mg.mL^{-1}$ and 1 $mg.mL^{-1}$), and then dried at 37 °C. It is noteworthy that all dipsticks run in this work were run in triplicate, image analysed and the average (mean) taken. A (commercial) gold nanoparticle (AuNP, 40 nm) functionalised with streptavidin was flowed down the surface of the dipstick to determine if the biotin-functionalised PVP sequestered the streptavidin-functionalised particles. As a negative mobile phase, a previously reported galactosamine-functionalised poly(hydroxyethyl acrylamide) ($PHEA_{72}$) gold nanoparticle (16 nm) system (Gal-$PHEA_{72}$@$AuNP_{16}$) was used, which has no affinity to biotin (Figure 5.3).[13]

All dipsticks that used a test line of biotin-functionalised PVPs successfully bound the streptavidin AuNPs at all concentrations of the applied test line. Example dipsticks and the surface image analysis are provided in Figure 5.4A. Images of all dipsticks and analysis are provided in Appendix 5 (Tables S4-S6 and Figures S20-S22). No nonspecific binding was observed to any of the triplicate controls at 20 $mg.mL^{-1}$ (except perhaps weak binding in one PVP_{50} test strip to the streptavidin-$AuNP_{40}$), although a "bleeding" effect (smearing of the test spot) was observed at higher test line concentrations (10 and 20 $mg.mL^{-1}$) indicating that the test line concentration impacts binding and likely saturates the nitrocellulose membrane (Figure 5.4B). Interestingly the best polymer system, i.e., the system that provided the highest signal response, varied by concentration of test line applied, although all gave a positive signal in all triplicates run, with no observable off-target binding to the unfunctionalised PVP test line seen in the 10 $mg.mL^{-1}$ or 1 $mg.mL^{-1}$ triplicates. This was first determined visually and then measured by digitally analyzing the image (Figure 5.4A) and signal-to-noise ratios determined (Figure 5.4C). The PVP_{80}-biotin system had the highest signal response at 10 $mg.mL^{-1}$ but the lowest at 20 $mg.mL^{-1}$, while the PVP_{50}-biotin system had the highest response at just 1 $mg.mL^{-1}$, while PVP_{80}-biotin and PVP_{150}-biotin were comparable. This indicates that the systems produced require tuning to find the correct test line and concentration for the application; this additional tuneability gained from varying polymer chain length is another benefit of the polymeric system versus protein-based systems.

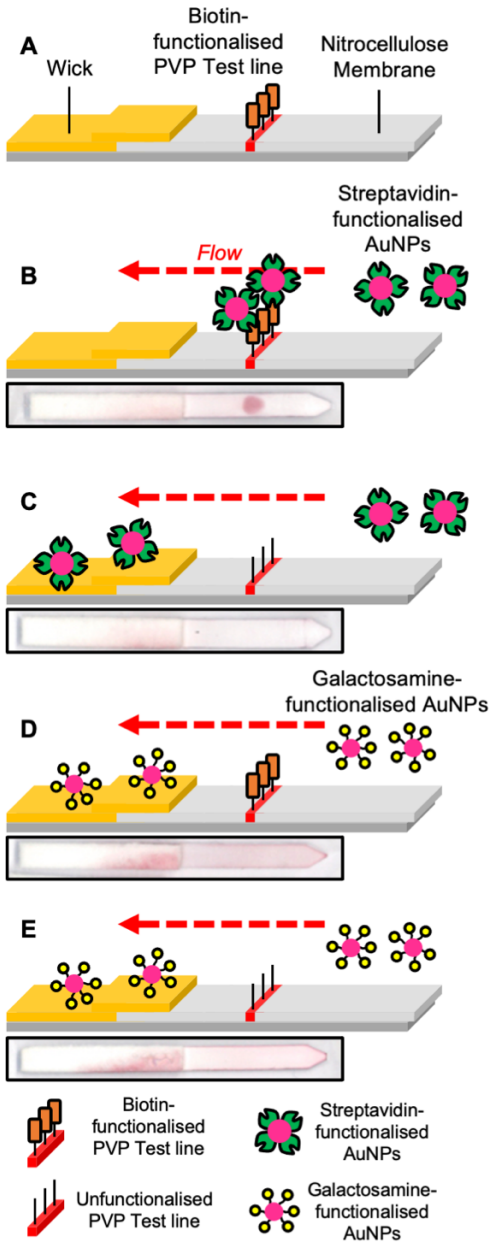

Figure 5.3. Schematic of dipstick flow-through assay and example dipsticks.

A) Design of dipstick; B) Flow-through with biotin-functionalised PVP test line where streptavidin-functionalised AuNPs flow and engage the test line - resulting in signal generation; C) Flow-through with unfunctionalised PVP test line where streptavidin-functionalised AuNPs flow and do not engage the test line - resulting in no signal generation; D) Flow-through with biotin-functionalised PVP test line where Gal-functionalised AuNPs flow and do not engage the test line - resulting in no signal generation; E) Flow-through with unfunctionalised PVP test line where Gal-functionalised AuNPs flow and do not engage the test line - resulting in no signal generation.

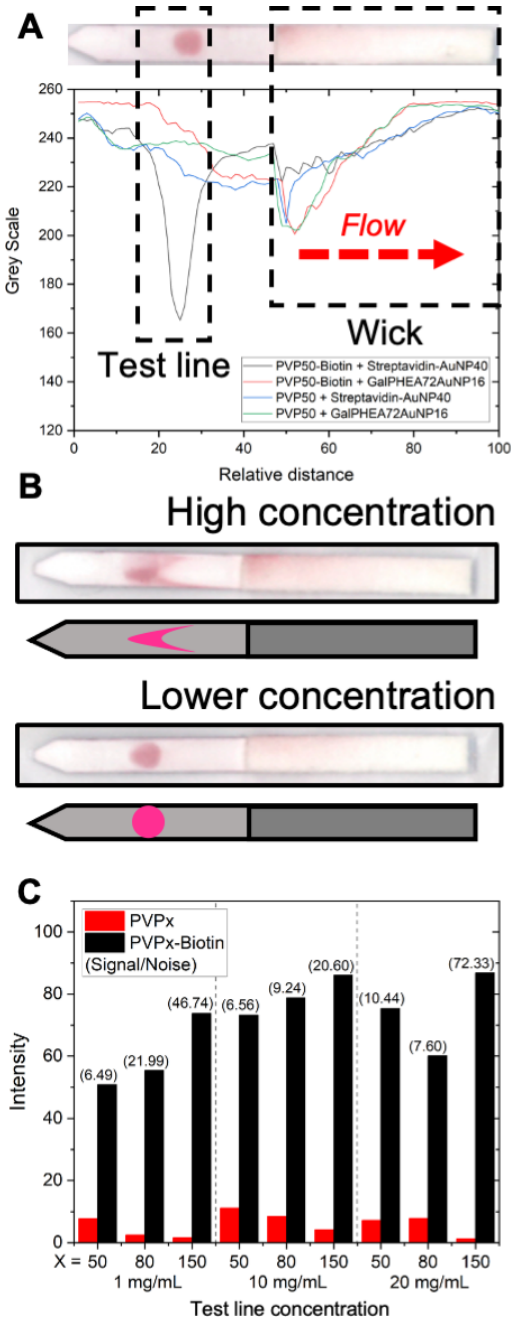

Figure 5.4. Analysis of flow-through dipstick assays.

A) Analysis of PVP_{50}-biotin and unfunctionalised PVP_{50} (1 $mg.mL^{-1}$) versus streptavidin-functionalised AuNPs and galactosamine-functionalised AuNPs, with example dipstick of PVP_{50}-biotin versus streptavidin-$AuNP_{40}$; B) Representative example dipsticks and graphical representation of test line "bleeding" effect at high (top, 20 $mg.mL^{-1}$) and lower test line concentrations (bottom, 1 $mg.mL^{-1}$); C) Intensity of PVP_x and PVP_x-biotin at varying concentrations versus streptavidin-functionalised $AuNP_{40}$, signal-to-noise ratio (PVP_x-biotin Intensity / PVP_x Intensity) is provided in brackets.

Following the successful demonstration of a flow-through system with biotin-functionalised PVPs as a test line, the next step was to create a lateral flow setup that sensed for free streptavidin in solution, which requires biotin-functionalised AuNPs, coated with a non-interacting water-soluble polymer. Therefore, a series of biotin-functionalised poly(*N*-hydroxyethyl acrylamide)s (PHEA) were synthesised and immobilised on 16 and 40 nm gold nanoparticles (Figure 5.5A&B). PHEA was chosen because of its colloidal stability,[36–38] solubility, and its established use to functionalise gold nanoparticles for lateral flow and flow-through devices.[13] Using a pentafluorophenyl-2-(dodecylthiocarbonothioylthio)-2-methylpropanoate (PFP-DMP) chain transfer agent (CTA) (see 5.6 Experimental section for a detailed synthetic procedure), a series of PHEA homopolymers were prepared (DP = 53, 72, 110, as determined by SEC, Figure 5.5C and Table 5.2, ^{1}H NMR spectra in Appendix 5) according to a previously described protocol.[13] Biotin installation as the end-groups of PHEA homopolymers was achieved by the reaction of the pentafluorophenol (PFP) end-group at the α-terminus with biotin-NH_2. The functionalised polymers were characterised by ^{1}H and ^{19}F NMR, and FTIR with successful conjugation of biotin-NH_2 confirmed by loss of the PFP fluorine peaks in ^{19}F NMR. The gold nanoparticles produced were characterised by UV-vis, DLS (Appendix 5 Figures S10-S19 and Table S3) and x-ray photoelectron spectroscopy (XPS) (Figure 5.5D and Appendix 5 Figures S32-S40 and Tables S20-S21). The increase in the N 1*s*/C 1*s* ratios in the XPS spectra for the polymer-coated particles and the increased presence of amine and amide in the C 1*s* spectra compared to the citrate-stabilised ("naked") nanoparticles confirmed the presence of polymers on the nanoparticles, alongside a shift in the UV-vis spectra. The library-based design approach to synthesising AuNP systems for lateral flow and flow-through assays has been established by Baker *et al.*[13] as a method to find the appropriately sized polymer-coated gold particle for the intended diagnostic application (Chapters 2 and 3).

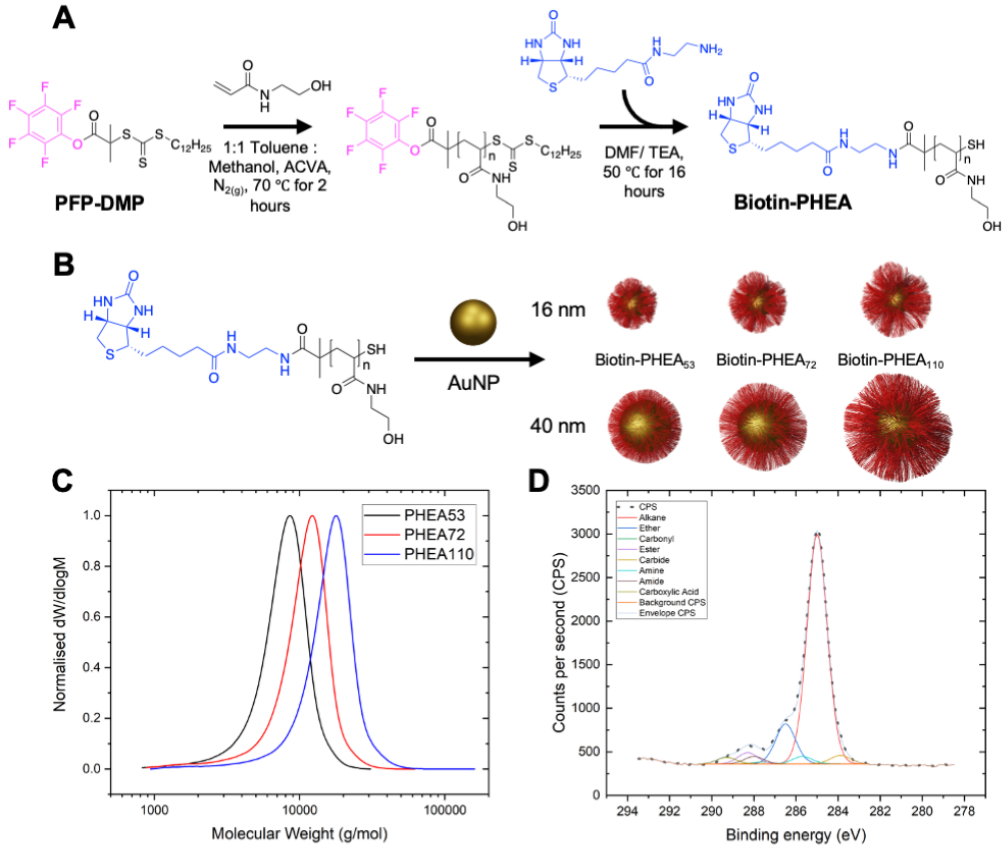

Figure 5.5. Synthesis of PHEA polymers and AuNPs.

A) Polymerisation of *N*-hydroxyethyl acrylamide (HEA) and post-functionalisation with a biotin derivative; B) Synthesis of polymer-functionalised AuNPs; C) Normalised size exclusion chromatography analysis of PHEA polymers from Table 5.2; D) C 1*s* XPS scan of biotin-PHEA$_{72}$@AuNP$_{40}$.

Table 5.2. PHEA polymers prepared for the detection of streptavidin

Polymer	[M]:[CTA]	$M_{n(theo)}$ (g.mol^{-1})[a]	$M_{n(SEC)}$ (g.mol^{-1})[b]	$M_{n(NMR)}$ (g.mol^{-1})[c]	$Đ_M$[b]
PHEA$_{53}$	28	3800	6600	6000	1.24
PHEA$_{72}$	40	5100	8900	8600	1.28
PHEA$_{110}$	70	8600	13000	14000	1.27

[a)] Determined from the feed ratio of the monomer to chain transfer agent; [b)] Calculated against poly(methyl methacrylate) standards using 5 mM NH_4BF_4 in DMF as eluent; [c)] Determined from ^{1}H NMR end-group analysis by comparing the integrations of the –CH_2CH_3 signals (δ ~0.9 - 0.7 ppm) of the dodecyl end-group with those of the corresponding signals of the polymer.

The DLS (dynamic light scattering) analysis of the biotin-functionalised 16 nm gold particles indicated some aggregation at all polymer lengths. This was observed in the dipsticks, run in triplicate, where the particles aggregated at the solvent front and on the PVP test lines even when no analyte and off-target protein (UEA, *Ulex europaeus* agglutinin I) at 0.05 $mg.mL^{-1}$ was present (Appendix 5 Tables S7-S9). However, greater aggregation at the solvent front was observed in systems containing streptavidin, indicating affinity toward streptavidin; this was observed visually by more intense colouration at the solvent front, decreased background along the strips, and decreased colouration in the wick – indicating that fewer AuNPs passed the solvent front. Note, a PVP test line concentration of 10 $mg.mL^{-1}$ was chosen to decrease the bleeding effect observed in the flow-through devices.

The biotin-PHEA-functionalised 40 nm gold particles were more stable in solution than the 16 nm particles. However, aggregation at the solvent front and with streptavidin at the solvent front was observed in the biotin-$PHEA_{72}$@$AuNP_{40}$ system but less so in the biotin-$PHEA_{110}$@$AuNP_{40}$ system (Appendix 5 Tables S10-12 and Figures S23-25). Furthermore, off-target binding to the 10 $mg.mL^{-1}$ PVP-biotin test lines was observed in all biotin-$PHEA_{110}$@$AuNP_{40}$ systems. Hence, the concentration of the test line was decreased to 1 $mg.mL^{-1}$. At this concentration, the biotin-$PHEA_{110}$@$AuNP_{40}$ system bound to streptavidin at a protein concentration of 0.05 $mg.mL^{-1}$, and this AuNP-analyte complex was successfully bound by the PVP_{150}-biotin test line (in all triplicates) with minimal nonspecific binding observed in the UEA or no analyte system (Figures 5.6 and 5.7, Appendix 5 Table S13 and Figure S26). Notably, aggregation of the AuNP system with streptavidin was observed at the solvent front likely reducing signal and leading to increased background in the controls. This experiment confirmed that functionalised PVP test lines could be used successfully in LFDs.

To confirm it is the biotin that the streptavidin specifically binds in the test lines; streptavidin at 0.05 $mg.mL^{-1}$ with biotin-$PHEA_{110}$@$AuNP_{40}$ particles was tested against biotin-functionalised and unfunctionalised PVP test lines at a test line concentration of 1 $mg.mL^{-1}$ (Appendix 5 Table S14 and Figure S27). While weak binding was observed to the unfunctionalised PVP_{50} test line, binding was far stronger to the PVP_{50}-biotin test line and all other biotin-functionalised test lines versus their unfunctionalised equivalents. With no binding to the unfunctionalised PVP_{150} test line

observed in any of the triplicates. It is notable, that signal intensity decreased with PVP chain length likely because relative biotin concentration on the test line decreases as polymer chain length increases (as test line concentration is measured by mass not molarity), although the decrease in off-target binding to unfunctionalised PVP_{150} led to a high signal-to-noise ratio for the PVP_{150}-biotin system (Figure 5.7B). Attempts to use a lower concentration of streptavidin (0.005 $mg.mL^{-1}$) and the PVP_{150}-biotin test line were unsuccessful, with a signal-to-noise ratio of ~1. However, binding to the PVP_{80}-biotin was observed at this concentration (0.005 $mg.mL^{-1}$ streptavidin) versus unfunctionalised PVP_{80} (signal-to-noise of > 7); likely due to decreased aggregation at the solvent front between the particles and streptavidin (Figure 5.7B, Appendix 5 Table S15 and Figure S28), indicating the need to tune the AuNP system for the target analyte and test line used in a finished device.

In comparison to antibody-based lateral flow immunoassays that often have limits of detection ranging from microgram to nanogram per millilitre,[39] this system when targeting streptavidin has a limit of detection (LoD) of ~0.05 - 0.005 $mg.mL^{-1}$ or ~0.8 - 0.08 $nmol.mL^{-1}$ for the PVP150-biotin and PVP80-biotin systems. This is higher than many commercially available lateral flow immunoassays but is comparable to commercial pregnancy test LFDs with molar LoDs of ~0.7 – 0.07 $nmol.mL^{-1}$.[40]

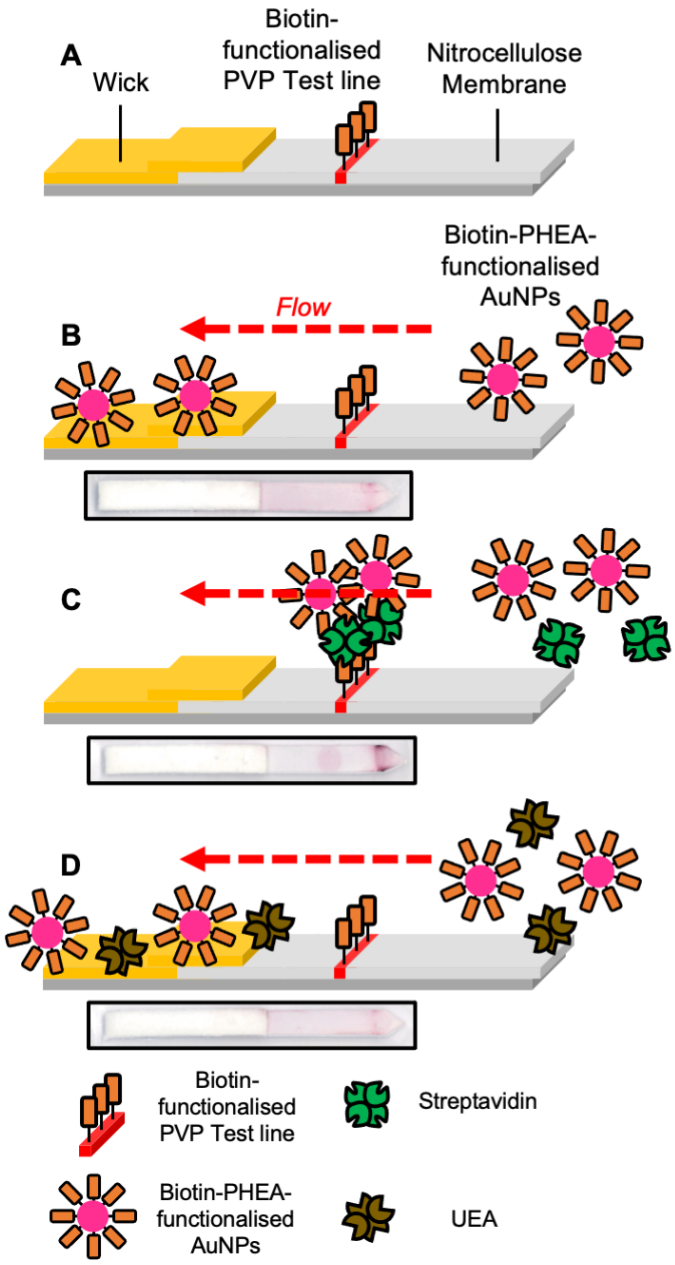

Figure 5.6. Schematic of dipstick lateral flow assay and example dipsticks.

A) Design of dipstick; B) Lateral flow with biotin-functionalised PVP test line with no analyte in solution and biotin-PHEA-functionalised AuNPs flow and do not engage the test line – resulting in no signal generation; C) Lateral flow with biotin-functionalised PVP test line with streptavidin (0.05 $mg.mL^{-1}$) in solution, and biotin-functionalised AuNPs flow and do engage the test line – resulting in signal generation; D) Lateral flow with biotin-functionalised PVP test line with UEA (0.05 $mg.mL^{-1}$) in solution, and biotin-functionalised AuNPs flow and do engage the test line – resulting in no signal generation.

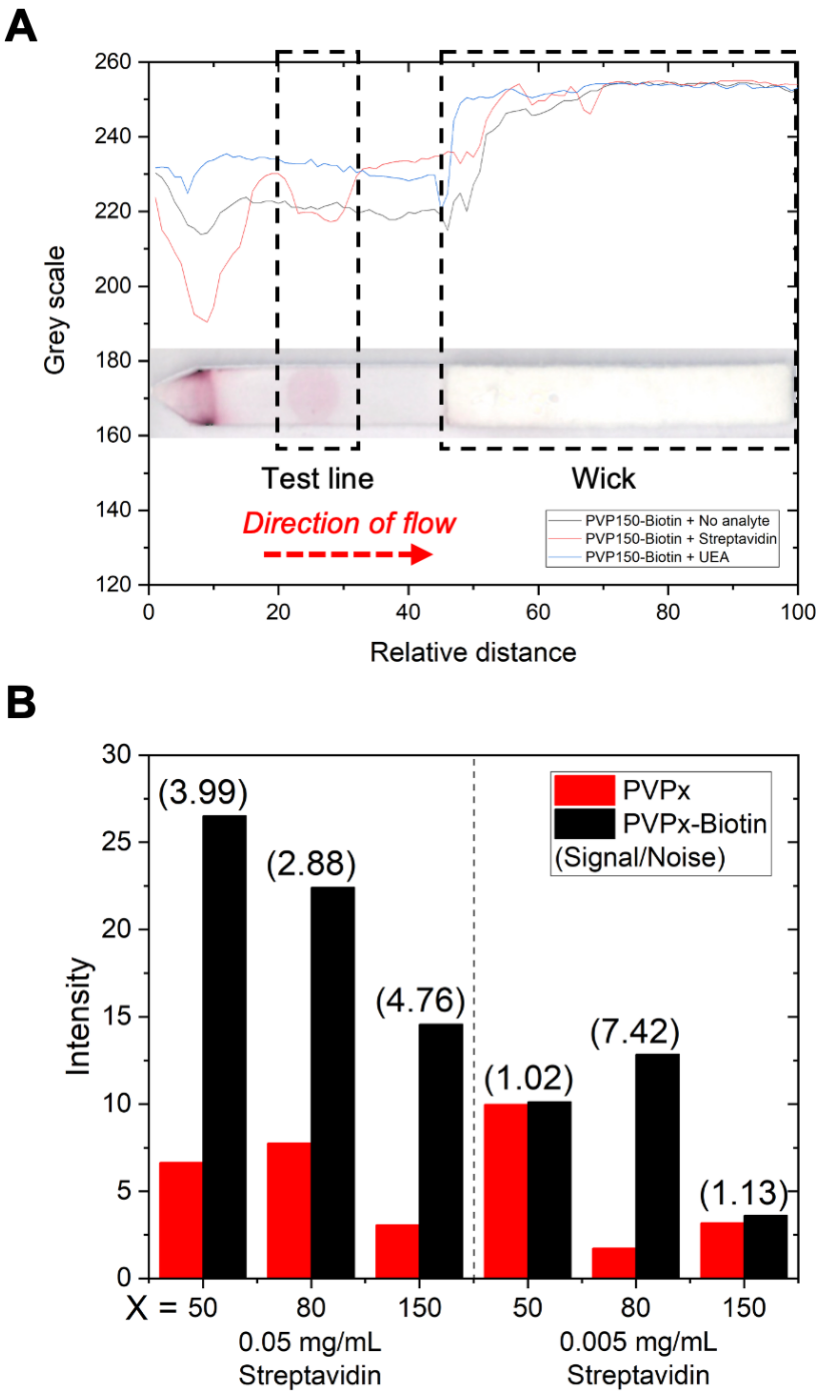

Figure 5.7. Analysis of scanned lateral flow strips using test lines of PVP_{150}-biotin.

A) PVP_{150}-biotin (1 $mg.mL^{-1}$) versus either no analyte, streptavidin (0.05 $mg.mL^{-1}$) or UEA (0.05 $mg.mL^{-1}$) using with biotin-$PHEA_{110}$@$AuNP_{40}$ (inset example dipstick from PVP_{150}-biotin versus streptavidin); B) Intensity of PVP_x (1 $mg.mL^{-1}$) and PVP_x-biotin (1 $mg.mL^{-1}$) versus streptavidin of varying concentrations with biotin-$PHEA_{110}$@$AuNP_{40}$, signal-to-noise ratio (PVP_x-biotin Intensity / PVP_x Intensity) is provided in brackets.

While biotin-streptavidin is an excellent model system, its low K_d (~10^{-14} mol.dm^{-3})[41] is not representative of many analyte-capture agent scenarios that have lower affinity (higher K_d). Therefore, soybean agglutinin (SBA), a lectin with a known affinity for galactosamine, was chosen as an analyte. We have previously designed and validated an appropriate gold nanoparticle system (Gal-PHEA$_{72}$@AuNP$_{16}$) to sense specifically for SBA in an LFD device using protein agents to immobilise the glycan to the stationary phase (Chapter 2).[13] It was anticipated that the PVP test lines functionalised with galactosamine may not perform as well as their glycan-BSA counterpart (Galα1-3Galβ1-4GlcNAc-BSA). This is likely due to the loss of the cluster glycoside effect (the glycan-BSA used carried > 20 glycans per BSA protein as reported by the manufacturer) and the use of galactosamine (with free anomeric position) as the binding glycan in the PVP system. Initial attempts, in triplicate, to use 20 mg.mL^{-1} galactosamine-functionalised PVPs and an SBA concentration in solution of 0.05 mg.mL^{-1} proved unsuccessful with no binding observed to the SBA (Appendix 5 Table S16). However, no off-target binding was observed to either the no-lectin, UEA, or unfunctionalised PVP systems (in any test), which was promising. A higher concentration of SBA (0.5 mg.mL^{-1}) was therefore chosen for the lateral flow glyco-assay (Appendix 5 Table S17 and Figure S29). While this concentration of SBA did lead to nonspecific binding of the SBA-particle complex to the unfunctionalised PVP test line in all cases and in all triplicates; stronger signals were observed in the PVP$_{150}$-Gal system (Figure 5.8), with the PVP$_{150}$-Gal system (signal) versus the unfunctionalised PVP$_{150}$ system (noise) having a signal-to-noise ratio of 2.44 (Figure 5.8C). This indicates that the limit of detection (LoD) of SBA is between ~0.5 - 0.05 mg.mL^{-1}. This compares well to a system using the same nanoparticles in a setup against a test line of Galα1-3Galβ1-4GlcNAc-BSA (1 mg.mL^{-1}), with a LoD of ~0.02 mg.mL^{-1} (Chapter 2). Considering the PVP does not (likely) benefit from the cluster glycoside effect to the same extent as a multi-valent protein surface[42] the LoD achieved is promising. Although, it is possible that the lectins can bind multiple PVP chains, depending on their exact orientation on the surface. Notably, the PVP-based system is not as sensitive as antibody based LFDs, such as those for ricin (LoD ~20 ng.mL^{-1})[43] or a concanavalin A (LoD ~0.1 μg.mL^{-1})[16], but it does indicate the potential for the integration of polymer systems into LFDs.

Decreasing the concentration of the PVP test line systems was attempted but yielded mixed results (Appendix 5 Table S18-19 and Figure S30-31), indicating that the 20 $mg.mL^{-1}$ PVP_{150}-Gal system is the optimum for this particular particle system and analyte. Interestingly this is different from the concentration used in the biotin-functionalised PVP lateral flow system and the optimum chain length in some of the flow-through assays. This indicates the need to tune each system depending on the application, again highlighting the tuneability benefits of polymer chemistry over protein-based systems. Furthermore, the background could be improved by adjusting the buffer, tuning the AuNP system, or treating the membrane. While the signal could be improved by printing the test line, rather than using "by hand" deposition of a test spot or using a more complex glycan with greater affinity for SBA. These sorts of modifications were however beyond the scope of this work that focusses on a proof-of-concept for polymeric test lines.

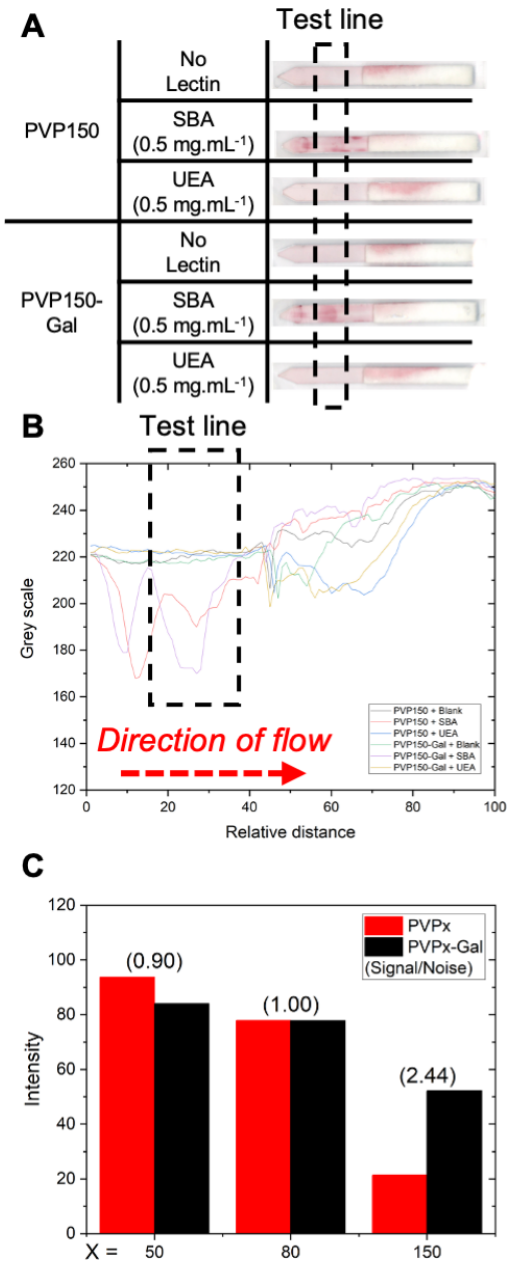

Figure 5.8. Lateral flow strips and analysis using test lines of PVP_{150}-Gal and PVP_{150} (20 $mg.mL^{-1}$).

A) Example lateral flow strips using test lines of PVP_{150}-Gal and PVP_{150} (20 $mg.mL^{-1}$) versus no analyte, SBA (0.5 $mg.mL^{-1}$) and UEA (0.5 $mg.mL^{-1}$), using Gal-$PHEA_{72}$@$AuNP_{16}$; B) Analysis of scanned lateral flow strips using test lines of PVP_{150}-Gal and PVP_{150} (20 $mg.mL^{-1}$) versus either no analyte, SBA (0.5 $mg.mL^{-1}$) and UEA (0.5 $mg.mL^{-1}$); C) Intensity of PVP_x (20 $mg.mL^{-1}$) and PVP_x-Gal (20 $mg.mL^{-1}$) versus SBA (0.5 $mg.mL^{-1}$), signal-to-noise ratio (PVP_x-Gal Intensity / PVP_x Intensity) is provided in brackets.

5.5 Conclusions

Here, the concept of a fully synthetic, protein-free, polymeric lateral flow test line is validated and explored for the first time. It is shown to be a promising alternative to the established protein-based anchoring reagents. Poly(vinyl pyrrolidone), PVP, was identified as a promising immobilisation agent, based on its widespread use as a "blocking agent", which is sufficiently hydrophobic to adhere to nitrocellulose stationary phases but still being water-soluble which is essential for production/printing of the test line. PVP was synthesised by RAFT/MADIX polymerisation using an *N*-hydroxysuccinimide (NHS) functionalised chain transfer agent, which allowed for subsequent installation of a glycan or biotin, as a capture ligand. The polymer anchor was shown to allow capture in flow-through and lateral flow systems leading to specific binding with limited off-target (nonspecific) binding. A key observation was that the chain length of the PVP (as well as the concentration applied) was crucial to optimise the signal generation and specificity. For example, in the flow-through system when targeting streptavidin-functionalised particles in the mobile phase, the best PVP-biotin chain length varied with the concentration of the test line used. While in the lateral flow system when targeting streptavidin, a 1 $mg.mL^{-1}$ test line of PVP_{150}-biotin was best and in the lateral flow glyco-assay when targeting SBA, a 20 $mg.mL^{-1}$ PVP_{150}-Gal test line was best.

We anticipate that the polymeric system discussed (PVP) could be used as a multifunctional scaffold or platform to present other capture agents such as short amino acid or nucleotide sequences and enable a wider range of end-group functionality beyond amide chemistry (i.e., click chemistry approaches). The ability to tune the molecular weight of a polymeric test line will allow further fine-tuning, in contrast to protein-based anchors. Furthermore, the addition of multivalency to the system could also be explored while maintaining synthetic control over the number of capture agents per polymer anchor unit. Plus, there exists many thousands of potential (co)polymer structures, which provide further opportunities to refine the polymer test line approach. In summary, the PVP scaffolds presented and validated here provide the first examples of a tuneable and multifunctional polymeric test line capture system for lateral flow devices and further epitomise the potential of applying polymer chemistry to LFDs.

5.6 Experimental

5.6.1 Physical and Analytical Methods

NMR Spectroscopy

^{1}H-NMR, ^{13}C-NMR and ^{19}F-NMR spectra were recorded at 300 MHz or 400 MHz on a Bruker DPX-300 or DPX-400 spectrometer respectively, with chloroform-*d* ($CDCl_3$), deuterated DMSO (DMSO-d_6), deuterated methanol (MeOD) or deuterium oxide (D_2O) as the solvent. Chemical shifts of protons are reported as δ in parts per million (ppm) and are relative to either $CDCl_3$ (7.26), DMSO-d_6 (2.50), MeOD (4.87, 3.31) or D_2O (4.79).

Mass Spectrometry

Low resolution mass spectra (LRMS) were recorded on a Bruker Esquire 2000 spectrometer using electrospray ionisation (ESI). m/z values are reported in Daltons.

FT-IR Spectroscopy

Fourier Transform-Infrared (FT-IR) spectroscopy measurements were carried out using an Agilent Cary 630 FT-IR spectrometer, in the range of 650 to 4000 cm^{-1}.

Size Exclusion Chromatography

Size exclusion chromatography (SEC) analysis was performed on an Agilent Infinity II MDS instrument equipped with differential refractive index (DRI), viscometry (VS), dual angle light scattering (LS) and variable wavelength UV detectors. The system was equipped with 2 x PLgel Mixed D columns (300 x 7.5 mm) and a PLgel 5 µm guard column. The mobile phase used was DMF (HPLC grade) containing 5 mM NH_4BF_4 at 50 °C at flow rate of 1.0 $mL.min^{-1}$. Poly(methyl methacrylate) (PMMA) standards (Agilent EasyVials) were used for calibration between 955,000 – 550 $g.mol^{-1}$. Analyte samples were filtered through a nylon membrane with 0.22 µm pore size before injection. Number average molecular weights (M_n), weight average molecular weights (M_w) and dispersities ($Đ_M = M_w/M_n$) were determined by conventional calibration using Agilent GPC/SEC software.

X-ray Photoelectron Spectroscopy (XPS)

The samples were attached to electrically-conductive carbon tape, mounted on to a sample bar and loaded into a Kratos Axis Ultra DLD spectrometer which possesses a

base pressure below 1 x 10^{-10} mbar. XPS measurements were performed in the main analysis chamber, with the sample being illuminated using a monochromated Al Kα x-ray source. The measurements were conducted at room temperature and at a take-off angle of 90° with respect to the surface parallel. The core level spectra were recorded using a pass energy of 20 eV (resolution approx. 0.4 eV), from an analysis area of 300 μm x 700 μm. The spectrometer work function and binding energy scale of the spectrometer were calibrated using the Fermi edge and $3d_{5/2}$ peak recorded from a polycrystalline Ag sample prior to the commencement of the experiments. In order to prevent surface charging the surface was flooded with a beam of low energy electrons throughout the experiment and this necessitated recalibration of the binding energy scale. To achieve this, the C-C/C-H component of the C 1*s* spectrum was referenced to 285.0 eV. The data were analyzed in the CasaXPS package, using Shirley backgrounds and mixed Gaussian-Lorentzian (Voigt) lineshapes. For compositional analysis, the analyser transmission function has been determined using clean metallic foils to determine the detection efficiency across the full binding energy range.

Dynamic Light Scattering

Hydrodynamic diameters (D_h) and size distributions of particles were determined by dynamic light scattering (DLS) using a Malvern Zetasizer Nano ZS with a 4 mW He-Ne 633 nm laser module operating at 25 ℃. Measurements were carried out at an angle of 173° (back scattering), and results were analyzed using Malvern DTS 7.03 software. All determinations were repeated 5 times with at least 10 measurements recorded for each run. D_h values were calculated using the Stokes-Einstein equation where particles are assumed to be spherical.

UV-vis Spectroscopy

Absorbance measurements were recorded on an Agilent Cary 60 UV-Vis Spectrophotometer and on a BioTek Epoch microplate reader.

Transmission Electron Microscopy

Dry-state stained TEM imaging was performed on a JEOL JEM-2100Plus microscope operating at an acceleration voltage of 200 kV. All dry-state samples were diluted with deionised water and then deposited onto formvar-coated copper grids.

Image Collection of Lateral Flow Dipsticks and Devices

All devices were scanned using a Kyocera TASKalfa 5550ci printer to a pdf file that was converted to a jpeg. The jpeg was analyzed in ImageJ 1.51.[44] None of the images in Appendix 5 have been image adjusted i.e. no changes/enhancements have been made from the original scan images. The main paper images may have been enhanced and/or cropped to improve clarity.

Solvent drying

4 Å molecular sieves were activated either by heat or using microwave energy (600W). A 20% w/v. of sieves:solvent was used, the solvent was degassed with nitrogen for 30 minutes with the sieves present and then left overnight before the solvent was used.

5.6.2 Materials

All chemicals were used as supplied unless otherwise stated. *N*-Hydroxyethyl acrylamide (97%), 4,4'-azobis(4-cyanovaleric acid) (ACVA, 98%), 4-dimethylaminopyridine (DMAP, > 98%), mesitylene (reagent grade), triethylamine (TEA, > 99%), sodium citrate tribasic dihydrate (> 99%), gold(III) chloride trihydrate (99.9%), potassium phosphate tribasic (≥ 98%, reagent grade), *N*,*N*'-diisopropylcarbodiimide (DIC, 99%), 1-vinyl-2-pyrrolidone (≥ 98.0% for synthesis), DMSO (ACS reagent, (≥ 99.9%), deuterated DMSO (DMSO-d_6, ≥ 99%), deuterium oxide (D_2O, 99.9%), deuterated chloroform ($CDCl_3$, 99.8%), deuterated methanol (CD_3OD, (≥ 99.8%), diethyl ether (≥ 99.8%, ACS reagent grade), methanol (≥ 99.8%, ACS reagent grade), toluene (≥ 99.7%,), di-*tert*-butyl dicarbonate (≥ 98.0%), Tween-20 (molecular biology grade), HEPES, PVP40 (poly(vinyl pyrrolidone)$_{400}$ (Average Mw ~40,000)), carbon disulphide (≥ 99.8%), acetone (≥ 99%), 1-dodecane thiol (≥ 98%), biotin (≥ 99%, HPLC lyophilised powder), 40 nm gold nanoparticles (OD1 in citrate buffer), streptavidin-gold (40 nm) from *Streptomyces avidinii*, pentafluorophenol (≥ 99%, reagent plus), *N*-hydroxysuccinimide (98%), ethylenediamine (≥ 99.5%), ethyl acetate (≥ 99.5%), trifluoroacetic acid (TFA, ≥ 99%, reagent plus), sodium azide (≥ 99.5%, reagent plus) and potassium permanganate (≥ 99%) were purchased from Sigma-Aldrich. Potassium ethyl xanthate (98%) was purchased from Alfa Aesar. DMF (> 99%) and 2-bromo-2-methyl-propionic acid (98%) were purchased from Acros Organics. Galactosamine HCl and 1-ethyl-3-(3-dimethylaminopropyl)carbodiimide hydrochloride (EDCI, > 98%) were purchased from Carbosynth. Hexane fraction from petrol (lab reagent grade), DCM (99% lab reagent grade), sodium hydrogen carbonate (≥ 99%), ethyl acetate (≥ 99.7%, analytical reagent grade), sodium chloride (≥ 99.5%), calcium chloride, 40-60 petroleum ether (lab reagent grade), hydrochloric acid (~37%, analytical grade), glacial acetic acid (analytical grade), magnesium sulphate (reagent grade), THF (HPLC), chloroform (≥ 99%), Molecular Sieve type 4 Å nominal pore size (general purpose grade) and 1,4-dioxane (≥ 99%) were purchased from Thermo Fisher Scientific. Ethanol absolute was purchased from VWR International.

Nitrocellulose Immunopore RP 90-150 s/4cm 25 mm was purchased from GE Healthcare. Lateral flow backing cards 60 mm by 301.58 mm (KN-PS1060.45 with KN211 adhesive) was purchased from Kenosha Tapes. Cellulose fibre wick material

20 cm by 30 cm by 0.825 mm (290 gsm and 180 mL/min) (Surewick CFSP223000) was purchased from EMD Millipore.

Soybean agglutinin and *Ulex Europaeus* Agglutinin I were purchased from Vector Laboratories.

Spectra/Por 7 Dialysis Membrane Pre-treated RC (regenerated cellulose) Tubing MWCO: 1 kD was purchased from Spectrum Laboratories. Streptavidin lyophilised was purchased from Stratech Scientific.

Ultra-pure water used for buffers was MilliQ grade 18.2 mΩ resistance.

5.6.3 Synthetic Methods

Synthesis of 2-(dodecylthiocarbanothionylthio)-2-methyl propionic acid (DMP)

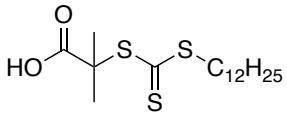

This was synthesised, according to a previously published procedure.[36] 2.00 g (9.88 mmol) of 1-dodecane thiol was added dropwise to stirring 2.10 g (9.89 mmol) of K_3PO_4 in 30 mL of acetone at RTP, the mixture was left to stir for 25 minutes to form a white suspension. 2.05 g (26.93 mmol) of carbon disulphide was then added and left for 10 minutes, a yellow solution formed. 1.5 g (8.98 mmol) of 2-bromo-2-methyl-propionic acid was then added and the solution left to stir for 16 hours. The solvent was removed under vacuum. The crude product was dissolved in 100 mL of 1 M HCl and extracted with DCM (2×100 mL). The organic layer was washed with 200 mL of water and 200 mL of brine. The organic layer was dried with $MgSO_4$ and filtered under gravity. The solvent was then removed from the filtrate under vacuum. The crude product was purified using a silica column (40-60 PET:DCM:glacial acetic acid 75:24:1) and recrystalised in n-hexane to give a yellow solid (58%). δ_H (300 MHz, $CDCl_3$) 3.28 (2H, t, *J* 7.5, SCH_2CH_2), 1.80 - 1.45 (8H, m, $C(CH_3)_2$ and SCH_2CH_2), 1.45 - 1.2 (18H, m, $(CH_2)_9CH_3$), 0.87 (3H, t, *J* 6.0, CH_3). δ_C (400 MHz, $CDCl_3$) 221.0 (1C, SC(S)S), 178.3 (1C, C(O)), 55.7 (1C, $C(CH_3)_2$), 37.7 (1C, SCH_2), 32.1 - 28.0 (9C, $SCH_2(CH_2)_9$), 25.4 (2C, $C(CH_3)_2$), 22.8 (1C, CH_2CH_3), 14.3 (1C, CH_2CH_3). m/z calculated as 364.16; found for ESI $[M+H]^+$ 365.3 and $[M+Na]^+$ 387.3. FTIR (cm^{-1}) – 2956, 2916.6 & 2850 (methyl and methylene), 1702 (ester C=O), 1459, 1437 & 1413 (methyl and methylene), 1280 ($C(CH_3)_2$), 1064 (S-C(S)-S).

Synthesis of pentafluorophenyl-2-(dodecylthiocarbonothioylthio)-2-methylpropanoate (PFP-DMP)

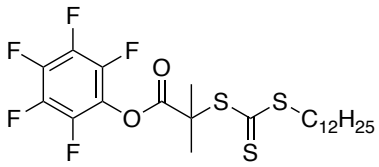

This was synthesised, according to a previously published procedure.[36] 4.06 g (11.13 mmol) of DMP, 3.65 g (19.04 mmol) of EDC and 2.30 g (18.82 mmol) of DMAP were dissolved in 160 mL of DCM and degassed for 30 minutes. 7.28 g (39.55 mmol) of pentaflurophenol was added in 20 mL of DCM and the mixture stirred for 18 hours at RTP. The organic layer was washed with 3 M HCl (200 mL), 1 M $NaHCO_3$ (200 mL) and 0.5 M NaCl (200 mL). The organic layer was dried with $MgSO_4$ and filtered under gravity. The solvent was then removed from the filtrate under vacuum. The crude product was recrystallised from ethyl acetate (or hexane) overnight at -8 °C and dried to give yellow crystals (90.9%). δ_H (300 MHz, $CDCl_3$) 3.31 (2H, t, *J* 7.5, SCH_2CH_2), 1.86 (6H, s, $C(CH_3)_2$), 1.69 (2H, qn, *J* 7.5, SCH_2), 1.48 - 1.16 (18H, m, $CH_2CH_2CH_2CH_2CH_2CH_2CH_2CH_2CH_3$), 0.94 - 0.82 (3H, m, CH_3). δ_C (300 MHz, $CDCl_3$) 220.1 (1C, SC(S)S), 169.7 (1C, C(O)), 143.1 (2C, meta C), 139.8 (1C, ipso C), 139.6 (1C, para C), 136.3 (2C, Ortho C), 55.5 (1C, $C(CH_3)_2$), 37.3 (1C, SCH_2), 32.0 - 22.8 (10C, $SCH_2(CH_2)_{10}$), 25.4 (2C, $C(CH_3)_2$), 14.1 (1C, CH_2CH_3). δ_F (300 MHz, $CDCl_3$) -151.4 - -151.6 (2F, m, $OCC_2H_2C_2H_2CH$), -148.5 (1F, t, *J* 21.5, $OCC_2H_2C_2H_2CH$), -162.2 - -162.5 (2F, m, $OCC_2H_2C_2H_2CH$). m/z calculated as 530.14; found for ESI $[M+Na]^+$ 553.3 and $[M+CH_3CN+Na]^+$ 593.5. FTIR (cm^{-1}) – 2956, 2917 & 2850 (methyl and methylene), 1702 (ester C=O), 1519 (aromatic C=C or C-F), 1460, 1437 & 1413 (methyl and methylene), 1280 ($C(CH_3)_2$), 1068 (S-C(S)-S).

Representative Polymerisation of 2-hydroxyethyl acrylamide (PHEA72)

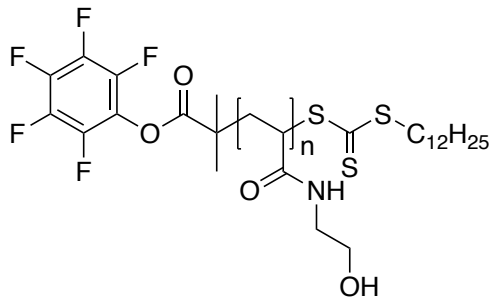

PHEA72 as representative example. 4.38 g (38 mmol) of 2-hydroxyethyl acrylamide, 0.0595 g (0.21 mmol) of ACVA and 0.5008 g (0.91 mmol) of PFP-DMP was added to 22 mL 1:1 toluene:methanol and degassed with nitrogen for 30 minutes. The reaction vessel was stirred and heated to 70 ℃ for 2 hours. The solvent was removed under vacuum. The crude product was dissolved in the minimum amount of methanol. Diethyl ether cooled in liquid nitrogen was added to the methanol to form a precipitate. The mixture was centrifuged for 2 minutes at 13 krpm and the liquid decanted off. The solid was dissolved in methanol and removed under vacuum to give a yellow crystalline solid.

PHEA72 - δ_H (300 MHz, D_2O) 8.30 - 7.96 (34H, m, N*H*), 3.96 - 3.52 (126H, m, NHC*H*$_2$), 3.52 - 3.07 (155H, m, C*H*$_2$OH & SC*H*$_2$), 2.36 - 1.88 (70H, m, $CH_2CHC(O)$ & $C(CH_3)_2$), 1.88 - 1.03 (148H, m, $CH_2CHC(O)$ & $CH_2CH_2CH_2CH_2CH_2CH_2CH_2CH_2CH_2CH_2CH_3$), 0.82 - 0.70 (5H, m, CH_2CH_3). δ_F (300 MHz, D_2O) - 151.0 - -165.0 (5F, m, C_6F_5). FTIR (cm^{-1}) – 3267 (OH, broad), 3088 & 2924 (C(O)NH and NH), 1638 & 1545 (C(O)NH). Yield - 73%

PHEA53 - δ_H (300 MHz, D_2O) 8.34 - 7.98 (4H, m, N*H*), 4.01 - 3.56 (90H, m, NHC*H*$_2$), 3.56 - 3.07 (91H, m, C*H*$_2$OH & SC*H*$_2$), 2.40 - 1.90 (47H, m, $CH_2CHC(O)$ & $C(CH_3)_2$), 1.90 - 0.99 (123H, m, $CH_2CHC(O)$ & $CH_2CH_2CH_2CH_2CH_2CH_2CH_2CH_2CH_2CH_2CH_3$), 0.82 - 0.72 (5H, m, CH_2CH_3)

PHEA110 - δ_H (300 MHz, D_2O) 8.24 - 8.02 (28H, m, N*H*), 3.83 - 3.51 (239H, m, NHC*H*$_2$), 3.51 - 3.08 (293H, m, C*H*$_2$OH & SC*H*$_2$), 2.40 - 1.90 (117H, m, $CH_2CHC(O)$ & $C(CH_3)_2$), 1.90 - 1.03 (273H, m, $CH_2CHC(O)$ & $CH_2CH_2CH_2CH_2CH_2CH_2CH_2CH_2CH_2CH_2CH_3$), 0.86 - 0.73 (5H, m, CH_2CH_3)

Representative Poly(N-hydroxyethyl acrylamide) (PHEA72) Glycan Functionalisation

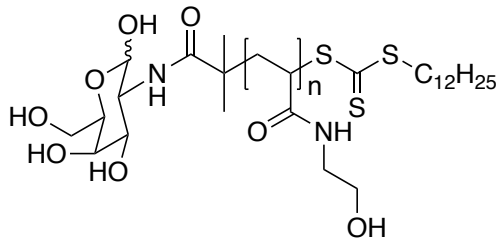

0.2516 g (0.028 mmol) of poly(2-hydroxyethyl acrylamide) and 0.093 g (0.43 mmol) of galactosamine HCl were added to 30 mL of DMF containing 0.05 M TEA. The reaction was stirred at 50 ℃ for 16 hours. Solvent was removed under vacuum. The crude product was dissolved in the minimum amount of methanol at RTP before cooling in a liquid nitrogen bath. Diethyl ether cooled in liquid nitrogen was added to the methanol to form a precipitate. The mixture was centrifuged for 2 minutes at 13 krpm and the liquid decanted off. The solid was dissolved in methanol and removed under vacuum to give an orange/brown crystalline solid. δ_H (400 MHz, D_2O) 8.33 - 8.01 (6H, m, NH), 4.95 - 4.89 (6H, anomeric protons), 3.99 - 3.54 (~145H, m, NHC*H*$_2$ & glycan protons), 3.54 - 3.19 (~233H, m, C*H*$_2$OH & SC*H*$_2$ & glycan protons + diethyl ether impurity), 2.37 - 1.87 (~60H, m, $CH_2CHC(O)$, $C(CH_3)_2$ & glycan protons), 1.87 - 1.07 (152H, m, C*H*$_2$CHC(O) & C*H*$_2$C*H*$_2$C*H*$_2$C*H*$_2$C*H*$_2$C*H*$_2$C*H*$_2$C*H*$_2$C*H*$_2$CH$_3$ + diethyl ether impurity), 0.93 - 0.72 (5H, m, CH_2CH_3). FTIR (cm^{-1}) – 3274 (OH, broad), 3104 & 2929 (C(O)NH and NH), 1638 & 1552 (C(O)NH).

Representative Poly(N-hydroxyethyl acrylamide) (PHEA72) Biotin Functionalisation

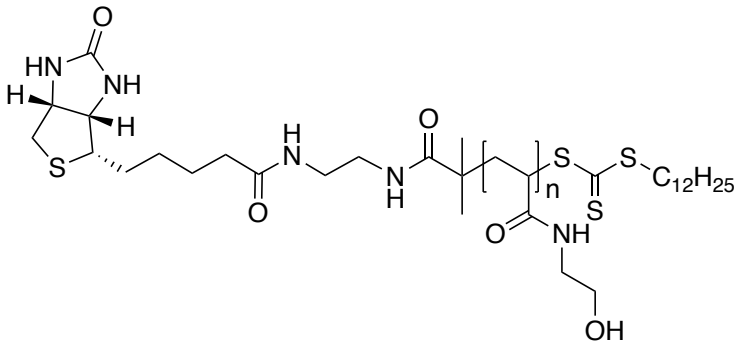

85.5 mg (0.0096 mmol) of PHEA72 and 19.45 mg (0.068 mmol) of biotin-NH_2 was dissolved in 10 mL of DMF containing 100 µL TEA. The reaction was stirred at 50 °C for 16 hours. Solvent was removed under vacuum. The crude product was dissolved in the minimum amount of methanol at RTP before cooling in a liquid nitrogen bath. Diethyl ether cooled in liquid nitrogen was added to the methanol to form a precipitate. The mixture was centrifuged for 2 minutes at 13 krpm and the liquid decanted off. The solid was dissolved in methanol and removed under vacuum to give an orange/yellow crystalline solid. δ_H (400 MHz, D_2O) 8.00 - 7.91 (4H, C(O)NH), 4.65 - 4.58 (1H, m, C*H*CH_2(S)), 4.47 - 4.39 (1H, m, C*H*CH(S)), 3.90 - 3.55 (85H, m, NHC*H*$_2$), 3.55 - 3.10 (141H, m, C*H*$_2$OH, C(O)NHC*H*$_2$$CH_2$NH, CHC*H*S, C(O)NHCH$_2$C*H*$_2$NH & CHCH*H*S), 2.82 - 2.68 (1H, m, CHC*H*HS), 2.45 - 1.87 (46H, m, CH_2C*H*C(O), $C(CH_3)_2$, C*H*$_2$C(O)NH), 1.87 - 1.07 (97H, m, C*H*$_2$CHC(O) & C*H*$_2$C*H*$_2$C*H*$_2$C*H*$_2$C*H*$_2$C*H*$_2$C*H*$_2$C*H*$_2$C*H*$_2$$CH_3$, SCHC*H*$_2$$CH_2$C*H*$_2$ & SCHCH$_2$C*H*$_2$$CH_2$), 0.86 -0.77 (1H, m, CH_2CH_3). FTIR (cm^{-1}) – 3248 (OH Broad), 1636 (C(O)NH).

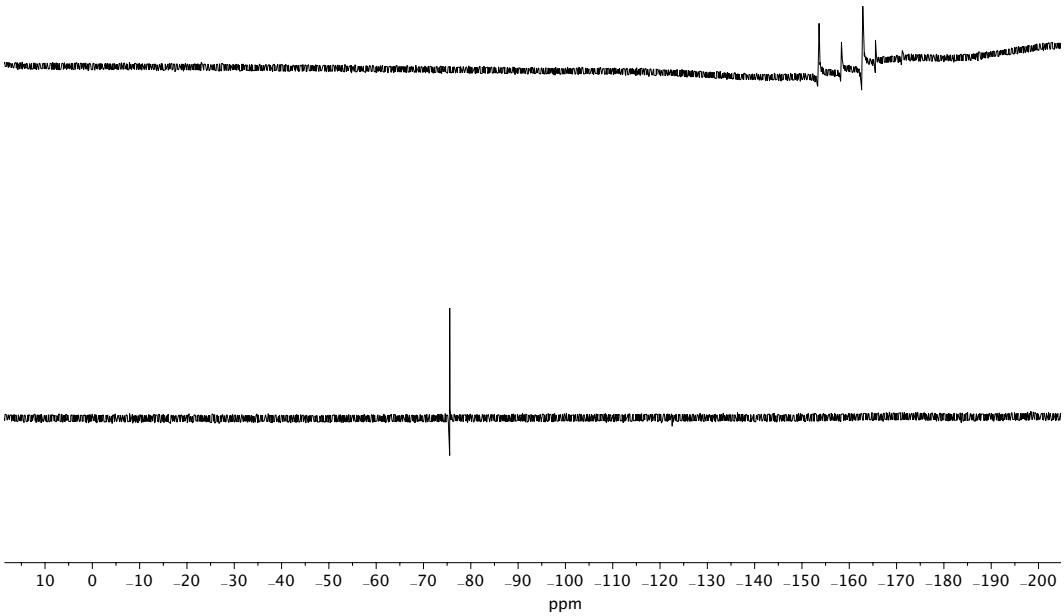

Figure E5.1. ^{19}F NMR of PHEA72 before (Top) and after (bottom) biotin functionalisation

MADIX Agent Synthesis. 2-(ethoxycarbonothioylthio)-2-methylpropanoic acid N-hydroxsuccinimide ester (MADIX1)

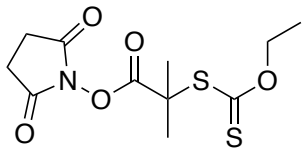

10.27g (61.50 mmol) of 2-bromo-2-methyl-propionic acid was dissolved in 60 mL of ethanol. 15.00 g (93.57 mmol) of potassium *O*-ethyl xanthate was added, and the mixture was stirred for 38 hours at RTP. The reaction mixture was filtered under gravity and the filtrate was diluted with 400 mL of diethyl ether. The organic layer was washed with water (200 mL ×3) and the aqueous layers were combined and acidified with 6 M HCl. The aqueous layers were extracted with diethyl ether (200 mL ×3) and combined with all organic layers. The solution was dried with $MgSO_4$ and filtered under gravity. The solvent was removed under vacuum to form a yellow oil.

8.83 g (42.45 mmol) of crude product (2-((ethoxycarbonothioyl)thio)-2-methylpropanoic acid) and 9.50 g (82.54 mmol) of *N*-hydroxysuccinimide were added to an empty RBF and purged with nitrogen before 40 mL of anhydrous THF was added, the solution was then degassed for a further 20 minutes. The solution was cooled to 0 ℃ and 8 mL (9.93 g, 78.65 mmol) of *N*-*N*-diisopropyl carbodiimide was added dropwise over 10 minutes. The flask was put under positive nitrogen pressure and stirred for 48 hours. The solution was filtered under gravity and the filtrate solvent removed under vacuum. The crude solid was dissolved in 100 mL of diethyl ether and 100 mL of saturated $NaHCO_3$ solution. The organic layer was washed with water (100 mL ×3) and 100 mL of brine once. The organic layer was dried with $MgSO_4$ and filtered under gravity. The solvent was then removed from the filtrate under vacuum. The crude product was recrystallised from ethyl acetate overnight at -8 ℃, washed with cold hexane and dried to give yellow crystals (25.2%). δ_H (300 MHz, $CDCl_3$) 4.69 (2H, q, *J* 7.0, OCH_2), 2.85 - 2.81 (4H, m, $C(O)CH_2CH_2C(O)$), 1.76 (6H, s, $C(CH_3)_2$), 1.37 (3H, t, *J* 7.0, CH_2CH_3). δ_C (300 MHz, $CDCl_3$) 208.9 (1C, SC(S)S), 171.4 (1C, OC(O)), 168.8 (2C, NC(O), 71.0 (1C, OCH_2), 52.4 (1C, $C(CH_3)_2$), 26.2 (2C, $C(O)CH_2CH_2C(O)$), 25.7 (2C, $C(CH_3)_2$), 13.1 (1C, CH_2CH_3). m/z calculated as 305.36; found for ESI $[M+Na]^+$ 328.1. FTIR (cm^{-1}) – 2989.32 & 2940.46 (methyl or methylene), 1779.80 (ester carbonyl), 1731.34 (amide), 1462 (methyl), 1202.06 (C=S), 1038.06 (S-C(S)-O).

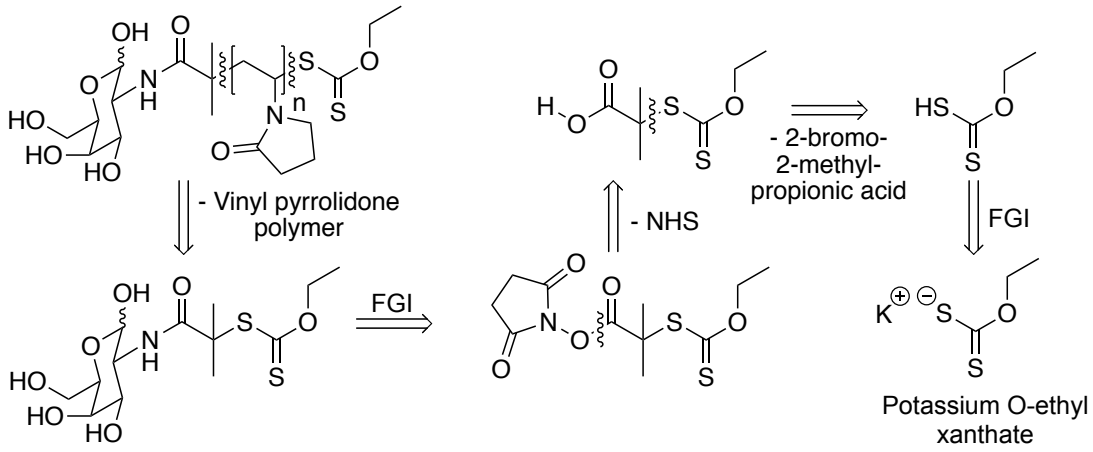

Figure E5.2. Retrosynthesis of MADIX agent

(FGI – functional group interconversion)

Representative Polymerisation of N-vinyl pyrrolidone (PVP80)

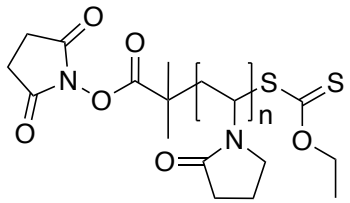

5.65 mL (5.43 g, 48.88 mmol) *N*-vinyl pyrrolidone, 0.010 g (0.036 mmol) ACVA and 0.0523 g (0.171 mmol) MADIX1 were added to 8.5 mL of dioxane and degassed with nitrogen for 20 minutes. The reaction was stirred at 80 °C for 3 days. The solvent was removed under vacuum and the solid dialyzed using 0.5 - 1 kDa cellulose ester tubing in water. The dialyzed product was freeze dried overnight to give a white powder. δ_H (300 MHz, $CDCl_3$) 4.06 - 3.48 (80H, m, NCH_2), 3.47 - 2.98 (184H, m, $NC(O)CH_2$) 2.85 - 2.77 (4H, m, $C(O)CH_2CH_2C(O)$), 2.58 - 2.13 (253H, m, $NC(O)CH_2$), 2.13 - 1.84 (206H, m, NCH_2CH_2), 1.84 - 1.03 (204H, m, $(CH_3)_2$ & $NCHCH_2$ & OCH_2CH_3). FTIR (cm^{-1}) – 2926 (alkyl stretch) 1655 (lactam amide), 1422 (CH_2)

PVP50 - δ_H (300 MHz, $CDCl_3$) 4.16 - 3.45 (50H, m, NCH_2), 3.51 - 2.96 (100H, m, $NC(O)CH_2$) 2.86 - 2.74 (4H, m, $C(O)CH_2CH_2C(O)$), 2.71 - 2.14 (129H, m, $NC(O)CH_2$), 2.14 - 1.85 (111H, m, NCH_2CH_2), 1.85 - 1.01 (159H, m, $(CH_3)_2$ & $NCHCH_2$ & OCH_2CH_3)

PVP150 - δ_H (300 MHz, $CDCl_3$) 4.11 - 3.46 (150H, m, NCH_2), 3.46 - 2.92 (305H, m, $NC(O)CH_2$) 2.85 - 2.75 (4H, m, $C(O)CH_2CH_2C(O)$), 2.69 - 2.12 (428H, m, $NC(O)CH_2$), 2.12 - 1.84 (320H, m, NCH_2CH_2), 1.84 - 1.17 (306H, m, $(CH_3)_2$ & $NCHCH_2$ & OCH_2CH_3)

Representative Poly(N-vinyl pyrrolidone) (PVP80) Glycan Functionalisation

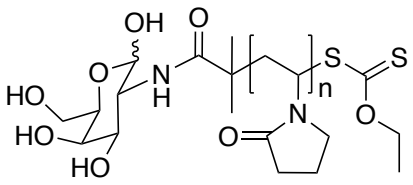

26.6 mg (2.8 μmol) of polymer and 21.2 mg (0.099 mmol) of galactosamine HCl were dissolved in the minimum amount of DMSO and 37.5 μL TEA, stirred for 3 days at RTP and dialyzed using 0.5 - 1 kDa regenerated cellulose membrane tubing in water. The dialyzed product was freeze dried overnight to give a pale-yellow powder (23.5 mg).

δ_H (300 MHz, $CDCl_3$) 5.35 - 4.75 (anomeric 1H, m, C(O)OH), 4.04 - 3.51 (84H, m, CHN & glycan protons), 3.38 - 2.96 (184H, m, NCH_2 & glycan protons), 2.51 - 2.11 (176H, m, $NC(O)CH_2$ & glycan protons), 2.11 - 1.84 (172H, m, NCH_2CH_2), 1.84 - 1.01 (215H, m, $(CH_3)_2$ & $NCHCH_2$ & OCH_2CH_3). FTIR (cm^{-1}) – 2920, 2877 (alkyl stretch) 1655 (lactam amide), 1422 (CH_2)

Representative Poly(N-vinyl pyrrolidone) (PVP80) Biotin Functionalisation

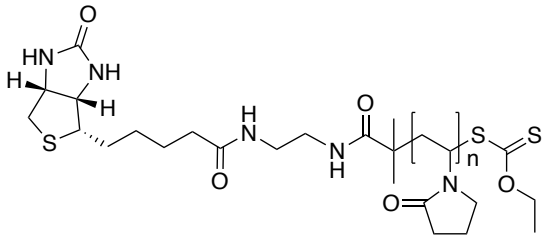

6.5 mg (0.7 μmol) of polymer, 5 mg (17.46 μmol) of biotin-NH_2 and 27.5 μL of TEA was dissolved in the minimum volume of DMSO and stirred at RTP for 72 hours. The reaction mixture was dialyzed using 1 kDa regenerated cellulose membrane in water and freeze dried to give a white solid (5.6 mg). δ_H (300 MHz, $CDCl_3$) 4.08 - 3.52 (82H, m, CHN & $C(O)NHCH_2$), 3.42 - 2.97 (167H, NCH_2, CHCHS, CH_2NH_2, CHCHHS, CHCHHS), 2.55 - 2.12 (226H, $NC(O)CH_2$ & $CH_2C(O)NH$), 2.12 - 1.85 (180H, NCH_2CH_2), 1.85 - 1.07 (193H, m, $(CH_3)_2$, $NCHCH_2$, OCH_2CH_3, $SCHCH_2CH_2CH_2$ & $SCHCH_2CH_2CH_2$). FTIR (cm^{-1}) – 1634 (lactam amide)

Synthesis of diamine t-BOC

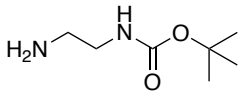

Synthesised by a previously reported protocol.[33] 14 mL (200 mmol) of 1,2-diaminethane (ethylene diamine) was added to 200 mL of chloroform and cooled to 0 °C. 4.44 g (20 mmol) of di-*tert*-butyl decarbonate (BOC_2O) was added to 100 mL of chloroform and added dropwise to the ethylene diamine solution over three hours. The reaction mixture was then stirred at RTP for 16 hours. After 16 hours the reaction mixture was washed with brine (3 × 100 mL) and then water (50 mL), before drying with magnesium sulphate. This was filtered to remove the magnesium sulphate and excess solvent was removed under vacuum to give a pale-yellow oil (3.28 g, 10.2%). δ_H (400 MHz, $CDCl_3$) 4.97 (1H, s, C(O)NH), 3.14 (2H, q, *J* 5.5, NHCH_2), 2.76 (2H, t, *J* 6.0, CH_2NH_2), 1.42 (9H, s, $C(CH_3)_3$), 1.30 (2H, s, NH_2). δ_C (400 MHz, $CDCl_3$) 156.3 (1C, C(O)), 43.5 (1C, NH*C*H_2), 42.0 (1C, *C*H_2NH_2), 28.5 (3C, C(*C*$H_3)_3$) - *C*$(CH_3)_3$ hidden by solvent peak. FTIR (cm^{-1}) – 3357 (amine and amide N-H), 2972, 2931 & 2870 (methyl and methylene), 1684 (amide carbonyl), 1507 (methyl). m/z calculated as 160.12; found for ESI $[M+H]^+$ 161.2 & $[2M+H]^+$ 321.5

Synthesis of biotin diamine t-BOC

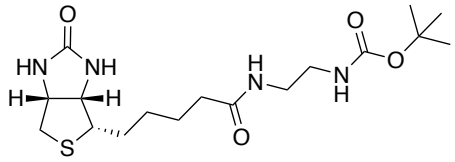

Synthesised by a previously reported protocol.[33] 0.253 g (1.04 mmol) of biotin, 0.217 g (1.36 mmol) of diamine *t*-BOC and 0.265g (1.70 mmol) of EDC were added to a mixture of 5 mL of methanol and 15 mL of acetonitrile under nitrogen. The solution was stirred at 50 ℃ for 5 hours. Excess solvent was removed under vacuum and the crude resuspended in methanol before filtering through a Celite plug®. The solvent was removed under vacuum and the product purified by silica column chromatography (DCM:MeOH 9:1) using a $KMnO_4$ stain to give a white powder (0.193 g, 48.1%). δ_H (400 MHz, MeOD) 7.65 - 7.55 (1H, m, N*H*C(O)O), 7.45 - 7.34 (1H, m, $CH_2C(O)N$*H*), 6.75 - 6.62 (1H, m, C(O)N*H*CHCH), 6.15 - 6.07 (1H, m, C(O)N*H*CHCH$_2$), 4.57 - 4.47 (1H, m, C*H*CH$_2$(S)), 4.37 - 4.28 (1H, m, C*H*CH(S)), 3.82 (2H, q, *J* 7, $CH_2C(O)NHC$*H*$_2$), 3.22 - 3.04 (3H, m, C*H*$_2$NHC(O)O & SC*H*), 2.78 (1H, t, *J* 8.5, CHC*H*HC(S)), 2.71 (1H, t, *J* 7, CHCH*H*C(S)), 2.22 (2H, t, J 7.5, C*H*$_2$C(O)), 1.72 - 1.47 (4H, m, C*H*$_2$CH$_2$C*H*$_2$CH$_2$C(O)), 1.43 (9H, s, OC(CH$_3$)$_3$), 1.30 - 1.10 (2H, m, C*H*$_2$CH$_2$CH$_2$C(O)NH). δ_C (400 MHz, MeOD) 176.4 (1C, CH$_2$*C*(O)NH) 166.1 (1C, NHC(O)NH), 80.1 (1C, *C*(CH$_3$)$_3$), 63.3 (1C, C(O)NH*C*HCH$_2$), 61.6 (1C, C(O)NH*C*HCH), 56.9 (1C, C(O)NHCH*C*H), 41.03, 41.96 & 40.5 (3C, C(O)NHCH*C*H$_2$, C(O)NH$_2$*C*H$_2$*C*H$_2$NH$_2$), 36.8 (1C, *C*H$_2$C(O)NH), 29.8 & 29.5 (2C, C(*C*H$_3$)$_3$), 28.8 & 26.8 (2C, SCH*C*H$_2$*C*H$_2$). FTIR (cm^{-1}) – 3291 (amine and amide N-H), 2931 & 2864 (methyl and methylene), 1687 & 1647 (amide carbonyls), 1528 (methyl/aromatic). m/z calculated as 386.20; found for ESI $[M+Na]^+$ 409.2 & $[M-H]^-$ 385.2

Synthesis of biotin-NH_2

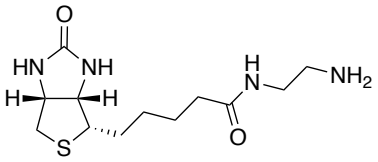

Synthesised by a previously reported protocol.[34] 0.1 g (0.26 mmol) of biotin diamine *t*-BOC was added to 6 mL of DCM containing 1.5 mL of TFA. This was stirred for 2 hours at RTP. The reaction mixture solvent was removed under vacuum and the crude solid dissolved in 50 mL of water before washing with diethyl ether (3× 50 mL). The aqueous layer solvent was removed under vacuum and dried to give a clear colourless oil (0.08 g). δ_H (400 MHz, D_2O) 4.62 (1H, dd, *J* 7.5, 5.0 C*H*CH_2(S)), 4.44 (1H, dd, *J* 8, 4.5, C*H*CH(S)), 3.51 (2H, t, *J* 6, C(O)NHC*H*$_2$), 3.39 - 3.32 (1H, m, CHC*H*S), 3.15 (2H, t, *J* 6, C*H*$_2$$NH_2$), 3.01 (1H, dd, *J* 13, 5, CHCH*H*S), 2.89 - 2.69 (1H, m, CHC*H*HS), 2.31 (2H, t, *J* 7.5 C*H*$_2$C(O)NH), 1.81 - 1.52 (4H, m, SCHC*H*$_2$$CH_2$C*H*$_2$), 1.49 - 1.36 (2H, m, SCHCH$_2$C*H*$_2$$CH_2$). δ_C (400 MHz, D_2O) 177.9 (1C, CH_2*C*(O)NH), 62.1 (1C, *C*HCHS), 60.3 (1C, *C*HCH$_2$S), 55.3 (1C, CH*C*HS), 39.6 (1C, CH*C*H$_2$S) 39.1 (1C, *C*H$_2$$NH_2$), 36.7 (1C, C(O)NH*C*H$_2$), 35.3 (1C, *C*H$_2$C(O)NHCH$_2$), 27.9 & 27.6 (2C, S*C*H$_2$CH$_2$*C*H$_2$), 24.8 (1C, SCH$_2$*C*H$_2$CH$_2$). FTIR (cm^{-1}) – 3390, 3272 (amine and amide N-H), 1685 & 1662 (amide carbonyls). m/z calculated as 286.39; found for ESI $[M+H]^+$ 287.1 $[M+Na]^+$ 309.1

Citrate-Stabilised 16 nm Gold Nanoparticle Synthesis

Synthesised by a previously reported protocol.[45] To 500 mL of water was added 0.163 g (0.414 mmol) of gold(III) chloride trihydrate, the mixture was heated to reflux and 14.6 mL of water containing 0.429 g (1.46 mmol) of sodium citrate tribasic dihydrate was added. The reaction was allowed to reflux for 30 minutes before cooling to room temperature over 3 hours. The solution was centrifuged at 13 krpm for 30 minutes and the pellet resuspended in 40 mL of water to give an absorbance at 520 nm of ~1Abs.

Gold Nanoparticle Polymer Coating Functionalisation – 16 nm

10 mg of polymer was agitated overnight with 10 mL of 16 nm AuNPs ~1Abs at UV_{max}. The solution was centrifuged at 13 krpm for 30 minutes and the pellet resuspended in 10 mL of water, the solution was centrifuged again at 13 krpm for 30 minutes and the pellet resuspended in 1 mL aliquots and centrifuged at 14.5 krpm for 10 minutes. The pellets were combined into a 1 mL solution with an absorbance at 520 nm of ~10 Abs.

Gold Nanoparticle Polymer Coating Functionalisation – 40 nm

10 mg of polymer was agitated overnight with 10 mL of 40 nm AuNPs ~1Abs at UV_{max}. The solution was centrifuged at 6 krpm for 10 minutes and the pellet resuspended in 10 mL of water, the solution was centrifuged again at 6 krpm for 10 minutes and the pellet resuspended in 1 mL aliquots and centrifuged at 6 krpm for 10 minutes. The pellets were combined into a 1 mL solution with an absorbance at UV_{max} of ~10 Abs.

5.6.4 Lateral Flow Strip Production, Running and Analysis Protocols

The procedure to produce flow-through and lateral flow devices was identical, apart from the deposition of the analyte directly to the nitrocellulose (flow-through), versus application of tests lines to the nitrocellulose (lateral flow). This is a truncated protocol from Baker *et al.*, provided for clarity.[13]

Protocol for Manufacturing Lateral Flow Strips

Backing cards were cut to size by removal of 20 mm using a guillotine. Nitrocellulose was added to the backing card by attaching the plastic backing of the nitrocellulose to the self-adhesive on the card. The wick material was then added to the backing card so it overlaps with the nitrocellulose by ~5 mm. The lateral flow strips were cut to size of width 2 - 3 mm.

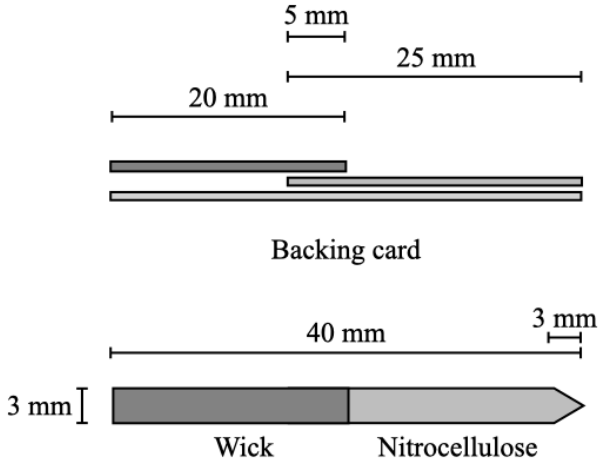

Figure E5.3. Lateral flow strip dimensions

Protocol for Test Line Addition to the Lateral Flow Strips

1 µL of the test line solution was added to the test strip using a micropipette fitted with 10 µL tip, the test line was spotted ~1 cm from the non-wick end of the strip. The strips were dried at 37 ℃ in an oven for 30 minutes. The test strips were allowed to cool to room temperature before testing.

Protocol for Running Lateral Flow Test Without Target Analyte in Buffer

The running buffer of total volume 50 µL was made as follows; 5 µL AuNPs (OD10), 5 µL lateral flow assay buffer – 10 × HEPES buffer, 40 µL water. The running solution was then agitated on a roller for 5 minutes. 45 µL of this solution was added to a 0.2 mL PCR tube, standing vertically.

A small “v” (~3 mm) was cut into the test strips at the non-wick end and the strips added to the PCR tubes, so they protrude from the top and the immobile phase (1 cm from non-wick end) is not below the solvent line. There was one test per tube. All tests were run in triplicate.

The tests were run for 20 minutes before removal from the tubes. The test strips were allowed to dry at room temperature for ~5 minutes. The test strips were mounted test-face down onto a clear and colourless piece of acetate sheeting.

The *Protocol for Running Lateral Flow Test Without Target Analyte in Buffer* was used for the flow-through assays as the target analyte is deposited on the nitrocellulose as a “test line” i.e. the analyte is not in the running buffer.

Protocol for Running Lateral Flow Test with Target Analyte in Buffer

The running buffer of total volume 50 µL was made as follows; 5 µL AuNPs (OD10), 5 µL lateral flow assay buffer – 10 × HEPES buffer, 40 µL of water - *x* µL, where *x* is the volume of target analyte added to make the required concentration of the lectin. The running solution was then agitated on a roller for 5 minutes. 45 µL of this solution was added to a 0.2 mL PCR tube, standing vertically.

A small “v” (~3 mm) was cut into the test strips at the non-wick end and the strips added to the PCR tubes, so they protrude from the top and the immobile phase (1 cm from non-wick end) is not below the solvent line. There was one test per tube. All tests were run in triplicate.

The tests were run for 20 minutes before removal from the tubes. The test strips were allowed to dry at room temperature for ~5 minutes. The test strips were mounted test-face down onto a clear and colourless piece of acetate sheeting.

Standard Protocol for Lateral Flow Strip Analysis

The acetate sheets were scanned using a Kyocera TASKalfa 5550ci printer to a pdf file that was converted to a jpeg, scans were taken within 1 hour of strip drying. The jpeg was analyzed in ImageJ 1.51[44] using the plot profile function to create a data set exported to Microsoft Excel for Mac. The data was exported to Origin 2019 64Bit and trimmed to remove pixel data not from the strip surface. The data was aligned and averaged (mean). The data was then reduced by number of groups to 100 data points

(nitrocellulose and wick) and plotted as Grey value (scale) vs Relative distance along the 100 data points.

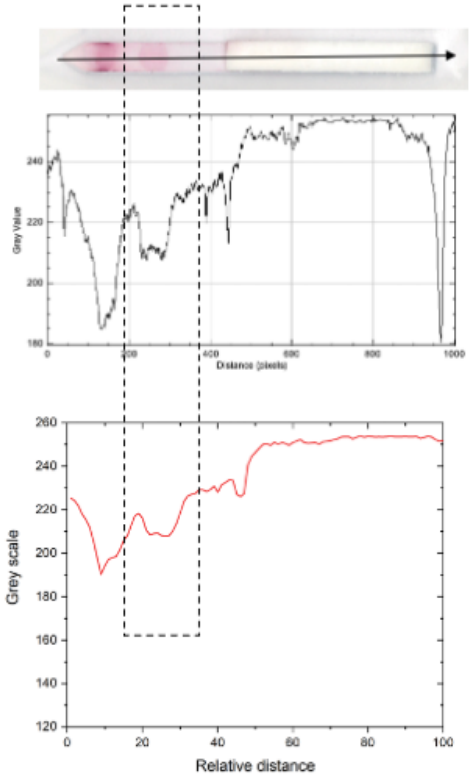

Figure E5.4. Representative dipstick (Top), raw grey value plot (Middle) and processed grey value plot (Bottom)

Lateral Flow Assay Buffer - 10× HEPES buffer (10% PVP_{400}) in 100 mL H_2O

2.38 g (100 mmol.dm^{-3}) of HEPES, 8.77 g (1.50 mol.dm^{-3}) of NaCl, 0.011 g (1.0 mmol.dm^{-3}) of $CaCl_2$, 0.8 g (0.8% w/v., 123 mmol.dm^{-3}) of NaN_3, 0.5 g (0.5% w/v., 4.07 mmol.dm^{-3}) of Tween-20 and 10 g (10% w/v.) of poly(vinyl pyrrolidone)$_{400}$ (PVP_{400}, Average Mw ~40,000) were dissolved in 100 mL of water. The buffer was not pH adjusted.

Intensity Calculations

The average background was determined by calculating the mean grey value of points between 0 - 60 relative distance units, subtracted from 255 (the grey value of clean nitrocellulose); excluding points from aggregation at the solvent front, points contributing to the signal peak and points in the wick. This average background value

was subtracted from the lowest grey value of the signal peak (subtracted from 255) to give intensity.

Signal-to-Noise Calculations

The signal (intensity of test) was then divided by the noise (intensity of control) value to give a signal-to-noise value.

5.7 References

(1) St John, A.; Price, C. P. Point-of-Care Testing Technologies Existing and Emerging Technologies for Point-of-Care Testing. *Clin Biochem Rev* **2014**, *35* (3), 155–167.

(2) Braunstein, G. D.; Khanlian, SA.; Cole, LA.; Wade, ME. The Long Gestation of the Modern Home Pregnancy Test. *Clinical chemistry* **2014**, *60* (1), 18–21.

(3) Crane, M. M.; Organon MV. *Diagnostic Test Device - US3579306A*; 1969.

(4) Wu, J.; Ma, J.; Wang, H.; Qin, D.; An, L.; Ma, Y.; Zheng, Z.; Hua, X.; Wang, T.; Wu, X. Rapid and Visual Detection of Benzothiostrobin Residue in Strawberry Using Quantum Dot-Based Lateral Flow Test Strip. *Sensors and Actuators B: Chemical* **2019**, *283*, 222–229.

(5) Yu, L.; Li, P.; Ding, X.; Zhang, Q. Graphene Oxide and Carboxylated Graphene Oxide: Viable Two-Dimensional Nanolabels for Lateral Flow Immunoassays. *Talanta* **2017**, *165*, 167–175.

(6) Hassan, A. H. A.; Bergua, J. F.; Morales-Narváez, E.; Mekoçi, A. Validity of a Single Antibody-Based Lateral Flow Immunoassay Depending on Graphene Oxide for Highly Sensitive Determination of E. Coli O157:H7 in Minced Beef and River Water. *Food Chemistry* **2019**, *297*, 124965.

(7) Yao, L.; Teng, J.; Zhu, M.; Zheng, L.; Zhong, Y.; Liu, G.; Xue, F.; Chen, W. MWCNTs Based High Sensitive Lateral Flow Strip Biosensor for Rapid Determination of Aqueous Mercury Ions. *Biosensors and Bioelectronics* **2016**, *85*, 331–336.

(8) Carrio, A.; Sampedro, C.; Sanchez-Lopez, J.; Pimienta, M.; Campoy, P. Automated Low-Cost Smartphone-Based Lateral Flow Saliva Test Reader for Drugs-of-Abuse Detection. *Sensors* **2015**, *15* (11), 29569–29593.

(9) Wonderly, B.; Jones, S.; Gatton, M. L.; Barber, J.; Killip, M.; Hudson, C.; Carter, L.; Brooks, T.; Simpson, A. J. H.; Semper, A.; Urassa, W.; Chua, A.; Perkins, M.; Boehme, C. Comparative Performance of Four Rapid Ebola Antigen-Detection Lateral Flow Immunoassays during the 2014-2016 Ebola Epidemic in West Africa. *PLOS ONE* **2019**, *14* (3), e0212113.

(10) Jarvis, J. N.; Percival, A.; Bauman, S.; Pelfrey, J.; Meintjes, G.; Williams, G. N.; Longley, N.; Harrison, T. S.; Kozel, T. R. Evaluation of a Novel Point-of-Care Cryptococcal Antigen Test on Serum, Plasma, and Urine From Patients With HIV-Associated Cryptococcal Meningitis. *Clinical Infectious Diseases* **2011**, *53* (10), 1019–1023.

(11) Carter, L. J.; Garner, L. V.; Smoot, J. W.; Li, Y.; Zhou, Q.; Saveson, C. J.; Sasso, J. M.; Gregg, A. C.; Soares, D. J.; Beskid, T. R.; Jervey, S. R.; Liu, C. Assay Techniques and Test Development for COVID-19 Diagnosis. *ACS Central Science* **2020**, *6* (5), 591–605.

(12) Posthuma-Trumpie, G. A.; Korf, J.; van Amerongen, A. Lateral Flow (Immuno)Assay: Its Strengths, Weaknesses, Opportunities and Threats. A Literature Survey. *Analytical and Bioanalytical Chemistry* **2009**, *393* (2), 569–582.

(13) Baker, A. N.; Richards, S.-J.; Guy, C. S.; Congdon, T. R.; Hasan, M.; Zwetsloot, A. J.; Gallo, A.; Lewandowski, J. R.; Stansfeld, P. J.; Straube, A.; Walker, M.; Chessa, S.; Pergolizzi, G.; Dedola, S.; Field, R. A.; Gibson, M. I. The SARS-COV-2 Spike Protein Binds Sialic Acids and Enables Rapid Detection in a Lateral Flow Point of Care Diagnostic Device. *ACS Central Science* **2020**, *6* (11), 2046–2052.

(14) Damborský, P.; Koczula, K. M.; Gallotta, A.; Katrlík, J. Lectin-Based Lateral Flow Assay: Proof-of-Concept. *The Analyst* **2016**, *141* (23), 6444–6448.

(15) Baker, A. N.; Richards, S.-J.; Pandey, S.; Guy, C. S.; Ahmad, A.; Hasan, M.; Biggs, C. I.; Georgiou, P. G.; Zwetsloot, A. J.; Straube, A.; Dedola, S.; Field, R. A.; Anderson, N. R.; Walker, M.; Grammatopoulos, D.; Gibson, M. I. Glycan-Based Flow-Through Device for the Detection of SARS-COV-2. *ACS Sensors* **2021**, *6* (10), 3696–3705.

(16) Ishii, J.; Toyoshima, M.; Chikae, M.; Takamura, Y.; Miura, Y. Preparation of Glycopolymer-Modified Gold Nanoparticles and a New Approach for a Lateral Flow Assay. *Bulletin of the Chemical Society of Japan* **2011**, *84* (5), 466–470.

(17) Mansfield, M. A. Nitrocellulose Membranes for Lateral Flow Immunoassays: A Technical Treatise. In *Lateral Flow Immunoassay*; 2009; pp 95–114.

(18) Mansfield, M. M. The Use of Nitrocellulose Membranes in Lateral Flow Assays. In *Drugs of Abuse: Body Fluid Testing*; 2005; pp 74–85.

(19) Aoyama, S.; Akiyama, Y.; Monden, K.; Yamada, M.; Seki, M. Thermally Imprinted Microcone Structure-Assisted Lateral-Flow Immunoassay Platforms for Detecting Disease Marker Proteins. *The Analyst* **2019**, *144* (5), 1519–1526.

(20) Ledesma-Osuna, A. I.; Ramos-Clamont, G.; Vázquez-Moreno, L. Characterization of Bovine Serum Albumin Glycated with Glucose, Galactose and Lactose. *Acta biochimica Polonica* **2008**, *55*, 491–497.

(21) Jorgensen, P.; Chanthap, L.; Rebueno, A.; Tsuyuoka, R.; Bell, D. Malaria Rapid Diagnostic Tests in Tropical Climates: The Need for a Cool Chain. *American Journal of Tropical Medicine and Hygiene* **2006**, *74* (5), 750–754.

(22) Pai, N. P.; Vadnais, C.; Denkinger, C.; Engel, N.; Pai, M. Point-of-Care Testing for Infectious Diseases: Diversity, Complexity, and Barriers in Low- And Middle-Income Countries. *PLoS Medicine* **2012**, *9* (9), e1001306.

(23) Aung, M. N.; Koyanagi, Y.; Yuasa, M. Health Inequality among Different Economies during Early Phase of COVID-19 Pandemic. *Journal of the Egyptian Public Health Association* **2021**, *96* (1), 3.

(24) Hansch, C.; Leo, A.; Hoekman, D. *Exploring QSAR: Hydrophobic, Electronic, Steric Constants*; ACS, Washington DC, 1995.

(25) Franco, P.; De Marco, I. The Use of Poly(N-Vinyl Pyrrolidone) in the Delivery of Drugs: A Review. *Polymers* **2020**, *12* (5), 1114.

(26) Ieong, N. S.; Redhead, M.; Bosquillon, C.; Alexander, C.; Kelland, M.; Oreilly, R. K. The Missing Lactam-Thermoresponsive and Biocompatible Poly(N -Vinylpiperidone) Polymers by Xanthate-Mediated RAFT Polymerization. *Macromolecules* **2011**, *44* (4), 886–893.

(27) Congdon, T.; Notman, R.; Gibson, M. I. Antifreeze (Glyco)Protein Mimetic Behavior of Poly(Vinyl Alcohol): Detailed Structure Ice Recrystallization Inhibition Activity Study. *Biomacromolecules* **2013**, *14* (5), 1578–1586.

(28) Perrier, S. *50th Anniversary Perspective*: RAFT Polymerization—A User Guide. *Macromolecules* **2017**, *50* (19), 7433–7447.

(29) Stenzel, M. H.; Cummins, L.; Roberts, G. E.; Davis, T. P.; Vana, P.; Barner-Kowollik, C. Xanthate Mediated Living Polymerization of Vinyl Acetate: A Systematic

Variation in MADIX/RAFT Agent Structure. *Macromolecular Chemistry and Physics* **2003**, *204* (9), 1160–1168.

(30) Congdon, T. R.; Notman, R.; Gibson, M. I. Influence of Block Copolymerization on the Antifreeze Protein Mimetic Ice Recrystallization Inhibition Activity of Poly (Vinyl Alcohol). *Biomacromolecules* **2016**, *17* (9), 3033–3039.

(31) Keddie, D. J.; Moad, G.; Rizzardo, E.; Thang, S. H. RAFT Agent Design and Synthesis. *Macromolecules* **2012**, *45* (13), 5321–5342.

(32) Bell, C. A.; Hedir, G. G.; O'Reilly, R. K.; Dove, A. P. Controlling the Synthesis of Degradable Vinyl Polymers by Xanthate-Mediated Polymerization. *Polymer Chemistry* **2015**, *6* (42), 7447–7454.

(33) Eisenführ, A.; Arora, P. S.; Sengle, G.; Takaoka, L. R.; Nowick, J. S.; Famulok, M. A Ribozyme with Michaelase Activity. *Bioorganic & Medicinal Chemistry* **2003**, *11* (2), 235–249.

(34) Kaufman, N. E. M.; Meng, Q.; Griffin, K. E.; Singh, S. S.; Dahal, A.; Zhou, Z.; Fronczek, F. R.; Mathis, J. M.; Jois, S. D.; Vicente, M. G. H. Synthesis, Characterization, and Evaluation of Near-IR Boron Dipyrromethene Bioconjugates for Labeling of Adenocarcinomas by Selectively Targeting the Epidermal Growth Factor Receptor. *Journal of Medicinal Chemistry* **2019**, *62* (7), 3323–3335.

(35) Kaufman, N. E. M.; Meng, Q.; Griffin, K. E.; Singh, S. S.; Dahal, A.; Zhou, Z.; Fronczek, F. R.; Mathis, J. M.; Jois, S. D.; Vicente, M. G. H. Synthesis, Characterization, and Evaluation of Near-IR Boron Dipyrromethene Bioconjugates for Labeling of Adenocarcinomas by Selectively Targeting the Epidermal Growth Factor Receptor. *Journal of Medicinal Chemistry* **2019**, *62* (7), 3323–3335.

(36) Richards, S.-J.; Gibson, M. I. Optimization of the Polymer Coating for Glycosylated Gold Nanoparticle Biosensors to Ensure Stability and Rapid Optical Readouts. *ACS Macro Letters* **2014**, *3* (10), 1004–1008.

(37) Richards, S.-J.; Keenan, T.; Vendeville, J.-B. B.; Wheatley, D. E.; Chidwick, H.; Budhadev, D.; Council, C. E.; Webster, C. S.; Ledru, H.; Baker, A. N.; Walker, M.; Galan, M. C.; Linclau, B.; Fascione, M. A.; Gibson, M. I. Introducing Affinity and Selectivity into Galectin-Targeting Nanoparticles with Fluorinated Glycan Ligands. *Chemical Science* **2021**, *12* (3), 905–910.

(38) Pancaro, A.; Szymonik, M.; Georgiou, P. G.; Baker, A. N.; Walker, M.; Adriaensens, P.; Hendrix, J.; Gibson, M. I.; Nelissen, I. The Polymeric Glyco-Linker Controls the Signal Outputs for Plasmonic Gold Nanorod Biosensors Due to Biocorona Formation. *Nanoscale* **2021**, *13* (24), 10837–10848.

(39) Bahadır, E. B.; Sezgintürk, M. K. Lateral Flow Assays: Principles, Designs and Labels. *TrAC Trends in Analytical Chemistry* **2016**, *82*, 286–306.

(40) Alfthan, H.; Björses, U.-M.; Tiitinen, A.; Stenman, U.-H. Specificity and Detection Limit of Ten Pregnancy Tests. *Scandinavian Journal of Clinical and Laboratory Investigation* **1993**, *53*, 105–113.

(41) Green, N. M. Avidin. *Advances in Protein Chemistry* **1975**, *29*, 85–133.

(42) Lundquist, J. J.; Toone, E. J. The Cluster Glycoside Effect. *Chemical Reviews* **2002**, *102*, 555–578.

(43) Simon, S.; Worbs, S.; Avondet, M.-A.; Tracz, D.; Dano, J.; Schmidt, L.; Volland, H.; Dorner, B.; Corbett, C. Recommended Immunological Assays to Screen for Ricin-Containing Samples. *Toxins* **2015**, *7* (12), 4967–4986.

(44) Schneider, C. A.; Rasband, W. S.; Eliceiri, K. W. NIH Image to ImageJ: 25 Years of Image Analysis. *Nature Methods* **2012**, *9* (7), 671–675.

(45) Ieong, N. S.; Brebis, K.; Daniel, L. E.; O'Reilly, R. K.; Gibson, M. I. The Critical Importance of Size on Thermoresponsive Nanoparticle Transition Temperatures: Gold and Micelle-Based Polymer Nanoparticles. *Chemical Communications* **2011**, *47* (42), 11627–11629.

Chapter 6

The Synthesis of C2 Aminated Monosaccharides with Conserved C2 Hydroxyl Functionality using Mannich Reactions

6.1 Abstract

Aminated glycans, such as mannosamine and 1-deoxy-1-amino-mannose, are convenient for conjugation reactions onto polymers. However, to create these aminated glycans a hydroxyl must be sacrificed in a substitution reaction for an amine. This is unfortunate, given the importance of a glycan's hydroxyl groups to lectin recognition. The Mannich reaction is a multicomponent reaction widely used to make pharmaceutical targets which could provide an opportunity to produce aminated glycan derivatives without the loss of hydroxyl groups at the C2 position. This study explores the use of the Mannich reaction with mannose and glucose derivatives. Although unsuccessful with the reagents used, it does highlight a potential avenue for future chemical exploration in novel glycan synthesis.

6.2 Declaration

This chapter is entirely the work of myself and has not been published.

6.3 Introduction

Multicomponent reactions allow access to a wide array of chemical space in a small number of synthetic steps. Examples include; the Ugi coupling reaction to form bisamides, the Strecker amino acid synthesis and the Mannich reaction.[1] The Mannich reaction was discovered in 1917 following the reaction of acetophenone (an aromatic ketone) with methanal (formaldehyde) and ammonium chloride by the reaction's namesake.[2] Since then, it has been extensively studied[3] and its mechanism elucidated.

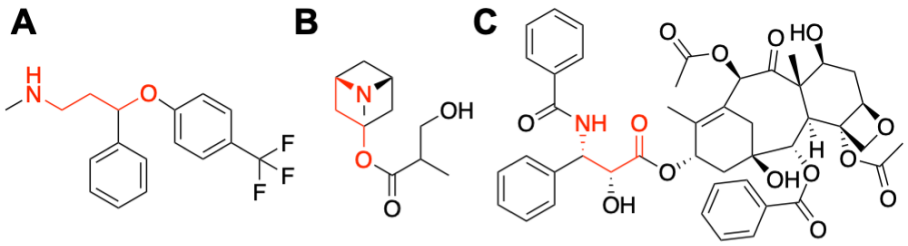

Figure 6.1. Drugs with Mannich base pharmacophores (highlighted in red).

A) Fluoxetine; B) Atropine and C) Paclitaxel

The Mannich reaction synthesises β-aminoketones and β-aminoaldehydes – termed "Mannich bases". Mannich bases are a pharmacophore in many drugs, such as fluoxetine (Figure 6.1A) and atropine (Figure 6.1B).[4] These bases are also of interest due to their similarities with α-hydroxy-β-amino motifs found in therapeutics, for example, paclitaxel (Figure 6.1C) and docetaxel.[5] For this reason, the Mannich reaction has been utilised *en route* to pharmaceuticals.[6] The reaction requires an acidic proton, an aldehyde and an amine in a (usually) acid catalysed reaction. The first step is the attack of the amine with the non-enolisable, often protonated, carbonyl (Figure 6.2). After tautomerisation, an iminium ion forms and acts as the electrophile in a reaction with an enolate to form the Mannich base. The utilisation of iminium salts has allowed for milder and faster reaction conditions.[7]

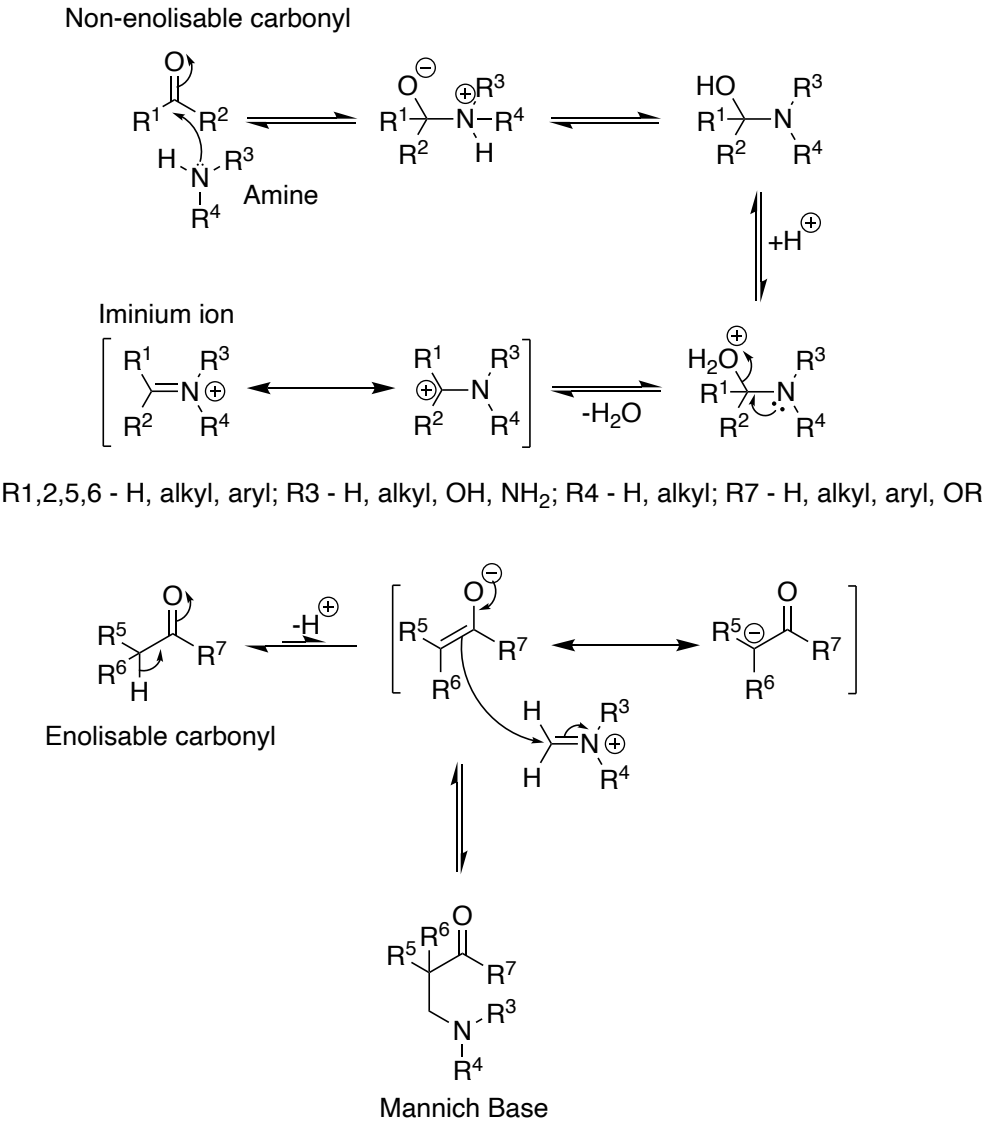

Figure 6.2. Mannich Reaction mechanism

Aminated glycans at the C1 (1-amino-1-deoxyhexoses) or C2 (2-amino-2-deoxyhexoses) position, for example glucosamine, galactosamine and mannosamine (Figure 6.3A), are functionally useful monosaccharides as they can act as nucleophiles for conjugations, such as additions onto polymer end groups. Cho and Kim[8] have developed a convenient synthesis for glucosamine and mannosamine from glucose, while addition of an amine to the C1 position is possible using hydrazides[9] and ammonium solutions.[10,11] In all these glycans, the hydroxyls at the C1 or C2 positions are substituted for amine groups. This is of concern since the removal of hydroxyls from a monosaccharide can influence its affinity for a lectin.[12,13]

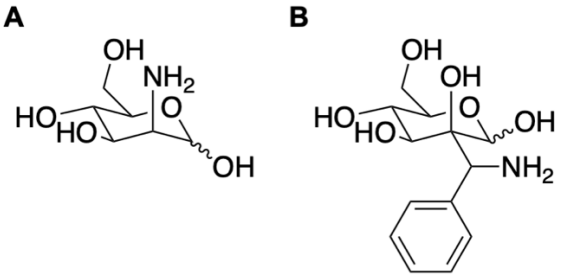

Figure 6.3. Mannose derivatives

A) Mannosamine and B) a mannose derivative (2-*C*-phenylmethanamine mannose) with an amine linker at the C2-position.

The Mannich reaction could offer access to a variety of novel aminated glycan molecules via a carbon linker (Figure 6.3B). The Córdova group has previously shown that the Mannich reaction can be used to add *N*-(phenylmethylene)benzamides to aldehydes[14] to form α-hydroxy-β-amino acids in a proline-catalysed reaction (Figure 6.4).[5]

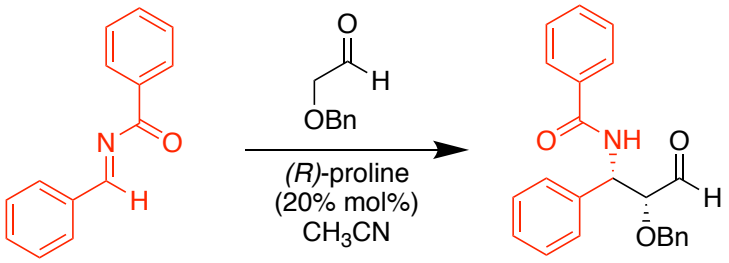

Figure 6.4. Scheme presented by Dziedzic *et al.* for the reaction of *N*-benzylidone benzamide with an aldehyde to form an α-hydroxy-β-amino acid[14]

The linear form of 2,3,4,6-tetra-benzyl-protected aldehydic glycans replicate the structures of the aldehydes used by Córdova, raising the potential for the formation of carbon-linked aminated glycans at the C2 position without replacing the hydroxyl (Figure 6.3B). By building on the transition state proposed by the Córdova group, it is possible to formulate a reaction mechanism for the reaction of a mannose derivative with an iminium compound, such as *N*-benzylidone benzamide (Figure 6.5).

The aim of this chapter is to synthesise the compound shown in Figure 6.3B using the method developed by Córdova for both mannose and glucose derivatives.

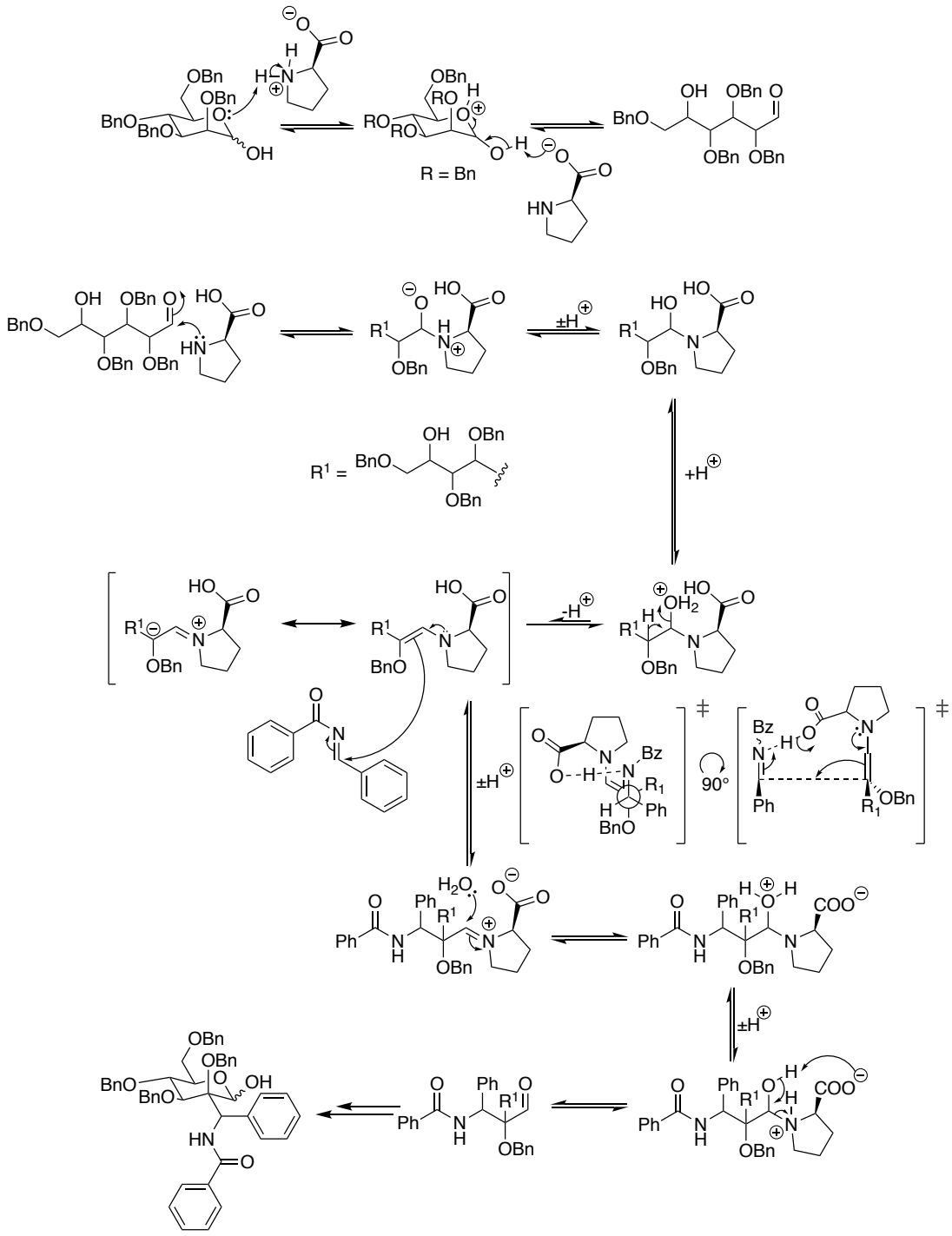

Figure 6.5. Proposed Mannich Reaction of mannose derivative adapted from transition state proposed by Córdova group[5]

6.4 Results and Discussion

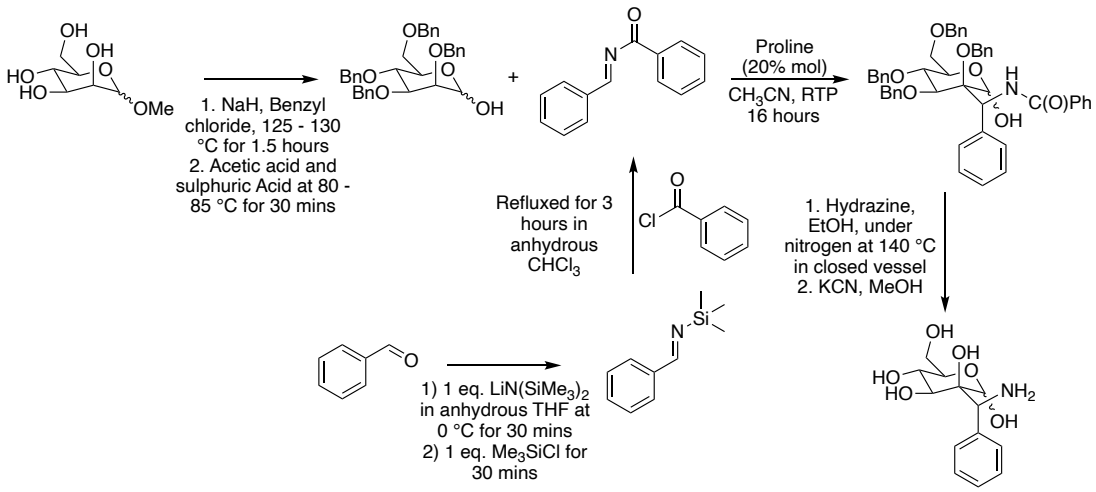

Figure 6.6. Proposed reaction scheme for the synthesis of 2-*C*-phenylmethanamine mannose

The proposed synthesis for 2-*C*-phenylmethanamine mannose (Figure 6.6) utilises the work of the Córdova group, specifically their work on the Mannich reaction (Figure 6.4).[5,14] Notably, the linear (open-chain) form of 2,3,4,6-tetra-*O*-benzyl-protected mannose replicates the core structure of the aldehydes used by Córdova. Following the proline-catalysed Mannich reaction step, the benzyl and benzoyl protecting groups can be removed to leave the 2-*C*-phenylmethanamine mannose product

6.4.1 Synthesis of 2,3,4,6-tetra-O-benzyl mannose

Two methods were trialled for the synthesis of 2,3,4,6-tetra-*O*-benzyl mannose from methylmannoside. The first method, based on work by Koto *et al.*,[15] provided a pure product observed by ^{1}H NMR with a 17% yield – marginally greater than that reported by Koto (Figure 6.7A). The second method (Bulman Page *et al.*) offered yields in the literature of ~40% but required anhydrous solvents and a more arduous synthesis (Figure 6.7B).[16] Initial attempts with the Bulman Page method delivered only trace yields too small to characterise successfully by NMR with partial benzylation shown by mass spectrometry.

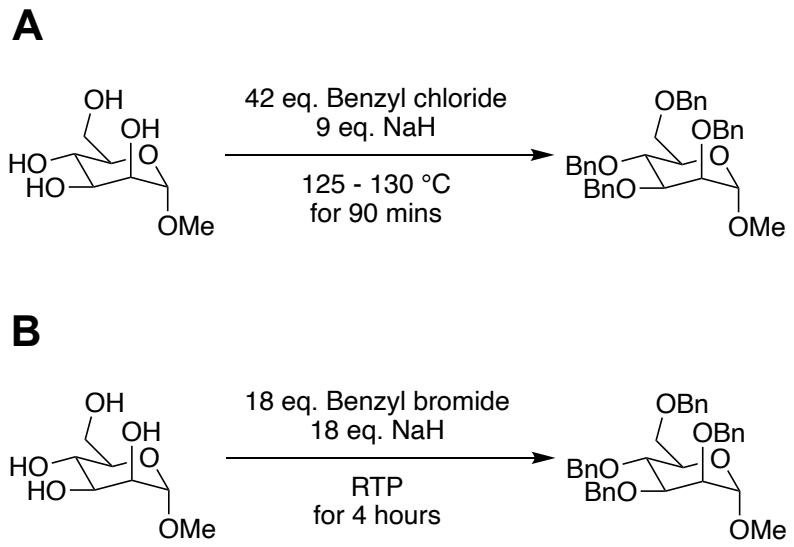

Figure 6.7. Reaction schemes for the Koto (A) and Bulman Page (B) approaches for the synthesis of 2,3,4,6-tetra-*O*-benzyl methylmannoside

Alterations to the temperature and reaction time (from RTP to 70 °C and 3 hours to 16 hours) of the Bulman Page method for benzylation provided yields of 57%. This diverges from other literature sources that favour low reaction temperatures,[17] but did remove the excess use of benzyl chloride as in the Koto method, favouring benzyl bromide instead.

A series of reactions, that did not require the use of methyl protecting groups, was also attempted to produce glycan reagents for the Mannich reaction step. It was decided that 1-acetyl-mannopyranoside using the Lim and Fairbanks method[18] was a possible alternative to 1-methyl-mannopyranoside. However, in all cases the reaction did not stop at the monoacetylated anomeric product, but progressed to various degrees of acetylation as shown by mass spectrometry.

Using a less stable protecting group at the anomeric position also necessitated exploration of global benzylation without the loss of the acetyl group. Therefore, sodium hydride could not be used.[19] A feasible method in the literature involved the use of bis[acetylacetonato]nickel,[20] however this reaction has not been discussed in the literature for monosaccharides. The reaction was unsuccessful in all cases, in the synthesis of 1,2,3,4,6-penta-*O*-benzyl-mannopyranoside, as it required the use of high temperatures that led to degradation of the monosaccharide. Therefore, the use of methylmannoside was favoured since a more facile method using acetyl groups could not be achieved.

With the 2,3,4,6-tetra-*O*-benzyl methylmannoside (and glucose equivalent) to hand, following the aforementioned adapted Bulman Page method, the next step was removal of the C1 methyl protecting group. Both Koto's and Bulman Page's demethylation methods utilise glacial acetic acid, however Bulman Page (Figure 6.8B) favours hydrochloric acid instead of sulphuric acid used by Koto (Figure 6.8A). Both approaches were attempted, and it was found that the Koto method, when carried out over approximately four hours, led to near-complete demethylation. Therefore, the Koto method was used to synthesise both 2,3,4,6-tetra-*O*-benzyl mannose and 2,3,4,6-tetra-*O*-benzyl glucose.

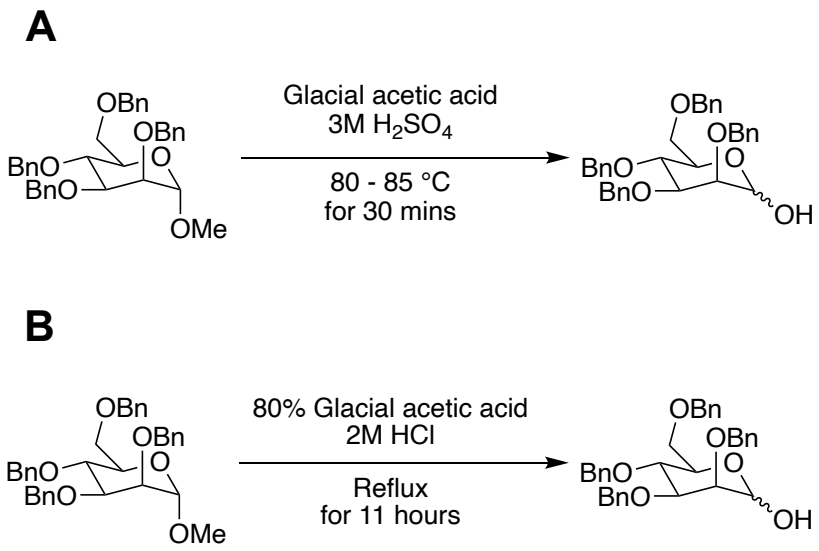

Figure 6.8. Reaction schemes for Koto (A) and Bulman Page (B) approaches for the synthesis of 2,3,4,6-tetra-*O*-benzyl mannose

6.4.2 Synthesis of N-benzylidone benzamide

Various methods were used to synthesise the silyl imine and the imide. Two methods were used to synthesise the silyl imine; the Bongini method[21] that did not require anhydrous solvents; and the Panunzio method[22] that required anhydrous THF (Figure 6.9). All approaches obtained good yields and product as shown by ^{1}H NMR and EI mass spectrometry.

While the Panunzio method obtained marginally higher yields (83%) compared to the Bongini method (79%), the Panunzio method required solvent removal for use in the imide synthesis. Solvent removal proved problematic, as extended exposure to moisture in the air led to degradation of the silyl imine. Therefore, the Bongini method was initially favoured as it was anticipated that this method could be used in conjunction with the Bongini-Kupfer[21,23] imide synthesis without solvent removal.

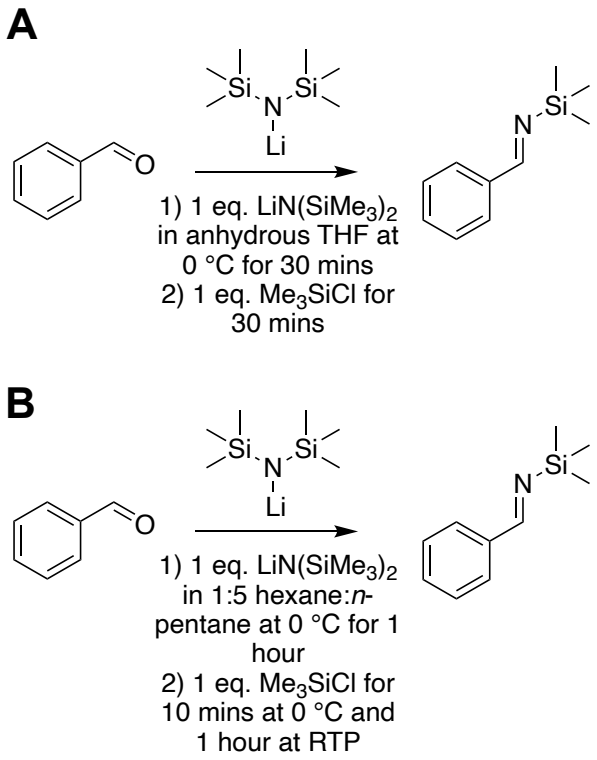

Figure 6.9. Reaction schemes for Panunzio (A) and Bongini (B) approaches for the synthesis of *N*-trimethylsilylbenzaldimine

Synthesis of the imide from the silyl imine was carried out by two methods; Bongini-Kupfer[21,23] (Figure 6.10A) and Colvin-Kupfer[23,24] (Figure 6.10B). It should be noted that the syntheses of the imide were carried out following the Bongini imine synthesis using methods adapted from both Bongini and Kupfer (Bongini-Kupfer) or both

Colvin and Kupfer (Colvin-Kupfer), with cis or trans isomerism not determinable. While the Bongini-Kupfer method does not require anhydrous solvents, it delivered higher yields (75%) compared to Colvin-Kupfer (69%) and could be carried out consecutively without removing the imine adduct from solution (protecting the imine adduct from degradation). However, it was found that the Colvin-Kupfer method was more reproducible and provided a purer product following removal of the solvent and excess *N*-trimethylsilylbenzaldimine under vacuum.

The consecutive Bongini and Colvin-Kupfer syntheses were tracked by ^{1}H NMR integration of the imine's hydrogen (C*H*NSi) versus the benzaldehyde α-hydrogen in the silyl imine synthesis, and the shift of the imine hydrogen on conjugation to benzoyl chloride in the imide synthesis. This showed the reaction processes to almost near-completion, with the final product observable by ESI mass spectrometry. The *N*-benzylidone benzamide product was not purified beyond removal of both the solvent and *N*-trimethylsilylbenzaldimine under vacuum.

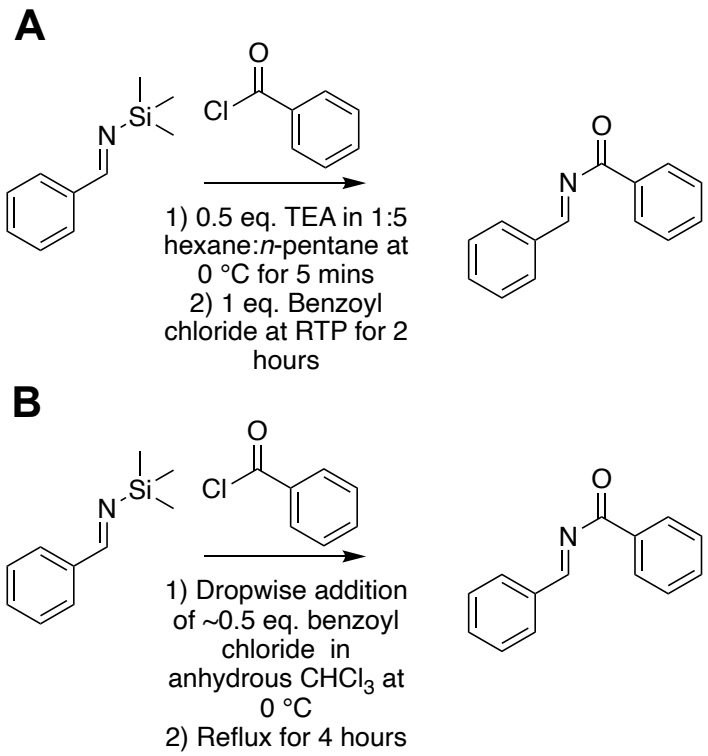

Figure 6.10. Reaction schemes for Bongini-Kupfer (A) and Colvin-Kupfer (B) approaches for the synthesis of *N*-benzylidone benzamide

6.4.3 Mannich reaction

With *N*-benzylidone benzamide, 2,3,4,6-tetra-*O*-benzyl mannose and 2,3,4,6-tetra-*O*-benzyl glucose synthesised, the Mannich reaction step was attempted as described by the Córdova group.[5,14] In order to avoid issues with enantioselective control, as described by Dziedzic,[14] both the *R* (levo, L) and *S* (dextro, D) enantiomers of proline were used with both glycans in four separate reaction combinations (Figure 6.11).

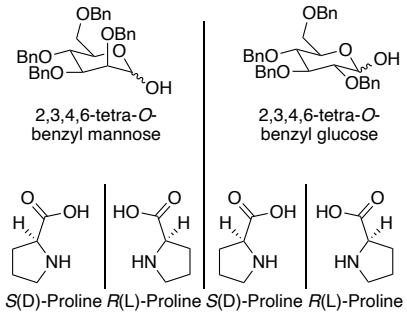

Figure 6.11. Mannich reaction proline and glycan combinations

The Mannich reaction step was attempted on a milligram scale. Mass spectrometry analysis was promising with a peak in all four proline and glycan combinations at ~772 Da (m/z calculated as 749.3; found for ESI $[M+Na]^+$ ~772), but is likely due to a π-π stacking adduct of the glycan and imide reagents. Further characterisation by TLC, after a washing step to remove the proline catalyst, also showed no new products formed (Figure 6.12).

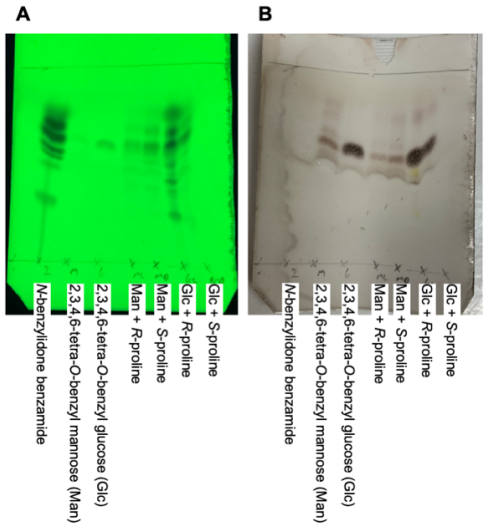

Figure 6.12. TLC analysis of Mannich reaction crudes

A) TLC under UV light; B) TLC after a 5% sulphuric acid in ethanol stain

An in-depth analysis of the NMR data, including the HSQC and HMBC data, collected after a washing step to remove the proline catalyst, also confirmed that no Mannich product was formed (all spectra can be found in Appendix 6). Figure 6.13 shows the overlaid ^{1}H NMR spectra from a representative Mannich reaction (2,3,4,6-tetra-*O*-benzyl glucose + L-proline). It is clear from Figure 6.13 that no new product forms as all peaks (except impurities and solvents) can be accounted for in both the higher region of the ^{1}H spectra (8.5 ppm to 6.3 ppm, Figure 6.13B) and the lower range (5.3 ppm to 3.3 ppm, Figure 6.13C) by the presence of the benzylated glycan and *N*-benzylidone benzamide.

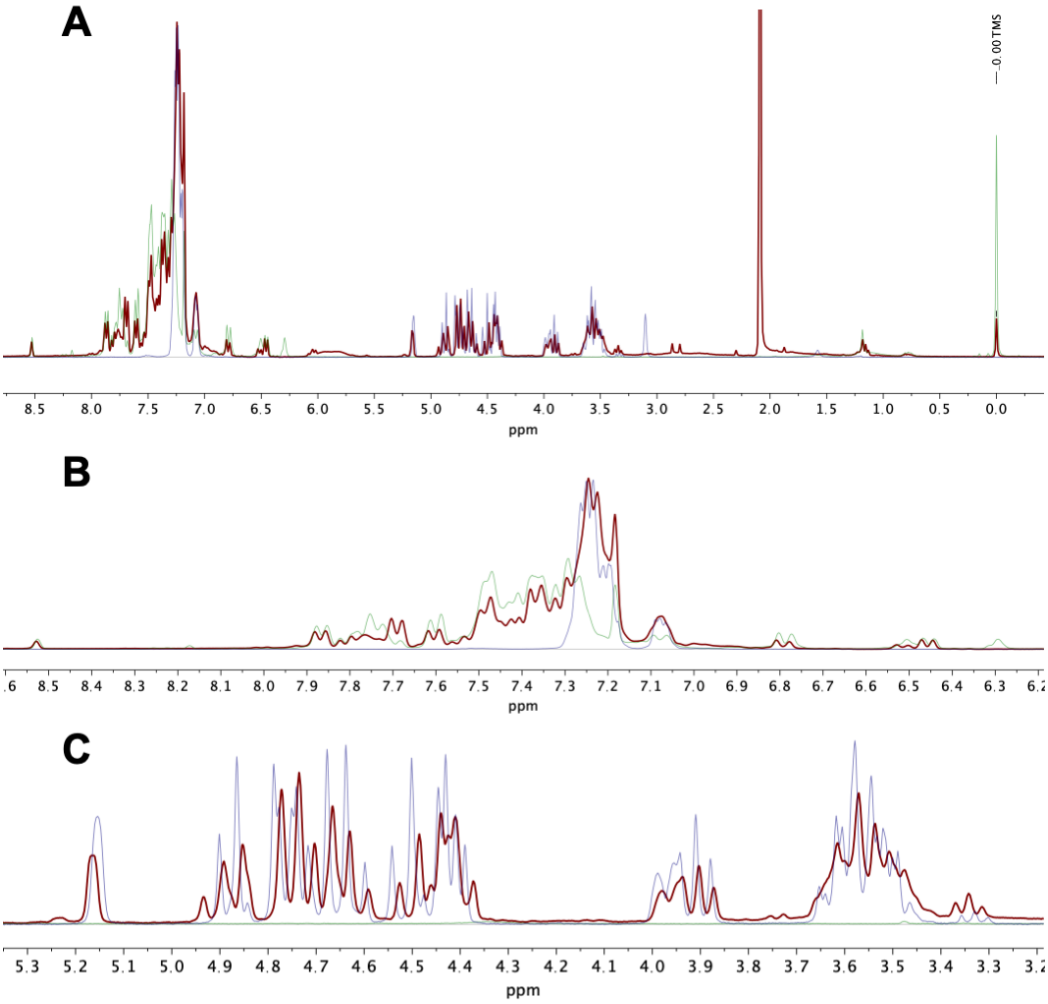

Figure 6.13. Overlaid representative ^{1}H NMR analysis of Mannich reaction crude products and reagents

A) ^{1}H NMR; B) zoomed ^{1}H NMR from 8.5 - 6.3 ppm; C) zoomed ^{1}H NMR from 5.3 - 3.3 ppm. 2,3,4,6-tetra-*O*-benzyl glucose + L-proline, -, red; *N*-benzylidone benzamide, -, green; and 2,3,4,6-tetra-*O*-benzyl glucose, -, lilac.

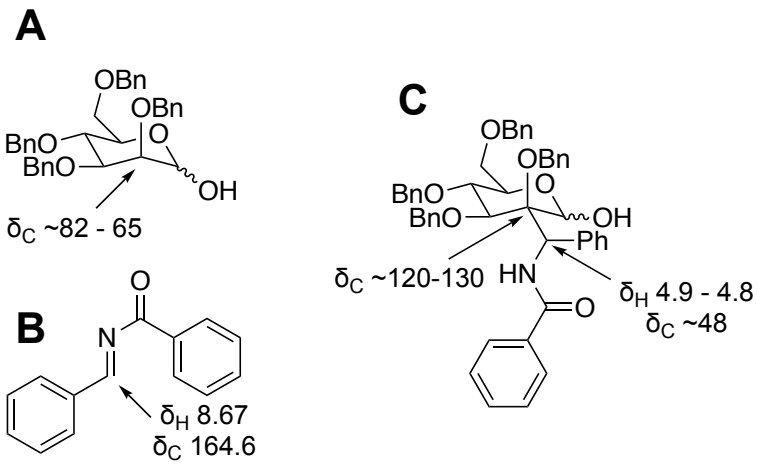

Figure 6.14. Observed and anticipated chemical shifts (ppm) for reagents and products in the Mannich reaction

A) 2,3,4,6-tetra-*O*-benzyl mannose; B) *N*-benzylidone benzamide; C) target product

Furthermore, a consideration of the chemical shifts anticipated in the target product (Figure 6.14C) would suggest the movement of a proton peak in the ^{1}H spectra from 8.67 ppm (C(*H*)NC(O), Figure 6.14B) to ~4.9 ppm (Figure 6.14C) in the target molecule, as the electron withdrawing π-system is lost to form the new C-C bond – this is not observed. It is also anticipated that the carbon of the shifting proton will become more electron shielded: so, move to ~48 ppm (Figure 6.14C) from ~164.59 ppm (Figure 6.14C). This change should be observable in the HSQC spectrum (Figure 6.15A); however, it is not observed with no signal forming in this region (black circle on Figure 6.15A), further indicating that the anticipated product does not form. The HMBC spectrum also shows no change in the shift of the glycan's C2 signal (Figure 6.15B, as the anticipated quaternary carbon does not form in the ^{13}C NMR attached proton test spectrum. It can therefore be concluded that the Mannich reactions were all unsuccessful.

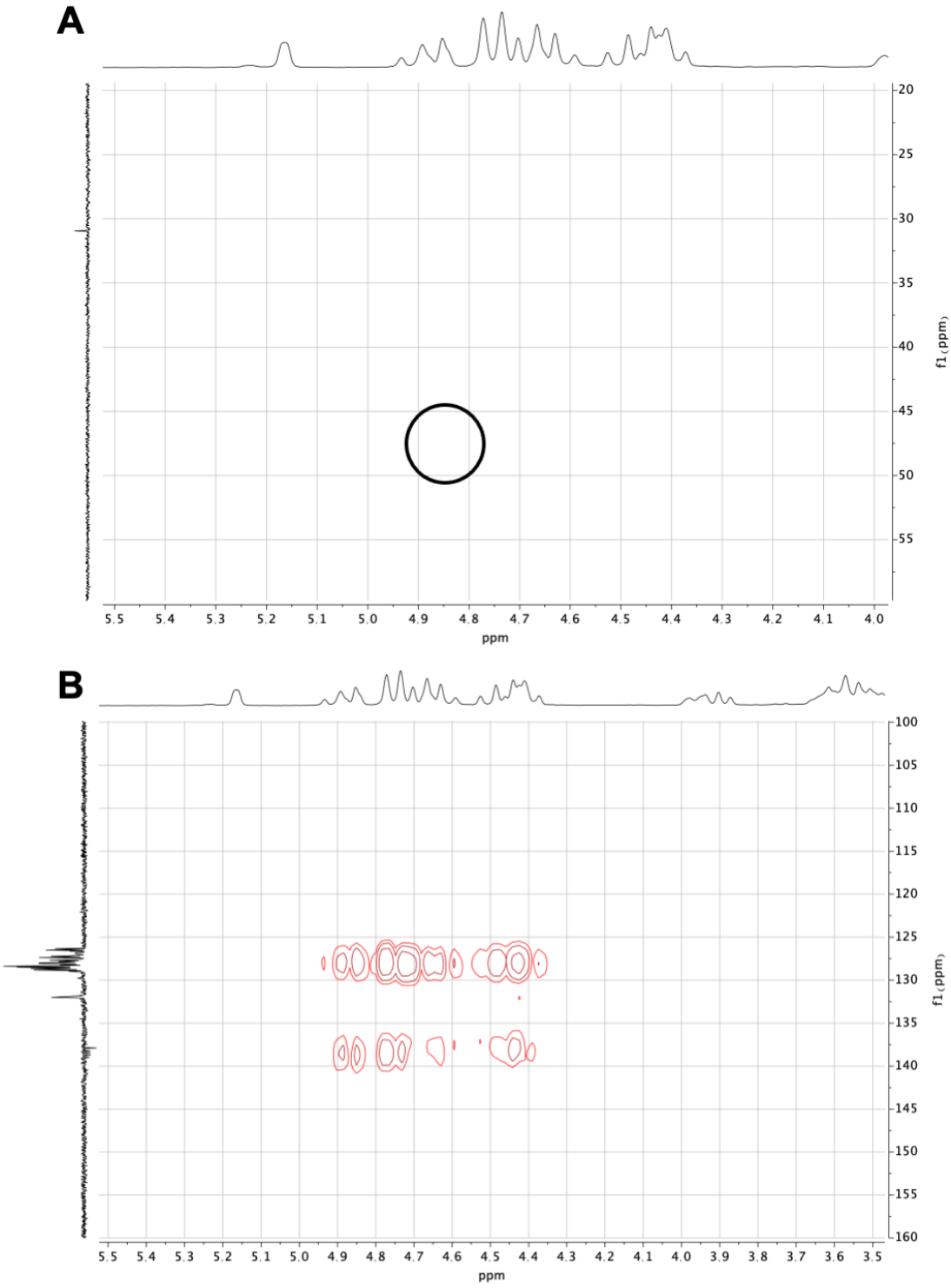

Figure 6.15. Representative 2D NMR analysis of Mannich reaction crude products (2,3,4,6-tetra-*O*-benzyl glucose + L-proline)

A) HSQC of crude with predicted signal circled in black; B) HMBC of crude

A potential reason for the failure of the reactions could be slow mutarotation steps caused by a non-aqueous solvent. This is because the addition of the *N*-benzylidone benzamide to the glycan can only occur with the linear form of the glycan. The linear form of the glycan can only be accessed when the glycan undergoes a mutarotation reaction, catalysed in nature by water, in a solvent-assisted process. In this process water is not only the catalyst, but also stabilises the intermediates by hydrogen bonding. However, because water would degrade the *N*-benzylidone benzamide it could not be used. Therefore, proline was used in its place as a zwitterionic amphiphilic catalyst, alongside acting as a catalyst for the Mannich steps. It is likely that the proline catalysed mutarotation does not occur as rapidly as water catalysed mutarotation, as illustrated by decreased rates of mutarotation in non-aqueous solvents.[25] It is also likely that the acetonitrile solvent is not stabilising the intermediates in a solvent-assisted manner.

6.5 Conclusions

In conclusion, this work aimed to synthesise novel 2-*C*-phenylmethanamine pyranoses that maintain C2 hydroxyl functionality, even with the addition of an amine at the C2 position. To this end, two benzylated monosaccharides (2,3,4,6-tetra-*O*-benzyl mannose and 2,3,4,6-tetra-*O*-benzyl glucose) and *N*-benzylidone benzamide were synthesised and used in a Mannich reaction adapted from the Córdova group.[5,14] This reaction was, however, unsuccessful as shown by TLC and NMR. It is likely this reaction failed due to a slow monosaccharide ring-opening step caused by an organic solvent, and a catalyst that did not replicate the conditions found in aqueous solvent, specifically water's catalytic impact on mutarotation.

While this study was unsuccessful in its primary purpose, it does highlight a potential avenue for future chemical exploration in novel glycan synthesis using the Mannich reaction. Future work based on this study should focus on investigating the other imides discussed by Dziedzic *et al.*,[14] with further consideration of the conditions required for proline-catalysed mutarotation.

6.6 Experimental

6.6.1 Physical and Analytical Methods

NMR Spectroscopy

^{1}H-NMR, ^{13}C-NMR and ^{19}F-NMR spectra were recorded at 300 MHz or 400 MHz on a Bruker DPX-300 or DPX-400 spectrometer respectively, with chloroform-*d* ($CDCl_3$) as the solvent. Chemical shifts of protons are reported as δ in parts per million (ppm) and are relative to $CDCl_3$ (7.26) or tetramethylsilane (TMS, 0.00).

Mass Spectrometry

Low resolution mass spectra (LRMS) were recorded on a Bruker Esquire 2000 spectrometer using electrospray ionisation (ESI) or an Agilent 5977B GC-MS spectrometer using electron ionisation (EI). m/z values are reported in Daltons.

FT-IR Spectroscopy

Fourier Transform-Infrared (FT-IR) spectroscopy measurements were carried out using an Agilent Cary 630 FT-IR spectrometer, in the range of 650 to 4000 cm^{-1}.

Solvent drying

4 Å molecular sieves were activated either by heat or using microwave energy (600W). A 20% w/v. of sieves:solvent was used, the solvent was degassed with nitrogen for 30 minutes with the sieves present and then left overnight before the solvent was used.

6.6.2 Materials

All chemicals were used as supplied unless otherwise stated. Triethylamine (> 99%), deuterated chloroform ($CDCl_3$, 99.8%), 60% sodium hydride in a mineral oil suspension, methanol (≥ 99.8%, ACS reagent grade), toluene (≥ 99.7%), benzaldehyde (≥ 99%, reagent plus), benzoyl chloride (99% ACS reagent), chlorotrimethylsilane (≥ 98.0%) and silica gel 60 Å pore size (Supelco technical grade) were purchased from Sigma-Aldrich.

HPLC grade acetonitrile (≥ 99.8%), hexane fraction from petrol (lab reagent grade), DCM (99% lab reagent grade), sodium hydrogen carbonate (≥ 99%), ethyl acetate (≥ 99.7%, analytical reagent grade), sodium chloride (≥ 99.5%), 40-60 petroleum ether (lab reagent grade), hydrochloric acid (~37%, analytical grade), Molecular Sieve type 4 Å nominal pore size (general purpose grade), THF (HPLC), chloroform (≥ 99%) glacial acetic acid (analytical grade), sulphuric acid (≥ 99.5% analytical grade) and magnesium sulphate (reagent grade) were purchased from Thermo Fisher Scientific.

Benzyl bromide (99%), n-pentane (98%) and lithium bis(trimethylsilyl)amide were purchased from Alfa Aesar

DMF (> 99%) and benzyl chloride (99.5%) were purchased from Acros Organics

Ethanol absolute was purchased from VWR International.

TLCs were imaged under UV light or using a 5% H_2SO_4 stain in ethanol.

Ultra-pure water used for washing and aqueous solutions was MilliQ grade 18.2 mΩ resistance.

6.6.3 Synthetic Methods

NMR spectra for the synthesised molecules can be found in Appendix 6.

Synthesis of 2,3,4,6-tetra-O-benzyl mannose – Bulman Page method

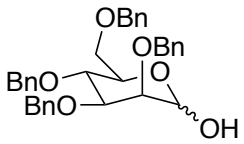

Synthesised by a previously reported protocol.[16] 1 g (5.15 mmol) of methyl α-D-mannopyranoside was added to 45 ml of anhydrous DMF under nitrogen and cooled in an ice bath. 3.7 g (92.51 mmol) of 60% NaH in oil was slowly added under nitrogen and the reaction vessel was vigorously stirred for 30 minutes in the ice bath. 11.3 ml (16.25 g, 95.00 mmol) of benzyl bromide was added dropwise over 30 minutes to the reaction vessel still in an ice bath. The reaction was allowed to reach RTP and stir for a further 4 hours. 7.4 ml of methanol was added and the reaction vessel stirred for a further 10 minutes. The solvent was then removed under vacuum. 100 ml of water and 100 ml of ethyl acetate were used to dilute the solid before filtration under gravity. The organic filtrate layer was washed with water and brine before drying with $MgSO_4$. The reaction was filtered under gravity to give a filtrate, this was concentrated under vacuum to give the crude intermediate (methyl 2,3,4,6-tetra-*O*-benzyl-D-mannopyranoside).

Adaptations to this method of a 70 ℃ reaction temperature and a reaction time of 16 hours increased the yield to 57.4%. A pure product could be achieved by silica chromatography using 1:9 ethyl acetate: 40-60 petroleum ether.

The crude intermediate was dissolved in 80% glacial acetic acid and 2 M HCl, using ~45 ml of acid solution per gram of crude. The reaction mixture was heating to reflux for 11 hours before diluting with DCM (25 ml of DCM per gram of crude) and washing with saturated sodium hydrogen carbonate (50 ml of solution per gram of crude). The aqueous layer was extracted using DCM (25 ml of DCM per gram of crude). All organic layers were combined, dried using $MgSO_4$ and the solvent removed under vacuum. The crude product was purified by silica chromatography with 1:2 ethyl acetate: 40-60 petroleum ether. There was too low a yield to purify by silica chromatography.

Synthesis of 2,3,4,6-tetra-O-benzyl mannose – Koto method

Synthesised by a previously reported protocol.[15] 1 g (5.15 mmol) of methyl α-D-mannopyranoside was added to 25 ml (27.5 g, 217.25 mmol) of benzyl chloride and cooled in an ice bath. 1.7 g (45.99 mmol) of 60% NaH in oil was slowly added and the reaction vessel heated to 125 - 130 ℃, under nitrogen, with vigorous stirring for 90 minutes. The reaction was filtered under gravity to give a yellow filtrate, this was concentrated under vacuum.

The crude product (2,3,4,6-tetra-*O*-benzyl methyl mannoside) was purified by silica chromatography using 1:9 ethyl acetate:40-60 petroleum ether to give a pale yellow oil (17%). Anomeric ratio of OCH_3 - α:β : 45:55. δ_H (300 MHz, $CDCl_3$) 7.53 - 7.16 (20H, m, phenyl protons), 4.98 (1H, s, β-C^1 proton), 4.95 (1H, s, α-C^1 proton), 4.89 - 4.71 (4H, m, C^3 & C^4 PhCH_2), 4.71 - 4.67 (2H, m, C^6 PhCH_2), 4.67 - 4.56 (2H, m, C^2 PhCH_2), 4.07 (1H, t, *J* 9.0, C^4 proton), 3.97 (1H, dd, *J* 9.5, 2.5, C^3 proton), 3.82 - 3.67 (4H, m, C^2 and C^{5-6} protons), 3.42 (3H, s, C^1 OCH_3). δ_C (300 MHz, $CDCl_3$) 141.0 - 138.3 (4C, ipso phenyl carbons), 128.7 - 126.8 (20C, ortho, meta and para phenyl carbons), 98.1 (1C, C^1), 80.1 (1C, C^4), 75.1 - 69.4 (8C 4xCH_2Ph, C^{2-3} and C^{5-6}), 54.8 (1C, CH_3). m/z calculated as 554.27; found for ESI $[M+Na]^+$ 577.27. FTIR (cm^{-1}) – 3028.46 (aryl C-H), 2909.18 & 2864.46 (methyl and methylene), 1496.52 (aromatic alkene), 1453.66 (methyl), 1056.70 (ether)

0.25g (4.51 mmol) of (methyl 2,3,4,6-tetra-*O*-benzyl-D-mannopyranoside) was added to 50 ml of glacial acetic acid and 6 ml (3 M) H_2SO_4 and stirred for 2 hours at 85 ℃, to form a yellow liquid. Aliquots were taken for mass spectrometry every hour to determine reaction progress. The yellow liquid was diluted in 75 ml of toluene and 75 ml of water before washing the organic layer with (150 ml ×2) saturated sodium hydrogen carbonate solution then (150 ml ×2) water. The organic layer was concentrated under vacuum to give the crude product. This was purified by silica chromatography using 1:2 ethyl acetate:40-60 petroleum ether, to give a white solid/oil (22.5%). Anomeric ratio OH - α:β 0.33:0.66. δ_H (300 MHz, $CDCl_3$) 7.43 - 7.09 (20H, m, phenyl protons), 5.26 (1H, s, β-C^1 proton), 5.09 (1H, d, *J* 11.5, α-C^1 proton), 4.91 - 4.46 (8H, m, PhCH_2), 4.06 - 3.99 (1H, m, C^2 or C^5 or C^4 proton), 3.99 - 3.93 (1H, m, C^3 proton), 3.91 - 3.79 (2H, m, C^2 or C^5 or C^4 protons), 3.76 - 3.67 (2H, m, C^6 protons). δ_C (300 MHz, $CDCl_3$) ~140 - 135 (4C, ipso phenyl carbons (shown by HMBC)), 128.5 - 127.5 (20C, ortho, meta and para phenyl carbons), 92.9 (1C, C^1),

79.7 (1C, C^3), 75.2, 74.8, 71.9 (3C, C^2, C^4, C^5), 75.1, 73.4, 72.8, 72.2 (4C, *C*H_2 benzyl), 69.7 (1C, C^6). m/z calculated as 540.25; found for ESI $[M+Na]^+$ 563.2. FTIR (cm^{-1}) – 3304.3 (broad, hydroxyl), 3069.5, 2899.9 (C-H stretch), 1528.2 (aromatic alkene), 1047.4 (ether), 844.7 (aromatic)

Synthesis of Methyl 2,3,4,6-Tetra-O-Benzyl-Glucopyranoside

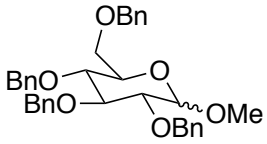

Adapted from the Bulman Page method.[16] 2.00 g (10.3 mmol) of methyl α-D-glucopyranoside was added to 60 ml of anhydrous DMF under nitrogen and cooled in an ice bath. 4.94 g (123.6 mmol) of 60% NaH in oil was slowly added under nitrogen and the reaction vessel was vigorously stirred for 30 minutes in the ice bath. 14.7 ml (21.14 g, 123.6 mmol) of benzyl bromide was added dropwise over 30 minutes to the reaction vessel still in an ice bath. The reaction was heated to 70 °C and stirred for 16 hours. 10 ml of methanol was added, and the reaction vessel stirred for a further 10 minutes. The solvent was then removed under vacuum. 200 ml of water and 200 ml of toluene were used to dilute the solid. The organic layer was washed with 2 × 200 mL of water before the organic layer was evaporated to give a crude product. The crude was purified by silica chromatography with 1:9 ethyl acetate:40-60 petroleum ether to give a pale-yellow oil (51%). δ_H (400 MHz, $CDCl_3$) 7.44 - 7.10 (20H, m, phenyl protons), 5.04 - 4.95 (1H, m, anomeric proton), 4.88 - 4.45 (9H, m, anomeric proton, PhCH_2), 3.84 - 3.50 (5H, m, C^2-C^6 protons), 3.45 - 3.30 (3H, m, OCH_3, including methanol impurity). δ_C (400 MHz, $CDCl_3$) 141.0 - 138.0 (4C, ipso phenyl carbons), 128.7 - 127.0 (20C, ortho, meta and para phenyl carbons), 97.7 (1C, C^1), 82.2 - 65.3 ($C^{2\text{-}6}$ and CH_2 benzyl) 55.2 (1C, OCH_3). m/z calculated as 544.27; found for ESI $[M+Na]^+$ 577.2 . FTIR (cm^{-1}) – 3062.0, 3030.3, 2905.3, 2808.2 (C-H stretch), 1647.5 (aromatic), 1451.8 (methyl), 1042.8 (ether)

Synthesis of 2,3,4,6-Tetra-O-Benzyl-Glucose

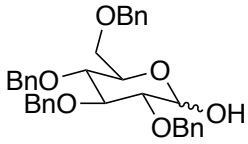

Adapted from the Koto method.[15] 0.5g (9.02 mmol) of (methyl 2,3,4,6-tetra-*O*-benzyl-D-glucopyranoside) was added to 100 ml of glacial acetic acid and 13 ml (3 M) H_2SO_4 and stirred for 2 hours at 85 °C, to form a yellow liquid. Aliquots were taken for mass spectrometry every hour to determine reaction progress. The yellow liquid was diluted in 150 ml of toluene and 150 ml of water before washing the organic layer with (300 ml ×2) saturated sodium hydrogen carbonate solution then (300 ml ×2) water. The organic layer was concentrated under vacuum to give the crude product. This was purified by silica chromatography with 1:2 ethyl acetate:40-60 petroleum ether, to give a white solid (6.7%). δ_H (400 MHz, $CDCl_3$) 7.44 - 6.96 (20H, m, phenyl protons), 5.18 - 5.13 (1H, m, anomeric proton), 4.93 - 4.31 (~8H, m, anomeric proton and PhCH_2), 4.01 - 3.91 (1H, m, C^5 proton), 3.88 (1H, d, *J* 9.5, C^3 proton), 3.74 - 3.43 (4H, m, C^2, C^6 and C^4 protons). δ_C (400 MHz, $CDCl_3$) 138.8, 138.3, 138.0, 138.0 (4C, ipso phenyl carbons), 128.8 - 127.6 (16C, ortho, meta and para phenyl carbons), 91.5 (1C, C^1), 81.9 (1C, C^3), 80.1, 77.8 (2C, C^2 and C^4), 75.9, 75.2, 73.6, 73.4 (4C, PhCH_2), 70.6, (1C, C^5), 68.7 (1C, C^6). m/z calculated as 540.25; found for ESI $[M+Na]^+$ 563.2. FTIR (cm^{-1}) – 3354 (broad, hydroxyl), 3084.4, 3060.1, 3028.5 (aryl C-H), 2916.6, 28657.0 (methyl and methylene), 1584.1 (aromatic alkene), 1086.5 (ether)

Synthesis of N-trimethylsilylbenzaldimine – method 1 – Bongini

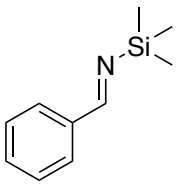

Synthesised by a previously reported protocol.[21] All reaction steps were carried out under nitrogen. 0.16 g (0.956 mmol) of lithium bis(trimethylsilyl)amide was to a mixture of 1 ml of hexane and 5 ml of n-pentane at 0 ℃. 0.1 ml (0.1044 g, 9.84 mmol) of benzaldehyde was added in 2 ml of n-pentane and the reaction stirred at 0 ℃ for one hour. 0.13 ml (0.11 g, 1.02 mmol) of chlorotrimethylsilane was added and the reaction stirred for a further 10 minutes at 0 ℃ and at RTP for 1 hour. A white precipitate formed (79%). δ_H (300 MHz, $CDCl_3$) 8.80 (1H, s, NCH), 7.69 - 7.58 (2H, m, ortho protons), 7.30 - 7.01(3H, m, para and meta) 0.08 (9H, s, $Si(CH_3)_3$). δ_C (300 MHz, $CDCl_3$) 168.7 (NCH), 139.0 (ipso), 132.0 (para), 128.9 (ortho), 128.4 (meta), -0.9 ($SiCH_3$). m/z calculated as 177.10; found for EI $[M]^+$ 177.1. FTIR (cm^{-1}) – 2950.15 (C-H stretch), 1649.35 (C=N stretch), 1248.86 ($SiMe_n$), 833.06 (C-H aromatic)

Synthesis of N-trimethylsilylbenzaldimine – method 2 – Panunzio[22]

To 20 ml of anhydrous THF was added 1.06 g (9.98 mmol) of benzaldehyde and 1.67 g (9.98 mmol) of lithium bis(trimethylsilyl)amide, the mixture was stirred for 30 minutes at 0 ℃ under nitrogen. The reaction was allowed to reach RTP and 1.08 g (9.94 mmol) of chlorotrimethylsilane was added and the reaction stirred for a further 30 minutes. The reaction mixture was filtered under gravity and the solvent removed under vacuum to give the product (83%).

Synthesis of N-benzylidone benzamide – method 1 – Bongini-Kupfer

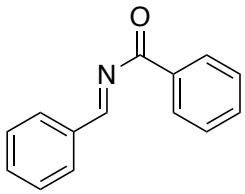

Adapted from the Bongini[21] and Kupfer[23] methods. All reaction steps were carried out under nitrogen. To 0.1 g (1.41 mmol) of *N*-trimethylsilylbenzaldimine 1 ml of hexane and 5 ml of n-pentane at 0 ℃, was added 0.1 ml (0.0725 g, 0.717 mmol) triethylamine. The reaction was stirred for 5 minutes before 0.044 g (0.348 mmol) of benzoyl chloride was added and the reaction allowed to return to RTP. The reaction was stirred for 2 hours, and the solvent removed under vacuum to give a white product (75%). No further purification was carried out, due to the instability of the product. δ_H (300 MHz, $CDCl_3$) 8.67 (1H, m, NCH), 8.15 - 7.11 (10H, m, phenyl protons). δ_C (300 MHz, $CDCl_3$) 181.0 (1C, C(O)), 164.6 (1C, *C*NC(O)), 133.2 - 125 (12C, phenyl carbons). m/z calculated as 209.08; found for ESI $[M+H]^+$ 210.0. FTIR (cm^{-1}) – 3062.0 & 3030.3 (C-H stretch), 1643.8 (amide carbonyl), 1522.6 (amide bend)

Synthesis of N-benzylidone benzamide – method 2 – Colvin-Kupfer[23,24]

Adapted from the Colvin[24] and Kupfer[23] methods. 0.25 g (3.525 mmol) of *N*-trimethylsilylbenzaldimine was added to 10 ml of anhydrous chloroform before 0.2 g (1.58 mmol) of benzoyl chloride was added dropwise to the stirring reaction under nitrogen at 0 ℃. The reaction was refluxed for 4.5 hours under nitrogen, an aliquot was taken every hour to determine reaction progress by mass spectrometry. The solvent was removed under vacuum to give a white powder (69%). No further purification was carried out, due to the instability of the product.

Mannich Reaction

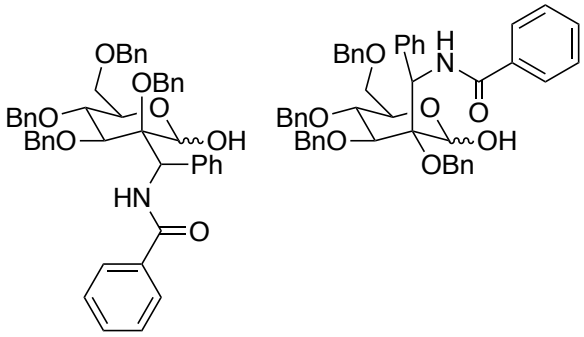

Carried out folowing a previously reported protocol.[14] 77 mg (0.37 mmol) of *N*-benzylidone benzamide, 40 mg (0.074 mmol) of 2,3,4,6-tetra-*O*-benzyl mannose (or 2,3,4,6-tetra-*O*-benzyl glucose) and 2.6 mg (0.023 mmol) of a proline isomer was added to 2 ml of acetonitrile and stirred for 48 hours at RTP. Solvent was removed under vacuum and the crude dissolved in 20 mL of DCM. The DCM layer was washed with water (10 mL ×3), the aqueous layers were extracted with 15 mL of DCM, the organic layers combined and solvent removed under vacuum to give a crude product that was analysed by mass spectrometry, NMR (in $CDCl_3$) and TLC (9:1:1% DCM:MeOH:acetic acid).

6.7 References

(1) Alvim, H. G. O.; da Silva Júnior, E. N.; Neto, B. A. D. What Do We Know about Multicomponent Reactions? Mechanisms and Trends for the Biginelli, Hantzsch, Mannich, Passerini and Ugi MCRs. *RSC Adv.* **2014**, *4* (97), 54282–54299.

(2) Mannich, C.; Krösche, W. Ueber Ein Kondensationsprodukt Aus Formaldehyd, Ammoniak Und Antipyrin. *Archiv der Pharmazie* **1912**, *250* (1), 647–667.

(3) Filho, J. F. A.; Lemos, B. C.; de Souza, A. S.; Pinheiro, S.; Greco, S. J. Multicomponent Mannich Reactions: General Aspects, Methodologies and Applications. *Tetrahedron* **2017**, *73* (50), 6977–7004.

(4) Bala, S.; Sharma, N.; Kajal, A.; Kamboj, S.; Saini, V. Mannich Bases: An Important Pharmacophore in Present Scenario. *International Journal of Medicinal Chemistry* **2014**, *2014*, 1–15.

(5) Dziedzic, P.; Vesely, J.; Córdova, A. Catalytic Asymmetric Synthesis of the Docetaxel (Taxotere) Side Chain: Organocatalytic Highly Enantioselective Synthesis of Esterification-Ready α-Hydroxy-β-Amino Acids. *Tetrahedron Letters* **2008**, *49* (47), 6631–6634.

(6) Sun, B.; Pluta, R.; Kumagai, N.; Shibasaki, M. Direct Catalytic Asymmetric Mannich-Type Reaction En Route to α-Hydroxy-β-Amino Acid Derivatives. *Organic Letters* **2018**, *20* (3), 526–529.

(7) Arend, M.; Westermann, B.; Risch, N. Modern Variants of the Mannich Reaction. *Angewandte Chemie International Edition* **1998**, *37* (8), 1044–1070.

(8) Kim, S.-J.; Cho, H. Convenient Synthesis of Glucosamine and Mannosamine Starting from Glucose. *Bulletin of the Korean Chemical Society* **2015**, *36* (7), 1916–1918.

(9) Godula, K.; Bertozzi, C. R. Synthesis of Glycopolymers for Microarray Applications via Ligation of Reducing Sugars to a Poly(Acryloyl Hydrazide) Scaffold. *Journal of the American Chemical Society* **2010**, *132* (29), 9963–9965.

(10) Campa, C.; Donati, I.; Vetere, A.; Gamini, A.; Paoletti, S. Synthesis of Glycosylamines: Indentification and Quantification of Side Products. *Journal of Carbohydrate Chemistry* **2001**, *20* (3–4), 263–273.

(11) Lubineau, A.; Augé, J.; Drouillat, B. Improved Synthesis of Glycosylamines and a Straightforward Preparation of N-Acylglycosylamines as Carbohydrate-Based Detergents. *Carbohydrate Research* **1995**, *266* (2), 211–219.

(12) Rao, V. S. R.; Lam, K.; Qasba, P. K. Three Dimensional Structure of the Soybean Agglutinin-Gal/GalNAc Complexes by Homology Modeling. *Journal of Biomolecular Structure and Dynamics* **1998**, *15* (5), 853–860.

(13) Yahara, I.; Edelman, G. M. Restriction of the Mobility of Lymphocyte Immunoglobulin Receptors by Concanavalin A. *Proceedings of the National Academy of Sciences* **1972**, *69* (3), 608–612.

(14) Dziedzic, P.; Schyman, P.; Kullberg, M.; Córdova, A. Highly Enantioselective Organocatalytic Addition of Aldehydes to N -(Phenylmethylene)Benzamides: Asymmetric Synthesis of the Paclitaxel Side Chain and Its Analogues. *Chemistry - A European Journal* **2009**, *15* (16), 4044–4048.

(15) Koto, S.; Morishima, N.; Miyata, Y.; and Shonosuke Zen. Preparation of 2,3,4,6-Tetra-O-Benzyl-D-Mannose. *Bull Chem Soc Jpn* **1976**, *49* (9), 2639–2640.

(16) Bulman Page, P. C.; Chan, Y.; Liddle, J.; Elsegood, M. R. J. Carbohydrate-Derived Iminium Salt Organocatalysts for the Asymmetric Epoxidation of Alkenes. *Tetrahedron* **2014**, No. 70, 7283–7305.

(17) Blaukopf, M.; Müller, B.; Hofinger, A.; Kosma, P. Synthesis of Neoglycoconjugates Containing 4-Amino-4-Deoxy-L-Arabinose Epitopes Corresponding to the Inner Core of Burkholderia and Proteus Lipopolysaccharides. *European Journal of Organic Chemistry* **2012**, *2012* (1), 119–131.

(18) Lim, D.; Fairbanks, A. J. Selective Anomeric Acetylation of Unprotected Sugars in Water. *Chemical Science* **2017**, *8* (3), 1896–1900.

(19) Wuts, P. G. M.; Greene, T. W. *Greene's Protective Groups in Organic Synthesis*, Fourth.; Wiley, 2007.

(20) Yamashita, M.; Takegami, Y. A Convenient Synthesis of Ethers from Alcohols and Alkyl Halides Catalysed by Bis[Acetylacetonato]Nickel. *Synthesis* **1977**, No. 11, 803.

(21) Bongini, A.; Panunzio, M.; Bandini, E.; Campana, E.; Martelli, G.; Spunta, G. Synthesis of Perhydroxazin-4-Ones. Competitive Mukaiyama versus Hetero Diels-

Alder Reaction in the Cycloaddition of 2-Aza-3-Trimethylsilyloxy-1,3-Butadiene and Aldehydes. *Tetrahedron Asymmetry* **2001**, No. 12, 439–454.

(22) Panunzio, M.; Zarantonello, P. Synthesis and Use of N-(Trimethylsilyl)Imines. *Organic Process Research & Development* **1998**, *2*, 49–59.

(23) Kupfer, R.; Meier, S.; Würthwein, E.-U. A Facile Method for the Synthesis of Substituted N-Methylenecarboxamides and Alkyl N-Methylenecarbamates. *Synthesis* **1984**, *8*, 688–690.

(24) Colvin, E. W.; McGarry, D. G. Reaction of Silyl Ketene Acetals with N-Trimethylsilyl Imines: A Route to N-Unsubstituted Azetidin-2-Ones. *Journal of the Chemical Society, Chemical Communications* **1985**, No. 9, 539.

(25) Capon, B. Mechanism in Carbohydrate Chemistry. *Chemical Reviews* **1969**, *69* (4), 407–498.

Chapter 7

X-ray Photoelectron Spectroscopy for the Elemental Analysis of Glycopolymer-Functionalised Gold Nanoparticles and the Elucidation of Grafting Density

7.1 Abstract

X-ray photoelectron spectroscopy (XPS) may provide a less resource intensive method to determine relative grafting density than thermogravimetric analysis. In this chapter the use of XPS to determine relative grafting density is explored using a range of glycan functionalised polymer coated gold particles of varying size and shape. While this study does not provide conclusive proof of the value of XPS to determine relative grafting density, it does provide broad evidence and impetus to further explore this method.

7.2 Declaration

This chapter contains materials synthesised for use in the following papers;

P. G. Georgiou, **A. N. Baker**, S-J. Richards, A. Laezza, M. Walker, M. I. Gibson, *Journal of Materials Chemistry B.*, 2020, *8*, 136-145.[1]

S-J. Richards, **A. N. Baker**, M. Walker, M. I. Gibson, *Biomacromolecules*, 2020, *21*, 4, 1604-1612.[2]

A. N. Baker, S-J. Richards, C. S. Guy, T. R. Congdon, M. Hasan, A. J. Zwetsloot, A. Gallo, J. R. Lewandowski, P. J. Stansfeld, A. Straube, M. Walker, S. Chessa, G. Pergolizzi, S. Dedola, R. A. Field, M. I. Gibson, *ACS Cent. Sci.,* 2020, *6*, 2046.[3]

A. N. Baker, S-J. Richards, C. S. Guy, T. R. Congdon, M. Hasan, A. J. Zwetsloot, A. Straube, M. Walker, S. Chessa, G. Pergolizzi, S. Dedola, R. A. Field, M. I. Gibson, *Chemrxiv,* 2020*, https://doi.org/10.26434/chemrxiv.12465680.v1*[4]

S-J. Richards, M. I. Gibson, M. A. Fasciae, B. Linclau, M. C. Galan, **A. N. Baker**, H. Ledru, C. S. Webster, C. E. Council, M. Walker, H. Chidwick, D. E. Wheatley, J-B. Vendeville, T. Keenan, D. Budhadev, *Chemical Science*, 2020, *12*, 905-910. [5]

A. Pancaro, M. Szymonik, P. G. Georgiou, **A. N. Baker**, M. Walker, P. Adriaensens, J. Hendrix, M. I. Gibson, I. Nelissen, *Nanoscale*, 202, *13* (24), 10837-10848.[6]

P. G. Georgiou, C. S. Guy, M. Hasan, A. Ahmad, S-J. Richards, **A. N. Baker**, N. V. Thakkar, M. Walker, S. Pandey, N. R. Anderson, D. Grammatopoulos, M. I. Gibson, *Plasmonic Detection of SARS-CoV-2 with Polymer-Stabilised Glycosylated Gold Nanorods* – Manuscript accepted

A. N. Baker, A. R. Muguruza, S-J. Richards, P. G. Georgiou, S. Goetz, M. Walker, S. Dedola, R. A. Field, M. I. Gibson, *Adv. Healthcare Mater.,* 2021, 2101784.[7]

Particles taken from the above papers were synthesised by the authors of the paper. All XPS analysis was carried out by myself with the support, advice and training of Marc Walker.

The thermogravimetric analysis was carried out by Ioanna Kontopoulou. The synthesis of the previously unpublished particles was carried out by myself with the assistance from Asier R. Muguruza, who also carried out the UV-vis and DLS analysis of the particles.

7.3 Introduction

7.3.1 Interfaces, Surfaces and Grafting Density

Interfaces decorated with macromolecules are crucial in a range of devices from medical implants[8,9] and cell scaffolds[10] to coatings for combating marine biofouling.[11] The functionality of the surface of these particles is determined by the macromolecule attached and its grafting density – the number of macromolecules in a determined surface area. Grafting density is driven by several characteristics of the attached macromolecule such as length and composition, as well as the size and shape of the surface/particle itself.[12]

If polymers are considered as simple ligands the Hill-Langmuir equation, equivalent to the Langmuir isotherm for ideal gases (Equation 7.3), is useful for considering grafting and grafting density. The Hill-Langmuir equation (Equation 7.2) describes the binding of ligands (L) to a macromolecule (M) with n binding sites as a function of K_D, the dissociation equilibrium constant, a ratio between k_d (dissociation rate constant) and k_a (association rate constant) (Equation 7.1), and total ligand concentration $[L_0]$.

$$M + nL \underset{k_d}{\overset{k_a}{\rightleftharpoons}} ML_n$$

Equation 7.1. Chemical equilibrium of bound (ML) and unbound ligand (L)

$$[ML_n] = [L_0] \times \frac{[L]^n}{K_D + [L]^n}$$

Equation 7.2. Hill-Langmuir Equation

$$\theta = \frac{L_{bound}}{L_{max}} = \frac{K_A \times [L]}{1 + K_A \times [L]}$$

Equation 7.3. Langmuir Adsorption Equation

(θ, fractional occupancy of adsorption sites, L_{bound}, number of bound ligands, L_{max}, number of ligands required to bind all binding sites, L, unbound ligand and K_A, association equilibrium constant

Two competing processes dominate polymer adsorption; the contraction of polymers to the surface as determined by the adsorption constant and the entropic repulsion of

polymer when confined to the surface.[13] When on the surface, since polymers can change their morphology by varying the distribution of their pervaded volume (size of a polymer in space at a given temperature), the number of binding sites is adaptable.

As polymers are brought into less than two radii of gyration lengths on a surface, polymers interact and move away from a half "sphere" morphology ("mushroom"), following the Flory theory, towards linear extended high-density chain brushes (Figure 7.1), increasing grafting density. The simplest model of a polymer brush system, a sufficiently dense system of polymer chains covalently bound to a surface at one end, is described by de Gennes[14] for flat surfaces. The model is dictated by two forces; the desire of a polymer to maximise its configurational entropy in a random walk versus its desire to be surrounded by solvent. This was further developed for curved surfaces by applying the Daoud and Cotton Blob model originally postulated for star-shaped polymers in 1982 (Figure 7.2).[15,16]

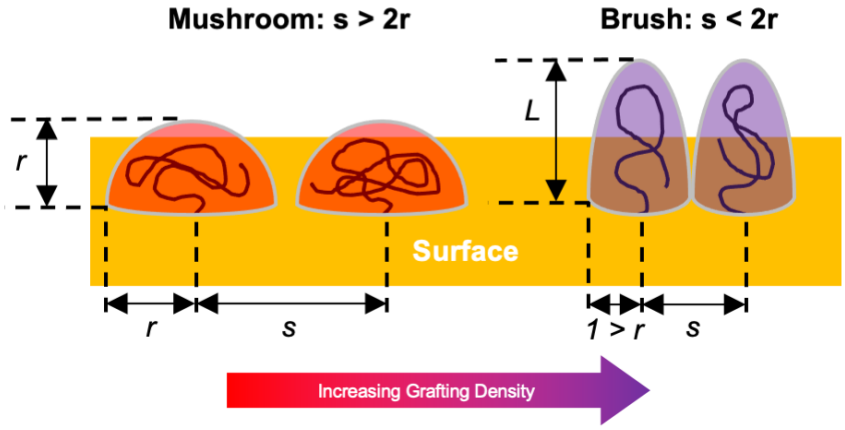

Figure 7.1. Diagrammatic representation of how polymer morphology changes with grafting density on a flat surface.

In the Daoud Cotton Blob model the space filled by a polymer chain (excluded volume) at distance R from a curved surface is dependent on the radius (R_{min}) of the surface, distance R of the blob and the diameter of the blob (r). The model shows that as a chain moves away from the surface its excluded volume sphere (blob) increases in size ($r_n < r_{n+1}$), in effect this creates "cone-shapes" of excluded volume. This means that as surface curvature decreases excluded volume spheres in the Doaud Cotton Blob model overlap unless packing decreases – therefore grafting density should decrease with curvature decrease.[17,18]

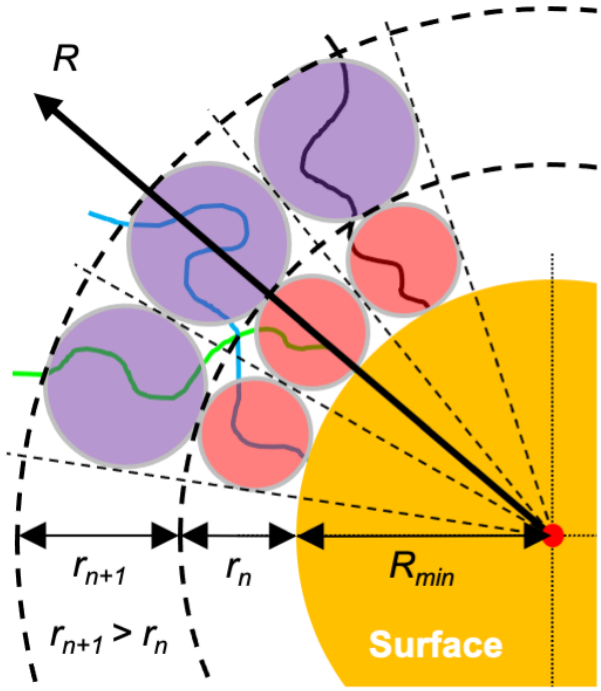

Figure 7.2. Diagrammatic representation of Daoud Cotton Blob model.

7.3.2 Determining Grafting Density

Grafting density can be characterised analytically in a variety of ways, the most common, according to Michalek *et al.*,[19] are; dry thickness measurements, swelling experiments[20] and gravimetric analysis. The first two methods rely on reflective and refractive spectroscopic techniques such as ellipsometry,[21,22] small angle x-ray scattering (SAXS),[23] neutron reflectometry[24] or x-ray reflectivity/reflectometry[25] in elucidating the relationship between the thickness of the polymer coating and grafting density. Beyond these methods, others have used the concentration of carbon on the nanoparticle surface for grafting density determination.[26] Or determined the grafting density of polymers (poly(3-methylthienyl methacrylate)) using GPC, reporting a positive relationship between the grafting density on glass and the thickness of the polymer layer.[27] Work by Hill *et al.* has also shown that surface loading of oligonucleotides onto gold surfaces can be calculated within error by considering the deflection angle i.e., the angle produced when considering the diameter of an excluded volume sphere to the centre of a nanoparticle in the Daoud Cotton Blob model.[28] Others such as Guo *et al.*[29] have sought to apply Hill's equations to larger polymeric systems – it is however debatable whether this methodology is valid for larger molecular weight systems. It is notable, that many works that consider polymer

grafting density also report XPS measurements, for example Wolski *et al.* and Liu *et al.*;[27,30] while Sofia *et al.* reported correlations between ellipsometry data and XPS for poly(ethylene oxide).[31]

7.3.3 X-ray Photoelectron Spectroscopy

X-ray Photoelectron Spectroscopy (XPS) or electron spectroscopy for chemical analysis (ESCA) is a photoelectronic, surface-sensitive, ultra-high vacuum technique used to measure elemental composition and elucidate the surface chemistry through spectral deconvolution. XPS is most commonly used to study inorganic systems particularly; metals/alloys,[32] insulators[33] and, semiconductors.[34,35] This has led to its use in myriad applications from photovoltaics[36] to hydrogen storage.[37]

In XPS, a focused beam of x-rays irradiates the sample surface, this leads to the emission of photoelectrons from the surface via the photoelectric effect.[38] The emitted flux of photoelectrons is recorded as a function of kinetic energy.[39] When the energy of the photoelectron released (E_{kin}) is considered versus the energy of the incident x-ray photon (hv), the binding energy (E_b) relative to the Fermi level of the atom can be determined (Equation 7.4). Necessary adjustments for the spectrometer and materials are made in the work function (ϕ), an expression of the minimum thermodynamic work required to remove an electron from the Fermi level to a vacuum immediately outside the surface. Using this data, the elemental species of the atom releasing the electron can be determined.

$$E_b = hv - (E_{kin} - \phi)$$

Equation 7.4. Simplified equation to calculate the binding energy of a photoelectron

Further information on the relative abundance of elements in the sample can be determined by considering the intensity of the electron flux. This data can be used to elucidate the empirical formula of a compound or its crystal structure. When considering different elements, the transmission function of the analyser, and kinetic energy change with sample depth, must also be considered. The latter comes from the inelastic mean free path length universal curve of an electron moving through a material, taking into account the take-off angle of 90°. To determine the elemental abundance (c_x) (Equation 7.5) the intensity of the peak, I_x, and the relative sensitivity factor of the element, S_x, can be divided by the total relative intensity (I_i/S_i) of the sample.

$$c_x = \frac{I_x/S_x}{\sum I_i/S_i}$$

Equation 7.5. Simplified equation to determine elemental abundance

Analysis of small changes in the binding energy of the photoelectrons (chemical shifts) can be used to obtain information about the bonding environment (chemical state) of the element being analysed. The change in binding energy, ΔE, is summarised in Equation 7.6 – Δq is the difference in valence charge of the atom (assumed to be a hollow sphere), multiplied by a factor, k, and ΔV is the change in the effective potential assuming surrounding atoms are point charges. Simply, the binding energy of an atom changes with its electron density. If an atom is electron deshielded by a neighbouring electronegative system, the binding energy of its remaining electrons to the nucleus increases.

$$\Delta E = k\Delta q + \Delta V$$

Equation 7.6. Simplified equation to estimate chemical shift as influenced by surrounding charged particles

Furthermore, the ability of XPS to analyse multiple elemental components simultaneously and in the nanogram range makes it an ideal technique for nanoparticle characterisation. This is especially true when nanoparticles are functionalised with glycans, whose presence can be hidden in NMR either by low concentrations (due to cost) or low integration ratios versus large polymeric systems.

7.3.4 X-ray Photoelectron Spectroscopy and Glycopolymer Grafting Density

Multiple studies have explored how grafting density varies with polymer chain length and composition. Both Georgiou *et al.* and Ieong *et al.* observed that increasing polymer chain length decreased grafting density. In addition, they showed that increasing steric hindrance in the polymer chain structure also decreased grafting density. Georgiou *et al.* illustrated this using AuNPs coated with biocompatible poly(*N*-(2-hydroxypropyl)-methacrylamide) (PHPMA) or poly(*N*-hydroxymethylacrylamide) (PHEA). While PHEA and PHPMA are very similar, PHPMA has additional methyl groups in both the backbone and pendent of the polymer, likely decreasing the packing efficiency of PHPMA vs PHEA, by decreasing PHPMA's linear morphology and so decreasing PHPMAs relative grafting density.[1] This effect was also seen by Pancaro *et al.* in gold nanorod systems by XPS.[6] Ieong *et al.* observed a similar trend using poly(oligoethyleneglycol methacrylates) and poly(*N*-vinyl pyrrolidones) (PVP), here PVP showed a higher relative grafting density by XPS.[40] These observations are supported by Sofia *et al.* who measured grafting density using both XPS and ellipsometry for varying lengths of poly(ethylene oxide). Sofia *et al.* found that increasing polymer length decreased grafting density but also showed good agreement between grafting density calculated by ellipsometry and XPS, when a standard sample is used to determine absolute grafting density.[31]

7.4 Results and Discussion

7.4.1 Building an XPS Model for Glycosylated Polymeric Gold Nanoparticle Systems

A range of gold nanoparticles of varying size and shape, coated with poly(hydroxyethyl acrylamide) (PHEA) and poly(*N*-(2-hydroxypropyl)-methacrylamide) (PHPMA) functionalised with varying glycans were taken from studies previously conducted by the Gibson Group (details in Appendix 7 and the Declaration of this chapter). In order to extract XPS data from these particles a model was developed based on a series of newly synthesised galactosamine functionalised poly(hydroxyethyl acrylamide)-coated 16 nm gold nanoparticles (detailed synthesis and analysis is provided in the Experimental and Appendix 7).

In this model the C 1*s*, O 1*s*, N 1*s* and Au 4*f*, were considered. It was anticipated in a theoretical C 1s spectrum that; alkane, ether (including hydroxyl), amide, and amine environments would be present in PHEA coated particles alongside the adventitious (background) carbon environments of; alkane (calibration peak), ether, ester, and carbonyl. Furthermore, carbides and carboxylic acid environments were also expected from silicon carbide at the silicon wafer/air interface and remnants of the gold nanoparticle citrate coating respectively.

Using these expected C 1*s* environments, the intensity of each environment was then considered for a theoretical PHEA system (Figure 7.3). In XPS the intensity of a peak is determined by the number of atoms in that specific environment (including adventitious atoms), with binding energy (BE, eV) determined by the environment itself. This was also done for the O 1*s* and N 1*s* environments (Figure 7.4), with the C 1*s* to N 1*s* ratio dictating the ratio of the amine and amide to the other C 1*s* environments in the C 1*s* model.

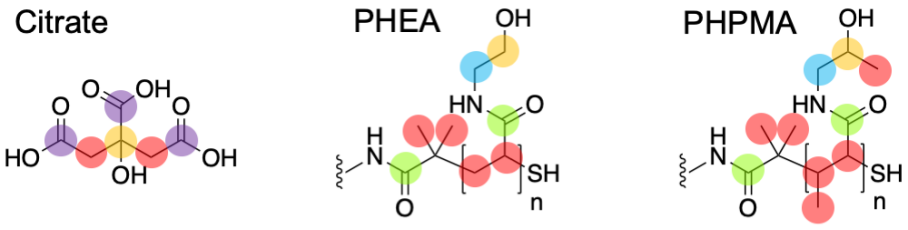

C 1s character	Binding energy (eV)
Alkane	285
Ether (including hydroxyl)	~286.5
Carbonyl	~287.6
Ester	~288.3
Carbide	~284
Amine	~285.7
Amide	~288
Carboxylic acid	~289.3

Figure 7.3. C 1*s* character of nanoparticle coatings

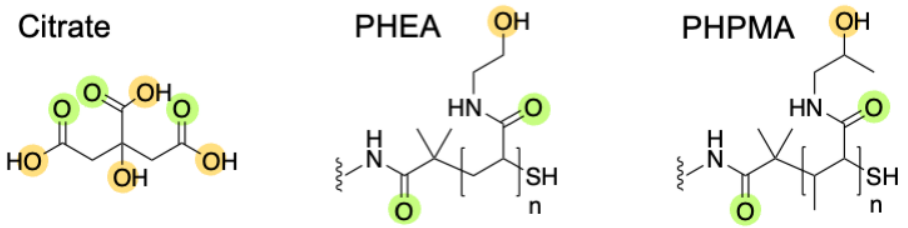

O 1s character	Binding energy (eV)
Carbonyl/amide	~531.5
Ether (including hydroxyl, ester and carboxylic acid)	>532

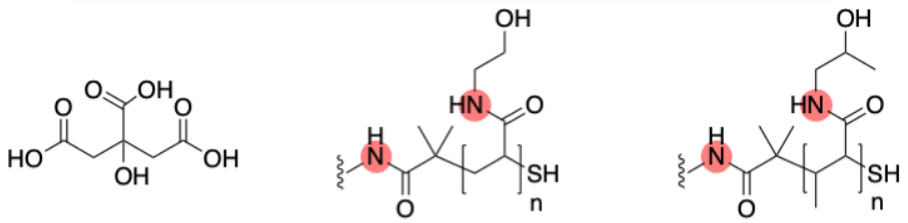

N 1s character	Binding energy (eV)
Amide	~399

Figure 7.4. O 1*s* and N 1*s* character of nanoparticle coatings

The proposed model (Figure 7.5) was then applied to the series of 16 nm glycosylated gold nanoparticles with different PHEA chain lengths (26, 40, 72 and 110) and an unfunctionalised AuNP (citrate stabilised). It was found that with minor adjustments

the model fitted well. (All fitted XPS spectra for the entire study can be found in Appendix 7).

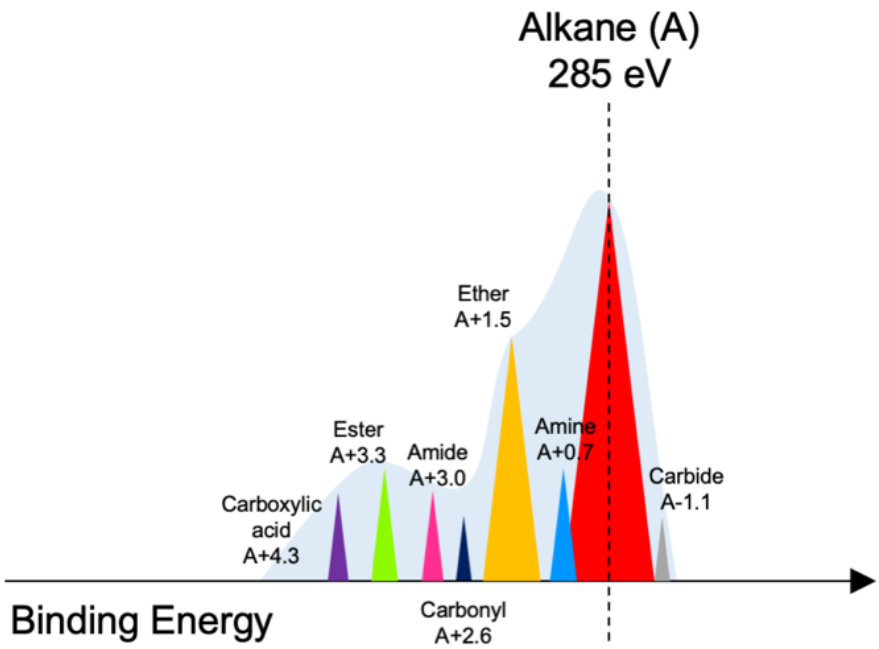

Figure 7.5. Graphical representation of proposed XPS C 1*s* model with approximate values versus alkane ("A") and approximate signal intensities

The addition of the glycopolymer could be observed versus the naked AuNP system through the presence of N 1*s* environments, that are not present in the naked particles or found commonly in background contaminants and a slight attenuation of the Au 4*f* signal. This confirmed the incorporation of the polymers onto the particle surface, alongside shifts in the UV-vis and DLS spectra (Appendix 7). An increase in the ether, amide and amine peaks was also observed in C 1*s* spectra and indicated glycopolymer incorporation, although the ether peak (C-O) often decreased in intensity as the polymer chain length increased (Figure 7.6). An increase in ether intensity on glycan addition was observed previously by Laezza *et al.*, where glycopolymer addition was carried out using an amino-oxy conjugation system with PHEA polymers and confirmed by an increase in the C 1*s* ether:amide ratio when a glycan is added to the system.[41]

Furthermore, the XPS method developed is compatible with the minute amounts (µg - ng) of material available for more complex glycans, where methods like NMR are not sufficiently sensitive. This allowed the models and methods produced to be used

to study complex fluorinated glycans on PHEA polymers and in some cases observe the presence of fluorinated glycans on the polymers, in F 1*s* scans, when NMR could not (Figure 7.7).[5] This further validates the potential of XPS to study glycosylated nanoparticle system.

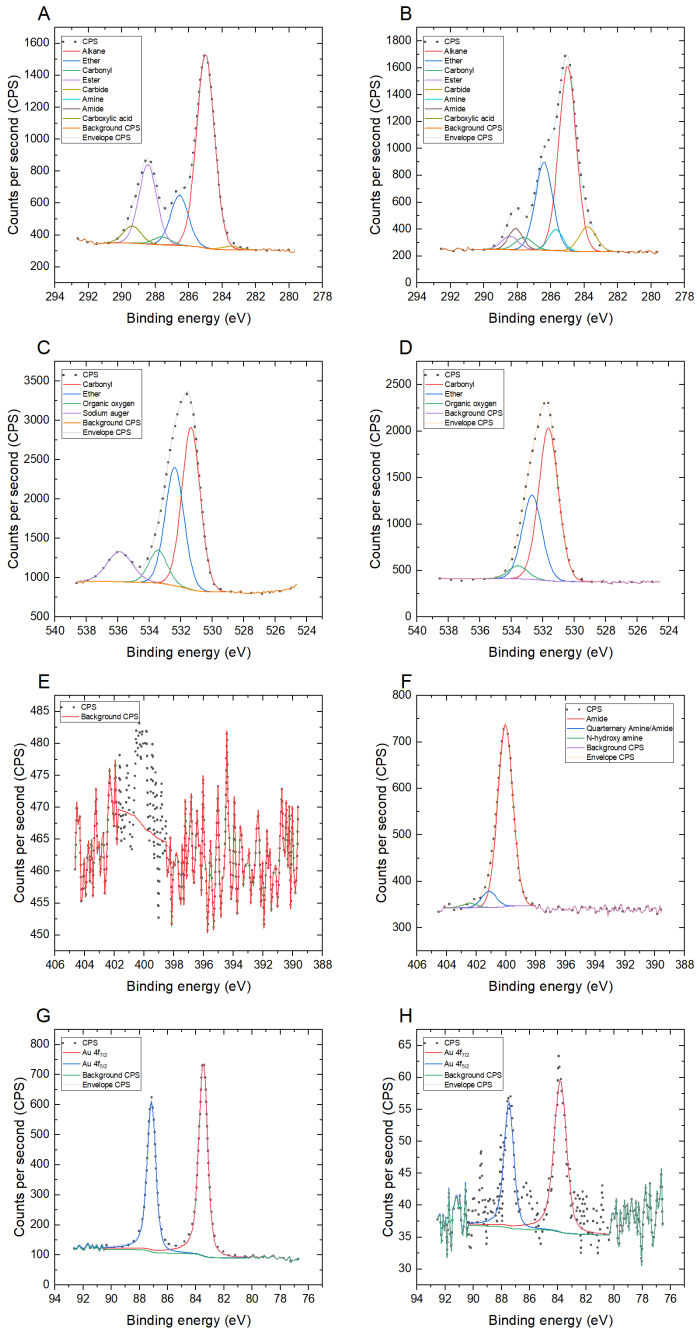

Figure 7.6. A comparative XPS spectra example of a citrate stabilised AuNP ($AuNP_{16}$, Left column) and a polymer coated AuNP (Galactosamine-$PHEA_{40}$@$AuNP_{16}$, Right column).

A&B) C 1*s*; C&D) O 1*s*; E&F) N 1*s* and G&H) Au 4*f*

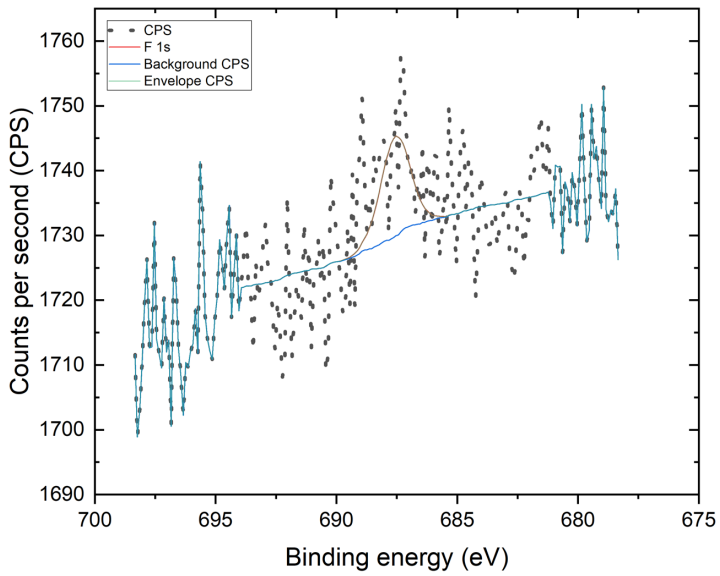

Figure 7.7. Representative F 1*s* of a fluorinated glycosylated nanoparticle (Gal β1,3 6,6-di-F-GlcNTFAc $PHEA_{45}$@$AuNP_{55}$)

7.4.2 Calculating Relative Grafting Density

Having illustrated that glycopolymer addition to gold nanoparticles could be analysed using XPS, it was considered if relative grafting density of the particles could be evaluated – as this was anticipated to vary from particle to particle and influence the characteristics of the nanoparticles. To study the relative grafting density of the particles, the five particles were analysed in triplicate by XPS and the N 1*s* to Au 4*f* ratio calculated. This compares the gold component present in the sample versus the nitrogen component, found only in the polymer-coated system, therefore this ratio provides a measure of polymer to gold concentration in the sample independent of background as no nitrogen components are present in the background.

When considered in relation to the molecular weight ($M_{n(SEC)}$) of the polymer systems (as determined by size exclusion chromatography, SEC) and the surface area of the gold nanoparticles (SA_{Au}), a relative grafting density can be calculated using equation 7.7. Results are presented in Figure 7.8. (all calculated relative grafting densities for the study can be found in Appendix 7). While this method does not give absolute grafting density in nm^{-2}, as no standard is used unlike in Sofia *et al.*,[31] it does allow for comparisons between samples as relative grafting density.

$$Relative\ Grafting\ Density = \frac{((N\ 1s: Au\ 4f)/M_{n(SEC)})}{SA_{Au}}$$

Equation 7.7. Equation to calculate relative grafting density from the N 1*s* to Au 4*f* ratio, as determined by XPS

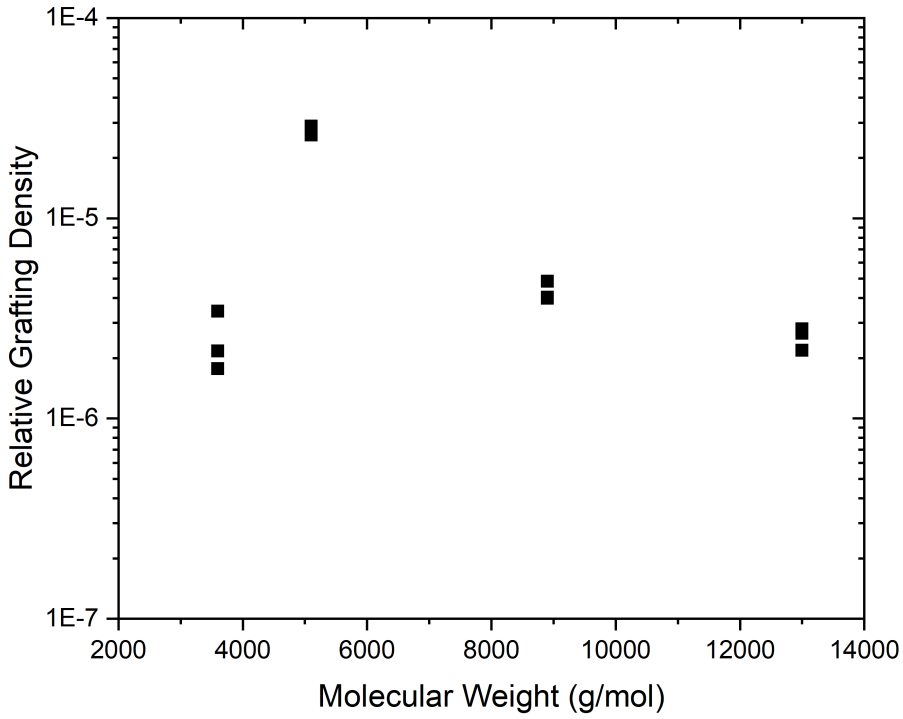

Figure 7.8. Relative grafting density calculated from XPS for synthesised PHEA coated samples on 16 nm gold nanoparticles.

To ascertain if this method is viable for determining relative grafting density, thermogravimetric analysis (TGA) was conducted on the polymer-coated AuNP systems to determine absolute grafting density (Figure 7.9). As previously discussed, TGA is widely used to determine grafting density. The grafting density was calculated for the TGA samples using the methods from Rahme *et al.*[42,43] and Gibson *et al.*.[44] Here the mass change before heating and after heating is considered as the mass of polymer; and the final weight after heating as the mass of gold alone. By calculating the moles of both polymer and gold, as well as the surface area of the gold; a grafting density value (nm^{-2}) can be determined.

Using this approach, the $PHEA_{72}$ system was found to have the highest grafting density followed by the $PHEA_{40}$ system, then the $PHEA_{26}$ and $PHEA_{110}$ both with similar grafting densities (Table 7.1). Notably the calculated values were found to be near to those of the literature for other polymer systems on similar sized nanoparticles; falling a little below the sterically smaller PEG systems (as determined by Rahme *et*

al.) and similar to sterically similar poly(poly(ethylene glycol) methacrylate systems.[43,44]

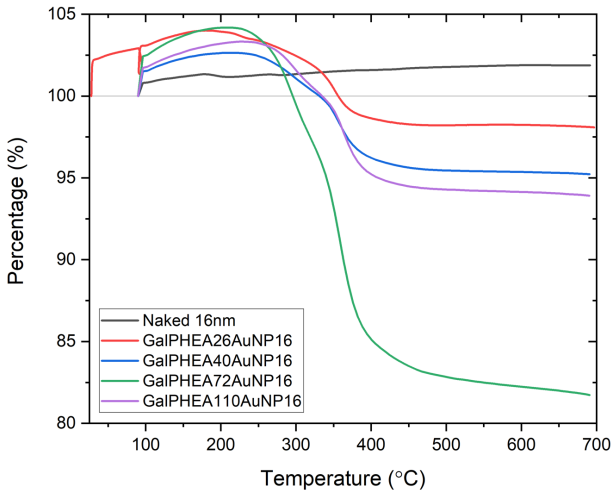

Figure 7.9. Thermogravimetric analysis of galactosamine (Gal) functionalised PHEA polymers on 16 nm AuNPs

AuNP	Weight loss in TGA (%)	PHEA chains per AuNP	Footprint (nm^2)	Grafting density by TGA (nm^{-2})	Highest relative grafting density by XPS
Gal-$PHEA_{26}$@$AuNP_{16}$	1.91	135	5.96	0.168	= 4th
Gal-$PHEA_{40}$@$AuNP_{16}$	4.78	245	3.28	0.328	1st
Gal-$PHEA_{72}$@$AuNP_{16}$	18.27	626	1.28	0.778	2nd
Gal-$PHEA_{110}$@$AuNP_{16}$	6.09	124	6.47	0.155	= 4th

Table 7.1. Equation to calculate relative grafting density from the N 1*s* to Au 4*f* ratio, as determined by XPS

While the triplicate data showed the reproducibility of XPS; when compared to TGA data there was only moderate agreement. For example, the XPS data aligned with the TGA data in determining that the $PHEA_{26}$ and $PHEA_{110}$ sample had the lowest grafting densities, in addition to correctly determining that the $PHEA_{40}$ system had a higher grafting density than both $PHEA_{26}$ and $PHEA_{110}$. However, XPS suggested that the $PHEA_{40}$ system has a higher grafting density than $PHEA_{72}$, at odds with the TGA results. Despite this one error and considering the reproducibility of the XPS data, it is likely that XPS can be used to probe relative grafting density, as previously explored by Sofia *et al.*.[31] Therefore the developed XPS methodology was applied to a variety of other gold nanoparticle systems.

7.4.3 Relative Grafting Density by Spherical Gold Diameter

To further consider the relationship between; polymer length, particle size and relative grafting density, a series of previously synthesised particles were analysed by XPS. These particles, taken from a range of published studies, provided a wide variety of AuNP sizes up to 70 nm and PHEA polymer mass up to ~20,000 Da (Figure 7.10). From the data, particle size has a greater impact on grafting density than polymer length in PHEA systems, with larger diameter AuNPs having lower grafting densities, as determined by XPS, than higher curvature, smaller diameter AuNPs. This is unsurprising considering the Daoud Cotton Blob model and its implications for grafting density on decreased curvature surfaces. This model describes how as surface curvature decreases excluded volume spheres overlap leading to decreased packing – therefore grafting density should decrease with curvature decrease.[17,18] This is modelled in end-functionalised polymers by Oyerokun *et al. in silico*.[45] Notably, a decreasing grafting density with increasing polymer chain length trend was also observed following expectation.[12]

Therefore, the model used here to compare relative grafting density across different nanoparticle sizes is appropriate and follows the predicted trends. There is however the potential that the effectiveness of measuring relative grafting density by XPS decreases as the AuNP diameter increases beyond the penetration depth of the x-ray beam and the sampling depth of ~10 nm, beyond which photoelectrons are extremely likely to have undergone inelastic scattering events (losing kinetic energy) and therefore contributing to the background intensity. This could artificially decrease the N 1*s* to Au 4*f* ratio.

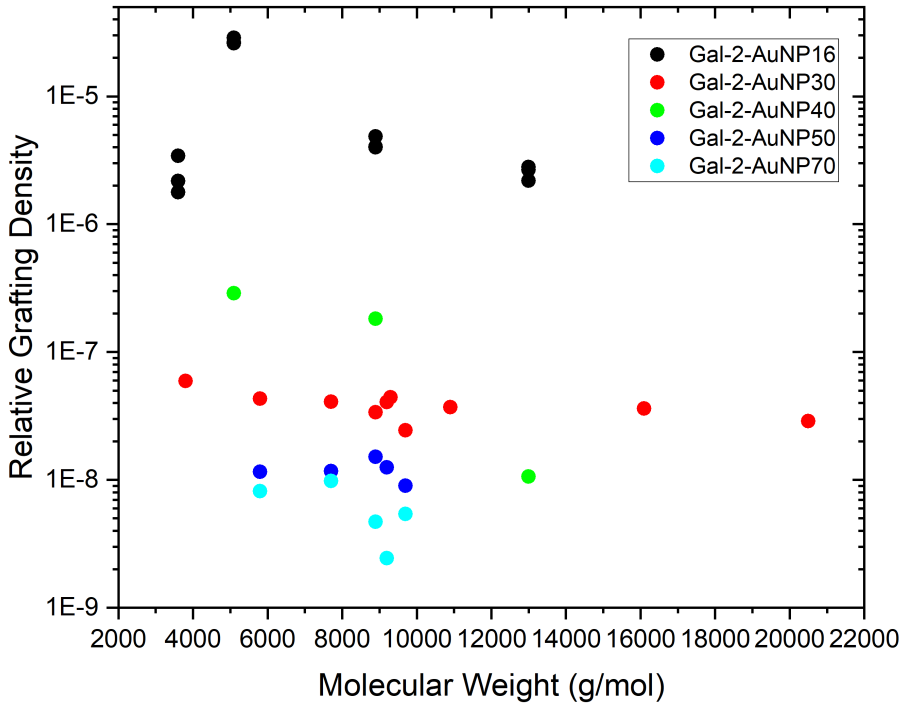

Figure 7.10. Relative grafting density calculated from XPS for galactosamine (Gal-2) functionalised PHEA coated samples on varying diameter gold nanoparticles (spheres).

7.4.4 Relative Grafting Density by Polymer

The relationship between monomer structure and grafting density was explored next, using previously synthesised PHEA and PHPMA (poly(*N*-(2-hydroxypropyl) methacrylamide) coated AuNPs of diameter 30 nm. Using Equation 7.7, higher relative grafting densities on the nanoparticle surface were observed in the PHEA systems versus the PHPMA systems (Figure 7.11). These ratios provide evidence for differing surface grafting behaviors between PHEA and PHPMA demonstrating how simple modification of the polymer ligand can tune the surface and the observed properties as discussed by Georgiou *et al.*.[40]

It is likely that the Gibbs free energy conformations of the dihedral angles in the polymer backbone are influential in determining grafting density differences between PHEA and PHPMA. This is because the PHEA backbone can potentially access a lower antiperiplanar Gibbs free energy conformer, when considered in a Newman projection, compared to PHPMA due to the additional methyl group in the PHPMA backbone increasing steric hinderance (Figure 7.12). The radius of gyration of PHPMA would therefore be greater than PHEA, leading to less tight packing in PHPMA. In the context of Hill *et al.*,[28] this means that the deflection angle of PHPMA is greater than PHEA so has a lower grafting density. This explanation is supported in the literature by Barner and co-workers, who have shown how lower molecular weight polymers more favourably graft to nanoparticles due to radius of gyration (R_g) effects.[46]

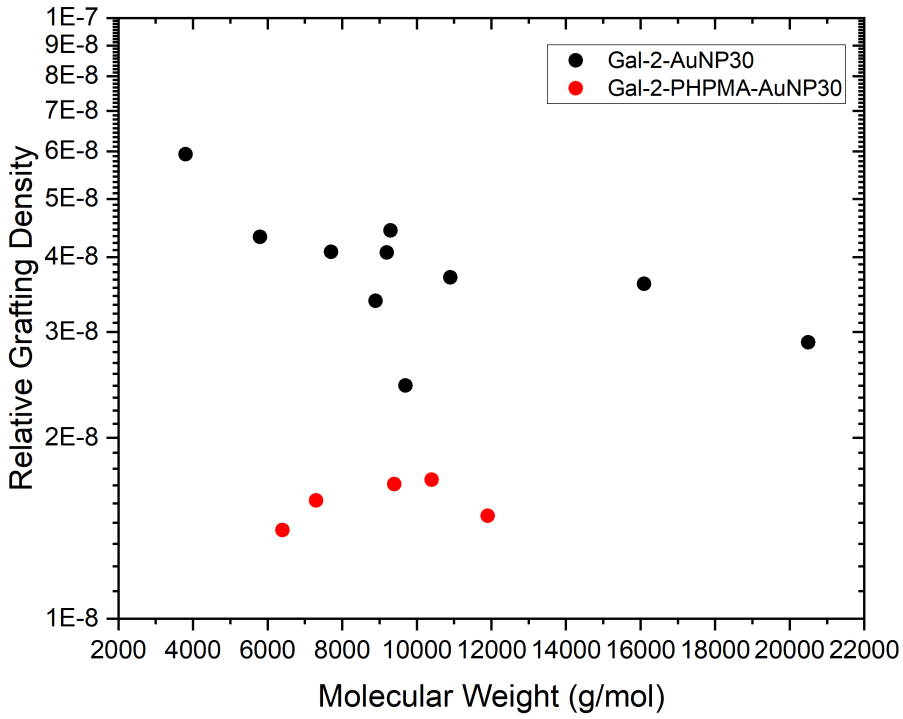

Figure 7.11. Relative grafting density calculated from XPS for galactosamine functionalised PHEA (Gal-2-AuNP30) and PHPMA (Gal-2-PHPMA-AuNP30) coated samples on 30 nm gold nanoparticles (spheres).

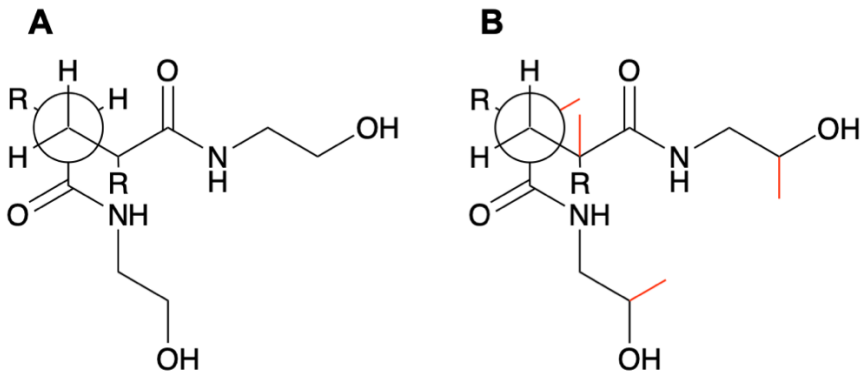

Figure 7.12. Newman projection considering the proposed lowest energy conformer of PHEA (A) and PHPMA (B) polymers.

"R" is polymer chain and additional methyl groups in PHMPA versus PHEA are highlighted in red.

7.4.5 Relative Grafting Density by Glycan

It is likely that varying glycan functionalisation of the nanoparticle system influences the grafting density of the glycopolymer on the surface of the nanoparticle. To explore this hypothesis a series of nanoparticle systems utilizing PHEA glycopolymers but bearing varying glycans were analysed by XPS (Figure 7.13). Figure 7.14 shows the outcome of the XPS analysis.

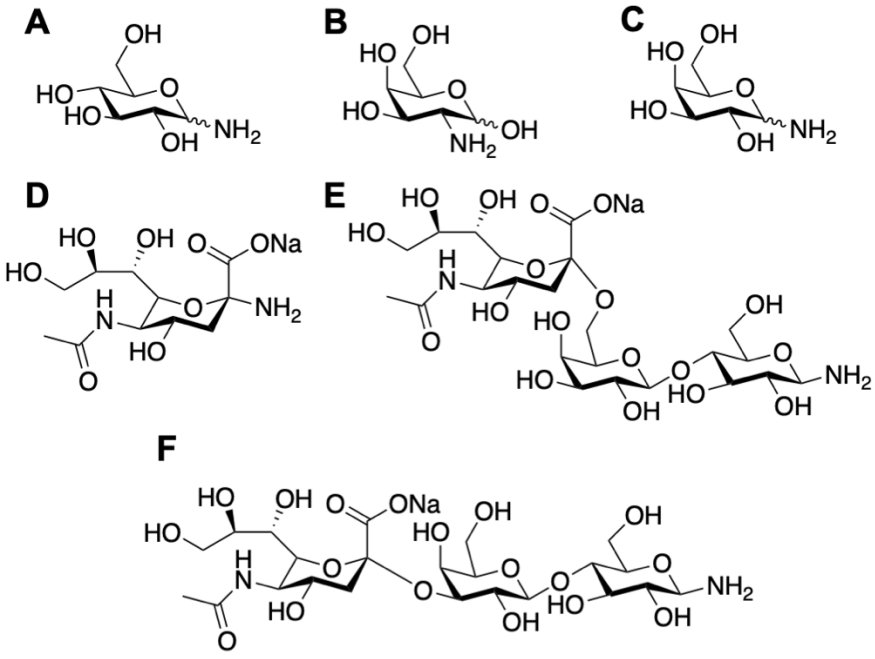

Figure 7.13. Glycans used to functionalise polymer.

A) 1-deoxy-1-amino-glucose (Glc-1); B) galactosamine (2-deoxy-2-amino-galactose, Gal-2); C) 1-deoxy-1-amino-galactose (Gal-1); D) neuraminic acid (NeuNAc); E) 2,6-sialyllactosamine (2,6SL) and F) 2,3-sialyllactosamine (2,3SL)

In all cases the larger the AuNP the lower the grafting density even as glycan functionalisation changes, supporting evidence presented previously that as particle size increases so grafting density decreases. While changing the glycan impacts grafting density too, no clear trends are evident, other than the impact on 16 nm AuNPs of exchanging a monosaccharide (galactosamine) for a trisaccharide (sialyllactosamine). An explanation for this is that the glycan used likely impacts the solvation energy of the polymer by increasing its hydrophilicity through the addition of hydroxyl groups. This in turn may influence the solubility of the polymer and alter the energy change on binding to the AuNP surface. This may explain the difference

between the mono- and trisaccharide systems. However, as the glycan is only on the polymer terminus it has only a minimal impact on grafting density. Notably the structural isomer of sialyllactosamine also has an impact on relative grafting density (although minor), with the "kinked" 2,6 configuration regularly having a lower grafting density than the more linear 2,3-sialyllactosamine (consistent with the greater excluded volume of the 2,6 isomer).

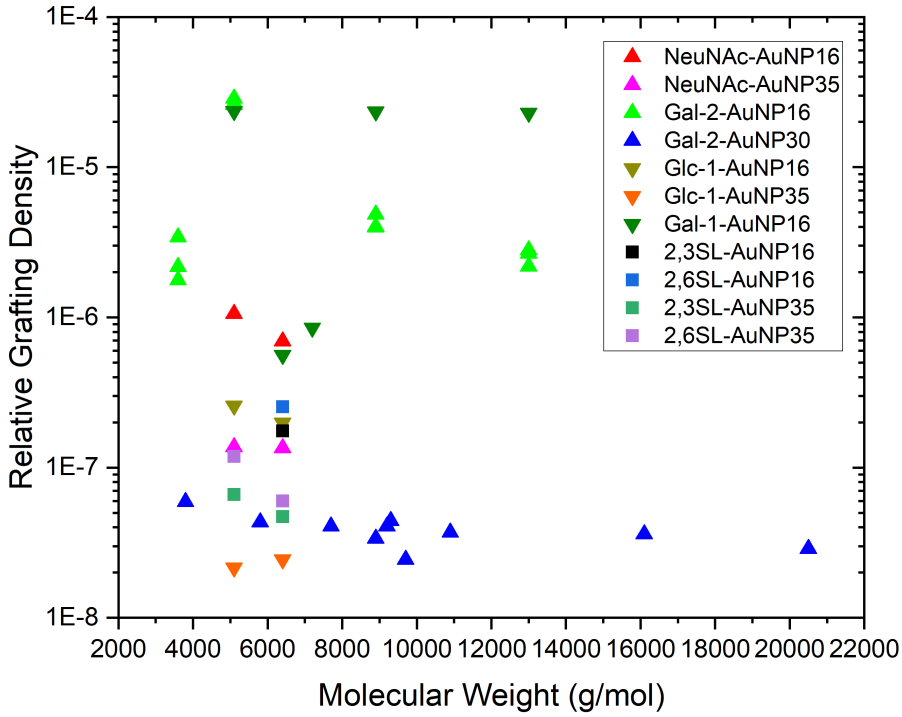

Figure 7.14. Relative grafting density calculated from XPS for PHEA polymer coated samples on varying diameter gold nanoparticles (spheres) functionalised with various glycans (coding from Figure 7.13).

In summary, while the glycan used does impact grafting density, no clear trends are observable between glycans of similar molecular weight, but a minor decrease is seen as glycan size increases from mono- to trisaccharide. Further studies would be needed to explore these trends as there is currently a lack of literature exploring this. Although trends using the same glycan are noticeable and predictable in some cases.

7.4.6 Relative Grafting Density of Spherical Gold versus Gold Rods

To explore how grafting density changes from gold spheroids to rods, a series of PHEA and PHPMA coated spheres (30 nm) and rods (10 nm by 38 nm) were analysed by XPS. The two sizes of rod and sphere were chosen as the surface areas are comparable: 2.51×10^3 nm and 2.83×10^3 nm, respectively. However, the curvature of the particles differs, with the diameter of the rod being only 10 nm versus the 30 nm gold AuNP. This leads to a higher curvature in the rod system and therefore a higher grafting density as seen in Figure 7.15, comparing the galactosamine system using PHEA on the spheroid versus the rod. It is also notable that the PHEA polymer maintains a higher grafting density in the rod system too versus PHPMA.

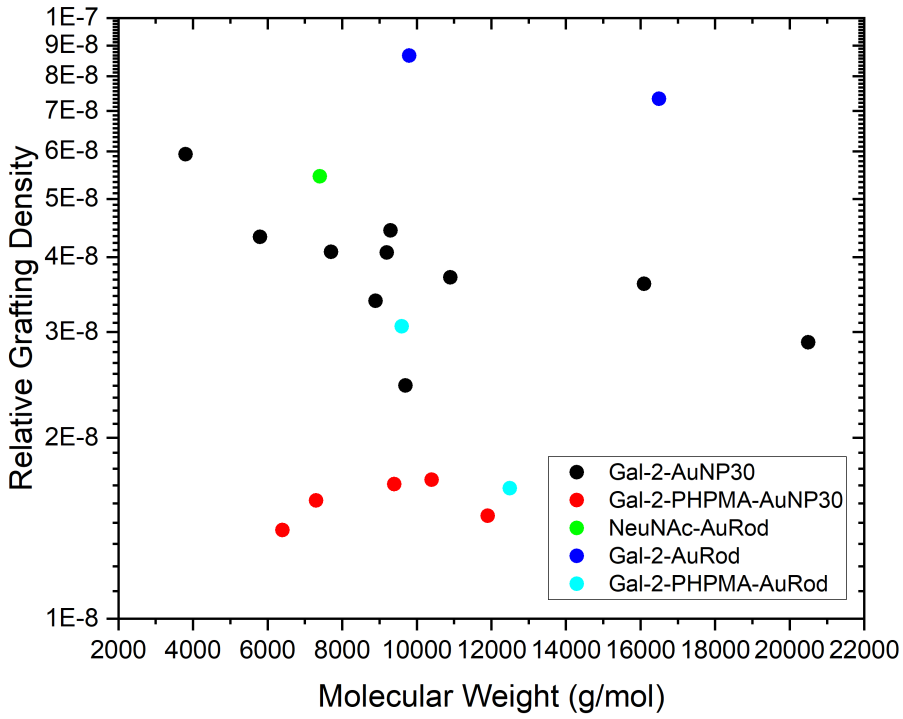

Figure 7.15. Relative grafting density calculated from XPS for PHEA (Glycan-AuNP/AuRod) and PHPMA (Glycan-PHPMA-AuNP/AuRod) coated samples coated on gold spheres (AuNP) and rods (10 nm by 38 nm, AuRod)

7.5 Conclusions

To summarise, the viability of using XPS as a less resource intense method to determine grafting density was explored versus TGA. This was done using a variety of different size and shape gold nanoparticles coated with either PHEA or PHPMA and a variety of glycan end groups. An XPS model was developed using a series of galactosamine functionalised PHEA polymers of different sizes coated onto 16 nm spherical AuNPs. The relative grafting density was then calculated and compared to TGA data taken from the same particles. The XPS and TGA data compared well, although not perfectly. Building on this the effects of gold sphere size, polymer coating and glycan were explored. It was found that, by XPS, gold size has the greatest effect on grafting density, though the glycan used, and polymer length also influence grafting density too.

While this study does not provide conclusive proof of the value of XPS to determine relative grafting density, it does provide broad evidence (alongside Sofia *et al.*[31]) and impetus to further explore this method. As such, future work should further explore the effects of chain length and glycan on relative grafting density determined by XPS with PHEA and PHPMA polymers, and this should be compared with TGA measurements or another accepted approach for determining grafting density.

7.6 Experimental

7.6.1 Physical and Analytical Methods

NMR Spectroscopy

^{1}H-NMR, ^{13}C-NMR and ^{19}F-NMR spectra were recorded at 300 MHz or 400 MHz on a Bruker DPX-300 or DPX-400 spectrometer respectively, with chloroform-*d* ($CDCl_3$) or deuterium oxide (D_2O) as the solvent. Chemical shifts of protons are reported as δ in parts per million (ppm) and are relative to either $CDCl_3$ (7.26) or D_2O (4.79).

Mass Spectrometry

Low resolution mass spectra (LRMS) were recorded on a Bruker Esquire 2000 spectrometer using electrospray ionisation (ESI). m/z values are reported in Daltons.

FT-IR Spectroscopy

Fourier Transform-Infrared (FT-IR) spectroscopy measurements were carried out using an Agilent Cary 630 FT-IR spectrometer, in the range of 650 to 4000 cm^{-1}.

Size Exclusion Chromatography

Size exclusion chromatography (SEC) analysis was performed on an Agilent Infinity II MDS instrument equipped with differential refractive index (DRI), viscometry (VS), dual angle light scattering (LS) and variable wavelength UV detectors. The system was equipped with 2 x PLgel Mixed D columns (300 x 7.5 mm) and a PLgel 5 µm guard column. The mobile phase used was DMF (HPLC grade) containing 5 mM NH_4BF_4 at 50 °C at flow rate of 1.0 $mL.min^{-1}$. Poly(methyl methacrylate) (PMMA) standards (Agilent EasyVials) were used for calibration between 955,000 – 550 $g.mol^{-1}$. Analyte samples were filtered through a nylon membrane with 0.22 µm pore size before injection. Number average molecular weights (M_n), weight average molecular weights (M_w) and dispersities ($Đ_M = M_w/M_n$) were determined by conventional calibration using Agilent GPC/SEC software.

X-ray Photoelectron Spectroscopy (XPS)

The samples were attached to electrically-conductive carbon tape, mounted on to a sample bar and loaded into a Kratos Axis Ultra DLD spectrometer which possesses a base pressure below 1 x 10^{-10} mbar. XPS measurements were performed in the main analysis chamber, with the sample being illuminated using a monochromated Al Kα

x-ray source. The measurements were conducted at room temperature and at a take-off angle of 90° with respect to the surface parallel. The core level spectra were recorded using a pass energy of 20 eV (resolution approx. 0.4 eV), from an analysis area of 300 μm x 700 μm. The spectrometer work function and binding energy scale of the spectrometer were calibrated using the Fermi edge and $3d_{5/2}$ peak recorded from a polycrystalline Ag sample prior to the commencement of the experiments. In order to prevent surface charging the surface was flooded with a beam of low energy electrons throughout the experiment and this necessitated recalibration of the binding energy scale. To achieve this, the C-C/C-H component of the C 1*s* spectrum was referenced to 285.0 eV. The data were analysed in the CasaXPS package, using Shirley backgrounds and mixed Gaussian-Lorentzian (Voigt) lineshapes. For compositional analysis, the analyser transmission function has been determined using clean metallic foils to determine the detection efficiency across the full binding energy range.

Dynamic Light Scattering

Hydrodynamic diameters (D_h) and size distributions of particles were determined by dynamic light scattering (DLS) using a Malvern Zetasizer Nano ZS with a 4 mW He-Ne 633 nm laser module operating at 25 °C. Measurements were carried out at an angle of 173° (back scattering), and results were analysed using Malvern DTS 7.03 software. All determinations were repeated 5 times with at least 10 measurements recorded for each run. D_h values were calculated using the Stokes-Einstein equation where particles are assumed to be spherical.

UV-vis Spectroscopy

Absorbance measurements were recorded on an Agilent Cary 60 UV-Vis Spectrophotometer and on a BioTek Epoch microplate reader.

Transmission Electron Microscopy

Dry-state stained TEM imaging was performed on a JEOL JEM-2100Plus microscope operating at an acceleration voltage of 200 kV. All dry-state samples were diluted with deionised water and then deposited onto formvar-coated copper grids.

Thermogravimetric Analysis

2 mL of functionalised AuNPs with ~10 Abs was centrifugated and the maximum amount of solvent removed. Then, samples were heated in a sand bath at 70 ℃ for 2 days until they were completely dry. The drying process was monitored by measuring the samples until no weight change was observed.

7.6.2 Materials

All chemicals were used as supplied unless otherwise stated. *N*-Hydroxyethyl acrylamide (97%), 4,4'-azobis(4-cyanovaleric acid) (ACVA, 98%), 4-dimethylaminopyridine (DMAP, > 98%), mesitylene (reagent grade), triethylamine (> 99%), sodium citrate tribasic dihydrate (> 99%), gold(III) chloride trihydrate (99.9%), potassium phosphate tribasic (≥ 98%, reagent grade), deuterium oxide (D_2O, 99.9%), deuterated chloroform ($CDCl_3$, 99.8%), diethyl ether (≥ 99.8%, ACS reagent grade), methanol (≥ 99.8%, ACS reagent grade), toluene (≥ 99.7%,), carbon disulphide (≥ 99.8%), acetone (≥ 99%), 1-dodecane thiol (≥ 98%) and pentafluorophenol (≥ 99%, reagent plus) were purchased from Sigma-Aldrich. DMF (> 99%) and 2-bromo-2-methyl propionic acid (98%) were purchased from Acros Organics. Galactosamine HCl and 1-Ethyl-3-(3-dimethylaminopropyl)carbodiimide hydrochloride (EDCI, > 98%) were purchased from Carbosynth. HPLC grade acetonitrile (≥ 99.8%), hexane fraction from petrol (lab reagent grade), DCM (99% lab reagent grade), sodium hydrogen carbonate (≥ 99%), ethyl acetate (≥ 99.7%, analytical reagent grade), 40-60 petroleum ether (lab reagent grade), hydrochloric acid (~37%, analytical grade), glacial acetic acid (analytical grade) and magnesium sulphate (reagent grade) were purchased from Thermo Fisher Scientific.

Ultra-pure water used for buffers was MilliQ grade 18.2 mΩ resistance.

Further details of materials used, and synthesis of the particles can be found in the respective papers the particles are taken from.

7.6.3 Synthetic Methods

Synthesis of 2-(dodecylthiocarbanothionylthio)-2-methyl propionic acid (DMP)

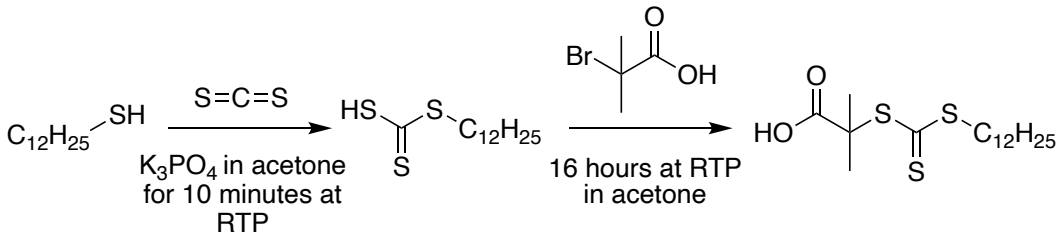

This was synthesised, according to a previously published procedure.[47] 2.00 g (9.88 mmol) of 1-dodecane thiol was added dropwise to stirring 2.10 g (9.89 mmol) of K_3PO_4 in 30 mL of acetone at RTP, the mixture was left to stir for 25 minutes to form a white suspension. 2.05 g (26.93 mmol) of carbon disulphide was then added and left for 10 minutes, a yellow solution formed. 1.5 g (8.98 mmol) of 2-bromo-2-methyl-propionic acid was then added and the solution left to stir for 16 hours. The solvent was removed under vacuum. The crude product was dissolved in 100 mL of 1 M HCl and extracted with DCM (2×100 mL). The organic layer was washed with 200 mL of water and 200 mL of brine. The organic layer was dried with $MgSO_4$ and filtered under gravity. The solvent was then removed from the filtrate under vacuum. The crude product was purified using a silica column (40-60 PET:DCM:glacial acetic acid 75:24:1) and recrystalised in n-hexane to give a yellow solid (58%). δ_H (300 MHz, $CDCl_3$) 3.28 (2H, t, *J* 7.5, SCH_2CH_2), 1.80 - 1.45 (8H, m, $C(CH_3)_2$ and SCH_2CH_2), 1.45 - 1.2 (18H, m, $(CH_2)_9CH_3$), 0.87 (3H, t, *J* 6.0, CH_3). δ_C (400 MHz, $CDCl_3$) 221.0 (1C, SC(S)S), 178.3 (1C, C(O)), 55.7 (1C, $C(CH_3)_2$), 37.7 (1C, SCH_2), 32.1 - 28.0 (9C, $SCH_2(CH_2)_9$), 25.4 (2C, $C(CH_3)_2$), 22.8 (1C, CH_2CH_3), 14.3 (1C, CH_2CH_3). m/z calculated as 364.16; found for ESI $[M+H]^+$ 365.3 and $[M+Na]^+$ 387.3. FTIR (cm^{-1}) – 2956, 2916.6 & 2850 (methyl and methylene), 1702 (ester C=O), 1459, 1437 & 1413 (methyl and methylene), 1280 ($C(CH_3)_2$), 1064 (S-C(S)-S).

Synthesis of pentafluorophenyl-2-dodecylthiocarbonothioylthio)-2-methylpropanoate (PFP-DMP)

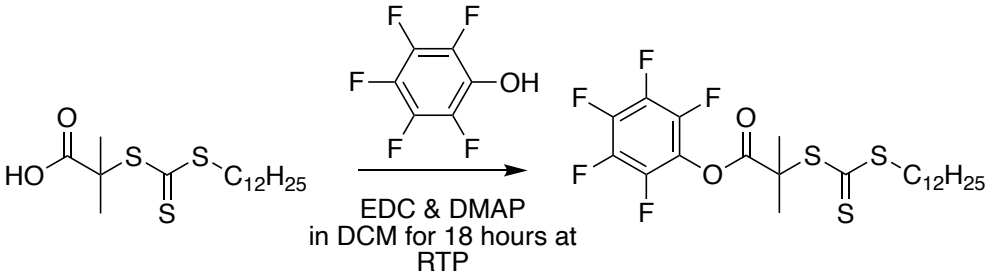

This was synthesised, according to a previously published procedure.[47] 4.06 g (11.13 mmol) of DMP, 3.65 g (19.04 mmol) of EDC and 2.30 g (18.82 mmol) of DMAP were dissolved in 160 mL of DCM and degassed for 30 minutes. 7.28 g (39.55 mmol) of pentaflurophenol was added in 20 mL of DCM and the mixture stirred for 18 hours at RTP. The organic layer was washed with 3 M HCl (200 mL), 1 M $NaHCO_3$ (200 mL) and 0.5 M NaCl (200 mL). The organic layer was dried with $MgSO_4$ and filtered under gravity. The solvent was then removed from the filtrate under vacuum. The crude product was recrystallised from ethyl acetate (or hexane) overnight at -8 °C and dried to give yellow crystals (90.9%). δ_H (300 MHz, $CDCl_3$) 3.31 (2H, t, *J* 7.5, SC*H*$_2$CH$_2$), 1.86 (6H, s, C(CH$_3$)$_2$), 1.69 (2H, qn, *J* 7.5, SCH$_2$), 1.48 - 1.16 (18H, m, C*H*$_2$C*H*$_2$C*H*$_2$C*H*$_2$C*H*$_2$C*H*$_2$C*H*$_2$C*H*$_2$CH$_3$), 0.94 - 0.82 (3H, m, CH$_3$). δ_C (300 MHz, $CDCl_3$) 220.1 (1C, SC(S)S), 169.7 (1C, C(O)), 143.1 (2C, meta C), 139.8 (1C, ipso C), 139.6 (1C, para C), 136.3 (2C, Ortho C), 55.5 (1C, *C*(CH$_3$)$_2$), 37.3 (1C, SCH$_2$), 32.0 - 22.8 (10C, SCH$_2$(*C*H$_2$)$_{10}$), 25.4 (2C, C(*C*H$_3$)$_2$), 14.1 (1C, CH$_2$*C*H$_3$). δ_F (300 MHz, $CDCl_3$) -151.4 - -151.6 (2F, m, OCC$_2$*H*$_2$C$_2$H$_2$CH), -148.5 (1F, t, *J* 21.5, OCC$_2$H$_2$C$_2$H$_2$C*H*), -162.2 - -162.5 (2F, m, OCC$_2$H$_2$C$_2$*H*$_2$CH). m/z calculated as 530.14; found for ESI $[M+Na]^+$ 553.3 and $[M+CH_3CN+Na]^+$ 593.5. FTIR (cm^{-1}) – 2956, 2917 & 2850 (methyl and methylene), 1702 (ester C=O), 1519 (aromatic C=C or C-F), 1460, 1437 & 1413 (methyl and methylene), 1280 (C(CH$_3$)$_2$), 1068 (S-C(S)-S).

Representative Polymerisation of 2-hydroxyethyl acrylamide (PHEA40)

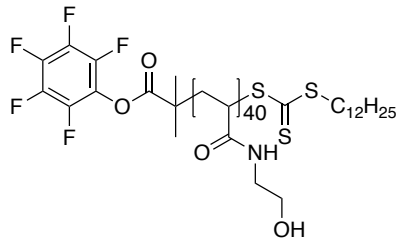

PHEA40 as representative example. 2.0 g (17.37 mmol) of 2-hydroxyethyl acrylamide, 0.043 g (0.15 mmol) of ACVA and 0.368 g (0.69 mmol) of PFP-DMP was added to 16 mL 1:1 toluene:methanol and degassed with nitrogen for 30 minutes. The reaction vessel was stirred and heated to 70 °C for 2 hours. The solvent was removed under vacuum. The crude product was dissolved in the minimum amount of methanol. Diethyl ether cooled in liquid nitrogen was added to the methanol to form a precipitate. The mixture was centrifuged for 2 minutes at 13 krpm and the liquid decanted off. The solid was dissolved in methanol and removed under vacuum to give a yellow crystalline solid.

PHEA40 - δ_H (300 MHz, D_2O) 8.35 - 7.95 (21H, m, N*H*), 3.97 - 3.56 (78H, m, NHC*H*$_2$), 3.56 - 3.03 (80H, m, C*H*$_2$OH & SC*H*$_2$), 2.41 - 1.90 (41H, m, $CH_2CHC(O)$ & $C(CH_3)_2$), 1.90 - 0.99 (108H, m, $CH_2CHC(O)$ & $CH_2CH_2CH_2CH_2CH_2CH_2CH_2CH_2CH_2CH_2CH_3$), 0.83 - 0.72 (5H, m, CH_2CH_3). δ_F (300 MHz, D_2O) -152.0 - -164.3 (5F, m, C_6F_5).

PHEA26 - δ_H (300 MHz, D_2O) 8.38 - 7.88 (13H, m, N*H*), 3.96 - 3.54 (55H, m, NHC*H*$_2$), 3.55 - 3.09 (78H, m, C*H*$_2$OH & SC*H*$_2$), 2.53 - 1.90 (31H, m, $CH_2CHC(O)$ & $C(CH_3)_2$), 1.90 - 1.01 (86H, m, $CH_2CHC(O)$ & $CH_2CH_2CH_2CH_2CH_2CH_2CH_2CH_2CH_2CH_2CH_3$), 0.84 - 0.73 (5H, m, CH_2CH_3)

PHEA72 - δ_H (300 MHz, D_2O) 8.30 - 7.96 (34H, m, N*H*), 3.96 - 3.52 (126H, m, NHC*H*$_2$), 3.52 - 3.07 (155H, m, C*H*$_2$OH & SC*H*$_2$), 2.36 - 1.88 (70H, m, $CH_2CHC(O)$ & $C(CH_3)_2$), 1.88 - 1.03 (148H, m, $CH_2CHC(O)$ & $CH_2CH_2CH_2CH_2CH_2CH_2CH_2CH_2CH_2CH_2CH_3$), 0.82 - 0.70 (5H, m, CH_2CH_3)

PHEA110 - δ_H (300 MHz, D_2O) 8.24 - 8.02 (28H, m, N*H*), 3.83 - 3.51 (239H, m, NHC*H*$_2$), 3.51 - 3.08 (293H, m, C*H*$_2$OH & SC*H*$_2$), 2.40 - 1.90 (117H, m, $CH_2CHC(O)$ & $C(CH_3)_2$), 1.90 - 1.03 (273H, m, $CH_2CHC(O)$ & $CH_2CH_2CH_2CH_2CH_2CH_2CH_2CH_2CH_2CH_2CH_3$), 0.86 - 0.73 (5H, m, CH_2CH_3)

Representative Poly(N-hydroxyethyl acrylamide) (PHEA40) Glycan Functionalisation

0.25 g (0.088 mmol) of poly(2-hydroxyethyl acrylamide) and 0.090 g (0.50 mmol) of galactosamine HCl were added to 25 ml of DMF containing 0.05 M TEA. The reaction was stirred at 50 ℃ for 16 hours. Solvent was removed under vacuum. The crude product was dissolved in the minimum amount of methanol at RTP before cooling in a liquid nitrogen bath. Diethyl ether cooled in liquid nitrogen was added to the methanol to form a precipitate. The mixture was centrifuged for 2 minutes at 13krpm and the liquid decanted off. The solid was dissolved in methanol and removed under vacuum to give an orange/brown crystalline solid. δ_H (300 MHz, D_2O) 8.03 - 7.86 (6H, m, NH), 4.96 - 4.87 (2H, anomeric protons), 4.13 - 3.51 (~90H, m, NHCH_2 & glycan protons), 3.51 - 3.09 (~80H, m, CH_2OH & SCH_2 & glycan protons), 2.47 - 1.90 (~50H, m, $CH_2CHC(O)$, $C(CH_3)_2$ & glycan protons), 1.90 - 1.42 (98H, m, CH_2CHC(O) & CH_2CH_2CH_2CH_2CH_2CH_2CH_2CH_2CH_2CH$_3$), 0.93 - 0.72 (5H, m, CH_2CH_3). FTIR (cm^{-1}) – 3267 (OH, broad), 3094 & 2926 (C(O)NH and NH), 1638 & 1545 (C(O)NH).

Citrate-Stabilised 16 nm Gold Nanoparticle Synthesis

Synthesised by a previously reported protocol.[48] To 500 mL of water was added 0.163 g (0.414 mmol) of gold(III) chloride trihydrate, the mixture was heated to reflux and 14.6 mL of water containing 0.429 g (1.46 mmol) of sodium citrate tribasic dihydrate was added. The reaction was allowed to reflux for 30 minutes before cooling to room temperature over 3 hours. The solution was centrifuged at 13 krpm for 30 minutes and the pellet resuspended in 40 mL of water to give an absorbance at 520 nm of ~1Abs.

Gold Nanoparticle Polymer Coating Functionalisation – 16 nm

100 mg of glycopolymer was agitated overnight with 10 mL of 16 nm AuNPs ~1Abs at UV_{max}. The solution was centrifuged at 13 krpm for 30 minutes and the pellet resuspended in 10 mL of water, the solution was centrifuged again at 13 krpm for 30 minutes and the pellet resuspended in 1 mL aliquots and centrifuged at 14.5 krpm for 10 minutes. The pellets were combined into a 1 mL solution with an absorbance at 520 nm of ~10 Abs.

7.7 References

(1) Georgiou, P. G.; Baker, A. N.; Richards, S.-J.; Laezza, A.; Walker, M.; Gibson, M. I. Tuning Aggregative versus Non-Aggregative Lectin Binding with Glycosylated Nanoparticles by the Nature of the Polymer Ligand. *Journal of Materials Chemistry. B* **2020**, *8* (1), 136–145.

(2) Richards, S.-J.; Baker, A. N.; Walker, M.; Gibson, M. I. Polymer-Stabilized Sialylated Nanoparticles: Synthesis, Optimization, and Differential Binding to Influenza Hemagglutinins. *Biomacromolecules* **2020**, *21* (4), 1604–1612.

(3) Baker, A. N.; Richards, S.-J.; Guy, C. S.; Congdon, T. R.; Hasan, M.; Zwetsloot, A. J.; Gallo, A.; Lewandowski, J. R.; Stansfeld, P. J.; Straube, A.; Walker, M.; Chessa, S.; Pergolizzi, G.; Dedola, S.; Field, R. A.; Gibson, M. I. The SARS-COV-2 Spike Protein Binds Sialic Acids and Enables Rapid Detection in a Lateral Flow Point of Care Diagnostic Device. *ACS Central Science* **2020**, *6* (11), 2046–2052.

(4) Baker, A. N.; Richard, S.-J.; Guy, C. S.; Congdon, T. R.; Hasan, M.; Zwetsloot, A. J.; Straube, A.; Walker, M.; Chessa, S.; Pergolizzi, G.; Dedola, S.; Field, R.; Gibson, M. The SARS-COV-2 Spike Protein Binds Sialic Acids, and Enables Rapid Detection in a Lateral Flow Point of Care Diagnostic Device. *chemrxiv.org* **2020**.

(5) Richards, S.-J.; Keenan, T.; Vendeville, J.-B. B.; Wheatley, D. E.; Chidwick, H.; Budhadev, D.; Council, C. E.; Webster, C. S.; Ledru, H.; Baker, A. N.; Walker, M.; Galan, M. C.; Linclau, B.; Fascione, M. A.; Gibson, M. I. Introducing Affinity and Selectivity into Galectin-Targeting Nanoparticles with Fluorinated Glycan Ligands. *Chemical Science* **2021**, *12* (3), 905–910.

(6) Pancaro, A.; Szymonik, M.; Georgiou, P. G.; Baker, A. N.; Walker, M.; Adriaensens, P.; Hendrix, J.; Gibson, M. I.; Nelissen, I. The Polymeric Glyco-Linker Controls the Signal Outputs for Plasmonic Gold Nanorod Biosensors Due to Biocorona Formation. *Nanoscale* **2021**, *13* (24), 10837–10848.

(7) Baker, A. N.; Muguruza, A. R.; Richards, S.-J.; Georgiou, P. G.; Goetz, S.; Walker, M.; Dedola, S.; Field, R. A.; Gibson, M. I. Lateral Flow Glyco-Assays for the Rapid and Low-Cost Detection of Lectins–Polymeric Linkers and Particle Engineering Are Essential for Selectivity and Performance. *Advanced Healthcare Materials* **2021**, 2101784.

(8) Gao, G.; Lange, D.; Hilpert, K.; Kindrachuk, J.; Zou, Y.; Cheng, J. T. J.; Kazemzadeh-Narbat, M.; Yu, K.; Wang, R.; Straus, S. K.; Brooks, D. E.; Chew, B. H.; Hancock, R. E. W.; Kizhakkedathu, J. N. The Biocompatibility and Biofilm Resistance of Implant Coatings Based on Hydrophilic Polymer Brushes Conjugated with Antimicrobial Peptides. *Biomaterials* **2011**, *32* (16), 3899–3909.

(9) Raynor, J. E.; Capadona, J. R.; Collard, D. M.; Petrie, T. A.; García, A. J. Polymer Brushes and Self-Assembled Monolayers: Versatile Platforms to Control Cell Adhesion to Biomaterials (Review). *Biointerphases* **2009**, *4* (2), FA3–FA16.

(10) Nie, Z.; Kumacheva, E. Patterning Surfaces with Functional Polymers. *Nature Materials* **2008**, *7* (4), 277–290.

(11) Yang, W. J.; Neoh, K. G.; Kang, E. T.; Teo, S. L. M.; Rittschof, D. Polymer Brush Coatings for Combating Marine Biofouling. *Progress in Polymer Science*. **2014**, 39 (5), 1017–1042.

(12) Dahal, U.; Dormidontova, E. E. Chain Conformation and Hydration of Polyethylene Oxide Grafted to Gold Nanoparticles: Curvature and Chain Length Effect. *Macromolecules* **2020**, *53* (19), 8160–8170.

(13) de Gennes, P. G. Polymers at an Interface; a Simplified View. *Advances in Colloid and Interface Science* **1987**, *27* (3–4), 189–209.

(14) de Gennes, P. G. Conformations of Polymers Attached to an Interface. *Macromolecules* **1980**, *13* (5), 1069–1075.

(15) Daoud, M.; Cotton, J. P. Star Shaped Polymers : A Model for the Conformation and Its Concentration Dependence. *Journal de Physique* **1982**, *43* (3), 531–538.

(16) Johner, A.; Lee, N.-K. The Daoud and Cotton Blob Model and the Interaction of Star-Shaped Polymers. *The European Physical Journal E* **2018**, *41* (7), 88.

(17) Dan, N.; Tirrell, M. Polymers Tethered to Curves Interfaces: A Self-Consistent-Field Analysis. *Macromolecules* **1992**, *25* (11), 2890–2895.

(18) Birshtein, T. M.; Borisov, O. V.; Zhulina, Ye. B.; Khokhlov, A. R.; Yurasova, T. A. Conformations of Comb-like Macromolecules. *Polymer Science U.S.S.R.* **1987**, *29* (6), 1293–1300.

(19) Michalek, L.; Barner, L.; Barner-Kowollik, C. Polymer on Top: Current Limits and Future Perspectives of Quantitatively Evaluating Surface Grafting. *Advanced Materials* **2018**, *30* (21), 1706321.

(20) Lv, B.; Zhou, Y.; Cha, W.; Wu, Y.; Hu, J.; Li, L.; Chi, L.; Ma, H. Molecular Composition, Grafting Density and Film Area Affect the Swelling-Induced Au–S Bond Breakage. *ACS Applied Materials & Interfaces* **2014**, *6* (11), 8313–8319.

(21) Liu, Y.; Klep, V.; Zdyrko, B.; Luzinov, I. Synthesis of High-Density Grafted Polymer Layers with Thickness and Grafting Density Gradients. *Langmuir* **2005**, *21* (25), 11806–11813.

(22) Sofia, S. J.; Premnath, V.; Merrill, E. W. Poly(Ethylene Oxide) Grafted to Silicon Surfaces: Grafting Density and Protein Adsorption. *Macromolecules* **1998**, *31* (15), 5059–5070.

(23) Grünewald, T. A.; Lassenberger, A.; Van Oostrum, P. D. J.; Rennhofer, H.; Zirbs, R.; Capone, B.; Vonderhaid, I.; Amenitsch, H.; Lichtenegger, H. C.; Reimhult, E. Core−Shell Structure of Monodisperse Poly(Ethylene Glycol)-Grafted Iron Oxide Nanoparticles Studied by Small-Angle X-Ray Scattering. *Chem. Mater* **2015**, *27*, 48.

(24) Rodriguez-Loureiro, I.; Scoppola, E.; Bertinetti, L.; Barbetta, A.; Fragneto, G.; Schneck, E. Neutron Reflectometry Yields Distance-Dependent Structures of Nanometric Polymer Brushes Interacting across Water. *Soft Matter* **2017**, *13* (34), 5767–5777.

(25) Fernandes, A. E.; Ye, Q.; Collard, L.; Le Duff, C.; d'Haese, C.; Deumer, G.; Haufroid, V.; Nysten, B.; Riant, O.; Jonas, A. M. Effects of Thickness and Grafting Density on the Activity of Polymer-Brush-Immobilized Tris(Triazolyl) Copper(I) Catalysts. *ChemCatChem* **2015**, *7* (5), 856–864.

(26) Benoit, D. N.; Zhu, H.; Lilierose, M. H.; Raymond, V. A.; Naushaba, A.; Morrison, A. N.; Fortner, J. D.; Avendano, C.; Colin, V. L. Measuring the Grafting Density of Nanoparticles in Solution by Analytical Ultracentrifugation and Total Organic Carbon Analysis. *Analytical Chemistry* **2019**, *176* (3), 139–148.

(27) Wolski, K.; Gruszkiewicz, A.; Wytrwal-Sarna, M.; Bernasik, A.; Zapotoczny, S. The Grafting Density and Thickness of Polythiophene-Based Brushes Determine the

Orientation, Conjugation Length and Stability of the Grafted Chains. *Polym. Chem.* **2017**, *8* (40), 6250–6262.

(28) Hill, H. D.; Millstone, J. E.; Banholzer, M. J.; Mirkin, C. A. The Role Radius of Curvature Plays in Thiolated Oligonucleotide Loading on Gold Nanoparticles. *ACS Nano* **2009**, *3* (2), 418–424.

(29) Guo, Y.; Nehlmeier, I.; Poole, E.; Sakonsinsiri, C.; Hondow, N.; Brown, A.; Li, Q.; Li, S.; Whitworth, J.; Li, Z.; Yu, A.; Brydson, R.; Turnbull, W. B.; Pöhlmann, S.; Zhou, D. Dissecting Multivalent Lectin–Carbohydrate Recognition Using Polyvalent Multifunctional Glycan-Quantum Dots. *Journal of the American Chemical Society* **2017**, *139* (34), 11833–11844.

(30) Liu, Y.; Klep, V.; Zdyrko, B.; Luzinov, I. Synthesis of High-Density Grafted Polymer Layers with Thickness and Grafting Density Gradients. *Langmuir* **2005**, *21* (25), 11806–11813.

(31) Sofia, S. J.; Premnath, V.; Merrill, E. W. Poly(Ethylene Oxide) Grafted to Silicon Surfaces: Grafting Density and Protein Adsorption. *Macromolecules* **1998**, *31* (15), 5059–5070.

(32) Watson, R. E.; Hudis, J.; Perlman, M. L. Charge Flow and Compensation in Gold Alloys. *Physical Review B* **1971**, *4* (12), 4139–4144.

(33) Pantano, C, G. Surface and In-Depth Analysis of Glass and Ceramics. *American Ceramic Society Bulletin* **1981**, *60* (11), 1154–1163.

(34) Rinta-Möykky, A.; Uusimaa, P.; Suhonen, S.; Valden, M.; Salokatve, A.; Pessa, M.; Likonen, J. Study of Ohmic Multilayer Metal Contacts to P-Type ZnSe. *Journal of Vacuum Science & Technology A: Vacuum, Surfaces, and Films* **1999**, *17* (2), 347–353.

(35) New, E.; Hancox, I.; Rochford, L. A.; Walker, M.; Dearden, C. A.; McConville, C. F.; Jones, Tim. S. Organic Photovoltaic Cells Utilising ZnO Electron Extraction Layers Produced through Thermal Conversion of ZnSe. *J. Mater. Chem. A* **2014**, *2* (45), 19201–19207.

(36) Tyler, M. S.; Hutter, O. S.; Walker, D. M.; Hatton, D. R. A. A Silver-Free, Reflective Substrate Electrode for Electron Extraction in Top-Illuminated Organic Photovoltaics. *ChemPhysChem* **2015**, *16* (6), 1203–1209.

(37) Ramadass, K.; Sathish, C. I.; Johns, A.; Ruban, S. J.; Singh, G.; Lakhi, K. S.; Almajid, A. M.; Belperio, T.; Vinu, A. Characterization and Hydrogen Storage Performance of Halloysite Nanotubes. *Journal of Nanoscience and Nanotechnology* **2019**, *19* (12), 7892–7898.

(38) Einstein, A. Über Einen Die Erzeugung Und Verwandlung Des Lichtes Betreffenden Heuristischen Gesichtspunkt. *Annalen der Physik* **1905**, *322* (6), 132–148.

(39) Oswald, S. X-Ray Photoelectron Spectroscopy in Analysis of Surfaces. In *Encyclopedia of Analytical Chemistry*; John Wiley & Sons, Ltd: Chichester, UK, 2013.

(40) Sze Ieong, N.; Biggs, C. I.; Walker, M.; Gibson, M. I. Comparison of RAFT Derived Poly(Vinylpyrolidone) Verses Poly(Oligoethyleneglycol Methacrylate) for the Stabilization of Glycosylated Gold Nanoparticles. *Journal of Polymer Sciences* **2017**, *55* (7), 1200–1208.

(41) Laezza, A.; Georgiou, P. G.; Richards, S.-J.; Baker, A. N.; Walker, M.; Gibson, M. I. Protecting Group Free Synthesis of Glyconanoparticles Using Amino–Oxy-Terminated Polymer Ligands. *Bioconjugate Chemistry* **2020**, *31* (10), 2392–2403.

(42) Rahme, K.; Chen, L.; Hobbs, R. G.; Morris, M. A.; O'Driscoll, C.; Holmes, J. D. PEGylated Gold Nanoparticles: Polymer Quantification as a Function of PEG Lengths and Nanoparticle Dimensions. *RSC Adv.* **2013**, *3* (17), 6085–6094.

(43) Rahme, K.; Chen, L.; Hobbs, R. G.; Morris, M. A.; O'Driscoll, C.; Holmes, J. D. Correction: PEGylated Gold Nanoparticles: Polymer Quantification as a Function of PEG Lengths and Nanoparticle Dimensions. *RSC Advances* **2017**, *7* (15), 8798–8799.

(44) Gibson, M. I.; Paripovic, D.; Klok, H.-A. Size-Dependent LCST Transitions of Polymer-Coated Gold Nanoparticles: Cooperative Aggregation and Surface Assembly. *Advanced Materials* **2010**, *22* (42), 4721–4725.

(45) Oyerokun, F. T.; Vaia, R. A. Distribution in the Grafting Density of End-Functionalized Polymer Chains Adsorbed onto Nanoparticle Surfaces. *Macromolecules* **2012**, *45* (18), 7649–7659.

(46) Michalek, L.; Mundsinger, K.; Barner-Kowollik, C.; Barner, L. The Long and the Short of Polymer Grafting. *Polymer Chemistry* **2019**, *10* (1), 54–59.

(47) Richards, S.-J.; Gibson, M. I. Optimization of the Polymer Coating for Glycosylated Gold Nanoparticle Biosensors to Ensure Stability and Rapid Optical Readouts. *ACS Macro Letters* **2014**, *3* (10), 1004–1008.

(48) Ieong, N. S.; Brebis, K.; Daniel, L. E.; O'Reilly, R. K.; Gibson, M. I. The Critical Importance of Size on Thermoresponsive Nanoparticle Transition Temperatures: Gold and Micelle-Based Polymer Nanoparticles. *Chemical Communications* **2011**, *47* (42), 11627–11629.

Chapter 8

Conclusions

This work has introduced, and explored, the emerging technology of lateral flow glyco-assays. The key components of the lateral flow glyco-assay have been systematically interrogated and investigated, notably; glycosylated polymer-coated nanoparticles in the mobile phase, and polymeric anchors as test line scaffolds in the stationary phase. Additionally, the relative grafting density of the glycosylated polymer-coated nanoparticles has been probed, and the synthesis of novel glycans using the Mannich reaction studied.

Through the synthesis of a library of glycosylated polymer-coated nanoparticles, utilising RAFT polymerisation, the concept of the lateral flow glyco-assay has been introduced and validated for the first time. Unlike immunoassays, the nanoparticle's polymer-coating could be optimised for the detection of different analytes; SBA, RCA_{120}, SARS-COV-2 S1 spike protein etc. This is a unique advantage of employing polymeric tethers, in that the final device's performance and specificity can be tuned by macromolecular engineering, in addition to varying the glycan. The "whole particle" impact of adjusting; polymer length, glycan and gold particle used, was explored by x-ray photoelectron spectroscopy. Succinctly, the changes to relative grafting density likely explain some of the variations in binding seen between different particle systems.

The approach of "tuning" lateral flow glyco-assay systems enabled the rapid detection (in under 20 minutes) of model proteins (SBA) as low as 5 $\mu g.mL^{-1}$ (0.042 $nmmol.mL^{-1}$). This is below the (molar) detection limits of commercial lateral flow pregnancy tests which use antibody-functionalised gold nanoparticles and falls within the range of values (microgram to nanogram per millilitre) for antibody-based LFDs. Moreover, these glycan-based devices were used to probe the glycan-binding specificity of the SARS-COV-2 S1 spike protein. It was discovered that this "biologically new" protein, and its respective virus, have an affinity for α,*N*-acetyl neuraminic acid; with successful detection of a virus mimic particle bearing SARS-COV-2 S1 achieved in under 30 mins using a lateral flow glyco-assay. This discovery was built upon by colleagues who have shown the importance of sialic acids in mediating the viral entry of SARS-COV-2 into the cell; and lays the foundations for a greater understanding of SARS-COV-2's biology beyond proteins.

Furthermore, the α,*N*-acetyl neuraminic acid-based system was developed into a prototype flow-through glyco-assay device, capable of detecting SARS-COV-2

infection. This prototype device was demonstrated versus spike bearing lentiviruses and patient samples containing the SARS-COV-2 virus itself – achieving, after silver staining, a sensitivity of 85% and specificity of 93%. The devices were also shown to detect recombinant spike proteins from several variants, indicating that these mutations do not remove glycan-binding function. While the cassettes themselves displayed good robustness following prolonged exposure to the environment and temperatures in excess of 70 °C. This affirmed that, not only can lateral flow and flow-through glyco-assay technology be deployed in a "real-world" setting, but the predicted advantages of glyco-assays, namely increased robustness and low-cost, are attainable too.

To develop lateral flow glyco-assay technology further, and remove protein components completely from the devices, a polymeric lateral flow test line was synthesised and tested. The poly(vinyl pyrrolidone) anchor synthesised, by MADIX, was shown to be a promising alternative to the established protein-based anchoring reagents. This validated the concept of a fully synthetic, protein-free, polymeric lateral flow test line and protein-free ("vegan") lateral flow test. It is anticipated that this first-generation of adjustable polymeric anchor systems could be used as multifunctional scaffolds or platforms to present other capture agents, such as short amino acid or nucleotide sequences, and enable a wider range of end-group functionality beyond amide chemistry.

In summary, lateral flow glyco-assays and flow-through glyco-assays present a viable alternative to lateral flow immunoassays. The benefits of these glycan-based systems compared to proteomic or immuno-based systems are the ease of both storage and manufacture, low-cost, increased robustness, and additional synthetic optionality, tuneability and control. The potential for glycopolymer-functionalised AuNPs, integrated into lateral flow systems as POC devices is vast: with this thesis only scratching the surface. These low-cost, immuno-free glycopolymer-based lateral flow diagnostic devices, lateral flow glyco-assays, could be ideal for low- and middle-income countries, and more economically developed countries alike, in closing the diagnostic health inequalities we see in both the COVID-19 pandemic and beyond.

End of Volume 1 of 2